Exploration of 3d, 4*f* and 3d-4*f* coordination clusters for potential industrial applications.

Zur Erlangung des akademischen Grades eines

DOKTORS DER NATURWISSENSCHAFTEN

(Dr. rer. nat.)

von der KIT-Fakultät für Chemie und Biowissenschaften

des Karlsruher Instituts für Technologie (KIT)

Genehmigte

DISSERTATION
Von

M.Sc. Firas Khalil Atyyeh Al-Zeidaneen

Mutah University, JORDAN, 2012

Dekan: Prof. Dr. Manfred Wilhelm

Referent: Prof. Dr. Annie Powell

Korreferent: Prof. Dr. Mario Ruben

Tag der mündlichen Prüfung: 10.12.2020

Acknowledgements

First and foremost, I would like to thank Almighty Allah for giving me the ability, patience and strength to complete my doctoral thesis and achieve this milestone. I express my sincere gratitude to Tafila Technical University (TTU), Jordan for awarding me a PhD grant. I also thank Karlsruhe Institute of Technology (KIT) for providing me a research opportunity and facility.

The accomplishment of this work would not have been possible without the help of various people.

I would like to show my deepest gratitude to my PhD supervisor Prof. Dr. Annie K. Powell for giving me the chance to work on this project. I have highly appreciated her brilliant academic guidance and encouragement. In addition, her polite nature and easygoing attitude made my stay pleasant at KIT in a very comfortable atmosphere. I would like to extend my deep gratitude to Dr. Ghulam Abbas for his excellent lab supervision and for his invaluable discussions on the subject of my research. I also thank him for the entertainment and joyous moments that he provided in the lab. My special thanks and heartfelt gratitude go to Dr. Masooma Ibrahim, from whom I received lots of intensive supports, constructive discussions and suggestions. Dr. Masooma Ibrahim was the first member of our group that I met on my first day in Germany. She picked me up from the main station to my room. I do not forget her favour, kindness and support. I would also like to express my sincere appreciation to Dr. Christopher Anson, Dr. Olaf Fuhr and Prof. Dr. Dieter Fenske for their expertise as crystallographers and chemists.

I would like to thank Dr. Yan Peng, Nithin Suryadevara, Sören Schlittenhardt and Ruby Singh for performing magnetic studied on the obtained compounds. I would like to thank Dr. Anthony Carter and Umaira Shuaib for their proof-reading of this thesis. In addition, I would like to thank Dr. Mohammed Reda Chellali, Dr. Mohammed Hammad Fawey, Dr. Tawheed Hashem, Dr. Andreas Eichhöfer, Dr. Stefan Walheim, Dr. Roland Gröger, Dr. Leonardo Velasco Estrada and Simone Dehm for the various instrument trainings and constructive discussions.

I would like to thank Mrs. Gertraud Amschlinger for her kindness and her assistance in understanding administrative documents and forms. In addition, I would like to thank Mr. Hartmut Speck, Ms. Anna Navickas and Mr. Florian Döring for their support in residence permit process.

I would like to thank Ms. Nicole Klaassen for measuring the elemental analyses. Also, I would like to thank Ms. Lena Friedrich and Ms. Gabi Leichle for their help in the chemical stores and ordering chemicals.

My acknowledgements also to all my colleagues: PhD students and Postdoctoral fellows, past and present (Dr. Marcel Merkel, Dr. Krisana Peewasan, Dr. Sebastian Schmidt, Dr. Mahdi Dadfar, Dr. Konstantis F. Konidaris, Dr Muhammad Moazzam Naseer, Dr. Markus Schroth, Dr. Nicolas Leblanc, Thomas Ruppert, Rouven Pfleger, Hagen Kämmerer, Jonas Braun, Samer Daradkah and Surya Abhishek Singaraju). It has been a pleasure to work with you all.

I owe my loving thanks to my supportive and encouraging parents Mr. Khalil and Ms. Ameera. Without their prayers, support and encouragement it would not have been possible to reach this stage. I also would like to acknowledge my brothers, sisters, my relatives and friends for their support and encouragements.

Last but not least, my very special thanks go to my wife Safa who sacrificed much to enable me to accomplished my doctoral task. In addition, I would like to thank my children Alyaman and Mira for their lovely support. This journey would not have been possible without the support of my loving family.

DEDICATION

Lovingly, I dedicate my dissertation work to my parents, Mr. Khalil Al-Zeidaneen and Mrs. Ameera Al-Masdeen, my wife Safa Al-Masdeen, my children Alyaman and Mira, my brothers Ayham, Bilal and Mohammad, my sisters Areej and Alaa who have given me so much love and support throughout the process.

Abstract

This doctoral research saw the production of a large library of compounds which exhibit a wide range of structural motifs. The goal of this work was to produce novel compounds which may prove to be industrially relevant for incorporation into magnetic and optical devices. The work has been divided into three chapters each presenting a series of compounds which feature interesting magnetic and/or optical properties.

Chapter 3 reports thirteen homometallic lanthanide complexes featuring multiple amino-polyalcohol-based ligands. This consists of three distinct series of dinuclear complexes (**1**), (**2-5**), and (**6-9**) as well as a series of tetranuclear complexes (**10-13**). The complexes were synthesised aerobically and were crystallised by slow evaporation of the solvent. The crystal structures, optical and magnetic properties of these crystalline complexes were collected and analysed. Magnetic measurements were carried out on complexes **1**, **5**, **9** and **13** and all exhibited weak antiferromagnet interactions with complexes **1**, **5** and **9**, also showing slow relaxation. Investigations into the magnetocaloric effect were carried out on complex **3**, whilst complexes **2** and **4** were studied for their potential to act as luminescent materials.

Chapter 4 present thirty-three heterometallic iron-lanthanide (Fe-Ln) complexes which all utilise the ligand *N*-methyldiethanolamine (mdeaH_2). These heterometallic complexes consist of a series of tetranuclear complexes (**14-20**) and three distinct hexanuclear complexes (**21-29**), (**30-39**) and (**40-46**). The crystal structures, optical and magnetic properties of these complexes were investigated and discussed in detail. Magnetic measurements were carried on compounds **20**, **26**, **27**, **32**, **33** and **43**. Complexes **20**, **32** and **33** exhibit weak antiferromagnetic interactions, whilst **26**, **27** and **43** exhibit weak ferromagnetic interactions. The magnetic investigations revealed that complex **43** shows the slow relaxation typical of a single molecule magnetic. The magnetocaloric effect of complexes **25** and **31** was studied. Finally, complexes **24**, **26** and **46** underwent an investigation into their luminescence properties to assess their potential as phosphorescent materials.

Chapter 5 presents two homometallic copper complexes which both feature 2,2′-bipyridine and benzylphosphonic acid as ligands (**47-48**). The crystal structures and optical properties of these complexes were collected and analysed. Complexes **47** and **48** both absorb in the NIR range whilst

remaining largely optically transparent, these complexes also demonstrated thermal stability up to 250 °C and 207 °C, respectively. Finally, thin films (up to 34 μm) of complexes **47** and **48** were prepared on a glass substrate and the optical properties were re-investigated and found to resemble that of the bulk crystalline material.

Zusammenfassung

Diese Dissertation hat Verbindungen mit einem breiten Spektrum an strukturellen Motiven hervorgebracht. Das Ziel dieser Arbeit war es neuartige Verbindungen zu synthetisieren, welche mit industrieller Relevanz in magnetische und optische Instrumente integriert werden können. Die Arbeit ist in drei Kapitel unterteilt, welche jeweils unterschiedliche Gruppen von Verbindungen diskutieren welche interessante magnetische und/oder optische Eigenschaften besitzen.

Kapitel 3 stellt dreizehn homometallische Lanthanidkomplexe basierend auf der Verwendung diverser Amino-Polyalkoholbasierter Liganden vor. Es besteht aus drei separaten Serien dinuklearer (**1**), (**2-5**) und (**6-9**), sowie einer Art tetranuklearer Komplexe (**10-13**). Die Synthese der Komplexe wurde unter aeroben Bedinungen durchgeführt, die Kirstallisation erfolgte durch das langsame Verdampfen einer Acetonitrillösung. Die Einkristallstrukturen sowie optische und magnetische Eigenschaften wurden gesammelt und analysiert. Messungen der magnetischen Eigenschaften wurde an den Komplexen **1**, **5**, **9** und **13** durchgeführt, alle diese Komplexe zeigten schwache antiferromagnetische Wechselwirkungen, wobei die Komplexe **1**, **5** und **9** ebenfalls eine langsame Relaxation der Magnetisierung aufweisen. An Komplex **3** wurden Untersuchungen des magnetokalorischen Effekts durchgeführt, während Komplex **2** und **4** hinsichtlich potentieller Anwendungen als luminszierende Materialien untersucht wurden.

Kapitel 4 führt dreiunddreißig heterometallische Eisen-Lanthanidkomplexe (Fe-Ln) ein, welche unter Verwendung von N-Methyldiethanolamin ($mdeaH_2$) synthetisiert werden. Diese heterometallischen Komplexe bestehen aus einer Serie von tetranuklearen (**14**-**20**) und drei unterschiedlichen Serien von hexanuklearen Komplexen (**21**-**29**), (**30**-**39**) und (**40**-**46**). Die Einkristallstrukturen, optischen und magnetischen Eigenschaften dieser Komplexe wurden untersucht und im Detail diskutiert. Messungen der magnetischen Eigenschaften wurden für die Verbindungen **20**, **26**, **27**, **32**, **33** und **43** durchgeführt. Die Komplexe **20**, **32** und **33** zeigen schwache antiferromagnetische Wechselwirkungen, während **26**, **27** und **43** schwache ferromagnetische Wechselwirkungen aufweisen. Zusätzlich zeigten die magnetischen Untersuchungen, dass Komplex **43** eine langsame Relaxation der Magnetisierung aufweist, eine typische Eigenschaft für Einzelmolekülmagneten. An den Komplexen **25** und **31** wurde eine Untersuchung des magnetokalorischen Effekts durchgeführt. Abschließend wurden die

Lumineszenz der Komplexe **24**, **26** und **46** im Hinblick auf deren Nutzen als phosphoreszierende Materialien untersucht.

In **Kapitel 5** werden zwei homometallische Kupferkomplexe präsentiert, welche beide unter Verwendung von 2,2‘-Bipyridin und Benzylphosphonsäure als Liganden synthetisiert werden (**47**-**48**). Die Einkristallstrukturen und optischen Eigenschaften dieser Komplexe wurden untersucht. Beide Komplexe zeigen eine Absorption im NIR Bereich währenddessen sie weithin optisch transparent bleiben, außerdem weisen diese Komplexe eine thermische Stabilität bis zu 250°C und 207°C auf. Zu guter Letzt wurden die Komplexe **47** und **48** als Dünnschicht (bis zu 34 µm) auf einer Glassoberfläche aufgetragen und die optischen Eigenschaften erneut untersucht, diese stimmten mit den für die kristallinen Phasen gefundenen Eigenschaften überein.

Declaration

I am Firas Khalil Atyyeh Al-Zeidaneen. I declare that this thesis entitled "Exploration of 3d, 4f and 3d-4f coordination clusters for potential industrial applications" and the work presented in it is my own and was performed under the supervision of Prof. Dr. Annie Powell at the Institute of Nanotechnology (INT) and Institut für Anorganische Chemie, at the Karlsruhe Institute of Technology (KIT). I confirm that:

- This work was done wholly while in candidature for a research degree at KIT.
- The whole thesis was written by me and no other sources other than the specified were used.
- The rules for ensuring good scientific practice of the Karlsruhe Institute of Technology (KIT) have been used and the submission and archiving of the primary data, in accordance with section A(6) of the rules for ensuring good scientific practice of KIT, has been ensured.
- The electronic version of the work is consitent with the written version.
- Where I have consulted the published work of others, this is always clearly attributed.
- I have acknowledged all main sources of help.
- Where the thesis is based on work done by myself joinly with others, I have made clear exactly what was done by other and what I have contributed myself.
- Furthermore, I declare that I did not undertake any previous doctoral studies and that I am currently not enrolled in any other ongoing doctoral procedure.

Signature: ……

Date: ……

Contents

Chapter 1. Introduction

In this chapter, a number of potential applications for the types of coordination clusters in this thesis are described. The scope for coordination compounds is vast and potential applications have been limited to those involving open-shell 4*f* and 3d/4*f* multinuclear compounds.

This chapter represents a general introduction of chapter three and four of this thesis.

1.1. Introduction to molecular magnetism

1.1.1. History of magnetism

Historically, magnetism was discovered in ancient times. Magnes in Crete discovered the intriguing phenomenon of magnetism around (900 B.C.) [1-5]. He noticed that the natural magnet lodestone (a form of magnetite, Fe_3O_4) attracted the iron nails from his sandals and metal tip of his staff while he walked over a deposit. This took place in a region later named Magnesia in Greece [1-4]. The Chinese used this phenomenon to create a floating compass [2].

In 1269, the French scientist Petrus Peregrinus de Maricourt identified that magnets have poles. He called them the North (N) and South (S) poles which are maintained even upon breaking the magnet. He noticed that the opposite poles are attracted to each other whilst the similar poles repelled each other [1-3].

In the 1800s, researchers began to explore the relationship between magnetism and electricity leading to rapid advancements. In 1819, the Danish physicist and chemist Hans Christian Oersted discovered that electric current in a wire could deflect a magnetised compass needle. In 1823, the English scientist Michael Faraday invented the electromagnet. He used magnets to build the first electric generator in order to produce low-cost electricity. In the 1860s, the Scottish physicist James Clerk Maxwell combined the fields of magnetism, electricity and optics to give the first unified theory of physics. In 1885, the German physicist Heinrich Rudolf Hertz showed that Maxwell's theory of electromagnetism was correct and that heat and light are forms of electromagnetic radiation [1-4].

In 1907, the French physicist Pierre-Ernest Weiss developed the theory of ferromagnetism based on the presumption that the interaction between the magnetic molecules could be described

empirically considering an internal molecular field. In 1913, the Danish physicist Niels Bohr detailed the fundamental physics from which magnetism result, alluding to the spin associated with an unpaired electron [3, 6-9].

The spins on the magnetic centres interact with their neighbors in the 3D lattice of a conventional magnet. Their spontaneous magnetisation relies on the alignment of the very high number of spin centres in the bulk material [1-3].

In the absence of an applied field the magnetic moments in the bulk magnetic structure are canceled out because it is divided into many domains and although the spins are aligned in one domain the different domains have different alignments and the overall spin is canceled out. By applying an external field on the material, all magnetic moments in all domains can orient in the same direction of the externally applied field the magnetisation is retained after removal of the field, the material is a permanent magnet [1-3].

In recent times, magnetism has been applied in various applications, ranging from electric motors and generators to communication devices such as televisions and telephones. It has important uses in data storage. Because the capacity of data storage is limited by the size of the domains in conventional magnets, there is a need to explore new materials. These materials may exhibit magnetic behaviour that could therefore allow significantly higher data storage density.

In 1993, a major breakthrough in nanomagnetism was reported as the first metal complex, $[Mn^{III}_8Mn^{IV}_4O_{12}(O_2CMe)_{16}(H_2O)_4]$ $2CH_3CO_2H$ $4H_2O$ {abbreviated as Mn_{12}} displaying SMM (i.e. molecule based) properties was identified [10-14]. Mn_{12} was prepared in 1980 by Lis while trying to oxidise Mn^{II} ions by using permanganate $(MnO_4)^-$ in acetic acid [15]. Mn_{12} was reported many times to explore its properties [10-14]. Mn_{12} shows magnetisation hysteresis below a certain blocking temperature T_B (below 2 K) and quantum tunneling of magnetisation (QTM)[15].

Over the last decades of research in the field of SMM, many metal complexes were synthesised and characterised. This includes inorganic, organic and organometallic coordination complexes in order to achieve a better understanding of the structural aspects which shows SMM behaviour through different synthetic approaches. The research target is to develop such systems with higher blocking temperature (T_B).

SMMs are of global interest. It is advanced for the fundamental scientific and technological purpose. SMMs have potential applications due to magnetic bistability which resulting from energy barriers, such as information storage devices and could act as the smallest unit in magnetic memory [16].

There are many approaches to develop specific properties of the material such as the blocking temperature or high effective energy barrier. One of these approaches is to synthesise heterometallic complexes that hold metal centres together by bridging units which are commonly an oxygen atom. Oxygen can be derived from hydroxide, oxide, carboxylate and alkoxide. These compounds can have intrinsic properties of the magnetic units such as quantum effects, Ising type anisotropy and high spin state [17].

The chemical and physical properties of the metal complex are derived from the molecular composition and the bonding within the molecule and the lanthanides are useful for different applications. Typically, Dy^{III} and Tb^{III} (anisotropic) analogues exhibit SMM behaviour, Tb^{III} and Eu^{III} analogues exhibit luminescence while the Gd^{III} (isotropic) analogue can be used as a molecular magnet refrigerant and is currently used as a contrast agent for MRI.

1.1.2. Magnetic bulk behaviour classifications

Magnetic properties depend on the orbital and spin motion of electron interaction. Some substances have very high magnetic interaction between the magnetic moments while some materials do not have collective interactions of atomic magnetic moments [6-9, 18, 19].

The various classes of magnetic behaviour are described in more detail in a number of test books. The main thing to note is that cooperative magnetic behaviour can arise when paramagnetic species are present in a material. In this sense, they are all special cases of paramagnetism and this can be conveniently summarised in one overview digram (Figure 1.1).

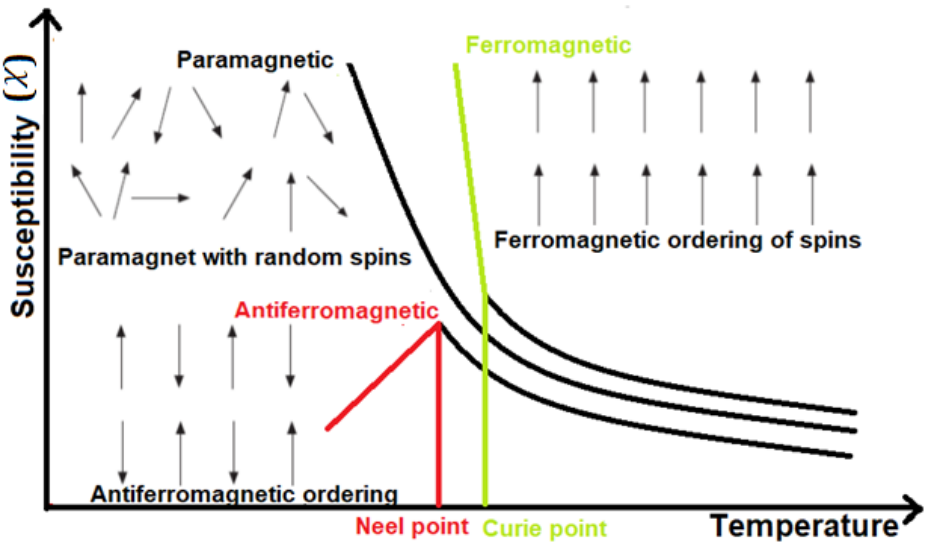

Figure 1.1. Spin interactions for common magnetic behaviours (a) paramagnetic (b) ferromagnetic (c) antiferromagnetic (image adapted from reference [19, 20]).

As shown in Figure 1.1, the classifications of the magnetic behaviour of the materials are divided into three group:

1-Ferromagnet

Below the critical Curie temperature, T_C, the domains align paralled and susceptibility (χ) increases for beyond the paramagnetic limit. Above T_C the system is paramagnetic.

2-Paramagnet

No cooperative effects so χ decreases with increasing temperature with inverse proportionality. This follows the Curie law

χ α 1/T or χ= C/T. Where C is the Curie-constant.

3- Antiferromagnet

Below the critical Neél temperature, T_N, the domains align antiparallel and cames each other so that at 0 K the χ value is theoretically 0. Above T_N the substance is only paramagnetic.

Two further possibilities, which can be regarded as special cases of Antiferromagnet coupling, are:

1- Ferrimagnetism

Spins with antiparallel orientation (AF coupling) but different magnitudes give rise to a residual magnetic moment and below the critical temperature the material acts in a similar way to a ferromagnet. The first and most famous example for such a ferrimagnet is provided by magnetite, Fe_3O_4 (Figure 1.2, a).

2- Canted antiferromagnetism also called weak ferromagnetism

The spins are oriented such that there is a competition between parallel alignments of spins with canted parallel aligned spins of opposite direction (Figure 1.2, b).

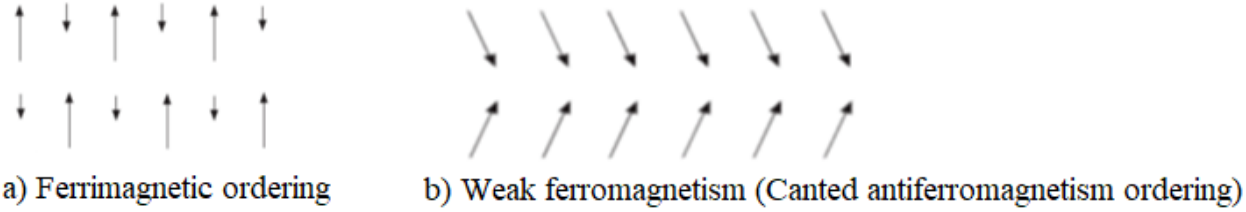

Figure 1.2. Spin interactions for magnetic behaviours (a) Ferrimagnetism (b) Canted antiferromagnetism (weak ferromagnetism) (taken from reference [19, 20]).

It turns out that all of these situations can be observed in molecular-based magnetic materials. For systems based on zero-dimensional materials (i.e on molecules) the most important spin arrangements are a) A molecular-based form of ferrimagnetisum as seen in Mn_{12} [10-14] and b) molecular-based ferromagnetism as seen in Co_2Dy_2 [21, 22]. Although compounds containing only one type of spin carrier can be overall AF coupled, competing coupling constants amongst the spin carriers has led to these being termed as ferromagnetic.

1.1.3. Single-Molecule Magnet (SMM) behaviour

So-called SMM behaviour can be observed when a zero-dimensional system (i.e. molecule) possesses a spin structure which creates a hindrance to the inversion of the total spin on the molecule. This is actually a simplification since the assumption is made that the molecule carries a "giant" spin, but it is helpful for describing some key parameters. Taking Mn_{12} as an example it eventually became clear that this molecule could be treated as having a giant spin of S=10. This arises from the central tetrahedral arrangement of 4x Mn^{IV} being ferromagnetically coupled to give

S=4x (3/2)=6, but then also being antiferromagnetically coupled to the surrounding ring of the 8 ferromagnetically coupled Mn^{III} with S=8x (4/2)=16. This leads to the total spin for the molecule of S=16-6=10.

The arrangement of the 8x Mn^{III} in an essentially planar ring allows the Jahn-Teller axes of all of these (arising from the d^4 distorted octahedral geometry for the high spin ion) to a point in the same direction which gives the whole system a significant axial zero-field splitting parameter D of -0.4 cm^{-1}. Once a relationship between anisotropy barrier height, D and S had been figured out as ΔE or U_{eff} =lDl S^2, the barrier height of 40 cm^{-1} was firmly established.

The basic requirements for this phenomenon (SMM):

1- High spin bistable ground state (±S).

2- High zero-field splitting/magnetic anisotropy.

3- Negligible magnetic interaction between molecules.

As a result of their molecular nature SMMs have long-term stability in air and are soluble in organic solvents and are excellent candidates for the different novel technological applications. Industrial applications such as high-density information storage data, electrical motors, ATM cards, information/telecommunications devices, generators, magnetic shielding [23], as optics [24], luminescence [25, 26], magnetic resonance [27], catalysis [28, 29], magnetic refrigeration [30-34], molecular magnetism [35], biomedical applications such as magnetic resonance imaging, production of frictionless bearings, medical implants, magnetic separators, acoustic devices and sensors [36-38] have all been suggested.

Moreover, SMM consideres as ideal candidates for substances to function in many advanced applications such as quantum bits (qubits) in quantum computing [39-45] , spintronic devices [39, 40, 46] and molecular electronics [47].

However, it is difficult to completely control all parameters during the synthesis of metal complexes. Likewise, this difficult extends to the magnetic properties of metal complexes and SMM behaviour [48].

Some factors that are difficult to control:

(1) The arrangement of the metal ions in the complex.

(2) The magnetic exchange interactions between the atoms.

(3) The relative orientations of the single ion in the anisotropy axes.

These factors have a profound effect on the magnetic properties:

(1) The high effective energy barrier to spin re-orientation.

(2) The splitting of a magnetic state.

(3) The existence of Quantum Tunnelling of the Magnetisation (QTM).

The review of the literature reveals that the coordination chemistry and the structural modification can tap into processing the magnetic properties of Ln complexes to achieve the maximum height energy barrier and minimising Quantum Tunnelling of the Magnetisation (QTM).

In order to optimise the properties, many attempts are centralised on:

(1) Increasing the nuclearity of the metal complex.

(2) Increasing the high-energy barrier (U_{eff}).

(3) The blocking temperature (T_B).

(4) The spin ground state.

SMM behaviour can be identified through two methods on a modern SQUID:

(1) Alternating-current (AC) is the magnetic susceptibility with an oscillating magnetic field. AC susceptibility magnetic data method can be separated into two components, the in-phase (χ') and out-of-phase (χ''), to detect and quantitatively examine the SMM behaviour. The effective energy barrier (U_{eff}) and pre-exponential factor (τ_0) can be calculated by the help of the Arrhenius equation (Equation 1.1).

$$\tau = \tau_0 e^{\left(\frac{U_{eff}}{k_B T}\right)}$$ Equation 1.1

Where τ is the relaxation time for magnetisation, τ_0 is a pre-exponential factor (the relaxation rate between attempts of thermal excitations over the energy barrier), U_{eff} is an effective energy barrier, T is the temperature in Kelvin and k_B is the Boltzmann constant.

The plot of temperature dependence between out of phase (χ'') versus temperature displays the maximum peak at the temperature where the switching of the magnetic field matches the relaxation rate $1/\tau$ (Equation 1.2).

$$\tau = \frac{1}{2\pi\nu}$$ Equation 1.2

When τ is relaxation time of magnetisation, ν is the frequency in the maximum peak for every temperature that has a peak.

Moreover, when the switching frequency increases, the peak must shift to higher temperatures due to an increase in $1/\tau$ with increasing temperature.

The relaxation time of magnetisation can be extracted from the frequency dependence from the out-of-phase (χ'') diagram.

Constructing a plot between $\ln(\tau)$ versus the inverse of temperature (1/T) creates a linear fit. From the linear fitting of the Arrhenius plot, the slope of the data can be precisely U_{eff}/k_B which means U_{eff} = slope k_B and the intercept $=\ln(\tau_0)$ that means $\tau_0=10^{-\text{ intercept}}$ s [49-53].

Various relaxation pathways dominate the diverse temperature regimes which may participate in the overall relaxation process which are characterised by a single U_{eff} and τ_0 [49-53].

Beside U_{eff} and τ_0 there is another parameter used to describe SMM behaviour. This is the blocking temperature (T_B) which can be extracted from the magnetic data. In the plot between out-of-phase versus temperature, the maximum at a particular frequency is called blocking temperature (T_B). The substance can act as an SMM below T_B.

(2) Direct-current (DC) is the magnetic susceptibility which studies the hysteresis loop. The hysteresis loop is the relationship between the magnetisations versus fields. Experimentally, the

hysteresis loop is characterised by micro-SQUID magnetometer performance at extremely low temperatures.

The field dependence is the plot between the magnetisations and the field (M vs. H) Figure 1.3. The field (H) starts to increase from zero to reach the maximum magnetisation and value of +H which is equivalent to the saturated magnetisation. The magnetisation remains at a high level and requires an inverse field to reverse magnetisation. That means the cycle comes back from +H to –H and again to +H [54]. The absence of a magnetic hysteresis loop means that the material does not exhibit SMM behaviour. The magnetic hysteresis is necessary for memory storage devices since it depends on the development of the magnetic hysteresis loop with perceived coercivity.

Most of the time, using the commercial SQUID does not help to characterise the hysteresis loops. Due to the limited temperature that is in the range 1.8-400 K, the hysteresis loops are not noticable. Therefore, using the micro-SQUID apparatus is useful to measure the hysteresis loops because micro-SQUID can go to temperatures below 1.8 K and also measures oriented single crystals [55].

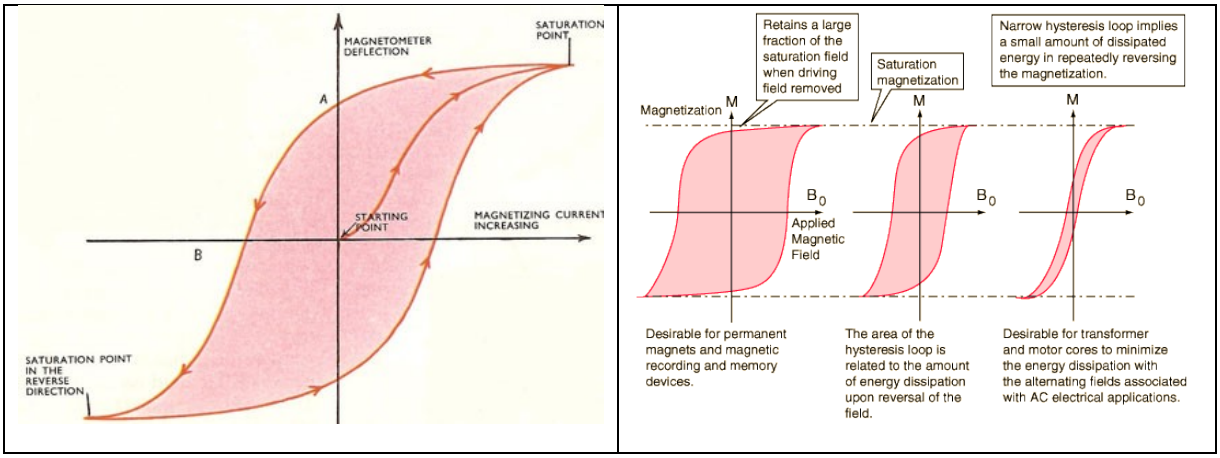

Figure 1.3. Hysteresis loops of magnetisations pattern (taken from reference [56-58]).

Based on the hysteresis loops, there are two different types of magnets. The first one is a hard or permanent magnet; this is a material has a broad hysteresis loop and a large magnetisation. The material has magnetised in the presence of an applied field and retains a large portion of the saturation field a magnetisation for a long time after removing the applied field [59-61]. This is desirable for permanent magnets, magnetic recording and memory devices.

The second type is a soft magnet has a narrow hysteresis loop with small magnetisation, which is more responsive to changed applied fields. These are suitable to be used in transformers and motors where a quick response to a rapidly oscillating field is needed [59-61].

Another parameter that shows in the hysteresis loop is the blocking temperature (T_B). It is the first temperature when a hysteresis loop is opened and the highest temperature when SMM can exhibit hysteresis loops. Below the blocking temperature (T_B), the SMM retains the magnetisation for a while during the remove of the externally applied field and the SMM metal complexes act as nanomagnets. Above blocking temperature (T_B), the material acts as paramagnetic material without retaining the magnetisation.

1.1.3.1. Mn_{12} SMM

The first complex that displayed SMM behaviour was $[Mn^{III}_8Mn^{IV}_4O_{12}(O_2CMe)_{16}(H_2O)_4]$ $2CH_3CO_2H$ $4H_2O$ {abbreviated as Mn_{12}} (Figure 1.4) reported in 1993 [10-14]. Mn_{12} was prepared in 1980 by Lis [15]. Mn_{12} has been reported later many times to explore the SMM properties [10-14]. Mn_{12} shows magnetisation hysteresis at lower temperatures and quantum tunnelling of magnetisation (QTM) (Figure 1.5).

The spin ground state of the Mn_{12} structure equates S =10 and to schematised by eight spins pointing up (Mn^{3+}) and four down (Mn^{4+}).

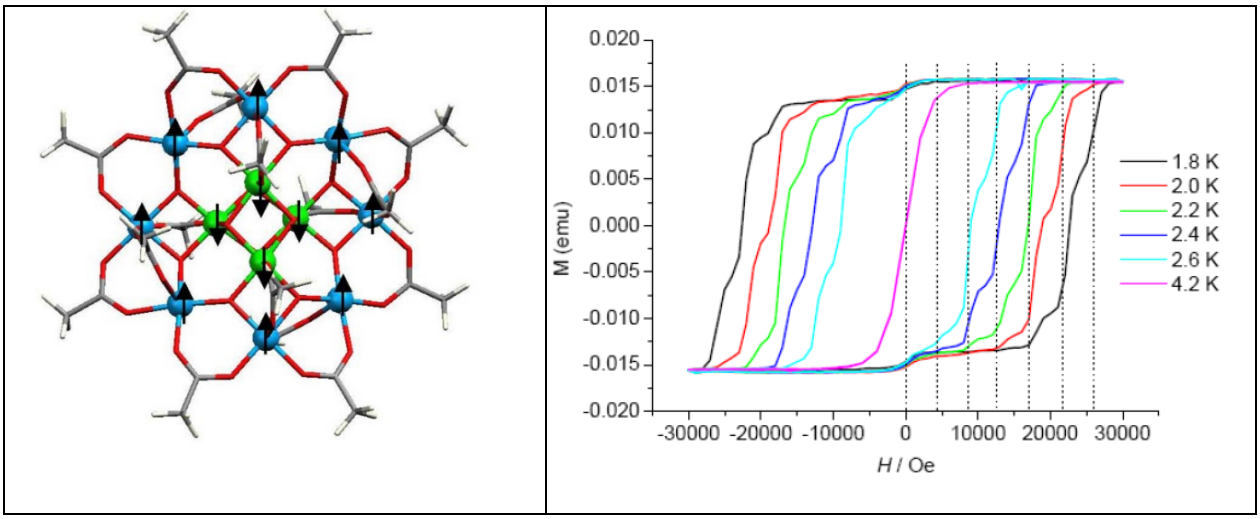

Figure 1.4 Molecular structure of $[Mn^{III}_8Mn^{IV}_4O_{12}(O_2CMe)_{16}(H_2O)_4]$. Colour code: blue, green, red, gray and white represent Mn^{3+}, Mn^{4+}, O, C and H, respectively (left) (taken from reference [4]). Hysteresis loop of a Mn_{12} for single crystal at different temperatures with an axially applied magnetic field (right) (taken from reference [4]). The steps indicate the relative change in magnetisation upon tunnelling.

1.1.4. Lanthanide complex SMM

There are 14 4*f* elements. These together with Sc, Y and La make up the rare earth elements. The ionic radius of lanthanides decreases sharply from left to right in the series due to the poor shielding of the increasing nuclear charge by the f-orbitals. The effect of spin-orbital coupling increases as the atomic number increases, except for the $4f^7$configuration which has no first-order angular momentum. The magnetic ground states of $Ln^{3+}$are summarised in Table 1.1.

Lanthanide ions mostly adopt a trivalent Ln^{3+} state although stable dipositive Eu^{2+} and Yb^{2+} are known as the tetravalent state for Ce^{4+} and Pr^{4+}. The characteristics for trivalent Ln^{3+} ions are summarised in Figure 1.5 and Table 1.1. As a result of the poor shielding of the orbitals, the electronic and spin character of Ln complexes are affected more by spin-orbit coupling effects than by the ligand field, opposite to what is seen for 3d metal ions. The large spin-orbit coupling means that the anisotropy of a Ln^{3+}, as can be defined by an anisotropy ellipsoid as shown in Figure 1.5, plays a key role in steering magnetic and optical properties [62].

Lanthanide tri-positive charge are divided into four classes (as shown in Figure 1.5) due to the quadrupole moment of their *f* electron cloud (electron density) [63]:

1- Axially elongated (prolate) comprises Pm^{3+}, Sm^{3+}, Er^{3+}, Tm^{3+} and Yb^{3+}.

2- Equatorially elongated (oblate) comprises Ce^{3+}, Pr^{3+}, Nd^{3+}, Tb^{3+}, Dy^{3+} and Ho^{3+}.

3- Spherical (isotropic) comprises Gd^{3+}, Lu^{3+} and Y^{3+}.

4- For Eu^{3+} (J=0).

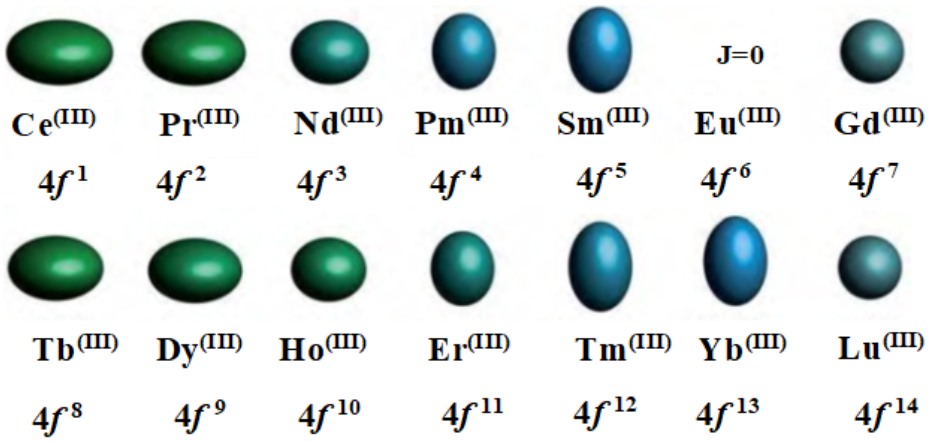

Figure 1.5. Quadrupole approximations of the 4*f*-shell electron distribution for the trivalent state of lanthanides (taken from reference [63]).

Lanthanide ions have a high coordination number in the range (7-12) with various coordination geometries due to their high ionic radius. Often, the coordination number is eight or nine.

Lanthanides play a special role in magnetism. Especially, Dy^{III} ions display the superiority in magnetism over transition metal (SMMs) [64] due to:

1- High magnetic moment.

2- High anisotropy of the spin-orbital coupled.

3- The electron configurations have odd number $4f^{9}$, thus insuring the kramers doublet ground state [65], a critical factor in the presence of typical SMM behaviour.

However, lanthanide complexes have a drawback. They present a very weak exchange interaction between lanthanide ions which result from the efficient shielding of the unpaired electrons in 4*f* orbitals [66, 67].

Table 1.1. Magnetic ground states of lanthanide tri-positive charge (Ln^{3+}) (taken from reference [63]).

Ln^{3+}	4*f*	Ground state	g_J	χT ($cm^3mol^{-1}K$)
Ce	f^1	$^2F_{5/2}$	6/7	0.80
Pr	f^2	$^3H_4$	4/5	1.6
Nd	f^3	$^4I_{9/2}$	8/11	1.64
Pm	f^4	$^5I_4$	3/5	0.90
Sm	f^5	$^6H_{5/2}$	2/7	0.09
Eu	f^6	$^7F_0$	-	0
Gd	f^7	$^8S_{7/2}$	2	7.87
Tb	f^8	$^7F_6$	3/2	11.82
Dy	f^9	$^6H_{15/2}$	4/3	14.17
Ho	f^{10}	$^5I_8$	5/4	14.07
Er	f^{11}	$^4I_{15/2}$	6/5	11.48
Tm	f^{12}	$^3H_6$	7/6	7.15
Yb	f^{13}	$^2F_{7/2}$	8/7	2.57
Lu	f^{14}	$^1S_0$	0	0

Lanthanide complexes govern the SMM behaviour via the interplay between ligand field effect, the strength of the magnetic interaction coupling between the lanthanide sitses and the coordination geometry [68].

Based on the theory of (hard and soft acids and bases), lanthanide ions are high Lewis acids due to $5p^66s^2$ orbital shielding the 4*f* orbitals [16]. So lanthanide ions prefer to bind with oxygen donors (neutral or /and negative charge) [69].

Figure 1.6, presents the geometry of the nuclearity of the lanthanide complex (less than six) which display SMM behaviour [70].

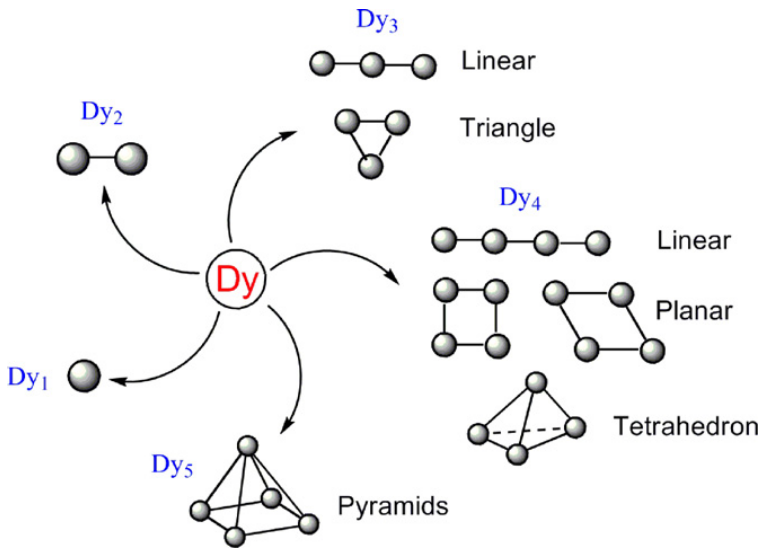

Figure 1.6. The basic structural motifs in Dy_{1-5} complexes (taken from reference [70]).

1.1.4.1. Pc_2Ln

The first lanthanide complex displaying SMM properties was $[Pc_2Ln]^-$ TBA^+, as shown in Figure 1.7 [71], where Pc is phthalocyanine and TBA^+ is $N(C_4H_9)_4^+$. The presence of one (TBA^+) cation implies that the mononuclear complex is a monovalent anion. Phthalocyanine double-decker of lanthanides $[Pc_2Ln]$ was prepared in 1965 [72] and the structure reported in 1979 [73]. Studies of the magnetic properties and an investigation into the SMM behaviour of $[Pc_2Ln]$ was carried out in 2003 [71].

For Tb and Dy respectively, the magnetic measurements revealed that the effective energy barrier $U_{eff,}$ was 230 and 28 cm^{-1} with pre-exponential factors ($1/\tau_0$) of 1.6×10^7 and 1.6×10^5 s^{-1} for Tb and Dy, respectively.

The magnetic properties of lanthanide complexes are interesting because they show the slow relaxation of magnetisation and the behaviour is higher than the 3d complexes that show SMM behaviour.

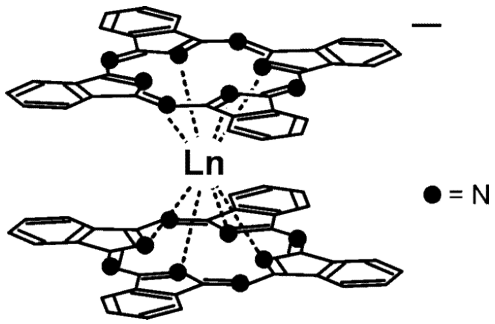

Figure 1.7. $[Pc_2Ln]^-$ (Ln = Tb, Dy, Ho, Er, Tm or Yb) (taken from reference [71]).

1.1.4.2. $[Dy_3(\mu_3\text{-}OH)_2L_3Cl(H_2O)_5]Cl_3\ 4H_2O\ 2MeOH\ 0.7\ MeCN$

The Dy_3 triangle was reported in 2006 [74]. Dy_3 is synthesised by using *o*-vanillin (HL), as shown in Figure 1.8. The presence of three (Cl) anion implies that the trinuclear complex is a trivalent cation. Dy_3 has antiferromagnetic interaction between the Dy atoms, as shown in Figure 1.9. Dy_3 with the toroidal moment arrangement of spins on the dysprosium sites has changed the chemistry of lanthanide complexes by presenting a new concept for magnetic memory without a net magnetic moment [74, 75]. It shows a disappearing susceptibility at low temperatures which is unexpected in systems having an odd number of unpaired electrons. The magnetic measurements of Dy_3 display SMM behaviour and reveal that an effective energy barrier (U_{eff}) is 61.7 K at a relaxation time (τ_0) of 2.2×10^{-8} s.

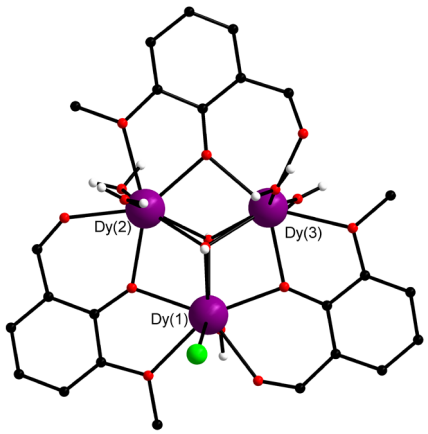

Figure 1.8. Molecular structure of $[Dy_3]$. Colour code: black, red, violet, green and white spheres represent C, O, Dy, Cl and H respectively.

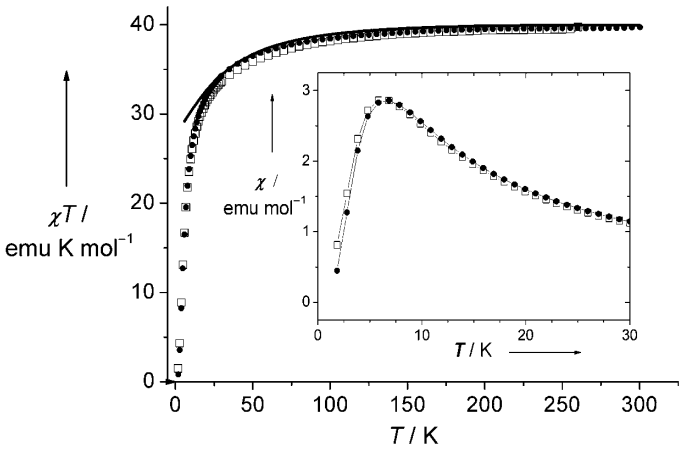

Figure 1.9. Temperature dependence of the χT products (per trimeric unit) for 1 (&) and 2 (*). The solid line represents the calculated value for three uncorrelated Dy^{III} ions. Inset: low-temperature susceptibility (taken from reference [74]).

1.1.5. 3d-4*f* metal complex as SMM

To begin with, researchers focused on homometallic 3d complexes and their nuclearity making modifications of the ligands to explore them further. Then research moved to the discovery of lanthanide complexes and their properties. Different approaches were taken to increase their nuclearity whilst also exploring their properties like SMM behaviour. After discovering 3d-4*f* combined complexes, different approaches to increase the nuclearity gave promising candidates that showed SMM behaviour.

One of the ideas to improve the SMM behaviour of 4*f* and 3d separate systems is to construct 3d-4*f* heterometallic complexes by combining 4*f* metal ions with 3d metal ions. The development of approaches and synthetic strategies towards high nuclearity 4*f* and 3d-4*f* metal complexes may show a better SMM behaviour. The first 3d-4*f* complex $[Nd_2(Co(CN)_6)_2 \cdot 9H_2O]$ was prepared by Cleve and Hoeglund in 1873 [76]. The reaction between a lanthanide chloride and potassium cobalticyanide that gave tetranuclear Co-Ln. The first 3d/4*f* SMM reported was Cu_2Tb_2 in 2004 [77], while the first Fe-Ln SMM reported was Fe_2Dy_2 in 2006 [78].

Orbital degeneracy could be limited by mixing metals Fe and Ln because the coupling interactions between Fe-Ln are often antiferromagnetic or very weak [79], but regardless they are bigger than the homonuclear lanthanide complexes.

The ionic radius of Ln^{III} is bigger than Fe^{III}. Therefore, the volume of the complex occupied by Ln^{III} ions will be bigger than Fe^{III} ions. It is difficult to predict the magnetic characteristics of any compound based purely on the crystal structure.

Contrary to lanthanide-transition metal alloys, SMMs are molecular superparamagnets and derive their properties from the combination of a high value of spin ground state (*S*) and a high magneto-anisotropy (negative zero-field splitting parameter, *D*).

The advantages of using 3d-4*f* together are:

1- 4*f* metal ions can provide both high spin and molecular magnetic anisotropy.

2- 3d metal ions can generate a high-spin ground states.

3- 3d-4*f* can be synthesised by assisted self-assembly reactions since 3d clusters can provide donors with the ions acting as accepters.

The 3d-4*f* metal complexes can exhibit a strong magnetic coupling. This may be through dipolar or superexchange between the 3d and 4*f* metal ions.

The combination of iron and lanthanide metals gives rise to a significant energy barrier to magnetisation reversal and slow relaxation of the magnetisation which is observed at low temperature like in case of Fe_7Dy_3 with U_{eff} =33.40 K with pre-exponential relaxation time, τ_o $=6.6\times10^{-8}$ s [80].

There are two efficient approaches widely used to combine 3d and 4*f* ions into one aggregate. The first approach is to design and synthesise the ligand. This should provide two or more coordination pockets in order to accommodate the 3d and 4*f* ions. The second approach which is used in this work, is an assisted self-assembly approach by using co-ligands that connect the 3d and 4*f* ions. In addition, co-ligands are suitable to stabilise the complex by completing the coordination spheres.

A review of the literature reveals that the source of Fe can be divided into commercially available salts such as: iron (chloride (anhydrous, $4H_2O$ and $6H_2O$), nitrate, sulfate and tosylate) [4, 80-87]. Moreover, we can synthesise the Fe triangle $[Fe_3(\mu_3\text{-}O)(carboxylate)_6(solvent)_3]\cdot carboxylate$. Carboxylate is used as a bridging ligand to synthesise Fe-Ln for example with benzoate ($PhCO_2$),

substituted benzoate in meta and para position with (CN, Cl, CH_3, NO_2), Pivalate (Piv) and acetate (OAc). A review of the literature reveals that various methods have been used to synthesise Fe-Ln metal complexes such as: stirring at room temperature, reflux, solvothermal, microwave irradiation, vapor and liquid diffusion [4, 80-89].

Fe-Ln metal complexes exist in different geometry topologies such as butterfly, wheel, S-shape, Z-shape, linear, planar cyclic, propeller alongside many others [4, 80-90]. Due to the promising results of the Fe-Ln metal complex, this work aims to construct and increase the family of Fe-Ln metal complexes and study their ability to be used in potential applications like quantum computing, magnetic refrigerant and luminescence.

1.1.5.1. Cu_2Tb_2 SMM

The first 3d-4*f* metal complex to display SMM properties was $[Cu^{II}LTb^{III}(hfac)_2]_2$, as shown in Figure 1.10, had been reported in 2004 [77]. A cyclic tetranuclear Cu_2Tb_2 was obtained, where H_3L is 1-(2-hydroxybenzamido)-2-(2-hydroxy-3-methoxy-benzylideneamino) ethane and Hhfac = hexafluoroacetylacetone. Magnetic studies of Cu_2Tb_2 reveal the presence of ferromagnetic interaction coupling, as shown in Figure 1.11. Fitting the data to the Arrhenius equation reveals an effective energy barrier U_{eff} as 21 K with pre-exponential relaxation time and $\tau_0 = 2.7 \times 10^{-8}$ s.

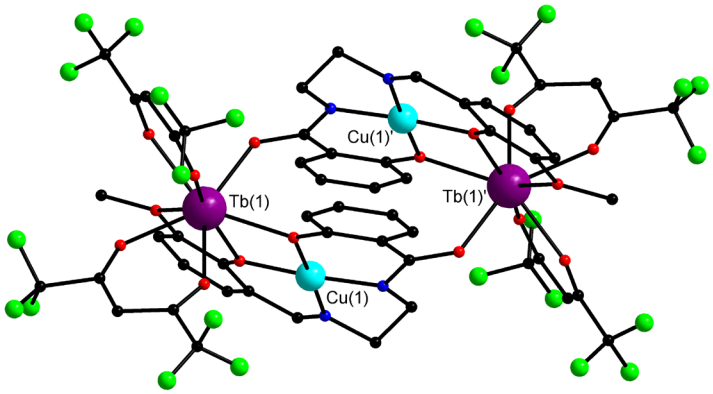

Figure 1.10. Molecular structure of $[Cu_2Tb_2]$. Colour code: black, red, blue, green, turquoise and violet spheres represent C, O, N, F, Cu and Dy, respectively.

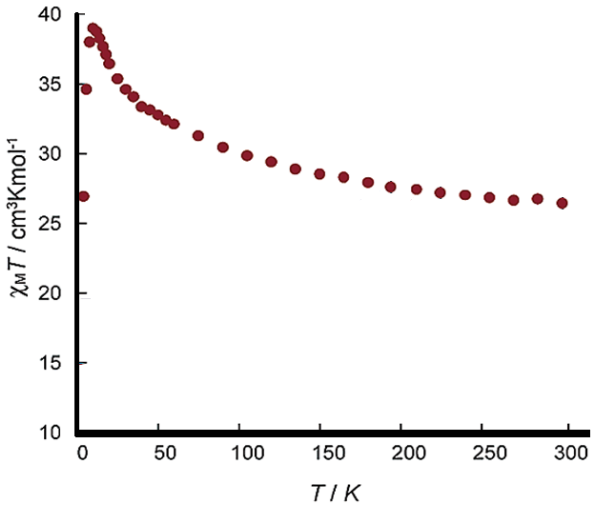

Figure 1.11. Plots of $\chi_M T$ versus T for $[Cu^{II}LTb^{III}(hfac)_2]_2$.

1.1.5.2. Fe_2Ln_2

The first Fe-Ln complex displaying SMM properties was reported in 2006 [78]: $[Fe_2Ho_2(\mu_3\text{-}OH)_2(teaH)_2(PhCO_2)_4(NO_3)_2]\cdot 4(MeCN)\cdot 3(H_2O)$ and $[Fe_2Dy_2(OH)_2(teaH)_2(PhCO_2)_6]$ where $teaH_3$= triethanolamine and $PhCO_2$ = benzoate. Fe_2Ln_2 has butterfly geometry, as shown in Figure 1.12.

The difference between the Fe_2Ho_2 and Fe_2Dy_2 clusters is the replacement of the terminal chelating nitrate groups in the Fe_2Ho_2 to the benzoate group in the Fe_2Dy_2. Magnetic studies of both compounds reveal the presence of antiferromagnetic exchange interactions.

These compounds are SMMs as shown by the observation of hysteresis loops at lower temperatures for Fe_2Dy_2 at 4K, 1.1 K and for Fe_2Ho_2 very small coercivity observed at 0.3 K. The presence of quantum tunnelling at zero-field gives a rapid decrease of the magnetisation and effective energy barrier U_{eff} values could not be extracted.

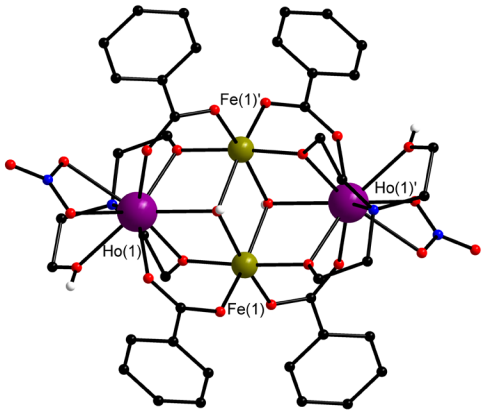

Figure 1.12. Molecular structure of $[Fe_2Ho_2(mdea)_2(mdeaH)_2(\mu_3\text{-}OH)_2(N_3)_2(PhCO_2)_8]$ 3MeCN. Colour code: black, red, blue, green, white and violet spheres represent C, O, N, Fe, H and Ho respectively.

1.1.5.3. Binuclear $Fe^{III}Dy^{III}$

The first Fe-Ln metal complex displaying SMM behaviour evaluated by AC- susceptibility was $[Fe(bpca)(\mu\text{-}bpca)Dy(NO_3)_4]$, is shown in Figure 1.13 was reported in 2006 [91], where Hbpca = bis(2-pyridylcarbonylamine). Magnetic studies of binuclear FeDy reveal the presence of antiferromagnetic interaction. The magnetic measurements reveal that the effective energy barrier U_{eff} is 8.98 cm^{-1} with pre-exponential factors (τ_0) of 7.77×10^{-8} s.

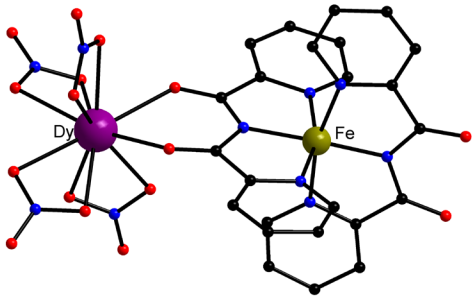

Figure 1.13. Molecular structure of $[Fe(bpca)(\mu\text{-}bpca)Dy(NO_3)_4]$. Colour code black, red, blue, green and violet spheres represent C, O, N, Fe and Dy, respectively.

1.1.5.4. Fe_7Dy_3

$[Fe_7Dy_3(\mu_4\text{-}O)_2(\mu_3\text{-}OH)_2(mdea)_7(PhCO_2)_4(N_3)_6]\cdot 7(MeOH)\cdot 2(H_2O)$ as shown in Figure 1.15, was reported in 2009 [79]. Where mdea is *N*- methyldiethanolamine ($mdeaH_2$), $PhCO_2$ is benzoate and

N_3 is azide. Magnetic studies of Fe_7Dy_3 reveal the presence of antiferromagnetic interactions, as shown in Figure 1.14. Micro SQUID measurements observed below 1.8 K gave rise to a hysteresis loop at 0.035 T/s sweep rate. The magnetic measurements reveal that the effective energy barrier (U_{eff}) is 33.4 K at a relaxation time (τ_0) of 6.6×10^{-8} s. For this reason, *N*- methyldiethanolamine ($mdeaH_2$) has been used as the main ligand to synthesise 3d-4*f* aggregates in chapter four of this work.

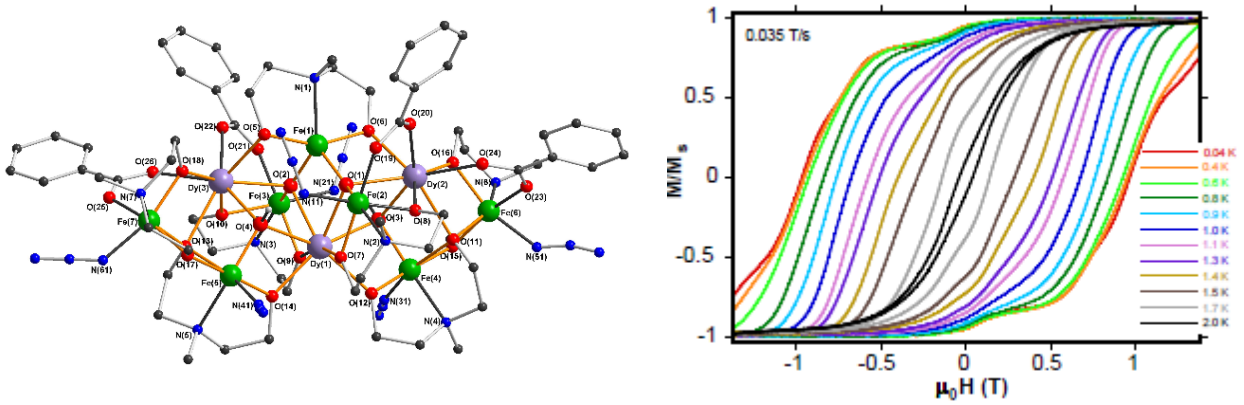

Figure 1.14. Molecular structure of $[Fe_7^{III}Dy_3^{III}(\mu_4\text{-}O)_2(\mu_3\text{-}OH)_2(N_3)_6(mdea)_7(PhCO_2)_4]$. Colour code grey, red, blue, green and lavender spheres represent C, O, N, Fe and Dy, respectively (on the left) (taken from reference [79]). Magnetisation (M) versus applied DC field (H) hysteresis loops for single crystals of Fe_7Dy_3 at the indicated temperatures and a fixed sweep rate of 0.035 T/s (on the right) (taken from reference [79]).

1.2. Optical properties of Ln ions

The luminescence from lanthanide complexes was first studied in the 1940s [62]. Most of the lanthanide ions have luminescence properties. After exciting an electron from its ground state to a higher electronic state, it exhibits long-lived luminescence. This is noticeable from sharp lines that are related to f–f transitions of the Ln^{III} ion.

The 4*f* orbitals are shielded by $5p^66s^2$ subshells so that the orbitals do not participate in the construction of coordination bonds significantly. So, the luminescent lanthanide bands originate from the electronic transitions which are located inside their valence 4*f* orbitals [92]. Therefore, the luminescence of the lanthanide ions appears as their atom-like sharp emission bands. In addition, the wavelengths are mostly unaffected by the lanthanide ions coordination environment.

The electronic spectra of lanthanide complexes are similar to their free ions. Moreover, the lanthanide complexes have almost the same colour as their aqua ions. This phenomenon is seen in the solid-state, in which there is a small competition from other non-radiative deactivation sources. This increased the attention of scientists to explore the application of lanthanide complexes in chemosensors, bioimaging probes and optical communications. For example, currently, there is a growing interest in the synthesis of lanthanide complexes and investigation into their fascinating magnetic and extremely interesting optical properties [93-95], in which the emission bands range from the visible to the near-infrared (NIR) regions. Lanthanide ions and complexes have found applications in modern everyday technologies such as: television, computer displays, optical amplifiers, lasers, economical luminescent lamps, optical fibers and light-emitting diodes. Lanthanide complexes are used in biological media as luminescent labels for analysis. In addition, they are used as responsive luminescent stains for medical diagnosis, biomedical analysis and cell imaging that depends on lanthanide ions heavily [96-98]. There are unique features in the lanthanide ions with potential candidates in conversion or amplification of light, fluorescent probes and light-emitting diodes [99, 100]. These features are long-lived emission, high Stokes shifts and high luminescence quantum yield [101-105] leading to applications in fluoroimmunoassays, optical telecommunication [106, 107], solar energy conversion [108, 109] and organic light-emitting diodes (OLEDs) [110, 111] synthesis of Ln^{III} (Nd, Yb or Er) complexes are highly desired.

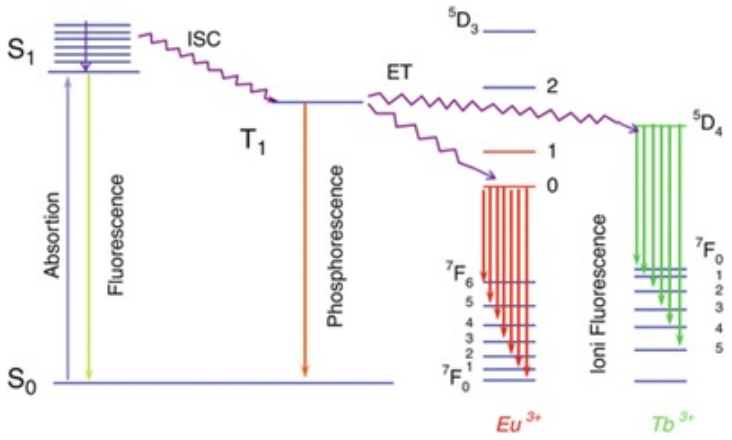

Figure 1.15. The energy transfer pathway of Europium and Terbium emission (taken from reference [112]).

As shown in Figure 1.15, the energy transfer pathway consists of absorption, fluorescence, phosphorescence and photodegradation.

The ligand is excited from the ground state (S_0) into the single state (S_1) by absorbtion of photons. Fluorescence is the energy transfer from the excited single-state (S_1) to ground state (S_0) followed by the light emission due to internal conversion of the ligand. Intersystem crossing (ISC) is a nonradiative conversion from the singlet state (S_1) to the triplet state (T_1). Phosphorescence is a conversion from the lowest triplet level of the ligand to the excited state of the lanthanide ion accompanied by light emission [112, 113]. Efficient energy transfer is a requirement for luminescence. This can be done by matching the triplet state of the ligand to the excited-state of the lanthanide. To ensure a forward exothermic process occurs, it is preferred that the triplet state of the ligand has slightly lower energy than the lanthanide excited state. When the energy gap is too small between the triplet state of the ligand and the excited state of the lanthanide ion, a problem may occur with the energy transfer from the excited state of the lanthanide to the triplet state of the antenna. Thus this process will affect the intensity of the emission [114].

The lanthanide ions are classified into three groups according to luminescence properties:

1. The first group contains four lanthanide ions (Sm^{3+}, Eu^{3+}, Tb^{3+} and Dy^{3+}). They exhibit a strong luminesce and their emission are easily detected in the visible region [115, 116]. The emission spectra of Eu^{3+} (red), Tb^{3+} (green), Sm^{3+} (orange) and Dy^{3+} (yellow) in their complexes are shown in Figure 1.16. These complexes have characteristic long lifetimes in the range (microsecond or millisecond).
2. The second group contains five lanthanide ions (Pr^{3+}, Gd^{3+}, Ce^{3+}, Ho^{3+} and Tm^{3+}). These five lanthanide ions appear in the visible region with weaker luminescence.
3. The third group contains six lanthanide ions (Pr^{3+}, Nd^{3+}, Er^{3+}, Ho^{3+}, Tm^{3+} and Yb^{3+}). They emit strong luminesce in the NIR region due to the small energy differs between their energy levels [117].

Lu^{3+} ($4f^{14}$) has no f-f transitions so no emissions have been observed in the visible range due to the filled 4*f* orbital.

This work focuses on looking for europium and terbium complexes that exhibit optically interesting properties making them suitable probes or labels for biological and chemical applications. Their electronic spectra display very narrow bands. Adjusting the coordination environments or temperature can shift the wavelengths no more than $\pm 2 cm^{-1}$. Using the sensitised

emission leads to the Stokes shift so it is unlikely to have overlap of the emission bands with the high absorption bands.

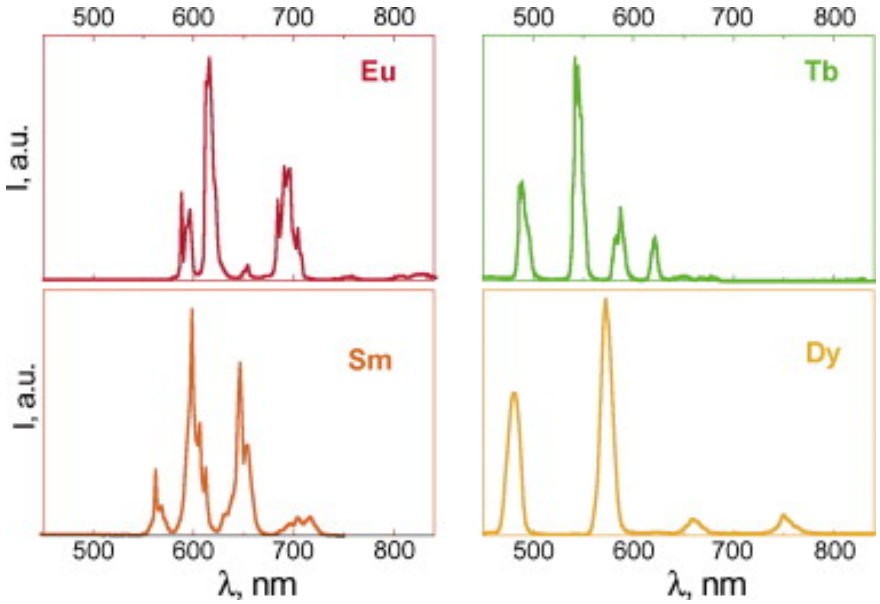

Figure 1.16. Luminescence spectra of Eu^{III}, Tb^{III}, Sm^{III} and Dy^{III} complexes (taken from reference[118]).

In Figure 1.17, NR arrows indicate non-radiative processes while other arrows indicate radiative processes.

For the Eu^{III} complexes, all emissions emanate from the $^5D_0$ level. The emission line in Eu^{III} complexes result predominately from electric dipole character (ED), although magnetic dipole radiation (MD) is often jointly responsible [119, 120]. The electrons in the 4*f* orbitals are shielded from ligand interactions very well by intervening $5p^6 5s^2$ octet so that the extent of removing the degeneracy depends upon both the symmetry and strength of the ligand field [119, 120]. The emission spectrum of the Eu^{III} complex exhibits a sharp emission band from the interaction between f-f transition of Eu^{III} corresponding to the $^5D_0 \rightarrow {}^7F_J$ (J = 1-4) transitions of the Eu^{III} ion $^5D_0 \rightarrow {}^7F_1$ (590 nm), $^5D_0 \rightarrow {}^7F_2$ (619 nm), $^5D_0 \rightarrow {}^7F_3$ (650 nm) and $^5D_0 \rightarrow {}^7F_4$ (700 nm).

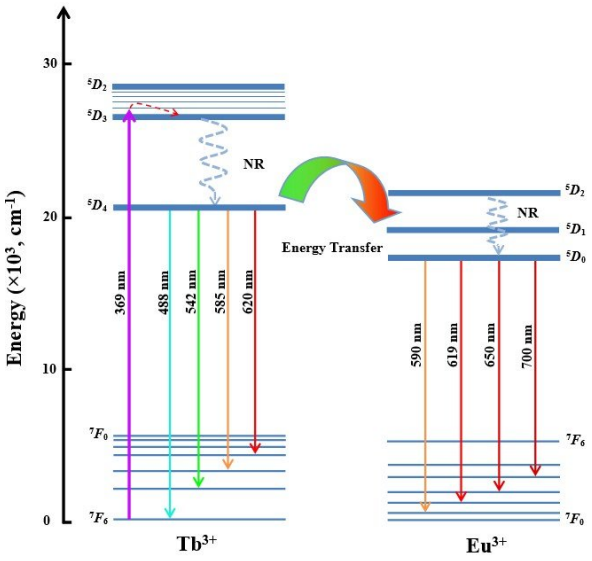

Figure 1.17. Schematic energy–level diagram of Tb^{III} and Eu^{III} [121].

The emission band at 619 nm corresponds to the hypersensitive $^5D_0 \rightarrow {}^7F_2$ transition. It dominates the emission spectra (high intensity) including the Eu^{III} ion which is not on an inversion centre. It is most likely at a site with low symmetry and non-centrosymmetric ligand [122]. The $^5D_0 \rightarrow {}^7F_2$ and the $^5D_0 \rightarrow {}^7F_1$ transitions have been referred to as hypersensitive electric-dipole (ED) and magnetic-dipole (MD) transitions, respectively [122-125]. For Tb^{III} complex, all emissions emanate from the $^5D_4$ level. The emission spectrum of the Tb^{III} complex exhibits a sharp emission bands from the intra f-f transition of Tb^{III} corresponding to the $^5D_4 \rightarrow {}^7F_J$ (J = 3–6) transitions of the Tb^{III} ion $^5D_4 \rightarrow {}^7F_6$ (488 nm), $^5D_4 \rightarrow {}^7F_5$ (542 nm), $^5D_4 \rightarrow {}^7F_4$ (585 nm) and $^5D_4 \rightarrow {}^7F_3$ (620 nm). The emission at 488 nm ($^5D_4 \rightarrow {}^7F_6$) was assigned to the magnetic dipole transition whilst the emission at 542 nm ($^5D_4 \rightarrow {}^7F_5$) was assigned to the electric dipole transition [126]. The emission intensity at 542 nm ($^5D_4 \rightarrow {}^7F_5$) dominates the emission spectra (high intensity) that deduces the Tb^{3+} ion is located on an asymmetric coordination [122].

Tb^{III} complexes are not as useful as Eu^{III} complexes for probing asymmetry of its complex. It only exhibits moderate sensitivity when compared to the Eu complex. It exhibits hypersensitivity to ligand environment.

Lanthanide ions face two problems for luminescence. The first one is the lower absorption bands with absorption coefficients normally less than 1 M^{-1} cm^{-1}. Therefore, the molar absorption

coefficients of the lanthanide ions are very low usually because the f–f transitions are parity forbidden making the direct excitation of lanthanide ions inefficient [92].

The second problem is the deactivation of the emissive states of the metal by vibrational energy transfer. This effect emerges through the process of energy transfer from the excited state of metal to O-H stretching vibrations of the coordinated or closely diffusing water molecules [127]. The 4*f* orbitals are shielded by 5p and 6s orbitals so that lanthanide ions are strong Lewis acids [128-131].

To overcome the second problem, we can use antenna ligands. By designing the antenna ligand in such a way, sufficient shielding of the lanthanide ions from water molecules can take place. In addition, this provides a non-radiative deactivation for excited state lanthanide ions through vibrational modes. Using the antenna chelates to synthesise the lanthanide complex has an advantage that one ligand can produce many different wavelengths by changing the metal (where not all metals have the same efficiency).

The ligand must have two features combined to synthesise luminescent lanthanide complexes:

(1) The ligand must include a chromophoric moiety which can prosses a large molar absorptivity. In addition, the ligand has the ability to coordinate with various lanthanide ions emitting in visible or/and near-infrared regions.

(2) The ligand must minimise nonradiative deactivation pathways so that it can protect the lanthanide cation.

Synthesising 3d-lanthanide complexes by using a ligand and trying to modify the ligand could produce complexes that have optical properties, magnetic properties or show SMM behaviour. This approach has been used in the literature [48, 81, 132].

Nevertheless, it is difficult to predict and assess how the modification will affect the luminescence properties of a complex.

1.3. Magnetocaloric effect and molecular magnetic refrigerants

The magnetocaloric effect (MCE) is another area of solid-state chemistry and physics where molecules are showing some advantages in terms of processability and reduced dimension. MCE

used to cool systems offers the possibility to achieve sub-Kelvin temperatures. On a more everyday note, cooling via magnesium offers several environmental advantages to standard refrigeration methods. The principle behind MCE is to use changes in entropy to either cool or heat locally. For cooling this can be best illustrated diagrammatically.

Two parameters are key to evaluate the performance of the magnetocaloric effect (MCE). These are the magnetic entropy change ($-\Delta S_m$) or/and the adiabatic temperature (ΔT_{ad}). This is shown schematically in Figure 1.18 and Figure 1.19.

In order to achieve good saturation of magnetisation, a material ideally be isotopic. All spins are aligned with the field. On removing the field the spins take heat out of the (adiabatic) system to randomise because the universe wants disorder (increasing entropy) $\Delta H=T\Delta S$ when ΔS +ve so ΔH +ve and T given by $\Delta S/\Delta H$.

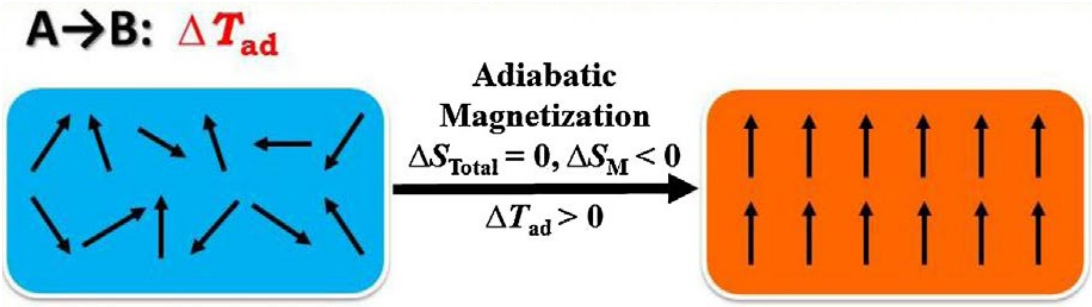

Figure 1.18. The schematic illustration of the adiabatic process (taken from reference [34]).

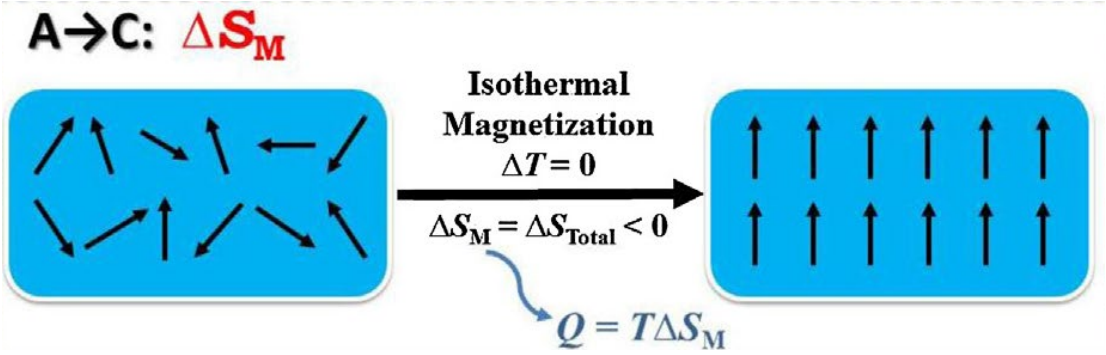

Figure 1.19. The schematic illustration of the isothermal process (taken from reference [34]).

1.4. Outlook for Quantum Computing

Whilst the idea of a Quantum computer offers ways to use interently quantum-based systems such as molecules to provide ultrafast processing coupled with sufficient storage (magnetic memory), the realisation of this concept is far from simple.

Whilst it is possible to find and optimise systems which provide rapid information processing, as gauged by relaxation times of the magnetisation, actually delivering and accessing the information is still a significant challenge.

In this thesis, some molecules have been identified as having the potential to be developed for Quantum computing applications but in common with similar systems, we are still far from finding ways to control the spin properties of these systems in terms of creating a Quantum Computer.

Table 1.2 summarises the features of quantum computers compared with their solid state counterparts.

Table 1.2. Comparison between conventional and quantum computers.

	Conventionally	Quantum
Information carriers	The states are reliably distinguishable and it can be observed without disturbing the system.	In general, the attempting of observation for the information carriers state disturbs the system. While it obtain only partial information about the state (uncertainty principle).
	To specify the joint state of two or more systems, it is sufficient to specify the state of each one separately.	Two systems can exist in an entangled state and causing them to behave in ways that cannot be explained by supposing that each particle has some state of its own.
The Bits	The information is reducible to bits 0 and 1.	Quantum information is reducible to qubits $\alpha\|0\rangle + \beta\|1\rangle$.
	All processing can be done by simple logic gates (AND, NOT) acting on bits one and two bits.	Quantum information processing is reducible to one and two-qubit gate operations.

As shown in Table 1.2, in classic computation, the basic element of information is a bit which can take two values (1 and 0). Its material realisation is a classical physical with two well-defined

states. Quantum computing is a quantum system termed qubit with quantum microstates (ms) that can take |1> or |0> but also any arbitrary superposition of these two (namely, $| \varphi > = \alpha|0> + \beta|1>$).

The physical implementation of quantum computing (QC) is considered one of the most difficult challenges in nanoscience. Quantum computing (QC) aims to use the quantum mechanics laws to implement tasks of the information processing [133].

The "quantum parallelism" is correlated using such superposition and is expected to enormously increase the potential of information processing [134-136]. It means that the possibility to extract and manipulate the information from a quantum system becomes reliable.

1.5. Methodology used to access 4*f* and 3d-4*f* cluster

There are three techniques to get crystals:

1.5.1. Evaporation technique

This technique is used widely. It is the simplest method used to create crystals, as shown in Figure 1.20. Large and high-quality crystals can be obtained by slow evaporation when the solution is left without disturbance and more solvent evaporates. In this work, all crystals are obtained by the slow evaporation technique by making holes in the cap of the vial. The number of holes controls the rate of evaporation based on the boiling point of the solvent. A lower boiling point like acetone needs fewer holes. On the other hand, the higher boiling point like toluene or water needs more holes even without closed cap [88].

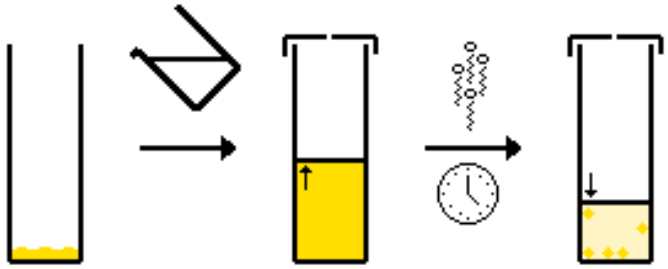

Figure 1.20. Schematic of the slow evaporation method (taken from reference [137]).

1.5.2. Vapour and Liquid diffusion

This technique is used to obtain crystals when slow evaporation does not work. Usually two solvents are allowed to diffuse together to aid the crystallisation.

There is a difference between liquid and vapour diffusion. In liquid diffusion, as shown in Figure 1.21, the solvents must be insoluble (immiscible) so the diffused solvent must be added slowly on the wall of vial. It will be on the top of the solution because it has lower density. If this method is successfully, the crystal will grow up in the interface of two layers. If precipitation is formed, the system will need another carefully selected solvent which is immiscible in both. The third solvent will separate the two layers by slowing down the reactions and allowing the crystal to grow up [88].

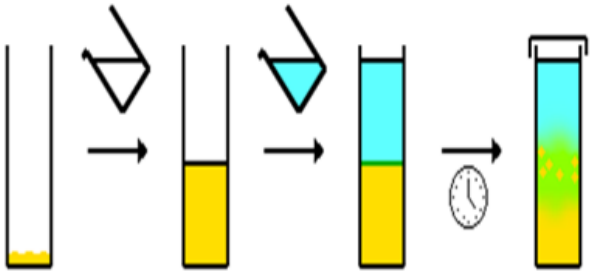

Figure 1.21. Schematic of the liquid diffusion method (taken from reference [138]).

In vapour diffusion, as shown in Figure 1.22, the solvents must be soluble (miscible). The solution will be placed in the small vial inside a bigger vial with another solvent. The solution must be less soluble in the new solvent than in the closed outer vial. The vapour from the bigger vial will diffuse into the small vial. That leads to supersaturation and crystallisation may take place. These good conditions may enable the crystals to grow [88].

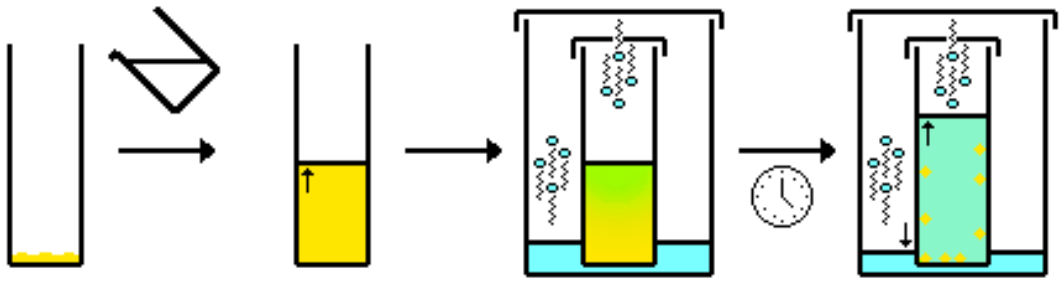

Figure 1.22. Schematic of the vapour diffusion method (taken from reference [137]).

1.5.3. Cooling method (Thermal gradient)

This technique is used to create crystals by decreasing the temperature of the solution, as shown in Figure 1.23.

The mechanism of this method converts the saturated to a supersaturated solution. If the solubility decreases with the temperature of the solution, the lower solubility of the product will lead to crystals. The advantage of this method is a high quality crystal [139].

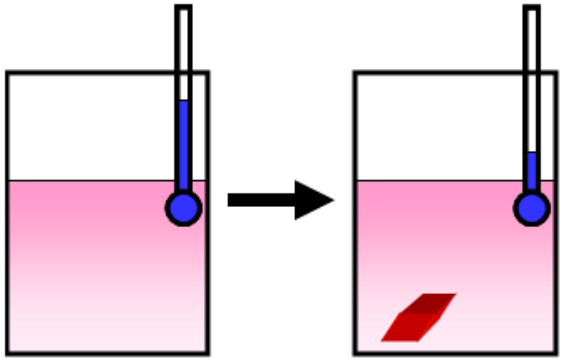

Figure 1.23. Schematic of the cooling method (taken from reference [140]).

1.6. Ligand Selection

The main goal of this research is to construct *4f* and *Fe-4f* coordination clusters in order to study their magnetic and electronic properties and potential applications.

Amino-polyalcohol ligands have been widely used in the synthesis of high spin molecules and SMM.

These ligands combine a central N-donor with oxygen from the alcohol arms which chelate to a metal ion in conjunction with the central N donor as well as forming bridges to further metals through the alkoxy oxygens. Based on HSAB (hard-soft acid-base), the hard-donor oxygen tends to be connected with lanthanide ions while the soft-donor nitrogen tends to be connected with transition-metal ions.

In chapter, three and four different amino-polyalcohol ligands have been used to synthesise four different types of homometallic lanthanide complexes as seen from their topology and magnetic properties.

Amino-polyalcohol ligands represent the major ingredient of the synthesis, often acting as the main ligand. In some cases, amino polyalcohol ligand is absent from the final product, but is a necessary ingredient in this synthesis since there is no product without it. The amino polyalcohol acts as a base to deprotonate the oxygens. It can be a protecting buffer of the lanthanide towards further hydrolysis.

1,3-bis-diethanolamino-2-propanol (H_5bdp) ligand (Figure 1.24, a) has been used in chapter three. It is a flexible ligand and it can bind metals in many ways or/and with many coordination modes. It has two N and five O atoms that allow the ligand to coordinate with metal depending on the basicity of the conditions. A review of the literature reveals that the H_5bdp ligand has been bound to the metal in the form of a singly-deprotonated $(H_4bdp)^-$ (Figure 1.24, b), with four-deprotonated $(Hbdp)^{4-}$ (Figure 1.24, c) and five-deprotonated oxygens $(bdp)^{5-}$ (Figure 1.24, d).

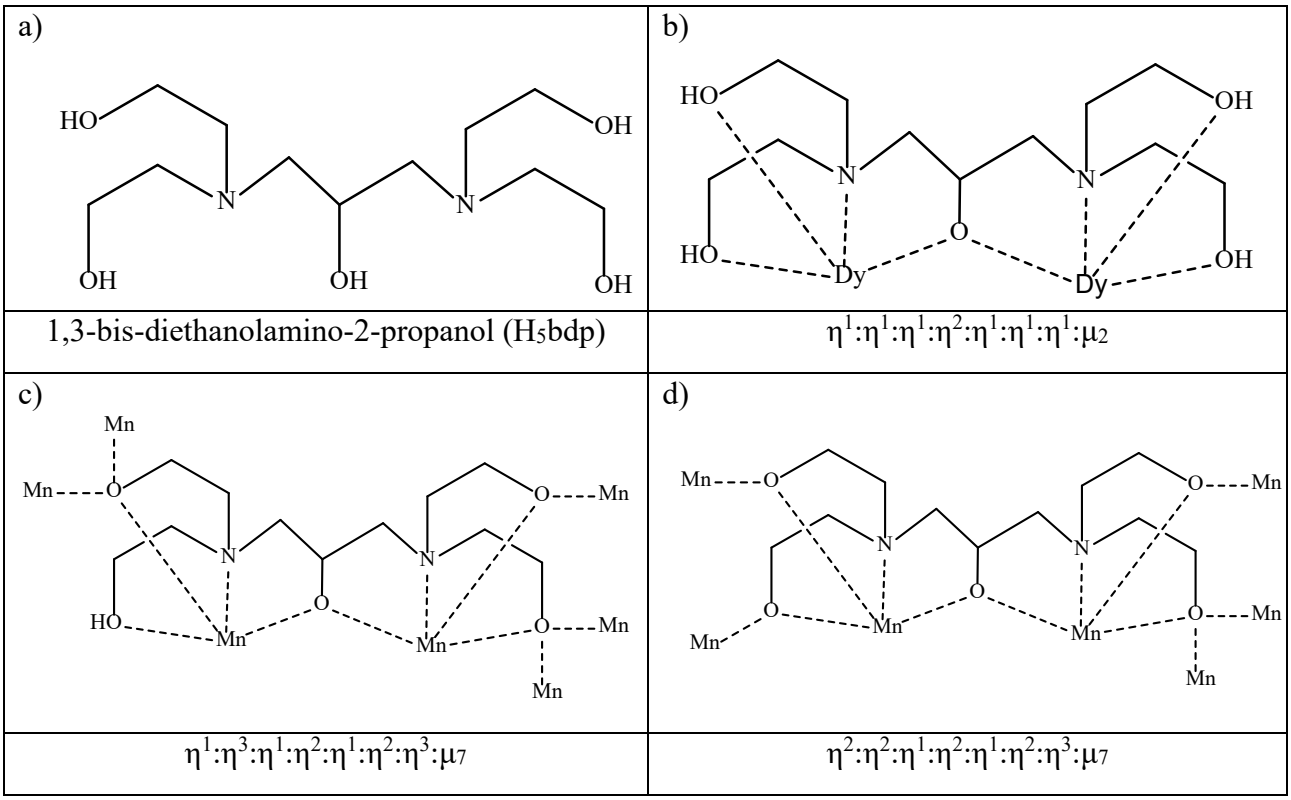

Figure 1.24. H_5bdp ligand (a) coordination mode of H_5bdp ligand Dy_2 from this work (b) and reported (c-d) [141].

Triisopropanolamine ($TipaH_3$) ligand was employed in the synthesis 4*f* (Yb_2 [82]), 3d (Ti [142, 143], V [143, 144], Cu [145, 146]) and 3d-4*f* (Fe-Gd [84]) with different coordination modes and different topologies.

Triisopropanolamine ($TipaH_3$) ligand was used in chapter three as a ligand with chirality. It has three stereogenic centres as shown in (Figure 1.25, a). It can bond to metals in many ways or/and with many coordination modes. It has one N and three O atoms which allow the ligand to coordinate with metal depending on the basicity of the conditions. A review of the literature reveals that the $TipaH_3$ ligand has been bound to the metal in a singly-deprotonated form $(TipaH_2)^-$ (Figure 1.25, b), triply-deprotonated $(Tipa)^{3-}$ (Figure 1.25, c) and also fully protonated ($TipaH_3$) (Figure 1.25, d).

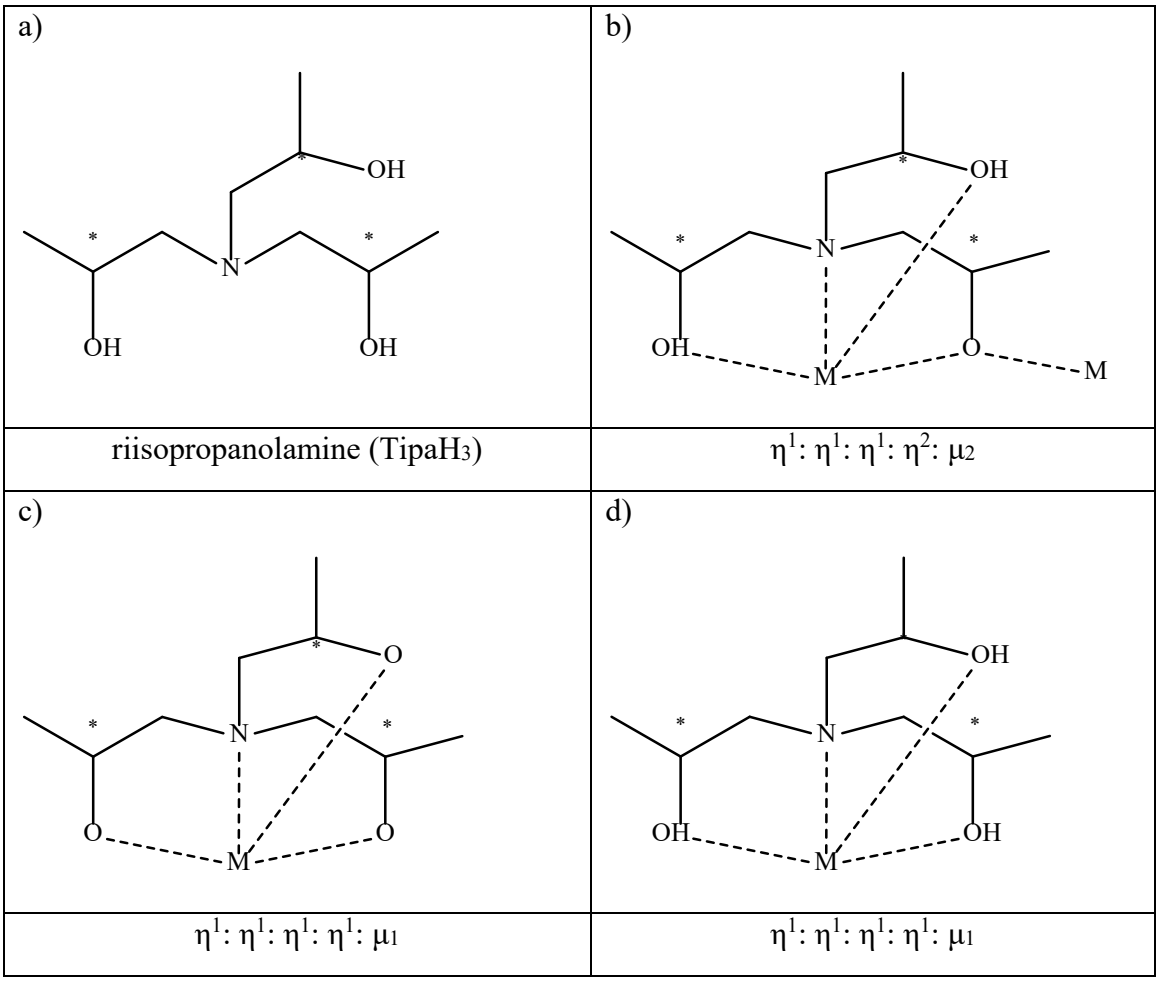

Figure 1.25. Triisopropanolamine ($TipaH_3$) ligand (a) stereocentres marked with (*) and reported coordination modes (b) mode I [82, 145], (c) mode II [142, 143] and (d) mode III [84, 146]

Diisopropanolamine ($dipaH_3$) ligand is employed to synthesise 3d (Fe and Co [147]) with different coordination modes and different topologies.

Diisopropanolamine ($dipaH_3$) ligand (Figure 1.26, a) has been used in chapter three as chiral ligand. It can bond to metals in many ways or/and with many coordination modes. It has one N and two O atoms allowing the ligand to coordinate with the metal depending on the basicity of the conditions. A review of the literature reveals that the $dipaH_3$ ligand has been bound to the metal in singly-deprotonated $(dipaH_2)^-$ (Figure 1.26, b-c) and doubly-deprotonated $(dipaH)^{2-}$ form (Figure 1.26, d).

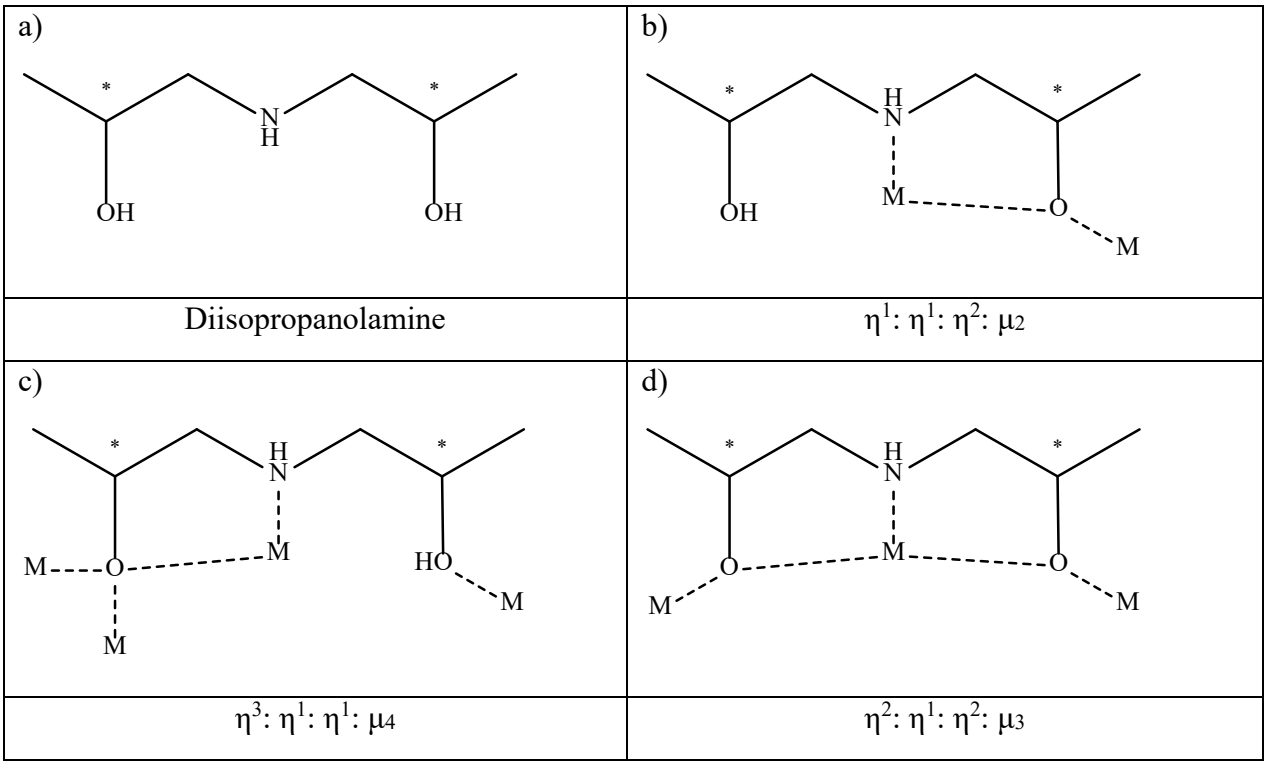

Figure 1.26. Diisopropanolamine ($dipaH_3$) ligand (a) stereocentres marked with (*) and (b-d) coordination modes with reported [147].

In this work, diisopropanolamine ligand is absent in the final product of the Ln_2 (1D polymer) complex but is a necessary in this synthesis. The diisopropanolamine ligand acts as a buffer that protects the dysprosium from further hydrolysis. The benzoate ligand selected to be an auxiliary ligand then becomes the main ligand.

In chapter three, *N*-methyldiethanolamine ligand is absent in the final product of Ln_4 complex but is a necessary in this synthesis. The *N*-methyldiethanolamine ligand acts as a base to deprotonate oxygen from the *o*-vanillin ligand. The *o*-vanillin ligand has selected to be an auxiliary ligand then it becomes the main ligand.

The *o*-vanillin (*o*-van) ligand has three potential O donor atoms for coordination with the metal, e.g. 4*f* [74, 148-162], 3d (V [163], Mn [164], Fe [165, 166],Co [167-181], Ni [173, 175, 182-197], Cu [198-209], Zn [210-212]), 3d-3d (Mn-Ni [213]), Cu-Co [214], Cu-Ni [214], Cu-Zn [214]), 3d-4*f* (Mn-Ln [215], Co-Ln [216], Ni-Ln [217-222], Cu-Ln [223-225] and Zn-Ln [226-230]). There are many potential coordination modes giving rise to different topologies for the metal clusters with a variety of properties (Figure 1.27).

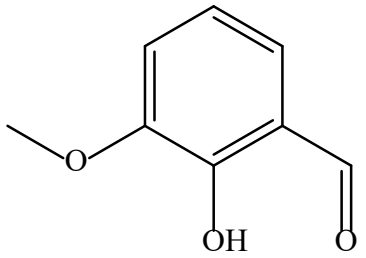	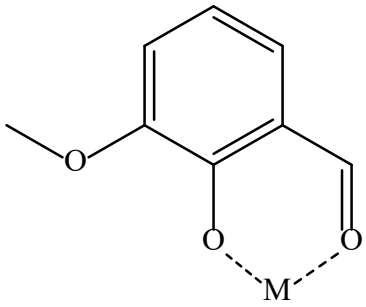	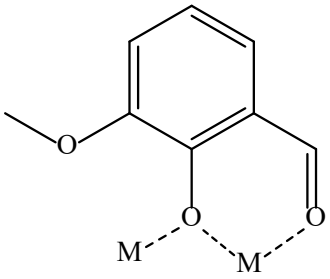
o-vanillin	$\eta^0:\eta^1:\eta^1:\mu_1$	$\eta^0:\eta^2:\eta^1:\mu_2$
	Mode 1	Mode 2
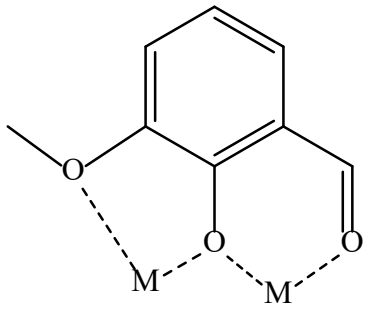	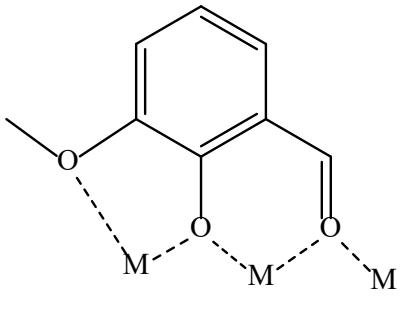	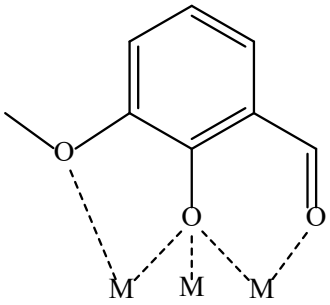
$\eta^1:\eta^2:\eta^1:\mu_2$	$\eta^1:\eta^2:\eta^2:\mu_3$	$\eta^1:\eta^3:\eta^1:\mu_3$
Mode 3	Mode 4	Mode 5

Figure 1.27. *o*-Vanillin and coordination modes reported for *o*-vanillin ligand mode I [149, 151, 153, 154, 163-165, 167-177, 181-192, 198-205, 210, 211, 214, 216, 217, 220, 223, 224, 226-228], mode II [162, 213], mode III [74, 148, 150, 152, 155-162, 166, 178-180, 192-197, 200, 206-209, 212, 218, 219, 221, 222, 225, 229, 230], mode IV [215] and mode V [214, 221].

In this work, different metal to ligand ratios were used along with different metal salt starting material, co-ligand and synthetic strategy.

In chapter four, the auxiliary ligand is the same as in chapter three but Pivalic acid is replaced with sodium azide. It is selected to encourage amino-polyalcohol ligands to construct high-nuclearity complexes. Sodium benzoate is used as an auxiliary ligands in chapter three and four to synthesise lanthanide complexes.

The carboxylic acid works as co-ligand in this work, in order to increase the nuclearity of homo-heterometallic clusters (Figure 1.28).

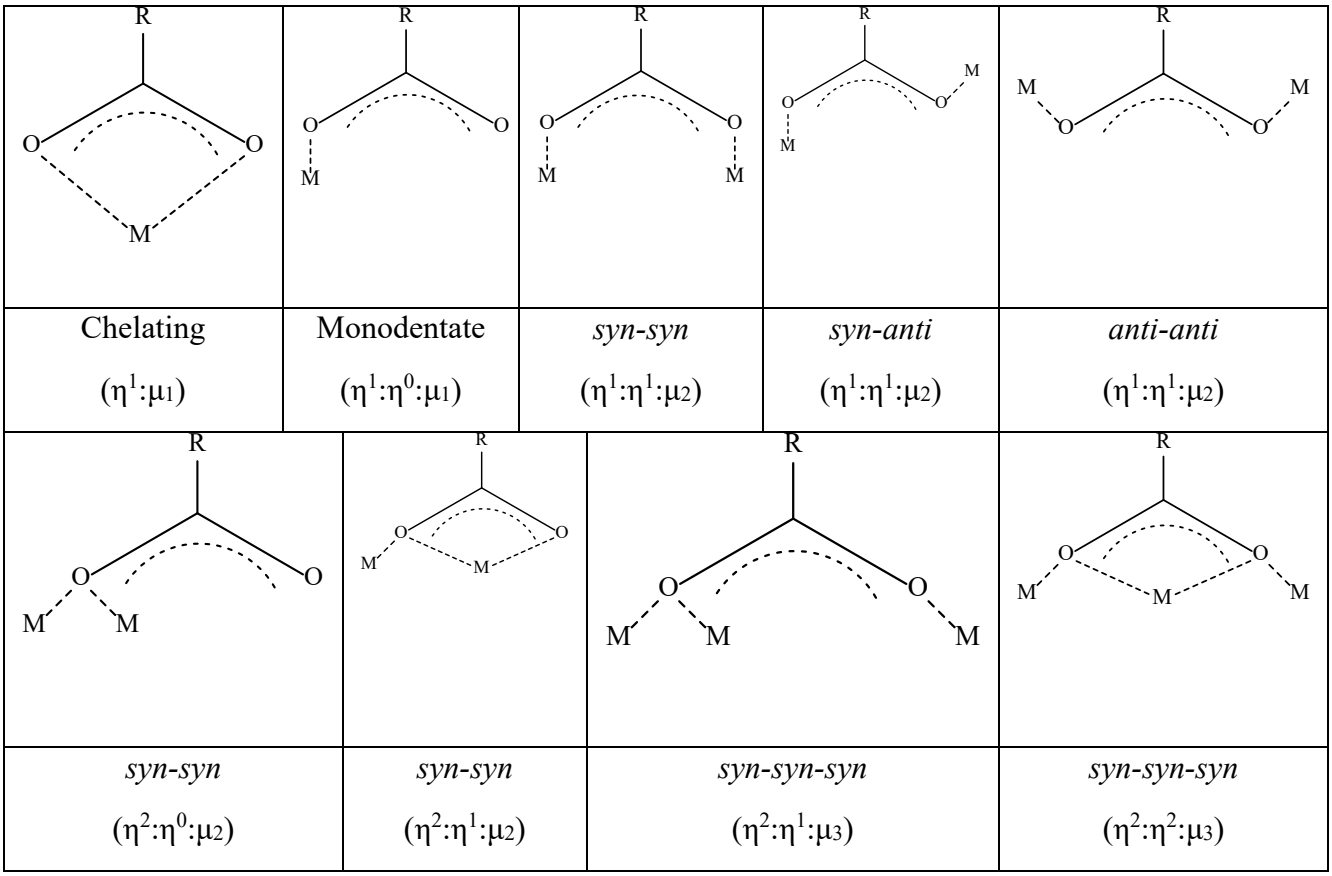

Figure 1.28. Coordination modes of the carboxylate group, commonly.

N-methyldiethanolamine ($mdeaH_2$) ligand is used in chapter four. It is a flexible ligand and it can bond to metals in many ways or/and with many coordination modes. It has one N and two O atoms, which allow the ligand to coordinate with the metal depending on the basicity of the conditions. A review of the literature reveals that the $mdeaH_2$ ligand has been bound to the metal in the form of a singly-deprotonated (mdeaH), doubly-deprotonated ($mdea^{2-}$) and with protonated oxygen atoms ($mdeaH_2$).

The *N*-methyldiethanolamine ligand is flexible and widely employed to synthesise 4*f* [231-234], 3d (Ti [235, 236], Fe [237, 238], Ni [239, 240], Cu [128-131], Zn [128, 241]) and 3d-4*f* (Cr-Ln [242-247], Mn-Ln [248-252], Fe-Ln [79, 80, 89, 253], Co-Ln [254-259], Cu-Ln [260]) with different coordination modes and different topologies. *N*-methyldiethanolamine and its coordination modes are shown in Figure 1.29.

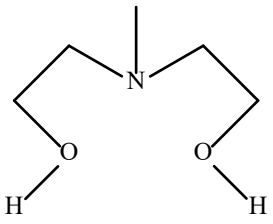	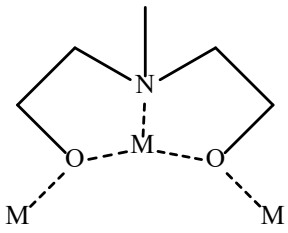	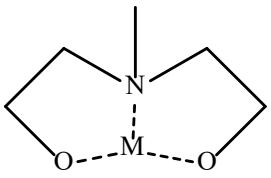
N-methyldiethanolamine	$\eta^2:\eta^1:\eta^2:\mu_3$	$\eta^1:\eta^1:\eta^1:\mu_1$
	Mode 1	Mode 2
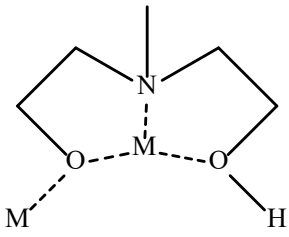	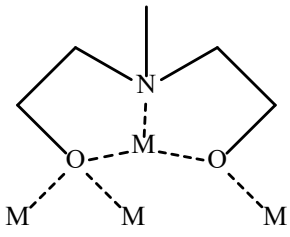	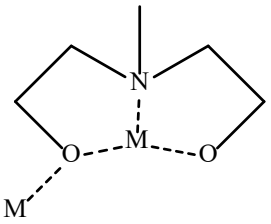
$\eta^2:\eta^1:\eta^1:\mu_2$	$\eta^3:\eta^1:\eta^2:\mu_4$	$\eta^2:\eta^1:\eta^1:\mu_2$
Mode 3	Mode 4	Mode 5
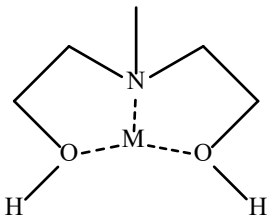	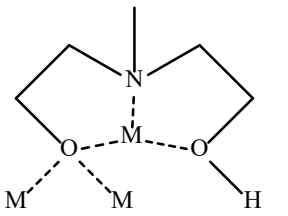	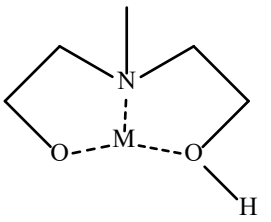
$\eta^1:\eta^1:\eta^1:\mu_1$	$\eta^3:\eta^1:\eta^1:\mu_3$	$\eta^1:\eta^1:\eta^1:\mu_1$
Mode 6	Mode 7	Mode 8

Figure 1.29. *N*-methyldiethanolamine and its coordination modes reported (mode I [79, 80, 233, 234, 242-249, 253-255, 257, 258], mode II [232, 241], mode III [231, 251, 259], mode IV [89, 251, 252, 256], mode V [235-238, 250], mode VI [128-131, 234], mode VII [239, 240, 260] and mode VIII [234]).

In chapter four *N*-methyldiethanolamine ($mdeaH_2$) is selected as the main ligand to synthesise four different series of Fe^{III}/Ln^{III} metal complexes. Magnetic studies indicate the influence of changing co-ligand and synthetic procedure.

Use of auxiliary ligands in conjunction with *N*-methyldiethanolamine ligands helps to construct high-nuclearity complexes. Often the auxiliary ligands are carboxylates such as benzoate and

Pivalate. These carboxylates act as a bridge or/and chelate and often act to complete the coordination sphere of metal. Therefore, benzoate and Pivalate have been used as an auxiliary ligand in this thesis to obtain Fe-Ln and 4*f* metal complex. In addition, sodium azide is common in Fe-Ln chemistry and can bridge or/and complete coordination sphere of metal ions.

1.7. Thesis Overview

This thesis describes the synthesis of homo-and heterometallic complexes which have been characterised crystallographically and it investigates the optical and magnetic properties. The research results are divided into three chapters (3, 4 and 5).

Chapter 3 describes the synthetic strategy, crystal structures, magnetic and optical investigations (photoluminescence) of homometallic lanthanide complexes by using four different amino-polyalcohol ligands (H_5bdp, dipaH_3, TipaH_3 and mdeaH_2) along with co-ligands such as (benzoate, Pivalate and *o*-vanillin). Some of these compounds are magnetically, optically investigated and presented.

Chapter 4 represents the synthetic strategy crystal structures, optical (photoluminescence) and magnetic investigations of heterometallic *Fe-4f* complexes using mdeaH_2 as the main ligand along with co-ligands such as benzoate, sodium azide, di(2-pyridyl) ketone or *o*-vanillin. Some of the compounds are optically and magnetically investigated and presented.

Chapter 5 describes the synthesis of two binuclear copper (II) complex incorporating with 2,2′-bipyridine (bpy) and benzylphosphonic acid ($PhCH_2PO(OH)_2$) ligands. These were tested for the transmission in the visible-NIR region of the electromagnetic spectrum. In addition, they were used as thin film on glass substrate to test their potential for use in energy saving glass. The compounds are promising for this application. Furthermore a preliminary test for microwave transmission showed that a mobile phone still receive signals when put in a box simulating the construction a modern office building.

Chapter 6 summarises the conclusion of the thesis.

Chapter 7 describes the experimental part of the thesis in detail.

Chapter 8 summarises crystallographic data and shape analysis of coordination complexes.

Chapter 9 describes characterisation techniques.

Chapter 10 contains all Appendix items.

Chapter 11 contains the bibliography which supports the whole research work structure.

Chapter 2. Goal and Objectives

It has been observed that coordination clusters can exhibit SMM behaviour and optical properties. In coordination chemistry, it is still difficult to control the key parameters for such behaviour in an existing cluster, because it is difficult to control the arrangement of the metal ions, the relative orientations of the single-ion anisotropy axes and the magnetic coupling between them. These factors all have profound effects on the height of the energy barrier to spin reorientation, the splitting of the magnetic states and the possibilities of Quantum Tunneling of the magnetisation.

The creation of a molecular compound that has multifunctionality is very important in many high-technology applications and everyday technology. Lanthanide and iron ions are considered as ideal candidates for the construction of complexes exhibiting magnetic (SMM behaviour and magnetic cooler) and optical (photoluminescent) properties.

Single-molecule magnets are considered as an interesting class of compounds with potential applications in fields of industrial and modern technology such as in highly efficient data storage systems, quantum computers, molecular coolers and contrast agents.

The key requirement for SMM behaviour is a combination of sufficient spin and uniaxial anisotropy within the molecule. Some metal ions such as Cr^{III}, Mn^{II}, Fe^{III} and Gd^{III} can contribute high spin but minimal anisotropy whereas others such as Mn^{III}, Co^{II} and most of the trivalent lanthanide ions can contribute high single-ion anisotropy.

The fact that the magnetic anisotropy is a major requirement to see SMM behaviour explains well the intense attention of many groups to incorporate lanthanide ions (homometallic complexes) or in combination with 3d transition metal ions in the same coordination complex (heterometallic 3d-4*f* complexes). Combining 3d and 4*f* means combining the high, predominantly anisotropic moments of lanthanide ions (e.g. Tb or Dy) with the high-spin states of many transition metal ions (Fe, Cr).

SMMs are among the most complex magnetic entities that show quantum phenomena like quantum tunneling of the magnetisation [261], quantum interference or quantum coherence and they have been postulated as candidates for spin qubits in quantum computing [136, 262, 263].

A further characteristic of lanthanide ions is the ability to emit radiation often in the visible range (we focus on those) as well as in NIR regions of the electromagnetic spectrum when excited with short wavelength light. The 4*f*-4*f* electronic transitions are responsible for light emission.

The present work has been motivated by the need to obtain new homometallic lanthanide complexes and heterometallic iron-lanthanide complexes and find the possible applications in industrial and everyday technology.

In order to construct such polynuclear complexes in the principle of self-assembly of the paramagnetic metal ions with suitable ligands like amino-polyalcohol ligand was applied. Amino-polyalcohol ligands have been used to synthesise 3d, 4*f* and a 3d-4*f* metal complexes. Based on the resulting structure, magnetic and optical properties, further attempts were made to extend the systems to explore optical and magnetic properties of homometallic lanthanide complexes and heterometallic iron-lanthanide complexes. This work examines the synthesis, structure, optical and magnetic properties of 3d–4*f* and 4*f* coordination compounds with amino-poly-alcohol ligands and their magnetic and optical properties.

Amongst the motivations for this was to investigate the possibility to use compounds in quantum computer devices through the properties of the metal complex as SMM behaviour, which can be employed to build the smallest magnetic memory. In addition, to explore their luminescence which may be used in OLEDs. The magnetocaloric effect, which can be used for refrigeration was also investigated.

In particular, Dy and Tb ions have magnetic anisotropy and high spins so that their complexes may show SMM behaviour. Gd as an isotopic metal is suited for magnetocaloric effects and these were evaluated for performances and efficiencies as magnetic refrigerants.

The optical properties have been studied of lanthanides and iron-lanthanide metal complex of Tb and Eu. These exhibit emission bands in the visible region. Therefore, the metal complexes have been studied to explore the electronic spectra and luminescence.

The goal of chapter five is to synthesise copper (II) complexes which are known to absorb in parts of the visible and NIR regions when coordinated by 2,2′-bipyridine and benzylphosphonic acid ($PhCH_2PO(OH)_2$) ligands. Such coatings have potential applictions in ESG.

Chapter 3. Structure, optical and magnetic properties of lanthanide aggregates

3.1. Introduction

Lanthanide complexes have gained the attention of researchers around the world due to their photo-physical and magnetic properties with potential applications in medicine (e.g. as photosensors or as agent for MRI) quantum materials with both unusual photophysical and exotic magnetic properties in addition to catalytic application, luminescent materials and commercial permanet magnets [264, 265]. Due to their unique and useful electronic, optical and magnetic properties [266], lanthanide complexes have potential application fields in industrial and in everyday technology such as in molecular optoelectronic devices, high-density data storage, laser materials, catalysis, quantum-based spintronic devices, OLEDs, metallurgy, MRI agents and electronic video displays [264-270]. Lanthanide complexes are uses in OLEDs because the luminescence lifetimes of lanthanide complexes (milliseconds-microseconds) are longer than organic dyes (nanoseconds) [271, 272]. Magnetic material in nanoscale has driven by the rapid growth in high-density magnetic storage devices and high-speed computers with the promise of a revolution in information technology [70, 273, 274]. Dy^{3+}, Tb^{3+}, Ho^{3+} and Er^{3+} ions have a higher magnetic anisotropy than the left side of lanthanide series ($4f^n$, $n < 7$), therefore they are widely uses to obtain SMM, especially the Dy^{III} ion [275, 276]. One of the objectives of this chapter is to produce lanthanide complexes that could be used to develop quantum computer.

A review of the literature shows that homonuclear lanthanide complexes have been reported using different types of ligand and co-ligand. The commercial and synthesised ligand contains one or more donor atoms (O, N and S donors) which allows access to coordination complexes with different nuclearity. Lanthanide ions prefer binding with oxygen donors (neutral or /and negative charge) or/ and nitrogen donors. Some triangular Dy_3 complexes present a new concept for magnetic memory without a net magnetic moment [74, 75]. These show a vanishing susceptibility at low temperature which is unexpected in a system having an odd number of unpaired electrons. Amino-polyalcohol ligands have been used in the literature due to containing polydentate chelating and having two donor atoms N and O. Many lanthanide complexes have been reported in the literature and those involving amino polyalcohol ligands and their modifications are an important subset.

A review of the literature reveals that amino-polyalcohol based ligand, their modifications, or a part of the ligand contains diethanolamine have been employed to synthesise 53 series of Ln complexes. Table 3.1, presents 53 series of Ln complexes from the literature and 2 compounds from this work which were synthesised using amino-polyalcohol ligands.

Table 3.1. Ln^{III} complexes based on amino-polyalcohol ligands with Dy SMM listed.

NO	Structure	Ln	Dy SMM	Ref
1	$[Ln(bheg)_2(MeCO_2)(H_2O)_4]$	La-Nd	NM	[277]
2	$[Ln(MeCO_2)(bicH_2)(phen)(H_2O)](ClO_4)\cdot phen\cdot 3H_2O$	Gd,Er,Pr,Nd	NM	[278]
3	$[Ln(teaH_3)_2(MeCO_2)](MeCO_2)_2]\cdot 0.5Py$	Ce, Pr	NM	[279]
4	$[Ln_2(MeCO_2)_4(teaH_2)_2]$	Gd, Dy-Er	Not	[279]
5	$[Dy_2(LH_2)_2(\mu^2\text{-Piv})](Cl)\cdot 2MeOH\cdot H_2O$	Dy	Not	[280]
6	$[Ln_2(mdeaH_2)_2(Piv)_6]$	La- Gd	NM	[232]
7	$[Ln_2(H_2L)_2(\mu\text{-Piv})_2(Piv)_2]\cdot 2CHCl_3$	Eu-Dy	SMM	[281]
8	$[Ln_2(TipaH_2)_2(Piv)_4]$ (**6-9**)	Gd-Er	SMM	This work
9	$[Dy_2(tea)_2(PhCO_2)_4\cdot 2H_2O]$	Dy	Not	[282]
10	$[Dy_2(teaH_2)_2(PhCO_2)_4]\cdot 2H_2O$	Dy	Not	[283]
11	$[Yb_2(TipH_2)_2(PhCO_2)_4]$	Yb	NM	[82]
12	$[Ln_2(H_4bdp)(PhCO_2)_2(NO_3)_2]\cdot(NO_3)$	Dy	SMM	This work
13	$[Dy_4(LH)_2(\mu_3\text{-}OH)_2(Piv)_4(MeOH)_2]\cdot 4MeOH\cdot 2H_2O$	Dy	SMM	[280]
14	$[Ln_4(\mu_3\text{-}OH)_2(mdeaH)_2(Piv)_8]$	Tb-Tm	SMM	[231]
15	$[Ln_4(LH)_2(\mu_2\text{-Piv})(Piv)(\mu_3\text{-}OH)_2]\cdot xH_2O\cdot yMeOH\cdot zCHCl_3$	Tb-Yb	SMM	[284]
16	$[Ln_4(LH_2)_2(O_3P^tBu)_2(\mu_2\text{–}\eta^1\eta^1\text{tfa})_2]\cdot(Cl)_2\cdot xMeOH\cdot yH_2O$	Gd-Dy	SMM	[285]
17	$[Ln_6(H_3L)_6(PhCO_2)_6]\cdot(2H_2O)_x\cdot(C_7H_8)_y$	Gd-Dy	Not	[286]

18	$[Ln_8(LH_2)_4(\mu_2\text{-}Piv)_4(Piv)_4(\mu_2\text{-}OMe)_4]\cdot xCH_3OH\cdot yH_2O$	Gd-Ho	SMM	[287]
19	$[NaCe_{10}O_7(OH)(ib)_{14}(HCO_2)(mdea)_5]$	Ce	NM	[233]
20	$[La(Bis\text{-}Tris)_2](Cl)_3$	La	NM	[288]
21	$[Pr(teaH_3)_2(NO_3)](NO_3)_2$	Pr	NM	[289]
22	$[La(Theen)(Pic)(H_2O)_2](Pic)_2]\cdot 2H_2O$	La	NM	[290]
23	$[Ln(teaH_3)_2](CF_3SO_3)_3$	Pr, Yb ,Lu	NM	[291]
24	$[La(NO_3)(teaH_3)_2](NO_3)_2$	La	NM	[292]
25	$[La(teaH_3)_2(H_2O)_2](Pic)_3$	La	NM	[290]
26	$[Dy_2(HL_1)_2(NO_3)_4]$	Dy	SMM	[293]
27	$[Dy_2(HL_3)_2(NO_3)_4]$	Dy	SMM	[293]
28	$[Gd_2(H_3L)_2(NO_3)_2](NO_3)_2$	Gd	NM	[294]
29	$[Eu(teaH_3)_2](ClO_4)_2$	Eu	NM	[295]
30	$[Yb(teaH_3)_2]_2(ClO_4)$	Yb	NM	[296]
31	$[Dy_2L(H_2L)(teaH_2)(o\text{-}van)(H_2O)](ClO_4)_2\cdot 2CH_3OH$	Dy	SMM	[153]
32	$[HNEt_3]_x[Ln_2(LH_4)_2(dbm)_2](NO_3)_y$	Gd, Dy	SMM	[297]
33	$[Ln_2(teaH_2)_2(NO_3)_4]$	Pr, Gd-Ho	Not	[289]
34	$[Gd(Hsabhea)(NO_3)]_2\cdot 2MeOH$	Gd	NM	[298]
35	$[Gd(teaH_2)(NO_3)_2]_2\cdot 2MeOH$	Gd	NM	[299]
36	$[Gd_3(HL)(H_2L)(NO_3)_4]\cdot C_2H_5OH$	Gd	NM	[294]
37	$[Dy_3(OH)(teaH_2)_3(paa)_3](Cl)\cdot 2MeCN\cdot 4H_2O$	Dy	Not	[157]
38	$[Ln_3(OH)(teaH_2)_3(paa)_3](Cl)_2$	Tb-Ho	Not	[300]
39	$[Dy_3(HL)(H_2L)(NO_3)_4]\cdot EtOH$	Dy	SMM	[301]
40	$[Gd_2(teaH_2)(teaH)(NO_3)_3]_2\cdot MeOH$	Gd	NM	[299]
41	$[Dy_4(dhampH_3)_4(NO_3)_2](NO_3)_2$	Dy	SMM	[302]
42	$\{[(C_5H_5)Ln(npdea)]_4(\mu_4\text{-}Cl)\}[Na(DME)_4]$	Sm, Yb	NM	[303]
43	$[Gd(teaH)(NO_3)]_6\cdot 8MeOH$	Gd	NM	[299]
44	$[Ln_6(teaH)_6(NO_3)_6]\cdot 8MeOH$	Tb-Er	SMM	[304]

45	$[Dy_6(Me\text{-}teaH)_6(NO_3)_6]\cdot 6MeCN$	Dy	Not	[305]
46	$[Dy_6(apadH_2)_6(NO_3)_6]\cdot 2THF$	Dy	SMM	[305]
47	$[Dy_6(teaH)_6(NO_3)_6]\cdot 3DMF\cdot H_2O$	Dy	Not	[304]
48	$[Dy_6(pdeaH)_6(NO_3)_6]$	Dy	SMM	[300]
50	$[Ln_6(teaH)_6(NO_3)_6]\cdot 8MeOH$	Gd, Dy	Not	[306]
51	$[Ln_6(teaH)_2(teaH_2)_2(CO_3)(NO_3)_2(chp)_7(H_2O)](NO_3)\cdot 4\cdot 5MeOH\cdot 1\cdot 5H_2O$	Gd-Dy	SMM	[307]
52	$[Dy_8(OH)_6(teaH)_6(teaH_2)_2(teaH_3)_2](CF_3SO_3)_4$ $0.5MeOH\ 2H_2O$	Dy	SMM	[157]
53	$[Gd_9(OH)_{10}(mdea)_4(mdeaH)_2(mdeaH_2)_2(NO_3)_7(CH_3OH)_4]$	Gd	NM	[234]
54	$[Ce_{13}O_8(phdea)_{18}]$	Ce	NM	[308]
55	$[Gd_{32}(OH)_{54}(mdea)_{12}(NO_3)_{12}(H_2O)_{24}](OH)_6\cdot 24CH_3OH\cdot 30H_2O$	Gd	NM	[234]

SMM means Dy is SMM, NM means not measured and Not means does not display SMM.

Carboxylate have been used widely as a co-ligand to build up high nuclearity lanthanide complexes. A review of the literature reveals that 17 series (1-19 of Table 3.1) out of 53 homometallic lanthanide complexes based on amino-polyalcohol ligand incorporating carboxylates have been reported so far. Four series incorporate acetic acid, four series incorporate benzoic acid, seven series incorporate Pivalic acid, one series incorporates trifluoroacetic acid and one series incorporates isobutyric acid.

In this thesis, four new series were successfully synthesised and characterised using amino-polyalcohol ligand as the main ligand supported by an auxiliary carboxylate co-ligand. The co-ligand was changed in the series in order to study the effect of the co-ligand on the structure as well as the magnetic and optical properties.

The nuclearity and topology depend on the strength of co-ligand and coordination modes of the ligand. The coordination modes of the carboxylate presented here can be divided into three types: bridging, bridging-chelating and terminal (monodentate and chelating). Changing the co-ligand leads to a change in nuclearity as well as in the resulting magnetic properties. The carboxylate group has proven to be a useful functional group to obtain high-nuclear clusters of lanthanide

species which can act as a main ligand or co-ligand. Carboxylate ligands include benzoate, Pivalate, acetate and isobutyrate are all commonly used for assembling Ln^{III} complexes. Changing ligand allowed change in magnetic properties.

The first series comprises one representative binuclear dysprosium complex and was obtained by using 1,3-bis-diethanolamino-2-propanol (H_5bdp) ligand, iron-benzoate ($Fe_3O(PhCO_2)$) and $Dy(NO_3)_3$. A binuclear $[Dy_2(H_4bdp)(PhCO_2)_2(NO_3)_2]$ (NO_3) MeCN, system with a novel core was successfully synthesised, characterised and the magnetic properties were investigated.

The second series comprises isostructural binuclear Ln complex and was obtained by using diisopropanolamine ligand ($dipaH_3$), iron-benzoate ($Fe_3O(PhCO_2)$) and $Ln(NO_3)_3$. A binuclear $[Ln_2(PhCO_2)_6(CH_3OH)_4]_\infty$ (Ln= Eu-Dy), system provides a novel core as 1D polymer and was fully synthesised, characterised, the optical and magnetic properties were also investigated.

The third series comprises the binuclear Ln complex and was obtained by using triisopropanolamine ($TipaH_3$), iron-Pivalate ($Fe_3O(Piv)$) and $Ln(NO_3)_3$. A binuclear $[Ln_2(TipaH_2)_2(Piv)_4]$ (Ln= Eu-Dy), system with a novel core was successfully synthesised, characterised and the magnetic properties were investigated.

The fourth series comprises isostructural tetranuclear Ln complexes and was obtained by using *N*-methyldiethanolamine ($mdeaH_2$), *o*-vanillin (*o*-van), Pivalic acid and $LnCl_3$. A tetranuclear butterfly complex $[Ln_4(\mu_3\text{-}OH)_2(o\text{-}van)_4(Piv)_6]$ 2MeCN (Ln= Eu-Dy) was successfully synthesised, characterised and the magnetic properties were investigated.

3.2. Structure and magnetic properties of $[Dy_2(H_4bdp)(PhCO_2)_2(NO_3)_2]NO_3 \cdot MeCN$ (1)

3.2.1. Synthetic description

The reaction of $[Fe_3O(PhCO_2)_6(H_2O)_3](PhCO_2)$, $Dy(NO_3)_3 \cdot 6H_2O$ and 1,3-bis-diethanolamino-2-propanol (H_5bdp) in a molar ratio of 1:1:4 in MeCN over stirring and heating for two hours and afforded colourless needles of a new binuclear Dy^{III} cluster $[Dy_2(H_4bdp)(PhCO_2)_2(NO_3)_2]NO_3 \cdot MeCN$ (**1**).

3.2.2. Crystal structure of $[Dy_2(H_4bdp)(PhCO_2)_2(NO_3)_2]$ $NO_3 \cdot MeCN$

The structure of compound **1** was characterised by single-crystal X-ray diffraction (full crystallographic data is given in Table 8.1) as shown in Figure 3.1. The purity of the phase is confirmed by powder X-ray diffraction (PXRD) (Figure 3.2).

The crystal structure of the binuclear complex $[Dy_2(H_4bdp)(PhCO_2)_2(NO_3)_2]NO_3 \cdot MeCN$ (**1**) is described in detail**.** The compound **1** crystallises in the orthorhombic space group *P*na2$_1$ with Z = 4. Compound **1** is a monocation complex with the charge balanced by a lattice nitrate and there is one lattice MeCN in the asymmetric unit of the lattice. However, it loses the lattice MeCN per molecule after dry according to elemental analyses.

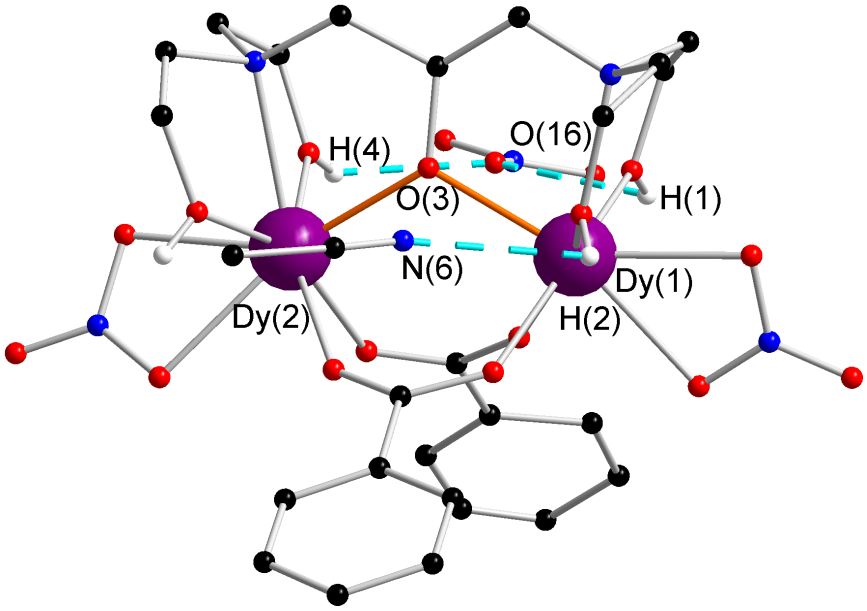

Figure 3.1. Molecular structure of compound **1**. Colour code: black, red, blue, white and violet spheres represent C, O, N, H and Dy, respectively. Some of the H atoms are omitted for clarity.

The H_5bdp ligand (Figure 3.3, a) and benzoate are coordinating to the metal centre of Dy atoms as shown in the crystal structure. The compound **1** consists of two Dy^{III} ions, a singly-deprotonated oxygen $(H_4bdp)^-$ ligand resulting in one negatively charged oxygen atom O(3) bridging two neighbouring Dy^{III} ions, two *syn-syn* -bridging benzoate and two chelated nitrate anions NO_3^-. A singly-deprotonated $(H_4bdp)^-$ ligand displays the (η^1: η^1: η^1: η^2: η^1: η^1: μ_2) coordination mode

both bridging and chelating the two Dy metal centres (Figure 3.3, b). The H_5bdp ligand has successfully been used to synthesise binuclear {Ln_2} complex.

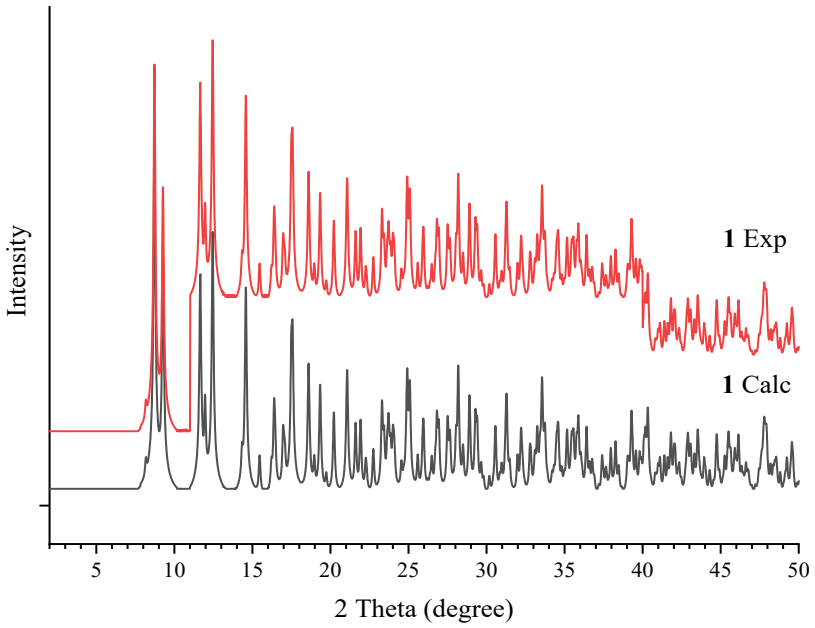

Figure 3.2. Calculated (black) and experimental (red) powder X-ray diffraction (PXRD) patterns of compound **1**.

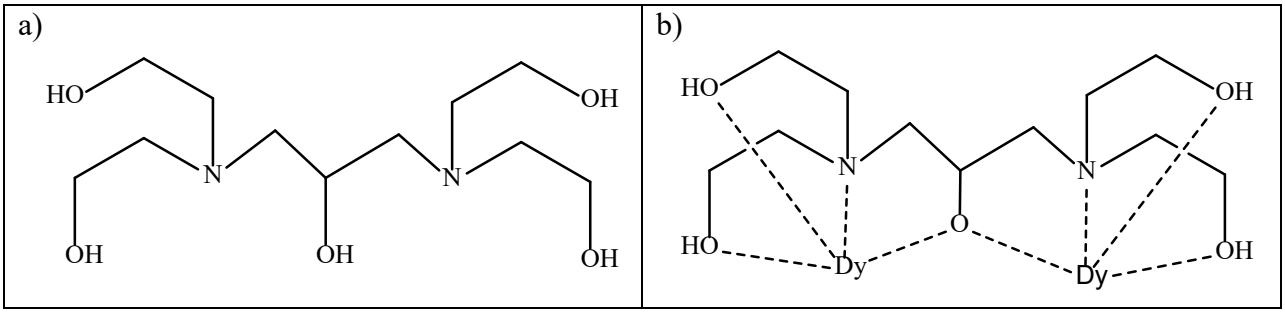

Figure 3.3. (a) H_5bdp ligand (b) the coordination mode of *(*H_4bdp)$^-$ ligand.

Both octa-coordinated Dy^{III} ion are surrounded by one N and seven O donor atoms (NO_7). One N and three O atoms come from the singly-deprotonated oxygen (H_4bdp)$^-$ ligand, two O atoms come from the *syn-syn* bridging benzoate ligand and two O atoms come from the chelating nitrate NO_3^- ligand. This results in a distorted triangular dodecahedron geometry which was confirmed by SHAPE analysis [309-312] with a deviation value of 2.02, (Figure 3.4, Table 8.7).

Using SHAPE software has afforded the value of continuous shape measurement (CShM), which is used to quantitatively evaluate how much a particular structure deviates from the ideal shape [312].

The Dy−O and Dy−N bond distances are in the range 2.250(15)−2.481(16) Å and 2.518(17)−2.887(18) Å, respectively. The Dy···Dy distance is 3.962(13) Å. The Dy−O−Dy angle is 119.2(5). Selected bond distances are summarised in Table 3.2.

Intra- and intermolecular interactions are stabilised the structure of compound **1** through hydrogen bonds. O(1)–H(1) and O(4)–H(4) from a single-deprotonated oxygen $(H_4bdp)^-$ ligand make intramolecular hydrogen bond to O(16) from uncoordinated nitrate NO_3^- group. The distances of O(1)···O(16) and O(4)···O(16) are 2.69 and 2.70 Å, respectively. In addition, O(2)–H(2) from a single-deprotonated oxygen $(H_4bdp)^-$ ligand makes an intramolecular hydrogen bond to N(6) from lattice MeCN molecule with a O(2)···N(6) distance of 2.87 Å. O(5)–H(5) from a single-deprotonated oxygen $(H_4bdp)^-$ ligand makes an intermolecular hydrogen bond to O(17) from nitrate NO_3^- counterion of a neighbouring molecule at {1-x, 1- y, -1/2+z} with an O(5)···O(17) distance of 2.70 Å. In addition, O(5)–H(5) from single-deprotonated oxygen $(H_4bdp)^-$ ligand of a neighbouring molecule at {1-x, 1- y, 1/2+z} make an intermolecular hydrogen bond to O(17) from uncoordinated NO_3^- group with an O(5)···O(17) distance of 2.70 Å. Intermolecular interaction results in a 2D supramolecular. The packing of compound **1** is presented in Figure 3.5.

Table 3.2. Selected bond distances (Å) of compound **1**.

Bond distances			Bond distances		
Atom	Atom	Distance /Å	Atom	Atom	Distance /Å
Dy(1)	O(1)	2.377(13)	Dy(2)	O(3)	2.282(12)
Dy(1)	O(2)	2.397(16)	Dy(2)	O(4)	2.388(14)
Dy(1)	O(3)	2.311(11)	Dy(2)	O(5)	2.390(2)
Dy(1)	O(6)	2.250(15)	Dy(2)	O(7)	2.300(14)
Dy(1)	O(8)	2.262(15)	Dy(2)	O(9)	2.358(16)
Dy(1)	O(10)	2.445(14)	Dy(2)	O(13)	2.432(15)
Dy(1)	O(11)	2.466(18)	Dy(2)	O(14)	2.481(16)
Dy(1)	N(1)	2.518(17)	Dy(2)	N(2)	2.584(16)
Dy(1)	Dy(2)	3.962(13)			

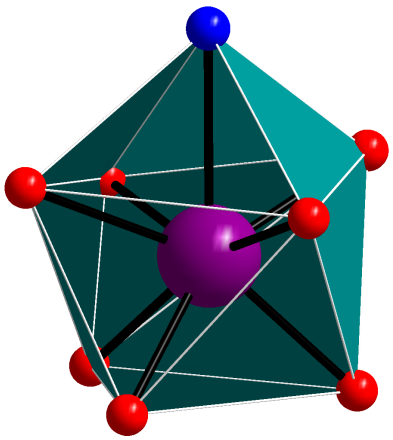

Figure 3.4. Distorted triangular dodecahedron geometry of the 8-coordinated Dy ion. Colour code: red, blue and violet spheres represent O, N and Dy, respectively.

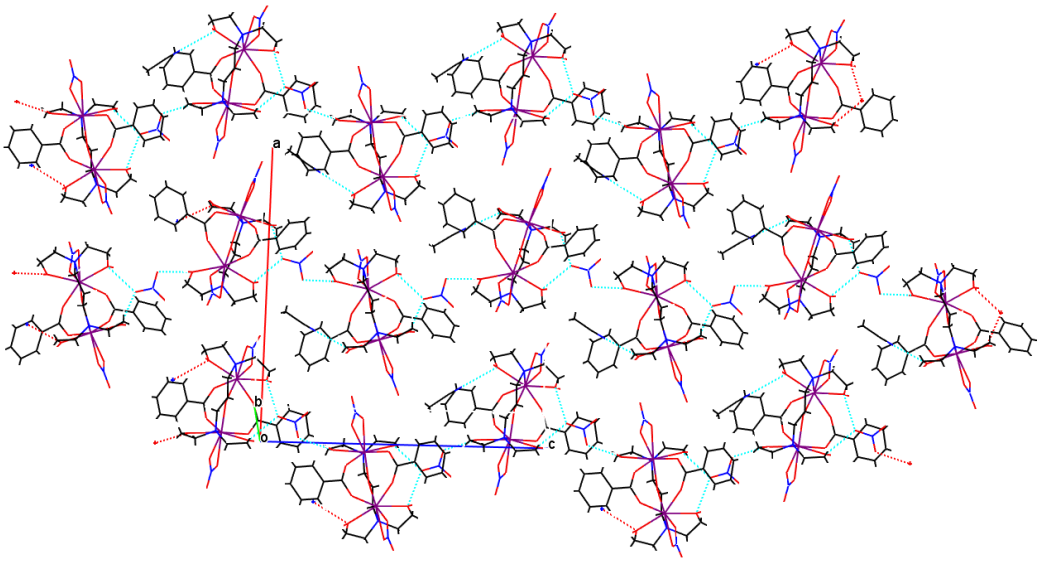

Figure 3.5. The packing structure of compound **1** (2D). Colour code: black, red, blue, white and violet spheres represent C, O, N, H and Dy, respectively.

3.2.3. Magnetic properties

DC magnetic susceptibility of compound **1** was carried out on freshly prepared polycrystalline sample in the temperature range 2-300 K under an applied DC magnetic field of 1000 Oe (0.1 T). The plot of χT versus T for compound **1** is shown in Figure 3.6.

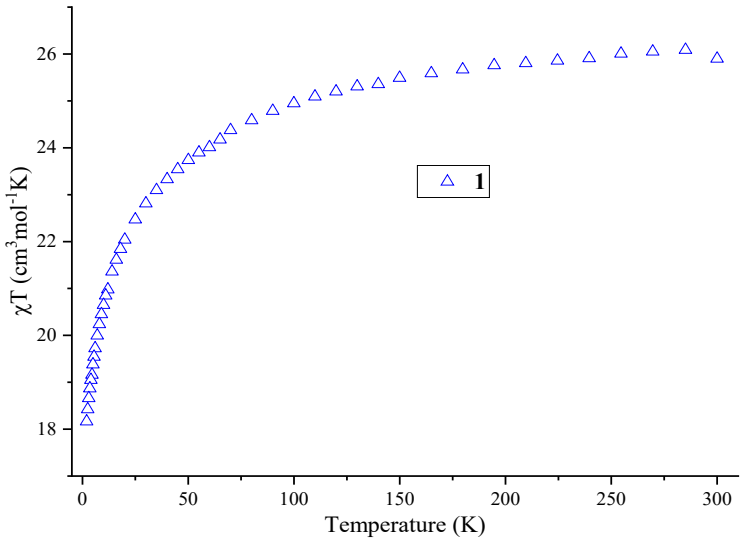

Figure 3.6. Temperature dependence of the χT products for compound **1** at 1000 Oe

The experimental χT value of compound **1** at 300 K is 25.90 $cm^3mol^{-1}K$ which is lower than the expected value of 28.34 $cm^3mol^{-1}K$ for two non-interacting Dy^{III} ions ($^6H_{15/2}$, S = 5/2, g = 4/3, L = 5, C = 14.17 $cm^3mol^{-1}K$) [276]. The χT product decreases slightly between 300 to 70 K followed by a rapid decrease from 70 to 2 K, reaching a value of 18.16 $cm^3mol^{-1}K$ at 2 K.

The decrease of χT experimental values with the temperature is probably due to the thermal depopulation of the Stark sublevels of Dy^{III} ions and/or antiferromagnetic interactions between the Dy^{III} ions [313, 314].

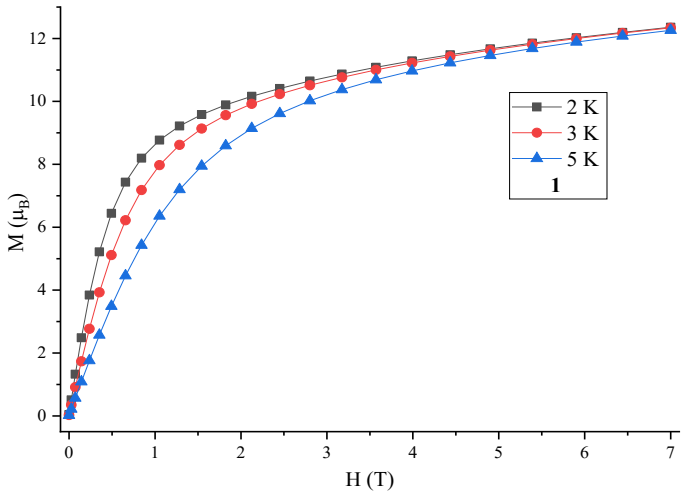

Figure 3.7. Field dependence of magnetisation at indicated temperatures of compound **1**.

The field dependence of the magnetisation of compound **1** was measured at fields ranging from 0 to 70000 Oe (0-7 T) at temperatures of 2 K, 3 K and 5 K.

Figure 3.7 shows the magnetisation values of compound **1** has a relatively rapid increase below 1 T followed by increase linearly up to 7 T, reaching a value of 12.36 μ_B at 2 K and 7 T without saturation indicating the presence of magnetic anisotropy or/and the population of low-lying excited states [315].

AC susceptibility measurements were performed in order to investigate the dynamic magnetic behaviour of compound **1**. The measurements were carried out in the frequency range 1-1488 Hz and in the temperature range 2-12 K. As shown in Figure 3.8, compound **1** shows slow relaxation of the magnetisation below 6 K under an applied DC field of 2500 Oe. The maximum out-of-phase signal has been noticed at 2 K at 2.6 Hz. The frequency dependence of the in-phase and out-of-phase susceptibility of compound **1** shown in Figure 3.9, indicates that compound **1** shows SMM behaviour. The characteristic SMM energy gap U_{eff} of 4.38 K and the pre-exponential factor of τ_o = 8.15× 10^{-3} s were estimated from linear fitting (Figure 3.10) of the data to an Arrhenius law.

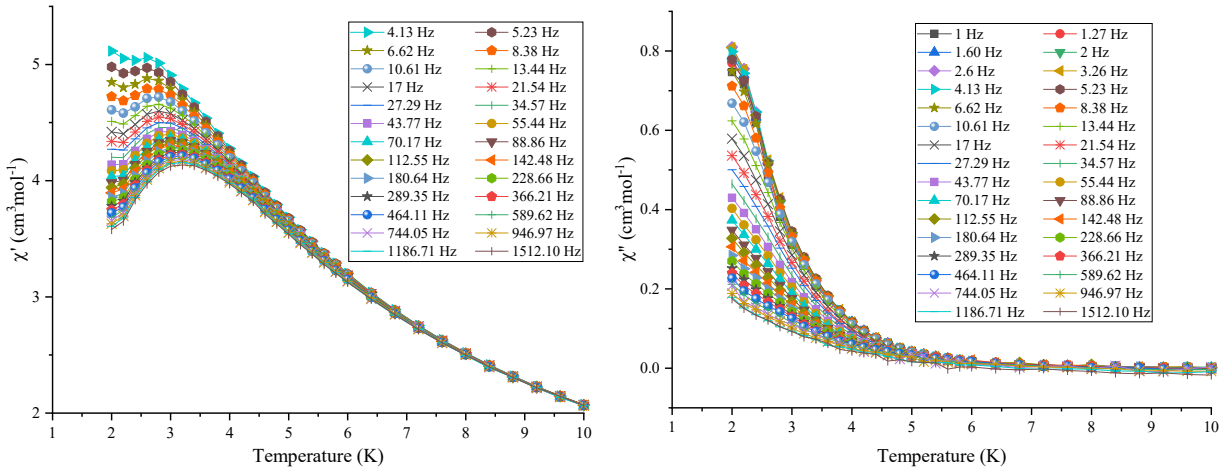

Figure 3.8. Temperature dependence of the in-phase (left) and the out-of-phase (right) components of the AC susceptibility of compound **1** under an applied DC field of 2500 Oe

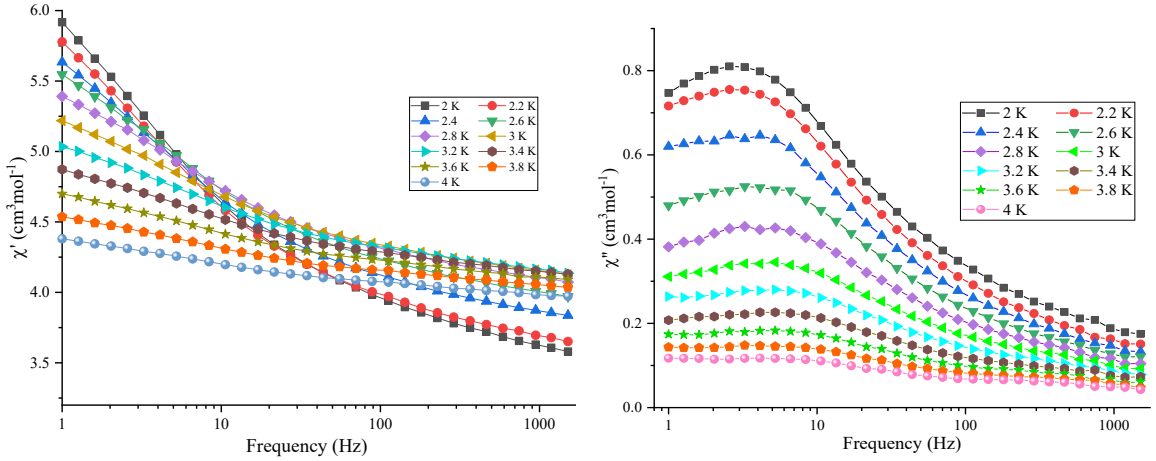

Figure 3.9 Frequency dependence of the in-phase (left) and the out-of-phase (right) components of the AC susceptibility of compound **1** under an applied DC field of 2500 Oe.

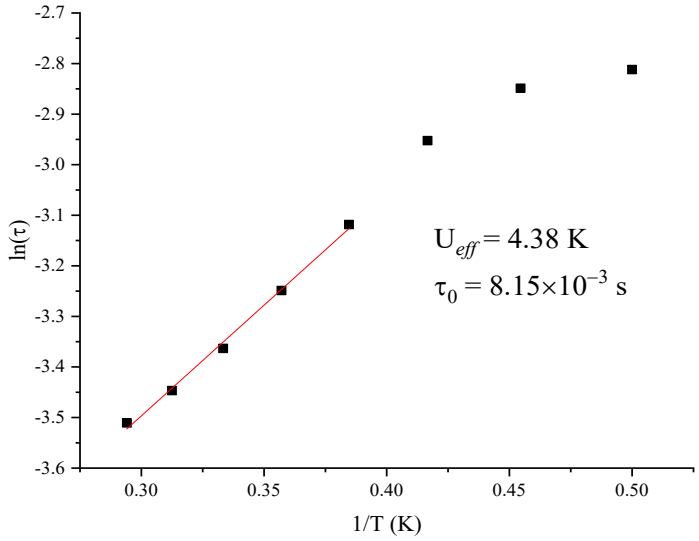

Figure 3.10. Arrhenius plot of compound **1** under an applied DC field of 2500 Oe.

The plot between out-of-phase (χ'') versus in-phase (χ') is to make the various relaxation processes visible; the resultant plot is called Cole-Cole diagram and is generally, useful in characterising the relaxation process and distribution of relaxation time in SMM and SCM. Out-of-phase (χ'') and in-phase (χ') are AC susceptibility components which are extracted from AC data at different temperatures. The Cole-Cole plot of compound **1** was constructed in the temperature range 2-3.2 K. The data were fitted using a generalised Debye model [316, 317] as shown in Figure 3.11. A fit to the plots gave α value are in the range 0.526-0.579 (Table 3.3) which indicate a wide distribution of relaxation time or multiple relaxation process within the compound **1**.

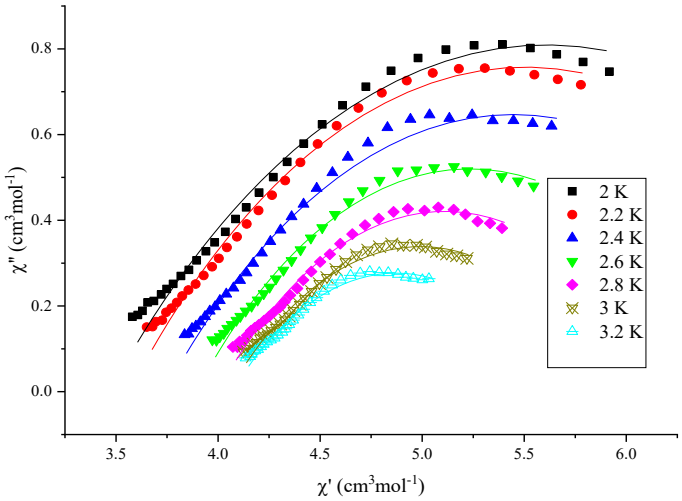

Figure 3.11. Cole-Cole plots of compound **1** under 2500 applied DC field. Solid lines for the fitting using a generalised Debye model.

Table 3.3. Analysis of the Cole-Cole plots of compound **1**.

Temperature (K)	χ_S	χ_T	τ	α	Residual
2	3.47E+00	7.75E+00	9.43E-02	0.540	4.20E-02
2.2	3.56E+00	7.45E+00	9.37E-02	0.526	2.75E-02
2.4	3.74E+00	7.15E+00	9.92E-02	0.539	2.28E-02
2.6	3.89E+00	6.57E+00	6.44E-02	0.528	1.44E-02
2.8	4.00E+00	6.22E+00	5.74E-02	0.539	1.15E-02
3	4.05E+00	5.93E+00	5.73E-02	0.560	8.21E-03
3.2	4.07E+00	5.68E+00	6.32E-02	0.579	6.32E-03

3.2.4. Comparison of the core structure

A review of the literature shows that homonuclear lanthanide complexes have been reported using amino-polyalcohol based ligand incorporating benzoic acid three times and all of them are binuclear, as shown in Table 3.4.

Table 3.4. Binuclear Ln^{III} synthesised using amino-polyalcohol ligands incorporating benzoic acid.

NO of compound	Structure	Ligand	SMMs		Coordination mode of benzoic acid	Ref
			Dy			
			U_{eff} (K)	τ_0 (s)		
1	$[Dy_2(tea)_2(PhCO_2)_4 \cdot 2H_2O]$	Triethanolamine	Not SMM		Chelating	[282]
2	$[Dy_2(H_2tea)_2(PhCO_2)_4]$ $2H_2O$	Triethanolamine	Not SMM		Chelating	[283]
3	$[Yb_2(TipH_2)_2(PhCO_2)_4]$	Triisopropanolamine	Not measured		Chelating and monodentate	[82]
4	$[Dy_2(H_4bdp)(PhCO_2)_2(NO_3)_2]$ (NO_3) (**1**)	1,3-bis-diethanolamino-2-propanol	4.38	8.15×10^{-3}	bridging	This work

As shown in Table 3.4, the first three compounds are absent of SMM behaviour and $\{Dy_2\}$ from this work shows weak SMM behaviour.

1,3-bis-diethanolamino-2-propanol (H_5bdp) ligand has been used to synthesised $\{Mn_{18}\}$ and $\{Mn_{21}\}$ [141], but not used to obtain lanthanide or iron–lanthanide metal complexes. From this perspective, in this work a combination of H_5bdp alongside benzoate as the co-ligand has been employed to obtain higher nuclearity cluster which could provide route toward compound potentially having optical or magnetic properties as well as SMM behaviour, With this synthetic approach $[Dy_2(H_4bdp)(PhCO_2)_2(NO_3)_2]$ (NO_3) MeCN (**1**) was produced.

There are many reported $\{Dy_2\}$ compounds in various topologies with different main ligand/co-ligand and synthetic procedures.

Compound **1** has a new core but similar to an existing core. The ligand previously used to synthesise a $\{Nd_2\}$ complex [318] is similar to the ligand used in compound **1**. The crystallographic and magnetic detail are compared in this section. The difference between the two ligands is carboxylic arms in $\{Nd_2\}$ and alcoholic arms in compound **1**. Therefore, the comparison of both compounds is summarised in Figure 3.12 and Table 3.5. $\{Nd_2\}$ is denoted by compound **A**.

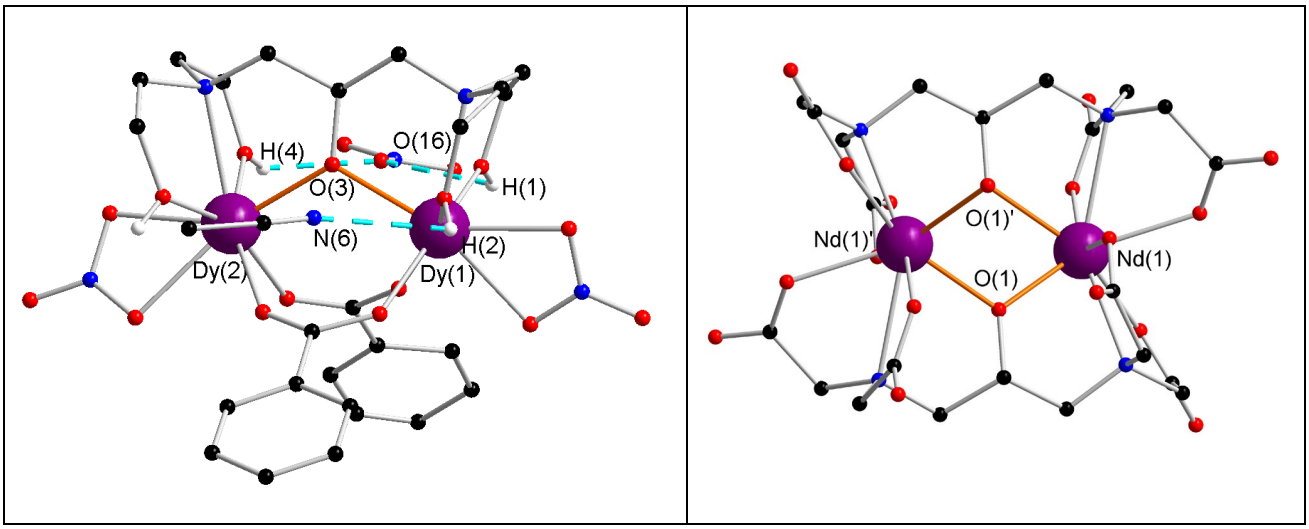

Figure 3.12. Molecular structure of compounds **1** (left) and **A** (right) (some H atoms omitted for clarity). Colour code: black, red, blue, white and violet spheres represent C, O, N, H and Dy/ Nd, respectively.

As shown in Table 3.5. Compound **1** was synthesised using 1,3-bis-diethanolamino-2-propanol (H_5bdp) as the main ligand and benzoate ($Fe_3O(PhCO_2)$) as co-ligand. While compound **A** was synthesised using 2-hydroxypropane-1,3-diamine-N,N,N',N'-tetraacetic acid as the main ligand.

Compound **1** is a cation neutralised by a nitrate, while compound **A** is an anion neutralised by four sodium ions. Compound **1** crystallises in the orthorhombic space group *P*na2$_1$, while compound **A** in the triclinic space group *P*$\bar{1}$.

Dy ions in compound **1** are eight-coordinate with a distorted triangular dodecahedron geometry, while Nd ions in compound **A** are nine-coordinate with a distorted capped square antiprism geometry.

The average Nd–O and Nd–N bond distances are longer than the Dy–O and Dy–N. The Nd···Nd distance is longer than the Dy···Dy. The average Nd–O–Nd angle is larger than Dy–O–Dy due to the bigger size of the Nd atom.

The magnetic studies of compounds **1** and **A** revealed that the Dy-Dy interaction is antiferromagnetic interaction. The magnetisation of compound **1** is higher than compound **A** at 2

K and 7 T (μ_B). Compound **1** demonstrate SMM behaviour with U_{eff} = 4.38 K and pre-exponential relaxation time τ_o =8.15x10^{-3} s, whereas compound **A** exhibits lack SMM.

Table 3.5. Comparison between compounds **1** and **A**.

Complex abbreviated as		Compound **1**	Compound **A** [318]
Structure		$[Dy_2(H_4bdp)(PhCO_2)_2(NO_3)_2].(NO_3)$ MeCN	$Na_4[\{Nd(H_2O)\}_2(\mu_2$-dptaO$)_2]$ $13H_2O$
Ligand		1,3-bis-diethanolamino-2-propanol (H_5bdp)	2-hydroxypropane-1,3-diamine-N,N,N',N'-tetraacetic acid
Co−ligand		Benzoate ($Fe_3O(PhCO_2)$)	----------
Charge of complex		Cation	Anion
Crystal system		Orthorhombic	Triclinic
Space group		$Pna2_1$	$P\bar{1}$
Volume		3547.98(18)	1112.97(6)
Colour of crystal		Colourless	Colourless
Shape of crystal		Needle	Platelet
Shape of Ln ions		Distorted triangular dodecahedron	Distorted spherical capped square antiprism
Average distance of	Ln−O	2.41	2.47
	Ln−N	2.65	2.72
Average angle of Ln−O−Ln		109.12	112.49(9)
Distance of Ln−Ln		3.92	3.93
Interactions		Antiferromagnetic	Antiferromagnetic
Magnetisation at 2 K and 7 T		12.36 μB	2.37 μB
Relaxation behaviour		SMM	Lack SMM

3.3. Structure, optical and magnetic properties of $[Ln_2(PhCO_2)_6(CH_3OH)_4]_\infty$ 1D polymer . (Ln = Eu(**2**), Gd(**3**), Tb(**4**) and Dy(**5**))

3.3.1. Synthetic description

The reaction of $[Fe_3O(PhCO_2)_6(H_2O)_3](PhCO_2)$, $Ln(NO_3)_3{\cdot}6H_2O$ and diisopropanolamine ($dipaH_3$) in a molar ratio of 1:1:2 in methanol under reflux for two hours and afforded colourless needles of a new family of binuclear Ln clusters $[Ln_2(PhCO_2)_6(CH_3OH)_4]_\infty$.

3.3.2. Crystal structure of $[Ln_2(PhCO_2)_6(CH_3OH)_4]_\infty$

In this series of binuclear lanthanide clusters, only compounds **3** and **5** have been characterised fully by single-crystal X-ray diffraction (full crystallographic data is given in Table 8.1); while the other compounds **2** and **4** were confirmed by their unit cell (Table 3.6). In addition, elemental analyses, FTIR spectroscopy and powder XRD studies (Figure 3.14) also support the suggestion that the whole series are isostructural, isomorphous and pure. Therefore, only the structure of $[Dy_2(PhCO_2)_6(CH_3OH)_4]_\infty$ (**5**) will be described in detail as a representative of the whole series. Compound **5** crystallises in the monoclinic space group $P2_1/c$ with Z = 8. The compound **5** is neutral complex.

The molecular structure of compound **5** is shown in Figure 3.13. The diisopropanolamine is a necessary reagent for the isolation of the compounds in this synthesis. The diisopropanolamine was not part of the obtained product, although it could act as a buffer protecting the dysprosium from further hydrolysis. The benzoate ligand coordinates to the metal centres as shown in the crystal structure. The benzoate ligand has been used successfully to synthesise binuclear $\{Ln_2\}$ complex.

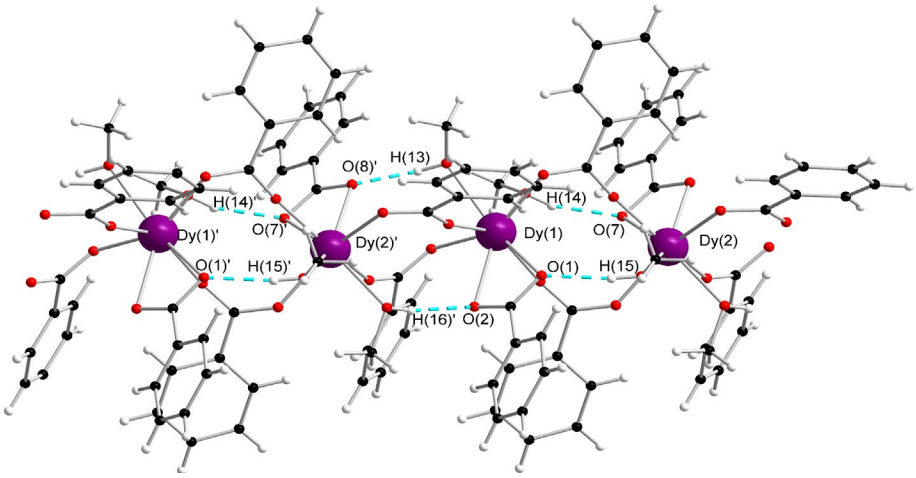

Figure 3.13. Molecular structure of compound **5**. Colour code: black, red, white and violet spheres represent C, O, H and Dy, respectively. Some of the H atoms are omitted for clarity.

The core central of compound **5** consists of two Dy^{III} ions, six benzoate ligands $(PhCO_2)^-$ (Figure 3.15) and four methanol molecules (CH_3OH).

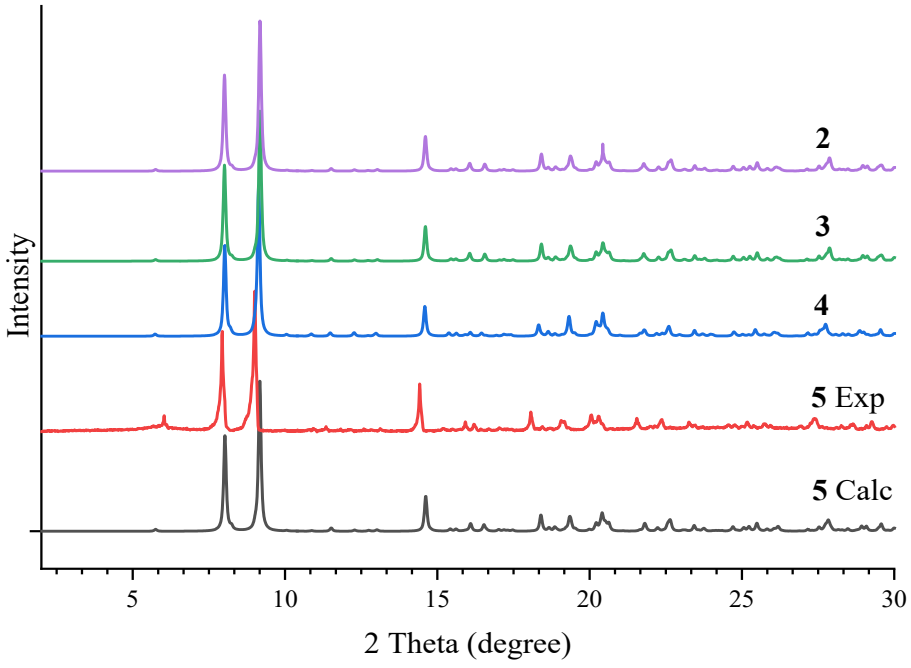

Figure 3.14. Calculated and experimental powder X-ray diffraction (PXRD) patterns of compounds **2-5**.

Table 3.6. The unit cells of compound **2**-**5**.

	a [Å]	b [Å]	c [Å]	α [deg]	β [deg]	γ [deg]	V [Å^3]
Eu_2(**2**)	9.6265(8)	21.4008(8)	22.0554(12)	90	90.764(5)	90	4550.4(5)
Gd_2(**3**)	9.6286(7)	21.4017(9)	22.0547(11)	90	90.799(5)	90	4544.3(4)
Tb_2(**4**)	9.6291(6)	21.4251(7)	22.0409(10)	90	90.801(3)	90	4541.2(3)
Dy_2(**5**)	9.6416(4)	21.4344(11)	22.0152(9)	90	90.837(4)	90	4549.2(4)

Six of benzoate ligands are in the crystal structure adopting two different coordination modes.

(i) Two of them are chelating to Dy(1) and Dy(2) with a (η^1:η^1:μ_1) coordination mode (Figure 3.15, a).

(ii) Four of them are *syn-syn* bridging to two $Dy^{(III)}$ ions with a (η^1:η^1:μ_2) coordination mode (Figure 3.15, b).

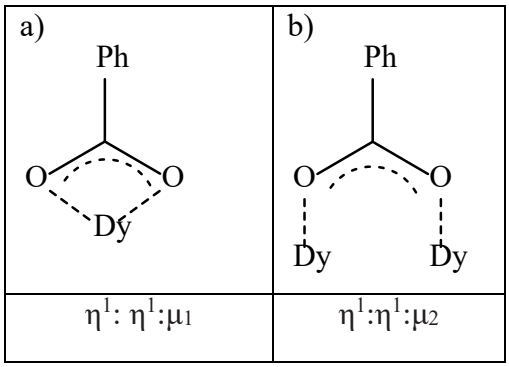

Figure 3.15. Bridging/coordination mode of benzoate ligand a) chelating b) bridging.

Both octa-coordinated Dy^{III} ion are surrounded by eight O donor atoms (O_8). Four O atoms come from *syn-syn* bridging benzoate ligand $(PhCO_2)^-$, two O atoms come from the chelating benzoate ligand $(PhCO_2)^-$ and two O atoms come from two methanol molecules (CH_3OH). This results in a distorted biaugmented trigonal prism geometry, which was confirmed by SHAPE analysis [309-312] with a deviation value of 1.28, (Figure 3.16, Table 8.8).

The Dy−O bond distances are in the range 2.259(4)−2.491(4) Å and the Dy···Dy distance is 4.848(5) Å. Selected bond distances are summarised in Table 3.7.

The structure is further stabilised by inter- and intramolecular interactions through hydrogen bonds. O(14)−H(14) and O(15)−H(15) from the methanol molecule (CH_3OH) make an intramolecular hydrogen bond to O(7) and O(1) from the chelating benzoate $(PhCO_2)^-$ ligand, respectively. The distance O(14)···O(7) and O(15)···O(1) are 2.85 and 2.76 Å, respectively.

In addition, O(13)−H(13) from the methanol molecule (CH_3OH) makes an intermolecular hydrogen bond to O(8), O(10) and O(12) from benzoate $(PhCO_2)^-$ ligand of the neighbouring molecule at {1+x, +y, +z}. The distance of O(13)···O(8), O(13)···O(10) and O(13)···O(12) are 2.73, 2.79 and 2.80 Å, respectively. Also, O(16)−H(16) from the methanol molecule (CH_3OH) makes an intermolecular hydrogen bond to O(2) from the benzoate $(PhCO_2)^-$ ligand of the neighbouring molecule at {1+x, +y, +z} with distance of 2.81 Å. The inter- and intramolecular interaction results in a 1D polymer, as shown in Figure 3.17.

Table 3.7. Selected bond distances (Å) for compound **5**.

Bond Distances			Bond Distances		
Atom	Atom	Distance/Å	Atom	Atom	Distance/Å
Dy(1)	O(1)	2.441(5)	Dy(1)	O(10)'	2.310(5)
Dy(1)	O(2)	2.489(4)	Dy(1)	O(12)'	2.261(4)
Dy(1)	O(3)	2.313(4)	Dy(1)	O(13)	2.465(5)
Dy(1)	O(5)	2.291(5)	Dy(1)	O(14)	2.445(5)

'-1+x, +y, +z

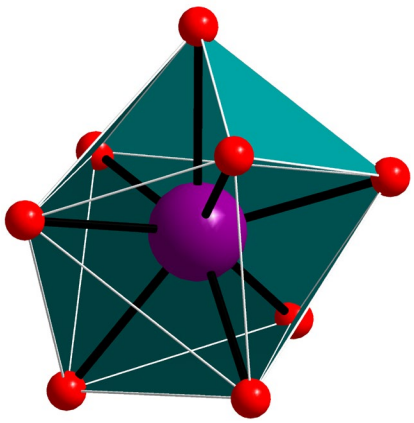

Figure 3.16. Distorted biaugmented trigonal prism geometry of the 8-coordinated Dy ion. Colour code: red and violet spheres represent O and Dy, respectively.

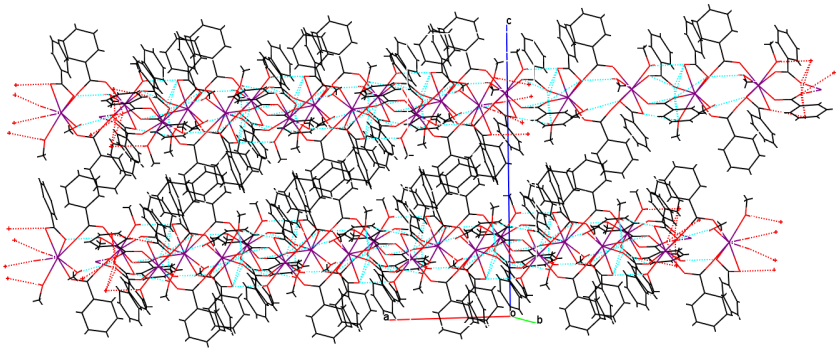

Figure 3.17. Packing structure of compound **5**. Colour code: black, red and violet spheres represent C, O and Dy, respectively.

3.3.3. Magnetic properties

DC magnetic susceptibilities of compounds **3** and **5** were carried out on freshly prepared polycrystalline samples in the temperature range 2-300 K under an applied magnetic field of 1000 Oe (0.1 T). The plot of χT versus T for compounds **3** and **5** is shown in Figure 3.18. DC data are summarised in Table 3.8.

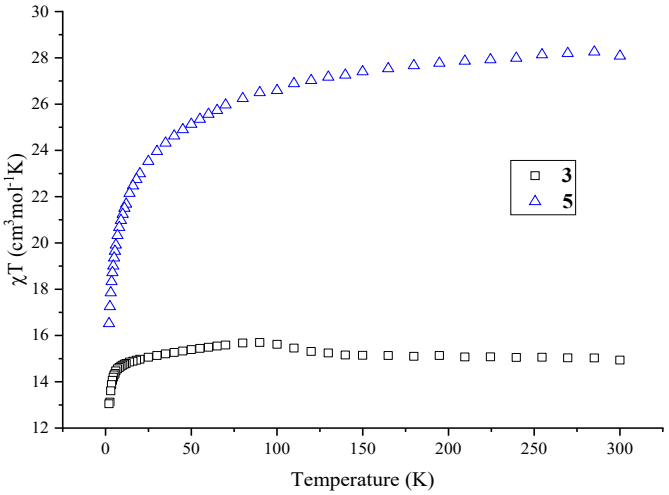

Figure 3.18. Temperature dependence of χT products for compounds **3** and **5** at 1000 Oe.

The experimental χT values of compounds **3** and **5** at 300 K are 14.94 cm^3 K mol^{-1} and 28.08 cm^3 K mol^{-1}, respectively, close to those expected values for two non-interacting ions of **3**: Gd_2 (15.76 cm^3Kmol^{-1}) and **5**: Dy_2 (28.34 cm^3Kmol^{-1}), respectively.

For compound **3**, upon cooling, the χT product stays almost constant to 120 K before a slight increase until reaching a maximum value of 15.70 cm^3 K mol^{-1} at 90 K followed by a sharp fall reaching minimum of 13.05 cm^3 K mol^{-1} at 2 K.

For compound **5**, upon cooling, the χT product slightly decreases to 70 K followed by a sharp fall reaching minimum of 16.51 cm^3 K mol^{-1} at 2 K.

The decreases of χT experimental value with the temperature are probably due to the thermal depopulation of the Stark sublevels of Ln^{III} ions and/or the presence of dominant antiferromagnetic interactions between the Ln^{III} ions in compounds **3** and **5** [313, 314].

Table 3.8. DC data for compounds **3** and **5**.

Compounds	Ground state of the Ln^{III} Ion	Curie Constant for each Ln ion at 300 K (cm^3K/mol) [180]	χT (cm^3mol^{-1}K) expected value for Ln_2 at RT	χT (cm^3mol^{-1}K) experimental value for Ln_2 at RT	χT (cm^3mol^{-1}K) experimental value for Ln_2 at 2 K	Magnetistion at 2 K and 7 T (μ_B)
Gd_2	$^8S_{7/2}$	7.88	15.76	14.94	13.05	13.08
Dy_2	$^6H_{15/2}$	14.17	28.34	28.08	16.51	12.75

The field dependence of the magnetisation for compound **5** was performed at fields from 0 to 70000 Oe (0–7 T) at temperatures of 2 K, 3 K and 5 K.

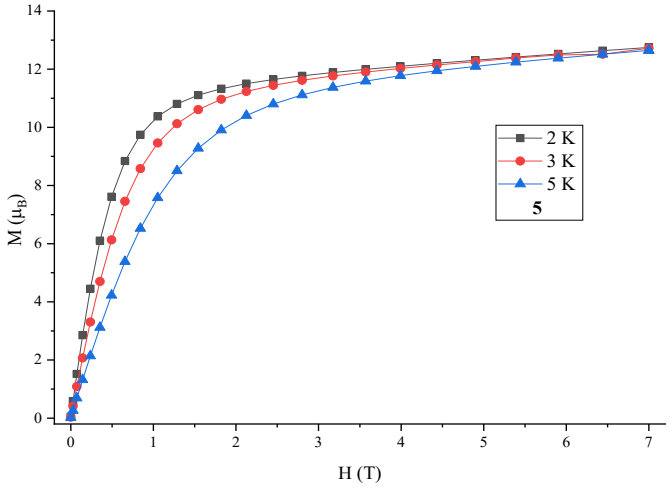

Figure 3.19. Field dependence of magnetisation at indicated temperatures for compound **5**.

Figure 3.19 shows the magnetisation values of compound **5** have a relatively rapid increase below 1 T followed by increase linearly up to 7 T reaching 12.75 μ_B without saturation. This behaviour indicates that the presence of magnetic anisotropy or/and the population of low-lying excited states [315].

AC susceptibility measurements were performed in order to investigate potential SMM behaviour. AC magnetic susceptibility measurements of compound **5** were carried out in the frequency range 1-1488 Hz and at temperature 2 K under different applied DC field. As shown in Figure 3.20, in the out of phase, slow relaxation was observed at 1000 Oe. The results indicate that compounds **5** is SMM behaviour but the energy barrier can‘t be obtained. There is a possibility that this system could be an SMM with a lower energy barrier and could potentially be observed at very low, sub Kelvin, temperatures.

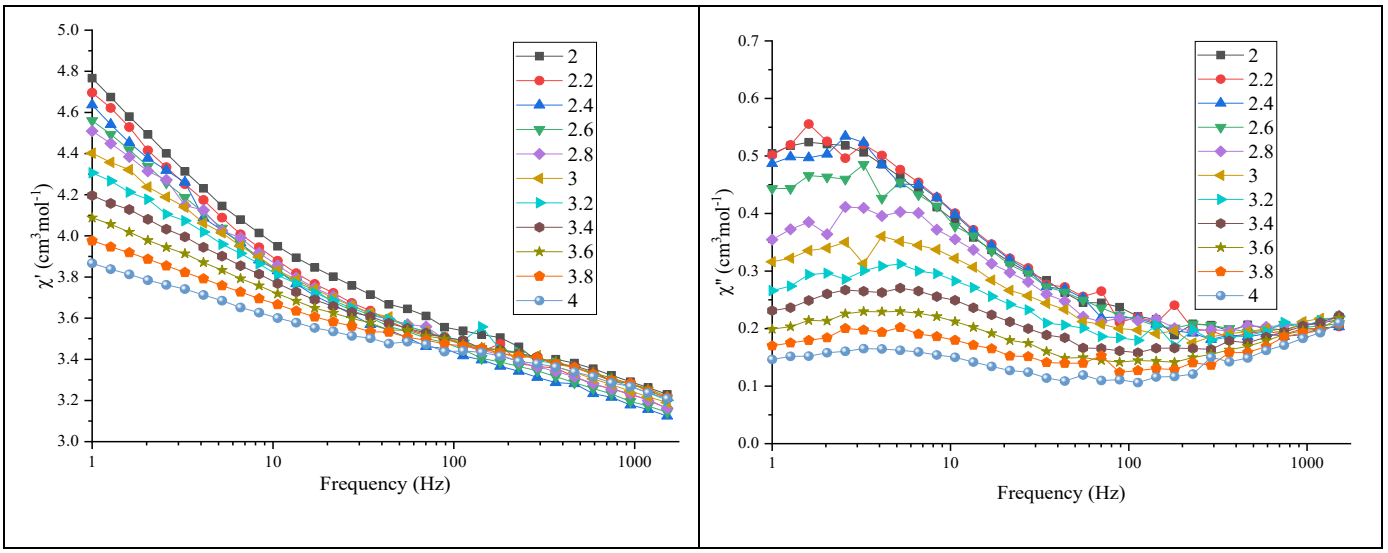

Figure 3.20. The plot of in-phase (left) and out-of-phase (right) against the frequency of compound **5** under 1000 Oe.

3.3.4. Comparison of the core structure

Diisopropanolamine ($dipaH_3$) ligand has been used as the main ligand once in the literature to synthesise Fe and Co metal complexes with different coordination modes and various topologies [147]. However, $dipaH_3$ has not used to obtain lanthanide or iron–lanthanide metal complexes.

Taking this into consideration, in the present work the combination of $dipaH_3$ alongside benzoate as the co-ligand has been employed to obtain higher nuclearity cluster which could provide route toward compounds potentially having optical or magnetic properties as well as SMM behaviour. With this synthetic approach, $[Ln_2(PhCO_2)_6(CH_3OH)_4]_\infty$ was produced as a 1D polymer. The $dipaH_3$ ligand was not present in the crystal structure as it only functioned as a buffer protecting the dysprosium from further hydrolysis.

There are many reports on $\{Dy_2\}$ compounds in various topologies with different main ligand/co-ligand and procedures.

A review of the literature reveals that lanthanide compounds with carboxylic acid as the main ligand only resulted in six complexes (Table 3.9).

Table 3.9. Lanthanide complexes based on carboxylic acid ligand.

NO	Structure	Carboxylic acid	Ln	Dy SMM	Ref
1	$[Dy_2(OAc)_6(H_2O)_4]_\infty \cdot 4H_2O$ (**B**)	Acetic acid	Dy	NO	[319]
2	$[Dy_2(BuCO_2)_6(MeOH)_2(H_2O)_2]$	Butyric acid	Dy	NO	[320]
3	$[Dy_2(3\text{-}Htzba)_2(3\text{-}tzba)_2(H_2O)_8]\cdot 4H_2O$	3-H_2tzba = 3-(1H-tetrazol-5-yl) benzoic acid	Dy	Yes	[321]
4	$[Dy_2(Acc)_4(H_2O)_8]\cdot Cl_6$ 5.89 H_2O	amino-cyclohexanecaboxylic acid	Dy	NO	[69]
5	$[Dy_2(phen)_2(L)_6]$ $2H_2O$	β-naphthoic acid (HL)	Dy	Yes	[322]
6	$[Dy_2(phen)_2(L)_6]$	β-naphthoic acid (HL)	Dy	Yes	[322]
7	$[Ln_2(PhCO_2)_6(CH_3OH)_4]_\infty$	Benzoic acid	Eu-Dy	Yes	This work

Compound **5** has chain topology similar to compound **B** which was previously reported by our group [319]. The crystallographic and magnetic details are compared in this section. The comparison of both compounds is summarised in Figure 3.21 and Table 3.10. In all cases, the Dy containing structure has chosen as representative of the whole lanthanide. Dy_2 [319] is abbreviated as compound **B**.

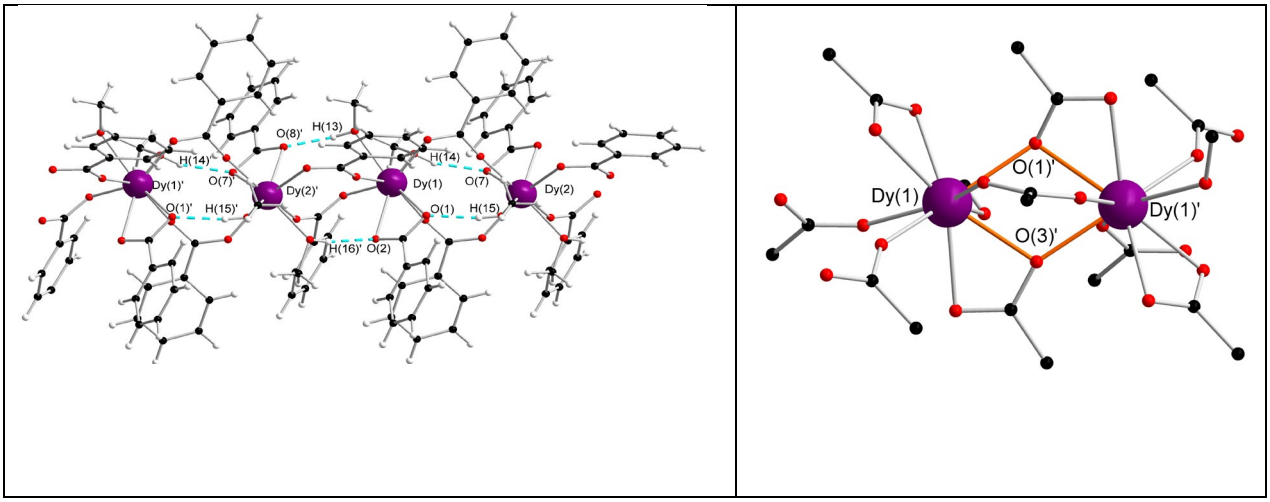

Figure 3.21. Molecular structure of compound **5** on the left and [Dy_2] had been reported on the right (some H atoms omitted for clarity). Colour code: black, red, white and violet spheres represent C, O, H and Dy, respectively.

Table 3.10. Comparison between compounds **5** and **B**.

Complex abbreviated as	Compound **5**	Compound **B**
Structure	$[Dy_2(PhCO_2)_6(MeOH)_4]_\infty$	$[Dy(OAc)_3(MeOH)]_\infty$
Ligand	Benzoate	Acetate
Crystal system	Monoclinic	Monoclinic
Space group	$P\,2_1/c$	$P\,2_1/c$
Volume	4549.2(4)	1077.2(3)
Colour of crystal	Colourless	Colourless
Shape of crystal	Needle	Needle
Shape of Ln ions	Distorted biaugmented trigonal prism	Distorted muffin
Average distance of Ln−O	2.38 Å	2.42 Å
Average angle of Ln−O−Ln	----------	111.65°
Distance of Ln−Ln	4.85 Å	4 Å
Interactions	Antiferromagnetic	Ferromagnetic
Magnetisation at 2 K and 7 T	16.51	----------
Relaxation behaviour	SMM	SCM

Compound **5** was synthesised using benzoate from $Fe_3O(PhCO_2)$ as a ligand while compound **B** was synthesised using acetate (Dy(acetate)) as a ligand. Both compounds **5** and **B** were crystallised in the monoclinic space group $P2_1/c$

Dy ions in compound **5** are eight-coordinate with a distorted biaugmented trigonal prism geometry while in compound **B** the Dy ions are nine-coordinate with a distorted muffin geometry.

The average Dy–O bond distance in compound **B** is longer than that in compound **5**. The Dy···Dy distance of compound **B** is shorter than that in compound **5**. The average Dy–O–Dy angle in compound **B** is (111.65°).

The magnetic studies of compound **5** revealed that the Dy–Dy interaction is antiferromagnetic while ferromagnetic interaction in compound **B**.

The magnetisation of Dy_2 in compound **5** is 16.51 μ_B at 2 K and 7 T whereas compound **B** has not been reported. Relaxation behaviour of compound **5** is SMM while compound **B** is SCM.

3.3.5. Magnetocaloric effect

Recently, Gd complexes have gained attention due to their potential applications for low-temperature magnetic coolers. Since, the compound **3**: $\{Gd_2\}$ exhibits an antiferromagnetic interaction between Gd ions therefore, it was decided to explore the magnetocaloric effect (MCE).

The field dependence of the magnetisation of compound **3** had performed under different fields range from 0 to 70000 Oe (0–7 T) at the temperatures range 2-10 K.

Figure 3.22 shows the magnetisation values of compound **3** arise gradually as the field increase to reach saturation value 13.05 μ_B at 2 K and 7 T close to the theoretical value of 14 μ_B for two Gd.

The MCE performance was evaluated by meaursing the magnetic entropy change ($-\Delta S_m$) using Maxwell relationship as shown in Figure 3.23.

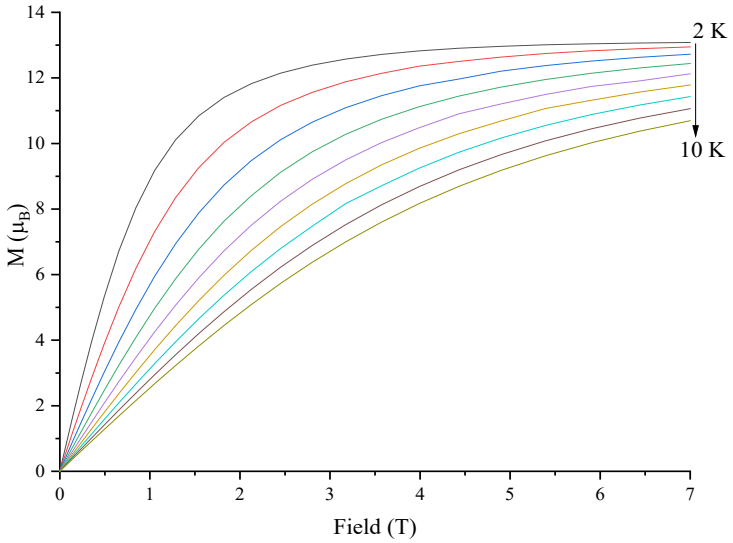

Figure 3.22. Field dependence of magnetisation at indicated temperatures of compound **3**

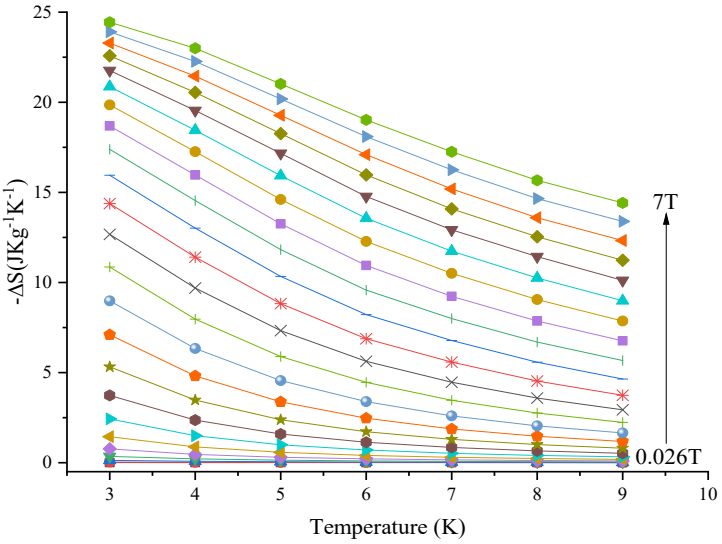

Figure 3.23. Changes in ($-\Delta S_m$) induced by magnetic field and temperatures of compound **3**.

Magnetic entropy change (-ΔSm) could be calculated from M versus H plots according to the Maxwell equation. The maximum entropy ($-\Delta S_m$) of compound **3** is 24.44 J kg^{-1} K^{-1} with ΔH =7T at 3 K which is lower than the theoretical ($-\Delta S_m$) value per mole (4.16R~34.59 J kg^{-1} K^{-1}) probably due to the antiferromagnetic coupling between Gd ions. From the value ($-\Delta S_m$) of compound **3** was found acts as a molecular magnetic refrigerant.

Table 3.11. Magnetic entropy changes for selected Gadolinium complexes.

Gadolinium complexes	-Δ Sm	T(K)	Δ H	Ref	AF/F
$[Gd(OAc)_3(H_2O)_2]_2{\cdot}4H_2O$	40.6	1.8	7 T	[323]	F
$[Gd_2(OAc)_2(Ph_2acac)_4(MeOH)_2]$	23.7	2.4	7 T	[324]	F
$[Gd_2(hfac)_4L_2]$	16.89	2	8 T	[325]	AF
$[Gd_2(2\text{-}TCA)_6(phen)_2]{\cdot}2H_2O$	21.8	2	7 T	[326]	AF
$[Gd_2(Piv)_6(phen)_2]$	19.21	2	7 T	[326]	AF
$[Gd_2(PhCO_2)_6(CH_3OH)_4]_\infty$(**3**)	24.44	3	7 T	This work	AF

As shown in Table 3.11 (AF= antiferremagnetic, F= ferromagnetic), the magnetic entropy change for $\{Gd_2\}$ in this work is higher than the others in the table except the $[Gd(OAc)_3(H_2O)_2]_2{\cdot}4H_2O$ [323].

3.3.6. Photoluminescence study

Photoluminescence spectra were recorded in the range from 200 to 800 nm in solid-state. of compounds **2** (Eu^{3+}) and **4** (Tb^{3+}).

The excitation spectrum of compound **2** monitored at 548 nm emission exhibits a high absorption in the range 200–400 nm (centred at 282 nm), (Figure 3. 24, a) presents the excitation and emission spectra of compound **2** in solid-state. The emission spectrum shows a sharp band which is a result of the intra f-f transition of Eu^{3+} corresponding to the $^5D_0 \rightarrow {}^7F_J$ (J = 0-4) transitions of the Eu^{3+} ion $^5D_0 \rightarrow {}^7F_0$ (548 nm), $^5D_0 \rightarrow {}^7F_1$ (581 nm), $^5D_0 \rightarrow {}^7F_2$ (617 nm), $^5D_0 \rightarrow {}^7F_3$ (655 nm) and $^5D_0 \rightarrow {}^7F_4$ (699 nm). Among all the transitions, the $^5D_0 \rightarrow {}^7F_2$ and the $^5D_0 \rightarrow {}^7F_1$ are referred to as hypersensitive electric-dipole (ED) and magnetic-dipole (MD) transitions, respectively [122-125].

The excitation spectrum of compound **4** monitored at 544 nm emission exhibits a high absorption in the range 200–400 nm (centred at 282 nm), (Figure 3.24, b) which presents the excitation and emission spectra of compound **4** in solid-state. The emission spectrum of Tb^{3+} exhibits a sharp bands which is a result of intra f-f transition of Tb^{3+} corresponding to the $^5D_4 \rightarrow {}^7F_J$ (J = 3–6) transitions of the Tb^{3+} ion $^5D_4 \rightarrow {}^7F_6$ (490 nm), $^5D_4 \rightarrow {}^7F_5$ (544 nm), $^5D_4 \rightarrow {}^7F_4$ (590 nm), $^5D_4 \rightarrow {}^7F_3$

(618 nm). The emission at 488 nm ($^5D_4 \rightarrow {}^7F_6$) was assigned to the magnetic dipole transition; while at 544 nm ($^5D_4 \rightarrow {}^7F_5$) was assigned to the electric dipole transition [126]. The emission intensity at 544 nm was the strongest which deduced that the Tb^{3+} ion is located in asymmetric coordination [122]. These results indicate that these compounds may be good candidates as emitting molecular materials such as those used in OLEDs which is one of the industrially relevant fields using coordination chemistry.

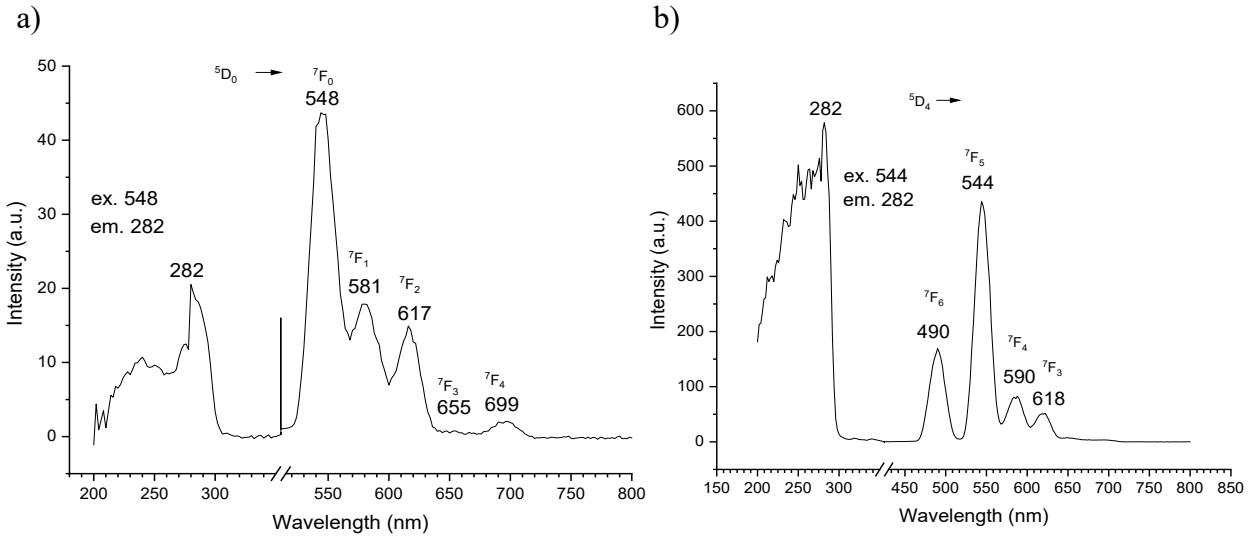

Figure 3.24. Excitation and emission spectra a) compound **2** b) compound **4**.

3.4. Structure and magnetic properties of [$Ln_2(TipaH_2)_2(Piv)_4$]. (Ln = Eu(**6**), Gd (**7**), Tb (**8**) and Dy(**9**))

3.4.1. Synthetic description

The reaction of $[Fe_3O(Piv)_6(H_2O)_3]Piv\cdot$, $Ln(NO_3)_3\cdot 6H_2O$ and triisopropanolamine ($TipaH_3$) in a molar ratio of 1:1:4 in MeCN in the presence of triethylamine (NEt_3) over stirring for one hour and afforded colourless crystals of a new family of binuclear Ln^{III} clusters [$Ln_2(TipaH_2)_2(Piv)_4$]. The NEt_3 acts as a base to facilitate the deprotonation of the $TipaH_3$ ligand.

3.4.2. Crystal structure of $[Ln_2(TipaH_2)_2(Piv)_4]$

Full structure determination was performed for compound **9** (Figure 3.25) by single-crystal X-ray diffraction (full crystallographic data is given in Table 8.2); while compounds **6-8** were found to be isostructural with **9** by checking their unit cells (Table 3.12). Analysis of the IR spectra, PXRD patterns (Figure 3.26) and elemental analyses further confirmed that compounds **6-9** are isomorphous and isostructural.

The structure of the binuclear complex $[Ln_2(TipaH_2)_2(Piv)_4]$ (**9**) will be described in detail as representative of the whole series. Compound **9** crystallises in the triclinic space group $P\bar{1}$ with Z=2. Compound **9** is neutral cluster. The unit cell has two molecules.

The structure of compound **9** is shown in Figure 3.25, the $TipaH_3$ and Pivalate ligands are coordinating to the Dy metal centres as shown in the crystal structure. $TipaH_3$ ligand is singly-deprotonated resulting in one negatively charged oxygen atom O(1) or O(1)' bridging two neighbouring Dy^{III} ions Dy (1) and Dy(1)'. The $TipaH_3$ ligand (Figure 3.27, a) has successfully been used to synthesise binuclear $\{Ln_2\}$ complex.

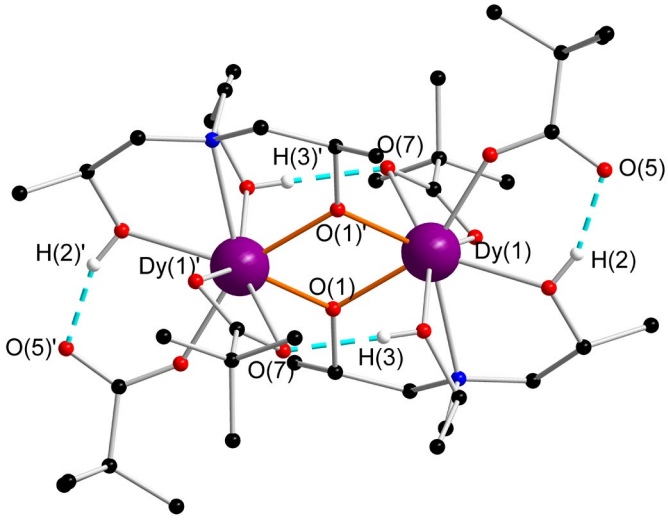

Figure 3.25. Molecular structure of compound **9**. Colour code: black, red, blue, white and violet spheres represent C, O, N, H and Dy, respectively. Some of the H atoms are omitted for clarity.

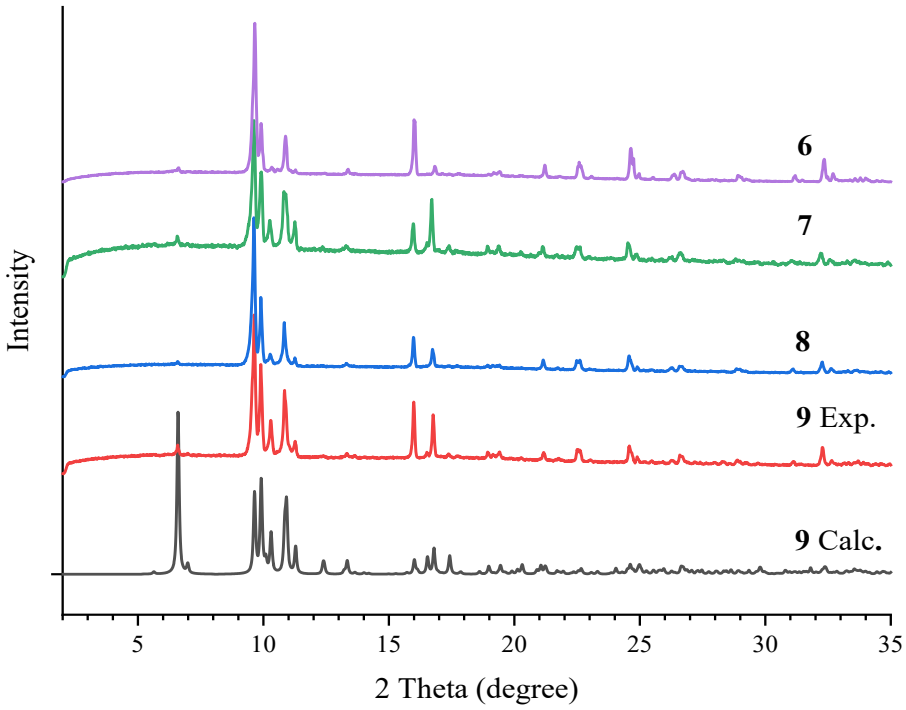

Figure 3.26. Calculated and experimental powder X-ray diffraction (PXRD) patterns of compounds **6-9**.

Table 3.12. The unit cells of compounds **6-9**

	a [Å]	b [Å]	c [Å]	α [deg]	β [deg]	γ [deg]	V [Å^3]
Eu_2(**6**)	10.599(4)	14.301(3)	16.89(3)	68.88(5)	89.69(8)	84.99(9)	2405.19(3)
Gd_2(**7**)	10.688(17)	14.314(3)	16.94(3)	68.89(18)	89.72(14)	84.94(15)	2407.20(7)
Tb_2(**8**)	10.842(2)	14.321(4)	16.80(4)	68.92(2)	89.81(17)	84.92(2)	2408.43(10)
Dy_2(**9**)	11.100(3)	14.375(5)	16.78(5)	69.17(3)	89.88(2)	85.31(3)	2492.50(14)

The compound **9** consists of two Dy^{III} ions, two singly-deprotonated oxygen $(TipaH_2)^-$ and four Pivalates ligands. Two of the singly-deprotonated oxygen $(TipaH_2)^-$ ligands are tetradentate coordinating to the Dy metal centre with a (η^1: η^1: η^1: η^2: μ_2) coordination mode (Figure 3.27, b). Four Pivalates are in the crystal structure adopting two different coordination modes:

(i) Two of them are chelating to Dy(1) and Dy(1)' with a (η^1:η^1:μ_1) coordination mode (Figure 3.27, c).

(ii) Two of them are monodentate coordinated with a (η^1:η^0:μ_1) coordination mode (Figure 3.27, d) on Dy(1) and Dy(1)'.

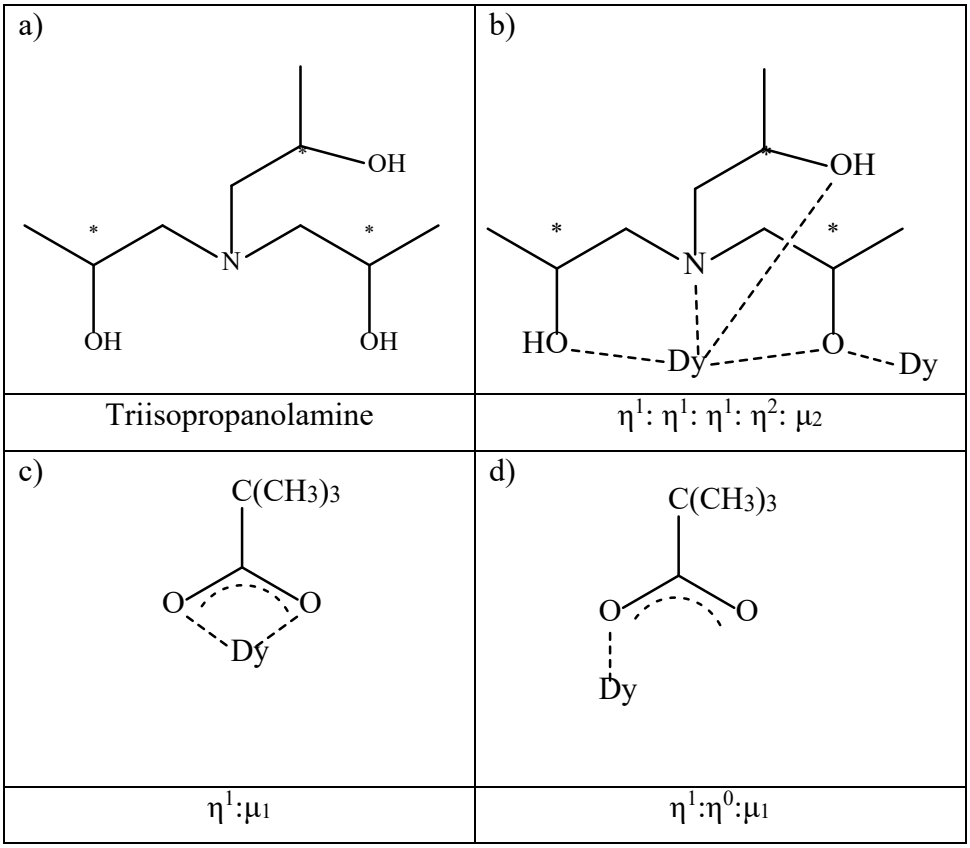

Figure 3.27. (a) Triisopropanolamine. The coordination modes of (b) $(TipaH_2)^-$ (c+d) Pivalate ligands found in compound **9**.

Both octa-coordinated Dy^{III} ion are surrounded by one N and seven O donor atoms (NO_7). One N and four O atoms (two deprotonated and two protonated) come from the singly-deprotonated oxygen $(TipaH_2)^-$ ligand, two O atoms come from the chelating Pivalate $(Piv)^-$ ligand and one O atom comes from the monodentate Pivalate ligand. This results in a distorted triangular dodecahedron geometry which was confirmed by SHAPE analysis [309-312] with a deviation value of 1.48, (Figure 3.28, Table 8.9).

The Dy–O bond distances are in the range 2.271(3)−2.516(4) Å. The Dy–N bond distance is 2.563(4) Å. The distance Dy⋯Dy is 3.688(5) Å. The Dy−O−Dy angle is 108.38 (13)°. Selected bond distances are summarised in Table 3.13.

The structure is stabilised by intramolecular interactions through hydrogen bonds. O(2)−H(2) and O(2)'−H(2)' from the singly-deprotonated oxygen $(TipaH_2)^-$ ligands make an intramolecular hydrogen bond to O(5) and O(5)' from the monodentate Pivalate ligand, respectively, with the distances of O(2)···O(5) and O(2)'···O(5)' are 2.54 Å. In addition, O(3)−H(3) and O(3)'−H(3)' from the singly-deprotonated oxygen $(TipaH_2)^-$ ligands make an intramolecular hydrogen bond to O(7) and O(7)' from the chelating Pivalate ligand, respectively. The distances of O(3)···O(7) and O(3)'···O(7)' are 2.72 Å. Figure 3.29 present packing of compound **9**.

Table 3.13. Selected bond distances (Å) of compound **9**

Bond distances			Bond distances		
Atom	Atom	Distance/Å	Atom	Atom	Distance/Å
Dy(1)	O(1)	2.271(3)	Dy(1)	O(4)	2.289(4)
Dy(1)	O(1)'	2.276(4)	Dy(1)	O(6)	2.373(4)
Dy(1)	O(2)	2.379(4)	Dy(1)	O(7)	2.516(4)
Dy(1)	O(3)	2.432(4)	Dy(1)	N(1)	2.563(4)

' 1-x, 1-y, 2-z

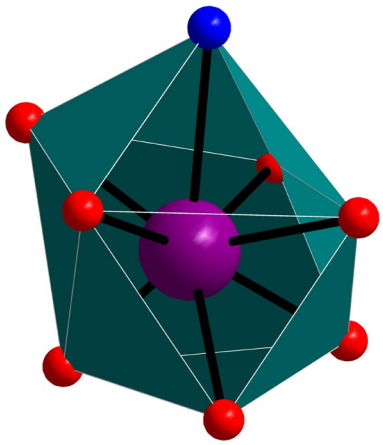

Figure 3.28. Distorted triangular dodecahedron geometry of the 8-coordinated Dy ion. Colour code: red, blue and violet spheres represent O, N and Dy, respectively.

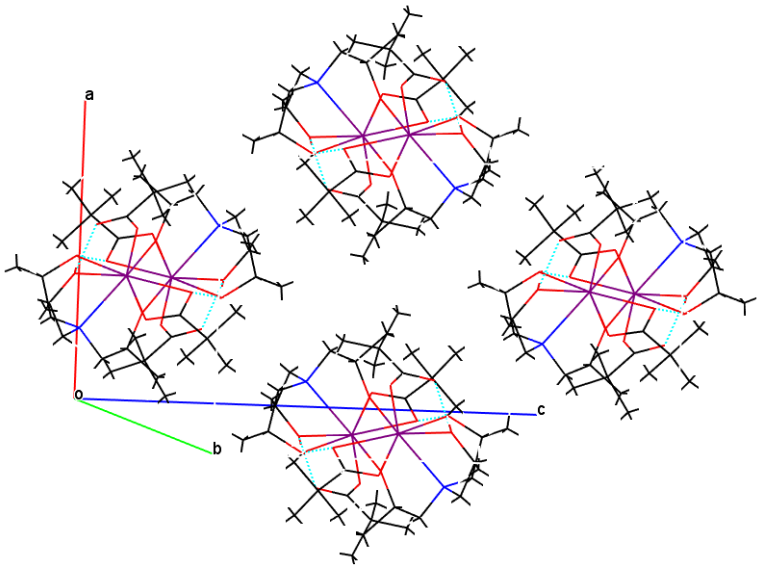

Figure 3.29. Packing structure of compound **9**. Colour code: black, red, blue, white and violet spheres represent C, O, N, H and Dy, respectively.

3.4.3. Magnetic properties

DC magnetic susceptibility of compound **9** was carried out on freshly prepared polycrystalline sample in the temperature range 2-300 K under an applied DC magnetic field of 1000 Oe (0.1 T). The plot of χT versus T for compound **9** is shown in Figure 3.30.

The χT product of compound **9** at 300 K is 25.65 $cm^3mol^{-1}K$ which is lower than the expected value of 28.34 $cm^3mol^{-1}K$ for two non-interacting Dy^{III} ions ($^6H_{15/2}$, S = 5/2, g = 4/3, L = 5, C = 14.17 $cm^3mol^{-1}K$) [276]. The χT product shows decreases slightly at the temperature from 300 to 100 K and is followed by a rapid decrease from 100-2 K, reaching a value of 7.81 $cm^3mol^{-1}K$ at 2 K.

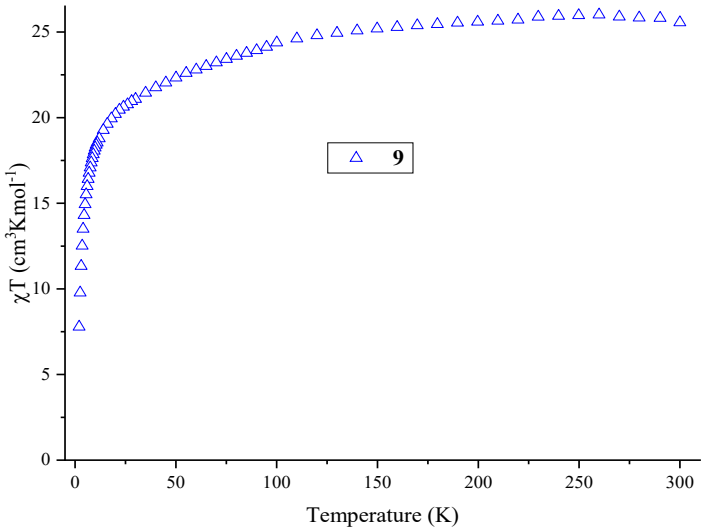

Figure 3.30. Temperature dependence of the χT products for compound **9** at 1000 Oe.

The decrease of χT experimental value with the temperature is probably due to the thermal depopulation of the Stark sublevels of Dy^{III} ions and/or antiferromagnetic interactions between the Dy^{III} ions [313, 314].

The field dependence of the magnetisation for compound **9** was measured at fields range from 0 to 70000 Oe (0-7 T) at temperatures of 2 K, 3 K and 5 K.

Figure 3.31 shows the magnetisation values of compound **9** has a relatively rapid increase below 2 T and then increase linearly up to 7 T, reaching a value of 11.59 μ_B at 2 K and 7 T without saturated which indicates the presence of magnetic anisotropy or/and the population of low-lying excited states [315].

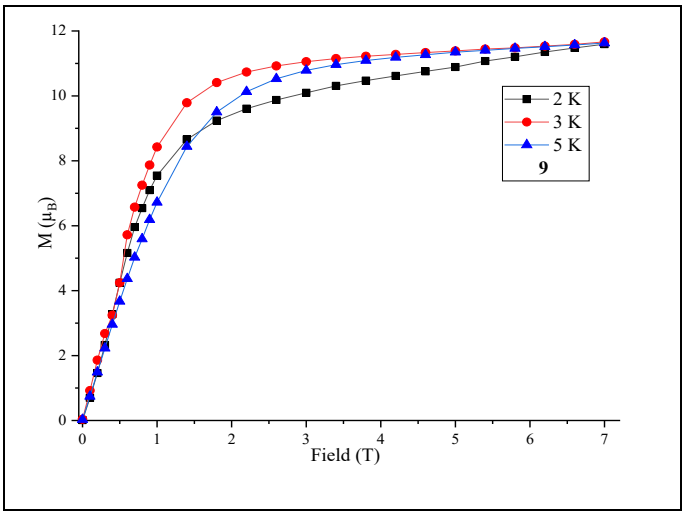

Figure 3.31. Field dependence of magnetisation at indicated temperatures for compound **9**.

AC susceptibility measurements of compound **9** were performed to investigate potential SMM behaviour. AC magnetic susceptibility measurements were carried out in the frequency range 1-1488 Hz and in the temperature range 2-12 K under different applied DC fields.

As shown in Figure 3.32, compound **9** shows slow relaxation of the magnetisation below 10 K under an applied DC field of 1500 and the out of phase signal, maxima peak has been observed at 7 K at 1488 Hz.

As shown in Figure 3.33, compound **9** shows SMM behaviour. The characteristic SMM energy barrier U_{eff} of 22.44 K and the pre-exponential factor of $\tau_o = 5.23 \times 10^{-6}$ s were estimated from linear fitting (Figure 3.34) of the data to an Arrhenius law.

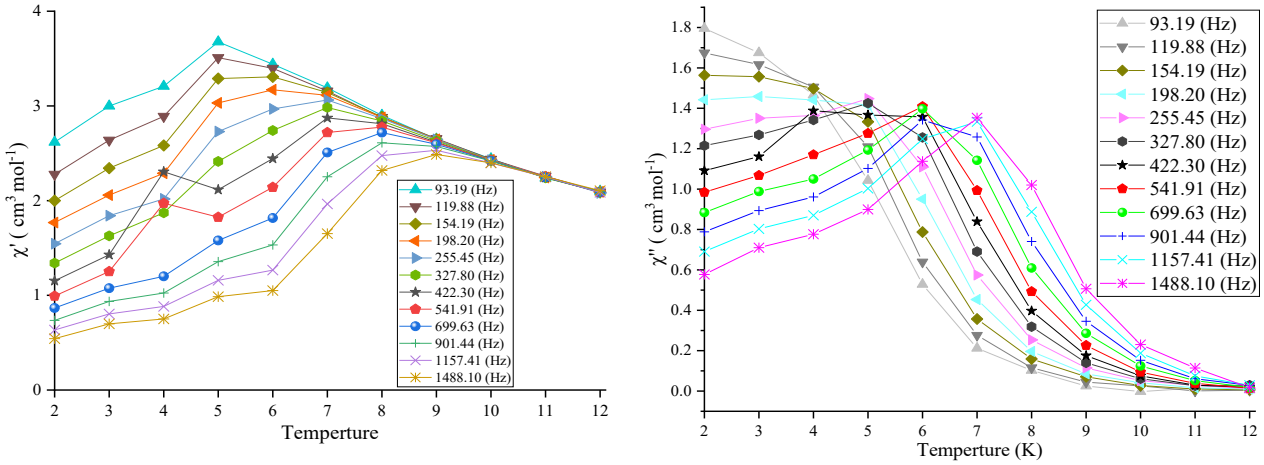

Figure 3.32. Temperature dependence of the in-phase (left) and the out-of-phase (right) components of the AC susceptibility for compound **9** under an applied DC field of 1500 Oe.

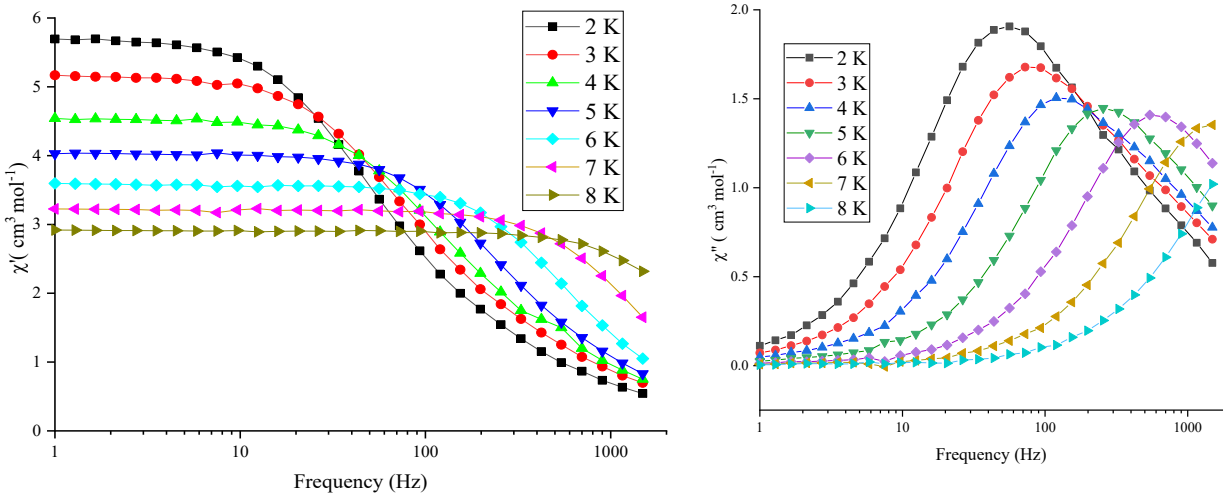

Figure 3.33. Frequency dependence of the in-phase (left) and the out-of-phase (right) components of the AC susceptibility for compound **9** under an applied DC field of 1500 Oe.

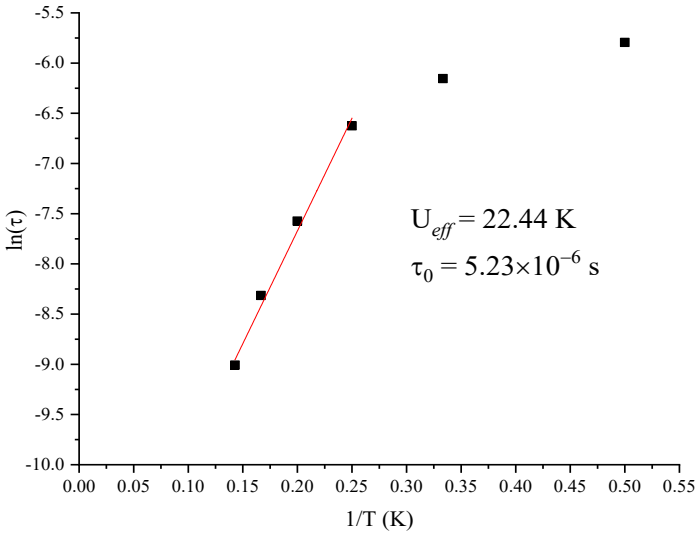

Figure 3.34. Arrhenius plot of compound **9** under an applied DC field of 1500 Oe.

The plot of out-of-phase (χ'') versus in-phase (χ') makes the various relaxation processes visible, the resultant plot is called Cole-Cole diagram and is generally useful in characterising the relaxation process and distribution of relaxation time in SMM and SCM. Out-of-phase (χ'') and in-phase (χ') are AC susceptibility components which are extracted from AC data at different temperature. The Cole-Cole plot of compound **9** was constructed in the temperature range 2-7 K. The data were fitted using a generalised Debye model [316, 317]. The Cole-Cole plot of **9**, as shown in Figure 3.35, has relatively symmetrical semicircles. As the temperature increases, the semicircle shape becomes smaller and smaller. A fit to the plots gave α values in range 0.052-0.222 (Table 3.14) which indicate a wide distribution of relaxation time or relaxation process within the compound **9**.

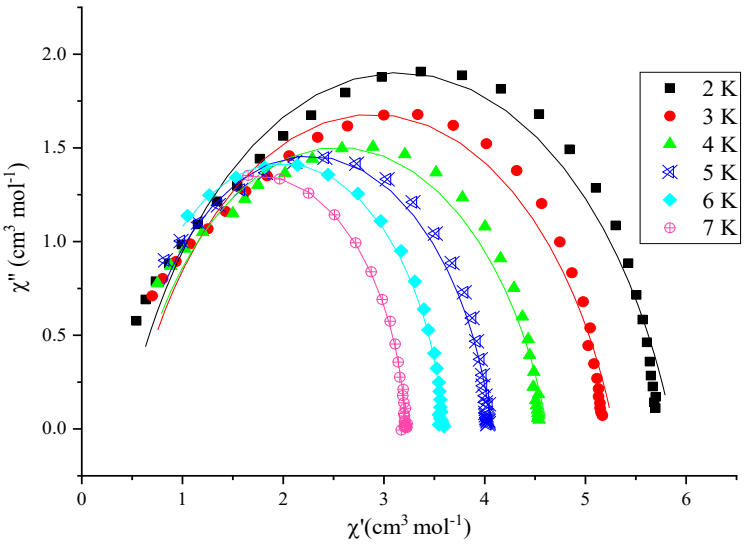

Figure 3.35 Cole-Cole plots of compound **9** under 1500 applied DC field. Solid lines for the fitting using a generalised Debye model.

Table 3.14. Analysis of the Cole-Cole plots of compound **9**

Temperature (K)	χ_S	χ_T	τ	α	Residual
2	4.30E-01	5.86E+00	2.28E-03	0.222	4.27E-01
3	4.90E-01	5.28E+00	1.47E-03	0.222	3.62E-01
4	4.72E-01	4.62E+00	9.24E-04	0.202	2.86E-01
5	4.46E-01	4.07E+00	5.23E-04	0.137	9.75E-02
6	3.92E-01	3.59E+00	2.57E-04	0.074	2.12E-02
7	2.78E-01	3.22E+00	1.17E-04	0.052	5.77E-03

3.4.4. Comparison of the core structure

A review of the literature on homonuclear lanthanide complexes reported using amino-polyalcohol based ligand incorporating Pivalic acid shows that all three are binuclear, as shown in Table 3.15.

Table 3.15. Binuclear Ln^{III} complexes incorporate Pivalic acid.

NO of compound	Structure	Ligand	SMMs Dy		Coordination mode of Pivalic acid	Ref
			U_{eff} (K)	τ_0 (s)		
1	$[Dy_2(LH_2)_2(\mu_2\text{-Piv})](Cl)\cdot 2MeOH \cdot H_2O$	6-((bis(2-hydroxyethyl)amino)methyl)-*N′*-((8-hydroxy-quinolin-2-yl)methylene)picolinohydrazide	Not		Chelating	[280]
2	$[Ln_2(mdeaH_2)_2(Piv)_6]$ (Ln=La-Gd)	Diethanolamine	Not measured		Bridging, monodentate, Bridging and chelating.	[232]
3	$Dy_2(H_2L)_2(\mu\text{-Piv})_2(Piv)_2]\cdot 2CHCl_3$	2,2'-(2-hydroxy-3-methoxy-5-methylbenzylazanediyl)diethanol	35.51	1.48×10^{-6}	[281]	[281]
4	$[Dy_2(TipaH_2)_2(Piv)_4]$ (**9**)	Triisopropanolamine	22.44	5.23×10^{-6}	This work	This work

As shown in Table 3.15, the first two compounds lack SMM behaviour and the other two compounds are showing SMM behaviour. The previously reported $Dy_2(H_2L)_2(\mu\text{-Piv})_2(Piv)_2]\cdot 2CHCl_3$ has a higher energy barrier than compound (**9**).

Triisopropanolamine ($TipaH_3$) ligand has been used to obtain $\{Fe_3Gd_2\}$ complex [84] and $\{Yb_2\}$ complex [82]. However, $TipaH_3$ has not used to obtain Dy or Tb metal complexes which show SMM behaviour. Bearing this fact in mind, in the present work a combination of $TipaH_3$ alongside Pivalate from ($Fe_3O(Piv)$) as the co-ligand has been employed to obtain higher nuclearity cluster which could provide route toward compounds potentially having optical or magnetic properties as well as SMM behaviour.

Thus, a little adjustment of synthetic strategy led to the isolation of compounds **6-9** $[Ln_2(TipaH_2)_2(Piv)_4]$. Many $\{Dy_2\}$ compounds have been already reported in the literature with various topologies, using different ligand and co-ligand.

Since $\{Yb_2\}$ [82] and **9** were synthesised using $TipaH_3$ ligand, the crystallographic and magnetic details will be compared in this section. The comparison between them is summarised in Figure 3.36 and Table 3.16. In all cases the Dy containing structure is chosen as representative for the whole lanthanide. $\{Yb_2\}$ is abbreviated as compound **C**.

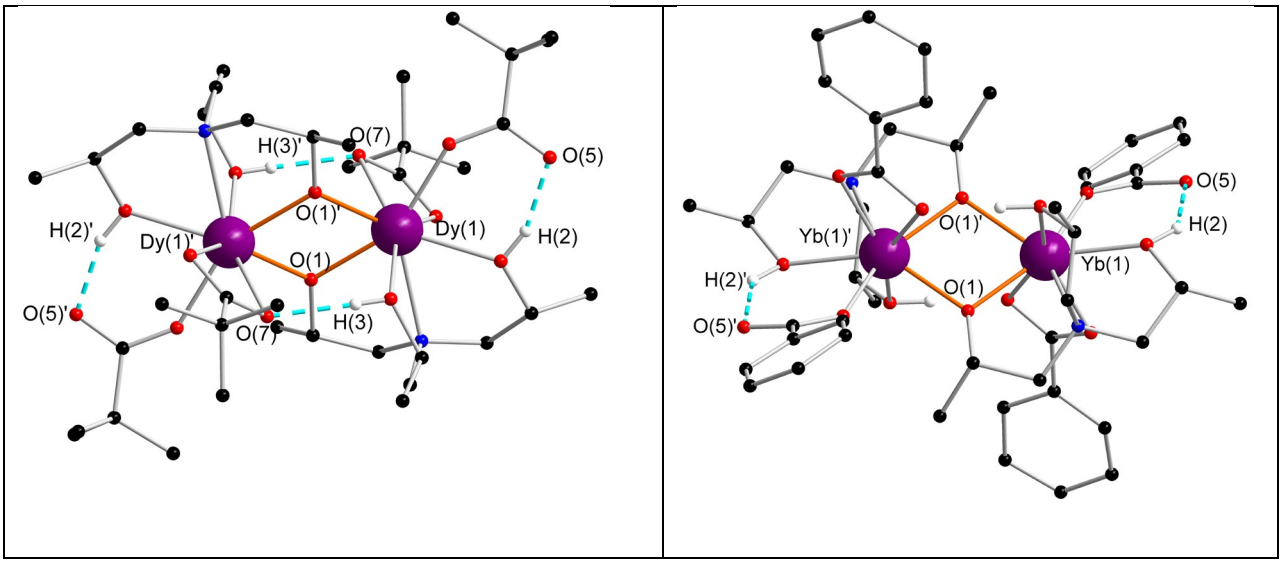

Figure 3.36. Molecular structure of compound **9** on the left and compound **C** on the right (some H atoms omitted for clarity). Colour code: black, red, blue, white and violet spheres represent C, O, N, H and Dy/Yb, respectively.

Table 3.16. Comparison between compounds **9** and **C**

Complex abbreviated as		Compound **9**	Compound **C** [82]
Structure		$[Dy_2(TipaH_2)_2(Piv)_4]$	$[Yb_2(TipaH_2)_2(PhCO_2)_4]$
Ligand		Triisopropanolamine	Triisopropanolamine
Co−ligand		Pivalate	Benzoate
Crystal system		Triclinic	Monoclinic
Space group		$P\bar{1}$	$P\ 2_1/n$
Volume		2492.50(14)	2394.0(6)
Colour of crystal		Colourless	Colourless
Shape of crystal		Block	Block
Shape of Ln ions		Distorted triangular dodecahedron	Distorted triangular dodecahedron
Average distance of	Ln−O	2.36	2.33
	Ln−N	2.56	2.50
Ln−O−Ln angle		108.38 (13)°	106.4(2)°
Distance of Ln−Ln		3.69	3.60
Interactions		Antiferromagnetic	-------
Magnetisation at 2 K and 7 T		11.59 μ_B	--------
Relaxation behaviour		SMM	---------

Compound **9** was synthesised with triisopropanolamine as the main ligand alongside Pivalate from ($Fe_3O(Piv)$) as the co-ligand while compound **C** was synthesised triisopropanolamine as the main ligand alongside benzoate from ($Fe_3O(PhCO_2)$) as the co-ligand.

Compound **9** crystallises in the triclinic space group $P\bar{1}$ while compound **C** in the monoclinic space group $P\ 2_1/n$. Dy and Yb ions are eight-coordinate with a distorted triangular dodecahedron geometry. The Dy–O and Dy–N bond distances are longer than Yb–O and Yb–N. The Dy···Dy distance is longer than Yb···Yb due to the bigger size of Dy. The Dy–O–Dy angle is higher than Yb–O–Yb.

The magnetic studies of compound **C** have not been reported. The magnetic studies of compound **9** revealed that the Dy–Dy interaction is antiferromagnetic. The magnetisation of compound **9** is 11.59 μ_B. Compound **9** demonstrates SMM behaviour U_{eff} = 22.44 K and τ_o =5.23x10^{-6} s.

3.5. Structure and magnetic properties of $[Ln_4(\mu_3\text{-}OH)_2(o\text{-}van)_4(Piv)_6]\cdot 2MeCN$. (Ln = Eu(**10**), Gd(**11**), Tb(**12**) and Dy(**13**))

3.5.1. Synthetic description

The reaction of $LnCl_3\cdot 6H_2O$, Pivalic acid (CMe_3CO_2H), *N*-methyldiethanolamine ($mdeaH_2$) and *o*-vanillin (*o*-van) in a molar ratio of 1:3:5:1.1 in MeCN over reflux for two hours and afforded yellow block crystals of a new family of tetranuclear planar Ln^{III} clusters $[Ln_4(\mu_3\text{-}OH)_2(o\text{-}van)_4(Piv)_6]\cdot 2MeCN$. *N*-methyldiethanolamine ligand was not present in the crystal structure as it only functioned as a base to facilitate the deprotonation of the *o*-vanillin ligands

3.5.2. Crystal structure of $[Ln_4(\mu_3\text{-}OH)_2(o\text{-}van)_4(Piv)_6]\cdot 2MeCN$

In the series of tetranuclear lanthanide clusters, only compound **13** has been characterised fully by single-crystal X-ray diffraction, as shown in Figure 3.37 (full crystallographic data is given in Table 8.2); while the other compounds **10**-**12** were confirmed by their unit cell (Table 3.17). In addition, elemental analyses, FTIR spectroscopy and powder XRD studies (Figure 3.38) also support the suggestion that the whole series are isostructural, isomorphous and pure. Therefore, only the crystal structure of $Dy_4(\mu_3\text{-}OH)_2(o\text{-}van)_4(Piv)_6]\cdot 2MeCN$ (**13**) is described in detail as a representative of the whole series. Compound **13** crystallises in the triclinic space group $P\bar{1}$ with Z = 1. Compound **13** is a neutral cluster along with two lattice MeCN molecules. However, it loses the lattice MeCN after dry according to elemental analyses.

The structure and the central core of compound **13** are shown in Figure 3.36. The *o*-vanillin (*o*-van) and Pivalic ligands are coordinating to the Dy metal centres as can be seen in the crystal structure and *o*-vanillin (*o*-van) ligand is singly-deprotonated resulting in one negatively charged oxygen atom O(2) or O(2)' or O(5) or O(5)' form bridges along the Dy···Dy edges. The *o*-vanillin ligand (Figure 3.39, a) has been successfully used to synthesise the tetranuclear $\{Ln_4\}$ complex.

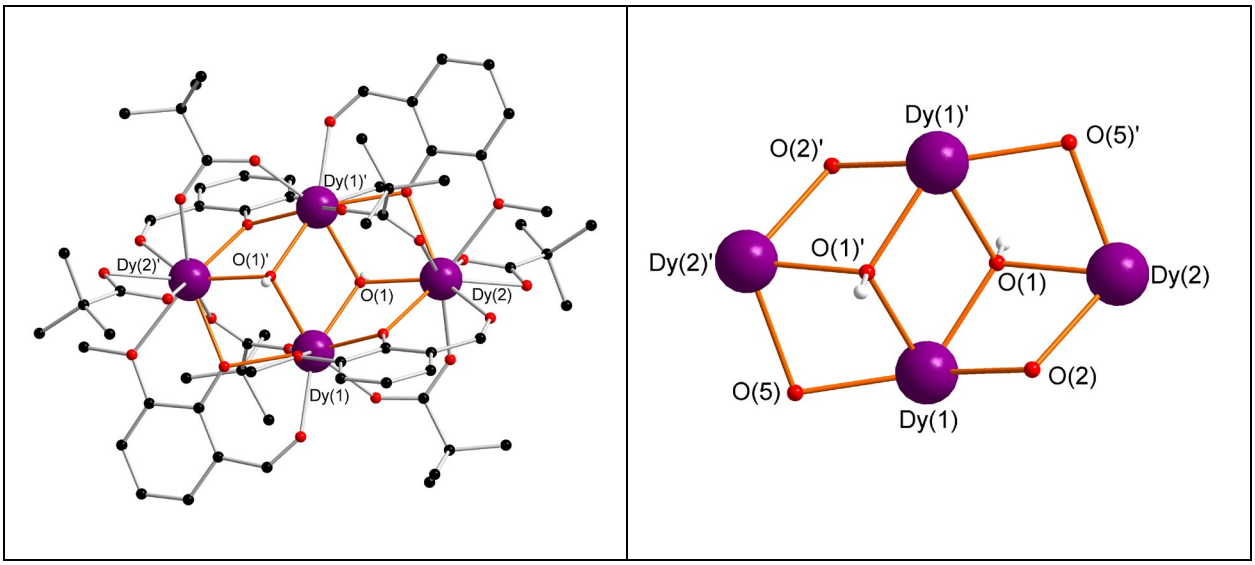

Figure 3.37. Molecular structure of compound **13**. Colour code: black, red, white and violet spheres represent C, O, H, and Dy, respectively. The core of compound **13** is shown on the right (*o*-vanillin and Pivalates are omitted for clarity).

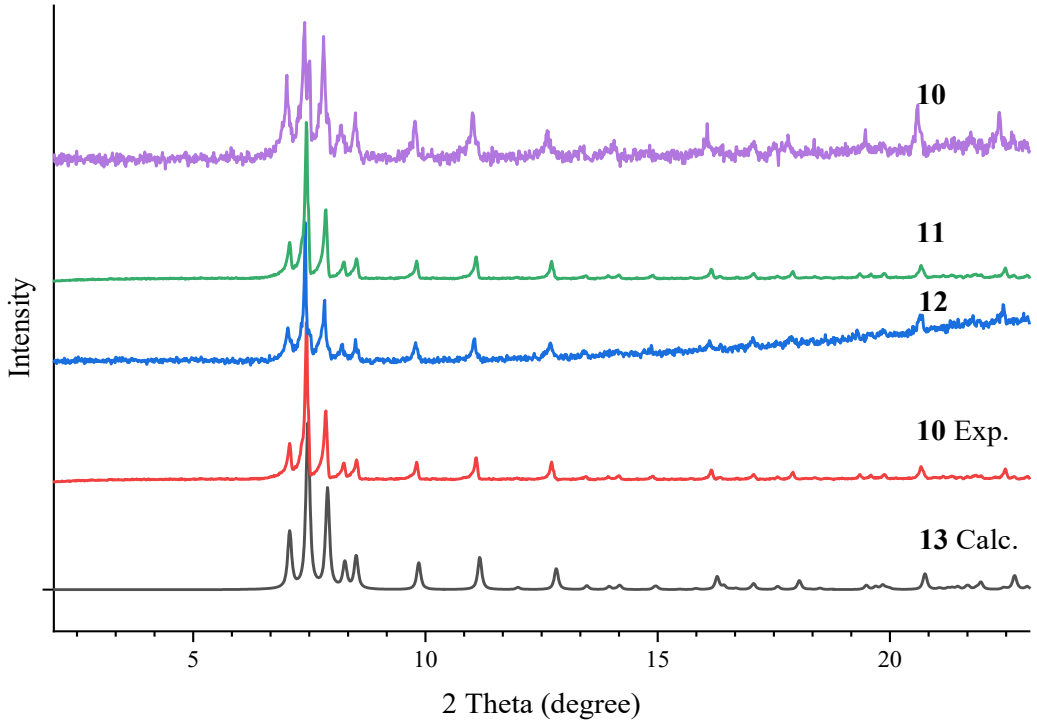

Figure 3.38. Calculated and experimental powder X-ray diffraction (PXRD) patterns of compounds **10-13**.

Table 3.17. The unit cells of compounds **10-13**

	a [Å]	b [Å]	c [Å]	α [deg]	β [deg]	γ [deg]	V [Å^3]
Eu_4(**10**)	12.10(5)	13.39(5)	13.64 (6)	69.94(8)	68.17(8)	88.06(9)	1919.12(13)
Gd_4(**11**)	12.12 (4)	13.40(4)	13.68 (4)	69.77(2)	68.15(2)	88.04(3)	1923.50(11)
Tb_4(**12**)	12.13 (7)	13.36 (7)	13.65 (8)	69.82(4)	67.96(4)	88.00(4)	1914.40(2)
Dy_4(**13**)	12.15(6)	13.36(7)	13.65 (7)	70.00(5)	67.94(5)	88.07(4)	1918.12(19)

The compound **13** consists of four Dy^{III} ions, four $(o\text{-van})^-$ and six Pivalates $(Piv)^-$. The compound **13** possesses a centrosymmetric $[Dy^{III}_4(\mu_3\text{-}OH)_2]^{10+}$ "butterfly" core, all four Dy atoms are in one plane. In this butterfly motif, two of the Dy^{III} ions occupy the body positions and the other two Dy^{III} ions occupy the outer wing-tips. Compound **13** has Dy_3 units in which the Dy_3 triangles are each bridged by a single $(\mu_3{-}OH)^-$ group, *syn-syn* bridging Pivalate and deprotonated oxygen $(o\text{-van})^-$ ligands. As shown in Figure 3.41, each of the Dy_3 triangles are bridged by a $(\mu_3{-}OH)^-$ groups through O (1) and O(1)', lying above and below the $\{Dy_4\}$ plane with a distance of 0.799 Å.

Four of deprotonated oxygen $(o\text{-van})^-$ ligands are tridentate coordinating to the Dy metal centre with a $(\eta^1{:}\ \eta^2{:}\ \eta^1{:}\ \mu_2)$ coordination mode (Figure 3.39, b). Six of the Pivalate ligands are in the crystal structure adopting two different coordination modes.

(i) Two of them are chelating to Dy(2) and Dy(2)' with a $(\eta^1{:}\eta^1{:}\mu_1)$ coordination mode (Figure 3.39, c).

(ii) Four of them are *syn-syn* bridging to two $Dy^{(III)}$ ions with a $(\eta^1{:}\eta^1{:}\mu_2)$ coordination mode (Figure 3.39, d).

a)	b)	c)	d)
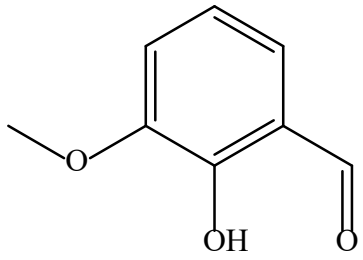	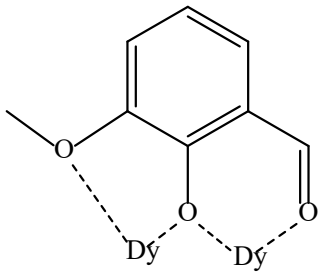	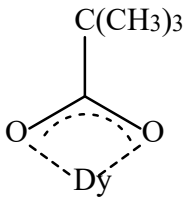	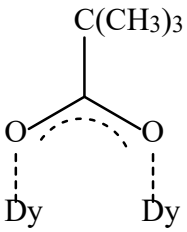
o-vanillin	$\eta^1{:}\eta^2{:}\eta^1{:}\mu_2$	$\eta^1{:}\eta1{:}\mu1$	$\eta^1{:}\ \eta^1{:}\mu_2$

Figure 3.39. (a) *o*-vanillin, (b) Coordination modes of $(o\text{-van})^-$ (c-d) Coordination modes of $(Piv)^-$ ligands found in compound **13**.

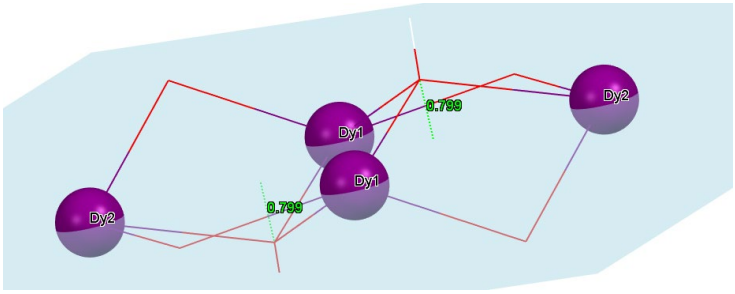

Figure 3.40. Single unit of the planar of compound **13**.

The Dy^{III} ions here present two different types of coordination spheres:

(i) Both octa-coordinated Dy(1) and Dy(1)' are surrounded by eight O donor atoms (O_8). Two O atoms come from the syn-syn bridging Pivalate ligand, four O atoms come from deprotonated oxygen $(o\text{–van})^-$ ligand and two O atoms come from $(\mu_3\text{–OH})^-$. This results in a slightly distorted triangular dodecahedron geometry which was confirmed by SHAPE analysis [309-312] with a deviation value of 0.56, (Figure 3.41, Table 8.10).

(ii) Both nine-coordinated Dy(2) and Dy(2)' are surrounded by nine O donor atoms (O_9). Two O atoms come from the chelating Pivalate ligand, two O atoms come from the *syn-syn* bridging Pivalate ligand, four O atoms come from deprotonated oxygen $(o\text{–van})^-$ ligand and one O atom comes from $(\mu_3\text{–OH})^-$. This results in a slightly distorted spherical capped square antiprism geometry which was confirmed by SHAPE analysis [309-312] with a deviation value of 0.98, Figure 3.41, Table 8.10).

The Dy−O bond distances are in the range 2.28(3)−2.59(3)Å. The Dy···Dy distances are in the range 3.80(4)−3.89(4) Å. The Dy−O−Dy angles are in the range 101.64(12)−111.14(13)°. Selected bond distances are summarised in Table 3.18.

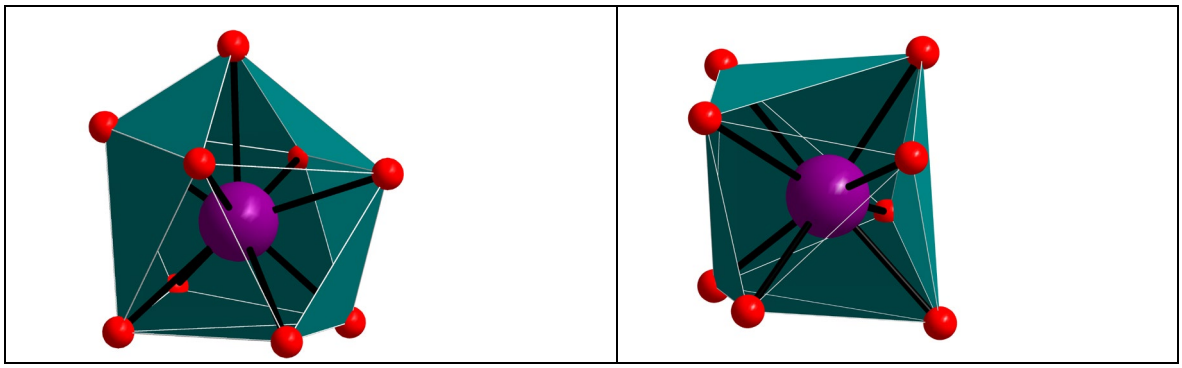

Figure 3.41. Slightly distorted triangular dodecahedron geometry of the 9-coordinated Dy(1) ion in the left and a distorted spherical capped square antiprism geometry of the 8-coordinated Dy(2) ion in the right. Colour code: red and violet spheres represent O and Dy, respectively.

Table 3.18. Selected bond distances (Å) and angles (°) of compound **13**

Bond distances				Bond distances			
Atom	Atom	Distance/Å		Atom	Atom	Distance/Å	
Dy(1)	O(1)	2.360(3)		Dy(2)	O(3)	2.361(3)	
Dy(1)	O(1)'	2.352(3)		Dy(2)	O(5)'	2.514(3)	
Dy(1)	O(2)	2.361(3)		Dy(2)	O(7)'	2.557(4)	
Dy(1)	O(4)	2.586(3)		Dy(2)	O(9)	2.317(4)	
Dy(1)	O(5)	2.386(3)		Dy(2)	O(11)'	2.337(3)	
Dy(1)	O(6)	2.383(4)		Dy(2)	O(12)	2.384(4)	
Dy(1)	O(8)	2.283(3)		Dy(2)	O(13)	2.489(3)	
Dy(1)	O(10)	2.301(4)		Dy(1)	Dy(1)'	3.823(6)	
Dy(2)	O(1)	2.353(3)		Dy(1)'	Dy(2)	3.799(4)	
Dy(2)	O(2)	2.456(3)		Dy(1)	Dy(2)	3.887(4)	
Bond Angles				Bond Angles			
Atom	Atom	Atom	Angles/°	Atom	Atom	Atom	Angles/°
Dy(1)	O(1)	Dy(2)	111.14(13)	Dy(1)	O(5)	Dy(2)'	101.64(12)
Dy(1)'	O(1)	Dy(2)	107.74(14)	Dy(1)	O(2)	Dy(2)	107.55(12)
Dy(1)	O(1)	Dy(1)'	108.48(13)				

'1-x, 1-y, 1-z

3.5.3. Magnetic properties

DC magnetic susceptibility of compound **13** was carried out on a freshly prepared polycrystalline sample in the temperature range 2-300 K under an applied DC magnetic field of 1000 Oe (0.1 T). The plot of χT versus T, for compound **13** is shown in Figure 3.42.

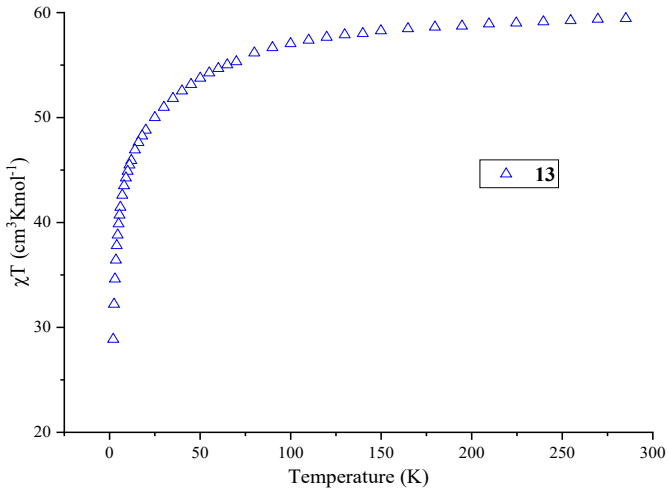

Figure 3.42. Temperature dependence of χT products for compound **13** at 1000 Oe.

The experimental χT of compound **13** at 300 K is 58.86 $cm^3mol^{-1}K$ which is slightly higher than the expected value of 56.68 $cm^3mol^{-1}K$ for four non-interacting Dy^{III} ions ($^6H_{15/2}$, S = 5/2, g = 4/3, L = 5, C = 14.17 $cm^3mol^{-1}K$) [276]. The χT product shows steady decrease at the temperature from 300 to 70 K, while at low-temperature it follows a sharp decrease down from 70-2 K reaching minimum value of 28.87 $cm^3mol^{-1}K$ at 2 K.

The decreasing of χT experimental values with the temperature is probably due to the thermal depopulation of the Stark sublevels of Dy^{III} ions and/or antiferromagnetic interactions between the Dy^{III} ions [313, 314].

AC susceptibility measurements were performed in order to investigate the dynamic magnetic behaviour of compound **13**. As shown in Figure 3.43, compound **13** shows no AC signal under zero applied DC field and even no signal under small-applied DC fields (1500 and 3000 Oe). These results indicate that compound **13** lacks SMM behaviour within the measurement parameters. However, the presence of a peak without a maximum in the Dy analogue, there is a possibility that

this system could be an SMM with a lower energy barrier which could be observed at very low, sub Kelvin, temperatures.

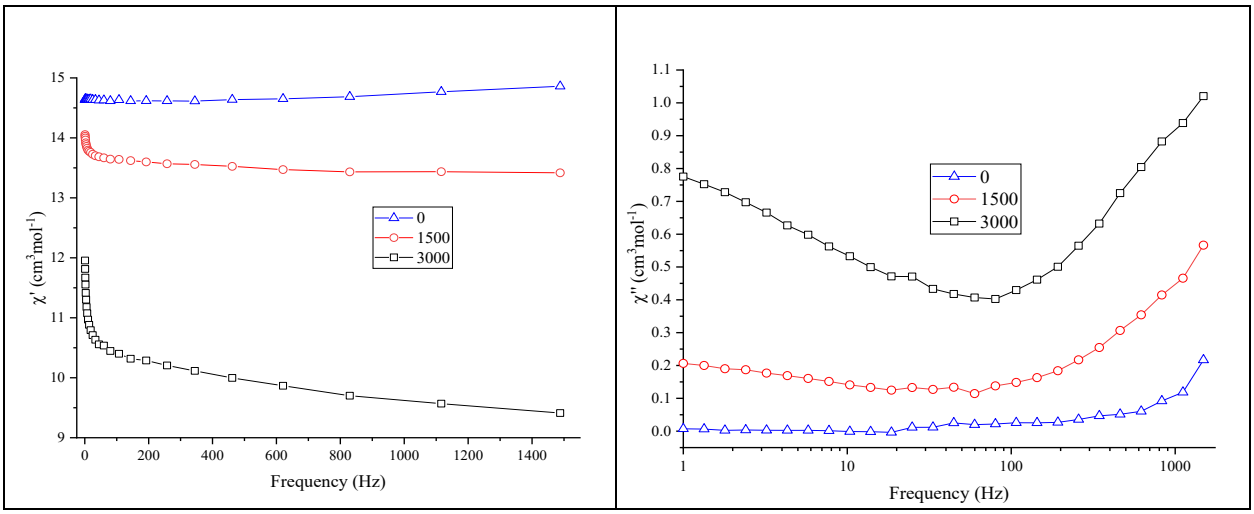

Figure 3.43. A plot of in-phase (left) and out-of-phase (right) versus frequency for compound **13** at 2 K at indicated applied magnetic fields.

3.5.4. Comparison of the core structure

The first lanthanide complex was synthesised in 2001 using *o*-vanillin (*o*-van) [148]. *o*-Vanillin has been widely used as a main ligand and co-ligand to synthesise lanthanide complexes with various topologies and also exhibiting interesting magnetic properties like SMM behaviour [32, 74, 148, 149, 151-157, 159-162]. For example, the highest energy barrier in Dy mononuclear, U_{eff} =615 K [154].

o-Vanillin was also used to synthesise {Dy_3} which presents a new concept for magnetic memory without a net magnetic moment [74, 75]. {Dy_3} shows a vanishing susceptibility at low temperature which is unexpected in a system having an odd number of unpaired electrons. *N*-methyldiethanolamine ($mdeaH_2$) has been widely used as a main ligand to synthesise Fe-Ln and 4*f* metal complexes with various topologies and also exhibiting interesting magnetic properties like SMM behaviour [79, 80, 89, 253]. For example, the highest energy barrier in the {Fe_7Dy_3} cluster U_{eff} = 33.40 K with pre-exponential relaxation time $\tau_0=6.6\times10^{-8}$ s [80]. However, $mdeaH_2$ and *o*-vanillin together have not been used to obtain lanthanide or iron–lanthanide metal complexes. From this perspective, in present work a combination of $mdeaH_2$ alongside *o*-vanillin and Pivalic acid as the two co-ligands have been employed to obtain a higher nuclearity cluster which could

provide route toward compound potentially having optical or magnetic properties as well as SMM behaviour. With this synthetic approach $[Ln_4(\mu_3\text{-}OH)_2(o\text{-van})_4(Piv)_6]$ 2MeCN was produced. The *N*-methyldiethanolamine ligand was not present in the crystal structure and probably functions as a base to facilitate the deprotonation of the *o*-vanillin ligands. There are many reports on $\{Ln_4\}$ compounds in various topologies with different main ligand/co-ligand and synthesis procedures. A review of the literature reveals that *o*-vanillin based ligands have been employed to synthesise lanthanide complexes with nuclearity ranging from 1-10 with various *4f* metals.

Table 3.19. Lanthanide complexes based on *o*-vanillin ligand.

NO	Structure	Ln	Dy SMM	Ref
1	$[DyLz_2(o\text{-van})_2]$ Br. solvent	Dy	SMM	[154]
2	$[DyLz_2(o\text{-van})_2]$ NO_3.solvent	Dy	SMM	[154]
3	$[DyLz_2(o\text{-van})_2]CF_3SO_3$.solvent	Dy	SMM	[154]
4	$[Dy_2L(H_2L)(teaH_2)(o\text{-van})(H_2O)](ClO_4)_2\cdot 2CH_3OH\cdot H_2O$	Dy	SMM	[153]
5	$[Dy_2(Pc)_2(o\text{-van})_2(H_2O)]\cdot 2THF$	Dy	SMM	[161]
6	$[Dy_2(H_2O)_2(o\text{-van})L](NO_3)_2(H_2O)_2$	Dy	Not measured	[149]
7	$[Yb_2(o\text{-van})LL'(CH_3OH)(H_2O)_2](ClO_4)_2\cdot CH_3OH\cdot H_2O$	Yb	SMM	[162]
8	$[Ce_2(H_2L_1)(o\text{-van})_3(NO_3)_3]$	Ce	Not measured	[160]
9	$[Dy_3(\mu_3\text{-}OH)_2(o\text{-van})_3Cl(H_2O)_5](Cl)_3\cdot 4H_2O\cdot 2MeOH\cdot 0.7MeCN$	Dy	SMM	[74]
10	$[Gd_3(o\text{-van})_3(OH)_2(NO_3)_2(OH_2)_4](NO_3)_2(H_2O)_4$	Gd	Not measured	[32]
11	$[Yb_3(o\text{-van})_3(OH)_2Cl(H_2O)_5]\cdot(Cl)_3\cdot 4H_2O$	Yb	Not measured	[158]
12	$[Ln_4(\mu_3\text{-}OH)_2(o\text{-van})_4(Piv)_4(NO_3)_2]\cdot CH_2Cl_2\cdot 1.5H_2O$	Gd and Dy	SMM	[156]
13	$[Ln_4(\mu_3\text{-}OH)_2(o\text{-van})_4(Piv)_6]\cdot 2MeCN$	Eu-Dy	Not SMM	This work

14	$[Dy_6(\mu_3\text{-}OH)_4(\mu_2\text{-}OH)_2(o\text{-}van)_8(H_2O)_6](CF_3SO_3)_4\cdot 6H_2O$	Dy	SMM	[155]
15	$[Dy_6(\mu_3\text{-}OH)_4(o\text{-}van)_4(avn)_2(NO_3)_4(H_2O)_4](NO_3)_2\cdot(H_2O)\cdot 3(CH_3)_2CO$	Dy	SMM	[159]
16	$[Dy_3(\mu_3\text{-}OH)_2(o\text{-}van)_3Cl_2(H_2O)_4][Dy_3(\mu_3\text{-}OH)_2(o\text{-}van)_3Cl(H_2O)_5](Cl)_5\cdot 19H_2O$	Dy	SMM	[74]
17	$[Dy_6(\mu_3\text{-}OH)_4(o\text{-}van)_4L'_2(H_2O)_9Cl](Cl)_5\cdot 15H_2O$	Dy	SMM	[32]
18	$[Tm_6(\mu_3\text{-}OH)_4(o\text{-}van)_4L'_2(H_2O)_{10}](Cl)_6\cdot 18H_2O$	Tm	Not measured	[32]
19	$[Dy_8(\mu_3\text{-}OH)_4(o\text{-}van)_2(mvn)_2(p\text{-}NO_2bz)_{14}(CH_3OH)_2]\cdot 3.09CH_3CN\cdot 6CH_3OH\cdot H_2O$	Dy	SMM	[152]
20	$[Ln_9L_1(o\text{-}van)_2(OAc)_{15}(OH)_8(H_2O)_2(DMF)]$	Nd and Gd	Not measured	[151]
21	$[Dy_{10}(\mu_4\text{-}O)_2(\mu_3\text{-}OH)_6(o\text{-}van)_6(ISO)_{13}(H_2O)_2](NO_3)$	Dy	SMM	[157]

The core of compound **13** is similar to an existing Ln_4 core. As shown in Table 3.19, $\{Dy_4\}$complex has been reported [156]. The crystallographic and magnetic details are compared in this section.

Therefore, the comparison of both compounds is summarised in Figure 3.44 and Table 3.20. In all cases the Dy containing structure has chosen as representative for the whole lanthanide. The reported $\{Dy_4\}$ [156] is denoted by compound **D**.

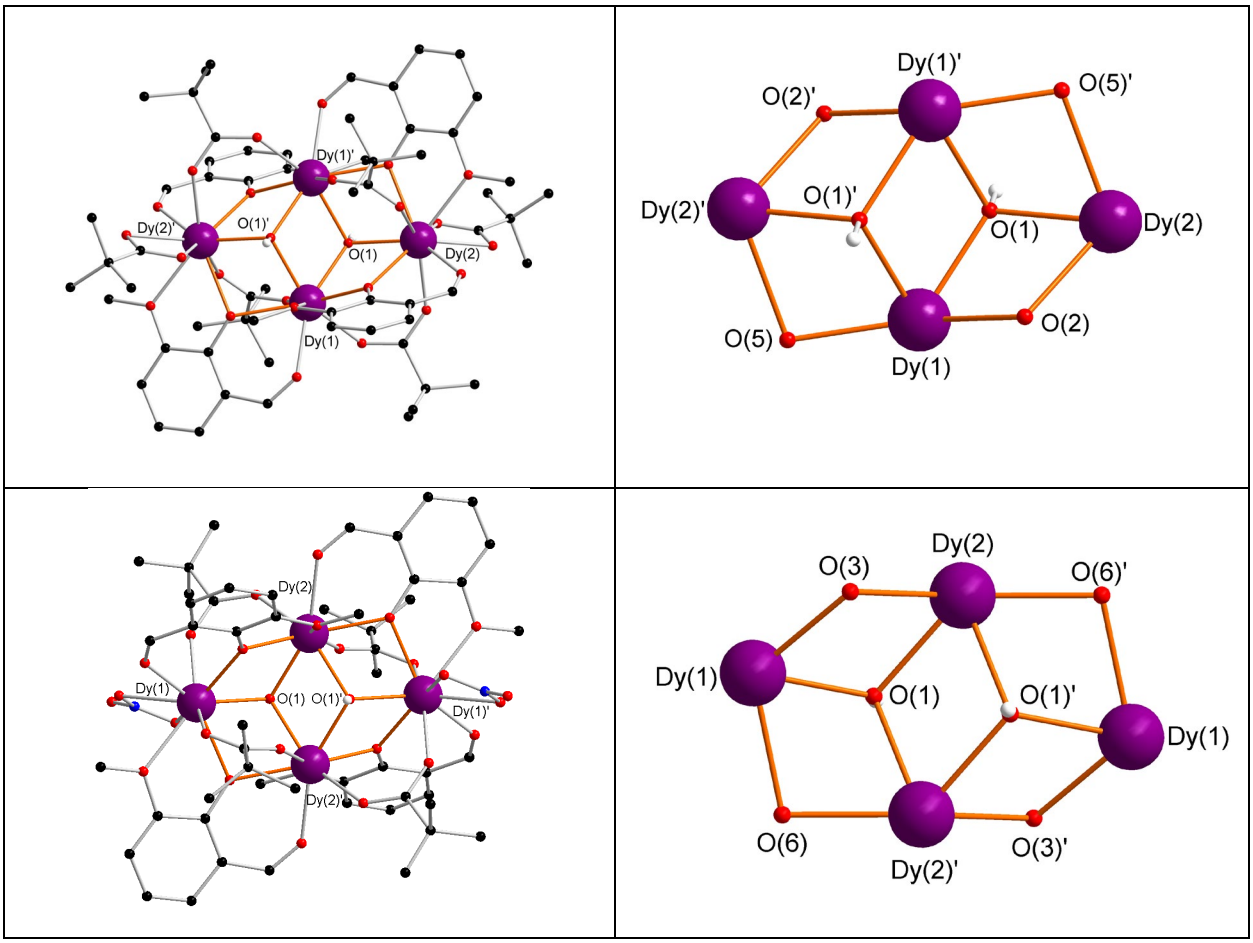

Figure 3.44. Molecular structure and the core of compound **13** on the top and compound **D** on the bottom (some H atoms omitted for clarity). Colour code: black, red, blue, white and violet spheres represent C, O, N, H and Dy, respectively.

Table 3.20. Comparison between compounds **13** and **D**.

Complex abbreviated as		Compound **13**	Compound **D** [156]	
Structure		$[Dy_4(\mu_3\text{-}OH)_2(o\text{-van})_4(Piv)_6]\cdot 2MeCN$	$[Dy_4(\mu_3\text{-}OH)_2(o\text{-van})_4(Piv)_4(NO_3)_2]\cdot CH_2Cl_2\cdot 1.5H_2O$	
Ligand		*o*-vanillin	*o*-vanillin	
Co−ligand		Pivalic acid	Pivalic acid	
Base		*N*-methyldiethanolamine	Triethylamine,	
Crystal system		Triclinic	Triclinic	
Space group		$P\bar{1}$	$P\bar{1}$	
Volume		1918.12(19)	1728.65(9)	
Colour of crystal		Yellow	Colourless	
Shape of crystal		Block	Block	
Positions in butterfly topology	body	Two Dy ions		
	wing-tips	Two Dy ions		
Position of $(\mu_3\text{−}OH)_2$		lying above and one below $\{Dy_4\}$ plane		
Distance between $(\mu_3\text{-}OH)$ and the $\{Dy_4\}$plane		0.799 Å	0.828 Å	
Shape of Dy ions		One atom distorted triangular dodecahedron and one atom distorted spherical capped square antiprism		
Average distance of Dy−O		2.40	2.39	
Average angle of	Dy−O−Dy	107.31	106.90	
Distance of	Dy−Dy	4.31	4.26	
Interactions		Antiferromagnetic		
Relaxation behaviour		Lack SMM	U_{eff} = 6.25 K	τ_0 =3.75 x10^{-5} s

Both compounds **13** and **D** were synthesised using *o*-vanillin as the main ligand alongside Pivalic acid as the co-ligand. The base in compound **13** was *N*-methyldiethanolamine whereas in compound **D** it was triethylamine. The counter ion of lanthanide in compound **13** is chloride, while in compound **D** it is nitrate. Both compounds **13** and **D** crystallises in the triclinic space group $P\bar{1}$. The colour and shape of the crystals of compound **13** is yellow blocks, while compound **D** is colourless blocks.

Both compounds **13** and **D** have butterfly core topology. In both compounds, the body and wing-tips of the butterfly topology are occupyied by two Dy^{III} ions. The two $(\mu_3\text{−}OH)$ are lying above and one below $\{Dy_4\}$ plane in compounds **13** and **D** with distance 0.799 and 0.828 Å, respectively. The Dy ions in compounds **13** and **D** two Dy ions are eight- coordinate with a distorted triangular

dodecahedron geometry and two Dy ions are nine-coordinate with a distorted spherical capped square antiprism geometry. The average Dy−O bond distance in compound **13** is longer than that in compound **D**. The Dy···Dy distance in compound **13** is longer than that in compound **D**. The average of Dy−O−Dy angle in compound **13** is larger than that in compound **D**.

The magnetic studies of compounds **13** and **D** revealed that the Dy−Dy interaction is antiferromagnetic interaction. Compound **D** demonstrates SMM behaviour U_{eff} = 6.25 K and τ_0 =3.75x10^{-5} s whereas compound **13** lacks SMM behaviour.

3.6. Conclusion

In this research, thirteen homometallic lanthanide complexes based on amino-polyalcohol ligands have been synthesised and characterised. Among dinuclear and tetranuclear Ln complexes, the crystal structures, optical and magnetic properties of Dy-based componds have been discussed in detail. Homometallic lanthanide complexes have been synthesised from the reactions of respective lanthanide cations, amino-polyalcohol ligand and co-ligand (benzoate, Pivalate and *o*-vanillin).

Three different dinuclear series $[Dy_2(H_4bdp)(PhCO_2)_2(NO_3)_2]\cdot NO_3\cdot MeCN$ (**1**), a series of four dinuclear $[Ln_2(PhCO_2)_8(MeOH)_4]_\infty$ (**2-5**) four dinuclear $[Ln_2(TipaH_2)_2(Piv)_4]$ (**6-9**) and four tetranuclear compounds $[Ln_4(\mu_3\text{-}OH)_2(o\text{-}van)_4(Piv)_6]\cdot 2MeCN$ (**10-13)** have been successfully synthesised, crystallographically characterised and magnetically studied.

Compound **1** was synthesised using 1,3-bis-diethanolamino-2-propanol (H_5bdp), iron-benzoate ($Fe_3O(PhCO_2)$) and $Dy(NO_3)_3$. Magnetic studies carried out on compound (**1**) revealed that antiferromagnetic interactions are dominant. Compound **1** exhibits slow relaxation of magnetisation and shows SMM behaviour. The energy barrier for **1** is 4.38 K with the pre-exponential factor τ_0 8.15×10^{-3} s. The Cole-Cole plots indicate a wide distribution of relaxation time or multiple relaxation process within the compound **1**.

Compounds **2-5** were synthesised using diisopropanolamine ligand, iron-benzoate ($Fe_3O(PhCO_2)$) and $Ln(NO_3)_3$. The diisopropanolamine is a necessary reagent for the isolation of the compounds in this synthesis, although it was not part of the obtained product it could act as a buffer protecting the dysprosium from further hydrolysis. The lanthanide ions are connected to benzoate and the coordination sphere completed by methanol.

Static magnetic studies show the presence of overall antiferromagnetic interactions in compounds **3-5**. Compound **5** exhibits slow relaxation of magnetisation with a maximum peak and the energy barrier is difficult to obtain. The maximum magnetic entropy (-ΔSm) value of 24.44 J kg^{-1} K^{-1} was obtained for compound **3** with ΔH =7T at 3 K. Such a feature may be of potential interest as molecular magnetic refrigerant systems. Luminescence studies performed on compounds **2** and **4** shows the emission bands emerging from f–f transitions. Compounds **2** and **4** were found to be luminescent materials.

Compounds **6-9** were synthesised using triisopropanolamine, iron-Pivalate ($Fe_3O(Piv)$) and $Ln(NO_3)_3$. Dominant antiferromagnetic interactions are observed in compound **9** and it displays slow relaxation of magnetisation and SMM behaviour. Fitting the AC data to an Arrhenius law results in an energy barrier of 22.44 K with the pre-exponential factor of 5.23×10^{-6} s. The Cole-Cole plots suggest that a single relaxation process occurs in compound **9**.

Compounds (**10-13)** were synthesised using *N*-methyldiethanolamine ($mdeaH_2$), *o*-vanillin (*o*-van), Pivalic acid and $LnCl_3$. The *N*-methyldiethanolamine ($mdeaH_2$) is an essential reagent for obtaining the compound. Although *N*-methyldiethanolamine ($mdeaH_2$) is not in the final product, it acts as a base catalyst to facilitate the deprotonation of the *o*-vanillin ligand. Magnetic studies carried out on compound (**13**) revealed that antiferromagnetic interactions are dominant and a lack SMM behaviour.

Chapter 4. Structure, optical and magnetic properties of iron-lanthanide aggregates

4. 1. Introduction

Fe-Ln metal complexes have gained the attention of researchers around the world due to their intriguing architectures and promising applications as single-molecule magnets (SMMs). SMMs have potential applications in industries such as a refrigeration, data storage, sensing and there is fucture expectation for use of SMM in quantum computing.

A review of the literature reveals that the synthesis of 3d-4*f* polynuclear metal complexes is a promising approach to SMM. Fe-Ln metal complexes have been reported in the literature using many different types of ligand and co-ligands, these can be mono- or multidentate to build the desired coordination complex.

Our group has long used the approach of incorporating N-substituted diethanolamine ligands along with carboxylic acids as a means of targeting 3d-4*f* coordination clusters (Scheme 4.1). This mixture of ligands provides various types of chelating and bridging modes allowing for "clustering" of 3d and 4*f* ions into favorable structural motifs. A large number of bridging possibilities for these ligands via hard O-donors means that the coordination environment and geometry preferences of both 3d and 4*f* ions can be accommodated. Stabilisation of a given motif is assisted through finding reaction conditions (temperature, pressure, solvents, etc...) to promote bulk crystallisation. We call this method "assisted self-assembly". It is clearly based on a serendipitous approach but with an eye to directing the system towards a "happy accident".

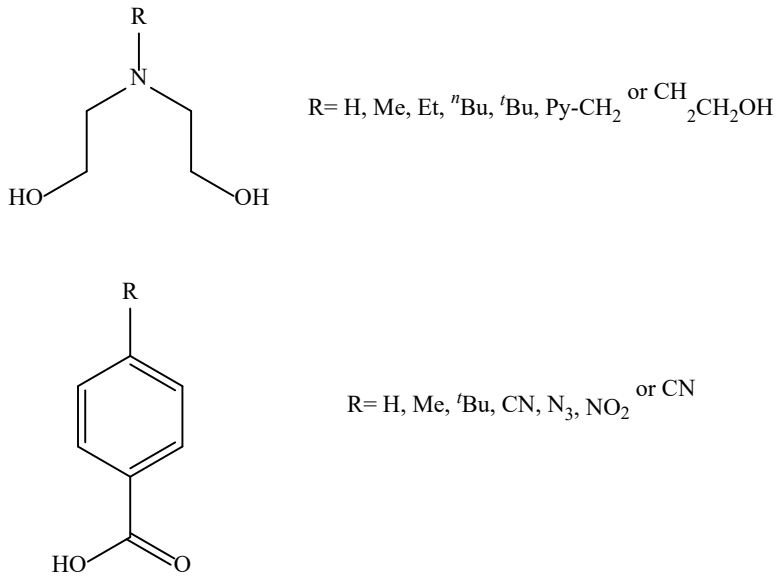

Scheme 4.1. The ligands and co-ligands used to assemble coordination clusters

A range of nuclearities has been achieved using this basic approach (from 2-10) with Fe or/and 4*f* ions [79, 80, 283]. This approach has been successfully used to synthesise 3d-metal complexes [327] and combine 3d and 4*f* metal in one aggregate [78-80, 328].

The fact that lanthanide/rare-earth ions (here we use the convention that Ln include the rare earths-ie. Sc, Y, La-Lu) adopt coordination geometries based principally on electrostatic considerations rather than ligand field stabilisation effects means that it is usually possible to study isostructural series of 3d-4*f* coordination clusters for a given 3d ion. In some case a series can be accessed for a large family of Ln^{3+} ions–rarely for La^{3+} and Ce^{3+} but, as here, for Pr-Ho or beyond (ideally to Lu).

The fact that such families are accessible means that the contribution of Ln ions to the properties of the coordination cluster (eg, magnetism, optical properties) can be surveyed. In addition, substituting a paramagnetic Ln^{3+} ion with diamagnetic Y^{3+}, La^{3+}, or Lu^{3+} (chosen according to which radius is most appropriate) means that the effect of the open 4*f* electron-shell on the properties can be determined as well as allowing for the investigation of the contribution of the 3d ions to the magnetic properties.

More specifically this work will investigate 3d-4*f* cluster complexes where 3d = Fe^{3+}. A large number of Fe/4*f* systems can be found in the literature where the majority, incorporate iron as the

high spin (hs) Fe^{3+} ion (note there are some high spin Fe^{2+} examples). As a d^5 ion, Fe^{3+} provides five spins in its high spin state, the maximum allowed in a d-block complex, making it a good choice in the search for new single-molecule magnet (SMM) systems. Indeed, mixing Fe^{3+} with 4*f* ions has led to the discovery of many SMM as well as compounds showing unusual features such as the reported '$Fe_{10}Gd_{10}$' from our group which is a system lying in close proximity to a Quantum Critical Point (QCP) [329]. Recently the highest nuclearity Fe-Ln cluster, the $Fe_{18}Dy_6$ SMM was reported by our group [330].

In terms of the cluster-based cooperative magnetic properties, the Fe-Ln pairing for Ln = Dy is generally the most promising first choice for finding SMM properties due to the large anisotropy and five unpaired electrons of Dy^{III}. Generally, the Fe-Dy interaction is ferromagnetic in nature. Using a third type of ligand in the system, normally the azide ion can guarantee ferromagnetic coupling when it acts as a bridging (η^1:η^1) ligand. The (η^1:η^2) mode tends to favour antiferromagnetic coupling.

A review of the literature reveals that 27 series of Fe-Ln metal complexes incorporating azide ligands have been reported, so far. Table 4.1, presents 30 compound families, of the 27 reported in the literature and 3 from this work.

Table 4.1. Fe-Ln metal complex incorporates azide ligands.

NO	Structure	Ln	SMM	Ref
1	$[Fe_2Ln_2(\mu_3\text{-}O)_4(H_2L)_2(mpm)_2(Piv)_2(N_3)_{4-x}(Cl)_x]$	Gd-Er	Not	[87]
2	$[Fe_2Ln_2(\mu_3\text{-}OH)_2(teg)_2(N_3)_2(Piv)_4]$	Dy, Ho and Y	Not	[331]
3	$[FeLn_2Fe(\mu_3\text{-}OH)_2(teg)_2(N_3)_2(PhCO_2)_4]$	Dy and Y	Not	[332]
4	$[Fe_2Ce_2Na_2(\mu_4\text{-}O)_2(Me_3CCO_2)_8(N_3)_2(ap)_2]F$	Ce	NM	[333]
5	$[Fe_2Ln_2(mdea)_2\{(py)_2C(OCH_3)O\}_2(\mu_4\text{-}O)(N_3)_2(NO_3)_2(CH_3OH)_2]\ H_2O$ (**14**-**20**)	Pr-Dy and Y	Not	This work 4.2
6	$[Fe_3Gd_2(N_3)_{15}(OH)_3(TipaH_3)_2]\ (TBA)_3$	Gd	NM	[84]
7	$[Fe_4Ln_2(OH)_2(N_3)_2(nbdea)_4(Me_3CCO_2)_5(H_2O)]NO_3\cdot 2EtOH$	Dy and Y	SMM	[334]

8	$[Fe_4Ln_2(OH)_2(N_3)_2(nbdea)_4(Me_3CCO_2)_4(NO_3)_2]\cdot 3EtOH$	Gd and Eu	NM	[334]
9	$[Fe_4Ln_2(\mu_3\text{-}OH)_2(nbdea)_4(Me_3CCO_2)_6(N_3)_2]\cdot 3MeCN$	Dy and Y	Not	[335]
10	$[Fe_4Ln_2(OH)_2(Me_2CHCO_2)_6(N_3)_2(nbdea)_4]\cdot 2MeOH$	Gd-Tm and Y	Dy and Tb are SMM	[336]
11	$[Fe_4Ln_2(Me_3CCO_2)_6(N_3)_4(teaH)_4]\cdot 2EtOH$	Dy-Er	Tb	[337]
12	$[Fe_4Tb_2(Me_3CCO_2)_6(N_3)_4(teaH)_4]$	Tb	Not	[337]
13	$[Fe_4Ln_2(Me_3CCO_2)_6(N_3)_4(teaH)_4]\cdot 2CH_2Cl_2$	Dy, Er	Not	[337]
14	$[Fe_4Ln_2(Me_3CCO_2)_4(N_3)_6(teaH)_4]\cdot 2EtOH\cdot 2CH_2Cl_2$	Dy, Er	Not	[337]
15	$[Fe_4Ln_2(teaH)_4(\mu\text{-}N_3)_4(N_3)_3(Piv)_3]$	Gd-Er and Y	Dy and Tb are SMM	[85]
16	$[Fe_4Ln_2(teaH)_4(N_3)_4(Piv)_6]$	Er and Lu	Not	[83]
17	$[Fe_2Ln_4(mdea)_2(mdeaH)_2(\mu_3\text{-}OH)_2(N_3)_2(PhCO_2)_8]\cdot 3MeCN$ (**21-29**)	Pr-Ho and Y	Not	This work 4.3
18	$[Fe_4Ln_2(mdea)_4(PhCO_2)_6(N_3)_2(\mu_3\text{-}OH)_2]\cdot MeCN$ (**40-46**)	Eu-Er and Y	SMM	This work 4.5
19	$[Fe_4Dy_4(teaH)_8(N_3)_8(H_2O)]\cdot H_2O\cdot 4CH_3CN\cdot$	Dy	SMM	[86]
20	$[Na_2Fe_6Dy_2(N_3)_4(HL)_4(CH_3O)_4(PhCO_2)_6]$	Dy	Not	[338]
21	$[Na_2Fe_6Dy_2(N_3)_4(L')_4(CH_3O)_4(PhCO_2)_6(H_2O)]$	Dy	Not	[338]
22	$[Na_2Fe_6Dy_2(N_3)_4(L')_4(CH_3O)_4(Me_3CCO_2)_6]$	Dy	Not	[338]
23	$[Na_2Fe_6Y_2(N_3)_4(L')_4(CH_3O)_4(PhCO_2)_6(H_2O)]$	Y	NM	[338]
24	$[Na_2Fe_6Gd_2(N_3)_4(L')_4(CH_3O)_4(PhCO_2)_6(CH_3OH)_2]$	Gd	NM	[338]
25	$[Fe_6Dy_3(\mu_7\text{-}C_2H_2O_4)(\mu_4\text{-}tea)_2(\mu_3\text{-}teaH)_4(\mu_2\text{-}N_3)_2(N_3)_6(NO_3)]\cdot 2EtOH$	Dy	SMM	[339]
26	$[Fe_6Ln_4(Me_2CHCO_2)_8(N_3)_2(nbdea)_{10}]\cdot n(methanol)$	Gd-Ho and Y	Tb	[336]
27	$[Fe_7Dy_3(\mu_4\text{-}O)_2(\mu_3\text{-}OH)_2(mdea)_7(\mu\text{-}PhCO_2)_4(N_3)_6]\cdot 2H_2O\cdot 7CH_3OH$	Dy	SMM	[80]

28	$[Fe_7Ln_3(\mu_4\text{-}O)_2(\mu_3\text{-}OH)_2(mdea)_7(\mu\text{-}PhCO_2)_4(N_3)_6]\cdot H_2O\cdot 4MeCN$	Gd, Tb	Tb	[79]
29	$[Fe_7Er_3(\mu_4\text{-}O)_2(\mu_3\text{-}OH)_2(mdea)_7(\mu\text{-}PhCO_2)_4(N_3)_5(MeOH)]Cl\cdot 7.5H_2O\cdot 11.5MeOH$	Er	Not	[79]
30	$[Fe_{18}Ln_6(Me_2CHCO_2)_{12}(teaH)_{18}(tea)_6(N_3)_6]\cdot$ n(solvent)	Sm-Ho and Y	Not	[337]

SMM means Dy is SMM, NM means not measured, Not means does not display SMM, Tb and means Tb is SMM.

Herein, the crystal structures, optical and magnetic properties are reported for 3 series of Fe-Ln metal complexes incorporating azide ligand plus a 4th without azide.

The four series of Fe-Ln metal complexes reported here used *N*-methyldiethanolamine ($mdeaH_2$) as the main ligand, supported by co-ligands. The co-ligand was changed in the series to study the magnetic and optical properties of the assembly and structures. The nuclearity and topology depend on the strength of co-ligand and possible coordination modes to complete the coordination sphere of the metal. The coordination modes presented here can be divided into bridging, bridging-chelating and terminal (monodentate and chelating). Changing the co-ligand allowed a change in nuclearity as well as the resulting magnetic and optical properties. The carboxylate group has proven a useful functional group as a main ligand or co-ligand for obtaining higher-nuclearity clusters of iron-lanthanide species. Carboxylate ligands include benzoate, Pivalate, acetate and isobutyrate which are all commonly used for Fe-Ln metal complexes.

To study the cooperative effect of combining Fe^{III} with paramagnetic Ln^{III}, the Ln can be replaced with diamagnetic ions such as Y^{III}, La^{III}or Lu^{III} or Fe^{III} can be replaced with Al^{III} or Ga^{III}.

The first series compound 5 in Table 4.1 comprises seven isostructural tetranuclear Fe-Ln metal complexes and was obtained by using *N*-methyldiethanolamine ($mdeaH_2$), di-2-pyridyl ketone (dpk), iron chloride, lanthanide nitrate and sodium azide (NaN_3). A tetranuclear Fe-Ln $[Fe_2Ln_2(mdea)_2\{(py)_2C(OCH_3)O\}_2(\mu_4\text{-}O)(N_3)_2(NO_3)_2(CH_3OH)_2]$ H_2O with a novel core was successfully synthesised, characterised and the magnetic properties were investigated

The second series compound 17 in Table 4.1 comprises nine isostructural hexanuclear Fe-Ln metal complexes and was obtained by using *N*-methyldiethanolamine ($mdeaH_2$), sodium benzoate ($PhCO_2Na$), iron chloride, lanthanide nitrate and sodium azide (NaN_3). A hexanuclear Fe-Ln butterfly complex $[Fe_2Ln_4(mdea)_2(mdeaH)_2(\mu_3\text{-}OH)_2(N_3)_2(PhCO_2)_8]$ 3MeCN with a novel core was successfully synthesised, characterised, the optical and magnetic properties were investigated.

The third series comprises ten isostructural hexanuclear Fe-Ln metal complexes and was obtained by using *N*-methyldiethanolamine ($mdeaH_2$), sodium benzoate ($PhCO_2Na$), iron chloride, lanthanide nitrate and *o*-vanillin (*o*-van). A hexanuclear Fe-Ln $[Fe_2Ln_4(mdea)_2(o\text{-}van)_2(\mu_4\text{-}O)_2(PhCO_2)_8]$ (2·5 MeCN) with a novel core was successfully synthesised, characterised and the magnetic properties were investigated.

The fourth series compound 18 in Table 4.1 comprises seven isostructural hexanuclear Fe-Ln metal complexes and was obtained by using *N*-methyldiethanolamine ($mdeaH_2$), sodium benzoate ($PhCO_2Na$), iron chloride, lanthanide chloride and sodium azide (NaN_3). A hexanuclear Fe-Ln with butterfly topology $[Fe_4Ln_2(mdea)_4(\mu_3\text{-}OH)_2(N_3)_2(PhCO_2)_6]$ MeCN was successfully synthesised, characterised, the optical and magnetic properties were investigated.

The content in the fourth series is similar to that presented in the second series. However changing the counter ion of the lanthanide provided a new series which may feature very different in magnetic and optical properties.

4.2. Structure and magnetic properties of $[Fe_2Ln_2(mdea)_2\{(py)_2C(OCH_3)O\}_2(\mu_4\text{-}O)(N_3)_2(NO_3)_2(CH_3OH)_2]\cdot H_2O$. (Ln = Pr(**14**), Nd(**15**), Sm(**16**), Eu(**17**), Gd(**18**), Tb(**19**) and Dy(**20**))

4.2.1. Synthetic description

The reaction of anhydrous $FeCl_3$, $Ln(NO_3)_3\cdot 6H_2O$, sodium azide (NaN_3), *N*-methyldiethanolamine ($mdeaH_2$) and di(2-pyridyl) ketone (dpk) in a molar ratio of 10:10:30:50:11 in a mixture of MeCN/MeOH (1:1) under reflux for two hours subsequent cooling and afforded brown block crystals of a new family of tetranuclear Fe-Ln clusters $[Fe_2Ln_2(mdea)_2\{(py)_2C(OCH_3)O\}_2(\mu_4\text{-}O)(N_3)_2(NO_3)_2(CH_3OH)_2]\cdot H_2O$.

4.2.2. Crystal structure of $[Fe_2Ln_2(mdea)_2\{(py)_2C(OCH_3)O\}_2(\mu_4\text{-}O)(N_3)_2(NO_3)_2(CH_3OH)_2]\ H_2O$

Full structure determination was performed for compound **20** by single-crystal X-ray diffraction (Figure 4.1) (crystallographic data is given in Table 8.3); while compounds **14-19** were found to be isostructural with **20** by checking their unit cells (Table 4.2). Analysis of the IR spectra, PXRD patterns (Figure 4.2) and elemental analyses further confirmed that compounds **14-20** are isomorphous and isostructural.

The crystal structure of the tetranuclear complex $[Fe_2Dy_2(mdea)_2\{(py)_2C(OCH_3)O\}_2(\mu_4\text{-}O)(N_3)_2(NO_3)_2(CH_3OH)_2]\cdot H_2O$ **(20)** will be described in detail as representative of the whole series. The compound **20** crystallises in the monoclinic space group *Cc* with Z = 4. Compound **20** is a neutral cluster with one lattice water molecule form an intramolecular interaction with terminal azide and also an intermolecular interaction with the nitrate $(NO_3)^-$ group of the neighbouring molecule.

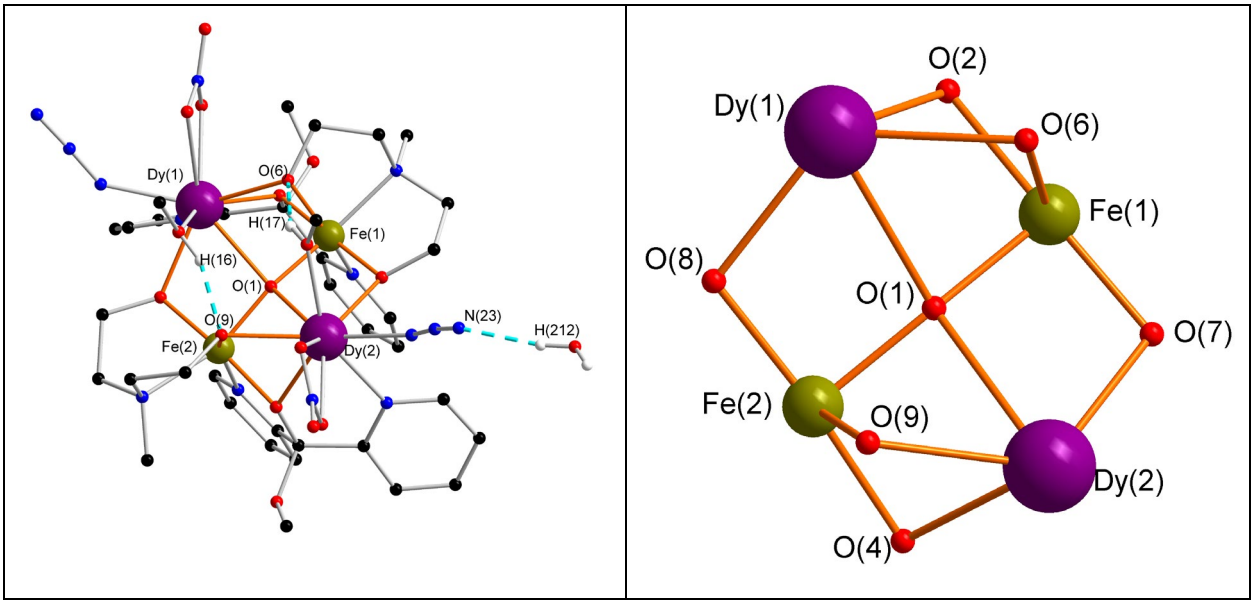

Figure 4.1. Molecular structure of compound **20**. Colour code: black, red, blue, green, white and violet spheres represent C, O, N, Fe, H and Dy, respectively. The core of compound **20** on the right (H atoms, $mdea^{2-}$ and $(py)_2C(OCH_3)O^-$ ligands are omitted for clarity).

The structure and the central core of compound **20** are shown in Figure 4.1, the compound **20** consists of two Fe^{III}, two Dy^{III}, two doubly-deprotonated $mdea^{2-}$, two singly-deprotonated

$((py)_2C(OCH_3)O)^-$ ligands, two terminal azide $(N_3)^-$ and two chelating nitrate $(NO_3)^-$ group. The compound **20** has $[Fe_2Dy_2(\mu_4\text{-}O)]^{10+}$ distorted square core. The $mdeaH_2$ and " modified dpk" ligands are coordinating to the metal centres as shown in the crystal structure and the $mdeaH_2$ is doubly–deprotonated resulting in two negatively charged oxygen atoms O(6), O(7), or O(8), O(9) form alkoxy bridges along the Fe···Dy edges, whilst $(py)_2C(OCH_3)OH$ is singly–deprotonated resulting in one negatively charged oxygen atom O(2) or O(4) form additional bridges along the Fe···Dy edges. The core is held together by the $(\mu_4\text{-}O)^{2-}$ group O(1) (Figure 4.1 right).

As commonly observed, the keto group of the dpk molecule forms a hemiacetal through reaction with the solvent MeOH [340] according to Scheme 4.2.

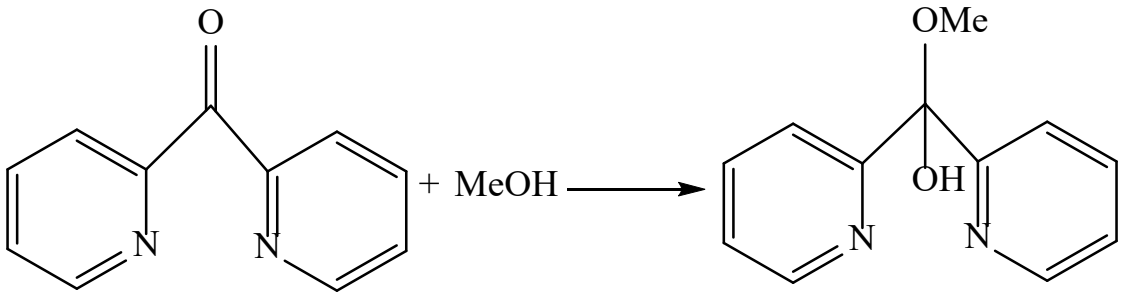

Scheme 4.3. Modification of dpk ligand by reaction methanol with dpk ligand

Table 4.2. The unit cells for compounds **14-20**.

	a [Å]	b [Å]	c [Å]	α [deg]	β [deg]	γ [deg]	V [Å^3]
Fe_2Pr_2(**14**)	18.28(7)	17.56(7)	16.32(3)	90.1(3)	98.15(2)	89.9(2)	5180(30)
Fe_2Nd_2(**15**)	18.41(3)	17.41(3)	16.48(3)	90.15(12)	98.12(14)	89.71(14)	5214(15)
Fe_2Sm_2(**16**)	18.32(13)	17.45(6)	16.16(11)	89.91(4)	97.99(6)	90.07(4)	5118(5)
Fe_2Eu_2(**17**)	18.35(4)	17.41(10)	16.24(13)	89.92(11)	97.82(11)	89.75(12)	5110(14)
Fe_2Gd_2(**18**)	18.28(10)	17.44(13)	16.17(12)	90(6)	97.97(5)	90.09(5)	5102(6)
Fe_2Tb_2(**19**)	18.45(2)	17.43(2)	16.31(3)	90.06(12)	97.63(12)	90.15(10)	5180(12)
Fe_2Dy_2(**20**)	18.13(4)	17.43(3)	15.85(3)	90(3)	97.52(2)	90(3)	4962.5(17)

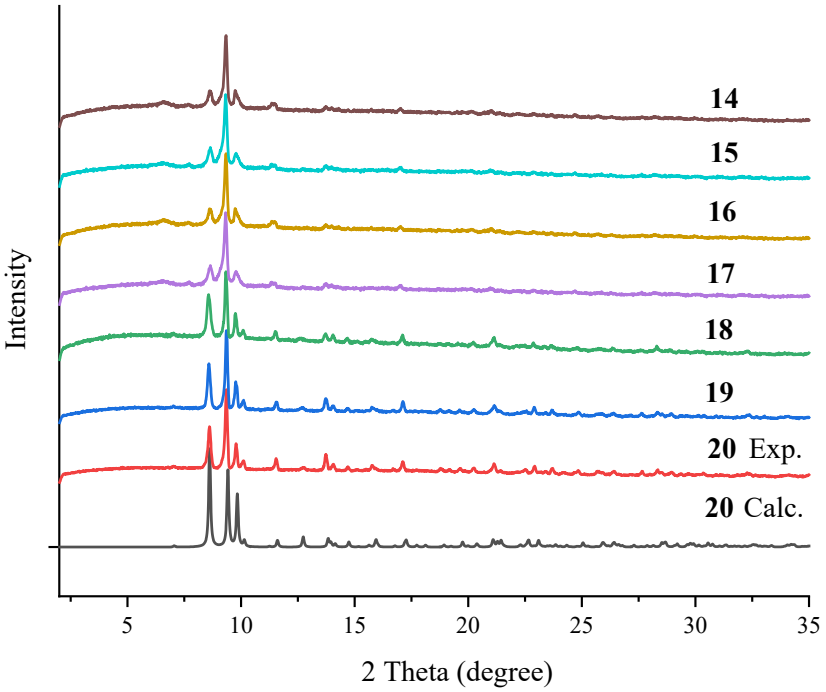

Figure 4.2. Calculated and experimental of PXRD patterns of compounds **14**–**20**.

The doubly-deprotonated $mdea^{2-}$ ligands are tridentate coordinating to the metal centre with a (η^2: η^1: η^2: μ_3) coordination mode (Figure 4.3, a). The doubly–deprotonated ligands are centred on the Fe^{III} ions through the N atom, while the singly-deprotonated $((py)_2C(OCH_3)O)^-$ ligands are tridentate coordinating to the metal centre with a (η^1: η^2: η^1: μ_2) coordination mode (Figure 4.3, b).

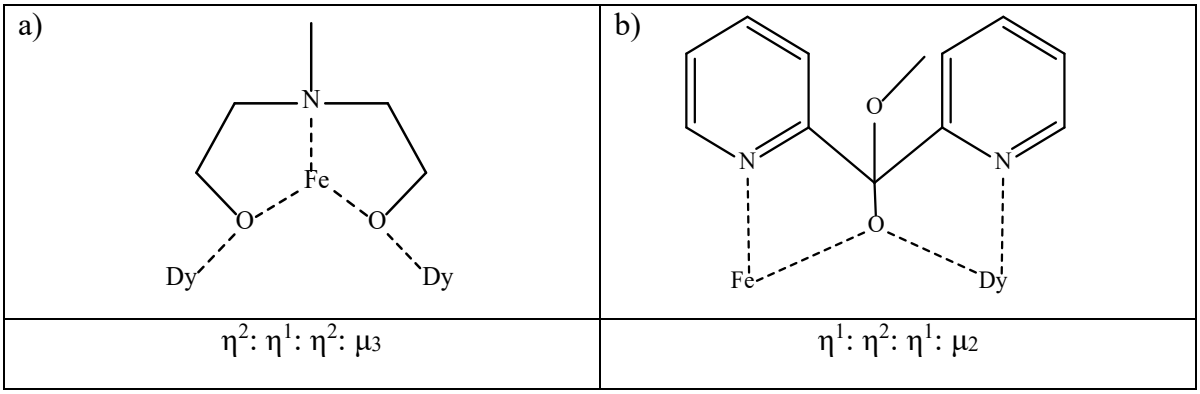

Figure 4.3. Coordination mode of ligands (a) $mdea^{2-}$, (b) $\{(py)_2C(OCH_3)O\}^-$.

Both hexa-coordinated Fe^{III} ion are surrounded by two N and four oxygen donor atoms (N_2O_4). One N and two O atoms come from the doubly-deprotonated oxygen $mdea^{2-}$ ligands. One N and one O atom come from the deprotonated oxygen of the $((py)_2C(OCH_3)O)^-$ ligand and one O atom

comes from the $(\mu_4\text{-O})^{2-}$ group. The Fe–O and Fe–N bond distances are in the range 1.890(6)−2.044(6) Å and 2.133(8)−2.217(8) Å, respectively. The Fe−Dy distance are in the range 3.1009(11)−3.4159(13). The Fe···Fe bond distance is 3.73(15) Å. The Fe−O−Fe angle is 161.4(3)°. Selected bond distances and bond angles are summarised in Table 4.3. This results in a distorted octahedron geometry with a ∑ parameter of 95.36. This octahedral geometry was confirmed by SHAPE analysis [309-312] with a deviation value of 2.73, (Figure 4.4, Table 8.11).

Both nine-coordinated Dy^{III} ion are surrounded by two N and seven O donor atoms (N_2O_7). One N atom comes from the terminal azide $(N_3)^-$, two O atoms come from doubly-deprotonated oxygens of the $mdea^{2-}$ ligand, one N atom and one O atom come from the deprotonated oxygen $((py)_2C(OCH_3)O)^-$ ligand, one O atom comes from the $(\mu_4\text{-O})^{2-}$, two O atoms come from the chelating nitrate anions NO_3^- and one O atom comes from the methanol molecule CH_3OH. The Dy−O and Dy−N bond distances are in the range 2.361(6)−2.579(6) Å and 2.371(9)−2.586 (8) Å, respectively. The Dy···Dy distance is 4.84(5) Å. The Fe−O−Dy angles are in the range 87.1(2)−104.4(2)° and Dy−O−Dy angle is 142.1(2)°. This results in a distorted spherical capped square antiprism geometry. This geometry was confirmed by SHAPE analysis [309-312] with a deviation value of 1.30, (Figure 4.4, Table 8.11).

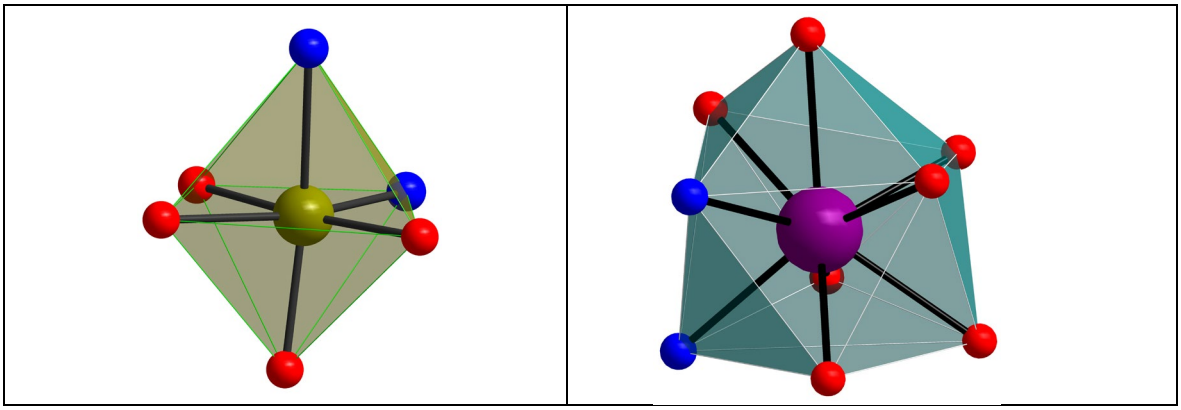

Figure 4.4. Distorted octahedron geometry of the 6-coordinated Fe ion on the left and distorted spherical capped square antiprism geometry of the 9-coordinated Dy ion on the right. Colour code: red, blue, green and violet spheres represent O, N, Fe and Dy, respectively.

The structure of compound **20** is further stabilised by intra- and intermolecular interactions. Intramolecular interactions stabilise the structure through π-π stacking and hydrogen bonds. The π-π stacking interaction is between the pyridine rings which are in the parallel (face-to-face) mode, where the distance between centroid-centroid is ~3.72 Å as shown in Figure 4.5.

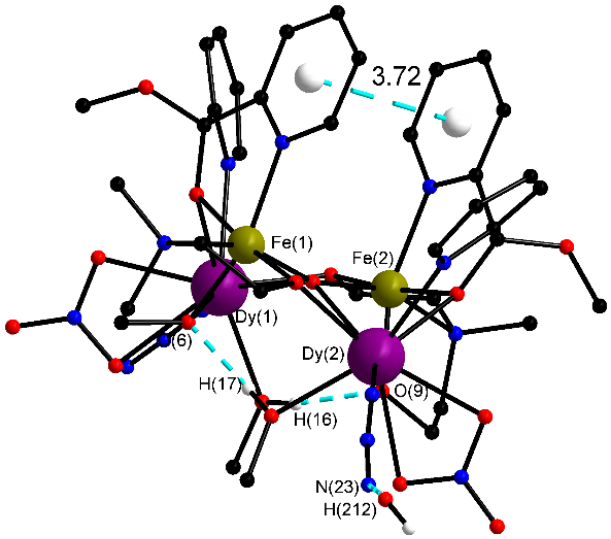

Figure 4.5. Intramolecular interactions of compound **20**. Colour code: black, red, blue, green, white and violet spheres represent C, O, N, Fe, H and Dy, respectively.

In addition, the intramolecular interaction has stabilised the structure through hydrogen bonds. O(16)−H(16) and O(17)−H(17) from the methanol molecule (CH_3OH) which make intramolecular hydrogen bonds to O(9) and O(6) from the doubly-deprotonated oxygen $(mdea)^{2-}$ ligands, respectively. The distances of O(16)···O(9) and O(17)···O(6) are 2.63 and 2.64 Å, respectively.

Also, O(21)−H(212) from the lattice water molecule (H_2O) makes an intramolecular hydrogen bond to N(23) from the terminal azide $(N_3)^-$ with a O(21)···N(23) distance of 2.91 Å. O(21)−H(211) from the lattice H_2O makes an intermolecular hydrogen bond to O(12) from nitrate group NO_3^- of a neighbouring molecule at {+x, 1-y, ½+z} with an O(21)···O(12) distance of 2.99 Å.

In addition, O(21)−H(212) from the lattice H_2O makes an intermolecular hydrogen bond to N(23) from the terminal azide N_3^- of the neighbouring molecule at {+x, 1-y, ½+z} with an O(21) ···N(23)

distance of 2.91 Å. The intra and intermolecular interaction result in a 3D supramolecular packing of compound **20** as shown in Figure 4.6.

Table 4.3. Selected bond distance (Å) and bond angles (°) of compound **20**

Bond distances				Bond distances			
Atom	Atom	Distance/Å		Atom	Atom	Distance/Å	
Fe(1)	O(1)	1.894(6)		Dy(1)	O(2)	2.391(6)	
Fe(1)	O(2)	2.013(6)		Dy(1)	O(6)	2.423(6)	
Fe(1)	O(6)	2.026(6)		Dy(1)	O(8)	2.367(7)	
Fe(1)	O(7)	1.931(6)		Dy(1)	O(10)	2.471(10)	
Fe(1)	N(2)	2.133(8)		Dy(1)	O(11)	2.565(9)	
Fe(1)	N(5)	2.211(8)		Dy(1)	O(16)	2.392(7)	
Fe(2)	O(1)	1.890(6)		Dy(1)	N(1)	2.586(8)	
Fe(2)	O(4)	1.999(6)		Dy(1)	N(11)	2.371(9)	
Fe(2)	O(8)	1.947(6)		Dy(2)	O(1)	2.543(6)	
Fe(2)	O(9)	2.044(6)		Dy(2)	O(4)	2.401(6)	
Fe(2)	N(4)	2.149(7)		Dy(2)	O(7)	2.361(6)	
Fe(2)	N(6)	2.217(8)		Dy(2)	O(9)	2.407(6)	
Fe(1)	Dy(1)	3.122(11)		Dy(2)	O(13)	2.470(7)	
Fe(1)	Dy(2)	3.400(12)		Dy(2)	O(14)	2.525(7)	
Fe(2)	Dy(1)	3.416(13)		Dy(2)	O(17)	2.384(7)	
Fe(2)	Dy(2)	3.101(11)		Dy(2)	N(3)	2.586(8)	
Dy(1)	O(1)	2.579(6)		Dy(2)	N(21)	2.387(9)	
Bond angles				Bond angles			
Atom	Atom	Atom	Angles/°	Atom	Atom	Atom	Angles/°
Fe(1)	O(1)	Dy(1)	87.1(2)	Fe(2)	O(1)	Dy(1)	98.5(2)
Fe(1)	O(2)	Dy(1)	89.9(2)	Fe(2)	O(8)	Dy(1)	104.3(3)
Fe(1)	O(6)	Dy(1)	88.7(2)	Fe(2)	O(1)	Dy(2)	87.5(2)
Fe(1)	O(1)	Dy(2)	99.0(2)	Fe(2)	O(4)	Dy(2)	89.1(2)
Fe(1)	O(7)	Dy(2)	104.3(2)	Fe(2)	O(9)	Dy(2)	87.9(2)
Fe(1)	O(1)	Fe(2)	161.4(3)	Dy(1)	O(1)	Dy(2)	142.1(2)

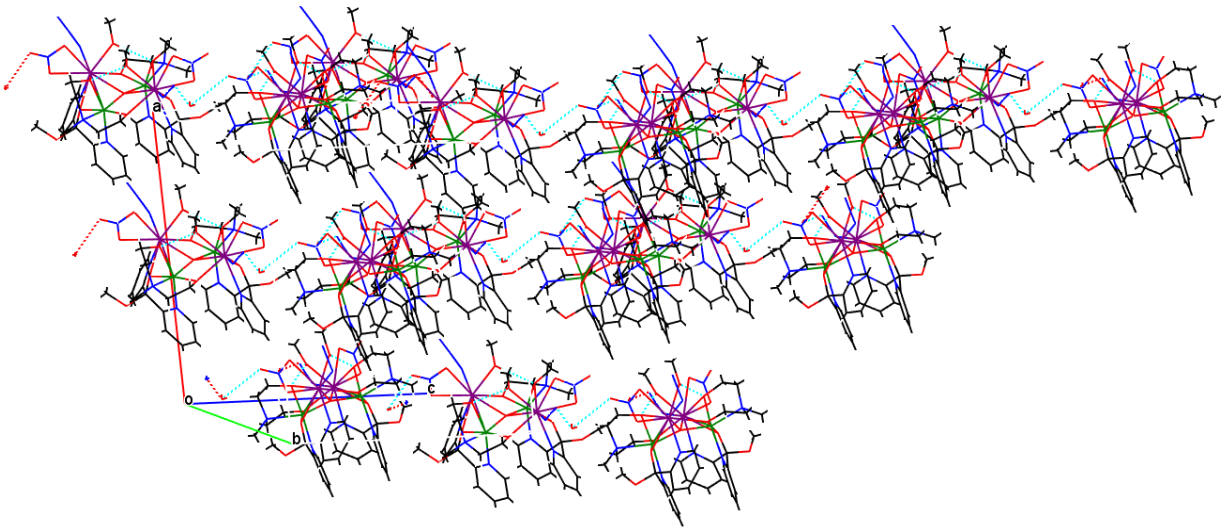

Figure 4.6. Packing of compound **20** (3 D supramolecular). Colour code: black, red, blue, green, white and violet spheres represent C, O, N, Fe, H and Dy, respectively.

4.2.3. Magnetic properties

DC magnetic susceptibility measurement of compound **20** was carried out on freshly prepared polycrystalline sample in the temperature range 1.8-300 K under an applied DC magnetic field of 1000 Oe (0.1 T). The plot of χT versus T, for compound **20** is shown in Figure 4.7.

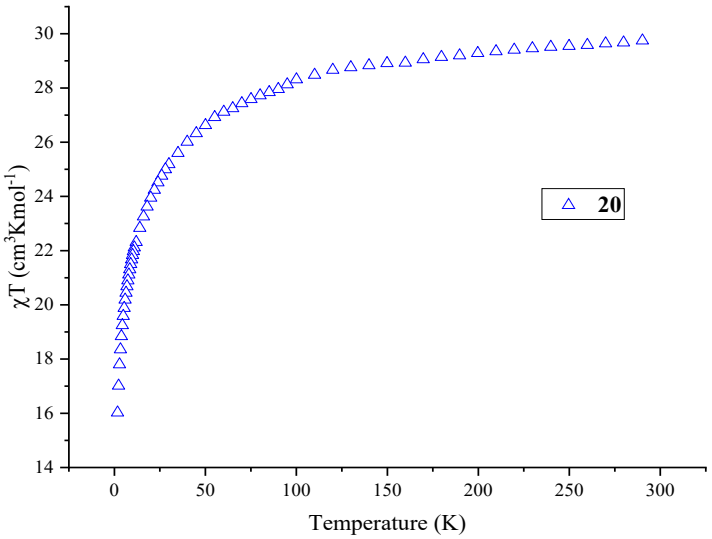

Figure 4.7. Temperature dependence of the χT products of compound **20** at 1000 Oe

The χT product of compound **20** value at 300 K is 32.01 $cm^3mol^{-1}K$ which is lower than the expected value of 37.09 $cm^3mol^{-1}K$ for four non interacting Fe^{III} and Dy^{III} (Fe^{III}, S = 5/2, g = 2, C = 4.375 $cm^3mol^{-1}K$) and (Dy^{III}, $^6H_{15/2}$, S = 5/2, g = 4/3, L = 5, C = 14.17 $cm^3mol^{-1}K$) [276]. The χT product shows a steady decrease between 300 to 100 K followed by a rapid drop from 100-1.8 K reaching a minimum value of 16.03 $cm^3mol^{-1}K$ at 1.8 K. The decreases of χT experimental values with the temperature is probably due to the thermal depopulation of the Stark sublevels of Dy^{III} ions within the complexes or with the individual Dy^{III} ions and/or antiferromagnetic interaction between the Dy^{III} ions or between Fe^{III}-Dy^{III} ions [313, 314].

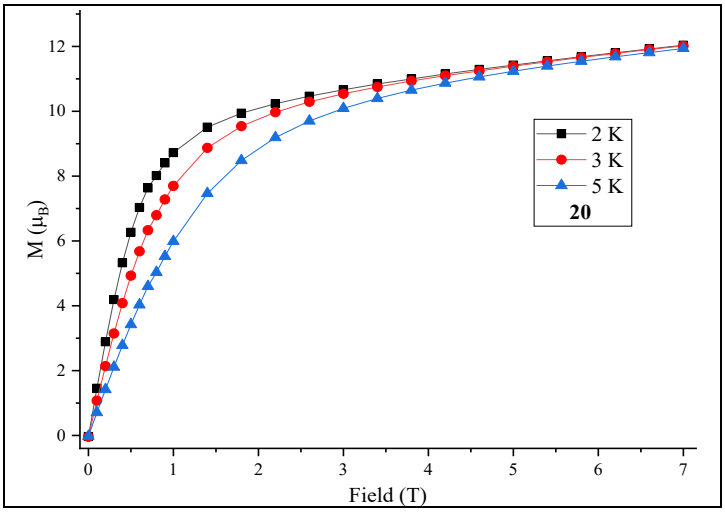

Figure 4.8. Field dependence of magnetisation at indicated temperatures of compound **20**.

The field dependence of the magnetisation of compound **20** was measured at field range from 0 to 70000 Oe (0-7 T) at temperatures of 2 K, 3K and 5 K. Figure 4.8 shows the magnetisation values for compound **20** increase rapidly below 2 T followed by a linear increase up to 7 T reaching a value of 12.04 μ_B at 2K and 7 T without saturation which indicates the presence of magnetic anisotropy or/and the population of low-lying excited states [315].

AC susceptibility measurements were performed in order to investigate potential SMM behaviour of compound **20**. As shown in Figure 4.9 compound **20**, shows no AC signals under zero applied DC field but shows slow relaxation without maxima under small-applied DC fields (500-3000 Oe). This result indicates that compound **20** lacks SMM behaviour. However, given the presence of a peak without a maxima in the Dy analogue, there is a possibility that this system could be an SMM

with a lower energy barrier and could potentially be observed at very low, sub Kelvin, temperatures.

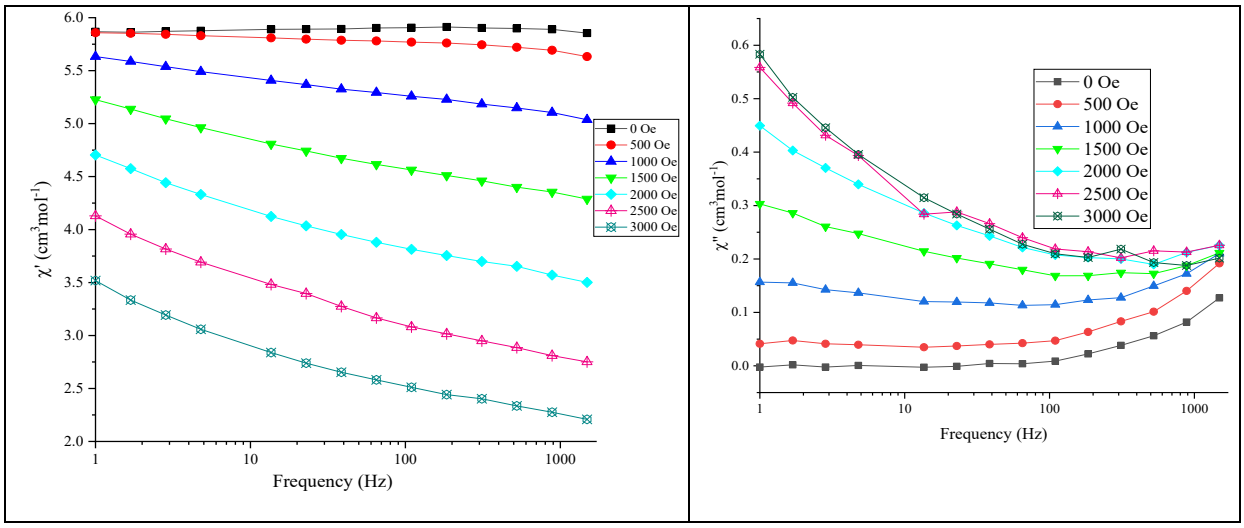

Figure 4.9. Frequency dependence of the In-phase (left) and the out-of-phase (right) components of the AC susceptibility of compound **20**, under different applied DC fields.

4.2.4. Comparison of the core structure

A review of the literature for heterometallic iron-lanthanide complexes reported incorporating azide ligands shows 4 of them are tetranuclear as shown in Table 4.4.

Table 4.4. Tetranuclear Fe-Ln metal complex incorporate azide ligands

NO	Structure	Ln	SMMs Dy	Core	Coordination mode of azide	Ref
1	$[Fe_2Ln_2(\mu_3\text{-}O)_4(H_2L)_2(mpm)_2(Piv)_2(N_3)_{4-x}(Cl)_x]$	Gd-Er	Not SMM	Inverse butterfly	Terminal	[87]
2	$[Fe_2Ln_2(\mu_3\text{-}OH)_2(teg)_2(N_3)_2(Piv)_4]$	Dy, Ho, Y	Not SMM	Butterfly	Terminal	[331]
3	$[FeLn_2Fe(\mu_3\text{-}OH)_2(teg)_2(N_3)_2(PhCO_2)_4]$	Dy, Y	Not SMM	Butterfly	Terminal	[332]
4	$[Fe_2Ce_2Na_2(\mu_4\text{-}O)_2(Me_3CCO_2)_8(N_3)_2(ap)_2]F$	Ce	-------	Chain	Bridging+ Terminal	[333]
5	$[Fe_2Ln_2(mdea)_2\{(py)_2C(OCH_3)O\}_2(\mu_4\text{-}O)(N_3)_2(NO_3)_2(CH_3OH)_2]\ H_2O$ (**14**-**20**)	Pr-Dy, Y	Not SMM	Distorted square	Terminal	This work 4.2

As shown in Table 4.4, all series are absent of SMM behaviour.

Di(2-pyridyl) ketone (dpk) has been used as a main ligand and co-ligand in the literature to synthesise Fe-Ln with various topologies and also exhibiting interesting magnetic properties like SMM behaviour [341-343]. For example, the highest energy barrier in an $\{Fe_4Dy_2\}$ cluster with U_{eff} =22.20 K and pre-exponential relaxation time $\tau_o = 1.20\times10^{-7}$ s [341].

N-methyldiethanolamine ($mdeaH_2$) has been widely used as a main ligand to synthesise Fe-Ln, with various topologies and also exhibiting interesting magnetic properties like SMM behaviour [79, 80, 89, 253]. For example, the highest energy barrier in an $\{Fe_7Dy_3\}$ cluster U_{eff}=33.40 K and pre-exponential relaxation time, $\tau_o = 6.6\times10^{-8}$ s [80].

However, $mdeaH_2$ and dpk together have not been used to obtain lanthanide or iron–lanthanide metal complexes. Taking this into consideration, in the present work a combination of $mdeaH_2$ alongside dpk and sodium azide as the two co-ligands has been employed to obtain higher nuclearity cluster which could provide a route towards compound potentially having optical or

magnetic properties as well as SMM behaviour. With this synthetic approach $[Fe_2Dy_2(mdea)_2\{(py)_2C(OCH_3)O\}_2(\mu_4\text{-}O)(N_3)_2(NO_3)_2(CH_3OH)_2]\,H_2O$ (**20**) was produced with the topology distorted square. There are many reports on $\{Fe_2Ln_2\}$ compounds in various topologies, with different main ligands/co-ligand and synthesis procedures [87, 313, 331, 332, 344-359]. Herein, the distorted square $[Fe_2Ln_2]$ topology is generally rare in Fe-Ln metal complexes but the topology of this tetranuclear $[Fe_2Ln_2]$ was initially reported for $[Mn_2Ln_2]$ complexes [360]. $[Mn_2Dy_2]$ is abbreviated as compound **E**.

Compounds **20** and **E** have the same distorted tetrahedral topology, "distorted square". The angles around the (μ_4-O) for Fe_2Dy_2 centre vary from 87.11 to 98.95° while for Mn_2Dy_2 centre vary from 92.11 to 101.60° both consistent with the distorted tetrahedral geometry. Therefore, the crystallographic and magnetic details are compared. The comparison between both compounds **20** and **E** is summarised in Figure 4.10 and Table 4.5. M=Fe, Mn and in all cases the Dy containing structure has chosen as representative for the whole lanthanide.

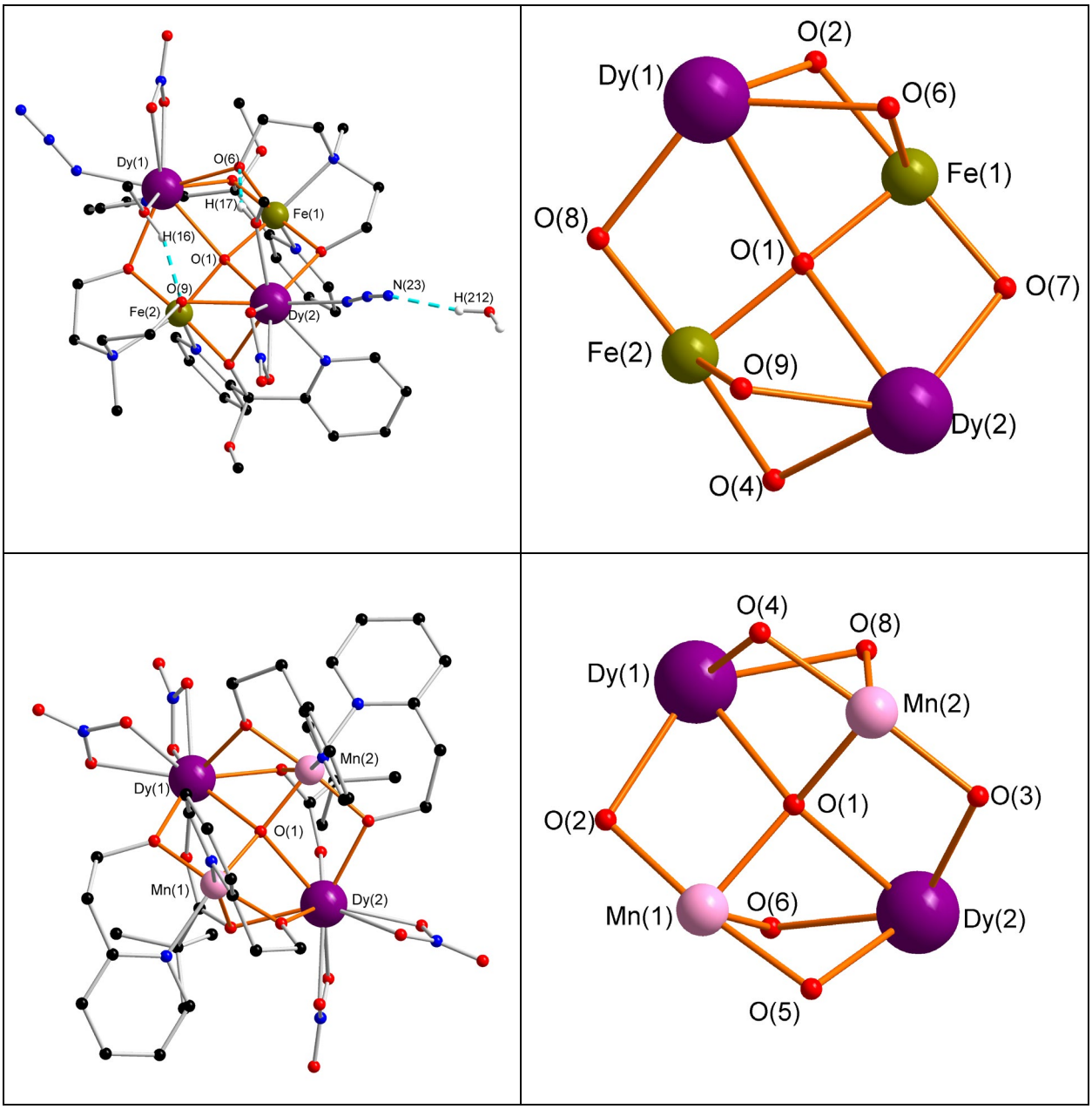

Figure 4.10. Molecular structure and the core of compound **20** on the top and compound **E** on the bottom (H atoms omitted for clarity). Colour code: black, red, blue, green, rose, white and violet spheres represent C, O, N, Fe, Mn, H and Dy, respectively.

Table 4.5. Comparison between compounds **20** and **E**

Complex abbreviated as		Compound **20**	Compound **E** [360]
Structure		$[Fe_2Dy_2(mdea)_2\{(py)_2C(OCH_3)O\}_2(\mu_4\text{-}O)(N_3)_2(NO_3)_2(CH_3OH)_2]\ H_2O$	$[Mn_2Dy_2(\mu_4\text{-}O)(Piv)_2(hep)_4(NO_3)_4]\ 3MeCN$
Ligand		*N*-methyldiethanolamine	2-(2-hydroxyethyl)pyridine
Co−ligand		Di(2-pyridyl) ketone	Pivalate
Co−ligand		Azide	----------
Crystal system		Monoclinic	Orthorhombic
Space group		*Cc*	*Pbca*
Volume		4962.59(17)	10298.8 (15)
Colour of crystal		Brown	Dichroic (blue/brown)
Shape of crystal		Block	Octahedron
Shape of M ions		Distorted octahedron	Distorted octahedron
Shape of Dy ions		Distorted spherical capped square antiprism	One atom distorted muffin and one atom distorted spherical capped square antiprism
Average distance of	M−O	1.97 Å	2.05 Å
	M−N	2.18 Å	2.14 Å
	Dy−O	2.45 Å	2.41 Å
Average angle of	M−O−M	161.40°	145.35°
	M−O−Dy	93.63°	94.74°
	Dy−O−Dy	142.10°	130.06°
Distance of	M−M	3.73(15) Å	3.63 Å
	Dy−Dy	4.84(5) Å.	4.38 Å
	M−Dy	3.26Å	3.25 Å
Interactions		Antiferromagnetic	Antiferromagnetic
Magnetisation at 2 K and 7 T		12.04 μ_B	10.9 μ_B
Relaxation behaviour		Lack SMM	Lack SMM

Compound **20** was synthesised using *N*-methyldiethanolamine as the main ligand and di(2-pyridyl) ketone and azide as the two co-ligands. While compound **E** was synthesised using 2-(2-hydroxyethyl) pyridine as the main ligand and Pivalate from (Mn(Pivalate) as the co-ligand. Compound 20 crystallises in the monoclinic space group *Cc*, while compound **E** in the orthorhombic space group *Pbca.*

The average Mn−O bond distance is longer than Fe−O and the Mn−N is shorter than the Fe−N. The Dy−O bond distance in compound **E** is shorter than that in compound **20**.

The average Mn−O−Mn angle is shorter than Fe−O−Fe and Mn−O−Dy angle is larger than Fe−O−Dy. The Dy−O−Dy angle of compound **E** is shorter than that in compound **20**.

The Fe···Fe distance is longer than Mn···Mn. The Dy···Dy distance of compound **20** is longer than that in compound **E**. The Fe···Dy distance is longer than Mn···Dy. Fe and Mn in their respective compounds are hexa-coordinated with a distorted octahedron geometry.

Dy ions in compound **20** are nine coordinate with a distorted spherical capped square antiprism geometry, while in compound **E** the Dy ions are nine coordinate with two geometries a distorted muffin and a distorted spherical capped square antiprism.

The magnetic studies of both compounds revealed that the presence of antiferromagnetic interactions. The magnetisation of compound **20** is higher than in compound **E** at 2 K and 7 T (μB) because Fe has more unpaird electron than Mn. Both compounds lack SMM behaviour.

4.3. Structure, optical and magnetic properties of $[Fe_2Ln_4(mdea)_2(mdeaH)_2(\mu_3\text{-}OH)_2(N_3)_2(PhCO_2)_8]\cdot 3MeCN$

(Ln = Pr(**21**), Nd(**22**), Sm(**23**), Eu(**24**), Gd(**25**), Tb(**26**), Dy(**27**), Ho(**28**) and Y(**29**))

4.3.1. Synthetic description

The reaction of anhydrous $FeCl_3$, $Ln(NO_3)_3{\cdot}6H2O$, sodium benzoate ($PhCO_2Na$), *N*-methyldiethanolamine ($mdeaH_2$) and sodium azide (NaN_3) in a molar ratio of 1:1:3:5:3 in MeCN under reflux for two hours subsequent cooling and afforded yellow needles of a new family of hexanuclear Fe-Ln clusters $[Fe_2Ln_4(mdea)_2(mdeaH)_2(\mu_3\text{-}OH)_2(N_3)_2(PhCO_2)_8]$ 3MeCN.

4.3.2. Crystal structure of $[Fe_2Ln_4(mdea)_2(mdeaH)_2(\mu_3\text{-}OH)_2(N_3)_2(PhCO_2)_8]\cdot 3MeCN$

In this series of hexanuclear iron-lanthanide clusters only compounds **21**, **27** and **28** have been characterised fully by single-crystal X-ray diffraction (full crystallographic data is given in Table 8.3); while the other compounds **22**-**26** and **29** were confirmed by their unit cell (Table 4.6). In addition, elemental analyses, FTIR spectroscopy and powder XRD studies (Figure 4.12) also support the suggestion that the whole series are isostructural, isomorphous and pure. Therefore, only the structure of $[Fe_2Ln_4(mdea)_2(mdeaH)_2(\mu_3\text{-}OH)_2(N_3)_2(PhCO_2)_8]\cdot 3MeCN$ (**27**) will be described in detail as a representative of the whole series. Compound **27** crystallises in the triclinic

space group $P\bar{1}$ with Z = 1. Compound **27** is a neutral cluster containing three lattice MeCN molecules. However, it loses lattice MeCN after dry according to elemental analyses.

The structure and the central core of compound **27** are shown in Figure 4.11. The $mdeaH_2$ is coordinating to the metal centres as can be seen in the crystal structure and the $mdeaH_2$ ligands are either are singly or doubly-deprotonated oxygen.

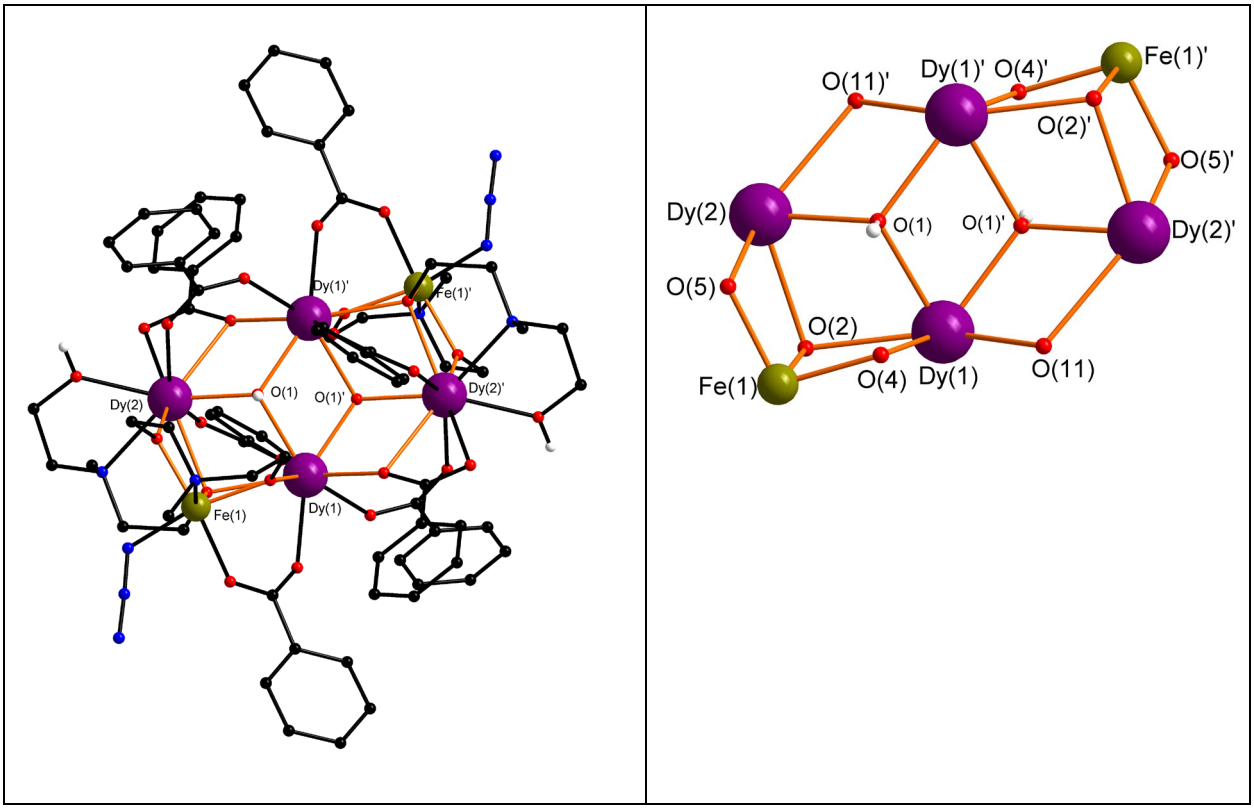

Figure 4.11. Molecular structure of compound **27**. Colour code: black, red, blue, green, white and violet spheres represent C, O, N, Fe, H and Dy, respectively. The core of compound **27** is shown on the right ($mdea^{2-}$, $mdeaH^{-}$and benzoates are omitted for clarity).

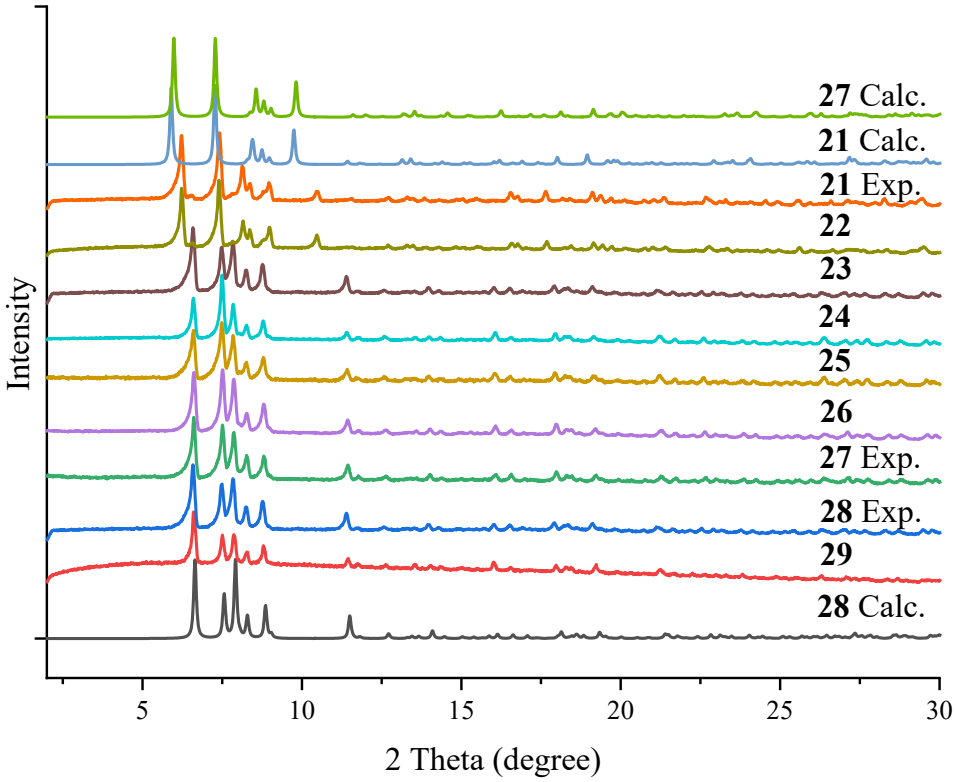

Figure 4.12. Calculated and experimental of PXRD patterns of compounds **21**-**29**.

Table 4.6. The unit cells data of compounds **21**-**29**

	a [Å]	b [Å]	c [Å]	α [deg]	β [deg]	γ [deg]	V [Å3]
Fe_2Pr_4(**21**)	12.50(3)	13.735(3)	15.99(4)	76.79(2)	69.89 (2)	62.50(2)	2280(11)
Fe_2Nd_4(**22**)	12.51(18)	13.75(3)	16.07(3)	85.51(17)	69.98(16)	63.07(17)	2310(8)
Fe_2Sm_4(**23**)	12.17(8)	13.49(18)	16.03(2)	85.01(1)	69.80(1)	63.02(11)	2262(50)
Fe_2Eu_4(**24**)	12.55(17)	13.81(19)	16.07(12)	84.40(9)	69.01(10)	63.08(1)	2304(40)
Fe_2Gd_4(**25**)	12.36(13)	13.65(13)	15.89(15)	84.83(8)	69.54(9)	63.15(10)	2233(4)
Fe_2Tb_4(**26**)	12.38(16)	13.66(6)	15.82(6)	83.94(9)	69.52(4)	63.06(5)	2229(2)
Fe_2Dy_4(**27**)	12.34(4)	13.62(5)	15.82(5)	85.01(3)	69.51(3)	63.21(4)	2213(15)
Fe_2Ho_4(**28**)	12.95(3)	13.92(3)	15.30(3)	63.40(2)	66.65(2)	62.52 (2)	2125(10)
Fe_2Y_4(**29**)	12.25(10)	13.65(15)	16.02(17)	84.58(7)	69.82(7)	63.10(8)	2246(6)

The compound **27** possesses a centrosymmetric $[Fe^{III}_2Dy^{III}_4(\mu_3\text{-}OH)_2]^{16+}$ "butterfly" core and consists of two Fe^{III}, four Dy^{III}, two terminal azide $(N_3)^-$, two doubly-deprotonated $mdea^{2-}$, two singly-deprotonated $mdeaH^-$ and eight of benzoate ligands. All four Dy atoms are in one plane. In this butterfly motif two of the Dy^{III} ions occupy the body positions and the other two Dy^{III} ions occupy the outer wing-tips, whilst the two Fe^{III} ions are lying above and below the Dy_4 plane at a

distance of 2.048 Å. Moreover, compound **27** has a $FeDy_3$ unit, in which the Dy_3 triangles are each bridged through single $(\mu_3\text{-}OH)^-$ group, singly-deprotonated $mdeaH^-$, doubly-deprotonated $mdea^{2-}$, *syn-syn* bridging benzoate and chelating and bridging benzoate. The Fe^{III} ions are each bridging through O(2) or O(2)' from the singly deprotonated $mdeaH^-$ ligand, *syn-syn* bridging benzoate and O(4), O(5), or O(4)', O(5)' from the doubly deprotonated $mdea^{2-}$ ligand to the tetranuclear core. The two Dy_3 triangles which share a Dy (1) and Dy (1)' backbone. The core is held together by two $(\mu_3\text{-}OH)^-$ groups O (1) and O(1)' lying above and below the Dy_4 plane with a distance of 0.799 Å.

There are two doubly-deprotonated $mdea^{2-}$ ligands and two singly-deprotonated $mdeaH^-$ ligands bridging to the metal centres. Interestingly the doubly–deprotonated ligands are centred on the outer Fe^{III} ions through the N atom and resulting in two negatively charged oxygen atoms O(4), O(5), or O(4)', O(5)' form alkoxy bridges along the Fe···Dy edges with a $(\eta^2\text{: }\eta^1\text{: }\eta^2\text{: }\mu_3)$ coordination mode (Figure 4.13, a). The two singly-deprotonated $mdeaH^-$ ligands are centred on the outer Dy^{III} ions through the N atom resulting in one negatively charged oxygen atom O(2) or O(2)' form alkoxy bridges along the Fe···Dy and Dy···Dy edges with a $(\eta^1\text{: }\eta^1\text{: }\eta^3\text{: }\mu_3)$ coordination mode (Figure 4.13, b).

Eight of benzoate ligands are in the crystal structure adopting three different coordination modes:

(i) Four of them are *syn-syn* bridging to two Dy^{III} ions with a $(\eta^1\text{:}\eta^1\text{:}\mu_2)$ coordination mode (Figure 4.13, c) either ((Dy(1) and Dy(2)), (Dy(1)' and Dy(2)'), (Dy(1)' and Dy(2)) and (Dy(1) and Dy(2)')).

(ii) Two of them are *syn-syn* bridging to Fe^{III} ion and Dy^{III} ion with a $(\eta^1\text{:}\eta^1\text{:}\mu_2)$ coordination mode (Figure 4.13, d) either ((Fe(1) and Dy(1)) and ((Fe(1)' and Dy(1)')).

(iii) Two of them are chelating and bridging to two Dy^{III} ions with a $(\eta^1\text{:}\eta^2\text{:}\mu_2)$ coordination mode (Figure 4.13, e) η^2 by O(10) and O(10)' either (Dy(1), Dy(2)' and Dy(1)) and (Dy(1)', Dy(2) and Dy(1)').

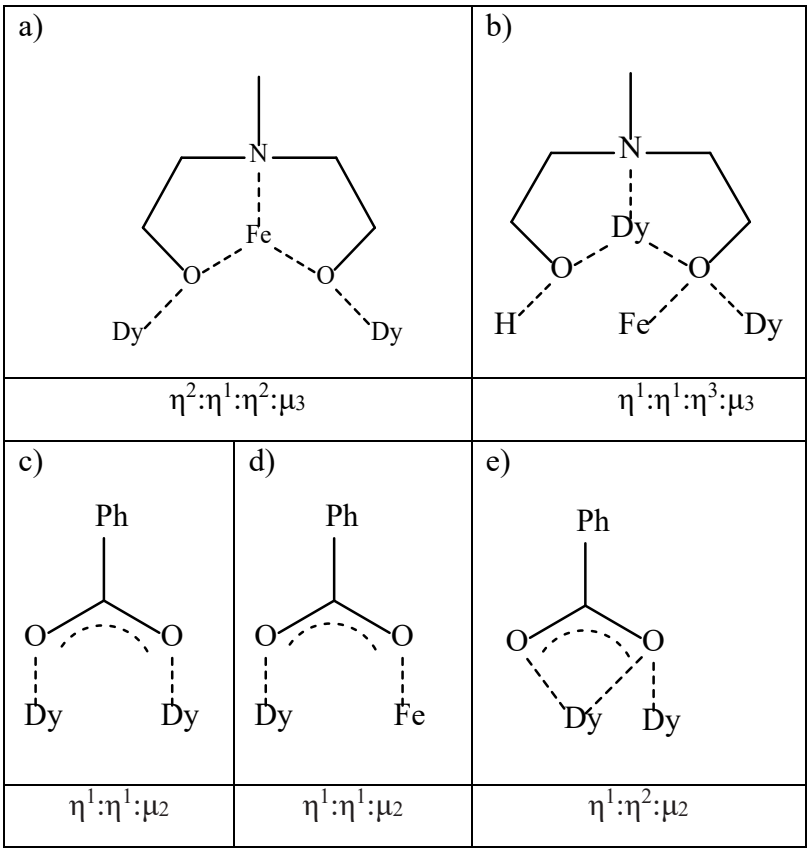

Figure 4.13. Coordination modes of (a) doubly-deprotonated $mdea^{2-}$ (b) singly-deprotonated $mdeaH^{-}$ and (c-e) benzoate ligands.

Both hexa-coordinated Fe^{III} ion are surrounded by two N and four O donor atoms (N_2O_4). One N and two O atoms come from doubly-deprotonated oxygen $mdea^{2-}$ ligands. One N comes from the terminal azide $(N_3)^{-}$, one O comes from *syn-syn* bridging benzoate and one O comes from a singly-deprotonated oxygen $mdeaH^{-}$ ligand. The Fe−O and Fe−N bond distances are in the range 1.970(3)−2.065(3) Å and 2.025(4)−2.266(4) Å, respectively. The Fe–Dy distance is 3.447(7). The Fe–O–Dy angles are in the range 98.29(12)−112.61(14)°. Selected bond distances and angles are summarised in Table 4.7. This results in a distorted octahedron with a ∑ parameter of 103°. This geometry was confirmed by SHAPE analysis [309-312] with a deviation value of 2.71, (Figure 4.14, Table 8.12).

The Dy^{III} ions present two different types of coordination spheres:

(i) Both octa-coordinated Dy(1) and Dy(1)' are surrounded by eight O donor atoms (O_8). Four O atoms come from *syn-syn* bridging benzoate, two O atoms come from the $(\mu_3\text{-}OH)^-$ group, one O atom comes from the doubly-deprotonated oxygen $mdea^{2-}$ ligand and one O atom comes from the singly-deprotonated oxygen $mdeaH^-$ ligand. This results in a distorted triangular dodecahedron geometry. This geometry was confirmed by SHAPE analysis [309-312] with a deviation value of 0.94, (Figure 4.14, Table 8.12).

(ii) Both nine-coordinated Dy(2) and Dy(2)' are surrounded by one N and eight O donor atoms (NO_8). One N atom and two O atoms come from the singly-deprotonated oxygen $mdeaH^-$ ligand, two O atoms come from the chelating and bridging benzoate ligands, two O atoms come from *syn-syn* bridging benzoate ligands, one O atom comes from the doubly-deprotonated oxygen $mdea^{2-}$ ligand and one O atom comes from $(\mu_3\text{-}OH)^-$ group. This results in spherical capped square antiprism geometry. This geometry was confirmed by SHAPE analysis [309-312] with a deviation value of 2.35, (Figure 4.14, Table 8.12).

The Dy–O bond distances are in the range 2.304(3)−2.768(3) Å and Dy–N bond distance is 2.653(4) Å. The Dy···Dy distances are in the range 3.904(4)−4.019(4) Å. The Dy–O−Dy angles are in the range 101.48(10)−117.99(12)°.

The structure is further stabilised by intermolecular interactions through hydrogen bonds. O(3)-H(3) from a singly-deprotonated $mdeaH^-$ ligand makes an intermolecular hydrogen bond to O(11) from the chelating and bridging benzoate ligand $(PhCO_2)^-$ of a neighbouring complex at (2-x, 1-y, 1-z). In addition, O(3)-H(3) from a singly-deprotonated $mdeaH^-$ ligand of a neighbouring complex at (1+x, +y, +z) makes an intermolecular hydrogen bond to O(11) from a chelating and bridging benzoate ligand $(PhCO_2)^-$. The O(3)···O(11) distance is 2.86 Å. Intermolecular interaction results in a 1D chain structure. The packing structure of compound **27** is presented in Figure 4.15.

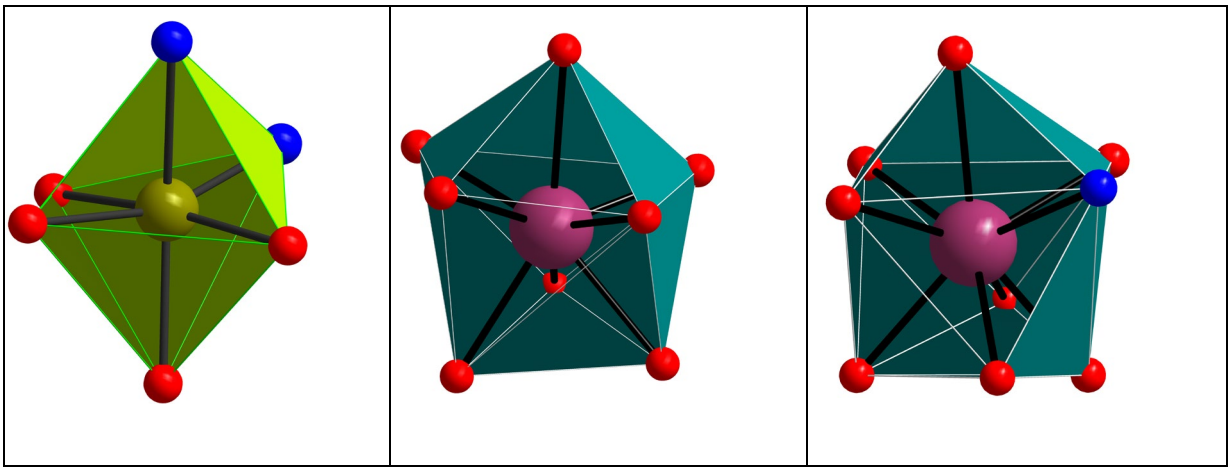

Figure 4.14. Octahedral geometry of the 6-coordinated Fe ion on the left, triangular dodecahedron geometry of the 8-coordinated Dy ion on the centre and spherical capped square antiprism geometry of the 9-coordinated Dy ion on the right. Colour code: red, blue, green and violet spheres represent O, N, Fe and Dy, respectively.

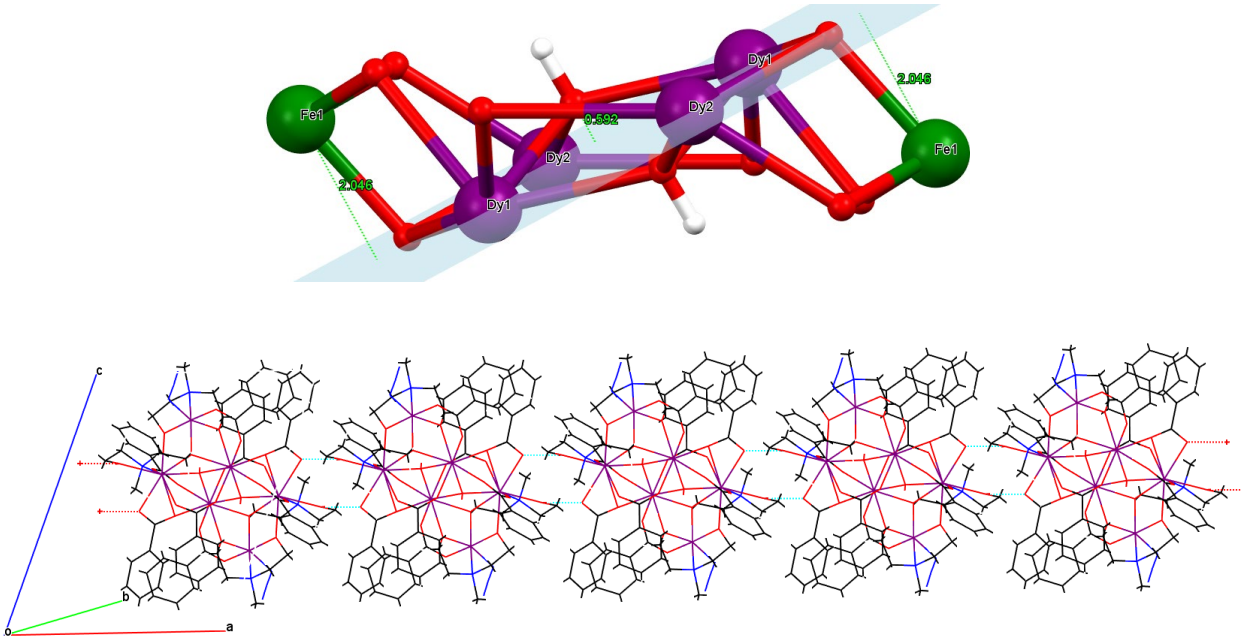

Figure 4.15. Single unit of the planar of compound **27** on the top and packing of compound **27** on the bottom. Colour code: black, red, blue, green, white and violet spheres represent C, O, N, Fe, H and Dy, respectively.

Table 4.7. Selected bond distances (Å) and bond angles (°) of compound **27**

Bond distances			Bond distances		
Atom	Atom	Distance/Å	Atom	Atom	Distance/Å
Fe(1)	O(2)	2.031(3)	Dy(1)	O(13)	2.351(3)
Fe(1)	O(4)	1.985(3)	Dy(2)	O(1)	2.308(3)
Fe(1)	O(5)	1.970(3)	Dy(2)	O(2)	2.535(3)
Fe(1)	O(6)	2.065(3)	Dy(2)	O(3)	2.449(3)
Fe(1)	N(2)	2.266(4)	Dy(2)	O(5)	2.304(3)
Fe(1)	N(11)	2.025(4)	Dy(2)	O(9)	2.320(3)
Dy(1)	O(1)	2.381(3)	Dy(2)	O(10)	2.768(3)
Dy(1)	O(1)'	2.388(3)	Dy(2)	O(11)	2.461(3)
Dy(1)	O(2)	2.507(3)	Dy(2)	O(12)	2.323(3)
Dy(1)	O(4)	2.328(3)	Dy(2)	N(1)	2.653(4)
Dy(1)	O(7)	2.356(3)	Fe(1)	Dy(1)	3.447(7)
Dy(1)	O(8)	2.329(4)	Dy(1)	Dy(1)'	3.934(5)
Dy(1)	O(10)	2.378(3)	Dy(1)	Dy(2)	3.904(4)
Bond angles				Bond angles			
Atom	Atom	Atom	Angle/°	Atom	Atom	Atom	Angle/°
Fe(1)	O(2)	Dy(1)	98.29(12)	Dy(2)	O(1)	Dy(1)	112.49(13)
Fe(1)	O(2)	Dy(2)	101.95(12)	Dy(1)	O(1)'	Dy(2)'	117.99(12)
Fe(1)	O(4)	Dy(1)	105.82(14)	Dy(1)	O(2)	Dy(2)	101.48(10)
Fe(1)	O(5)	Dy(2)	112.61(14)	Dy(1)	O(10)	Dy(2)'	102.45(12)
Dy(1)	O(1)'	Dy(1)'	111.19(12)				
'1-x,1-y,1-z							

4.3.3. Magnetic properties

DC magnetic susceptibilities of compounds **25**-**27** and **29** were carried out on freshly prepared polycrystalline samples in the temperature range 1.8-300 K under an applied DC magnetic field of 1000 Oe (0.1 T). The plot of χT versus T for compounds **25**-**27** and **29** is shown in Figure 4.16. The DC data are summarised in Table 4.8.

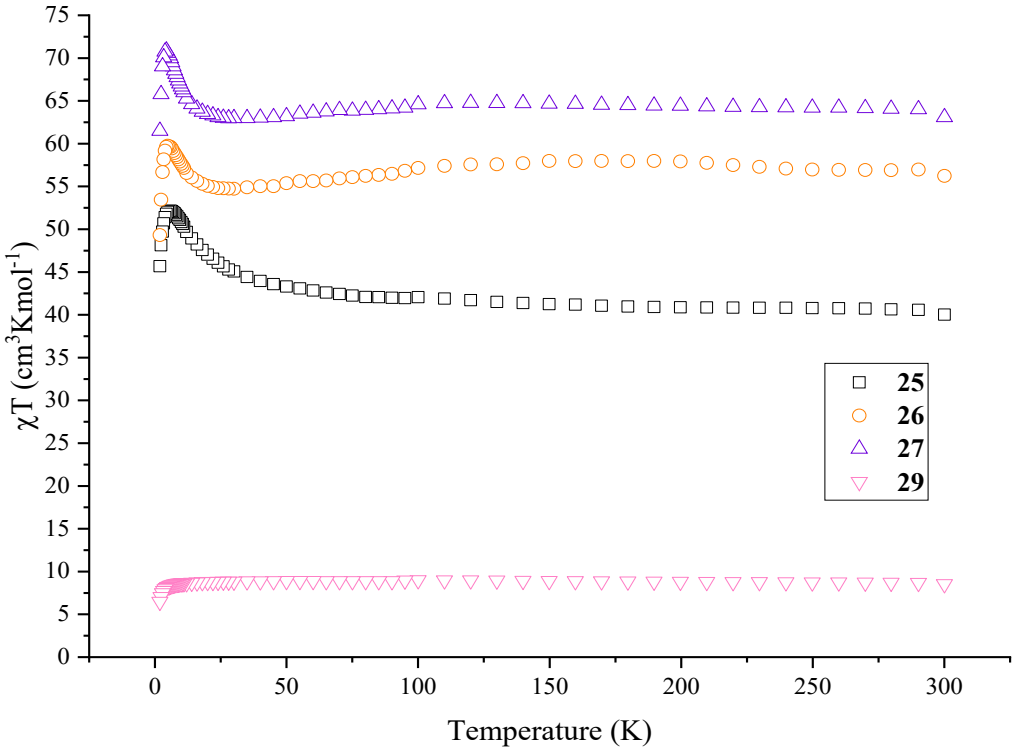

Figure 4.16. Temperature dependence of χT products for compounds **25-27** and **29** at 1000 Oe.

The χT products of compounds **25-27** and **29** at 300 K are 40.40 cm^3 K mol^{-1}, 55.70 cm^3 K mol^{-1}, 64.07 cm^3 K mol^{-1} and 8.80 cm^3 K mol^{-1}, respectively, close to those expected for six non-interacting ions of **25**: Fe_2Gd_4 (40.27 cm^3Kmol^{-1}), **26**: Fe_2Tb_4 (56.03 cm^3Kmol^{-1}), **27**: Fe_2Dy_4 (65.43 cm^3Kmol^{-1}) and **29**: Fe_2Y_4 (8.75 cm^3Kmol^{-1}), respectively. Upon lowering the temperature, the χT product of compound **29** stays almost constant down to 15 K before rapidly decreasing down to 6.47 cm^3Kmol^{-1} at 1.8 K, indicating that the interaction between the two separated Fe centres is very weak and antiferromagnetic. For compound **25**, the χT product continuously increases to 25 K until a maximum value of 52.17 cm^3 K mol^{-1} at 5.90 K reached this is followed by sharp fall to 45.67 cm^3Kmol^{-1} at 1.8 K. Compounds **26** and **27** show similar behaviour. χT remains essentially constant to 100 K and decreases slightly between 100 and 20 K. Below 20 K, the χT product increases to reach maximum values of 60.12 cm^3Kmol^{-1} at 4.9 K for compound **26** (70.86 cm^3 K mol^{-1} at 4.3 K for **27,** Fe_2Dy_4) followed by sharp fall to reach 49.61 cm^3 K mol^{-1} for **26** (61.49 cm^3 K mol^{-1} for **27**, Fe_2Tb_4) at 1.8 K. These indicate a dominant ferromagnetic interaction in compounds **25-27**.

Table 4.8. DC data of compounds **25-27** and **29**

Compounds	Ground state of the Ln ^{III} Ion	Curie Constant for each Ln ion at 300 K (cm^3K/mol) [276]	χT ($cm^3mol^{-1}K$) expected value for Fe_2Ln_4 at RT	χT ($cm^3mol^{-1}K$) experimental value for Fe_2Ln_4 at RT	χT ($cm^3mol^{-1}K$) experimental value for Fe_2Ln_4 at 1.8 K	Magnetistion at 2 K and 7 T (μ_B)
Fe_2Gd_4 (**25**)	$^8S_{7/2}$	7.88	40.27	40.40	45.67	38.08
Fe_2Tb_4 (**26**)	$^7F_6$	11.82	56.03	55.70	49.61	30.84
Fe_2Dy_4 (**27**)	$^6H_{15/2}$	14.17	65.43	64.07	61.49	33.89
Fe_2Y_4 (**29**)	--------	--------	8.75	8.80	6.47	10.31

The field dependence of the magnetisation of compounds **25-27** and **29** were performed at fields range from 0 to 70000 Oe (0-7 T) at temperatures of 2K, 3 K and 5 K.

Figure 4.17 shows the magnetisation values of compounds **25** and **29** increase rapidly below 3 T and then follow steady increases to reach saturation values 38.08 μ_B for compound **25** (Fe_2Gd_4, $2*5\ \mu_B + 4*7\mu_B$) and 10.31μ_B for compound **29** (Fe_2Y_4, $2*5\mu_B$) at 2 K and 7 T.

For compounds **26** and **27**, the magnetisation values increase rapidly below 1.5 T and then increase linearly up to 7 T reaching values of 30.84 μ_B for compound **26** and 33.89 μ_B for compound **27**. The magnetisations for compounds **26** and **27** at 7 T are lower than the expected values, suggesting a lack of saturation. This behaviour indicates that the presence of magnetic anisotropy or/and the population of low-lying excited states [315].

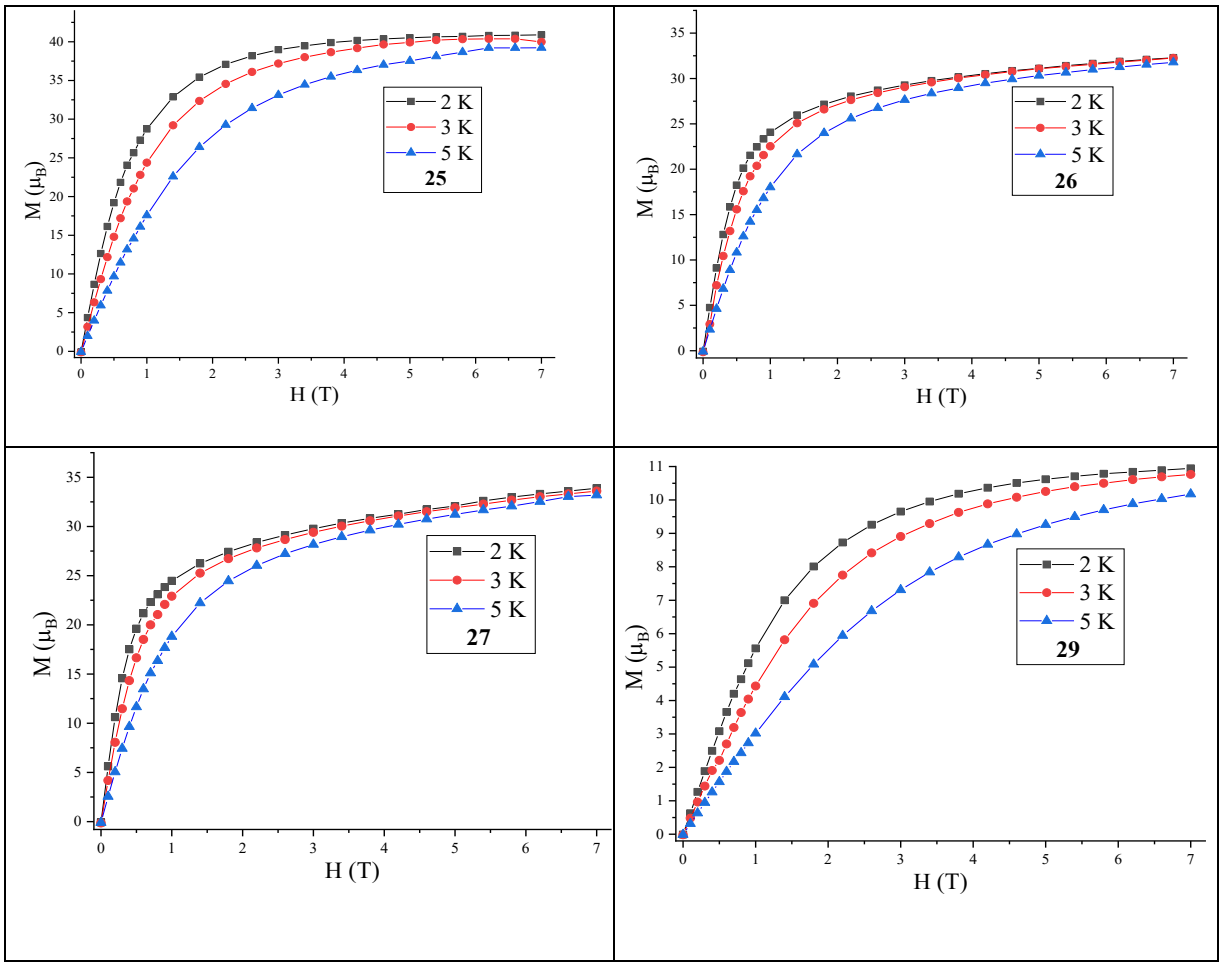

Figure 4.17. Field dependence of magnetisation at indicated temperature of compounds **25-27** and **29**.

AC susceptibility measurements of compounds **26** and **27** were performed in order to investigate potential single molecule magnetic behaviour of compounds **26** and **27**. AC magnetic susceptibilities measurements of compounds **26** and **27** were carried out in the frequency range 1-1488 Hz and at temperature 2 K under different applied DC fields. As shown in Figure 4.18, compound **26** shows slow relaxation under zero applied DC field but without maxima even under small-applied DC fields (500-3000 Oe). Compound **27** shows no AC signals under zero applied DC field but shows slow relaxation without maximum under a small-applied DC field (500-3000 Oe). These results indicate that both compounds **26** and **27** show lack SMM behaviour, however given the presence of a peak without maximum in the Dy analogue. There is a possibility that this system could be an SMM with a lower energy barrier which could potentially be observed at very low, sub Kelvin, temperatures.

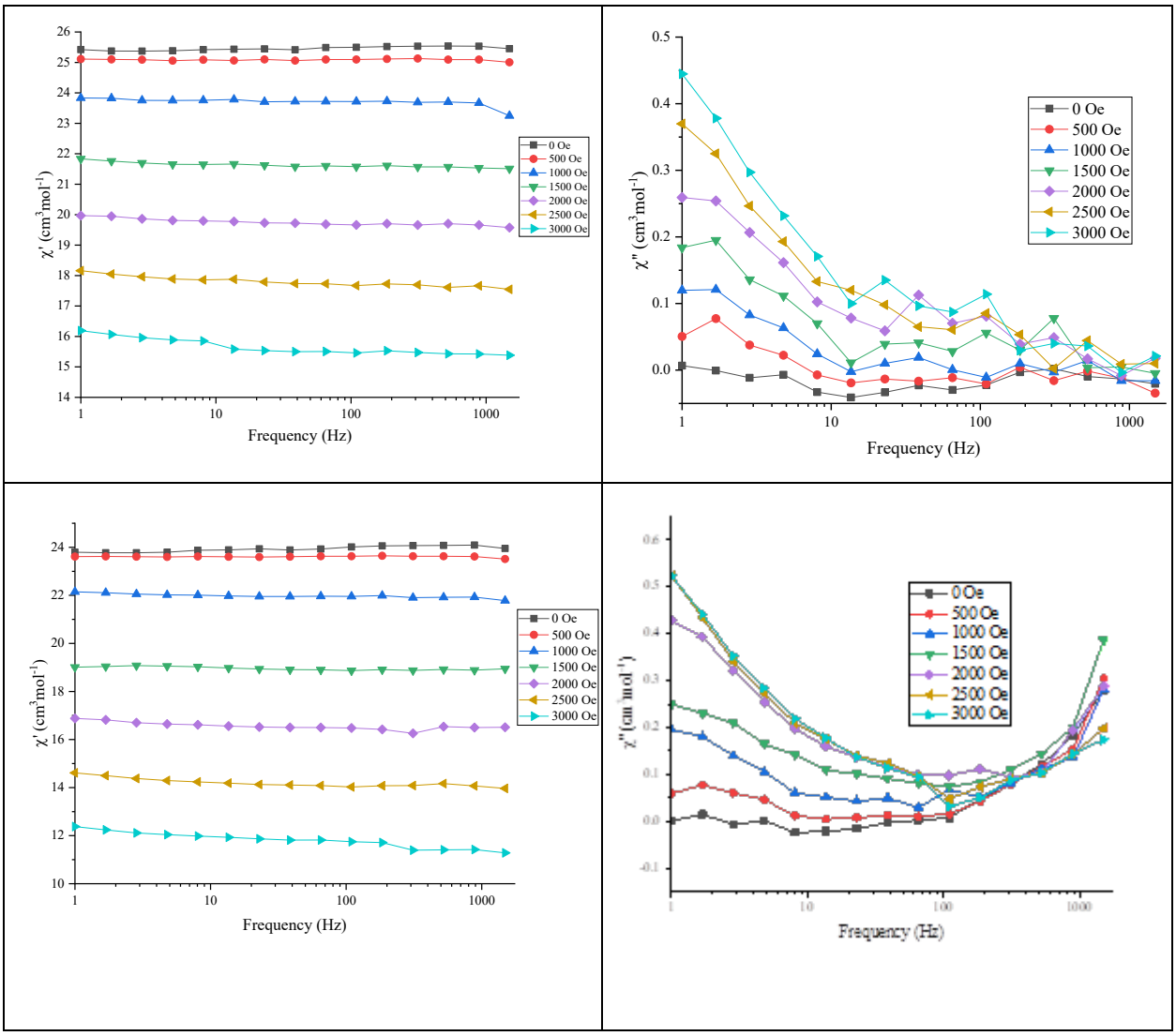

Figure 4.18. Frequency dependence of the In-phase (left) and the out-of-phase (right) components of the AC susceptibility for compounds **26** (top) and **27** (bottom) under different applied DC fields.

4.3.4. Comparison of the core structure

N-methyldiethanolamine ($mdeaH_2$) has been widely used as a main ligand to synthesise Fe-Ln clusters with various topologies and also exhibiting interesting magnetic properties like SMM behaviour [79, 80, 89, 253]. For example, the highest energy barrier in an $\{Fe_7Dy_3\}$ cluster is U_{eff}=33.40 K with pre-exponential relaxation time $\tau_o = 6.6\times10^{-8}$ s [80].

Bearing this fact in mind, in the present work a combination of $mdeaH_2$ alongside benzoate and sodium azide as the two co-ligands has been employed to obtain a higher nuclearity cluster which

could provide routes toward compounds potentially having optical or magnetic properties as well as SMM behaviour. With this synthetic approach $[Fe_2Ln_4(mdea)_2(mdeaH)_2(\mu_3\text{-}OH)_2(N_3)_2(PhCO_2)_8]$ 3MeCN was produced with a butterfly-shaped topology. There many reports on $\{Fe_2Ln_4\}$ compounds with various topologies with different main ligands/co-ligand and synthesis procedures, such as squashed octahedral [361] and butterfly-shaped [362]. The same nuclearity has been reported with different topologies in other 3d-4*f* complexes e.g. Cr_2Dy_4 [363], Ni_2Dy_4 [364], Zn_2Dy_4 [229], Mn_2Dy_4 [365-367] and Co_2Dy_4 [368-373]. The $\{Fe_2Ln_4\}$ (**27**) is in general rare for hexanuclear [3d-4*f*] coordination but this butterfly topology motif has initially been reported for the $\{Fe_2Ln_4\}$ complexes [362]. Both compounds have the same butterfly-shaped geometry. The crystallographic and magnetic details are compared in this section. The comparison of both compounds is summarised in Figure 4.19 and Table 4.9. In all cases the Dy containing structure has chosen as representative for the whole lanthanide. $\{Fe_2Dy_4\}$ is abbreviated as compound **F** [362].

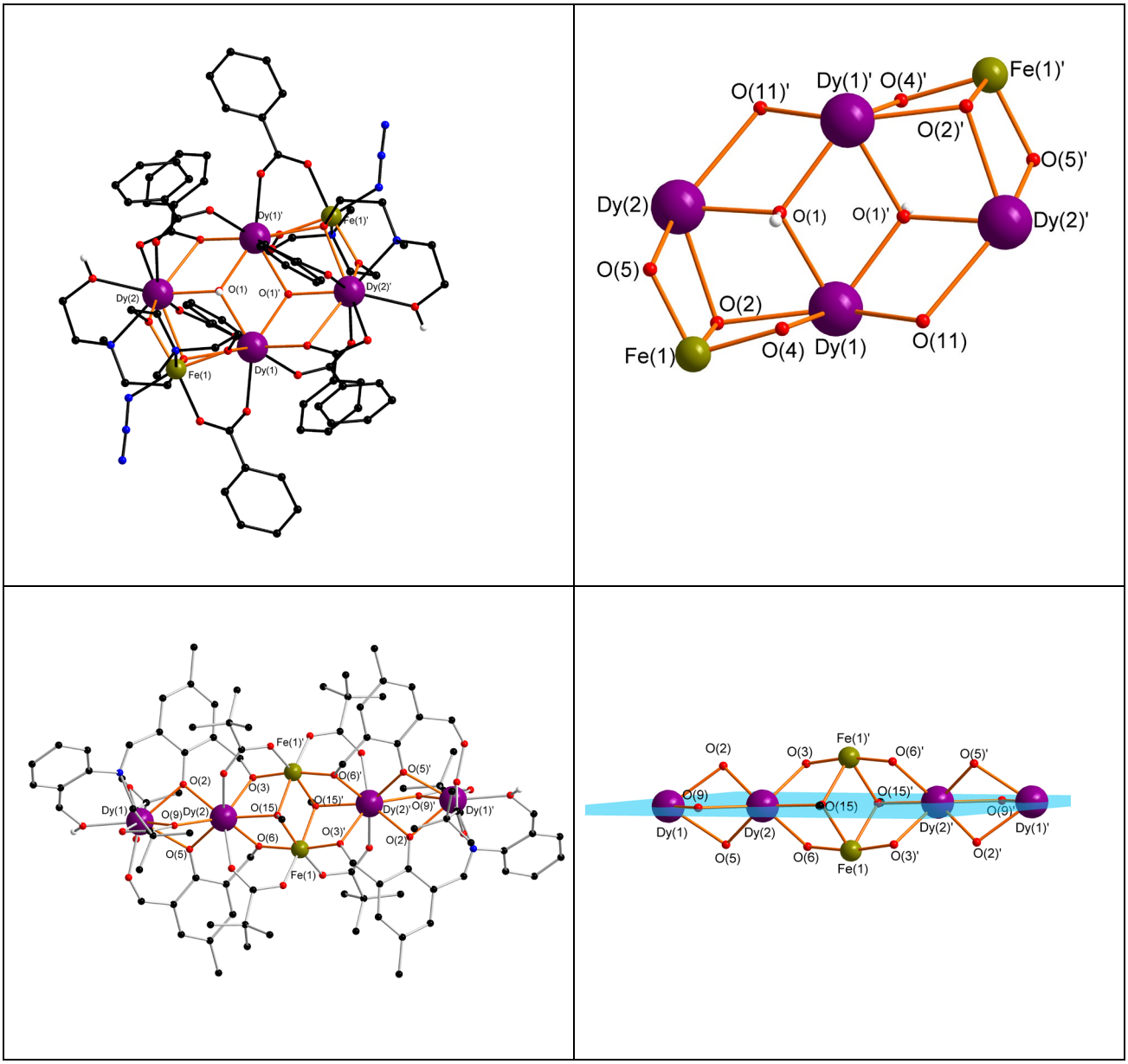

Figure 4.19. Molecular structure and the core of compound **27** on the top and compound **F** on the bottom (H atoms omitted for clarity). Colour code: black, red, blue, green, white and violet spheres represent C, O, N, Fe, H and Dy, respectively.

Table 4.9 Comparison between Compounds **27** and **F**

Compound abbreviated as		Compound **27**	Compound **F** [362]
Structure		$[Fe_2Dy_4(mdea)_2(mdeaH)_2(\mu_3\text{-}OH)_2(N_3)_2(PhCO_2)_8].3MeCN$	$[Fe_2Dy_4(L'H)_2(L)_2(\mu\text{-}Piv)_4(\eta^2\text{-}Piv)_2(\mu 2\text{-}\eta^2\text{-}Piv)_2(\mu 3\text{-}OMe)_2]$
Ligand		*N*-methyldiethanolamine ($mdeaH_2$)	(*E*)-2-(hydroxymethyl)-6-((2-(hydroxymethyl)phenylimino)methyl)-4-methylphenol
Co−ligand		Sodium benzoate ($PhCO_2Na$)	Pivalic acid
Co−ligand		Sodium azide (NaN_3)	----------
Crystal system		Triclinic	Triclinic
Space group		$P\bar{1}$	$P\bar{1}$
Volume		2213.32(15)	2622.7(16)
Colour of crystal		Yellow	Brown
Shape of crystal		Block	Plate
Positions in butterfly topology	body	Two Dy ions	Two Fe ions
	wing-tips	Two Dy ions	Two Dy ions
$(\mu_3\text{-}OR)_2$		R= H	R= CH_3
Position of $(\mu_3\text{−}OR)_2$		Lying above and below the $\{Dy_4\}$ plane	Lying same directions “in the plane”
Distance between $(\mu_3\text{−}OR)$ and the $\{Dy_4\}$plane		0.592 Å	----------
Distance between Fe and the $\{Dy_4\}$plane		2.05 Å	1.60 Å
Shape of Fe ions		Distorted octahedron	Distorted octahedron
Shape of Dy ions		Two atoms distorted triangular dodecahedron and two atom distorted spherical capped square antiprism	Two atom distorted muffin and two atom distorted square antiprism
Average distance of	Fe−O	2.01	2.00
	Dy−O	2.41	2.38
	Dy−N	2.65	2.37
Average angle of	Fe−O−Dy	104.67	103.38
	Dy−O−Dy	109.12	96.97
Distance of	Dy−Dy	3.92	3.58
	Fe−Dy	3.45	3.42
Interactions		Ferromagnetic	Antiferromagnetic
Magnetisation at 2 K and 7 T		33.89 μB	24.0 μB
Relaxation behaviour		Lack SMM	Lack SMM

Compounds **27** was synthesised using *N*-methyldiethanolamine as the main ligand and sodium benzoate and sodium azide as the two co-ligands, while compound **F** was synthesised using (*E*)-2-(hydroxymethyl)-6-((2-(hydroxymethyl)phenylimino)methyl)-4-methylphenol as the main ligand and Pivalic acid as the co-ligand.

Both compounds **27** and **F** were crystallise in the triclinic space group $P\bar{1}$. The colour and shape of the crystals of compound **27** are yellow blocks, while compound **F** are brown plates.

Both compounds **27** and **F** have butterfly topology geometry. The body of the butterfly topology are occupied by two Dy ions and two Fe ions for compounds **27** and **F**, respectively. The wing-tips of the butterfly topology are occupied by two Dy ions in both compounds **27** and **F**.

The core of the compound is held together by two of $(\mu_3\text{-OR})^-$ groups in compound **27** (R=H) and compound **F** (R=CH_3). The two of (μ_3-OH) groups in compound **27** lying above and below the {Dy_4} plane at distance 0.592 Å, while compound **F** two (μ_3-OCH_3) groups are lying in the {Dy_4} plane.

Fe ions in both compounds **27** and **F** are six-coordinate with a distorted octahedron geometry lying above and below the {Dy_4} plane with distances 2.048 and 1.603 Å, respectively.

Dy ions in compounds **27** and **F** are eight and nine-coordinate. Dy ion in compound **27** is eight-coordinate with a distorted triangular dodecahedron geometry and nine-coordinate with a distorted spherical capped square antiprism shape geometry. While Dy ion in compound **F** is eight-coordinate with a distorted square antiprism geometry and nine-coordinate with a distorted muffin geometry.

The average Fe−O distance in compound **27** is longer than that in compound **F**. The average Dy−O bond and Dy−N distances in compound **27** is longer than that in compound **F**. The Fe···Dy distance in compound **27** is longer than that in compound **F** and the Dy···Dy distance in compound **27** is longer than that in compound **F**. The average Fe−O−Dy angles in compound **27** are larger than t in compound **F** and the average Dy−O−Dy angles in compound **27** are larger than that in compound **F**.

The magnetic studies of compound **27** revealed that the Dy-Dy interaction is ferromagnetic, while antiferromagnetic interaction in compound **F**. The magnetisation of compound **27** is higher than in compound **F** at 2 K and 7 T (μB). Both compounds lack SMM behaviour.

4.3.5. Magnetocaloric effect

Recently, Gd-based-3d metal complexes have gained attention due to their potential application for low-temperature magnetic coolers. Since the compound **25** {Fe_2Gd_4} exhibits a ferromagnetic interaction between Fe-Gd ions therefore, it was decided to explore the magnetocaloric effect (MCE).

The field dependence of the magnetisation of compound **25** was performed under different fields ranging from 0 to 70000 Oe (0-7 T) at the temperatures of 2-10 K.

Figure 4.20 shows the magnetisation values of compound **25** rise gradually as the field increases to reach a saturation value of 38.90 μ_B at 2 K and 7 T close to the theoretical value of 38 μ_B for two Fe and four Gd.

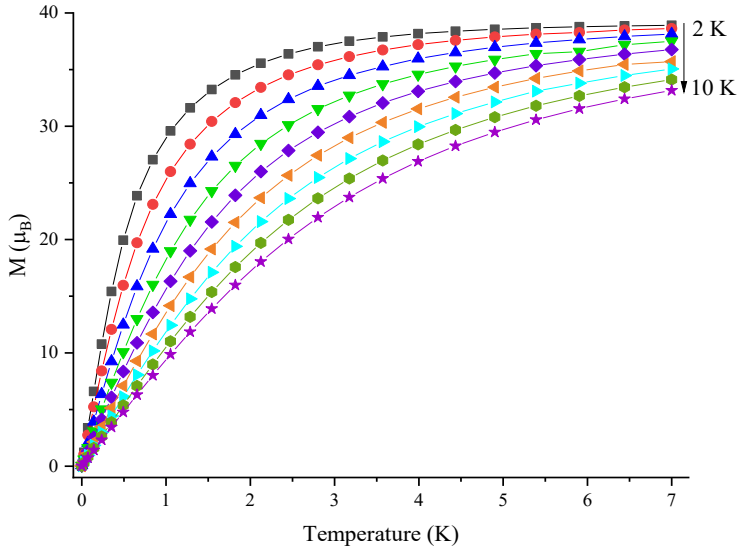

Figure 4.20. Field dependence of magnetisation at an indicated temperature of compound **25**.

Magnetic entropy change (-ΔSm) could be calculated from M versus H plots according to the Maxwell equation. The maximum entropy (-ΔS_m) of compound **25** is 27.50 J kg^{-1} K^{-1} with ΔH =7T at 4 K (Figure 4.21) which is lower than the theoretical (-ΔS_m) value per mole (69.17 J kg^{-1} K^{-1})

probably due to the ferromagnetic interaction between Fe-Gd ions. From the value ($-\Delta S_m$) compound **25** was found to act as a molecular magnetic refrigerant. To use such a material as a magnetic coolant, it should have higher MCE under a small magnetic field. Comparing compound **25** with reported Fe-Gd metal complexes, the maximum entropy ($-\Delta S_m$) of compound **25** (27.50 J kg $^{-1}$ K^{-1}) is higher than Fe_5Gd_8 (7.9 J kg $^{-1}$ K^{-1})[374] and also higher than Fe_3Gd_2 (21.1 J kg $^{-1}$ K^{-1}) [84] due to ferromagnetic interaction coupling of compound **25**.

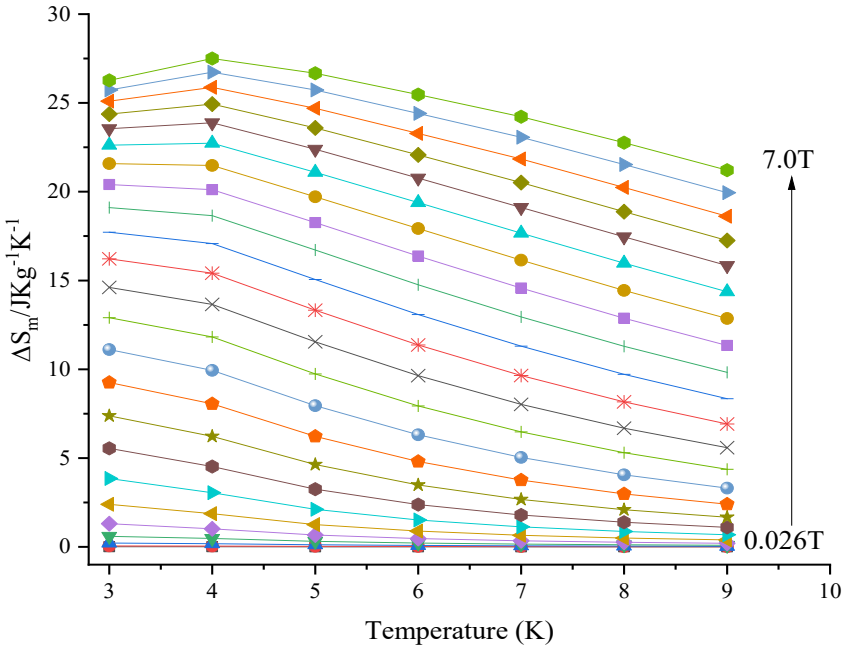

Figure 4.21. Changes in ($-\Delta S_m$) induced by magnetic field and temperatures of compound **25**.

4.3.6. Photoluminescence study

Photoluminescence spectra were recorded in the range from 200 to 800 nm in both solution and solid-state. Compounds **24** and **26** were measured in methanol and dichloromethane (1:1) at low concentration (100 µM) and were prepared at room temperature.

The excitation spectrum of compound **24** monitored at 614 nm emission exhibits high absorption in the range 200–400 nm (centred at 235 nm), Figure 4.22 presents the excitation and emission spectra of compound **24** in solution and solid-state.

The emission spectrum of compound **24** exhibits a sharp band which is a result of the f-f transition of Eu^{3+} corresponding to the $^5D_0 \rightarrow {}^7F_J$ (J = 0-4) transitions of the Eu^{3+} ion $^5D_0 \rightarrow {}^7F_0$ (544 nm), $^5D_0 \rightarrow {}^7F_1$ (590 nm), $^5D_0 \rightarrow {}^7F_2$ (614 nm), $^5D_0 \rightarrow {}^7F_3$ (650 nm) and $^5D_0 \rightarrow {}^7F_4$ (698 nm).

The emission band at 614 nm dominates the emission spectra (high intensity) corresponding to the hypersensitive $^5D_0 \rightarrow {}^7F_2$ transition, indicating that the Eu^{3+} ion is not on an inversion centre but is most likely at a site with low symmetry and non-centrosymmetric ligand field [122].

Among all the transitions, the $^5D_0 \rightarrow {}^7F_2$ and the $^5D_0 \rightarrow {}^7F_1$ are referred to as hypersensitive electric-dipole (ED) and magnetic-dipole (MD) transitions, respectively [122-125].

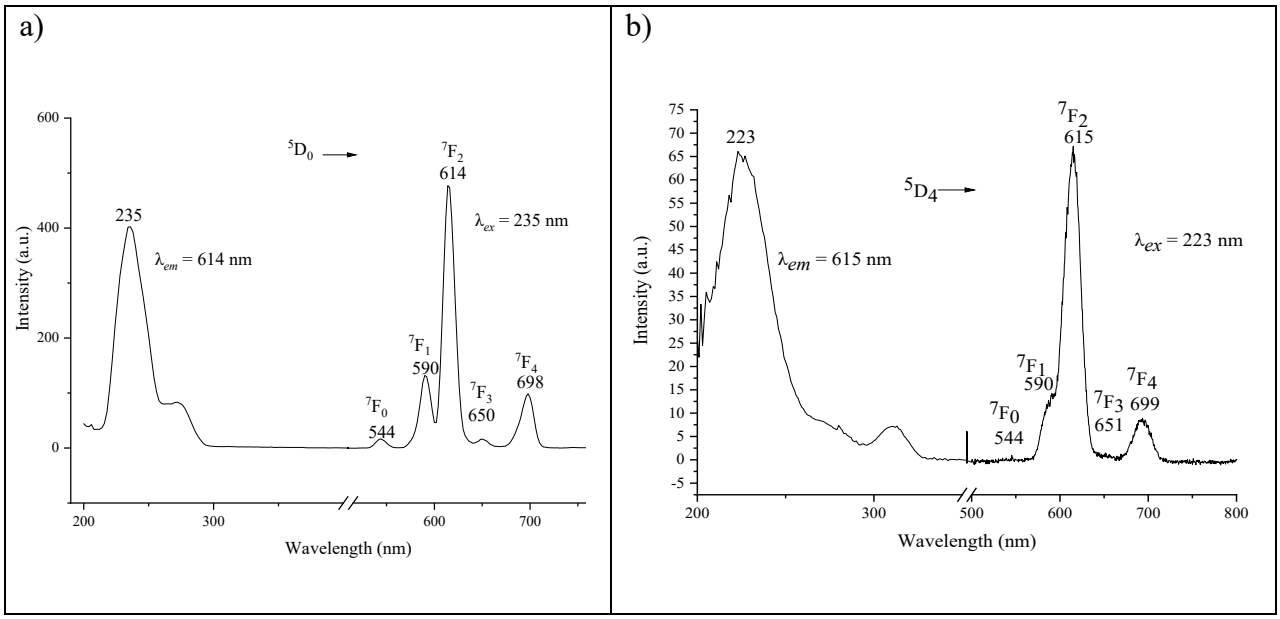

Figure 4.22. Excitation and emission spectra of compound **24** a) in solution b) solid-state.

The excitation spectrum of compound **26** monitored at 544 nm emission exhibits high absorption in the range 200–400 nm (centred at 235 nm), Figure 4.23 presents the excitation and emission spectra of compound **24** in solution and solid-state. The emission spectrum of compound **24** exhibits a sharp bands which is a result of the intra f-f transition of Tb^{3+} corresponding to the $^5D_4 \rightarrow {}^7F_J$ (J = 3–6) transitions of the Tb^{3+} ion $^5D_4 \rightarrow {}^7F_6$ (488 nm), $^5D_4 \rightarrow {}^7F_5$ (544 nm), $^5D_4 \rightarrow {}^7F_4$ (584 nm) and $^5D_4 \rightarrow {}^7F_3$ (620 nm). The emission at 488 nm ($^5D_4 \rightarrow {}^7F_6$) was assigned to the magnetic dipole transition; while at 544 nm ($^5D_4 \rightarrow {}^7F_5$) was assigned to the electric dipole transition [126]. The emission intensity at 544 nm was the strongest which deduced that the Tb^{3+} ion was located

on an asymmetric coordination [122]. This result indicates that these compounds may be good candidates as emitting molecular materials such as those used in OLEDs, which is one of the industrially relevant fields using coordination chemistry.

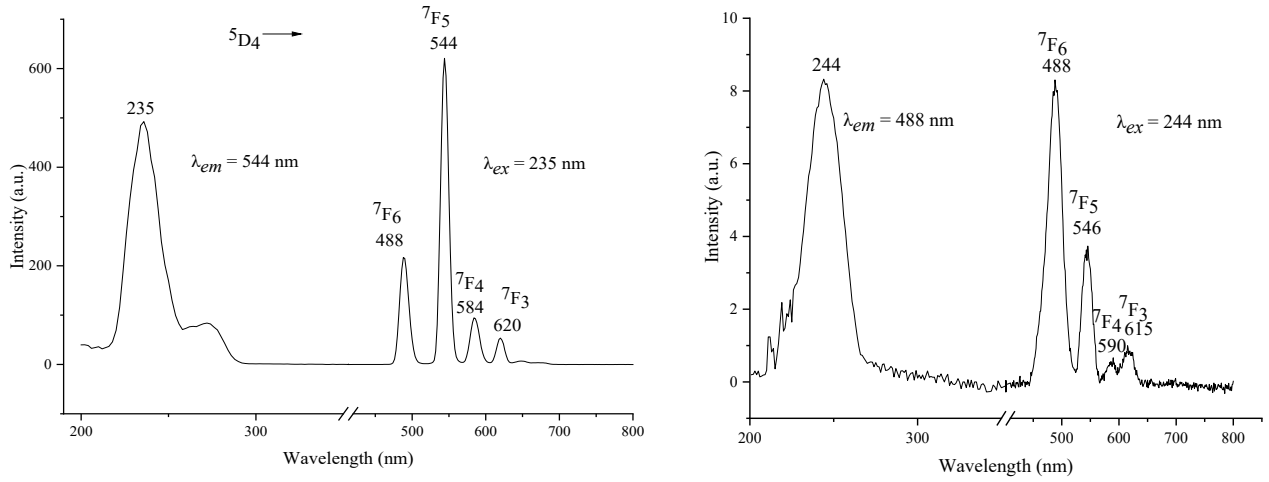

Figure 4.23. Excitation and emission spectra of compound **26** the solution-state on the left and the solid-state on the right.

4.4. Structure and magnetic properties of $[Fe_2Ln_4(mdea)_2(o\text{-van})_2(\mu_4\text{-}O)_2(PhCO_2)_8]$ **2·5MeCN**. (Ln = Eu(**30**), Gd(**31**), Tb(**32**), Dy(**33**), Ho(**34**), Er (**35**), Tm(**36**), Lu(**37**), Yb(**38**) and Y(**39**))

4.4.1. Synthetic description

The reaction of anhydrous $FeCl_3$, $Ln(NO_3)_3{\cdot}6H_2O$, sodium benzoate ($PhCO_2Na$), *N*-methyldiethanolamine ($mdeaH_2$) and *o*-vanillin (*o*-van) in a molar ratio of 1:1:3:5:1.1 in MeCN over reflux for two hours and afforded yellow block crystal of a new family of hexanuclear Fe-Ln clusters $[Fe_2Ln_4(mdea)_2(o\text{-van})_2(\mu_4\text{-}O)_2(PhCO_2)_8]{\cdot}2{\cdot}5MeCN$.

4.4.2. Crystal structure of $[Fe_2Ln_4(mdea)_2(o\text{-van})_2(\mu_4\text{-}O)_2(PhCO_2)_8]{\cdot}2{\cdot}5MeCN$

Full structure determination was performed for compounds **31** and **33** by single-crystal X-ray diffraction (full crystallographic data is given in Table 8.4); while the other compounds **30, 32** and **34-39** were found to be isostructural with **31** and **33** by checking their unit cells (Table 4.10).

Analysis of the IR spectra, PXRD patterns (Figure 4.25) and elemental analyses further confirmed that compounds **30**–**39** are isomorphous, isostructural and pure.

The structure of the hexanuclear complex $[Fe_2Dy_4(mdea)_2(o\text{-van})_2(\mu_4\text{-}O)_2(PhCO_2)_8]\cdot 2\cdot 5MeCN$ (**33**) will be described in detail as a representative of the whole series. Compound **33** crystallises in the triclinic space group $P\bar{1}$ with Z = 1. Compound **33** is a neutral cluster crystallising with 2·5 lattice MeCN molecules. However, it loses the lattice MeCN after dry according to elemental analyses.

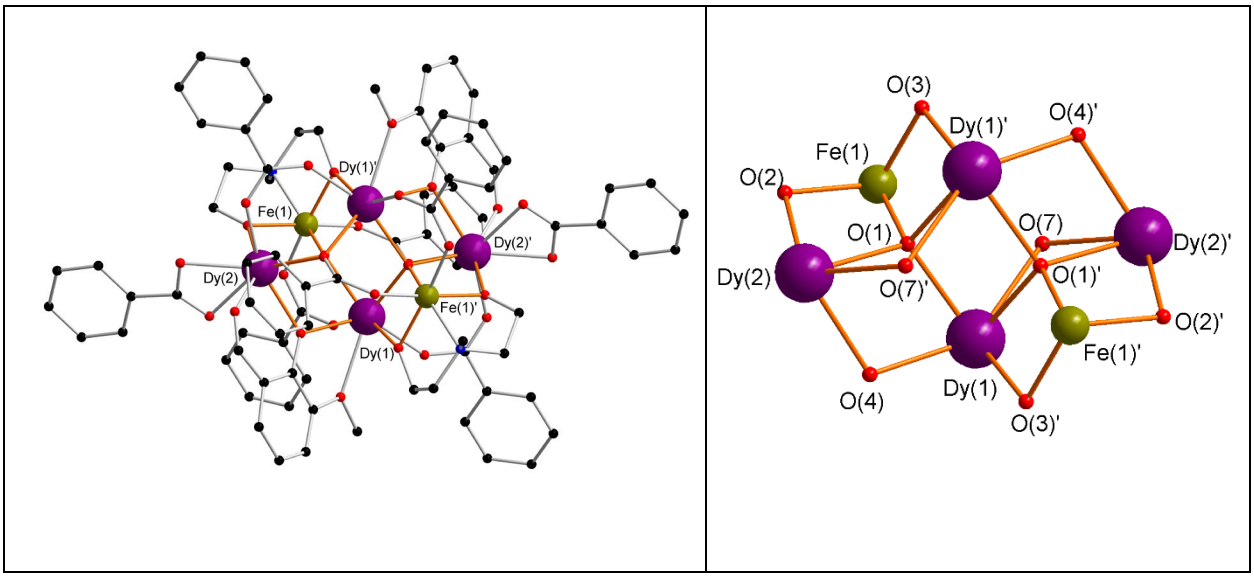

Figure 4.24. Molecular structure of compound **33**. Colour code: black, red, blue, green, white and violet spheres represent C, O, N, Fe, H and Dy, respectively. The core of compound **33** is shown on the right ($mdea^{2-}$, *o*-van^{-} and some benzoates are omitted for clarity).

The structure and the central core of compound **33** are shown in Figure 4.24, the $mdeaH_2$ and *o*-vanillin ligands are coordinating to the metal centres and doubly-deprotonated. The $mdeaH_2$ ligands are centred on the outer Fe^{III} through the N atom resulting in two negatively charged oxygen atoms O(2), O(3), or O(2)', O(3)' form alkoxy bridges along the Fe···Dy edges, whilst *o*-vanillin (*o*-van) ligand is a singly-deprotonated resulting in one negatively charged oxygen atom O(4) or O(4)' form bridges along the Dy···Dy edges.

Table 4.10. The unit cells data of compounds **30-39**

	a [Å]	b [Å]	c [Å]	α [deg]	β [deg]	γ [deg]	V [Å^3]
Fe_2Eu_4(**30**)	12.25(5)	12.87(7)	15.42(11)	73.45(5)	71.61(5)	89.54(5)	2190.39(17)
Fe_2Gd_4(**31**)	12.27(4)	12.85(5)	15.30(8)	73.41(4)	71.58(4)	89.56(3)	2185.80(17)
Fe_2Tb_4(**32**)	12.22(15)	12.86(13)	15.35(19)	73.58(18)	71.46(19)	89.54(18)	2182.16(40)
Fe_2Dy_4(**33**)	12.21(4)	12.84(5)	15.27(5)	73.35(3)	71.42(3)	89.44(3)	2166.26(14)
Fe_2Ho_4(**34**)	12.24(6)	12.83(6)	15.28(7)	73.31(4)	71.16(4)	89.30(4)	2167 28(2)
Fe_2Er_4(**35**)	12.14(8)	12.83(8)	15.30(12)	73.23(6)	71.28(7)	89.20(5)	2152 51(3)
Fe_2Tm_4(**36**)	12.18(6)	12.81(4)	15.28(9)	73.24(4)	71.29(5)	89.30(3)	2154 14(2)
Fe_2Lu_4(**37**)	12.17(7)	12.80(8)	15.29(9)	73.28(6)	70.98(5)	89.25(5)	2149.32(2)
Fe_2Yb_4(**38**)	12.24(12)	12.94(18)	15.41(5)	73.23(19)	71.16(17)	89.29(10)	2205.11(8)
Fe_2Y_4(**39**)	12.32(4)	12.81(3)	15.28(2)	73.41(17)	70.6(2)	89.20(2)	2172.04(10)

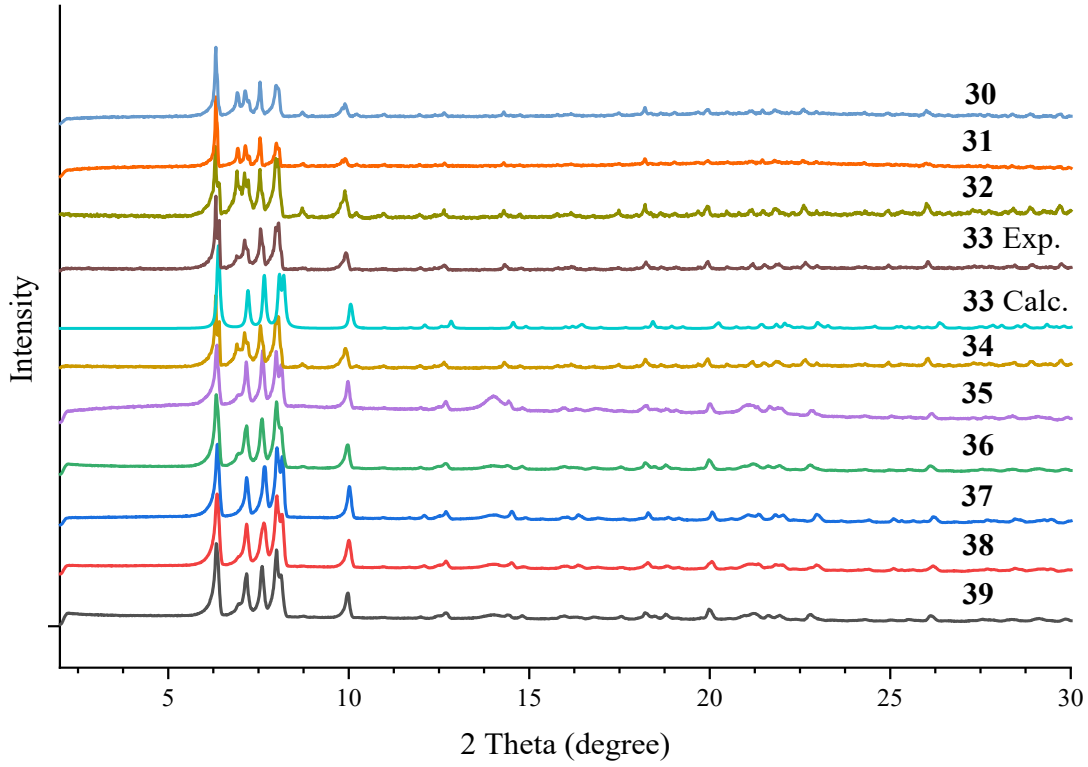

Figure 4.25. Calculated and experimental of PXRD patterns of compounds **30-39**.

The compound **33** possesses a centrosymmetric $[Fe_2Dy_4(\mu_4\text{-}O)_2]^{14+}$core with all four Dy atoms in one plane in a butterfly manner. In this butterfly motif two of the Dy^{III} ions occupy the body positions and the other two Dy^{III} ions occupy the outer wing-tips, whilst the two Fe^{III} ions are lying above and below the Dy_4 planner at a distance of 2.644 Å. Moreover, the compound **33** has $FeDy_3$

unit each bridged through single $(\mu_4\text{-O})^-$ group, *syn-syn*, doubly-deprotonated $mdea^{2-}$, $(o\text{-van})^-$ and *syn-syn-syn* bridging benzoate resulting in distorted tetrahedral $\{FeDy_3(\mu_4{-}O)\}$ geometry. The core is held together by two $(\mu_4{-}O)^{2-}$ groups O(1) or O(1)' lying above and below the Dy_4 plane at a distance of 0.781 Å (Figure 4.28). The structure does not have any inter or intramolecular interactions.

Thus compound **33** consists of two Fe^{III} and four Dy^{III}, two doubly-deprotonated $mdea^{2-}$, two singly-deprotonated $(o\text{-van})^-$ and eight of benzoate ligands. Two doubly-deprotonated $(mdea)^{2-}$ ligands are tridentate coordinating to the metal centres with a $(\eta^2{:}\ \eta^1{:}\ \eta^2{:}\ \mu_3)$ coordination mode (Figure 4.26, a). Two deprotonated oxygen $(o\text{-van})^-$ ligands are tridentate coordinating to the metal centres with a $(\eta^1{:}\ \eta^2{:}\ \eta^1{:}\ \mu_2)$ coordination mode (Figure 4.26, b).

Eight of benzoate ligands are in the crystal structure adopting three different coordination modes:

(i) Two of them are chelating to Dy(2) and Dy(2)' with a $(\eta^1{:}\eta^1{:}\mu_1)$ coordination mode (Figure 4.26, c).

(ii) Two of them are *syn-syn* bridging to two Dy^{III} ions with a $(\eta^1{:}\eta^1{:}\mu_2)$ coordination mode (Figure 4.26, d).

(iii) Two of them are *syn-syn* bridging to Fe^{III} ion and Dy^{III} ion with a $(\eta^1{:}\eta^1{:}\mu_2)$ coordination mode (Figure 4.26, e).

(iv) Two of them are *syn-syn-syn* bridging to two Dy^{III} ions and one Fe^{III} ion with a $(\eta^2{:}\eta^1{:}\mu_3)$ coordination mode (Figure 4.26, f).

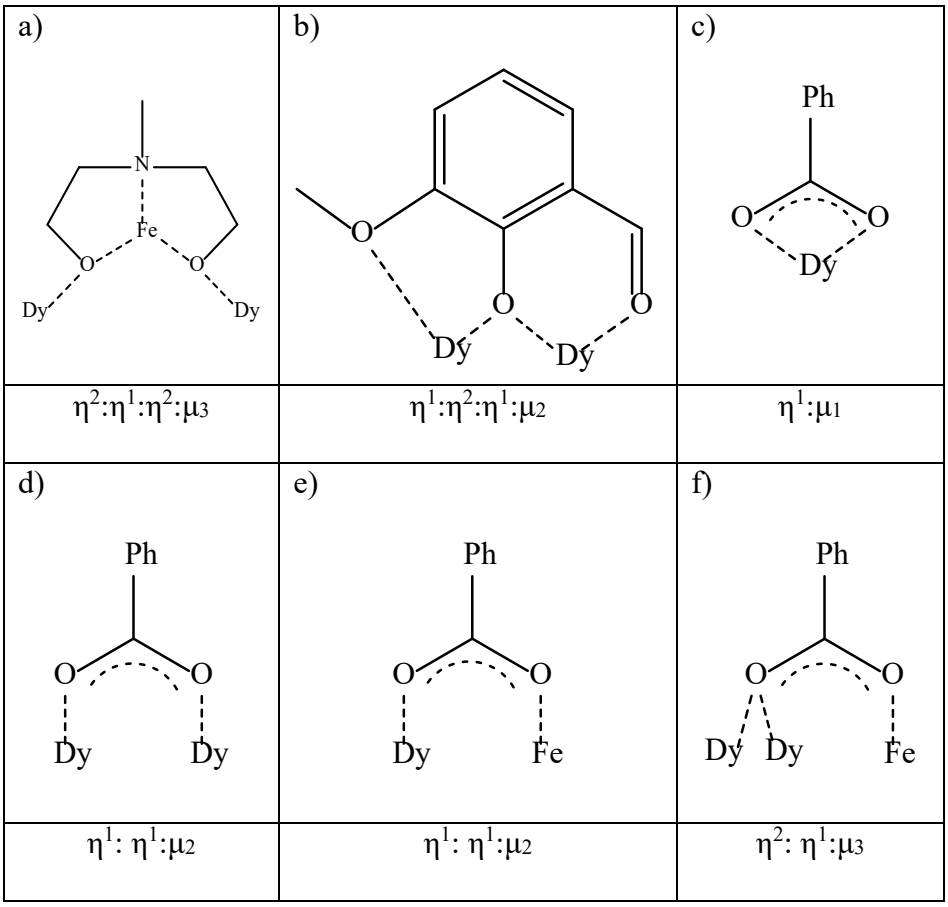

Figure 4.26. Coordination modes a) $mdea^{2-}$, b) (*o*-vanillin)$^{-}$ and c-f) benzoate ligands.

Both hexa-coordinated Fe^{III} ion are surrounded by one N and five O donor atoms (NO_5). One N and two O atoms come from the doubly-deprotonated oxygen $(mdea)^{2-}$ ligands, one O atom comes from *syn-syn*, one O atom comes from *syn-syn-syn* bridging benzoate and one O atom comes from the $(\mu_4{-}O)^{2-}$ group. The Fe–O bond distances are in the range 1.902(3)−2.213(5) Å and the Fe–N bond distance is 2.213(5) Å. The Fe···Dy distances are in the range 3.307(9)–3.337(9) Å. Selected bond distances and angles are summarised in Table 4.11. This results in a distorted octahedron geometry with a $\sum$ parameter of 91.82. This geometry was confirmed by SHAPE analysis [309-312] with a deviation value of 2.09, (Figure 4.27, Table 8.13).

The Dy^{III} ions here have eight O donors but present two different types of coordination environmental based on the source of O atom:

(i) Both octa-coordinated Dy(1) and Dy(1)' are surrounded by eight O donor atoms (O_8). One O atom comes from the doubly-deprotonated oxygen $mdea^{2-}$ ligand, two O atoms

come from *syn-syn* bridging benzoate, one O atom comes from *syn-syn-syn* bridging benzoate, two O atoms come from the deprotonated oxygen *o*-vanillin $(o\text{-van})^{-}$ ligand and two O atoms come from $(\mu_4\text{–O})^{2-}$ group. This results in a distorted triangular dodecahedron geometry. This geometry was confirmed by SHAPE analysis [309-312] with a deviation value of 1.31, (Figure 4.27, Table 8.13).

(ii) Both octa-coordinated Dy(2) and Dy(2)' ions are surrounded by eight O donor atoms (O_8). One O atom comes from the doubly−deprotonated oxygen $mdea^{2-}$ ligand, one O atom comes from *syn-syn* bridging benzoate, one O atom comes from *syn-syn-syn* bridging benzoate, two O atoms come from chelated benzoate, two O atoms come from the deprotonated oxygen *o*-vanillin $(o\text{-van})^{-}$ ligand and one O atoms comes from the $(\mu_4\text{–O})^{2-}$ group. This results in a distorted triangular dodecahedron geometry which was confirmed by SHAPE analysis [309-312] with a deviation value of 1.31, (Figure 4.27, Table 8.13).

The Dy−O bond distances are in the range 2.259(4)−2.589(3) Å. The Dy···Dy distances are in the range 3.664(6)−3.786(5) Å. The Dy−O−Fe and Dy−O−Dy angles are in the range 101.33(15)−121.79(16)° and 94.26(11)−112.03(13)°, respectively.

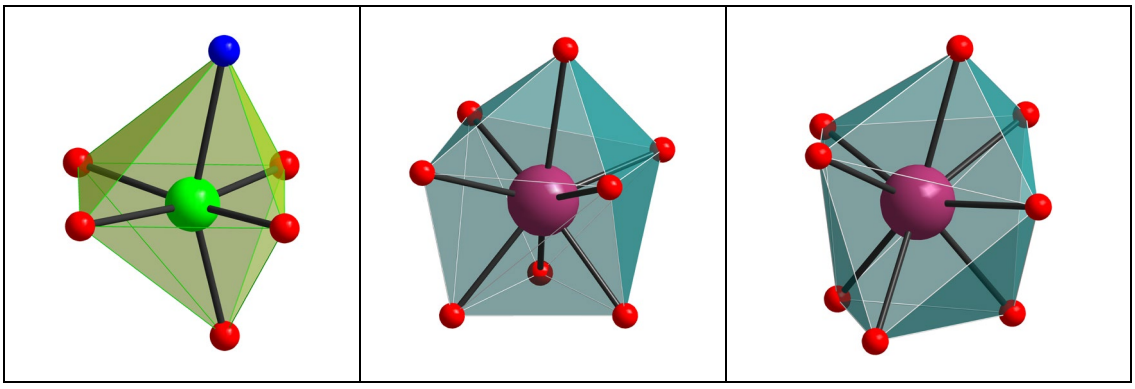

Figure 4.27. Distorted octahedral geometry of 6-coordinated Fe ion on the left, triangular dodecahedron geometry of 8-coordinated of Dy(1) ion on the centre and triangular dodecahedron geometry of 8-coordinated of Dy(2) ion on the right. Colour code: red, blue, green and violet spheres represent O, N, Fe and Dy, respectively.

Table 4.11 Selected bond distances (Å) and angles (°) of compound **33**

Bond distances			Bond distances		
Atom	Atom	Distance/Å	Atom	Atom	Distance/Å
Fe(1)	O(1)	1.902(3)	Dy(2)	O(1)	2.298(3)
Fe(1)	O(2)	1.978(4)	Dy(2)	O(2)	2.259(4)
Fe(1)	O(3)	1.995(4)	Dy(2)	O(4)	2.336(3)
Fe(1)	O(8)	2.053(4)	Dy(2)	O(5)	2.369(4)
Fe(1)	O(10)	2.051(4)	Dy(2)	O(7)	2.548(4)
Fe(1)	N(1)	2.213(5)	Dy(2)	O(12)	2.307(4)
Dy(1)	O(1)'	2.323(3)	Dy(2)	O(13)	2.420(4)
Dy(1)	O(1)	2.267(3)	Dy(2)	O(14)	2.439(4)
Dy(1)	O(3)	2.311(4)	Fe(1)	Dy(1)'	3.337(9)
Dy(1)	O(4)	2.385(4)	Fe(1)	Dy(2)	3.307(9)
Dy(1)	O(6)	2.575(4)	Dy(1)	Dy(1)'	3.664(6)
Dy(1)	O(7)	2.589(3)	Dy(1)	Dy(2)'	3.765(5)
Dy(1)	O(9)	2.315(4)	Dy(1)	Dy(2)	3.786(5)
Dy(1)	O(11)	2.321(4)			

Bond angles				Bond angles			
Atom	Atom	Atom	Angles/°	Atom	Atom	Atom	Angles/°
Fe(1)	O(1)	Dy(1)	121.79(16)	Dy(1)	O(1)	Dy(1)'	105.93(14)
Fe(1)	O(1)	Dy(1)'	103.85(14)	Dy(1)	O(1)	Dy(2)	112.03(13)
Fe(1)	O(1)	Dy(2)	103.45(15)	Dy(1)'	O(1)	Dy(2)	109.13(13)
Fe(1)	O(2)	Dy(2)	102.40(16)	Dy(1)	O(4)	Dy(2)	106.63(13)
Fe(1)	O(3)	Dy(1)'	101.33(15)	Dy(1)	O(7)	Dy(2)'	94.26(11)

'1-x, 1-y, 1-z

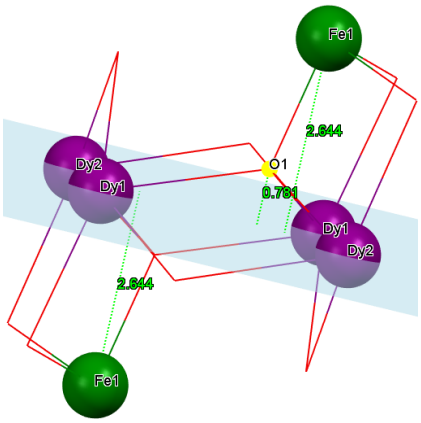

Figure 4.28. Single unit of the planar of compound **33**. Colour code: red, blue, green and violet spheres represent O, N, Fe and Dy, respectively.

4.4.3. Magnetic properties

DC magnetic susceptibilities of compounds **31-33** were carried out on freshly prepared polycrystalline samples in the temperature range 1.8-300 K under an applied magnetic field of 1000 Oe (0.1 T). The plot of χT versus T for compounds **31-33** is shown in Figure 4.29. The DC data are summarised in Table 4.12.

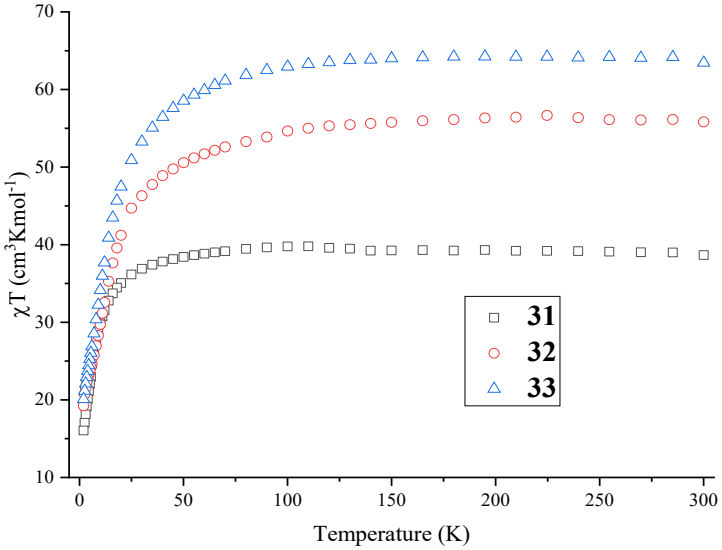

Figure 4.29. Temperature dependence of χT products for compounds **31-33** at 1000 Oe.

The χT products of compounds **31-33** at 300 K are 38.66 cm^3 K mol^{-1}, 55.82 cm^3 K mol^{-1} and 63.44 cm^3 K mol^{-1}, respectively, close to those expected values for six non-interacting ions of **31**:

Fe_2Gd_4(40.27 cm^3Kmol^{-1}), of **32**: Fe_2Tb_4 (56.03 cm^3Kmol^{-1}) and **33**: Fe_2Dy_4 (65.43 cm^3Kmol^{-1}) respectively. For compound **31**, the χT product stays almost constant from 300 to 120 K and then slightly increases from 120 to 70 K, followed by a slight decrease from 70-30 K, then a drop from 30-1.8 K, reaching a minimum value of 16.05 cm^3 K mol^{-1} at 1.8 K.

Compounds **32** and **33** are similar χT remain essentially constant from 300-110 K and decrease slightly from 110-70 K, followed by a drop from 70-1.8 K, reaching a minimum value of 19.23 cm^3 K mol^{-1} for compound **32** and 20.09 cm^3 K mol^{-1} for compound **33** at 1.8 K

The decrease of χT experimental values with the temperature is probably due to the thermal depopulation of the Stark sublevels of Ln^{III} ions within the complexes or with the individual Ln^{III} ions and/or antiferromagnetic interaction between the Ln^{III} ions or between Fe^{III}-Ln^{III} ions [313, 314].

Changing the co-ligand from azide in compound **27** to *o*-vanillin allow to obtain new compound **33** and changes the magnetic properties. Compound **27** has ferromagnetic while compound **33** has antiferromagnetic interaction.

Table 4.12. DC data for compounds **31-33**

Compounds	Ground state of the Ln^{III} Ion	Curie Constant for each Ln ion at 300 K (cm^3K/mol)[276]	χT ($cm^3mol^{-1}K$) expected value for Fe_2Ln_4 at RT	χT ($cm^3mol^{-1}K$) experimental value for Fe_2Ln_4 at RT	χT ($cm^3mol^{-1}K$) experimental value for Fe_2Ln_4 at 1.8 K	Magnetistion at 2 K and 7 T (μ_B)
Fe_2Gd_4 (**31**)	$^8S_{7/2}$	7.88	40.27	38.66	16.05	38.03
Fe_2Tb_4 (**32**)	$^7F_6$	11.82	56.03	55.82	19.23	26.94
Fe_2Dy_4 (**33**)	$^6H_{15/2}$	14.17	65.43	63.44	20.09	

AC susceptibility measurements of compounds **32** and **33** were performed in order investigate potential SMM behaviour of compounds **32** and **33**. AC magnetic susceptibility measurements of compounds **32** and **33** were carried out in the frequency range 1-1488 Hz and at temperature 2 K under different applied DC field. As shown in Figure 4.30, compounds **32** and **33** shows slow

relaxation without maxima under a small-applied DC fields (0-3000 Oe). The results indicate that both compounds **32** and **33** lack SMM behaviour, however given the presence of a peak without a maxima in the Dy analogue, there is possibility that this system could be an SMM with a lower energy barrier and could potentially be observed at very low, sub Kelvin, temperatures.

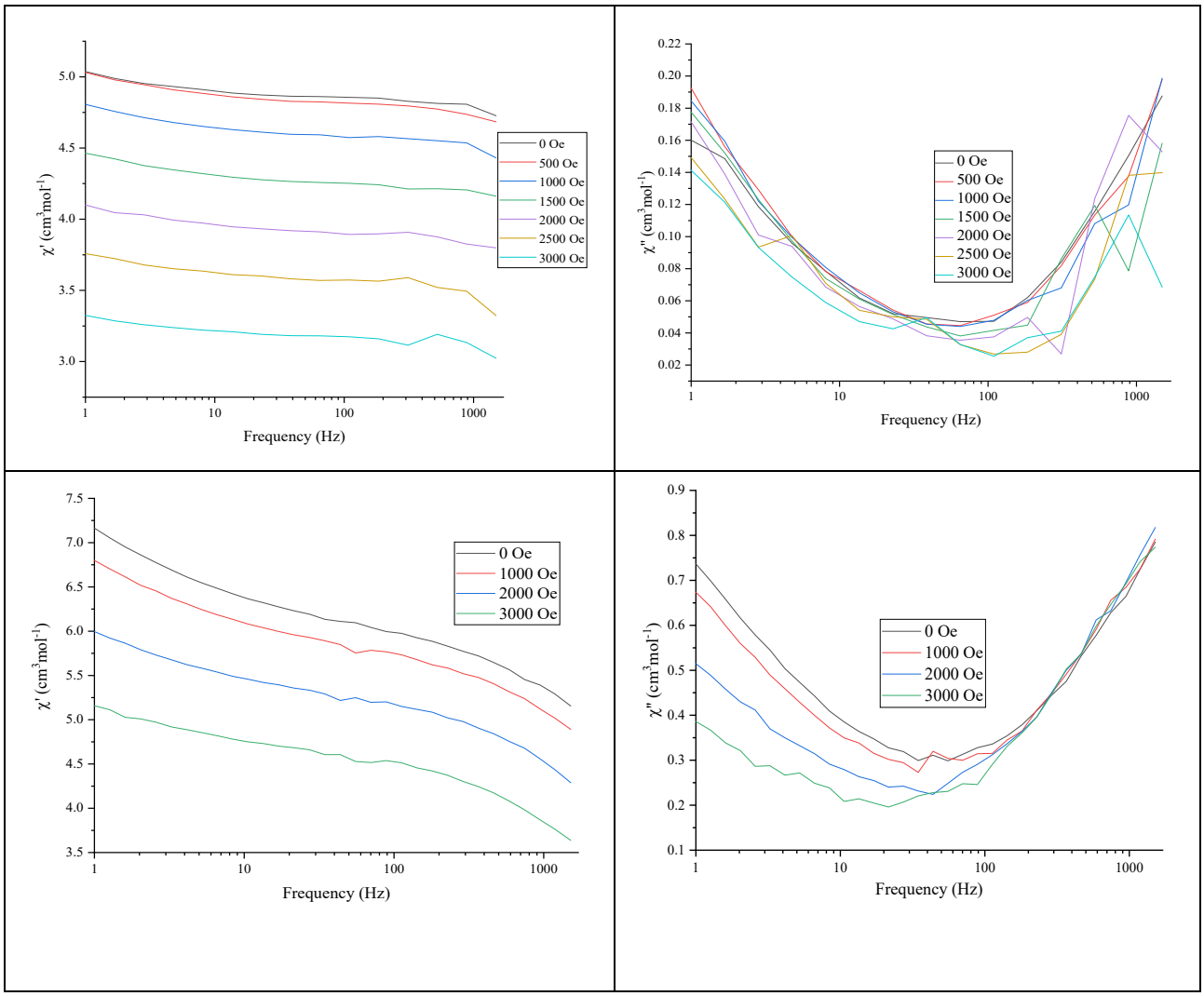

Figure 4.30. Frequency dependence of the In-phase (left) and the out-of-phase (right) components of the AC susceptibility for compounds **32** (top) and **33** (bottom) under different applied DC fields.

4.4.4. Comparison of the core structure

N-methyldiethanolamine ($mdeaH_2$) has been widely used as a main ligand to synthesise Fe-Ln, with various topologies and also exhibiting interesting magnetic properties like SMM behaviour

[79, 80, 89, 253]. For example, the highest energy barrier in an $\{Fe_7Dy_3\}$ cluster is U_{eff}=33.40 K with pre-exponential relaxation time, $\tau_o = 6.6\times10^{-8}$ s [80].

o-Vanillin has been widely used as a main ligand and co-ligand to synthesise lanthanide metal complexes with various topologies and also exhibiting interesting magnetic properties like SMM behaviour. *o*-Vanillin was also used to synthesise $\{Dy_3\}$ which presents a new concept for magnetic memory without a net magnetic moment [74, 75]. $\{Dy_3\}$ shows a vanishing susceptibility at low temperature which is unexpected in a system having an odd number of unpaired electrons. Nevertheless, *o*-vanillin has not been used to obtain iron–lanthanide metal complexes and also $mdeaH_2$ and *o*-vanillin together have not been used to obtain lanthanide or iron–lanthanide metal complexes. From this perspective, in the present work a combination of $mdeaH_2$ alongside *o*-vanillin and benzoate as the two co-ligands have been employed to obtain higher nuclearity cluster which could provide route toward compounds potentially having optical or magnetic properties as well as SMM behaviour, with this synthetic approach, $[Fe_2Ln_4(mdea)_2(o\text{-van})_2(\mu_4\text{-}O)_2(PhCO_2)_8]$. 2·5 MeCN was produced with butterfly-shaped manner.

Changing the co-ligand from Pivalic acid in compound **13** to benzoate (sodium benzoate) in compound **33** and the counter ion of the lanthanide give the system the opportunity to increase the nuclearity of the resulting compound.

Herein, the $\{Fe_2Ln_4\}$ (**33**) is in general rare for hexanuclear complex [3d-4*f*] coordination but similar core is existing. The core topologies of reported $[Fe_4Ln_2]$ complex [375] is similar to the compound **33**. Both compounds have almost the same geometry. The crystallographic and magnetic details are compared in this section. The comparison between both compounds is summarised in Figure 4.31 and Table 4.13. In all cases, the Dy containing structure has chosen as representative for the whole lanthanide. $\{Fe_4Dy_2\}$ is denoted by compound **G** [375].

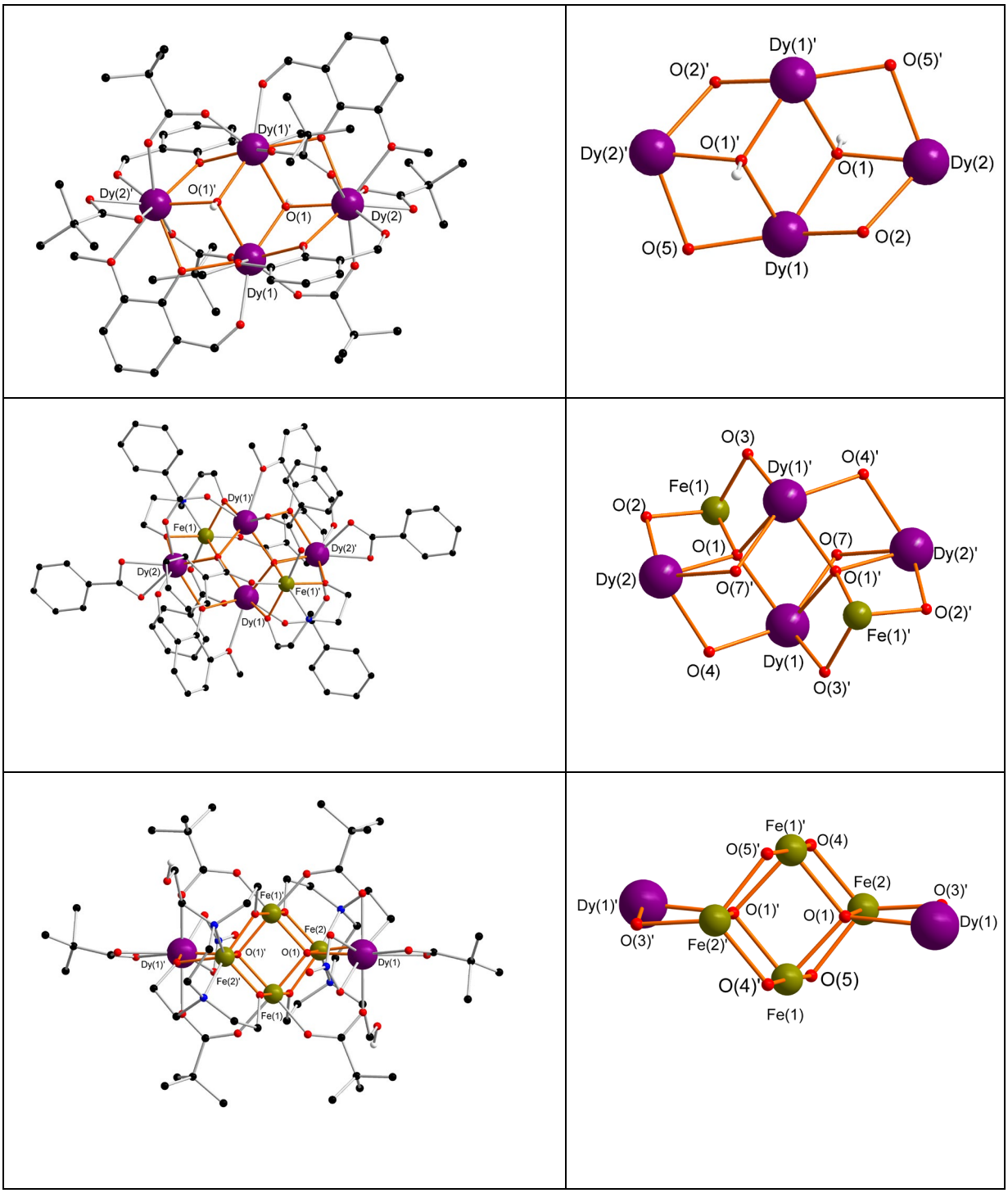

Figure 4.31. Molecular structure and the core of compound **13** on the top compound **33** on the middle and compound **G** on the bottom (H atoms omitted for clarity). Colour code: black, red, blue, green, white and violet spheres represent C, O, N, Fe, H and Dy, respectively.

Table 4.13. Comparison between compounds **33** and **G**

Complex abbreviated as		Compound **33**	Compound **G** [375]
Structure		$[Fe_2Dy_4(mdea)_2(o\text{-van})_2(\mu_4\text{-}O)_2(PhCO_2)_8]$ 2·5MeCN	$[Fe_4Dy_2(\mu_4\text{-}O)_2(Piv)_6(NO_3)_2(Hedte)_2]$ 4MeCN C_6H_5OH
Ligand		*N*-methyldiethanolamine ($mdeaH_2$)	N,N,N',N'-tetrakis-(2-hydroxyethyl) ethylenediamine
Co−ligand		*o*-Vanillin	Pivalic acid
Co−ligand		Sodium benzoate ($PhCO_2Na$)	
Crystal system		Triclinic	Monoclinic
Space group		$P\bar{1}$	$P2_1/n$
Volume		2166.26(14)	8251.2(6)
Colour of crystal		Yellow	Orange
Shape of crystal		Block	Block
Position of $(\mu_4\text{-}O)_2$		Lying above and below the $\{Dy_4\}$ plane	Lying above and below the $\{Fe_4\}$ plane
Distance between $(\mu_4\text{-}O)$ and the $\{Dy_4\}$ plane		0.78 Å	0.99 Å
Distance between the plane and rest metals		$\{Dy_4\}\cdots Fe$ =2.64Å	$\{Fe_4\}\cdots Dy$ = 3.14 Å
Shape of Fe ions		Distorted octahedron	Distorted octahedron
Shape of Dy ions		Distorted triangular dodecahedron	Distorted biaugmented trigonal prism
Average distance of	Fe−O	2.00	2.01
	Fe−N	2.21	2.25
	Dy−O	2.38	2.37
Average angle of	Fe−O−Dy	106.56	114.83
Average distance of	Fe−Dy	3.32	4.07
Interactions		Antiferromagnetic	Ferromagnetic
Relaxation behaviour		Lack SMM	SMM U_{eff}=30.85 K with a relaxation time $\tau_o = 3.7\text{x}10^{-8}$ s.

Compounds **33** was synthesised using *N*-methyldiethanolamine ($mdeaH_2$) as the main ligand and sodium benzoate and *o*-vanillin as the two co-ligands, while compounds **G** was synthesised using N,N,N',N'-tetrakis-(2-hydroxyethyl) ethylenediamine as the main ligand and Pivalic acid and phenol as the two co-ligands. Compound **33** crystallises in the triclinic space group $P\bar{1}$, while compound **G** in the monoclinic space group $P\ 2_1/n$. The colour and shape of the crystals of compound **33** are yellow block, while compound **G** are orange blocks. The core of compound **33**

and **G** is held together by two (μ_4-O) groups lying above and below the {Dy_4} plane at distances 0.78 and 0.99 Å, respectively.

Fe ions in both compounds **33** and **G** are six-coordinate with a distorted octahedron geometry. Fe ions in compound **33** lying above and below the {Dy_4} plane at distances 2.64 Å. Dy ions in compounds **33** and **G** are octa-coordinated with a distorted triangular dodecahedron and distorted biaugmented trigonal prism, respectively. Dy ions in compound **G** lying above and below the {Fe_4} plane at distances 3.14 Å.

The average Fe−O and Fe−N bond distances in compound **G** are longer than those in compound **33**, Dy−O bond distance in compound **G** is shorter than that in compound **33**. The average Fe···Dy distances in compound **G** is longer than that in compound **33**. The average Fe−O−Dy angle in compound **G** is larger than that in compound **33**.

The magnetic studies of compound **33** revealed the Dy−Dy interaction is antiferromagnetic, while ferromagnetic interaction that in compound **G**. Compound **G** demonstrate SMM behaviour U_{eff} = 30.85 K and τ_o =3.7x10^{-8} s while compound **33** lacks SMM behaviour.

4.4.5. Magnetocaloric effect

Recently, Gd-based-3d metal complexes have gained attention due to their potential application for low-temperature magnetic coolers. Since, the compound **31** {Fe_2Gd_4} exhibits an antiferromagnetic interaction between Fe-Gd ions therefore, it was decided to explore the magnetocaloric effect (MCE).

The field dependence of the magnetisation of compound **31** was performed under different fields ranging from 0 to 70000 Oe (0-7 T) at the temperatures range 2-10 K.

Figure 4.32 shows the magnetisation values of compound **31** arises gradually as the field increases to reach a saturation value of 38.03 μ_B at 2 K and 7 T close to the theoretical value of 38 μ_B for two Fe and four Gd.

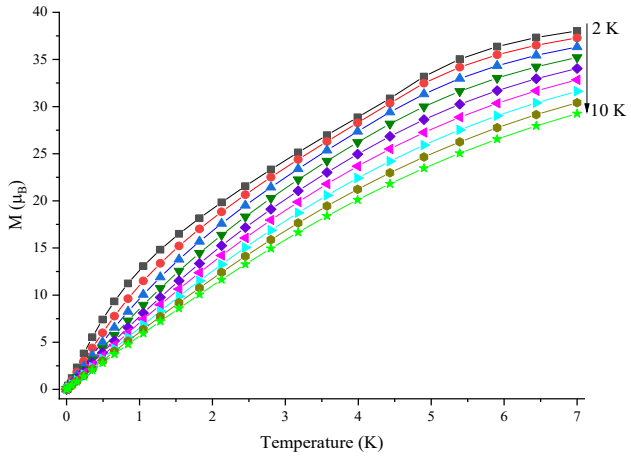

Figure 4.32. Field dependence of magnetisation at indicated temperatures of compound **31**

Magnetic entropy change (-ΔSm) could be calculated from M versus H plots according to the Maxwell equation. The maximum entropy ($-\Delta S_m$) of compound **31** was 18.41 J kg^{-1} K^{-1} with at ΔH =7T at 5 K (Figure 4.33) which is lower than the theoretical ($-\Delta S_m$) value per mole (69.17 J kg^{-1} K^{-1}) probably due to the antiferromagnetic interaction between Fe-Gd ions.

Comparing compound **31** with reported Fe-Gd metal complexes, the maximum entropy ($-\Delta S_m$) of compound **31** (18.41 J kg^{-1} K^{-1}) is higher than Fe_5Gd_8 (7.9 J kg^{-1} K^{-1}) [374], lower than Fe_3Gd_2 (21.1 J kg^{-1} K^{-1}) [84]. Compound **25** is the best 27.50 J kg^{-1} K^{-1} vs 18.41 J kg^{-1} K^{-1} for compound **31** which is quite a big improvement.

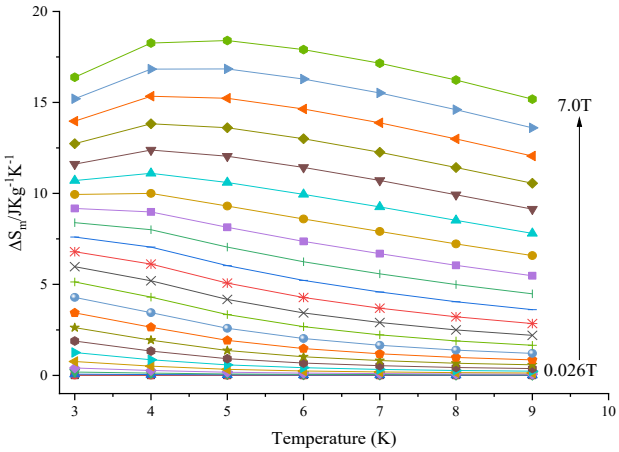

Figure 4.33. Changes in ($-\Delta S_m$) induced by the magnetic field and temperatures of compound **31**

4.5. Structure and magnetic properties of **$[Fe_4Ln_2(mdea)_4(PhCO_2)_6(N_3)_2(\mu_3\text{-}OH)_2]\cdot MeCN\cdot H_2O$**. (Ln = Eu(**40**), Gd(**41**), Tb(**42**), Dy(**43**), Ho(**44**), Er (**45**) and Y(**46**))

4.5.1. Synthetic description

The reaction of $[Fe_3O(PhCO_2)_6(H_2O)_3](PhCO_2)$, $LnCl_3\cdot 6H_2O$, *N*-methyldiethanolamine ($mdeaH_2$) and sodium azide (NaN_3) in a molar ratio of 1:1:4:8 in MeCN with stirring and heating for one hour and afforded orange plate crystals of a hexanuclear Fe-Ln clusters $[Fe_4Ln_2(mdea)_4(PhCO_2)_6(N_3)_2(\mu_3\text{-}OH)_2]\cdot MeCN\cdot H_2O$ after standing at room temperature overnight.

4.5.2. Crystal structure of $[Fe_4Ln_2(mdea)_4(PhCO_2)_6(N_3)_2(\mu_3\text{-}OH)_2]\cdot MeCN\cdot H_2O$

In this series of hexanuclear iron-lanthanide clusters, only compound **43** and **45** have been characterised fully by single-crystal X-ray diffraction (full crystallographic data is given in Table 8.5); while the other compounds **40**-**42**, **44** and **46** were confirmed by their unit cell (Table 4.14). In addition, elemental analyses, FTIR spectroscopy and powder XRD studies (Figure 4.35) also support the suggestion that compounds **40**-**46** are isostructural, isomorphous and pure. Therefore, only the structure of $[Fe_4Ln_2(mdea)_4(PhCO_2)_6(N_3)_2(\mu_3\text{-}OH)_2]\cdot MeCN\cdot H_2O$ (**43**) will be described in detail as a representative of the whole series. Compound **43** crystallises in the triclinic space group $P\bar{1}$ with Z = 2. Compound **43** is a neutral cluster containing one lattice MeCN and one lattice water molecule. However, it loses the lattice MeCN according to elemental analyses.

The structure and the central core of compound **43** are shown in Figure 4.34, the $mdeaH_2$ and benzoate ligands are coordinating to the metal centres as can be seen in the crystal structure. The $mdeaH_2$ is doubly-deprotonated resulting in two negatively charged oxygen atoms O(3), O(6) or O(7), O(10) or O(3), O(4) or O(7), O(8) form alkoxy bridges along the Fe···Dy edges. In addition, O(3), O(5) or O(7), O(9) form alkoxy bridges along the Fe···Fe edges.

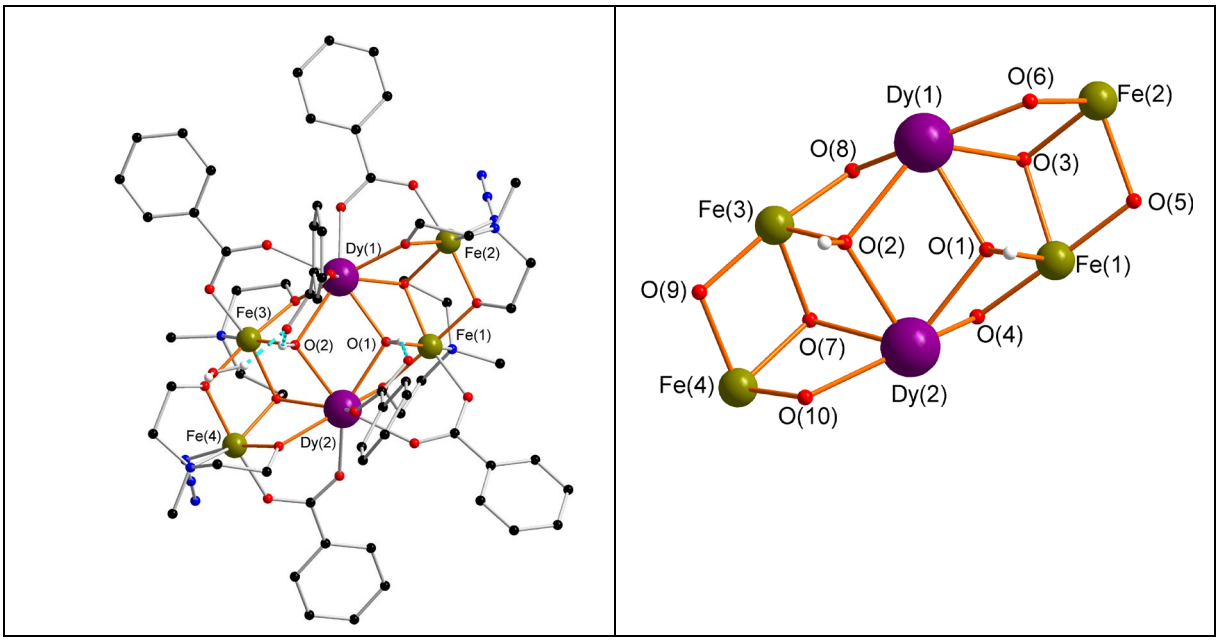

Figure 4.34. Molecular structure of compound **43**. Colour code: black, red, blue, green, white and violet spheres represent C, O, N, Fe, H and Dy, respectively. The core of compound **43** is shown on the right ($mdea^{2-}$, azides and benzoates are omitted for clarity).

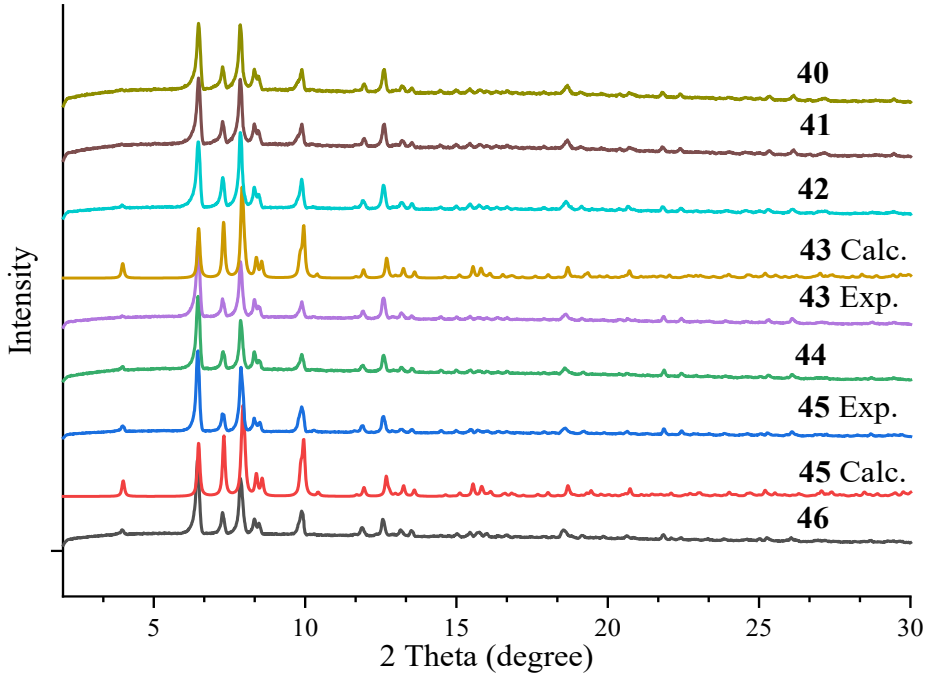

Figure 4.35. Calculated and experimental of PXRD patterns of compounds **40-46**.

Table 4.14. Unit cells data of compounds **40**-**46**

	a [Å]	b [Å]	c [Å]	α [deg]	β [deg]	γ [deg]	V [Å3]
Fe_4Eu_2(**40**)	12.18(3)	14.54(3)	23.26(4)	89.67(9)	74.80(9)	70.00(9)	3721.66(11)
Fe_4Gd_2(**41**)	12.20(2)	14.56(4)	23.23(5)	89.62(7)	74.88(8)	70.17(8)	3719.29(12)
Fe_4Tb_2(**42**)	12.15(4)	14.48(4)	23.22(6)	89.33(8)	75.10(9)	70.28(12)	3708.90(15)
Fe_4Dy_2(**43**)	12.16(2)	14.52(3)	23.08(4)	89.54(2)	75.03(10)	70.41(2)	3695.12(13)
Fe_4Ho_2(**44**)	12.18(4)	14.57(5)	23.00(7)	89.47(5)	74.95(5)	70.22(6)	3696.53(14)
Fe_4Er_2(**45**)	12.14(2)	14.53(2)	22.97(3)	89.57(10)	75.26(10)	70.33(10)	3674.00(10)
Fe_4Y_2(**46**)	12.14(3)	14.55(3)	23.08(5)	89.60(7)	75.16(8)	70.31(7)	3695.28(14)

The compound **43** possesses $[Fe^{III}_2Dy^{III}_2(\mu_3\text{-}OH)_2]^{10+}$ a non-planar butterfly. In this butterfly motif, two of the Dy^{III} ions occupy the body positions and two Fe^{III} ions occupy the outer wing-tips, whilst the two Dy ^{III} ions Dy(1) and Dy(2) are lying in the same directions above the Fe_4 planner at a distance of 0.811 and 0.992 Å, respectively. Moreover, the compound **43** has Fe_2Dy_2 unit, in which the $FeDy_2$ triangles are each bridged by a single $(\mu_3\text{-}OH)^-$ group, *syn-syn* bridging benzoate and doubly-deprotonated $mdea^{2-}$. The remaining Fe^{III} ions are each bridging through two deprotonated oxygens O(3), O(5) and O(6) or O(7), O(9) and O(10) from the doubly deprotonated $mdea^{2-}$ ligand and *syn-syn* bridging benzoate to the tetranuclear core. There are two $FeDy_2$ triangles which share a Dy(1) and Dy(2) backbone. The triangles are held together by two $(\mu_3\text{-}OH)^-$ groups O (1) and O(2) are lying in the same directions above the $\{Fe_4\}$ planner at a distance of 1.264 and 1.314 Å, respectively. Single unit of compound **43** is presented in Figure 4.38.

The compound **43** consists of four Fe^{III} and two Dy^{III}, two terminal azide $(N_3)^-$, four doubly-deprotonated $mdea^{2-}$ and six of benzoate ligands.

There are four doubly-deprotonated $mdea^{2-}$ ligands are centred on the outer Fe^{III} ions through the N atom present with two different types of coordination modes:

(i) Two of them are tridentate bridging to the metal centre with a $(\eta^2\text{: }\eta^1\text{: }\eta^2\text{: }\mu_3)$ coordination mode (Figure 4.36, a).

(ii) Two of them are tridentate bridging to the metal centre with a $(\eta^2\text{: }\eta^1\text{: }\eta^3\text{: }\mu_4)$ coordination mode (Figure 4.36, b).

Six of benzoate ligands are in the crystal structure adopting two different coordination modes.

(i) Four of them are *syn-syn* bridging to Fe^{III} ion and Dy^{III} ion with a (η^1: η^1: μ_2) coordination mode (Figure 4.36, c).

(ii) Two of them are monodentate to Dy(1) and Dy(2) with a (η^1:η^0:μ_1) coordination mode (Figure 4.36, d).

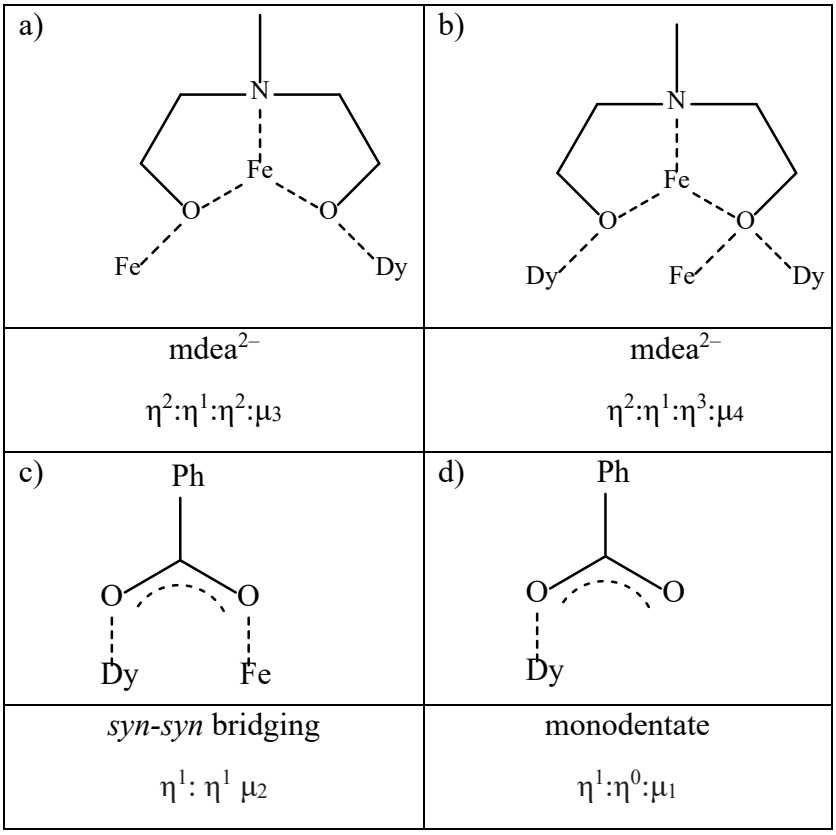

Figure 4.36. Coordination modes (a-b) $mdeaH_2$, (c-d) benzoate ligands.

Fe^{III} ions here present two different types of coordination environmental:

(i) Both hexa-coordinated Fe(1) and Fe(3) ions are surrounded by one N and five O donor atoms (NO_5). One N and three O atoms come from the doubly-deprotonated oxygen $mdea^{2-}$ ligands one O atom comes from *syn-syn* bridging benzoate and one O atom comes from the $(\mu_3\text{-}OH)^-$ group. This results in a distorted octahedron with a $\sum$ parameter of 88.64. This geometry was confirmed by SHAPE analysis [309-312] with a deviation value of 1.43, (Figure 4.37, Table 8.14).

(ii) Both hexa-coordinated Fe(2) and Fe(4) ions are surrounded by two N and four O donor atoms (N_2O_4). One N atom comes from the terminal azide $(N_3)^-$, one N and three O atoms come from the doubly-deprotonated oxygen $mdea^{2-}$ ligands and one O atom comes from *syn-syn* bridging benzoate. This results in a distorted octahedron with a $\sum$ parameter of 93.15. This geometry was confirmed by SHAPE analysis [309-312] with a deviation value of 2.92, (Figure 4.37, Table 8.14).

The Fe–O and Fe–N bond distances are in the range 1.934(3)−2.084(3) Å, 1.997(4)−2.197(4) Å, respectively. The Fe−Dy distances are in the range 3.371(6)−3.470(7) Å. The Fe−O−Fe angles are in the range 99.65(12)−105.09(13)°. Selected bond distances and angles are summarised in Table 4.15.

Both octa-coordinated Dy^{III} ion are surrounding by eight O donor atoms (O_8). Three O atoms come from the doubly-deprotonated oxygen $mdea^{2-}$ ligand, two O atoms come from *syn-syn* bridging benzoate, one O atom comes from the monodentate benzoate and two O atoms come from the $(\mu_3{-}OH)^-$ groups. This results in a slightly distorted square antiprism geometry which was confirmed by SHAPE analysis [309-312] with a deviation value of 0.70, (Figure 4.37, Table 8.14). The Dy−O bond distances are in the range 2.272(3)−2.602(3) Å. The Dy···Dy distance is 3.89(3) Å. The Fe−O−Dy and Dy–O−Dy angles are in the range 95.35(11)−110.34(12)° and 106.59(10)−110.02(11)°, respectively.

The structure is further stabilised by intramolecular interactions through hydrogen bonds. O(71)−H(71B) from a lattice water molecule (H_2O) makes an intramolecular hydrogen bond to O(22) from the monodentate $(PhCO_2)^-$ with an O(71)···O(22) distance of 2.78 Å. In addition, O(1)−H(1) from $(\mu_3\text{-}OH)^-$ group makes an intramolecular hydrogen bond to O(20) from the monodentate $(PhCO_2)^-$ with an O(71)···O(20) distance of 2.57 Å and O(2)−H(2) from $(\mu_3\text{-}OH)^-$ group makes an intramolecular hydrogen bond to O(22) from the monodentate $(PhCO_2)^-$ with an O(71)···O(22) distance of 2.63 Å.

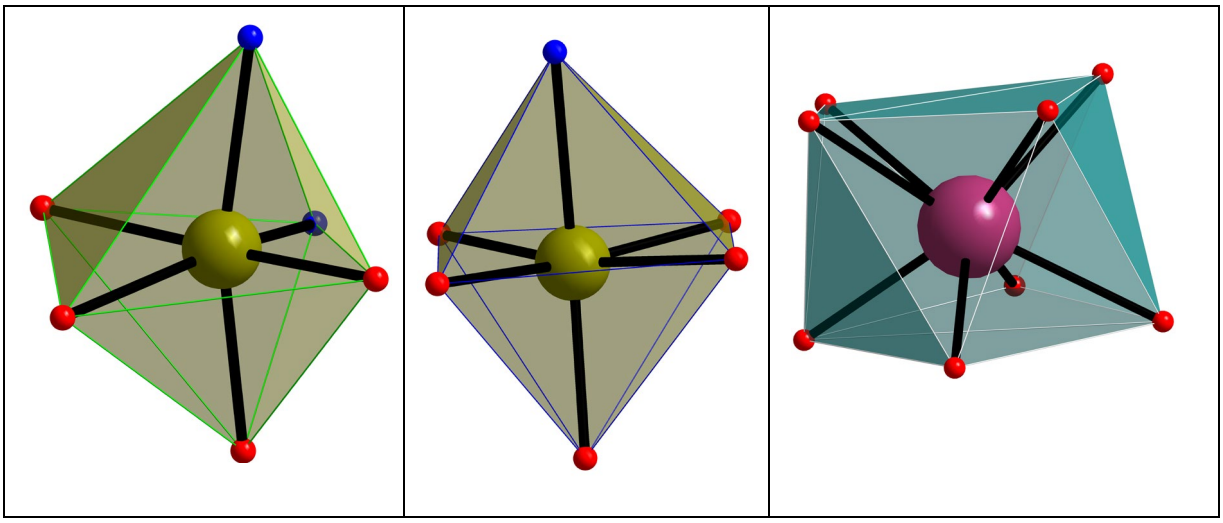

Figure 4.37. Distorted octahedral geometry of the 6-coordinated Fe (3) ion on the left, distorted octahedral geometry of the 6-coordinated of Fe(4) ion on the centre and a slightly distorted square antiprism geometry of 8-coordinated of Dy ion on the right. Colour code: red, blue, green and violet spheres represent O, N, Fe and Dy, respectively.

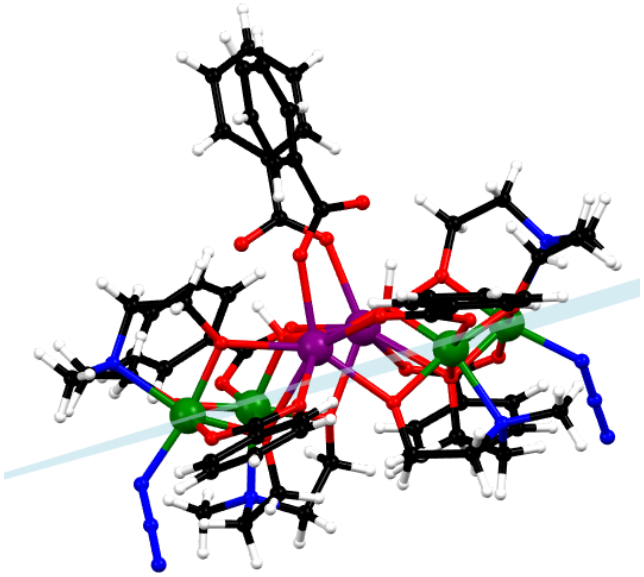

Figure 4.38. Single unit of the plane of compound **43**. Colour code: black, red, blue, green, white and violet spheres represent C, O, N, Fe, H and Dy, respectively.

Table 4.15. Selected Bond Distances (Å) and angles (°) of compound **43**

Bond distances			Bond distances		
Atom	Atom	Distance/Å	Atom	Atom	Distance/Å
Fe(1)	O(1)	1.953(3)	Fe(4)	N(8)	2.028(4)
Fe(1)	O(3)	2.082(3)	Dy(1)	O(1)	2.368(3)
Fe(1)	O(4)	1.989(3)	Dy(1)	O(2)	2.444(3)
Fe(1)	O(5)	1.970(3)	Dy(1)	O(3)	2.602(3)
Fe(1)	O(12)	1.992(3)	Dy(1)	O(6)	2.285(3)
Fe(1)	N(1)	2.185(4)	Dy(1)	O(8)	2.321(3)
Fe(2)	O(3)	2.066(3)	Dy(1)	O(13)	2.391(3)
Fe(2)	O(5)	2.022(3)	Dy(1)	O(16)	2.354(3)
Fe(2)	O(6)	1.961(3)	Dy(1)	O(21)	2.272(3)
Fe(2)	O(15)	2.037(3)	Dy(2)	O(1)	2.379(3)
Fe(2)	N(2)	2.197(4)	Dy(2)	O(2)	2.406(3)
Fe(2)	N(5)	1.997(4)	Dy(2)	O(4)	2.323(3)
Fe(3)	O(2)	1.934(3)	Dy(2)	O(7)	2.581(3)
Fe(3)	O(7)	2.084(3)	Dy(2)	O(10)	2.301(3)
Fe(3)	O(8)	1.984(3)	Dy(2)	O(11)	2.370(3)
Fe(3)	O(9)	1.971(3)	Dy(2)	O(18)	2.373(3)
Fe(3)	O(14)	1.991(3)	Dy(2)	O(19)	2.305(3)
Fe(3)	N(3)	2.197(4)	Fe(1)	Dy(2)	3.371(6)
Fe(4)	O(7)	2.044(3)	Fe(2)	Dy(1)	3.470(7)
Fe(4)	O(9)	2.017(3)	Fe(3)	Dy(1)	3.377(6)
Fe(4)	O(10)	1.961(3)	Fe(4)	Dy(2)	3.461(6)
Fe(4)	O(17)	2.017(3)	Dy(1)	Dy(2)	3.889(3)
Fe(4)	N(4)	2.197(4)			

Bond angles				Bond angles			
Atom	Atom	Atom	Angle/°	Atom	Atom	Atom	Angle/°
Fe(1)	O(1)	Dy(1)	110.34(12)	Fe(3)	O(7)	Dy(2)	98.96(10)
Fe(1)	O(3)	Dy(1)	98.12(11)	Fe(4)	O(7)	Dy(2)	96.19(11)
Fe(1)	O(1)	Dy(2)	101.72(11)	Fe(4)	O(10)	Dy(2)	108.32(13)
Fe(1)	O(4)	Dy(2)	102.55(12)	Fe(1)	O(3)	Fe(2)	99.65(12)
Fe(2)	O(3)	Dy(1)	95.35(11)	Fe(1)	O(5)	Fe(2)	105.09(13)
Fe(2)	O(6)	Dy(1)	109.39(13)	Fe(3)	O(7)	Fe(4)	99.73(12)
Fe(3)	O(2)	Dy(1)	100.31(12)	Fe(3)	O(9)	Fe(4)	104.61(13)
Fe(3)	O(8)	Dy(1)	103.06(12)	Dy(1)	O(1)	Dy(2)	110.02(11)
Fe(3)	O(2)	Dy(2)	109.81(12)	Dy(1)	O(2)	Dy(2)	106.59(10)

4.5.3. Magnetic properties

DC magnetic susceptibility of compound **43** was carried out on freshly prepared polycrystalline sample in the temperature range 1.8-300 K under an applied DC magnetic field of 1000 Oe (0.1 T). The plot of χT versus T for compound **43** is shown in Figure 4.39.

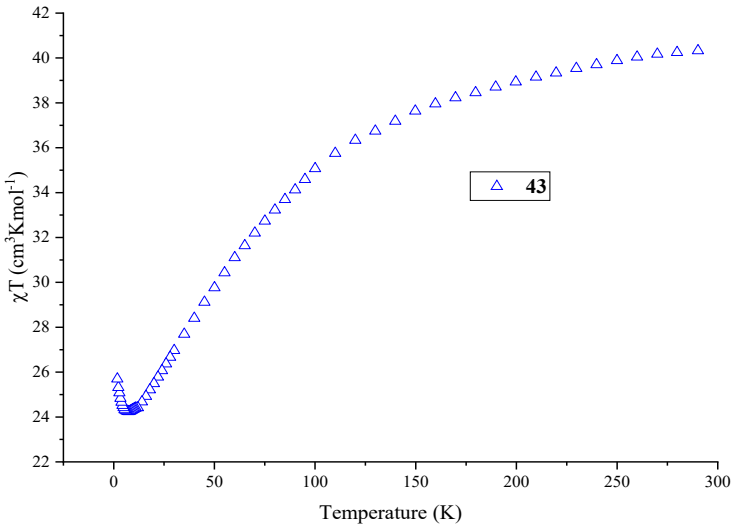

Figure 4.39. Temperature dependence of the χT products for compound **43** at 1000 Oe.

The χT product value of compound **43** at 300 K is 39.90 cm^3 K mol^{-1} which is lower than the expected value of 45.84 cm^3Kmol^{-1} for six non-interacting ions (four Fe^{III} and two Dy^{III}) (Fe^{III}, S = 5/2, g = 2, C = 4.375 $cm^3mol^{-1}K$) and (Dy^{III}, $^6H_{15/2}$, S = 5/2, g = 4/3, L = 5, C = 14.17 $cm^3mol^{-1}K$) [276]. The χT product shows a gradual decrease from 300-7.42 K, reaching a minimum value of 24.25 cm^3 K mol^{-1} at 7.42 K, followed by steep increase from 7.42-1.8 K, reaching value of 25.70 cm^3 K mol^{-1} at 1.8 K. This indicates a dominant ferromagnetic interaction at low temperature probably between Fe^{III}-Dy^{III} ions in compound **43**.

The low value of the room temperature χT vs T curve suggests that the pairs of iron (III) ions are antiferromagnetically coupled. The upturn in the χT vs T plot at very low temperatures suggests that at this point a ferromagnetic coupling between Fe and Dy becomes dominant. To investigate this idea a magnostructural correlation according to the equations proposed by christou et al [376, 377] gives antiferromagnetic interaction of -9 cm^{-1} in line with this suggestion.

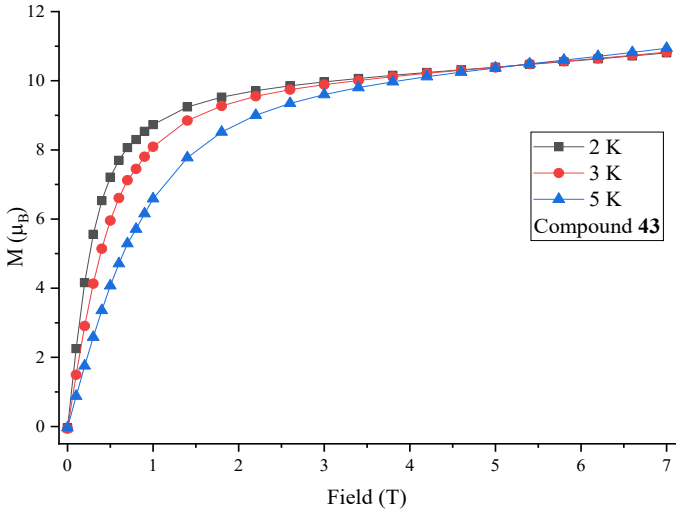

Figure 4.40. Field dependence of magnetisation at indicated temperatures for compound **43**.

The field dependence of the magnetisation for compound **43** was performed at a field range from 0 to 70000 Oe (0-7 T) at temperatures of 2 K, 3 K and 5 K.

Figure 4.40 shows the magnetisation values of compound **43** increases rapidly below 1 T and then increases linearly up to 7 T, reaching a value of 10.81 μ_B at 1.8 K and 7 T which indicates the presence of magnetic anisotropy or/and the population of low-lying excited states [315].

AC susceptibility measurements of compound **43** were performed in order to investigate potential single molecule magnetic behaviour of compound **43**. AC susceptibility measurements of compound **43** were carried out in the frequency range 1-1488 Hz and in the temperature range 2-12 K under zero applied DC field. As shown in Figure 4.41, compound **43** shows slow relaxation of the magnetisation below 5 K under zero applied DC field and the maximum out-of-phase signal is seen at 1.8 K at 80.13 Hz indicating slow relaxation of the magnetisation. The characteristic SMM energy gap, U_{eff} of 14.19 K and the pre-exponential factor $\tau_o=1.94\times10^{-6}$ s were estimated from linear fitting (Figure 4.43 left) of the data to an Arrhenius law. However, the fitting does not include the first point of the plot. This makes the analysis unreliable. Using the approach of fitting data to include further relaxation processes give a much more satisfactory model. It was found that the data could be fit using only QTM and Raman relaxation indicating the lack of an Orbach process.

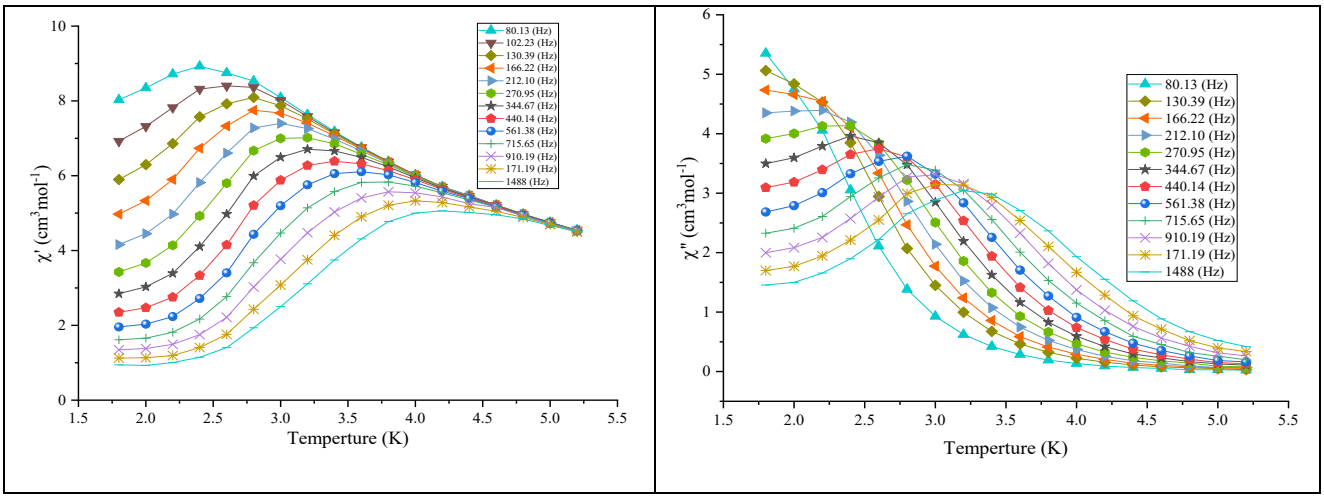

Figure 4.41. Temperature dependence of the in-phase (left) and the out-of-phase (right) components of the AC susceptibility of compound **43** under zero applied DC field.

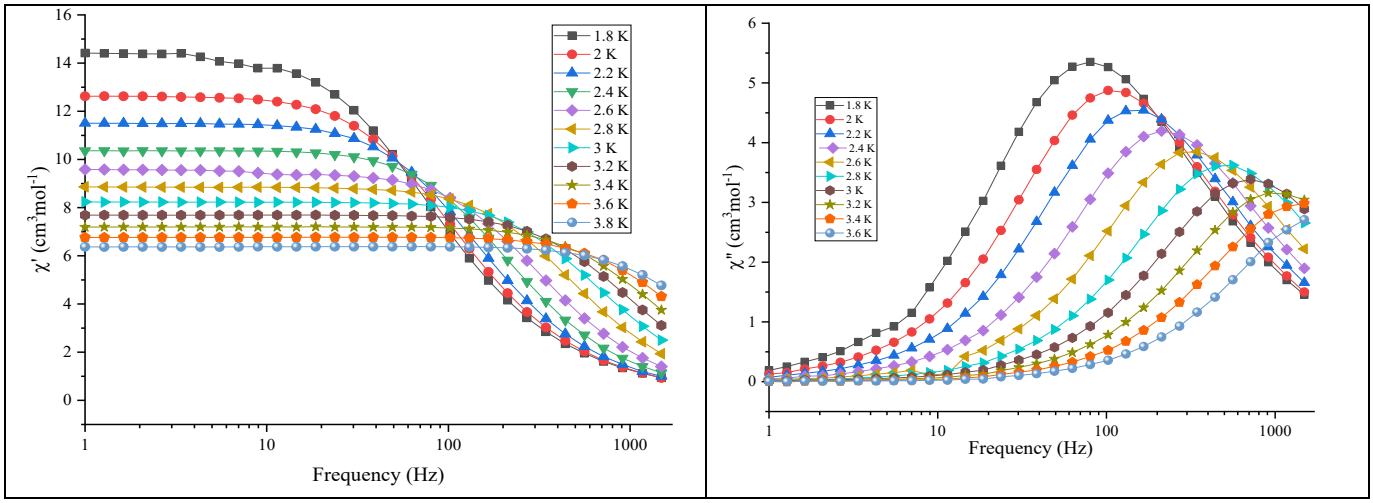

Figure 4.42. Frequency dependence of the in-phase (left) and the out-of-phase (right) components of the AC susceptibility of compound **43** under zero applied DC field.

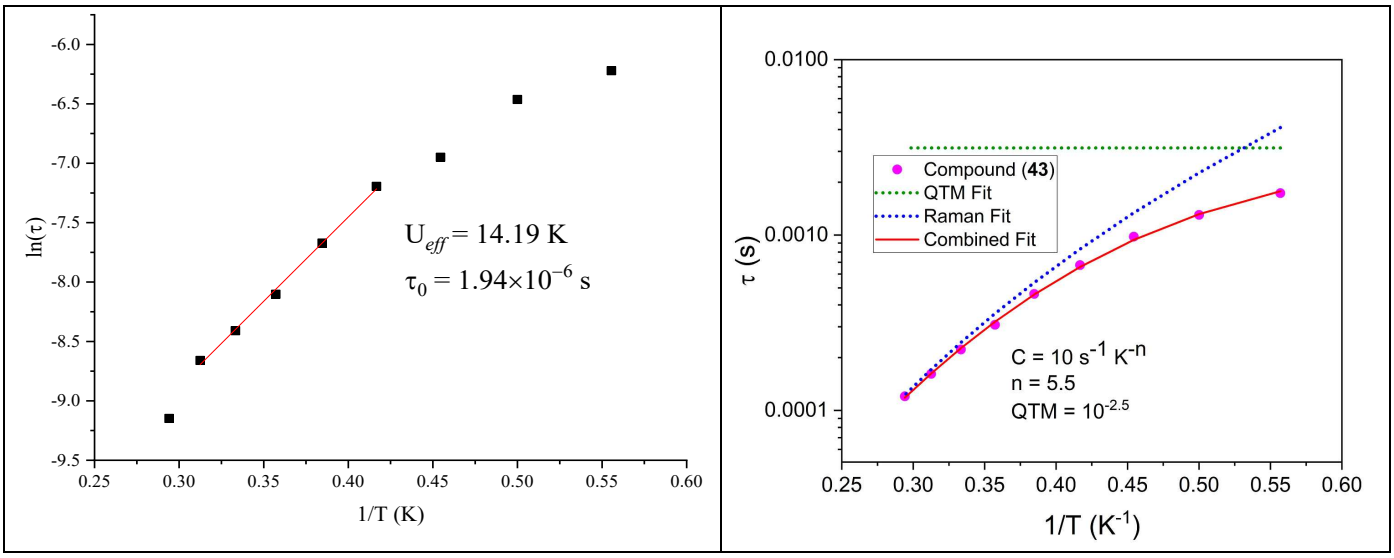

Figure 4.43. The maxima for the out-of-phase ac susceptibility data measured under zero applied field for compound 43 were fitted using an Arrhenius law with the parameters showing in the inset (left) and also modelled using only QTM and Raman processes (right).

The Cole-Cole plot of compound **43** was constructed in the temperature range 1.8-4K. The data were fitted using a generalised Debye model [316, 317]. The Cole-Cole plot of **43**, as shown in Figure 4.44, has relatively symmetrical semicircles. As the temperature increases, the semicircle shape becomes smaller and smaller. A fit to the plots gave α values in range 0.011-0.161 (Table 4.16) which indicate a single relaxation process within the compound **43**.

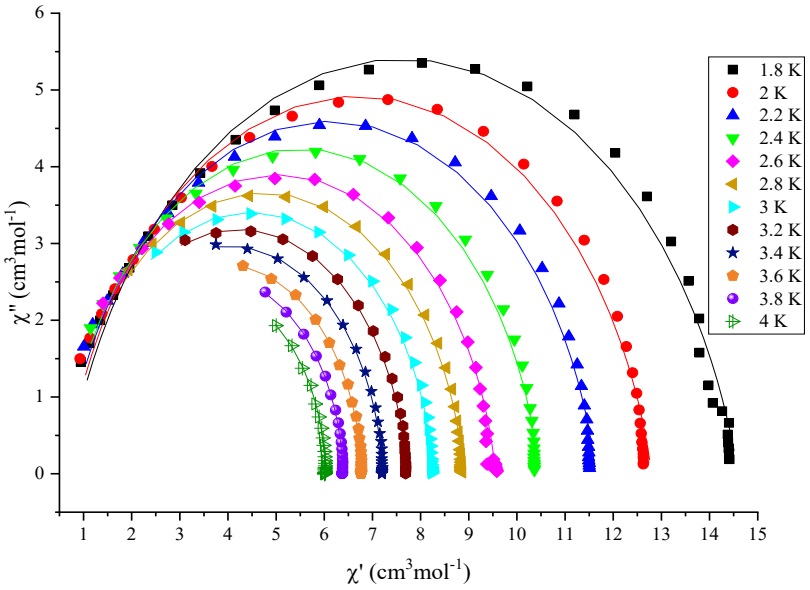

Figure 4.44. Cole-Cole plots of compound **43** under zero applied DC field. Solid lines for the fitting using a generalised Debye model.

Table 4.16. Analysis of the Cole-Cole plots of compound **43**

Temperature (K)	χ_S	χ_T	τ	α	Residual
1.8	6.41E-01	1.46E+01	1.75E-03	0.161	1.20E+00
2	6.12E-01	1.28E+01	1.30E-03	0.135	7.08E-01
2.2	5.81E-01	1.16E+01	9.80E-04	0.117	5.27E-01
2.4	5.68E-01	1.05E+01	6.73E-04	0.098	3.47E-01
2.6	5.27E-01	9.55E+00	4.62E-04	0.093	3.05E-01
2.8	5.84E-01	8.89E+00	3.08E-04	0.080	1.39E-01
3	6.99E-01	8.26E+00	2.22E-04	0.066	8.99E-02
3.2	7.43E-01	7.71E+00	1.62E-04	0.056	4.69E-02
3.4	8.33E-01	7.21E+00	1.20E-04	0.045	2.57E-02
3.6	1.05E+00	6.78E+00	9.30E-05	0.030	1.09E-02
3.8	1.03E+00	6.38E+00	6.94E-05	0.023	8.07E-03
4	1.15E+00	6.02E+00	5.43E-05	0.011	5.74E-03

4.5.6. Comparison of the core structure

A review of the literature reveals that 10 hexanuclear series of Fe-Ln metal complexes incorporating azide ligands have been reported so far, as shown in Table 4.17.

Table 4.17. Hexanuclear Fe/ Ln metal complex incorporate azide ligands

NO Of compound	Structure	SMMs				Core	Coordination mode of azide	Ref
		Dy		Tb				
		U_{eff} (K)	τ_0 (s)	U_{eff} (K)	τ_0 (s)			
1	$[Fe_4Ln_2(OH)_2(N_3)_2(nbdea)_4(Me_3CCO_2)_5(H_2O)](NO_3)\cdot 2EtOH$ (Ln=Dy, Y)	26.50	$1.0x10^{-7}$	NM	NM	B	T	[334]
2	$[Fe_4Ln_2(OH)_2(N_3)_2(nbdea)_4(Me_3CCO_2)_4(NO_3)_2]\cdot 3EtOH$ (Ln=Eu, Gd)	NM	NM	NM	NM	B	T	[334]
3	$[Fe_4Ln_2(\mu_3\text{-}OH)_2(nbdea)_4(Me_3CCO_2)_6(N_3)_2]$ 3MeCN (Ln= Dy, Y)	NM	NM	NM	NM	B	T	[335]
4	$[Fe_4Ln_2(OH)_2(Me_2CHCO_2)_6(N_3)_2(nbdea)_4]\cdot 2MeOH$ (Ln= Gd-Tm, Y)	13.97	$1.1x10^{-6}$	18.29	$5.2x10^{-8}$	B	T	[336]
5	$[Fe_4Ln_2(Me_3CCO_2)_6(N_3)_4(teaH)_4]\cdot 2$ EtOH (Ln= Gd-Er)	NM	NM	38.01	1.2×10^{-9}	W	B	[337]
6	$[Fe_4Tb_2(Me_3CCO_2)_6(N_3)_4(teaH)_4]$	Not SMM				W	B	[337]
7	$[Fe_4Ln_2(Me_3CCO_2)_6(N_3)_4(teaH)_4]\cdot 2$ CH_2Cl_2 (Ln= Dy, Er)	Not SMM				W	B	[337]
8	$[Fe_4Ln_2(Me_3CCO_2)_4(N_3)_6(teaH)_4]\cdot 2$ EtOH $2CH_2Cl_2$ (Ln= Dy, Er)	Not SMM				W	B+ T	[337]
9	$[Fe_4Ln_2(teaH)_4(\mu\text{-}N_3)_4(N_3)_3(Piv)_3]$ (Ln= Gd-Er, Y)	24	8×10^{-8}	36.9	6.8×10^{-10}	W	B+ T	[85]
10	$[Fe_4Ln_2(teaH)_4(N_3)_4(Piv)_6]$ (Ln= Er, Lu)	Not SMM				W	B	[83]
11	$[Fe_2Ln_4(mdea)_2(mdeaH)_2(\mu_3\text{-}OH)_2(N_3)_2(PhCO_2)_8]$ 3MeCN (**21-29**) (Ln= Pr-Ho, Y)	Not SMM				B	T	This work 4.3
12	$[Fe_4Ln_2(mdea)_4(PhCO_2)_6(N_3)_2(\mu_3\text{-}OH)_2]\cdot MeCN\ H_2O$ (**40-46**) (Ln= Eu-Er, Y)	14.19	1.9×10^{-6}	NM	NM	B	T	This work 4.5

Table 4.17 (B= Butterfly, W=wheel, NM not measured, T= Terminal and B= Bridging), 7 series are lack SMM behaviour and 5 series are SMMs.

N-methyldiethanolamine ($mdeaH_2$) has been widely used as a main ligand to synthesise Fe-Ln, with various topologies and also exhibiting interesting magnetic properties like SMM behaviour [79, 80, 89, 253].

Taking this into consideration, in the present work a combination of $mdeaH_2$ alongside benzoate and sodium azide as the two co-ligands has been employed to obtain higher nuclearity clusters which could provide routes toward compounds potentially having optical or magnetic properties as well as SMM behaviour. Thus, a little adjustment of synthetic strategy led to the isolation $[Fe_4Ln_2(mdea)_4(PhCO_2)_6(N_3)_2(\mu_3\text{-}OH)_2](MeCN)(H_2O)$ with a Fe_2Ln_2 butterfly core.

Changing of the procedure from reflux in compound **27** to stirring in compound **43** and counter ion of lanthanide give the opportunity to the system to change the nuclearity of the compound and changing the core.

There many reports on $\{Fe_4Ln_2\}$ compounds with various topologies with different main ligands/co-ligand and synthesis procedures. Such as in butterfly-shaped topology [89, 334-336, 378, 379] and in cyclic topology"wheel" [83, 85, 337, 341] and different topology [82, 90, 343, 375, 380-395]. The same nuclearity was also reported with different topology in other 3d-4*f* complexes e.g. Mn_4Dy_2 [84, 396-400], Co_4Dy_2 [401-405], Ni_4Dy_2 [406-409], Cu_4Dy_2 [410-412] and Zn_4Dy_2 [413]. Our group has reported $\{Fe_4Dy_2\}$ twice using the *N*-butyldiethanolamine ($nbdeaH_2$) ligand with the same core and butterfly-shaped topology. The crystallographic and magnetic detail are compared in this section.

The *N*-methyldiethanolamine ($mdeaH_2$) ligand possesses the same functional group as *N*-the butyldiethanolamine ($nbdeaH_2$) ligand. The difference between the two ligands is an additional propylene group in the case of *N*-butyldiethanolamine ($mbeaH_2$).

The comparison both of them is summarised in Figure 4.45 and Table 4.18. In all cases the Dy containing structure has chosen as representative for the whole lanthanide. $\{Fe_4Dy_2\}$ [379] is abbreviated as compound **H** and $\{Fe_4Dy_2\}$ [335] is abbreviated as compound **I**.

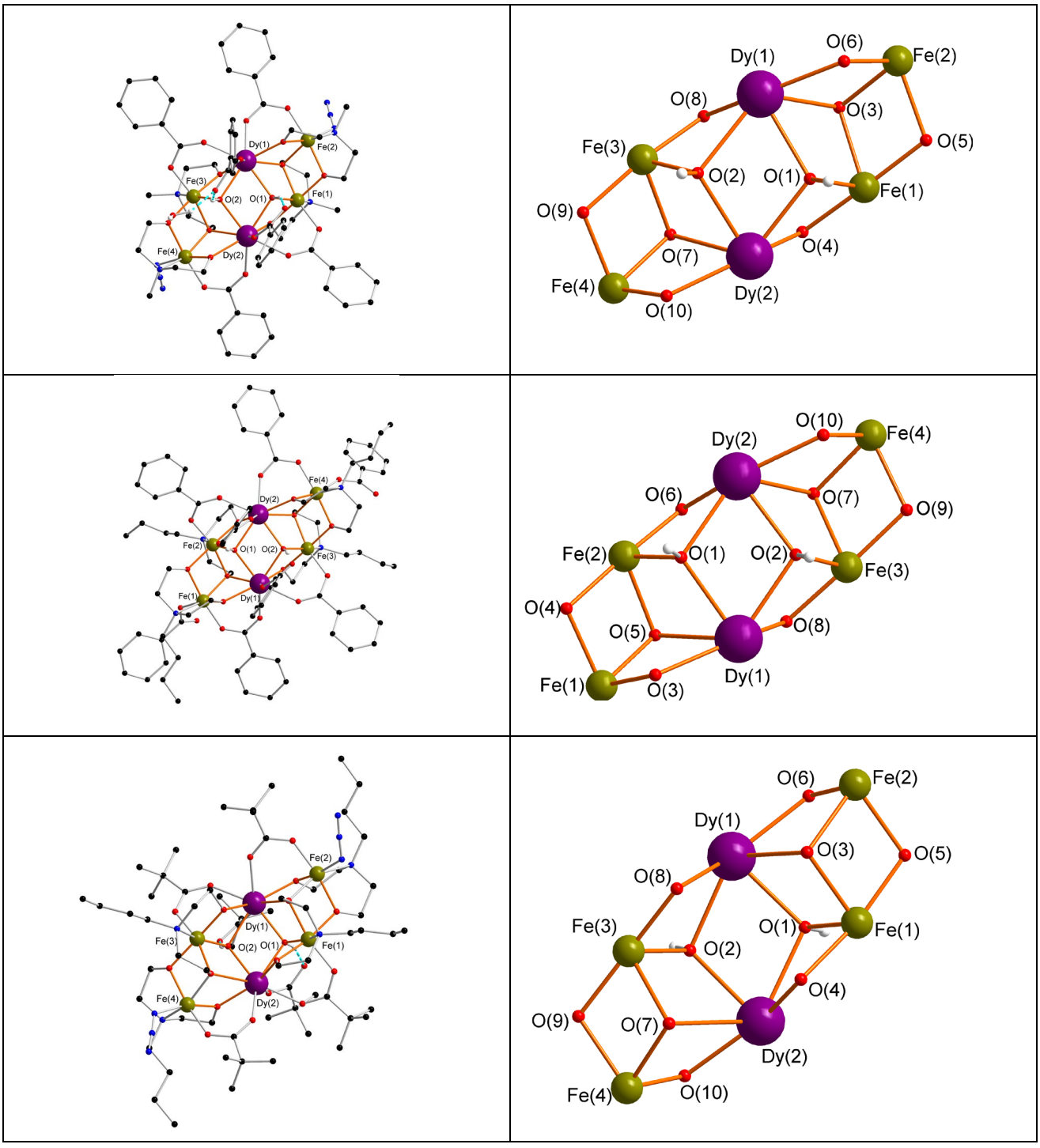

Figure 4.45. Molecular structure and the core of compound **43** on the top, compound **H** on the middle and compound **I** on the bottom (H atoms omitted for clarity). Colour code: black, red, blue, green, white and violet spheres represent C, O, N, Fe, H and Dy, respectively.

Table 4.18 Comparison between compounds **43**, **H** and **I**

Compound abbreviated as		Compound **43**	Compound **H** [379]	Compound **I** [335]
Structure		$[Fe_4Dy_2(mdea)_4(PhCO_2)_6(N_3)_2(\mu_3\text{-}OH)_2](MeCN)$	$[Fe_4Dy_2(\mu_3\text{-}OH)_2(n\text{-}bdea)_4(PhCO_2)_8]\cdot MeCN$	$[Fe_4Dy_2(\mu_3\text{-}OH)_2(nbdea)_4(Piv)_6(N_3)_2]\cdot 3(MeCN)$
Ln		Eu-Er	Dy-Er	Dy
Ligand		*N*-methyldiethanolamine ($mdeaH_2$)	*N*-butyldiethanolamine ($nbdeaH_2$)	*N*-butyldiethanolamine ($nbdeaH_2$)
Co−ligand		Benzoate	Benzoate	Pivalic acid
Co−ligand		Sodium azide (NaN_3)	----------	Sodium azide (NaN_3)
Crystal system		Triclinic	Monoclinic	Triclinic
Space group		$P\bar{1}$	P21/c	$P\bar{1}$
Volume		3695.12(13)	9564.5(18)	4542.9(4)
Colour of crystal		Orange	Orange	Orange
Shape of crystal		Plate	Block	Block
Positions in butterfly topology	body	Two Dy ions		
	wing-tips	Two Fe ions		
Position of 2 (μ_3−OH)		Lying in the same direction of plane		
Average distance between (μ_3−OH) and the $\{Fe_4\}$ plane		1.289 Å	1.3105 Å	1.328 Å
Position of Dy		Lying in the same direction		
Average distance between Dy and the $\{Fe_4\}$plane		0.9015 Å	1.0085 Å	0.9615 Å
Shape of Fe ions		Distorted octahedron		
Shape of Dy ions		Distorted square antiprism		
Average distance of	Fe−O	2.004	1.9912	2.0159
	Fe−N	2.1335	2.20825	2.1466
	Dy−O	2.380	2.369	2.384
Average angle of	Fe−O−Dy	102.843	102.916	102.415
	Fe−O−Fe	102.27	102.77	102.86
	Dy−O−Dy	108.306	108.615	108.025
Distance of	Dy−Dy	3.889	3.855	3.872
	Fe−Dy	4.075	4.070	4.089
	Fe−Fe	5.578	5.538	5.590
Interactions		10.81 μ_B	11 μ_B	---------

Magnetisation at 2 K and 7 T	Ferromagnetic				
Relaxation behaviour	14.19 K	1.94×10^{-6} s	21.4 K	2.7×10^{-8} s	SMM

Compound **43** was synthesised using *N*-methyldiethanolamine ($mdeaH_2$)) as the main ligand and benzoate and sodium azide as the two co-ligands. Compounds **H** and **I** were synthesised using *N*-butyldiethanolamine ($nbdeaH_2$) as the main ligand. Benzoate is a co-ligand of compound **H,** while Pivalic acid and sodium azide are the two co-ligands to synthesise compound **I**.

Both compounds **43** and **I** were crystallised in the triclinic space group $P\bar{1}$, while compound **H** in the monoclinic space group $P2_1/c$.

All compounds **43**, **H** and **I** have a butterfly topology geometry. In all compounds, the butterfly motif has the two Dy^{III} ions occupying the body positions and two Fe^{III} ions the outer wing-tips.

In all compounds, **43**, **H** and **I** the core is held together by two $(\mu_3\text{-OH})^-$ ligand lying in the same direction of $\{Fe_4\}$ plane. The average distance between (μ_3-OH) and $\{Fe_4\}$ plane of compound **H** are the largest and compound **43** is the shortest.

In all compounds, **43**, **H** and **I** the two Dy ions are lying in the same direction of $\{Fe_4\}$ plane, the average distances between Dy ions and $\{Fe_4\}$ plane compound **H** are the largest and compound **43** is the shortest.

In all compounds **43**, **H** and **I** each Fe ion is six-coordinate with a distorted octahedron geometry, while each Dy ions are eight coordinate with a distorted square antiprism geometry.

The average Fe−O and Dy−O distances in compound **I** are the longest and in compound **H** are the shortest, while average Fe−N distance in compound **H** is the longest and in compound **43** is the shortest.

The Fe···Fe and Fe···Dy distances in compound **I** are the longest and in compound **H** are the shortest. The Dy···Dy distances in compound **43** are the longest and in compound **H** are the shortest.

The average Fe−O−Dy and Dy−O−Dy angles in compound **H** are the biggest and in compound **I** are the smallest. The average Fe−O−Fe angle in compound **I** is the biggest and in compound **43** is the smallest.

The magnetic studies of all compounds **43**, **H** and **I** revealed the presence of ferromagnetic interaction. Both compounds **43** and **H** demonstrate SMM behaviour. The energy barrier (U_{eff}) for compound **H** is higher than that of compound **43**.

From this summary, it can be concluded that increasing the chain of a ligand can make a difference in the energy barrier.

4.5.5. Photoluminescence study

Photoluminescence spectra for compound **40** were recorded in the range from 200 to 800 nm in the solid-state.

The excitation spectrum of compound **40** monitored at 617 nm emission exhibits high absorption in the range 200–400 nm (centred at 242 nm), Figure 4.46 presents the excitation and emission spectra of compound **40**.

The emission spectrum of compound **40** exhibits a sharp band which is a result of the intra f-f transition of Eu^{3+} corresponding to the $^5D_0 \rightarrow {}^7F_J$ (J = 0-4) transitions of the Eu^{3+} ion $^5D_0 \rightarrow {}^7F_0$ (542 nm), $^5D_0 \rightarrow {}^7F_1$ (590 nm), $^5D_0 \rightarrow {}^7F_2$ (617 nm), $^5D_0 \rightarrow {}^7F_3$ (650 nm) and $^5D_0 \rightarrow {}^7F_4$ (699 nm).

The fact that the emission band at 617 nm has a dominates the emission spectra (high intensity) corresponding to the hypersensitive $^5D_0 \rightarrow {}^7F_2$ transition, indicating that the Eu^{3+} ion is not on an inversion centre. This is expected given the molecule is not on any symmetry centre [122].

Among all the transitions, the $^5D_0 \rightarrow {}^7F_2$ and the $^5D_0 \rightarrow {}^7F_1$ are referred to as hypersensitive electric-dipole (ED) and magnetic-dipole (MD) transitions, respectively [122-125]. This result which indicate that this compound may be good candidates as emitting molecular materials such as those used in OLEDs which is one of the industrially relevant fields using coordination chemistry.

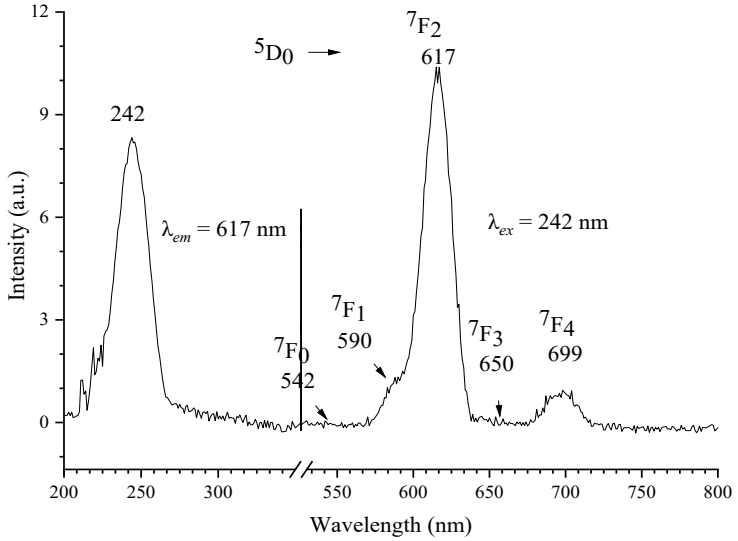

Figure 4.46. Excitation and emission spectra of compound **40**.

4.6. Conclusions

In this research, thirty-three heterometallic iron-lanthanide complexes based on *N*-methyldiethanolamine ($mdeaH_2$) ligands have been synthesised and characterised. These compounds have been synthesised from the reactions of *N*-methyldiethanolamine ligand and co-ligand (sodium benzoate, di(2-pyridyl) ketone (dpk), sodium azide and *o*-vanillin), iron and respective lanthanide cations. A series of seven tetranuclear $[Fe_2Ln_2(mdea)_2\{(py)_2C(OCH_3)O\}_2(\mu_4\text{-}O)(N_3)_2(NO_3)_2(CH_3OH)_2]\cdot H_2O$ (**14**-**20**) nine hexanuclear $[Fe_2Ln_4(mdea)_2(mdeaH)_2(\mu_3\text{-}OH)_2(N_3)_2(PhCO_2)_8]\cdot 3MeCN$ (**21**-**29**) ten hexanuclear $[Fe_2Ln_4(mdea)_2(o\text{-}van)_2(\mu_4\text{-}O)_2(PhCO_2)_8]\cdot 2\cdot 5MeCN$ (**30**-**39**) and seven hexanuclear $[Fe_4Ln_2(mdea)_4(PhCO_2)_6(N_3)_2(\mu_3\text{-}OH)_2]\cdot MeCN\cdot H_2O$ **(40-46)** have been successfully synthesised and structurally characterised by single crystal XRD and powder XRD, optically and magnetically investigated.

Slight changes in synthetic conditions allowed to change the nuclearity of the compound and the core from $[Fe_2Dy_4]$ (compound **27**) to $[Fe_4Dy_2]$ (compound **43**).

Compounds **14**-**20** were synthesised using *N*-methyldiethanolamine ($mdeaH_2$), di(2-pyridyl) ketone (dpk), sodium azide (NaN_3), iron chloride and lanthanide nitrate. Magnetic studies carried

out on compound **20** (Ln=Dy^{III}) revealed that antiferromagnetic interactions are dominant and showed lack SMM behaviour.

Compounds **21**-**29** were synthesised using *N*-methyldiethanolamine ($mdeaH_2$), sodium benzoate, sodium azide (NaN_3), iron chloride and lanthanide nitrate. Static magnetic studies show the presence of overall ferromagnetic interactions in compounds **26** (Ln=Tb^{III}) and **27** (Ln=Dy^{III}) were investigated for potential SMM behaviour. Compound **26** exhibits slow relaxation of magnetisation at a zero external DC field but without any maxima even under small-applied DC fields (500-3000 Oe). Compound **27** shows no AC signals under zero-DC field but displays slow relaxation of magnetisation without maxima under applied DC field of 500-3000 Oe. These analyses indicated that compounds **26** and **27** lack of SMM properties under these conditions. However, in order to confirm the SMM behaviour, the magnetisations of **26** and **27** can be studied on field-oriented single crystals by micro-SQUID at very low, sub Kelvin, temperatures.

The maximum entropy (-ΔSm) value of 27.50 J kg^{-1} K^{-1} was obtained for compound **25** (Ln=Gd^{III}) with ΔH =7T at 4 K. Such a feature may be of potential interest in molecular magnetic refrigerant systems.

Luminescence studies performed on **24** (Ln=Eu^{III}) and **26** (Ln=Tb^{III}**)** compounds shows the emission bands emerging from f–f transitions. Compounds **24** and **26** were found to be luminescence materials. The ability of compounds **24** and **26** to generate luminescence makes them potentially attractive materials for application in various optoelectronic devices.

Compounds **30**-**39** were synthesised using *N*-methyldiethanolamine ($mdeaH_2$), *o*-vanillin (*o*-van), sodium benzoate, iron chloride and lanthanide nitrate. Magnetic susceptibility data of **31**-**33** demonstrate the presence of dominant antiferromagnetic interactions in all compounds. Compound **32** (Tb^{III}**)** shows slow relaxation of magnetisation in zero applied DC field but without any maxima even under applied DC fields of 500-3000 Oe. Compound **33** (Ln=Dy^{III}) exhibits no AC signals at zero applied DC field but showed slow relaxation of magnetisation at applied DC fields of 500-3000 Oe. However, no clear peak maxima were observed. These results indicate that compounds **32** and **33** lack of SMM behaviour properties under these conditions. However, in order to confirm the SMM behaviour, the magnetisations of **32** and **33** can be studied on field-oriented single crystals by micro-SQUID at very low, sub Kelvin, temperatures.

The maximum entropy (-ΔSm) value of 18.41 J kg^{-1} K^{-1} was obtained for compound **31** ($Ln=Gd^{III}$) with ΔH =7T at 5 K. The obtained results on magnetocaloric properties suggest that compound **31** might be of interest in magnetic refrigeration applications.

Compounds **40-46** were synthesised using *N*-methyldiethanolamine ($mdeaH_2$), sodium benzoate, sodium azide (NaN_3), iron chloride and lanthanide chloride. Static magnetic studies show the presence of overall ferromagnetic interactions in compound **43** ($Ln=Dy^{III}$). The analysis of AC susceptibility data at a zero applied DC field illustrates that compound **43** displays slow relaxation of magnetisation and has SMM behaviour. Fitting the AC data to an Arrhenius law resulted in an energy barrier of 14.19 K with the pre-exponential factor of 1.94×10^{-6} s. The Cole-Cole plots suggest that a single relaxation process occurs in compound **43**.

Compounds with SMM properties are important because of their possible applications in data storage, quantum computing and molecule-based spintronics devices.

Luminescence studies performed on compound **40** ($Ln=Eu^{III}$) show emission bands arising from f–f transitions which could lead to optoelectronic applications.

Chapter 5. Structure and optical properties of copper complex as Near-Infrared (NIR) blocked

5.1. Introduction

The ozone layer protects the earth's surface from the harmful rays (UVA and UVB) that exist in sunlight. Day by day, global warming and environmental problems increase due to both nature and human activities which continue to contribute the expanded hole in the ozone. Protecting the population, automobiles and buildings from global warming by an improved of cooling efficiency has been promoted on a global scale. For example, shielding buildings by preventing the inflow of heat through windows.

Glass windows have undergone an energy-saving evolution from single panes to today's ultralow-emission windows [414]. Glass characteristically has high strength and is generally lighter in weight compared to metallic materials. Also, it retains its strength to relatively higher temperatures and corrosion at these elevated temperatures and is less susceptible to oxidation [415].

Windows are considered one of the least energy-efficient component of buildings. Building walls and roofs can be thermally insulated but glass has required properties for example it should be transparent, so for that reason we can not insulate glass [416]. However, for aesthetic purposes large glass windows have become increasingly popular in modern buildings leading to an increase in a building's heating in winter and cooling loads in summer [417] (Figure 5.1). The suitable arrangement of windows is a basic element for the bioclimatic design of buildings. In addition, large glass windows create a pleasant feeling for the inhabitants [418]. Curtains are the conventional prevention for blocking the sun's heat but unfortunately they also block the daylight [419]. Buildings in most warm climate countries get excessive heat gain throughout the year with average temperatures of 34˚C. A large amount of energy is consumed due to large glass surfaces, large internal loads, modern office having a high cooling demand during majority of the year [420, 421].

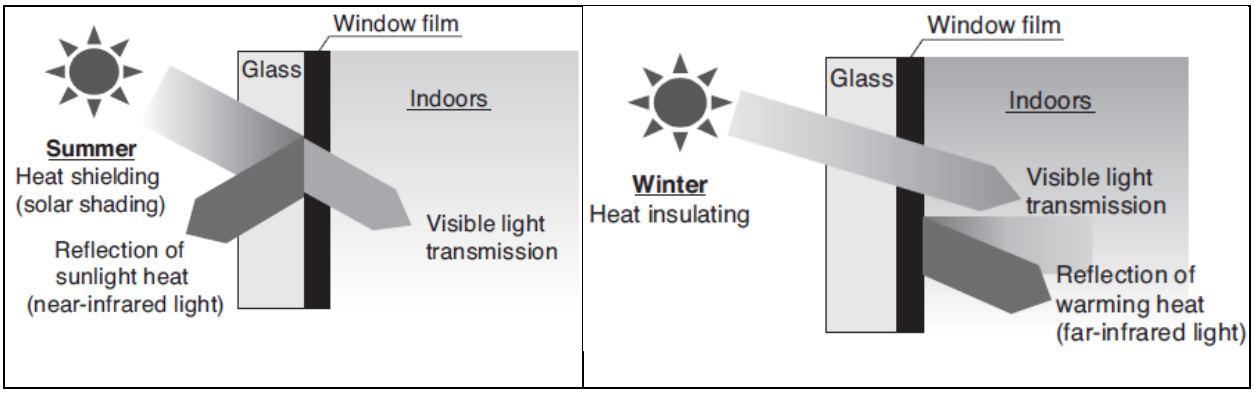

Figure 5.1. Functions of solar shading and heat insulating films in summer and winter seasons (taken from reference [422]).

Passive cooling can be accessed with an IR-shielding coating by blocking the NIR from solar light [423]. The most important factor that should be considered when applying IR-shielding coatings on smart windows is retaining the optical transparency in addition to effectiveness in blocking the NIR emissions. Therefore, there is a high demand for IR-shielding not only in windows of building but also in automobile windows which presenting infrared radiation (λ = 0.7–3 μm) from passing through window glass allows the indoors to remain cool in summer by blocking sun's radiation wheras in winter internal heat is prevented from passing through the windows..

Energy-saving windows (i.e containing Energy Saving Glass, ESG) contain low emissivity (Low-E) coatings that have a high transmittance in the visible region and reduce the ultraviolet (UV) and/or infrared (IR) radiation [423-425]. They are used in modern buildings in both hot and cold climates to provide isolation from severe temperatures [426].

Low-E coatings are known from the 1960s, but the main development took place in 1974 after the petroleum crisis. In the 1980s and 1990s, Low-E glass products dominated the markets [418]. Today's use of Low-E glass is very common in architecture for increasing the energy efficiency of buildings (reducing the large energy consumption of air conditioning), promote rational use of energy and reduce CO_2 emissions [418, 420, 427]. The heavy usage of air-conditioning contributes to global warming because it releases its gaseous refrigerants which are mainly Chlorofluorocarbons and Hydrofluorocarbon into the atmosphere [161, 162] leads to depletion of the ozone layer [418, 420, 427]. Therefore, more efficient use of energy is an important key to improving the environment [418, 420, 427].

ESG prevents the permeation of infrared radiation (heat waves) through its surface so the thermal effects inside buildings remain comfortable [428]. Hence a useful amount of energy is saved due to a lesser-load on the heating and cooling systems [428]. These windows provide certainty of keeping the heat within the indoor environment (thermal insulation), thus protecting the house from cooling for a longer period of time without significant heat loss during the winter seasons. This also reduces the cost of heating. In addition, ESGs protect the house from overheating from the solar radiation by blocking heat from entering the building during the summer seasons therefore reducing the cost of cooling [429].

It has been reported that using a single slide ESG in windows of the building could increase the temperature inside the building to 8 °C if the temperature outside is -10 °C, while a double glass ESG could increase the temperature inside the building to 15 °C if the temperature outside is -10 °C [430].

Low emissivity (Low-E) coatings usually consist of a stack of dielectric (8–15 layers) and metallic thin films (1–3 layers of silver) [431]. The Low-E glass includes panes with coatings of thin metal and/or metal oxides on one side of the glass [429, 432].

This coating has created radio propagation problems for communication systems; something that can be used to protect the building from intentional electromagnetic interference (IEMI) attacks and protecting against information leakage [414]. Low-E glass was deposited using different methods include evaporation [433, 434], chemical vapor deposition (CVD) [435, 436], spray pyrolysis [437, 438], magnetron sputtering [439, 440], sol-gel dip-coating processes [441, 442], rf sputtering [443, 444], immersion methods [445], photo-chemical vapor deposition [446], pulsed laser deposition [447], painting [448] and atomic layer epitaxy [449, 450]. These methods need large vacuum equipment or high electron or high glass substrate temperatures [451, 452] which are considered as disadvantages because of their associated high cost [453], low productivity and difficulty in retrofitting of existing architectural glass. Among these techniques, the drop-casting technique has the advantage of simple and inexpensive experimental arrangements.

Thin coating films are increasingly being applied to advanced technology today. Low-E window glassing and displays, functional layers in semiconductor chips, protective topcoats, stacks of recording films in optical storage disks, thin film in multilayer capacitors and hydrophobic layers

for keeping an adequate viewing field of mirrors on rainy days are some examples of their commercial applications [418, 454].

The most important application of thin-film technology for global energy conservation is a solar cell that converts solar radiation to electrical energy [453]. The main requirement for a solar cell is a material-coated the glass window which allows the maximum visible light to pass through and reflect IR radiation [453]. These types of thin films have been widely used in thermal insulation in lamps, solar photovoltaic conversion, window insulation, solar heating and solar thermal energy conversion [455].

Coating technology is divided into two different types based on the film thickness: Thick film with thicknesses above 10 mm and thin-film with thicknesses between 0.1 nm and 10 mm [456].

ESG can be divided into two types based on colour which are thin-film and tinted film. The tinted film has the properties to reflect heat and infrared light in the automotive application. Tinted film can be divided into few types based on the percentage of visible light and infrared transmission. The differences between thin-film and tinted film are the visibility of the glass and the features on it [454].

Tinting vehicle windows is a technique used to control undesirable solar heating. Optical thin films (like Low-E coatings) is another technique that has been applied on glass windows of automobile especially on windshields by utilising several layers of IR-shielding to allow a sufficient amount of visible light to be transmitted through the windows for the safe operation of the vehicle and to control solar energy passing through the automobile by absorbing or reflecting a portion of solar energy which has a lower wavelength and high energy [457].

Automobile glass has many problems that could be solved with coating technology in order to meet special requirements for automobiles, trucks, trains and other vehicles, such as light scattering from water droplets during rainy weather disturbing the driver's vision and can cause severe discomfort as well as restricted vision. To overcome this problem, hydrophobic thin film coatings have been used to keep adequate viewing on rainy days [456].

Thermal overheating due to sun load of more than 70% of solar radiation transmitted into a vehicle compartment through window glass, results in heat deposition and temperature increases of up to

80°C or more. To overcome this problem, IR-shielding is effective in controlling the heating inside the automobile and therefore reducing the loading on the air-conditioner maintaining a comfort level [454]. Therefore, blocking heating radiation can be done by absorption/reflection of NIR.

The main goal of using optical thin films is to have a high degree of transmission over the visible region of the electromagnetic energy spectrum and to control the amount of solar energy inflow through windows to heat the interior space which means having a low amount of transmission to non-visible solar radiation, therefore reducing undesirable solar heating of the automobile's interior. Moreover, this provides protection for a driver's skin, interior fabric, and protecting sheet materials from strong ultraviolet (UV) light irradiation (Figure 5.2).

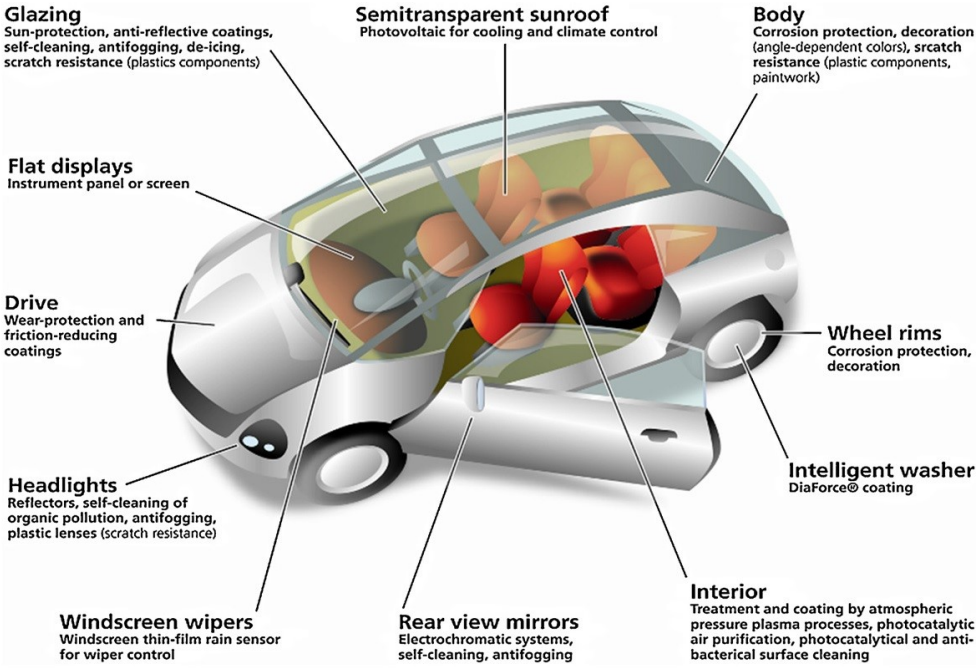

Figure 5.2. The application of surface technologies in a modern car (taken from reference [456]).

5.1.1. Electromagnetic spectrum

Solar radiation which is reaching the earth's surface is divided into the ultraviolet (UV 200-400 nm, 6.9%), visible light (400-700 nm, 42.2%), and near-infrared radiation (700-2500 nm, 37.7%) (Figure 5.3).

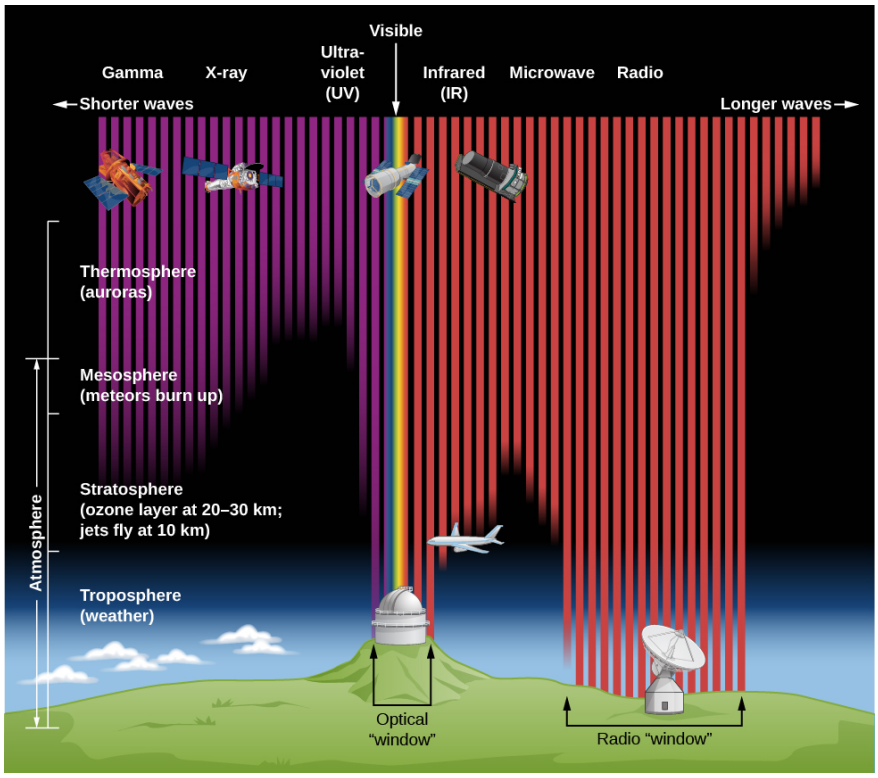

Figure 5.3. Radiation and earth's atmosphere (taken from reference [458]).

The ultraviolet radiation is distributed in UVA in the range 320-400 nm and it is believed to cause the pigmentation on human skin [459, 460], UVB in the range 290-320 nm and UVC in the range 200-290 nm [459]. UVC possesses a lower wavelength, higher energy and has the greatest potential for biological damage but fortunately UVC is effectively blocked by the ozone layer therefore not considered to be a factor in solar exposure of human beings [459] (Figure 5.4). The rest of the ultraviolet radiation that reaches the earth's surface consists of 3.5% UVB and 96.5% UVA during a typical summers day. Visible light is the wavelength range of general illumination in the range 400-700 nm.

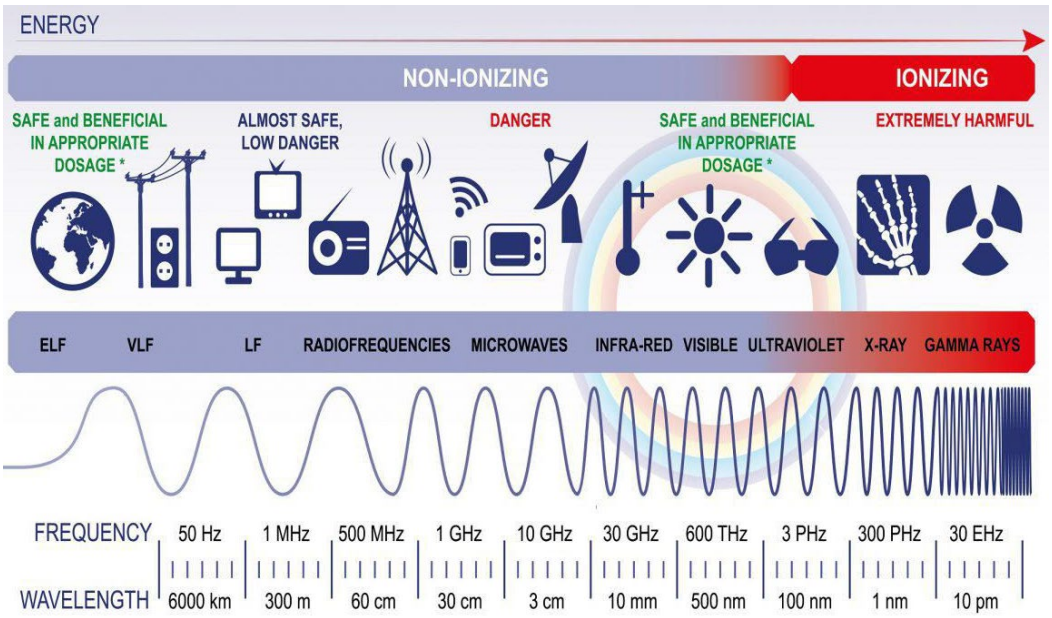

Figure 5.4. Electromagnetic spectrum (taken from reference [461]).

The German-British astronomer William Herschel discovered infrared light in 1800 when he investigated the temperature difference among the colours in the visible light spectrum by using thermometers [462]. He realised the temperature increased in the red light region of the visible wavelength range. Herschel assigned that region as infrared light and postulated that infrared light can be sensed as heat [463].

Infrared radiation is not visible to the human eye, it is between the visible and microwave regions of the electromagnetic spectrum ranging from 700 nm to 1 mm. The radiation responsible for heating is in the range 700-2500 nm and in the IR region, 35.9% of energy is in the 700–1200 nm range according to ASTM D173. The International Commission on Illumination has classified Infrared light based on photon energy into three categories as shown in Table 5.1 [464]. In addition, the International Organisation for Standardisation has classified Infrared light based on wavelength into three categories as shown in Table 5.2 [464]. As shown in Table 5.1 the highest photon energy and the lowest wavelength are for Near-Infrared in the range 700–1400 nm, which is considered as the heating range.

Table 5.1. CIE classification of IR radiations

Name	Wavelength	Frequency (THz)	Photon energy (meV)
Near infrared (IR-A)	0.7–1.4 μm (700–1400 nm)	215–430	886–1653
Mid-infrared (IR-B)	1.4–3.0 μm (1400–3000 nm)	100–215	155–413
Far-infrared (IR-C)	3.0–100 μm (3000–0.1 mm)	3–100	1.2–83

Table 5.2. ISO 20473 standard subdivision of IR

Name	Wavelength (μm)
Near infrared (NIR)	0.78–3 μm
Mid-infrared (MIR)	3–50 μm
Far-infrared (FIR)	50–1000 μm

There are requirements of glass coating on ESG as these need a high visible light transparency and a heat-shielding function (cut off NIR). NIR-absorbing dyes and metal nanoparticle dispersions are commonly used as transparent resin materials that absorb light in broad absorbance in the range 700–1200 nm and weak absorbance in the visible region is highly desirable for window materials [465-468]. Some examples of NIR-absorbing dyes are dithiolene complexes [469], nickel complexes [470], azo compounds [471], cyanines [472], phthalocyanines [473], polymethine [474], and boron–dipyrromethene [475]. Examples of NIR-absorbing metal nanoparticles are cesium tungsten oxide [476] and lanthanum hexaboride [477]. Unfortunately, these NIR-absorbing dyes are either strongly coloured owing to absorption in the visible (400-700 nm) region or provide insufficient heat shielding owing to a narrow NIR absorption band. Generally, organic dyes are unsuitable for use in environments like windows that are exposed to sunlight for long periods of time due to them having lower light stability [478].

Cu(II) often has a broad absorption band in the range 700 to 1200 nm which resulting from d–d transitions of Cu^{2+} (^2Eg-$^2T_{2g}$) electronic transition of the single unpaired electron and weak absorption in the visible region from 400 to 700 nm [478] (Figure 5.5). In addition, this broad absorption band results in the splitting of the orbital energy level by Jahn-Teller distortion [478]. Therefore, this was taken into account when making the decision to implement 3d-metal

complexes, in particular copper complexes, as NIR absorbers. The optical performance of copper complexes for NIR-absorbing has been illustrated by measuring their UV, visible and NIR spectra. The copper complexes have suitable absorption features for applications that require transparency or brightness [478]. Moreover, during thermal studies, some complexes showed decomposition at temperatures above 250 °C. Therefore, they are stable above the processing temperature of typical transparent resins [478].

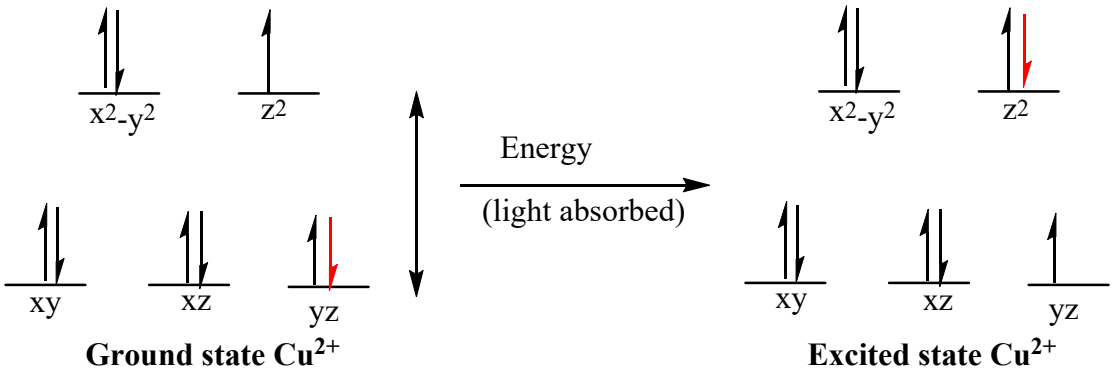

Figure 5.5. A d-d transition of Cu(II) ions (taken from reference[479, 480]).

NIR optical filtering has received much attention due to the rapid development of laser applications in various fields such as free-space optical telecommunication [481], night view imaging [482], satellite remote sensing [483, 484] and biological medicine [485, 486]. NIR optical filtering is a relation between optical attenuation and laser protection within a biological optical window of 800~1300 nm [469]. Often, optical filtering is applied in precision instruments, eye-protecting glasses, laser protections and photographs [469]. Due to their tense and broad absorption in the near-infrared region, copper metal complexes are also considered quite outstanding NIR optical filtering materials that will be discussed herein this research.

Modern windows, automobiles and trains include metal-containing coatings for ESG and to block heat penetration through the glass [431, 487, 488]. Unfortunately, these coatings have the problem of weakening the wireless transmission of Microwave/ Radio Frequency (RF) signals such as radio waves, television signals, shields radio signals, mobile phone signals [431, 452], Wi-Fi, security and personal communication signals which are used for mobile communications such as the Global System for Mobile communications (GSM) in the range 0.340-0.312 m (880–960 MHz), Universal Mobile Telecommunications System (UMTS) which is in the range 0.156-0.138 m (1920–2170

MHz), 0.1 m (3G) and GPS, etc. (<0.150 m (2 GHz)) signals, which affect the wireless communication between the inside and outside of those buildings which have ESG [431] (Figure 5.6).

Most developments of coatings of the panes are optimised with ultra-violet or infrared radiation but no attention has been paid for the microwave region of the electromagnetic spectrum. Modern windows have proven to block modern communication systems and lose radio signals [487, 489, 490]. It has been reported that this metallic shielding is opaque for microwaves [429, 487, 489-493].

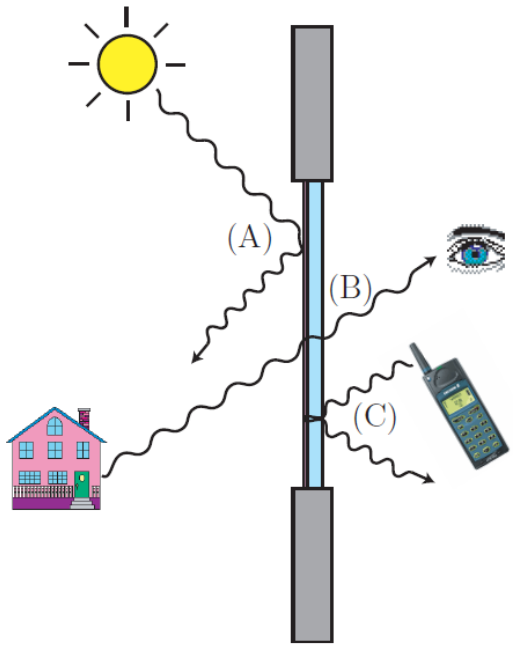

Figure 5.6. Illustration of the issues with ESG. The windowpane observes an opaque behaviour for heat, (A) IR-radiation, (B) transparent for the visible part of the spectrum, and (C) microwaves are stopped (taken from reference [494]).

The solution for attenuation consists of using repeaters to amplify the signal which is expensive because it needs to be used whenever communication standards change [431]. To overcome the weakening of the transmission of Microwave/RF signals, Frequency Selective Surface (FSS) is used as bandpass filter [431]. FSS is a technique that was applied to ESG to overcome the weakness useful microwave frequencies can pass through it whilst reflecting NIR by removing less than 4% of the coating area [431, 495]. The FSS structure etched on the metal oxide coated glass is designed to improve microwave transmission through it and reflects the infrared (IR) signal [496, 497].

5.1.2. Problem statement and Objective

Energy Saving Glass (ESG) is considered as a form of thermal insulation by keeping the room cold in the summer and warm in the winter. ESG can allow the visible light to pass through, reflect/absorb UV and IR radiations to reduce the consumption of energy, carbon emissions, and contribute to improving the environment. Unfortunately, ESG can attenuate/ reflect the useful electromagnetic wave (microwave frequencies) such as GSM mobile signal, wireless network, Bluetooth, and GPS signal in a certain area. Because of this, different approaches have been used to overcome this problem to reflect microwave frequencies. Herein, copper (II) complexes have been used to improve the transmission of microwave and cut off near infrared radiation of ESG.

The objective of this chapter of the research is the applications of copper(II) complexes as a near-infrared radiation-absorbing compounds, having a favorable shielding properties in a near-infrared range when used to produce films. The near-infrared radiation absorbing composition includes a copper (II) complex formed by reacting a 2,2′-bipyridine (bpy) and benzylphosphonate with two coordinating atoms form bonds using unshared electron pairs with the copper (II) component.

The goal of the coating is to combine three main properties: undisturbed visibility through the window, negligible losses in the thermal performances of the window and transparency to microwaves for telecommunications. To reach these goals, copper (II) complexes have been synthesised using a stirring method and glass substrate deposition using the drop-casting method to prepare structured low emissivity coatings that are optimised towards enhanced IR shielding properties and microwave transmission. Transparent IR shielding coatings were coated on the glass substrate in order to control the amount of solar radiation permitted to pass through the window, to heat the interior space with the remainder being reflected or absorbed by the coating layer while maintaining a desired visible light characteristic transmission. This coating can be also applied to vehicle glass windows to match special requirements for automobiles, trucks and trains. The optical and IR shielding performance of the coatings were evaluated. The IR shielding coating with a synthesised copper complex can block more than 90% NIR while it can maintain more than 80% transmittance in the visible range. Coated glass has been characterised by UV-Visible-NIR spectrophotometry and SEM.

5.1.2.1. Scope of Research

1- Employ a copper(II) coordination complex like copper complex in the application field and explore its properties including molecular structure in the solid-state.

2- Deposit the copper(II) complex on a glass substrate using drop-casting technique and characterise with FTIR, SEM and PXRD.

3- Provide and evaluate Ultraviolet Radiation-absorbing/reflecting composite having favorable shielding properties.

4- Provide coated glass that allows maximum transmission of visible light.

5- Provide and evaluate Near-Infrared Radiation-absorbing composition having favorable shielding properties.

6- Examine the surface morphology, optical and electrical properties of a copper complex thin film.

7- Evaluate the mobile radio signal transmission through the coated glass (Figure 5.7).

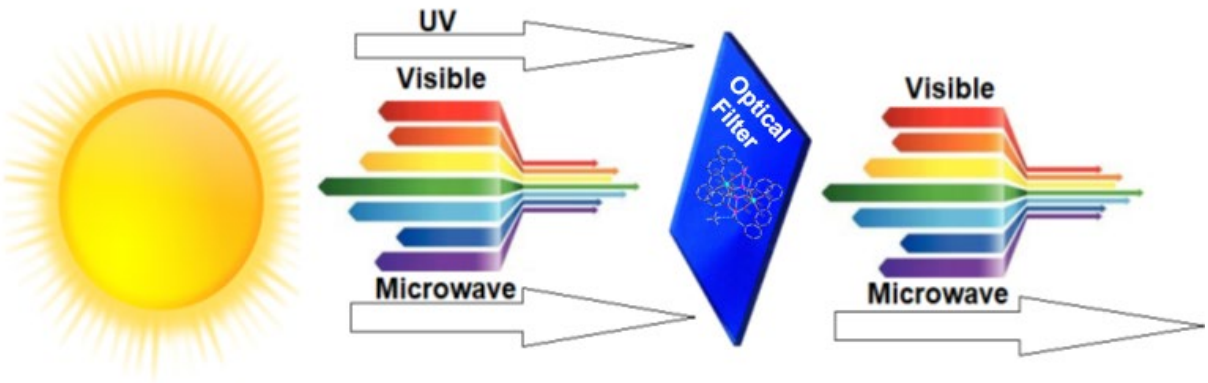

Figure 5.7 Optical Filter cut off UV and NIR.

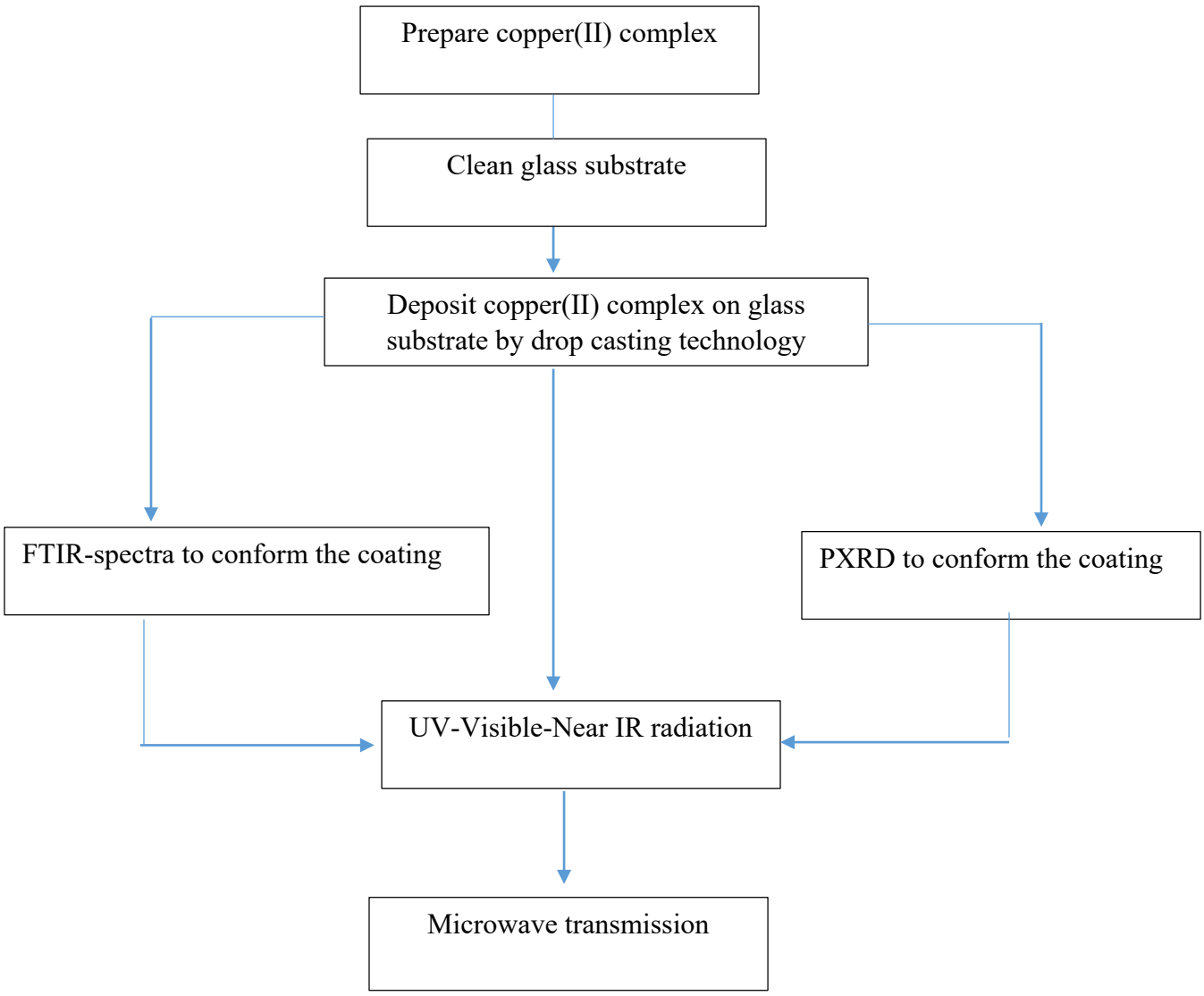

Scheme 5.1. Approach of copper(II) complex as NIR blocking.

In this chapter, copper complexes (**47** and **48**) were synthesised, characterisation and their solubility in different solvent such as: methanol, pyridine, and DMF were investigated.

The glass substrate was cleaned then these copper complexes were deposited on the glass substrate by drop-casting technique. The copper(II) complex coated on the glass substrate was confirmed by PXRD and FTIR. The dissolution and phase separation of the composites were investigated by scanning electron microscopy (SEM)/energy dispersive X-ray spectroscopy (EDX). The performances of copper(II) complexes as heat-shielding transparent window materials were determined the solar direct transmittance and visible light transmittance. The thermal properties were evaluated by thermogravimetric analysis (TGA).

The first binuclear copper (II) complex was obtained by using $Cu(OAc)_2\ H_2O$, benzylphosphonic acid ($PhCH_2PO(OH)_2$) and 2,2′-bipyridine (bpy). The binuclear Cu^{II} complex $[Cu_2(bpy)_2(PhCH_2PO_2OH)_4]\ CH_3OH$ (**47**) was successfully synthesised, characterised and the optical properties were investigated.

The second binuclear copper (II) complex was obtained by using $Cu(NO_3)_2\ 3H_2O$, benzylphosphonic acid ($PhCH_2PO(OH)_2$) and 2,2′-bipyridine (bpy). The a binuclear Cu^{II} complex $[Cu_2(bpy)_2(PhCH_2PO_2OH)_2(H_2O)_2]\ (NO_3)_2\ 4H_2O$ (**48**) was successfully synthesised, characterised and the optical properties were investigated.

5.2. Structure and optical properties of $[Cu_2(bpy)_2(PhCH_2PO_2OH)_4]\cdot CH_3OH$ (47)

5.2.1. Synthetic description

The reaction of $Cu(OAc)_2\ H_2O$, benzylphosphonic acid ($PhCH_2PO(OH)_2$) and 2,2′-bipyridine (bpy) in a molar ratio of 1:1:1 in MeOH with stirring for two hours and afforded blue block crystals of a new family of binuclear Cu^{II} complex $[Cu_2(bpy)_2(PhCH_2PO_2OH)_4]\cdot CH_3OH$.

5.2.2. Crystal structure of $[Cu_2(bpy)_2(PhCH_2PO_2OH)_4]\cdot CH_3OH$

The structure of compound **47** was characterised by single-crystal X-ray diffraction (full crystallographic data is given in Table 8.6) as shown in Figure 5.8. The purity of the phase is confirmed by powder X-ray diffraction (PXRD) (Figure 5.9).

The crystal structure of the binuclear complex $[Cu_2(bpy)_2(PhCH_2PO_2OH)_4]\cdot CH_3OH$ (**47**) crystallises in the triclinic space group $P\bar{1}$ with $Z = 2$.

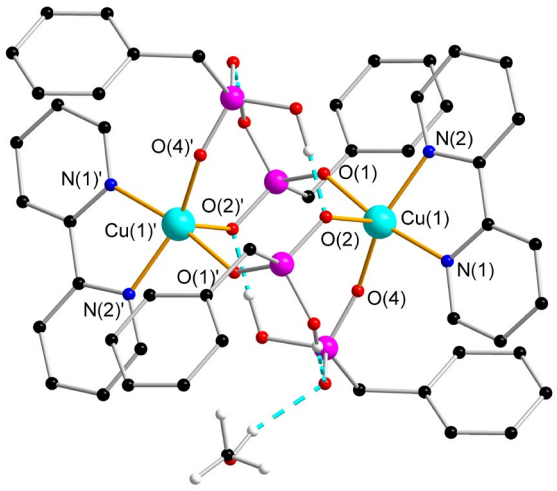

Figure 5.8. Molecular structure of compound **47**. Colour code: black, red, blue, white, pink and turquoise spheres represent C, O, N, H, P and Cu, respectively. Some of the H atoms are omitted for clarity.

As shown in Figure 5.8, the benzylphosphonate and 2,2′-bipyridine are coordinating to the metal centre of Cu atoms as shown in the crystal structure. The benzylphosphonic acid ligand is singly-deprotonated resulting in one negatively charged oxygen atom. The benzylphosphonate and 2,2′-bipyridine ligands have been successfully used to synthesise a new binuclear {Cu_2} complex consisting of two Cu^{II} ions, two 2,2′-bipyridine and four benzylphosphonate ligands.

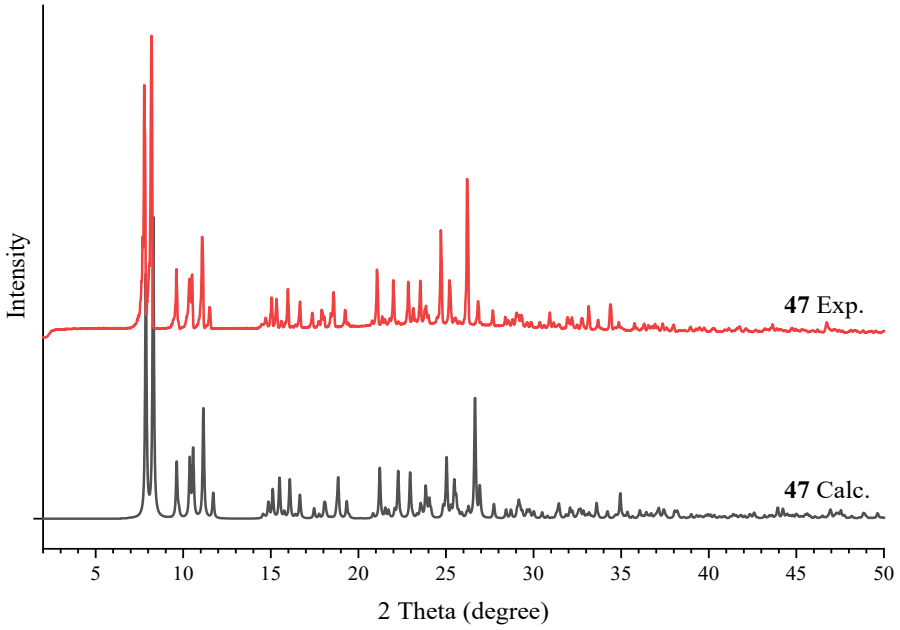

Figure 5.9. Calculated (black) and experimental (red) powder X-ray diffraction (PXRD) patterns of compound **47**.

Both penta-coordinated Cu^{II} ions are surrounded by two N and three O donor atoms (N_2O_3). Two N atoms come from the 2,2′-bipyridine ligand and three O atoms come from benzylphosphonate ligand. This results in a distorted spherical square pyramid geometry, which was confirmed by SHAPE analysis [215] with a deviation value of 1.07, (Figure 5.10, Table 8.15).

The Cu−O and Cu−N bond distances are in the range 1.930(2)−2.260(2) Å and 2.013(2)−2.016(2) Å, respectively. The Cu···Cu distance is 4.629(6) Å. Selected bond distances are summarised in Table 5.3.

Table 5.3. Selected bond distances (A°) for compound **47**

Bond distances			Bond distances		
Atom	Atom	Distance/Å	Atom	Atom	Distance/Å
Cu(1)	O(1)	1.936(2)	Cu(1)	N(1)	2.016(2)
Cu(1)	O(2)'	2.260(2)	Cu(1)	N(2)	2.013(2)
Cu(1)	O(4)	1.930(2)			
'1-x, 1-y, 1-z					

Intramolecular interaction has stabilised the structure of compound **47** through hydrogen bonds. O(6)–H(6) and O(6)'–H(6)' from the benzylphosphonate ligand make intramolecular hydrogen bonds to O(5) and O(5)' from the neighbouring benzylphosphonate ligand with distances of O(6)···O(5) and O(6)'···O(5)' 2.585 Å. In addition, O(3)–H(3) and O(3)'–H(3)' from the benzylphosphonate ligand makes intramolecular hydrogen bonds to O(5)' and O(5) from the neighbouring benzylphosphonate ligand with distances of O(3)···O(5)' and O(3)'···O(5) 2.588 Å. O(7)–H(7A) from the methanol (CH_3OH) makes intramolecular hydrogen bonds to O(5) from the benzylphosphonate ligand with distances of O(7)···O(5) is 2.834 Å.

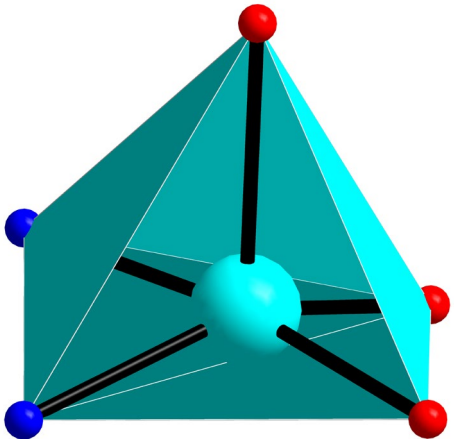

Figure 5.10. Distorted spherical square pyramid geometry of 5-coordinated of Cu ion. Colour code: red, blue and turquoise spheres represent O, N and Cu, respectively.

5.2.3. Thermal stability

Thermal Gravimetric Analysis (TGA) was used to evaluate the thermal stability of the copper complex **47** as shown in Figure 5.11. The decomposition temperature is the temperature of the crossing point of two tangential lines at the decomposition onset stage of the TGA curve.

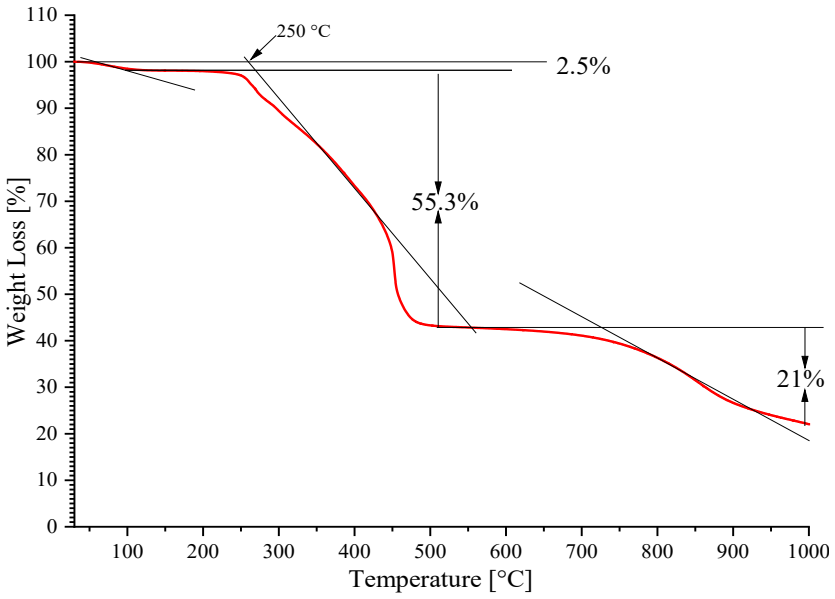

Figure 5.11. Thermogravimetric analysis curves of copper complex **47**.

Thermogravimetric analysis of **47** was performed between 30 and 1000 °C using a thermal gravimetric analysis (TGA Q-500, TA Instruments) under a nitrogen atmosphere to determine thermal stability. Complex **47** demonstrates thermal stability up to 250 °C. The weight loss of about 2.5% between 30 and 250 °C can be attributed to the loss of methanol molecule it should be 5% as theoretical might be sample more dry present in **47**. The continuous weight loss of about 55.3 % between 250 and 513 °C can be attributed to the loss of benzylphosphonate and the continuous weight loss of about 21 % between 513 and 1000 °C can be attributed to the loss of bpy present in **47**, it should be 26.3% as theoretical but the curve was stopped at 1000 °C.

5.2.4. Optical properties and Optical Filter

5.2.4.1. UV-visible and NIR study of Complex 47.

Optical transmission and absorption of complex **47** were measured in methanol with the concentration 2×10^{-3} M at room temperature on a Cary 5000 scan Spectrophotometer over the ultraviolet (UV), visible and NIR regions i.e from 200-1000 nm. Figure 5.12, shows the transmission with respect to the wavelength of copper complex **47**. The transmission in the visible region has been found to be 87.46 % at λ_{max} 474 nm for complex **47**. Generally, in the visible region (400-700 nm) of the spectrum, the transmission is high enough to observe interference

fringes. It is due to less absorption arising from the transfer of electrons from the valence to the conduction band owing to optical interference effects. The transmission in the NIR region has been found to be 15.17 % at λ_{min} 700 nm for complex **47**. In the absorption spectra as shown in Figure 5.13, the absorbance in the NIR region has been found to be 0.9 at λ_{max} 700 nm for complex **47**. Generally, in the NIR region there is a broad band from 700-1000 nm that is attributed to the d–d transitions of Cu^{2+} and weak absorption in the visible region [478].

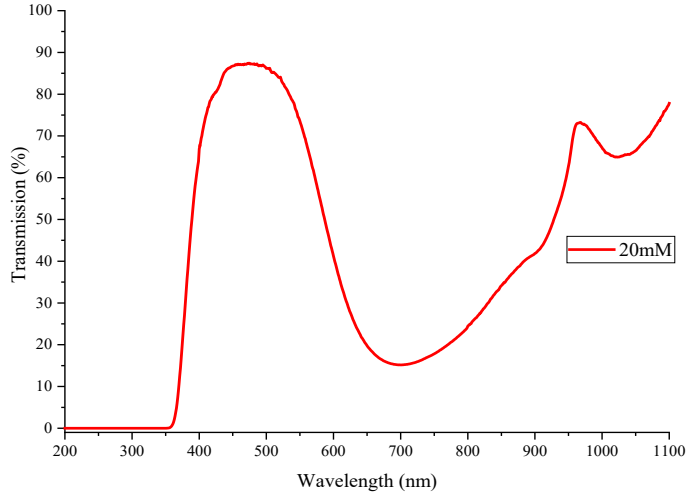

Figure 5.12. Transmission spectra of complex **47**.

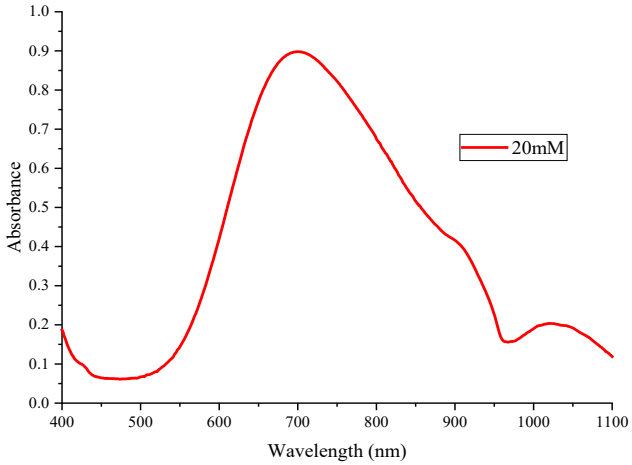

Figure 5.13. Absorption spectra of complex **47**.

5.2.4.2. Preparation of NIR-absorbing composition.

5.2.4.2.1. Preparation of glass substrate for coating

Commercial glass window has used with a thickness of 2 mm and a size of 2.5 cm x 2.5 cm. Glass substrates were cleaned first by dip it in " piranha" solution (H_2SO_4 75% and H_2O_2 25%) followed by rinsing several times with water and then sonicated for 20 min in isopropanol and dried in nitrogen. It was then placed in a plasma cleaner for 5 min prior to coating.

5.2.4.2.2. Film fabrication

The NIR optical filters were fabricated using a static solution drop-casting technique. The specific procedure is given below: 200 mg copper complex **47** was dissolved in 8 mL dry methanol with stirring for 10 minutes. Alternatively, the reaction between the components (see 7.2.47) without waiting for crystal growth gave the same result. This was followed by filtering the solution three times using pore diameter of the filter 0.45, 0.2 and 0.1 μm to reliably remove fine foreign substances while suppressing the filter clogging. Then 1.5 mL of solution is dropped to the cleaned glass substrate in three stages each 0.5 mL followed by increasing the temperature of hotplate to 50 °C. When the solvent had evaporated the temperature was decreased to room temperature. This was repeated three times using three 0.5 mL aliquots. Then film was further dried on the hotplate for 10 min at 75 °C. Another method drop-cast 0.75 mL all at once on the cleaned glass substrate and after an hour this was repeated with further 0.75 mL and left for 24 hours to dry completely.

Sometimes during evaporation of the solvent, some precipitate started to appear and this was avoided using poly(2-vinylpyridine) (PVP) for complex **47**.

Thus, 200 mg copper complex **47** was dissolved in 8 mL dry methanol and 200 mg PVP was dissolved in 2 mL dry methanol followed by mixing and stirring for 20 minutes then the solution filtered three times with 0.45, 0.2 and 0.1 μm pore diameter filter 0.7 mL. The final solution was dropped once on the cleaned glass substrate and after half an hour, the process repeated. The coated film was left to stand at room temperature for 24 hours to be dried.

5.2.4.3. Thin Film Characterisation

5.2.4.3.1. IR transmission of the coatings

The transmission of the coatings was measured in the middle infrared range using Fourier transform infrared spectrophotometer (FTIR), Bruker Alpha from wavenumber 4000–400 cm^{-1} (Figure 5.14). The IR of the pure complex and the film coating on glass substrate, for **47** shows that the complex and its thin film are identical.

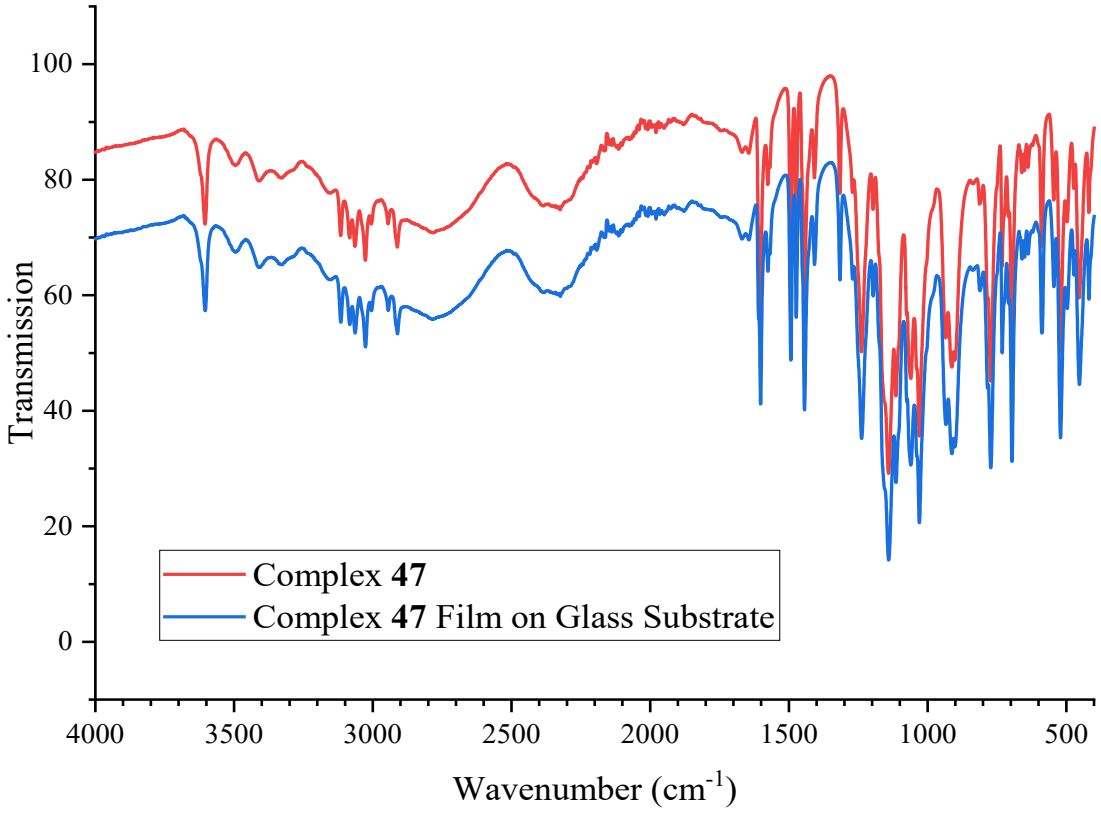

Figure 5.14. FTIR spectra for the pure complex and the film coating on glass substrate, for **47**.

5.2.4.3.2. Evaluation of the thickness of the coated film

The thickness of coated films complex **47** and **47** + PVP were evaluated by programmable surface profiler measuring system-DEKTAK 6m model. As shown in Figure 5.15, the thickness of complex **47**+PVP is 33.63 µm for 34.43 µm for complex **47**.

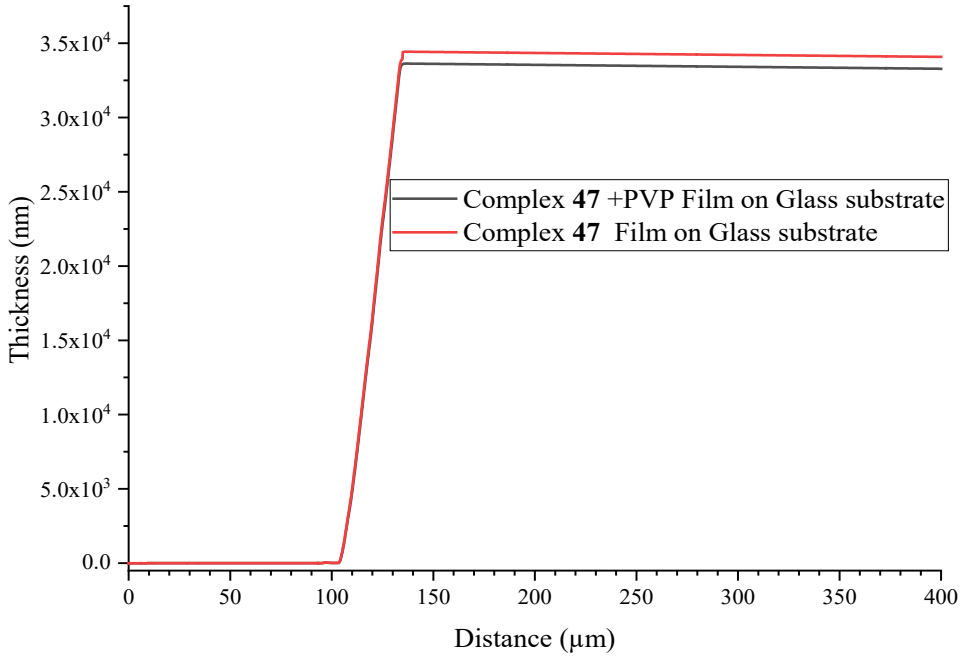

Figure 5.15. Thickness of coated film complex **47** and **47** + PVP.

5.2.4.3.3. Optical properties of the thin film

Optical transmission and absorbance of thin films of **47** and **47**+PVP were measured on a Cary 5000 scan Spectrophotometer UV-Vis-NIR in the ultraviolet (UV), visible and NIR 200-2000 nm as shown in Figure 5.16 and Figure 5.17.

The transmission in the visible region has been found to be 77.68% at λ_{max} 468 nm for copper complex **47** films and 80.56% at λ_{max} 470 nm for complex **47** film+ PVP. Generally, in the visible region (400-700 nm) of the spectrum, the transmission is high enough to observe interference fringes. It is less absorption due to the transfer of electrons from the valence to the conduction band owing to optical interference effects.

The transmission in the NIR region has been found to be 3.16 %at λ_{min} 674 nm for copper complex **47** films and 5.96 % at λ_{min} 675 nm for complex **47** film+ PVP. The absorbance in the NIR region has been found to be 1.5 at λ_{max} 673 nm for copper complex **47** films and 1.23 at λ_{max} 677 nm for complex **47** film+ PVP. Generally, in the NIR region there is a broad band from 700-1000 nm that is attributed to the d–d transitions of Cu^{2+} and weak absorption in the visible region [478].

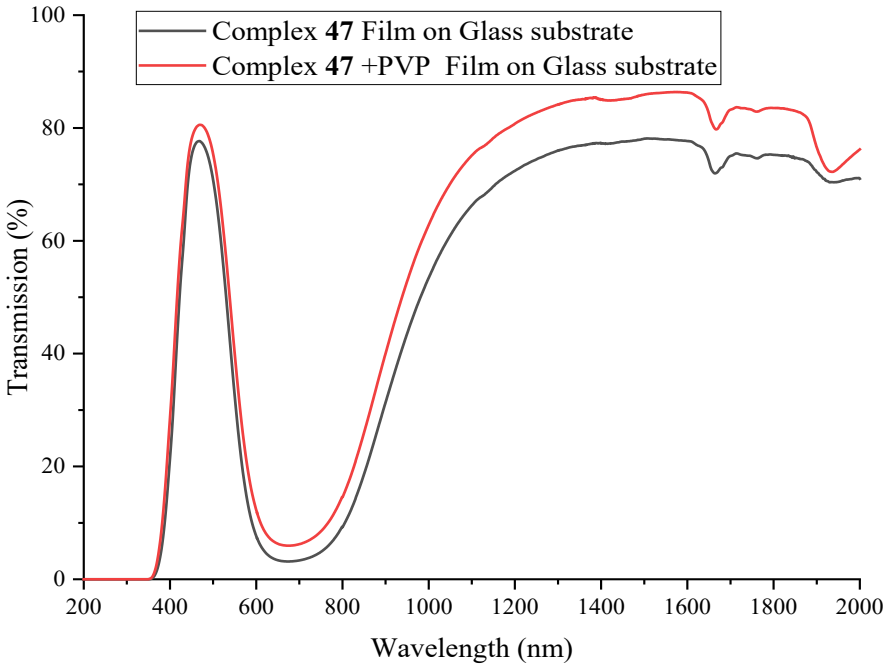

Figure 5.16. Transmission spectra of complex **47** film and complex **47**+PVP film.

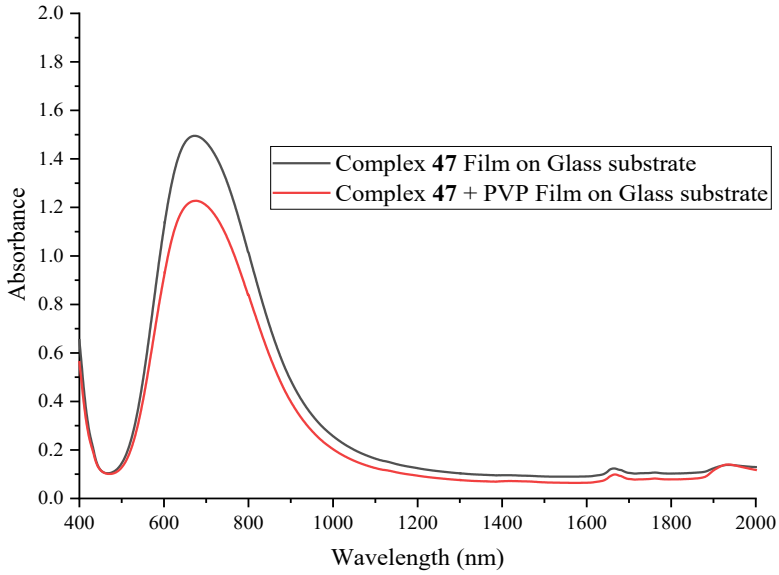

Figure 5.17. Absorbance spectra of complex **47** film and complex **47**+PVP film.

5.4.4.4.4. Scanning electron microscopy (SEM) /Energy-dispersive X-ray spectroscopy (EDX)

The copper complex **47** film was observed by SEM/EDX, analyse the surface morphology and the dissolved states of the complex **47** film was evaluated using Zeiss Auriga 60. The SEM images and EDX complex **47** film distribution maps are shown in Figure 5.18. There are no precipitates but like flexes on glass surface and Cu is homogeneously dispersed in the glass surface. The EDX mapping results show the composition of glass coated with **47**.

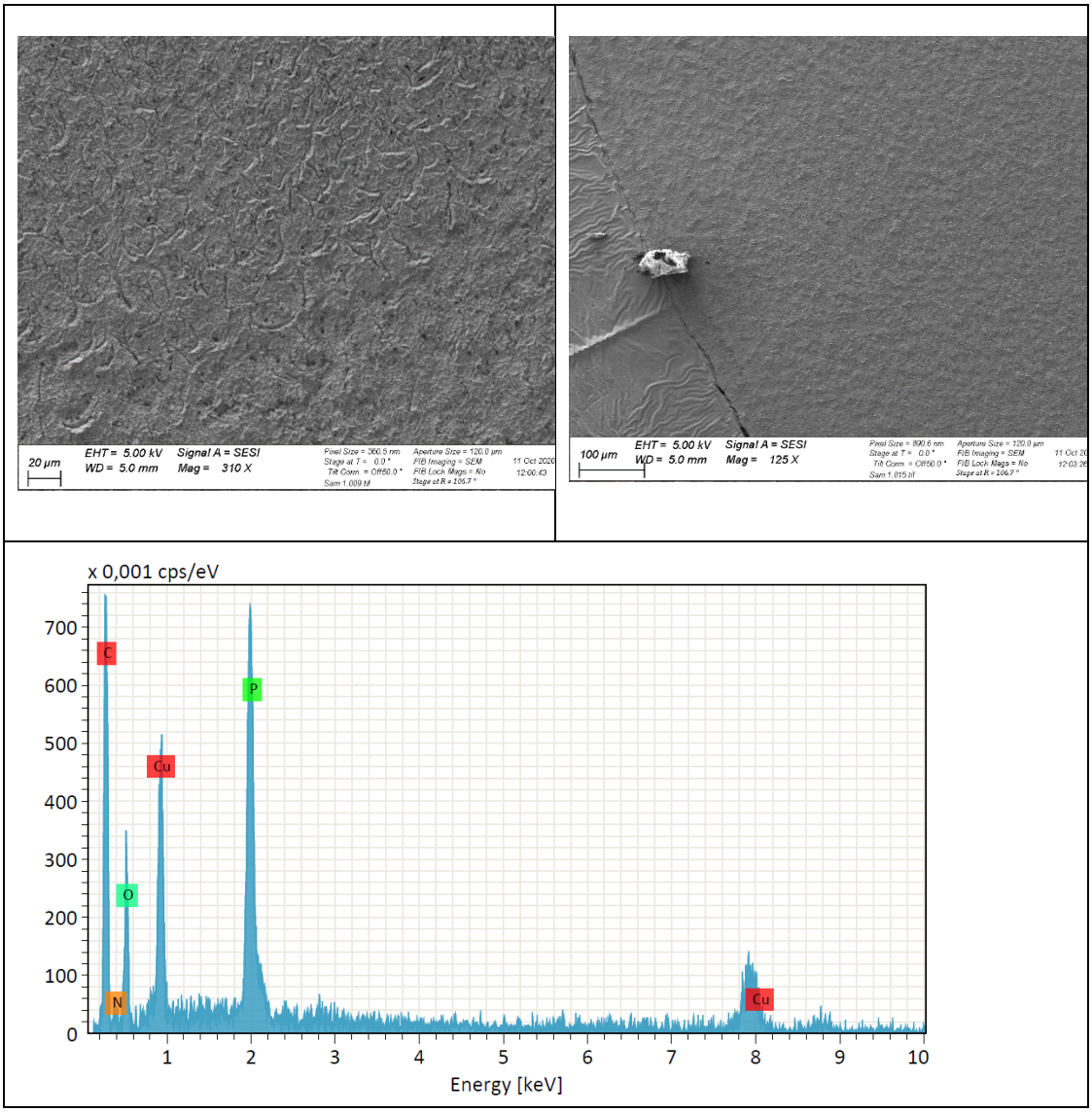

Figure 5.18 SEM and EDX spectra of complex **47** film.

5.2.4.3.5. Preliminary test of Microwave Transmission

A wide box was constructed from cement and sand opened from up with size 6 cm x 6 cm with depth 5cm was used to test microwave transmission.

A mobile phone was placed in the box which was then sealed with glass (10 cm x10 cm) coated with **47**. The phone showed a signal strength with 4 bars before being placed in the box. A call was made to the phone in box which received the signal still with a strength of 4 bars indicating successful microwave transmission.

5.3. Structure and optical properties of $[Cu_2(bpy)_2(PhCH_2PO_2OH)_2(H_2O)_2]$ $(NO_3)_2$ $4H_2O$ (**48**)

5.3.1. Synthetic description

The reaction of $Cu(NO_3)_2 \cdot 3H_2O$, benzylphosphonic acid ($PhCH_2PO(OH)_2$) and 2,2′-bipyridine (bpy) in a molar ratio of 1:1:1 in MeOH with stirring and heating at 70 °C for two hours and afforded blue block crystals of a new family of binuclear Cu^{II} complex $[Cu_2(bpy)_2(PhCH_2PO_2OH)_2(H_2O)_2] \cdot (NO_3)_2 \cdot 4H_2O$.

5.3.2. Crystal structure of $[Cu_2(bpy)_2(PhCH_2PO_2OH)_2(H_2O)_2] \cdot (NO_3)_2 \cdot 4H_2O$

The structure of compound **48** was characterised by single-crystal X-ray diffraction (full crystallographic data is given in Table 8.6) (Figure 5.19). The purity of the phase is confirmed by powder X-ray diffraction (PXRD) (Figure 5.20).

The binuclear complex $[Cu_2(bpy)_2(PhCH_2PO_2OH)_2(H_2O)_2] \cdot (NO_3)_2 \cdot 4H_2O$ (**48**) crystallises in the triclinic space group $P\bar{1}$ with Z = 1.

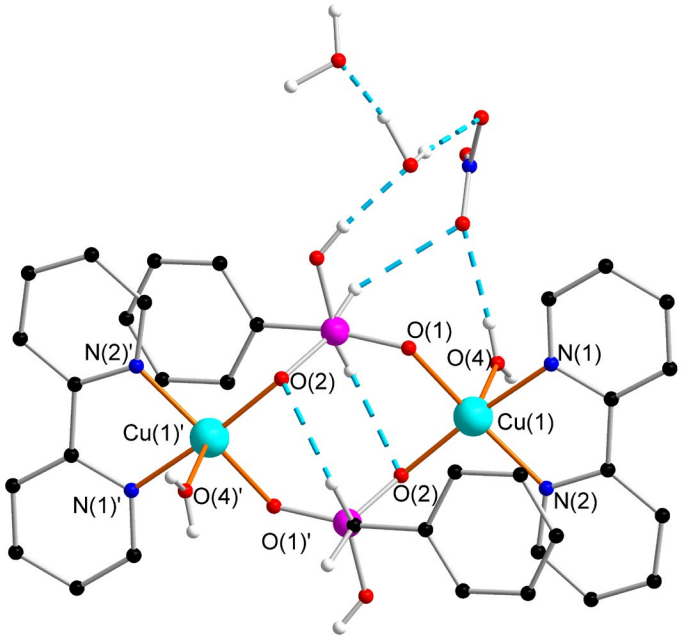

Figure 5.19. Molecular structure of compound **48**. Colour code: black, red, blue, white, pink and turquoise spheres represent C, O, N, H, P and Cu, respectively. Some of the H atoms are omitted for clarity.

The benzylphosphonate and 2,2′-bipyridine are coordinating to the metal centre of Cu atoms as shown in the crystal structure as shown in Figure 5.19. The benzylphosphonic acid ligand is singly-deprotonated resulting in one negatively charged oxygen atom. The benzylphosphonate and 2,2′-bipyridine ligands have successfully used to synthesise binuclear $\{Cu_2\}$ complex consisting of two Cu^{II} ions, two 2,2′-bipyridine ligand, two water, two nitrate groups and two benzylphosphonate ligands.

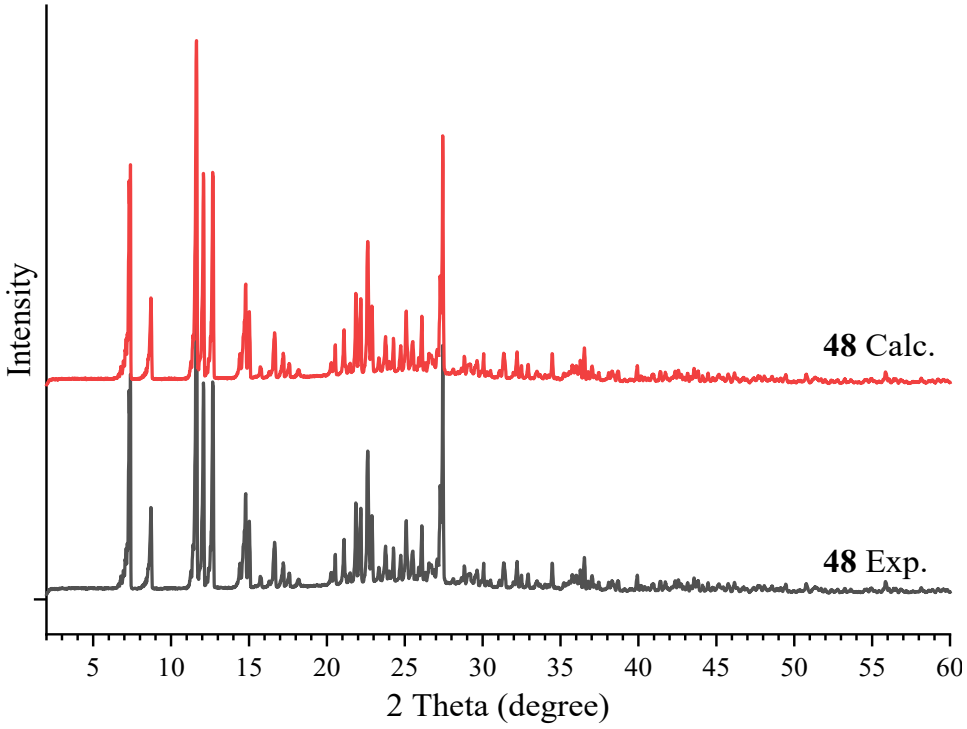

Figure 5.20. Calculated (black) and experimental (red) powder X-ray diffraction (PXRD) patterns of compound **48**.

Both penta-coordinated Cu^{II} ions are surrounded by two N and three O donor atoms (N_2O_3). Two N atoms come from the 2,2′-bipyridine ligand, two O atoms come from benzylphosphonate ligand and O atom comes from water (H_2O). This results in a distorted spherical square pyramid geometry which was confirmed by SHAPE analysis [215] with a deviation value of 0.85, (Figure 5.21, Table 8.16).

The Cu–O and Cu–N bond distances are in the range 1.940(14)–2.359(15) Å and 1.989(16)–2.006(17) Å, respectively. The Cu···Cu distance is 5.160(4) Å. Selected bond distances are summarised in Table 5.4.

Table 5.4. Selected bond distances (A°) for compound **48**

Bond distances			Bond distances		
Atom	Atom	Distance/Å	Atom	Atom	Distance/Å
Cu(1)	O(1)	1.940(14)	Cu(1)	N(1)	1.989(16)
Cu(1)	O(2)'	1.945(13)	Cu(1)	N(2)	2.006(17)
Cu(1)	O(4)	2.359(15)	'1-x, 1-y, 1-z		

Intramolecular interaction has stabilised the structure of compound **48** through hydrogen bonds. O(3)–H(3) from the benzylphosphonate ligand makes intramolecular hydrogen bond to O(8) from the lattice water molecule with distances of O(3)···O(8) 2.582 Å. In addition, O(8)–H(8A) from the lattice water molecule makes intramolecular hydrogen bond to O(9) from the another lattice water molecule with distances of O(8)···O(9) 2.662 Å, and O(8)–H(8B) from the lattice water molecule makes intramolecular hydrogen bonds to O(5) from the nitrate counteranion $(NO_3)^-$ group with distances of O(8)···O(5) 2.862 Å.

Intermolecular interaction has stabilised the structure of compound **48** through hydrogen bonds. O(8)–H(8B) from the lattice water molecule makes intermolecular hydrogen bond to O(5) from the nitrate NO_3^- counterion of a neighbouring molecule with O(8)···O(5) distance of 2.86 Å. In addition, O(9)–H(9A) from the lattice water molecule makes intermolecular hydrogen bond to O(7) from the nitrate NO_3^- counteranion of the neighbouring molecule with distances of O(9)···O(8) 2.94 Å, and O(8)–H(8B) from the lattice water molecule makes intramolecular hydrogen bond to O(3) from the benzylphosphonate ligand of the neighbouring molecule with distances of O(8)···O(3) 2.578 Å. Intra- and Intermolecular interaction results in a 3D supramolecular. The packing of compound **47** is presented in Figure 5.22.

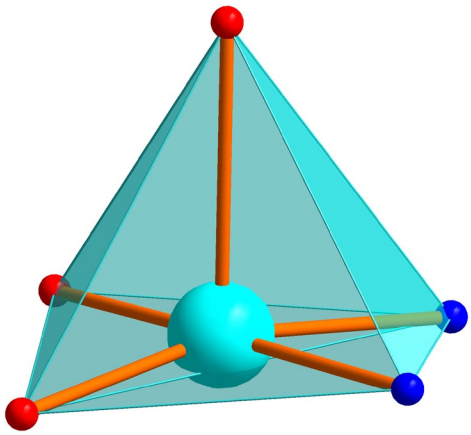

Figure 5.21. Distorted spherical square pyramid geometry of 5-coordinated of Cu ion. Colour code: red, blue and turquoise spheres represent O, N and Cu, respectively.

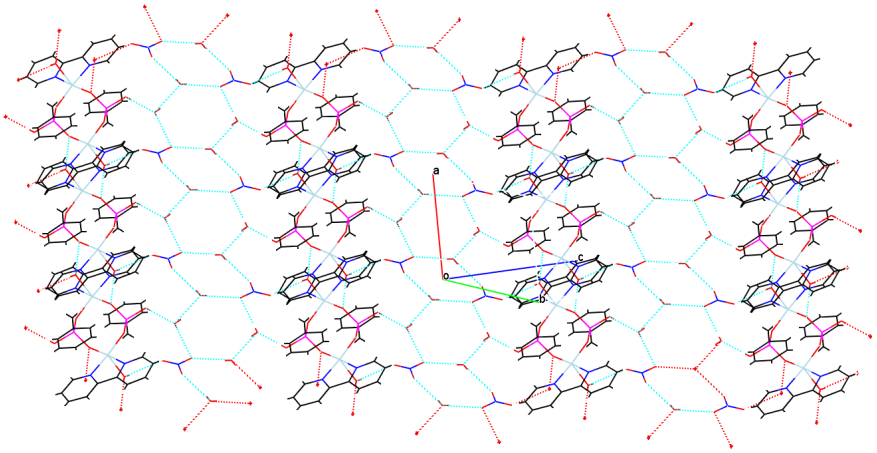

Figure 5.22. Packing of compound **48**. Colour code: black, red, blue, magenta and turquoise spheres represent C, O, N, P and Cu, respectively.

5.3.3. Thermal stability

Thermal Gravimetric Analysis (TGA) was used to evaluate the thermal stability of the copper complex **48** as shown in Figure 5.23. The decomposition temperature is the temperature of the crossing point of two tangential lines at the decomposition onset stage of the TGA curve.

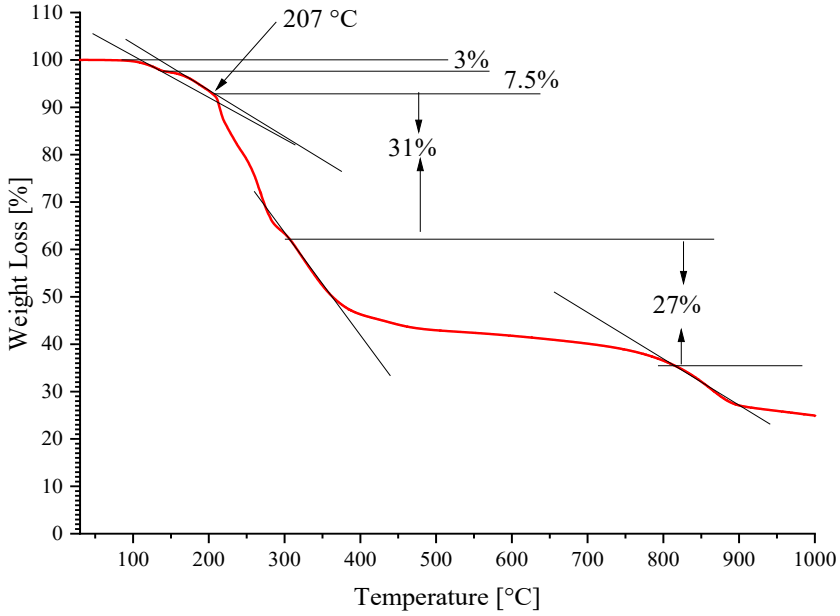

Figure 5.23. Thermogravimetric analysis curves of copper complex **48**.

Thermogravimetric analysis of **48** was performed between 30 and 1000 °C using a thermal gravimetric analysis (TGA Q-500, TA Instruments) under a nitrogen atmosphere to determine thermal stability. Complex **48** demonstrates thermal stability up to 207 °C. The weight loss of about 3% between 30 and 142 °C can be attributed to the loss of 2 water molecule, 7.5% between 142 and 207 °C can be attributed to the loss of 4 water molecule, 31 % between 207 and 293 °C can be attributed to the loss of benzylphosphonate and 27% between 293 and 762 °C can be attributed to the loss bpy present in **48.**

5.3.4. Optical properties and Optical Filter

5.3.4.1. UV-visible and NIR study of Complex 48

Optical transmission and absorption of complex **48** were measured in methanol with the concentration 2.3×10^{-3} M at room temperature on a Cary 5000 scan Spectrophotometer over the ultraviolet (UV), visible and NIR regions i.e from 200-1000 nm.

Figure 5.24, shows the transmission with respect to the wavelength of copper complex **48**. The transmission in the visible region has been found to be 88.16 % at λ_{max} 476 nm for the complex **48**. Generally, in the visible region (400-700 nm) of the spectrum, the transmission is high enough to observe interference fringes. It is due to less absorption arising from the transfer of electrons from the valence to the conduction band owing to optical interference effects.

The transmission in the NIR region has been found to be 14.92 % at λ_{min} 700 nm for copper complex **48**. In the absorption spectra as shown in Figure 5.25, the absorbance of the NIR region has been found to be 0.82 at λ_{max} 700 nm. Generally, in the NIR region there is a broad band from 700-1000 nm that is attributed to the d–d transitions of Cu^{2+} and weak absorption in the visible region [478].

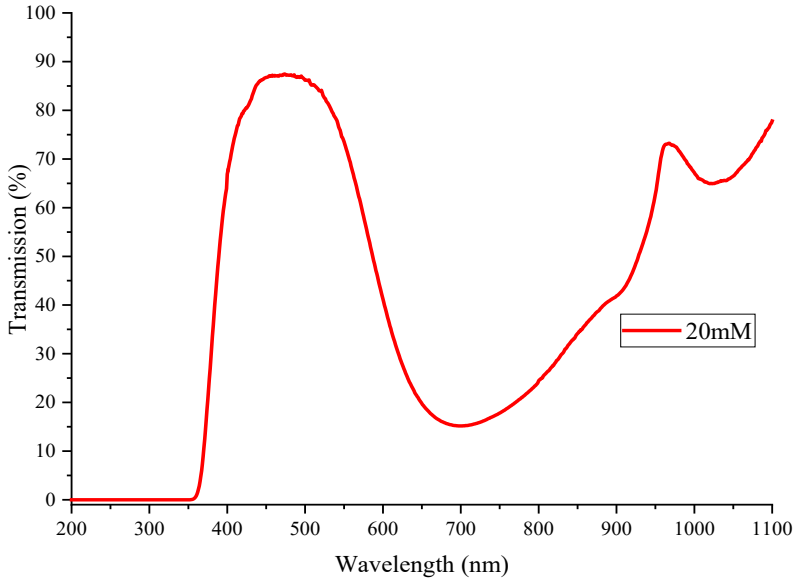

Figure 5.24. Transmission spectra of complex **48**.

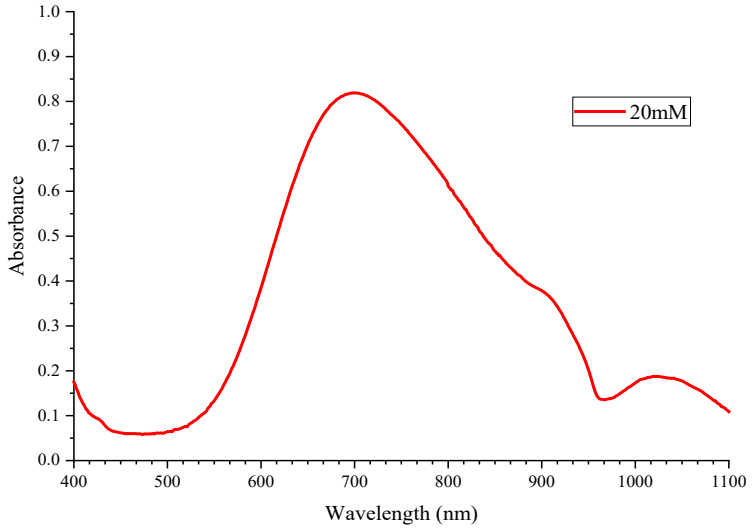

Figure 5.25. Absorption spectra of complex **48**.

5.3.4.2. Preparation of NIR-absorbing composition.

5.3.4.2.1. Film fabrication

The NIR optical filter was fabricated using a static solution drop-casting technique. The specific procedure is given below: 180 mg copper complex **48** was dissolved in 8 mL dry methanol with stirring for 10 minutes. Alternatively, the reaction between the components (see 7.2.48) without

waiting for crystal growth gave the same result. This was followed by filtering the solution three times using pore diameter of the filter 0.45, 0.2 and 0.1 μm to reliably remove fine foreign substances while suppressing the filter clogging. Then 1.5 mL of solution is dropped to the cleaned glass substrate (see 5.2.4.2.1**)** in three stage each 0.5 mL followed be increasing the temperature of hotplate to 50 °C. When the solvent had evaporated the temperature was decreased to room temperature. This was repeated three times using three 0.5 mL aliquots. Then film was further dried on the hotplate for 10 min at 75 °C. Another method drop-cast 0.75 mL all at once on the cleaned glass substrate and after an hour this was repeated with further 0.75 mL and left for 24 hours to dry completely.

Notably, the optical filters with copper complex **48** are impossibly achieved with poly(2-vinylpyridine) (PVP) as a matrix, mixing PVP with complex **48** form PVP was precipitated and not soluble this might be resulted from complex **48** since contains water lattice and PVP is form precipitated when mixed with water.

5.3.4.3. Thin Film Characterisation

5.3.4.3.1. IR transmission of the coatings

The transmission of the coatings was measured in the middle infrared range using Fourier transform infrared spectrophotometer (FTIR), Bruker Alpha from wavenumber 4000–400 cm^{-1} as shown in Figure 5.26. The IR for the pure complex and the film coating on glass substrate, for **48** shows that the complex and its thin film are identical.

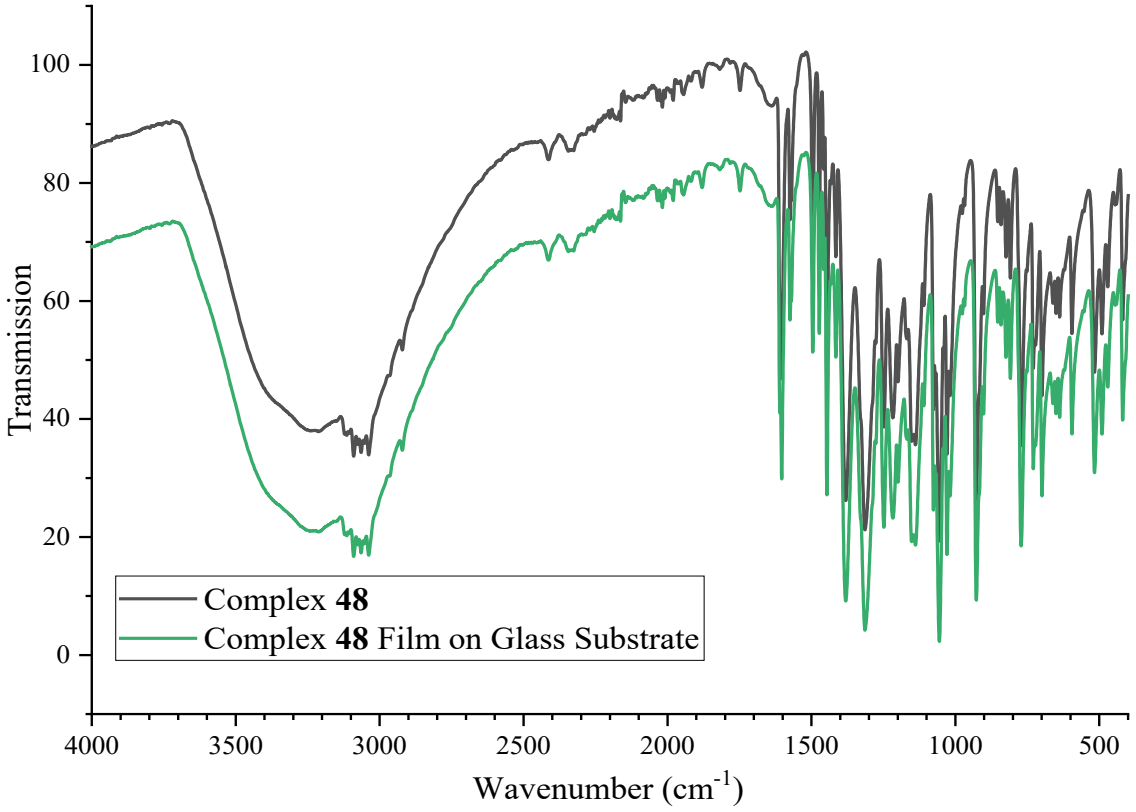

Figure 5.26. FTIR spectra for the pure complex and the film coating on glass substrate for **48**.

5.3.4.3.2. Evaluation of the thickness of the coated film

The thickness of coated film complex **48** was evaluated by programmable surface profiler measuring system- DEKTAK 6m model. As shown in Figure 5.27, the thickness of complex **48** is 26.78 μm.

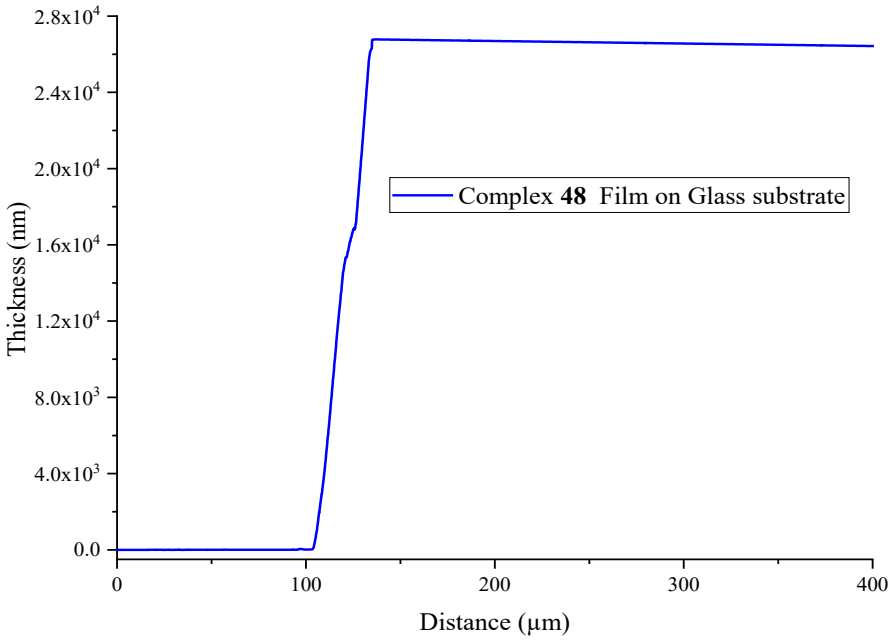

Figure 5.27. Thickness of coated film complex **48**.

5.3.4.3.3. Optical properties of the thin film

Optical transmission and absorbance of coated glass with **48** were measured on a Cary 5000 scan Spectrophotometer UV-Vis-NIR in the ultraviolet (UV), visible and NIR 200-2000 nm as shown in Figure 5.28 and Figure 5.29.

The transmission of copper complex **48** films in the visible region has been found to be 91.68 % at λ_{max} 461 nm. Generally, in the visible region (400-700 nm) of the spectrum, the transmission is high enough to observe interference fringes. It is less absorption due to the transfer of electrons from the valence to the conduction band owing to optical interference effects.

The transmission of copper complex **48** films in the NIR region has been found to be 11.66 %at λ_{min} 701 nm. The absorbance of copper complex **48** films in the NIR region has been found to be 0.95 at λ_{max} 700 nm. Generally, in the NIR region there is a broad band from 700-1000 nm that is attributed to the d–d transitions of Cu^{2+} and weak absorption in the visible region [478].

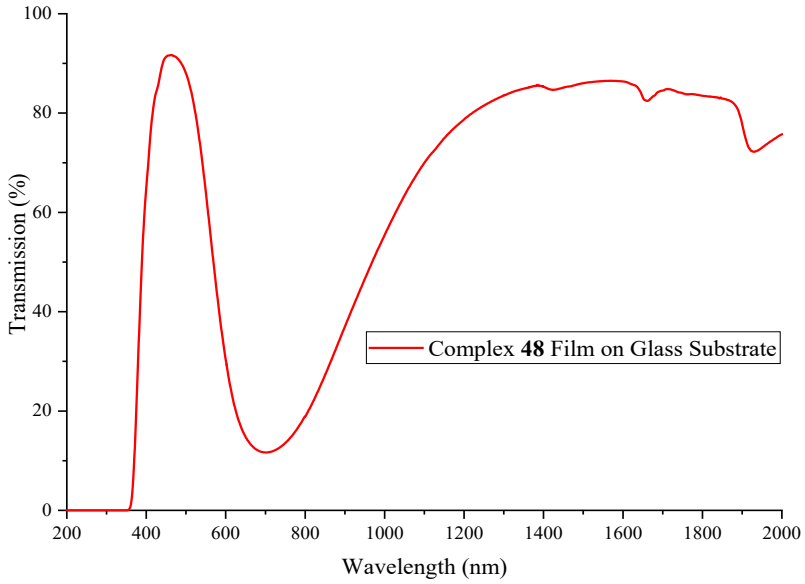

Figure 5.28. Transmission spectra of complex **48** film.

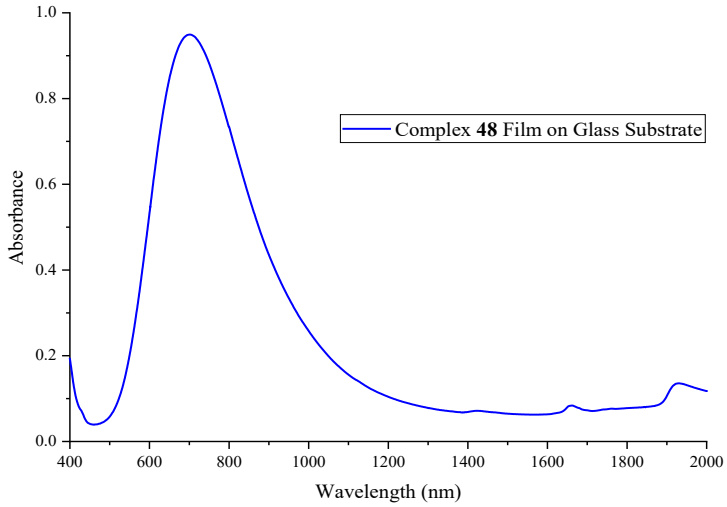

Figure 5.29. Absorbance spectra of complex **48** film.

5.5.4.3.4. Scanning electron microscopy (SEM) /Energy-dispersive X-ray spectroscopy (EDX).

The copper complex **48** film was observed by SEM/EDX, analyse the surface morphology and the dissolved states of the complex **48** film was evaluated using Zeiss Auriga 60. The SEM images and EDX complex **48** film distribution maps are shown in Figure 5.30. There are no precipitates

but like flexes on glass surface and Cu is homogeneously dispersed in the glass surface. The EDX mapping results show the composition of glass coated with **48**.

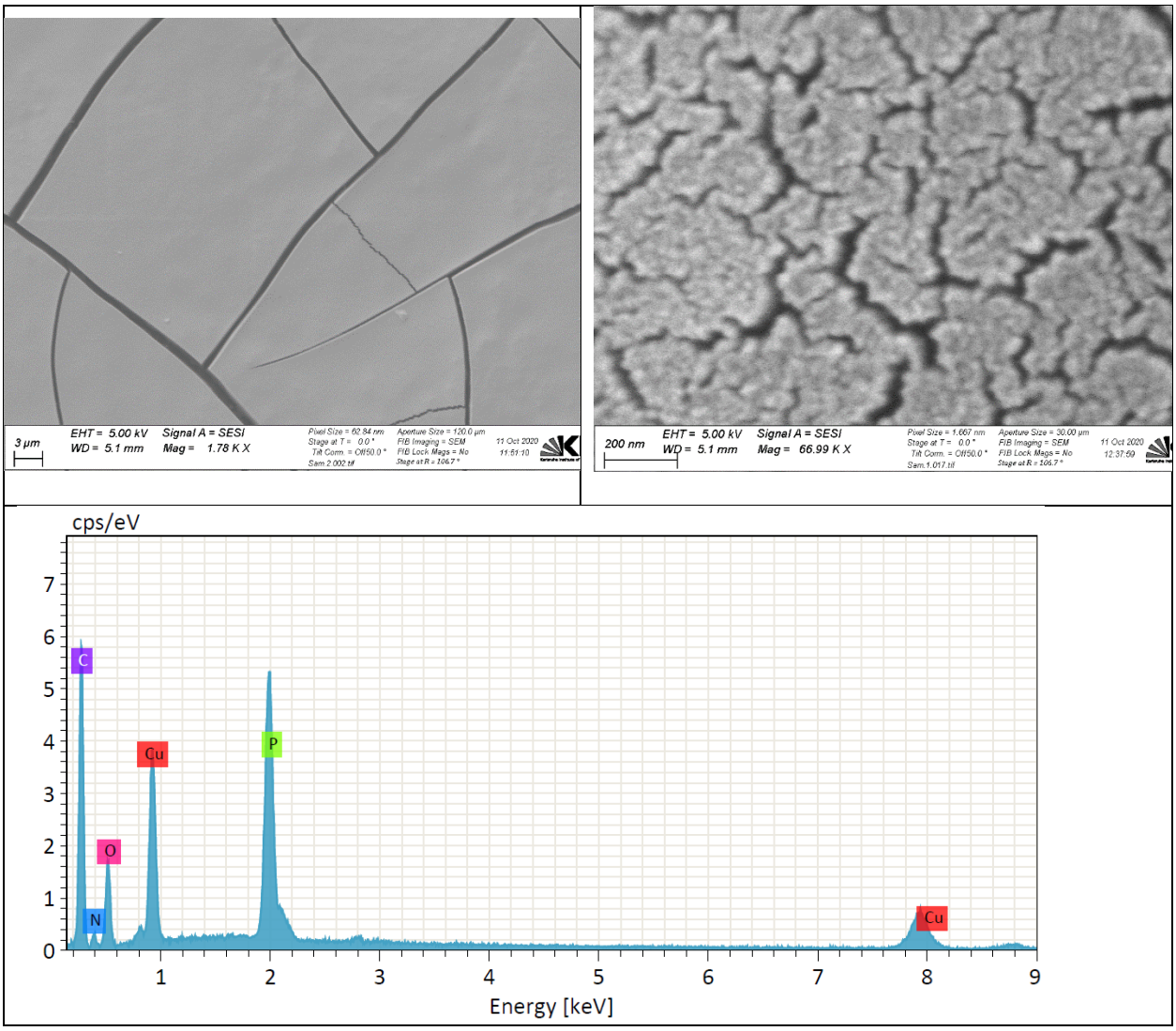

Figure 5.30. SEM and EDX spectra of complex **48** film.

5.3.4.3.5. Preliminary test of Microwave Transmission

A wide box was constructed from cement and sand opened from up with size 6 cm x 6 cm with depth 5cm was used to test microwave transmission.

A mobile phone was placed in the box which was then sealed with glass (10 cm x10 cm) coated with **48**. The phone showed a signal strength with 4 bars before being placed in the box. A call

was made to the phone in box which received the signal still with a strength of 4 bars indicating successful microwave transmission.

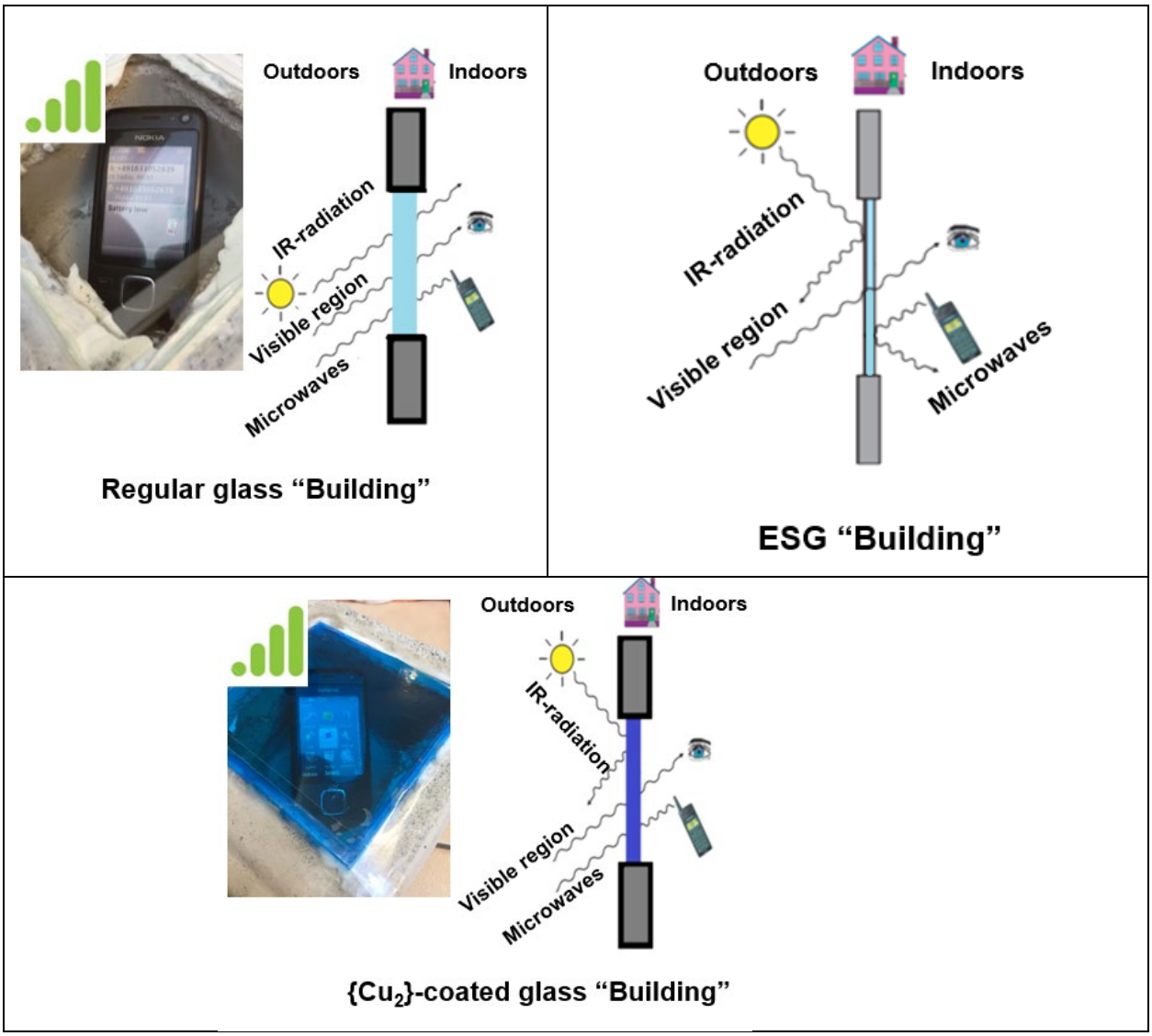

Figure 5.31. Comparisen of transmission of radiation through different glass substarte

5.4. Conclusion

In this research, two homometallic copper(II) complexes have been synthesised and characterised from the reactions of 2,2′-bipyridine (bpy) ligand, benzylphosphonic acid ($PhCH_2PO(OH)_2$) as co-ligand and copper salt. By changing the copper salt either $[Cu_2(bpy)_2(PhCH_2PO_2OH)_4]$ CH_3OH (**47**) or $[Cu_2(bpy)_2(PhCH_2PO_2OH)_2(H_2O)_2]$ $(NO_3)_2$ $4H_2O$ (**48**) could be obtained.

Compound **47** was synthesised using Cu(OAc) H_2O, benzylphosphonic acid and 2,2′-bipyridine (bpy) and structurally characterised by single crystal XRD and powder XRD, and investigated optically. Optical studies carried out on compound **47** revealed that it has a broad band absorption in the NIR region in the range 700-1000 nm.

Complex **47** was found to be thermally stable below 250 °C. The optical transmission in the visible region has been found to be 87.46 % at λ_{max} 474 nm while the transmission in the NIR region has been found to be 15.17 % at λ_{min} 700 nm. In the absorption spectra, the absorbance in the NIR region has been found to be 0.9 at λ_{max} 700 nm for complex **47**. Generally, in the NIR region there is a broad band from 700-1000 nm that is attributed to the d–d transitions of Cu^{2+} and weak absorption in the visible region [478].

The film was fabricated on glass substrate and some characterisation was taking place to confim the coating film on glass. The transmission of the coatings was measured in the middle infrared range by Fourier transform infrared spectrophotometer (FTIR), using Bruker Alpha spectrometer. The IR for the pure complex and the film coating on glass substrate, for **47** shows that the complex and its thin film are identical. The thickness of coated film complex **47** and **47** with PVP was evaluated 33.63 μm for complex **47**+PVP and 34.43 μm for complex **47**. Optical properties were investigated for complex **47** film and complex **47** film+ PVP. The transmission in the visible region was 77.68% at λ_{max} 468 nm for copper complex **47** films and 80.56% at λ_{max} 470 nm for complex **47** film+ PVP. The transmission in the NIR region was 3.16 %at λ_{min} 674 nm for copper complex **47** films and 5.96 % at λ_{min} 675 nm for complex **47** film+ PVP. The absorbance in the NIR region was 1.5 at λ_{max} 673 nm for copper complex **47** films and 1.23 at λ_{max} 677 nm for complex **47** film+ PVP. Generally, in the NIR region there is a broad band from 700-1000 nm that is attributed to the d–d transitions of Cu^{2+} and weak absorption in the visible region [478].

Compound **48** was synthesised using $Cu(NO_3)_2$ $3H_2O$, benzylphosphonic acid ($PhCH_2PO(OH)_2$) and 2,2′-bipyridine (bpy) and structurally characterised by single crystal XRD and powder XRD, and investigated optically. Optical studies carried out on compound **48** revealed that it has a broad band absorption in the NIR region in the range 700-1000 nm.

Complex **48** was found to be thermally stable below 207 °C. The optical transmission in the visible region has been found to be 88.16% at λ_{max} 476 nm while the transmission in the NIR region has

been found to be 14.92 % at λ_{min} 700 nm for complex **48**. In the absorption spectra, the absorbance of the NIR region has been found to be 0.82 at λ_{max} 700 nm for complex **48**. Generally, in the NIR region there is a broad band from 700-1000 nm that is attributed to the d–d transitions of Cu^{2+} and weak absorption in the visible region [478].

The film was fabricated on glass substrate and some characterisation was taking place to confimed the coating film on glass. The transmission of the coatings was measured in the middle infrared range by Fourier transform infrared spectrophotometer (FTIR), using Bruker Alpha spectrometer. The IR for the pure complex and the film coating on glass substrate, for **48** shows that the complex and its thin film are identical. The thickness of coated film complex **48** was evaluated 26.78 μm. Optical properties was investigated for complex **48** film. The transmission of complex **48** films in the visible region has been found to be 91.68 % at λ_{max} 461 nm. The transmission of complex **48** films in the NIR region has been found to be 11.66 %at λ_{min} 701 nm. In the absorption spectra, the absorbance of complex **48** films in the NIR region has been found to be 0.95 at λ_{max} 700 nm. Generally, in the NIR region there is a broad band from 700-1000 nm that is attributed to the d–d transitions of Cu^{2+} and weak absorption in the visible region [478].

The optical film was fabricated in order to construct an optical filter cuts off UV and NIR and allow the maximum visible radiation to pass through, together with microwave radiation. Low-emissivity coatings have been made from film of copper complexes **47** and **48**. These coatings exhibit superior solar infrared shielding with high visible transmittance and high environmental durability. It was found that copper complexes **47** and **48** both act as NIR-absorbers while allowing microwave transmission.

Chapter 6. Summary and Conclusions

This doctoral research work has produced compounds exhibiting a wide range of structural motifs and interesting magnetic and optical properties. The obtained results are divided into three chapters; each chapter contains one kind of cluster aggregate. In chapter 3, homometallic lanthanide complexes are discussed, whereas in chapter 4 heterometallic iron-lanthanide complexes (Fe-4*f*) are described while in chapter 5 homometallic copper(II) complexes are explained.

Chapter 3, Thirteen homometallic lanthanide complexes based on amino-polyalcohol ligands have been synthesised and characterised. Among dinuclear and tetranuclear Ln complexes, the crystal structures, optical and magnetic properties of Dy-based compounds have been discussed in detail. Homometallic lanthanide complexes have been synthesised from the reactions of the respective lanthanide cations, amino-polyalcohol ligands and co-ligands (benzoate, Pivalate or *o*-vanillin).

Three different dinuclear series $[Dy_2(H_4bdp)(PhCO_2)_2(NO_3)_2]\cdot NO_3\cdot MeCN$ (**1**), a series of four dinuclear $[Ln_2(PhCO_2)_8(MeOH)_4]$ (**2-5**), four dinuclear $[Ln_2(TipaH_2)_2(Piv)_4]$ (**6-9**) and four tetranuclear compounds $[Ln_4(\mu_3\text{-}OH)_2(o\text{-}van)_4(Piv)_6]\cdot 2MeCN$ **(10-13)** have been successfully synthesised, crystallographically characterised and magnetically studied. These syntheses were carried out under aerobic conditions.

Compound **1** was synthesised using 1,3-bis-diethanolamino-2-propanol (H_5bdp), benzoate and lanthanide nitrate. Moreover, intermolecular hydrogen bonding in compound **1** results in a 2D supermolecular. Magnetic studies carried out on compound **1** shows weak antiferromagnetic interactions. Compound **1** shows slow relaxation of the magnetisation below 6 K under an applied DC field of 2500 Oe. The maximum out-of-phase signal was noticed at 2 K at 2.6 Hz which indicates the presence of SMM behaviour in a compound **1** with energy barrier of 4.38 K and the pre-exponential factor of 8.15×10^{-3} s. The Cole-Cole plots suggest that a single relaxation process exists in compound **1**.

Compounds **2-5** were synthesised using diisopropanolamine ligand, benzoate from ($Fe_3O(PhCO_2)$) and lanthanide nitrate. The diisopropanolamine is a necessary reagent for the isolation of the

compounds in this synthesis. Although diisopropanolamine is not part of the obtained product it could act as a buffer protecting the dysprosium from further hydrolysis. Compound **5** (Ln=Dy^{III}) is further stabilised by intramolecular interaction through hydrogen bonding. These syntheses were carried out under aerobic conditions and products were crystallised in methanol by slow evaporation in air, resulting in dinuclear clusters. Static magnetic studies show the presence of antiferromagnetic interactions in compounds **3** and **5**. Compound **5** exhibits slow relaxation of magnetisation with a maximum peak.

The maximum entropy (-ΔSm) value of 24.44 J kg^{-1} K^{-1} was obtained for compound **3** (Ln=Gd^{III}) with ΔH =7T at 3 K. The MCE observed in **3** may be of the potential interest to the magnetic refrigeration technologies.

Luminescence studies performed on compounds **2** (Ln=Eu^{III}) and **4** (Ln=Tb^{III}) show the emission bands emerging from f–f transitions. This feature is important due to their potential applications as luminescent materials in areas such as: telecommunications, optical amplifiers and sensors.

Compounds **6-9** were synthesised using triisopropanolamine, iron-Pivalate and lanthanide nitrate. Dominant antiferromagnetic interactions are observed. Compound **9** (Ln=Dy^{III}) shows slow relaxation of magnetisation below 10 K under an applied DC field of 1500 Oe. The maximum out-of-phase signal observed at 7 K at 1488 Hz illustrates the SMM behaviour in **9**. Fitting the AC data to an Arrhenius law results in an energy barrier of 22.44 K with the pre-exponential factor of 5.23×10^{-6} s. The Cole-Cole plot suggest that a single relaxation process occurs in compound **9**.

Compounds **10-13** were synthesised using *N*-methyldiethanolamine ($mdeaH_2$), *o*-vanillin (*o*-van), Pivalic acid and respective lanthanide chloride. The *N*-methyldiethanolamine ($mdeaH_2$) is an essential reagent for obtaining the compound. Although *N*-methyldiethanolamine ($mdeaH_2$) is unlisted in the final product, it acts as a base to facilitate the deprotonation of the *o*-vanillin ligand. Tetranuclear compounds **10-13** are isostructural having a "butterfly" motif. Magnetic studies carried out on compound **13** (Ln=Dy^{III}) revealed that antiferromagnetic interactions are dominant. Compound **13** shows no AC signal under zero applied DC field and not even under small-applied DC fields (500-3000 Oe). These results indicate that compound **13** lacks SMM behaviour under these conditions; but it might be a SMM with lower energy barriers or at very low- temperatures

which cannot be measured in a standard SQUID. This can be studied using micro-SQUID at very low, sub Kelvin, temperatures.

Chapter 4, Thirty-three heterometallic iron-lanthanide complexes based on *N*-methyldiethanolamine ($mdeaH_2$) ligands have been synthesised and characterised. Among Fe-Ln complexes, the crystal structures, optical and magnetic properties of tetranuclear and hexanuclear have been discussed in detail. These complexes have been synthesised from the reactions of iron chloride and respective lanthanide cations, *N*-methyldiethanolamine ligand and co-ligand (sodium benzoate, di(2-pyridyl) ketone (dpk), sodium azide and *o*-vanillin).

A series of seven tetranuclear $[Fe_2Ln_2(mdea)_2\{(py)_2C(OCH_3)O\}_2(\mu_4\text{-}O)(N_3)_2(NO_3)_2(CH_3OH)_2]\cdot H_2O$ (**14-20**) nine hexanuclear $[Fe_2Ln_4(mdea)_2(mdeaH)_2(\mu_3\text{-}OH)_2(N_3)_2(PhCO_2)_8]\cdot 3MeCN$ (**21-29**) ten hexanuclear $[Fe_2Ln_4(mdea)_2(o\text{-}van)_2(\mu_4\text{-}O)_2(PhCO_2)_8]\cdot 2\cdot 5MeCN$ (**30-39**) and seven hexanuclear $[Fe_4Ln_2(mdea)_4(PhCO_2)_6(N_3)_2(\mu_3\text{-}OH)_2]\cdot MeCN\cdot H_2O$ (**40-46)** complexes have been successfully synthesised, crystallographically characterised, optically and magnetically studied.

Compounds **14-20** were synthesised using *N*-methyldiethanolamine ($mdeaH_2$), di(2-pyridyl) ketone (dpk), sodium azide (NaN_3), iron chloride and lanthanide nitrate. Tetranuclear compounds **14-20** are isostructural and having a distorted square core. Compound **20** ($Ln=Dy^{III}$) has been further stabilised by intramolecular interaction through hydrogen bonding resulting in a 2D extended structure. Magnetic studies carried out on compound **20** revealed that weak antiferromagnetic interactions are dominant. Compound **20**, shows no AC signals under zero applied DC field but shows slow relaxation without maxima under the small-applied DC field (500-3000 Oe). The results indicate that compound **20** lacks SMM behaviour. It is possible that compound **20** will be a SMM with lower energy barriers or at very low- temperatures which cannot be measured in a standard SQUID but with micro-SQUID at very low, sub Kelvin, temperatures.

Compounds **21-29** were synthesised using *N*-methyldiethanolamine ($mdeaH_2$), sodium benzoate, sodium azide (NaN_3) iron chloride and lanthanide nitrate. Hexanuclear compounds **21-29** are isostructural with a "butterfly" core. Compound **27** ($Ln=Dy^{III}$) has been further stabilised by intramolecular interaction through hydrogen bonds which result in a 1D polymeric structure. Static magnetic studies show the presence of overall ferromagnetic interactions in compounds **26**

(Ln=Tb^{III}) and **27** (Ln=Dy^{III}) were investigated for potential SMM behaviour. Compound **26** shows slow relaxation under zero applied DC field but without maxima even under small-applied DC fields (500-3000 Oe). Compound **27** shows no AC signals under zero applied DC field but shows slow relaxation without maxima under a small-applied DC field (500-3000 Oe). These analyses indicate that both compounds **26** and **27** are lacking SMM behaviour. They might be SMM with lower energy barriers or at very low-temperatures which cannot be measured in a standard SQUID.

The maximum entropy (-ΔSm) value of 27.50 J kg^{-1} K^{-1} was obtained for compound **25** (Ln=Gd^{III}) with ΔH =7T at 4 K. The magnetocaloric properties of **25** could of potential interest in molecular magnetic refrigerant systems.

Luminescence studies performed on compounds **24** (Ln=Eu^{III}) and **26** (Ln=Tb^{III}) shows the emission bands emerging from f–f transitions. Compounds **24** and **26** can acts as luminescence material.

Compounds **30-39** were synthesised using *N*-methyldiethanolamine ($mdeaH_2$), *o*-vanillin (*o*-van), sodium benzoate, iron chloride and lanthanide nitrate. Magnetic studies carried out on compounds **31-33** exhibit weak antiferromagnetic interactions in these compounds. Compound **32** (Ln=Tb^{III}) shows slow relaxation under zero applied DC field but without maxima even under small-applied DC fields (500-3000 Oe). Compound **33** (Ln=Dy^{III}) shows no AC signals under zero applied DC field but shows slow relaxation without maxima peak under a small-applied DC field (500-3000 Oe). The results indicate that both compounds **32** and **33** are lacking SMM behaviour under such conditions. They might be SMM with lower energy barriers or at very low-temperatures which cannot be measured in a standard SQUID but can be examined by micro-SQUID measurements.

The maximum entropy (-ΔSm) value of 18.41 J kg^{-1} K^{-1} was obtained for compound **31** (Ln=Gd^{III}) with ΔH =7T at 5 K. The investigation of magnetocaloric properties in compound **31** exhibits that it might be useful as magnetic cooler.

Compounds **40-46** were synthesised using *N*-methyldiethanolamine ($mdeaH_2$), sodium benzoate, sodium azide (NaN_3) iron chloride and lanthanide chloride. The hexanuclear compounds **40-46** are isostructural and possessing a “butterfly” core. Static magnetic studies show that both

antiferromagnetic and ferromagnetic interactions are dominant in compound **43** (Ln=Dy^{III}). Compound **43** shows slow relaxation of the magnetisation below 5 K under zero an applied DC field. The observation of maximain the out-of-phase signal at 1.8 K at 80.13 Hz indicates the SMM behaviour in **43**. Fitting the AC data to an Arrhenius law results in an energy barrier of 14.19 K with the pre-exponential factor of 1.94×10^{-6} s. The Cole-Cole plots suggest that a single relaxation process occurs in compound **43**. This result provides a path for developing novel molecular devices for information storage and quantum computing.

Luminescence studies performed on compound **40 (**Ln=Eu) shows the emission bands emerging from f–f transitions. Such properties can be of interest in developing light emitting materials.

Chapter 5, Two homometallic copper complexes have been synthesised and characterised. Among Cu complexes, the crystal structures, optical properties have been discussed in detail. These compounds have been synthesised from the reactions of 2,2′-bipyridine (bpy) ligand, benzylphosphonic acid ($PhCH_2PO(OH)_2$) as co-ligand and copper salt. $[Cu_2(bpy)_2(PhCH_2PO_2OH)_4]$ CH_3OH (**47**) and $[Cu_2(bpy)_2(PhCH_2PO_2OH)_2(H_2O)_2]\cdot(NO_3)_2\cdot 4H_2O$ (48) complexes have been successfully synthesised, crystallographically characterised, optically studied. Changing the copper salt allowed to obtained new compound.

Compound **47** (Cu^{II}) was synthesised using $Cu(OAc)_2\cdot H_2O$, benzylphosphonic acid and 2,2′-bipyridine (bpy) has been successfully synthesised and structurally characterised by single crystal XRD, powder XRD, and optically investigated. Compound **47** has been stabilised by intramolecular interaction through hydrogen bonding. Optical studies was investigated on compound **47** revealed that it has a broad band absorption in the range 700-1000 nm which act as NIR-absorbing. The transmission in the visible region has been found to be 87.46 % at λ_{max} 474 nm while the transmission in the NIR region has been found to be 15.17 % at λ_{min} 700 nm. In the absorption spectra, the absorbance of the NIR region has been found to be 0.9 at λ_{max} 700 nm for complex **47**. Complex **47** was found to be thermally stable below 250 °C. Generally, in the NIR region there is a broad band from 700-1000 nm that is attributed to the d–d transitions of Cu^{2+} and weak absorption in the visible region [478].

Complex **47** film was fabricated on glass substrate and some characterisation was taking place to confirm the coating film. The emissivity of the coatings was measured for investigating the optical

properties of thin films in the middle infrared range for the pure complex and the film coating on glass substrate, for **47** shows that the complex and its thin film are identical. The thickness of coated film was evaluated 33.63 μm for complex **47**+PVP and 34.43 μm for complex **47**. Optical properties was investigated on complex **47** film and complex **47** film+ PVP. The transmission in the visible region has been found to be 77.68% at λ_{max} 468 nm for complex **47** films and 80.56% at λ_{max} 470 nm for complex **47** film+ PVP. The transmission in the NIR region has been found to be 3.16 %at λ_{min} 674 nm for copper complex **47** films and 5.96 % at λ_{min} 675 nm for complex **47** film+ PVP. The absorbance in the NIR region has been found to be 1.5 at λ_{max} 673 nm for copper complex **47** films and 1.23 at λ_{max} 677 nm for complex **47** film+ PVP. Generally, in the NIR region there is a broad band from 700-1000 nm that is attributed to the d–d transitions of Cu^{2+} and weak absorption in the visible region [478].

Compound **48** (Cu^{II}) was synthesised using $Cu(NO_3)_2 \cdot 3H_2O$, benzylphosphonic acid ($PhCH_2PO(OH)_2$) and 2,2′-bipyridine (bpy) has been successfully synthesised and structurally characterised by single crystal XRD, powder XRD and optically investigated. Compound **48** has been further stabilised by intra- and intermolecular interaction through hydrogen bonding resulting in a 3D supramolecular. Optical studies was investigated on compound **48** revealed that it has a broad band absorption in the range 700-1000 nm which act as NIR-absorbing. The transmission in the visible region has been found to be 88.16 % at λ_{max} 476 nm while the transmission in the NIR region has been found to be 14.92 % at λ_{min} 700 nm for complex **48**. In the absorption spectra, the absorbance of the NIR region has been found to be 0.82 at λ_{max} 700 nm. Complex **48** was found to be thermally stable below 207 °C.

Complex **48** film was fabricated on glass substrate and some characterisation was taking place to confirm the coating film. The emissivity of the coatings was measured for investigating the optical properties of thin films in the middle infrared range for the pure complex and the film coating on glass substrate, for **48** shows that the complex and its thin film are identical. The thickness of coated film of complex **48** was evaluated 26.78 μm.

Optical properties was investigated of complex **48** film. The transmission of complex **48** films in the visible region has been found to be 91.68 % at λ_{max} 461 nm. The transmission of complex **48** films in the NIR region has been found to be 11.66 %at λ_{min} 701 nm. The absorbance of complex **48** films in the NIR region has been found to be 0.95 at λ_{max} 700 nm. Generally, in the NIR region

there is a broad band from 700-1000 nm that is attributed to the d–d transitions of Cu^{2+} and weak absorption in the visible region [478].

Optical film was fabricated in order construct an optical filter which cut off UV and NIR and allow maximum visible region to pass through. In addition, to allow microwave radiation to pass through without problem. Low-emissivity coatings has made from copper complex **47** and **48** films. These coatings exhibit superior solar infrared shielding with high visible transmittance and high environmental durability.

Generally, in the visible region (400-700 nm) of the spectrum, the transmission is high enough to observe optical interference fringes, due to the transfer of electrons from the valence to the conduction band. In addition, in the NIR region there is a broad band from 700-1000 nm that is attributed to the d–d transitions of Cu^{2+} and weak absorption in the visible region [478]. Complex **47** and **48** were found both act as NIR-absorbing and allow microwave transmission.

Chapter 7. Experimental

All chemicals were sourced commercially through Alfa aesar and were used without further purification. All synthetic procedures were carried out under aerobic conditions using commercial solvents.

7.1. Starting material

7.1.1. Synthesis of inorganic material

7.1.1.1. Synthesis of $[Fe_3O(PhCO_2)_6(H_2O)_3](PhCO_2)$

A solution of iron nitrate $Fe(NO_3)_3 \cdot 9H_2O$ (12.12 g, 30 mmol) in absolute ethanol (50 mL) was added to a second solution of sodium benzoate $PhCO_2Na$ (14.4 g, 100 mmol) in distilled water (90 mL). The combined solutions were stirred for two hours at 60 ˚C followed by a further two hours at room temperature. The product was washed with a combination of water/ethanol/ether (5 /5/5 mL), isolated and dried under vacuum [81].

Elemental analyses calculated (%) for, C 52.40, H 4.02; found: C 51.9, H 3.79.

7.1.1.2. Synthesis of $[Fe_3O(Piv)_6(H_2O)_3](Piv)$

Iron nitrate $Fe(NO_3)_3$. $9H_2O$ (10.0 g, 24.8 mmol) and Pivalic acid (HPiv, 28.0 g, 274.0 mmol) was heated to 200°C whilst stirring for 2h or longer until there was no more gas formation. After the reaction had cooled down to 80 °C, a mixture of ethanol and water (85:15) mL was added slowly whilst stirring for 10 min and then left to stand undisturbed overnight. Red-brown hexagonal prism-shaped crystals appeared. The crystals were collected, washed with hexane and dried under vacuum [85, 90].

Elemental analyses calculated (%) for, C 44.40, H 7.34; found: C 44.04, H 7.21.

7.1.1.3. Synthesis of $Ln(NO_3)_3 \cdot 6H_2O$

A mixture of Ln_2O_3 (15 mg) in H_2O (400 mL) was heated to reach 300 ˚C under stirring. Then Nitric acid (HNO_3 65%) was added dropwise until the oxide fully dissolved and the solution became transparent. Then the solvent was evaporated and the product was collected [88].

7.1.1.4. Synthesis of $LnCl_3 \cdot 6H_2O$

A mixture of Ln_2O_3(15 mg) in H_2O (400 mL) was heated to reach 300 ˚C under stirring. Then Hydrochloric acid (HCl 37%) was added dropwise of until the oxide fully dissolved and the solution became transparent. Then the solvent was evaporated and the product was collected [88].

7.1.2. Synthesis of organic material

7.1.2.1. Synthesis of 1,3-bis-diethanolamino-2-propanol (H_5bdp)

A mixture of diethanolamine (10.5 g, 100 mmol) and epichlorohydrin (9.3 g, 100 mmol) was stirred whilst cooling below 30° for over 2 h. Then an additional amount of diethanolamine (10.5 g, 100 mmol) was added to the reaction. The final reaction was heated on a water bath for 8 h. Then the product was acidified with concentrated hydrochloric acid. After one hour of stirring, the product was extracted with acetone and recrystallised from absolute ethanol [498].

7.2. Synthesis of inorganic complexes

7.2.1. Synthesis of $[Dy_2(H_4bdp)(PhCO_2)_2(NO_3)_2] \cdot NO_3 \cdot MeCN$ (1)

A mixture of 1,3-bis-diethanolamino-2-propanol (H_5bdp) (178 mg, 0.50 mmol), $[Fe_3O(PhCO_2)_6(H_2O)_3](PhCO_2)$ (125 mg, 0.125 mmol) and $Dy(NO_3)_3 \cdot 6H_2O$ (57 mg, 0.125 mmol) was dissolved in of acetonitrile (20 mL). The mixture was stirred at room temperature for 2 h then heated to boiling after which it was cooled to room temperature, filtered and left to stand undisturbed to crystllise via slow evaporation of the solvent. Colourless needles of compound **1** were obtained after three days. The crystals were filtrated and washed with MeCN. Yield; 52% based on Dy.

Elemental analyses calculated (%) of compound **1** (corresponds to a loss of all lattice MeCN): C 30.59, H 3.59, N 7.93; found: C 29.35, H 3.34, N 6.84.

IR: ν (cm^{-1}): 3328(w), 3158(w), 3054(w), 2991(w), 2966(w), 2911(w), 2861(w), 2741(w), 2519(w), 2290(w), 2246(m), 1769(w), 1608(s), 1562(s), 1494(m), 1448(w), 1429(w), 1406(vs), 1344(m), 1270(vs), 1218(w), 1181(w), 1162(m), 1110(m), 1074(m), 1058(w), 1041(w), 1022(vs),

999(m), 949(m), 897(vs), 859(m), 843(w), 807(m), 745(m), 724(vs), 672(s), 639(m), 569(w), 551(m), 509(m), 469(m), 448(w), 432(s).

7.2.2. Synthesis of $[Eu_2(PhCO_2)_8(MeOH)_4]_\infty$ (2)

A mixture of Diisopropanolamine ($dipaH_3$) (133 mg, 1 mmol) $Eu(NO_3)_3.6H_2O$ (112 mg, 0.25 mmol) and $[Fe_3O(PhCO_2)_6(H_2O)_3](PhCO_2)$ (250 mg, 0.25 mmol) was dissolved in methanol (20 mL). The mixture was heated under reflux for 2.5 h after which it was cooled to room temperature, filtered and left to stand undisturbed to crystllise via slow evaporation of the solvent. Colourless needles of compound **2** were obtained after three days. The crystals were filtrated and washed with MeOH. Yield; 32% based on Eu.

Elemental analyses calculated (%) of compound **2**: C 51.10, H 3.82, found: C 50.85, H 3.71.

IR: ν (cm^{-1}): 3648 (w), 3061 (w), 1590 (s), 1528 (vs), 1490 (w), 1409 (w), 1384 (vs), 1302 (w), 1276 (w), 1177 (m), 1148 (w), 1137 (w), 1113 (w), 1071 (m), 1012 (s), 999 (w), 871 (w), 844 (w), 825 (w), 806 (w), 712 (vs), 689 (s), 667 (m), 545 (w), 417 (s).

7.2.3. Synthesis of $[Gd_2(PhCO_2)_8(MeOH)_4]_\infty$ (3)

Compound **3** was prepared in the same way as compound **2** but using $Gd(NO_3)_3{\cdot}6H_2O$ (113 mg, 0.25 mmol) in place of $Eu(NO_3)_3{\cdot}6H_2O$. Yield; 33% based on Gd.

Elemental analyses calculated (%) of compound **3**: C 51.12, H 3.83, found: C 50.92, H 3.77.

IR: ν (cm^{-1}): 3649 (w), 3062 (w), 1589 (s), 1527 (vs), 1491 (w), 1408 (w), 1385 (vs), 1303 (w), 1277 (w), 1176 (m), 1149 (w), 1137 (w), 1114 (w), 1070 (m), 1012 (s), 999 (w), 872 (w), 845 (w), 824 (w), 805 (w), 713 (vs), 688 (s), 667 (m), 544 (w), 416 (s).

7.2.4. Synthesis of $[Tb_2(PhCO_2)_8(MeOH)_2]_\infty$ (4)

Compound **4** was prepared in the same way as compound **2** but using $Tb(NO_3)_3{\cdot}6H_2O$ (113 mg, 0.25 mmol) in place of $Eu(NO_3)_3{\cdot}6H_2O$. Yield; 34% based on Tb.

Elemental analyses calculated (%) of compound **4**: C 50.99, H 3.82, found: C 50.72, H 3.63.

IR: ν (cm^{-1}): 3064(w), 1625 (w), 1589 (s), 1519 (s), 1495 (w), 1410 (vs), 1302 (w), 1177 (m), 1160 (w), 1106 (m), 1068 (m), 1024 (vs), 932 (w), 857 (m), 819 (w), 711 (vs), 683 (w), 670 (m), 553 (m), 522(w), 483 (w), 466 (s), 417 (s).

7.2.5. Synthesis of $[Dy_2(PhCO_2)_8(MeOH)_2]_\infty$ (5)

Compound **5** was prepared in the same way as compound **2** but using $Dy(NO_3)_3 \cdot 6H_2O$ (114 mg, 0.25 mmol) in place of $Eu(NO_3)_3 \cdot 6H_2O$. Yield; 39% based on Dy.

Elemental analyses calculated (%) of compound **5**: C 50.74, H 3.81, found: C 50.42, H 3.57.

IR: ν (cm^{-1}): 3061 (w), 1589 (s), 1523 (vs), 1491 (m), 1442 (m), 1376 (vs), 1305 (w), 1174 (m), 1143 (w), 1067 (m), 1022 (m), 1001 (w), 974 (w), 935 (w), 858 (m), 821 (w), 711 (vs), 680 (s), 666 (m), 560 (w), 470 (w), 421 (s).

7.2.6. Synthesis of $[Eu_2(TipaH_2)_2(Piv)_4]$ (6)

A mixture of Triisopropanolamine ($TipaH_3$) (192 mg, 1 mmol), $Eu(NO_3)_3 \cdot 6H_2O$ (112 mg, 0.25 mmol) and $[Fe_3O(Piv)_6(H_2O)_3] \cdot Piv \cdot$(250 mg, 0.24 mmol) was dissolved in acetonitrile (20 mL). The mixture was stirred at ambient temperature for 10 minutes after which triethylamine (1 mL) was added dropwise to the solution followed by stirring at ambient temperature a further one hour. Then the solution was heated for 10 min to boiling after which it was cooled to room temperature, filtered and left to stand undisturbed to crystallise via slow evaporation of the solvent. Colourless block crystals of compound **6** suitable for X-ray crystallography were obtained after 2 weeks. The crystals were filtrated and washed with MeCN. Yield; 29% based on Eu.

Elemental analyses calculated (%) of compound **6**: C 41.99, H 6.81, N 2.58; found: C 41.82, H 6.73, N 2.54.

IR : ν (cm^{-1}): 3180(br), 2970(m), 2952(w), 2866(w), 1531(s), 1482(s), 1463(w), 1430(vs), 1418(vs), 1359(vs), 1312(m), 1297(w), 1262(w), 1222(vs), 1187(m), 1145(vs), 1123(w), 1072(vs), 1044(vs), 981(vs), 940(m), 896(s), 882(m), 871(s), 840(s), 809(m), 790(s), 750(w), 630(m), 602(s), 573(m), 551(m), 539(w), 495(vs), 478(m), 432(w).

7.2.7. Synthesis of $[Gd_2(TipaH_2)_2(Piv)_4]$ (7)

Compound **7** was prepared in the same way as compound **6** but using $Gd(NO_3)_3 \cdot 6H_2O$ (113 mg, 0.25 mmol) in place of $Eu(NO_3)_3 \cdot 6H_2O$. Yield; 34% based on Gd.

Elemental analyses calculated (%) of compound **7**: C 41.44, H 6.54, N 2.54; found: C 41.22, H 6.49, N 2.46.

IR : ν (cm^{-1}): 3181(br), 2971(m), 2953(w), 2865(w), 1530(s), 1483(s), 1464(w), 1429(vs), 1417(vs), 1358(vs), 1311(m), 1297(w), 1261(w), 1221(vs), 1186(m), 1144(vs), 1124(w), 1073(vs), 1044(vs), 980(vs), 939(m), 896(s), 881(m), 870(s), 841(s), 808(m), 791(s), 751(w), 629(m), 601(s), 572(m), 550(m), 538(w), 495(vs), 479(m), 433(w).

7.2.8. Synthesis of $[Tb_2(TipaH_2)_2(Piv)_4]$ (8)

Compound **8** was prepared in the same way as compound **6** but using $Tb(NO_3)_3 \cdot 6H_2O$ (113 mg, 0.25 mmol) in place of $Eu(NO_3)_3 \cdot 6H_2O$. Yield; 37% based on Tb.

Elemental analyses calculated (%) of compound **8**: C 41.49, H 6.55, N 2.54; found: C 41.29, H 6.43, N 2.47.

IR : ν (cm^{-1}): 3174(br), 2971(m), 2931(w), 2867(w), 1530(s), 1488(s), 1468(w), 1429(vs), 1417(vs), 1362(vs), 1314(m), 1298(w), 1263(w), 1223(vs), 1188(m), 1139(vs), 1127(w), 1071(vs), 1042(vs), 982(vs), 938(m), 894(s), 885(m), 868(s), 835(s), 806(m), 791(s), 755(w), 632(m), 605(s), 579(m), 550(m), 500(vs), 486(m), 446(m), 431(w).

7.2.9. Synthesis of $[Dy_2(TipaH_2)_2(Piv)_4]$ (9)

Compound **9** was prepared in the same way as compound **6** but using $Dy(NO_3)_3 \cdot 6H_2O$ (114 mg, 0.25 mmol) in place of $Eu(NO_3)_3 \cdot 6H_2O$. Yield; 39% based on Dy.

Elemental analyses calculated (%) of compound **9**: C 41.23, H 6.51, N 2.53; found: C 41.03, H 6.40, N 2.50.

IR: ν (cm^{-1}): 3174(w), 2966(m), 2929(w), 2869(w), 1532(s), 1481(s), 1464(w), 1429(vs), 1417(vs), 1358(vs), 1316(m), 1296(w), 1258(w), 1221(vs), 1186(m), 1141(vs), 1126(w), 1071(vs), 1049(vs),

983(vs), 938(m), 896(s), 883(m), 867(s), 841(s), 806(m), 793(s), 760(w), 636(m), 605(s), 579(m), 550(m), 500(vs), 485(m), 435(w).

7.2.10. Synthesis of $[Eu_4(\mu_3\text{-}OH)_2(o\text{-}van)_4(Piv)_6]\cdot 2MeCN$ (10)

A mixture of *N*-methyldiethanolamine ($mdeaH_2$) (149 mg, 1.25 mmol), Pivalic acid (HPiv) (77 mg, 0.75 mmol), *o*-vanillin (*o*-van) (42 mg, 0.275 mmol) and $EuCl_3\cdot 6H_2O$ (94 mg, 0.25 mmol) was dissolved in acetonitrile (20 mL). The mixture was heated under reflux for 2 h after which it was cooled to room temperature, filtered and left to stand undisturbed to crystallise via slow evaporation of the solvent. Yellow single crystals of compound **10** were obtained after two days. The crystals were filtrated and washed with MeCN. Yield; 38% based on Eu.

Elemental analyses calculated (%) of compound **10** (corresponds to a loss of all lattice MeCN): C 50.90, H 4.91, N 9.40; found: C 49.19, H 4.74, N 7.52.

IR: ν (cm^{-1}): 3604 (w), 2950(w), 2918(w), 2866(w), 1686(w), 1647(vs), 1612(m), 1564(s), 1542(m), 1481(m), 1422(vs), 1378(m), 1353(m), 1319(s), 1231(m), 1202 (vs), 1170(w), 1099(m), 1070(m), 955(s), 895(m), 855(m), 811(w), 795(m), 738(w), 727(m), 688(w), 648(m), 607(w), 594(m), 565(w), 550(w), 537(w), 503(w), 451(w).

7.2.11. Synthesis of $[Gd_4(\mu_3\text{-}OH)_2(o\text{-}van)_4(Piv)_6]\cdot 2MeCN$ (11)

Compound **11** was prepared in the same way as compound **10** but using $Gd(NO_3)_3\cdot 6H_2O$ (113 mg, 0.25 mmol) in place of $Eu(NO_3)_3\cdot 6H_2O$. Yield; 41% based on Gd.

Elemental analyses calculated (%) of compound **11** (corresponds to a loss of all lattice MeCN): C 50.35, H 4.86, N 9.30; found: C 48.74, H 4.70, N 7.48.

IR: ν (cm^{-1}): 3602 (w), 2948(w), 2918(w), 2864(w), 1684(w), 1648(vs), 1612(m), 1563(s), 1543(m), 1482(m), 1423(vs), 1377(m), 1352(m), 1319(s), 1230(m), 1205 (vs), 1172(w), 1097(m), 1072(m), 956(s), 897(m), 855(m), 812(w), 795(m), 739(w), 724(m), 689(w), 648(m), 610(w), 595(m), 566(w), 552(w), 537(w), 504(w), 454(w).

7.2.12. Synthesis of $[Tb_4(\mu_3\text{-}OH)_2(o\text{-}van)_4(Piv)_6]\cdot 2MeCN$ (12)

Compound **12** was prepared in the same way as compound **10** but using $Tb(NO_3)_3\cdot 6H_2O$ (113 mg, 0.25 mmol) in place of $Eu(NO_3)_3\cdot 6H_2O$. Yield; 37% based on Tb.

Elemental analyses calculated (%) of compound **12** (corresponds to a loss of all lattice MeCN): C 50.18, H 4.84, N 9.27; found: C 48.57, H 4.68, N 7.45.

IR: ν (cm^{-1}): 3601 (w), 2949(w), 2919(w), 2864(w), 1685(w), 1649(vs), 1613(m), 1563(s), 1540(m), 1482(m), 1422(vs), 1378(m), 1353(m), 1320(s), 1230(m), 1205 (vs), 1170(w), 1098(m), 1069 (m), 956(s), 897(m), 855(m), 811(w), 795(m), 739(w), 726(m), 688(w), 649(m), 610(w), 595(m), 566(w), 552(w), 537(w), 504(w), 453(w).

7.2.13. Synthesis of $[Dy_4(\mu_3\text{-}OH)_2(o\text{-}van)_4(Piv)_6]\cdot 2MeCN$ (13)

Compound **13** was prepared in the same way as compound **10** but using $Dy(NO_3)_3\cdot 6H_2O$ (114 mg, 0.25 mmol) in place of $Eu(NO_3)_3\cdot 6H_2O$. Yield; 42% based on Dy.

Elemental analyses calculated (%) of compound **13** (corresponds to a loss of all lattice MeCN): C 49.81, H 4.80, N 9.20; found: C 48.20, H 4.65, N 7.39.

IR: ν (cm^{-1}): 3603 (w), 2948(w), 2917(w), 2866(w), 1685(w), 1648(vs), 1611(m), 1563(s), 1541(m), 1480(m), 1422(vs), 1377(m), 1353(m), 1319(s), 1230(m), 1204 (vs), 1171(w), 1099(m), 1071(m), 956(s), 896(m), 855(m), 810(w), 795(m), 738(w), 726(m), 688(w), 648(m), 609(w), 595(m), 565(w), 552(w), 536(w), 504(w), 452(w).

7.2.14. Synthesis of $[Fe_2Pr_2(mdea)_2\{(py)_2C(OCH_3)O\}_2(\mu_4\text{-}O)(N_3)_2(NO_3)_2(CH_3OH)_2]\cdot H_2O$ (14)

A mixture of *N*-methyl diethanolamine ($mdeaH_2$) (149 mg, 1.25 mmol), $FeCl_3$ anhydrous (41 mg, 0.25 mmol), sodium azide (NaN_3) (49 mg, 0.75 mmol), 2,2′-Dipyridyl ketone(dpk) (51 mg, 0.275 mmol) and $Pr(NO_3)_3\cdot 6H_2O$ (109 mg, 0.25 mmol) was dissolved in a mixture of methanol /acetonitrile (20 mL, 1:1). The solution was heated under reflux for two hours after which it was cooled to room temperature, filtered and left to stand undisturbed to crystallise via slow evaporation of the solvent. Brown block crystals of compound **14** were obtained overnight. The crystals were filtrated and washed with MeCN / MeOH. Yield; 28% based on Pr.

Elemental analyses calculated (%) of compound **14**, C 31.66, H 3.96, N 14.36; found: C 31.49, H 3.79, N 14.17.

IR: ν (cm^{-1}): 3380(w), 2909(w), 2870(m), 2826(w), 2054(vs), 1603(m), 1573(w), 1432(vs), 1350(w), 1289(s), 1262(m), 1221(s), 1154(w), 1107(m), 1047(vs), 983(m), 952(w), 893(s), 820(m), 785(m), 762(w), 684(vs), 647(m), 620(s), 569(m), 520(m), 512(w), 490(w), 474(m), 421(w).

7.2.15. Synthesis of $[Fe_2Nd_2(mdea)_2\{(py)_2C(OCH_3)O\}_2(\mu_4\text{-}O)(N_3)_2(NO_3)_2(CH_3OH)_2]\ H_2O$(15)

Compound **15** was prepared in the same way as compound **14** but using $Nd(NO_3)_3\cdot 6H_2O$ (110 mg, 0.25 mmol) in place of $Pr(NO_3)_3\cdot 6H_2O$. Yield; 30 % based on Nd.

Elemental analyses calculated (%) of compound **15**, C 31.51, H 3.94,N 14.30; found : C 31.35, H 3.79, N 14.15

IR: ν (cm^{-1}): 3381(w), 2906(w), 2868(m), 2820(w), 2054(vs), 1600(m), 1573(w), 1432(vs), 1353(w), 1289(s), 1259(m), 1221(s), 1157(w), 1107(m), 1047(vs), 980(m), 952(w), 893(s), 821(m), 785(m), 762(w), 684(vs), 647(m), 620(s), 569(m), 520(m), 512(w), 490(w), 474(m), 421(w).

7.2.16. Synthesis of $[Fe_2Sm_2(mdea)_2\{(py)_2C(OCH_3)O\}_2(\mu_4\text{-}O)(N_3)_2(NO_3)_2(CH_3OH)_2]\ H_2O$(16)

Compound **16** was prepared in the same way as compound **14** but using $Sm(NO_3)_3\cdot 6H_2O$ (111 mg, 0.25 mmol) in place of $Pr(NO_3)_3\cdot 6H_2O$. Yield; 31 % based on Sm.

Elemental analyses calculated (%) of compound **16**, C 31.23, H 3.90,N 14.17; found :C 31.06, H 3.78, N 13.95.

IR: ν (cm^{-1}): 3383(w), 2906(w), 2864(m), 2826(w), 2058(vs), 1601(m), 1570(w), 1435(vs), 1350(w), 1303(s), 1258(m), 1228(s), 1154(w), 1107(m), 1054(vs), 983(m), 952(w), 897(s), 817(m), 781(m), 765(w), 685(vs), 646(m), 622(s), 571(m), 522(m), 510(w), 497(w), 478(m), 422(w).

7.2.17. Synthesis of $[Fe_2Eu_2(mdea)_2\{(py)_2C(OCH_3)O\}_2(\mu_4\text{-}O)(N_3)_2(NO_3)_2(CH_3OH)_2]\ H_2O$ (17)

Compound **17** was prepared in the same way as compound **14** but using $Eu(NO_3)_3{\cdot}6H_2O$ (112 mg, 0.25 mmol) in place of $Pr(NO_3)_3{\cdot}6H_2O$. Yield; 32 % based on Eu.

Elemental analyses calculated (%) of compound **17**, C 31.16, H 3.89,N 14.14 ; found: C 30.98, H 3.87, N 13.98.

IR: ν (cm^{-1}): 3387(w), 2909(w), 2867(m), 2825(w), 2061(vs), 1603(m), 1573(w), 1435(vs), 1350(w), 1305(s), 1258(m), 1225(s), 1156(w), 1107(m), 1052(vs), 983(m), 955(w), 896(s), 817(m), 784(m), 765(w), 687(vs), 648(m), 624(s), 571(m), 524(m), 512(w), 494(w), 475(m), 422(w).

7.2.18. Synthesis of $[Fe_2Gd_2(mdea)_2\{(py)_2C(OCH_3)O\}_2(\mu_4\text{-}O)(N_3)_2(NO_3)_2(CH_3OH)_2]H_2O$ (18)

Compound **18** was prepared in the same way as compound **14** but using $Gd(NO_3)_3{\cdot}6H_2O$ (113 mg, 0.25 mmol) in place of $Pr(NO_3)_3{\cdot}6H_2O$. Yield; 35 % based on Gd.

Elemental analyses calculated (%) of compound **18**, C 30.92, H 3.87, N 14.03; found: C 30.50, H 4.04, N 13.94.

IR: ν (cm^{-1}): 3391(w), 2915(w), 2872(m), 2826(w), 2060(vs), 1601(m), 1570(w), 1432(vs), 1350(w), 1305(s), 1256(m), 1228(s), 1156(w), 1107(m), 1054(vs), 983(m), 958(w), 894(s), 817(m), 781(m), 762(w), 687(vs), 649(m), 624(s), 569(m), 523(m), 512(w), 500(w), 472(m), 422(w).

7.2.19. Synthesis of $[Fe_2Tb_2(mdea)_2\{(py)_2C(OCH_3)O\}_2(\mu_4\text{-}O)(N_3)_2(NO_3)_2(CH_3OH)_2]\ H_2O$ (19)

Compound **19** was prepared in the same way as compound **14** but using $Tb(NO_3)_3{\cdot}6H_2O$ (113 mg, 0.25 mmol) in place of $Pr(NO_3)_3{\cdot}6H_2O$. Yield; 38 % based on Tb.

Elemental analyses calculated (%) of compound **19**, C 30.85, H 3.86,N 14.00; found: C 30.29, H 3.80, N 13.70.

IR: ν (cm^{-1}): 3391(w), 2917(w), 2872(m), 2824(w), 2062(vs), 1601(m), 1574(w), 1435(vs), 1352(w), 1307(s), 1258(m), 1228(s), 1154(w), 1109(m), 1052(vs), 983(m), 958(w), 894(s),

820(m), 784(m), 764(w), 686(vs), 649(m), 625(s), 569(m), 525(m), 512(w), 500(w), 472(m), 422(w).

7.2.20. Synthesis of $[Fe_2Dy_2(mdea)_2\{(py)_2C(OCH_3)O\}_2(\mu_4\text{-}O)(N_3)_2(NO_3)_2(CH_3OH)_2]\ H_2O$ (20)

Compound **20** was prepared in the same way as compound **14** but using $Dy(NO_3)_3{\cdot}6H_2O$ (114 mg, 0.25 mmol) in place of $Pr(NO_3)_3{\cdot}6H_2O$. Yield; 39 % based on Dy.

Elemental analyses calculated (%) of compound **20**, C 30.69, H 3.84,N 13.92; found: C 29.34, H 3.81, N 13.43

IR: ν (cm^{-1}): 3391(w), 2917(w), 2872(m), 2826(w), 2064(vs), 1598(m), 1573(w), 1434(vs), 1352(w), 1308(s), 1258(m), 1228(s), 1156(w), 1107(m), 1052(vs), 983(m), 958(w), 894(s), 820(m), 781(m), 762(w), 690(vs), 651(m), 627(s), 571(m), 525(m), 512(w), 500(w), 475(m), 422(w).

7.2.21. Synthesis of $[Fe_2Pr_4(mdea)_2(mdeaH)_2(\mu_3\text{-}OH)_2(N_3)_2(PhCO_2)_8]{\cdot}3MeCN$ (21)

A mixture of *N*-methyl diethanolamine ($mdeaH_2$) (149 mg, 1.25 mmol), $FeCl_3$ anhydrous (41 mg, 0.25 mmol), sodium benzoate ($PhCO_2Na$) (108 mg, 0.75 mmol), sodium azide (NaN_3) (49 mg, 0.75 mmol) and $Pr(NO_3)_3.6H_2O$ (109 mg, 0.25 mmol) was dissolved in acetonitrile (20 mL). The solution was heated under reflux for 2h after which it was cooled to room temperature, filtered and left to stand undisturbed to crystallise via slow evaporation of the solvent. Yellow needles of compound **21** were obtained after overnight. The crystals were filtrated and washed with MeCN. Yield; 37% based on Pr.

Elemental analyses calculated (%) of compound **21** (corresponds to a loss of all lattice MeCN): C 40.88, H 3.94, N 6.27; found: C 40.75, H 3.22, N 6.21

IR: ν (cm^{-1}): 2861 (w), 2061 (s), 1597 (s), 1556 (s), 1535 (s), 1395 (vs), 1338 (m), 1258 (w), 1198 (w), 1173 (w), 1141 (w), 1067 (m), 1024 (m), 996 (m), 888 (m), 869 (w), 836 (w), 756 (w), 716 (vs), 690 (m), 671 (s), 640 (m), 568 (m), 501 (m), 419 (s).

7.2.22. Synthesis of $[Fe_2Nd_4(mdea)_2(mdeaH)_2(\mu_3\text{-}OH)_2(N_3)_2(PhCO_2)_8]\cdot 3MeCN$ (22)

Compound **22** was prepared in the same way as compound **21** but using $Nd(NO_3)_3\cdot 6H_2O$ (110 mg, 0.25 mmol) in place of $Pr(NO_3)_3\cdot 6H_2O$. Yield; 40 % based on Nd.

Elemental analyses calculated (%) of compound **22** (corresponds to a loss of all lattice MeCN): C 40.64, H 3.91, N 6.24; found: C 40.47, H 3.78, N 6.22.

IR: ν (cm^{-1}): 2864 (w), 2060 (s), 1599 (s), 1556 (s), 1535 (s), 1399 (vs), 1338 (m), 1256 (w), 1198 (w), 1176 (w), 1143 (w), 1067 (m), 1024 (m), 999 (m), 895 (m), 865 (w), 836 (w), 756 (w), 715 (vs), 690 (m), 672 (s), 643 (m), 570 (m), 500 (m), 419 (s).

7.2.23. Synthesis of $[Fe_2Sm_4(mdea)_2(mdeaH)_2(\mu_3\text{-}OH)_2(N_3)_2(PhCO_2)_8]\cdot 3MeCN$ (23)

Compound **23** was prepared in the same way as compound **21** but using $Sm(NO_3)_3\cdot 6H_2O$ (111 mg, 0.25 mmol) in place of $Pr(NO_3)_3\cdot 6H_2O$. Yield; 43 % based on Sm.

Elemental analyses calculated (%) of compound **23** (corresponds to a loss of all lattice MeCN): C 40.20, H 3.87, N 6.16; found: C 40.04, H 3.78, N 6.09.

IR: ν (cm^{-1}): 2864 (w), 2059 (s), 1601 (s), 1562 (s), 1536 (s), 1395 (vs), 1336 (m), 1258 (w), 1201 (w), 1175 (w), 1140 (w), 1067 (m), 1027 (m), 999 (m), 895 (m), 871 (w), 836 (w), 755 (w), 715 (vs), 690 (m), 672 (s), 640 (m), 576 (m), 502 (m), 419 (s).

7.2.24. Synthesis of $[Fe_2Eu_4(mdea)_2(mdeaH)_2(\mu_3\text{-}OH)_2(N_3)_2(PhCO_2)_8]\cdot 3MeCN$ (24)

Compound **24** was prepared in the same way as compound **21** but using $Eu(NO_3)_3\cdot 6H_2O$ (112 mg, 0.25 mmol) in place of $Pr(NO_3)_3\cdot 6H_2O$. Yield; 44% based on Eu.

Elemental analyses calculated (%) of compound **24** (corresponds to a loss of all lattice MeCN): C 40.09, H 3.86, N 6.15; found: C 39.95, H 3.79, N 6.13

IR: ν (cm^{-1}): 2864 (w), 2064 (s), 1601 (s), 1562 (s), 1541 (s), 1402 (vs), 1338 (m), 1256 (w), 1201 (w), 1176 (w), 1143 (w), 1068 (m), 1027 (m), 999 (m), 897 (m), 869 (w), 834 (w), 754 (w), 718 (vs), 690 (m), 674 (s), 640 (m), 570 (m), 503 (m), 422 (s).

7.2.25. Synthesis of $[Fe_2Gd_4(mdea)_2(mdeaH)_2(\mu_3\text{-}OH)_2(N_3)_2(PhCO_2)_8]\cdot 3MeCN$ (25)

Compound **25** was prepared in the same way as compound **21** but using $Gd(NO_3)_3\cdot 6H_2O$ (113 mg, 0.25 mmol) in place of $Pr(NO_3)_3\cdot 6H_2O$. Yield; 53 % based on Gd.

Elemental analyses calculated (%) for of compound **25** (corresponds to a loss of all lattice MeCN): C 39.72, H 3.82, N 6.09; found: C 39.56, H 3.69, N 6.04

IR: ν (cm^{-1}): 2861 (w), 2061 (s), 1601 (s), 1565 (s), 1540 (s), 1395 (vs), 1338 (m), 1258 (w), 1201 (w), 1176 (w), 1143 (w), 1069 (m), 1027(m), 999 (m), 898 (m), 867 (w), 837 (w), 754 (w), 717 (vs), 690 (m), 673 (s), 638 (m), 570 (m), 504 (m), 422 (s).

7.2.26. Synthesis of $[Fe_2Tb_4(mdea)_2(mdeaH)_2(\mu_3\text{-}OH)_2(N_3)_2(PhCO_2)_8]\cdot 3MeCN$ (26)

Compound **26** was prepared in the same way as compound **21** but using $Tb(NO_3)_3\cdot 6H_2O$ (113 mg, 0.25 mmol) in place of $Pr(NO_3)_3\cdot 6H_2O$. Yield; 47 % based on Tb.

Elemental analyses calculated (%) of compound **26** (corresponds to a loss of all lattice MeCN): C 39.61, H 3.81, N 6.07; found: C 39.44, H 3.72, N 6.02

IR: ν (cm^{-1}): 2864 (w), 2059 (s), 1606 (s), 1567 (s), 1540 (s), 1399 (vs), 1338 (m), 1256 (w), 1201 (w), 1177 (w), 1145 (w), 1068 (m), 1027 (m), 999 (m), 897 (m), 868 (w), 839 (w), 756 (w), 718 (vs), 690 (m), 676 (s), 640 (m), 574 (m), 505 (m), 422 (s).

7.2.27. Synthesis of $[Fe_2Dy_4(mdea)_2(mdeaH)_2(\mu_3\text{-}OH)_2(N_3)_2(PhCO_2)_8]\cdot 3MeCN$ (27)

Compound **27** was prepared in the same way as compound **21** but using $Dy(NO_3)_3\cdot 6H_2O$ (114 mg, 0.25 mmol) in place of $Pr(NO_3)_3\cdot 6H_2O$. Yield; 50 % based on Pr.

Elemental analyses calculated (%) of compound **27** (corresponds to a loss of all lattice MeCN) : C 39.36, H 3.79,N 6.03; found: C 39.26, H 3.66, N 6.02.

IR: ν (cm^{-1}): 2864 (w), 2062 (s), 1606 (s), 1565 (s), 1543 (s), 1392 (vs), 1338 (m), 1256 (w), 1198 (w), 1176 (w), 1145 (w), 1069 (m), 1024 (m), 999 (m), 897 (m), 869 (w), 839 (w), 754 (w), 718 (vs), 690 (m), 671 (s), 649 (m), 571 (m), 505 (m), 422 (s).

7.2.28. Synthesis of $[Fe_2Ho_4(mdea)_2(mdeaH)_2(\mu_3\text{-}OH)_2(N_3)_2(PhCO_2)_8]\cdot 3MeCN$ (28)

Compound **28** was prepared in the same way as compound **21** but using $HoCl_3\cdot 6H_2O$ (95 mg, 0.25 mmol) in place of $Pr(NO_3)_3\cdot 6H_2O$. Yield; 41 % based on Ho.

Elemental analyses calculated (%) of compound **28** (corresponds to a loss of all lattice MeCN): C 39.19, H 3.77, N 6.01; found: C 39.06, H 3.66, N 6.02

IR: ν (cm^{-1}): 2864 (w), 2060 (s), 1605 (s), 1568 (s), 1541 (s), 1394 (vs), 1338 (m), 1257 (w), 1198 (w), 1176 (w), 1145 (w), 1065 (m), 1025 (m), 999 (m), 896 (m), 868 (w), 837 (w), 755 (w), 717 (vs), 689 (m), 670 (s), 649 (m), 571 (m), 505 (m), 424 (s).

7.2.29. Synthesis of $[Fe_2Y_4(mdea)_2(mdeaH)_2(\mu_3\text{-}OH)_2(N_3)_2(PhCO_2)_8]\cdot 3MeCN$ (29)

Compound **29** was prepared in the same way as compound **21** but using $Y(NO_3)_3\cdot 6H_2O$ (96 mg, 0.25 mmol) in place of $Pr(NO_3)_3\cdot 6H_2O$. Yield; 36 % based on Y.

Elemental analyses calculated (%) of compound **29** (corresponds to a loss of all lattice MeCN): C 45.08, H 4.34, N 6.92; found: C 44.95, H 4.25, N 6.85

IR: ν (cm^{-1}): 2864 (w), 2059 (s), 1605 (s), 1570 (s), 1541 (s), 1397 (vs), 1338 (m), 1258 (w), 1198 (w), 1176 (w), 1145 (w), 1067 (m), 1025 (m), 999 (m), 897 (m), 867 (w), 832 (w), 758 (w), 715 (vs), 687 (m), 674 (s), 640 (m), 572 (m), 505 (m), 425 (s).

7.2.30. Synthesis of $[Fe_2Eu_4(mdea)_2(o\text{-}van)_2(\mu_4\text{-}O)_2(PhCO_2)_8]\cdot 2\cdot 5MeCN$ (30)

A mixture of *N*-methyldiethanolamine ($mdeaH_2$) (149 mg, 1.25 mmol), $FeCl_3$ anhydrous (41 mg, 0.25 mmol), sodium benzoate ($PhCO_2Na$) (108 mg, 0.75 mmol), *o*-vanillin (*o*-van) (42 mg, 0.275 mmol) and $Eu(NO_3)_3\cdot 6H_2O$ (113 mg, 0.25 mmol) was dissolved in acetonitrile (20 mL). The solution was heated under reflux for 2 h after which it was cooled to room temperature, filtered and left to stand undisturbed to crystallise via slow evaporation of the solvent. Yellow single crystals of compound **30** were obtained in 3 days. The crystals were filtrated and washed with MeCN. Yield; 37% based on Eu.

Elemental analyses calculated (%) of compound **30** (corresponds to a loss of all lattice MeCN): C 43.59, H 3.37, N 1.24; found: C 43.29, H 3.26, N 1.20.

IR: ν (cm^{-1}): 3064 (w), 2841 (w), 1649 (m), 1598 (s), 1562 (s), 1545 (s), 1490 (m), 1463 (w), 1449 (w), 1397 (vs), 1307 (m), 1265 (w), 1244 (m), 1204 (s), 1169 (w), 1091 (s), 1064 (w), 1025 (m), 998 (m), 958 (m), 903 (m), 855 (m), 817 (w), 783 (w), 755 (m), 717 (vs), 690 (s), 670 (s), 631 (m), 606 (vs), 584 (w), 548 (m), 502 (m), 461 (w), 417 (m).

7.2.31. Synthesis of $[Fe_2Gd_4(mdea)_2(o\text{-van})_2(\mu_4\text{-}O)_2(PhCO_2)_8]\cdot 2\cdot 5MeCN$ (31)

Compound **31** was prepared in the same way as compound **30** but using $Gd(NO_3)_3\cdot 6H_2O$ (113 mg, 0.25 mmol) in place of $Eu(NO_3)_3\cdot 6H_2O$. Yield; 31% based on Gd.

Elemental analyses calculated (%) of compound **31** (corresponds to a loss of all lattice MeCN): C 43.19, H 3.35, N 1.22; found: C 42.94, H 3.23, N 1.20.

IR: ν (cm^{-1}): 3062 (w), 2843 (w), 1650 (m), 1598 (s), 1561 (s), 1548 (s), 1491 (m), 1465 (w), 1446 (w), 1398 (vs), 1305 (m), 1263 (w), 1242 (m), 1207 (s), 1170 (w), 1090 (s), 1066 (w), 1027 (m), 999 (m), 958 (m), 901 (m), 856 (m), 819 (w), 784 (w), 756 (m), 717 (vs), 691 (s), 671 (s), 630 (m), 604 (vs), 582 (w), 547 (m), 504 (m), 463 (w), 417 (m).

7.2.32. Synthesis of $[Fe_2Tb_4(mdea)_2(o\text{-van})_2(\mu_4\text{-}O)_2(PhCO_2)_8]\cdot 2\cdot 5MeCN$ (32)

Compound **32** was prepared in the same way as compound **30** but using $Tb(NO_3)_3\cdot 6H_2O$ (113 mg, 0.25 mmol) in place of $Eu(NO_3)_3\cdot 6H_2O$. Yield; 31% based on Tb.

Elemental analyses calculated (%) of compound **32** (corresponds to a loss of all lattice MeCN): C 43.06, H 3.32, N 1.22; found: C 42.97, H 3.31, N 1.18.

IR: ν (cm^{-1}): 3062(w), 2843(w), 1650(m), 1595(s), 1561(s), 1546(s), 1493(m), 1467(w), 1446(w), 1401(vs), 1307(m), 1261(w), 1237(m), 1207(s), 1170(w), 1096(s), 1070(w), 1025(m), 999(m), 955(m), 897(m), 853(m), 819(w), 782(w), 749(m), 714(vs), 688(s), 671(s), 630(m), 597(vs), 578 (w), 547(m), 506(m), 463(w), 417(m).

7.2.33. Synthesis of $[Fe_2Dy_4(mdea)_2(o\text{-van})_2(\mu_4\text{-}O)_2(PhCO_2)_8]\cdot 2\cdot 5MeCN$ (33)

Compound **33** was prepared in the same way as compound **30** but using $Dy(NO_3)_3\cdot 6H_2O$ (114 mg, 0.25 mmol) in place of $Eu(NO_3)_3\cdot 6H_2O$. Yield; 30 % based on Dy.

Elemental analyses calculated (%) of compound **33** (corresponds to a loss of all lattice MeCN): C 42.79, H 3.30,N 1.21; found : C 42.74, H 3.30, N 1.19

IR : *v* (cm^{-1}): 3054 (w), 2846 (w), 1648 (m), 1600 (s), 1561 (s), 1544 (s), 1494 (m), 1466 (w), 1444 (w), 1401 (vs), 1309 (m), 1259 (w), 1242 (m), 1211 (s), 1173 (w), 1097 (s), 1070 (w), 1027 (m), 999 (m), 958 (m), 899 (m), 853 (m), 819 (w), 784 (w), 756 (m), 717 (vs), 683 (s), 669 (s), 626 (m), 604 (vs), 580 (w), 550 (m), 506 (m), 463 (w), 417 (m).

7.2.34. Synthesis of $[Fe_2Ho_4(mdea)_2(o\text{-van})_2(\mu_4\text{-}O)_2(PhCO_2)_8]\cdot 2\cdot 5MeCN$ (34)

Compound **34** was prepared in the same way as compound **30** but using $Ho(NO_3)_3\cdot 6H_2O$ (115 mg, 0.25 mmol) in place of $Eu(NO_3)_3\cdot 6H_2O$. Yield; 30% based on Ho.

Elemental analyses calculated (%) of compound **34** (corresponds to a loss of all lattice MeCN): C 42.61, H 3.29, N 1.21; found: C 42.40, H 3.19, N 1.18.

IR: *v* (cm^{-1}): 3065 (w), 2858 (w), 1648 (m), 1600 (s), 1559 (s), 1562 (s), 1491 (m), 1474 (w), 1441 (w), 1405 (vs), 1313 (m), 1261 (w), 1240 (m), 1209 (s), 1170 (w), 1094 (s), 1068 (w), 1025 (m), 999 (m), 959 (m), 901 (m), 851 (m), 816 (w), 780 (w), 751 (m), 717 (vs), 693 (s), 675 (s), 640 (m), 600 (vs), 584 (w), 552 (m), 504 (m), 469 (w), 417 (m).

7.2.35. Synthesis of $[Fe_2Er_4(mdea)_2(o\text{-van})_2(\mu_4\text{-}O)_2(PhCO_2)_8]\cdot 2\cdot 5MeCN$ (35)

Compound **35** was prepared in the same way as compound **30** but using $Er(NO_3)_3\cdot 6H_2O$ (115 mg, 0.25 mmol) in place of $Eu(NO_3)_3\cdot 6H_2O$. Yield; 32% based on Er.

Elemental analyses calculated (%) of compound **35** (corresponds to a loss of all lattice MeCN): C 42.44, H 3.27, N 1.20; found: C 42.331, H 3.11, N 1.18.

IR: *v* (cm^{-1}): 3065 (w), 2843 (w), 1652 (m),1602 (s), 1563 (s), 1548 (s), 1493 (m), 1465 (w),1444 (w), 1409 (vs), 1309 (m), 1263 (w), 1240 (m), 1211 (s), 1173 (w), 1094 (s), 1070 (w), 1027 (m), 1000 (m), 955 (m), 901 (m), 851 (m), 819 (w), 786 (w), 756 (m), 717 (vs), 688 (s), 669 (s), 630 (m), 604 (vs), 578 (w), 552 (m), 506 (m), 467 (w), 417 (m).

7.2.36. Synthesis of $[Fe_2Tm_4(mdea)_2(o\text{-van})_2(\mu_4\text{-}O)_2(PhCO_2)_8]\cdot 2\cdot 5MeCN$ (36)

Compound **36** was prepared in the same way as compound **30** but using $Tm(NO_3)_3\cdot 6H_2O$ (116 mg, 0.25 mmol) in place of $Eu(NO_3)_3\cdot 6H_2O$. Yield; 34% based on Tm.

Elemental analyses calculated (%) of compound **36** (corresponds to a loss of all lattice MeCN): C 42.32, H 3.26, N 1.20; found: C 42.24, H 3.23, N 1.15.

IR: ν (cm^{-1}): 3060 (w), 2843 (w), 1650 (m), 1599 (s), 1563 (s), 1548 (s), 1491 (m), 1467 (w), 1448 (w), 1400 (vs), 1307 (m), 1261 (w), 1242 (m), 1214 (s), 1170 (w), 1092 (s), 1068 (w), 1029 (m), 999 (m), 964 (m), 899 (m), 856 (m), 816 (w), 784 (w), 751 (m), 719 (vs), 691 (s), 673 (s), 632 (m), 605 (vs), 578 (w), 547 (m), 508 (m), 469 (w), 417 (m).

7.2.37. Synthesis of $[Fe_2Yb_4(mdea)_2(o\text{-van})_2(\mu_4\text{-}O)_2(PhCO_2)_8]\cdot 2\cdot 5MeCN$ (37)

Compound **37** was prepared in the same way as compound **30** but using $Yb(NO_3)_3\cdot 6H_2O$ (117 mg, 0.25 mmol) in place of $Eu(NO_3)_3\cdot 6H_2O$. Yield; 28% based on Yb.

Elemental analyses calculated (%) of compound **37** (corresponds to a loss of all lattice MeCN): C 42.02, H 3.24, N 1.19; found: C 41.89, H 3.19, N 1.17.

IR: ν (cm^{-1}): 3062 (w), 2848 (w), 1648 (m), 1600 (s), 1563 (s), 1550 (s), 1491 (m), 1470 (w), 1441 (w), 1400 (vs), 1307 (m), 1261 (w), 1245 (m), 1211 (s), 1172 (w), 1096 (s), 1070 (w), 1027 (m), 999 (m), 962 (m), 901 (m), 853 (m), 836 (w), 816 (w), 786 (w), 754 (m), 719 (vs), 691 (s), 669 (s), 632 (m), 608 (vs), 586 (w), 552 (m), 510 (m), 471 (w), 417 (m).

7.2.38. Synthesis of $[Fe_2Lu_4(mdea)_2(o\text{-van})_2(\mu_4\text{-}O)_2(PhCO_2)_8]\cdot 2\cdot 5MeCN$ (38)

Compound **38** was prepared in the same way as compound **30** but using $Lu(NO_3)_3\cdot 6H_2O$ (117 mg, 0.25 mmol) in place of $Eu(NO_3)_3\cdot 6H_2O$. Yield; 27% based on Lu.

Elemental analyses calculated (%) of compound **38** (corresponds to a loss of all lattice MeCN): C 41.88, H 3.23, N 1.19; found: C 41.51, H 3.15, N 1.14.

IR: ν (cm^{-1}): 3060 (w), 2841 (w), 1648 (m), 1600 (s), 1563 (s), 1552 (s), 1494 (m), 1467 (w), 1446 (w), 1407 (vs), 1311 (m), 1263 (w), 1240 (m), 1209 (s), 1171 (w), 1094 (s), 1073 (w), 1025 (m),

999 (m), 958 (m), 900 (m), 851 (m), 819 (w), 784 (w), 751 (m), 719 (vs), 688 (s), 671 (s), 636 (m), 612 (vs), 584 (w), 552 (m), 506 (m), 476 (w), 417 (m).

7.2.39. Synthesis of $[Fe_2Y_4(mdea)_2(o\text{-van})_2(\mu_4\text{-}O)_2(PhCO_2)_8]\cdot 2\cdot 5MeCN$ (39)

Compound **39** was prepared in the same way as compound **30** but using $Y(NO_3)_3\cdot 6H_2O$ (96 mg, 0.25 mmol) in place of $Eu(NO_3)_3\cdot 6H_2O$. Yield; 38% based on Y.

Elemental analyses calculated (%) of compound **39** (corresponds to a loss of all lattice MeCN): C 49.08, H 3.79, N 1.39; found: C 48.88, H 3.62, N 1.25.

IR: ν (cm^{-1}): 3065 (w), 2845 (w), 1650 (m), 1602 (s), 1550 (s), 1544 (s), 1493 (m), 1470 (w), 1446 (w), 1405 (vs), 1313 (m), 1263 (w), 1242 (m), 1209 (s), 1168 (w), 1092 (s), 1068 (w), 1025 (m), 997 (m), 960 (m), 899 (m), 853 (m), 836 (w), 816 (w), 784 (w), 747 (m), 717 (vs), 691 (s), 669 (s), 632 (m), 602 (vs), 584 (w), 547 (m), 508 (m), 448 (w), 417 (m).

7.2.40. Synthesis of $[Fe_4Eu_2(mdea)_4(PhCO_2)_6(N_3)_2(\mu_3\text{-}OH)_2]\cdot MeCN\cdot H_2O$ (40)

Method A

A mixture *N*-methyl diethanolamine ($mdeaH_2$) (60 mg, 0.5 mmol), sodium azide (NaN_3) (65 mg, 1 mmol), $[Fe_3O(PhCO_2)_6(H_2O)_3](PhCO_2)$ (125 mg, 0.125 mmol) and $EuCl_3\cdot 6H_2O$ (46 mg, 0.125 mmol) was dissolved in acetonitrile (20 mL). The solution followed by stirring at room temperature for one hour. The solution was then heated to boiling, after which it was cooled to room temperature, filtered and left to stand undisturbed to crystallise via slow evaporation of the solvent. An orange plate crystals of compound **40** were obtained after overnight. The crystals were filtrated and washed with MeCN. Yield; 40% based on Eu.

Elemental analyses calculated (%) of compound **40** (corresponds to a loss of all lattice MeCN): C 40.47, H 4.26, N 8.10; found: C 40.23, H 4.19, N 7.99.

IR: ν (cm^{-1}): 3667 (w), 3369 (w), 2961 (w), 2869 (m), 2824 (w), 2061 (s), 1594 (m), 1536 (s), 1493 (w), 1450 (m), 1387 (vs), 1369 (w), 1330 (w), 1261 (w), 1199 (w), 1176 (w), 1154 (w), 1069 (s), 1046 (w), 1024 (m), 996 (s), 903 (m), 823 (m), 759 (m), 717 (vs), 689 (w), 673 (vs), 639 (m), 579 (s), 513 (s), 459 (s), 431(w), 416 (w).

Method B

A mixture of *N*-methyl diethanolamine ($mdeaH_2$) (149 mg, 1.25 mmol), $FeCl_3$ anhydrous (41 mg, 0.25 mmol), sodium benzoate ($PhCO_2Na$) (108 mg, 0.50 mmol), sodium azide (NaN_3) (49 mg, 0.75 mmol) and $EuCl_3 \cdot 6H_2O$ (92 mg, 0.25 mmol) was dissolved in acetonitrile (20 mL). The solution was heated under reflux for 2h after which it was cooled to room temperature, filtered and left to stand undisturbed to crystallise via slow evaporation of the solvent. An orange plate crystals of compound **40** was obtained after overnight. The crystals were filtrated and washed with MeCN. Yield; 37% based on Eu.

7.2.41. Synthesis of $[Fe_4Gd_2(mdea)_4(PhCO_2)_6(N_3)_2(\mu_3\text{-}OH)_2] \cdot MeCN \cdot H_2O$ (41)

Compound **41** was prepared in the same way as compound **40** but using $GdCl_3 \cdot 6H_2O$ (46 mg, 0.125 mmol) in place of $EuCl_3 \cdot 6H_2O$. Yield; 44% based on Gd.

Elemental analyses calculated (%) of compound **41** (corresponds to a loss of all lattice MeCN): C 40.24, H 4.24, N 8.06; found C 40.08, H 4.14, N 7.92.

IR: ν (cm^{-1}): 3665 (w), 3366 (w), 2964 (w), 2870 (m), 2823 (w), 2061 (s), 1595 (m), 1540 (s), 1493 (w), 1451 (m), 1388 (vs), 1369 (w), 1330 (w), 1258 (w), 1198 (w), 1176 (w), 1156 (w), 1069 (s), 1046 (w), 1024 (m), 995 (s), 905 (m), 823 (m), 759 (m), 716 (vs), 689 (w), 674 (vs), 633 (m), 580 (s), 512 (s), 462 (s), 431(w), 416 (w).

7.2.42. Synthesis of $[Fe_4Tb_2(mdea)_4(PhCO_2)_6(N_3)_2(\mu_3\text{-}OH)_2] \cdot MeCN \cdot H_2O$ (42)

Compound **42** was prepared in the same way as compound **40** but using $TbCl_3 \cdot 6H_2O$ (47 mg, 0.125 mmol) in place of $EuCl_3 \cdot 6H_2O$. Yield; 43% based on Tb.

Elemental analyses calculated (%) of compound **42** (corresponds to a loss of all lattice MeCN): C 40.17, H 4.23, N 8.04; found C 39.89, H 4.11, N 8.00.

IR: ν (cm^{-1}): 3664 (w), 3366 (w), 2961 (w), 2871 (m), 2823 (w), 2061 (s), 1595 (m), 1540 (s), 1490 (w), 1451 (m), 1388 (vs), 1369 (w), 1330 (w), 1258 (w), 1198 (w), 1176 (w), 1156 (w), 1069 (s), 1046 (w), 1024 (m), 996 (s), 905 (m), 823 (m), 759 (m), 716 (vs), 689 (w), 674 (vs), 633 (m), 580 (s), 512 (s), 462 (s), 431(w), 416 (w).

7.2.43. Synthesis of $[Fe_4Dy_2(mdea)_4(PhCO_2)_6(N_3)_2(\mu_3\text{-}OH)_2]\cdot MeCN\cdot H_2O$ (43)

Compound **43** was prepared in the same way as compound **40** but using $DyCl_3\cdot 6H_2O$ (47 mg, 0.125 mmol) in place of $EuCl_3\cdot 6H_2O$. Yield; 50% based on Dy.

Elemental analyses calculated (%) of compound **43** (corresponds to a loss of all lattice MeCN)**:** C 40.00, H 4.21, N 8.01; found: C 39.76, H 4.11 N 7.99.

IR: ν (cm^{-1}): 3665 (w), 3366 (w), 2961 (w), 2870 (m), 2820 (w), 2061 (s), 1595 (m), 1540 (s), 1490 (w), 1449 (m), 1388 (vs), 1369 (w), 1331 (w), 1258 (w), 1198 (w), 1176 (w), 1154 (w), 1069 (s), 1046 (w), 1024 (m), 996 (s), 905 (m), 820 (m), 759 (m), 716 (vs), 687 (w), 674 (vs), 633 (m), 580 (s), 514 (s), 462 (s), 431(w), 416 (w).

7.2.44. Synthesis of $[Fe_4Ho_2(mdea)_4(PhCO_2)_6(N_3)_2(\mu_3\text{-}OH)_2]\cdot MeCN\cdot H_2O$ (44)

Compound **44** was prepared in the same way as compound **40** but using $HoCl_3\cdot 6H_2O$ (47 mg, 0.125 mmol) in place of $EuCl_3\cdot 6H_2O$. Yield; 44% based on Ho.

Elemental analyses calculated (%) of compound **44** (corresponds to a loss of all lattice MeCN): C 39.92, H 4.20, N 7.99; found: C 39.54, H 4.09, N 7.96.

IR: ν (cm^{-1}): 3666 (w), 3369 (w), 2964 (w), 2870 (m), 2823 (w), 2061 (s), 1595 (m), 1540 (s), 1492 (w), 1452 (m), 1391 (vs), 1369 (w), 1330 (w), 1259 (w), 1198 (w), 1176 (w), 1154 (w), 1068 (s), 1046 (w), 1024 (m), 996 (s), 905 (m), 823 (m), 759 (m), 716 (vs), 689 (w), 674 (vs), 633 (m), 580 (s), 512 (s), 462 (s), 431(w), 416 (w).

7.2.45. Synthesis of $[Fe_4Er_2(mdea)_4(PhCO_2)_6(N_3)_2(\mu_3\text{-}OH)_2]\cdot MeCN\cdot H_2O$ (45)

Compound **45** was prepared in the same way as compound **40** but using $ErCl_3\cdot 6H_2O$ (48 mg, 0.125 mmol) in place of $EuCl_3\cdot 6H_2O$. Yield; 35% based on Er.

Elemental analyses calculated (%) of compound **45** (corresponds to a loss of all lattice MeCN): C 39.82, H 4.17, N 7.97; found: C 39.54, H 3.97, N 7.91.

IR: ν (cm^{-1}): 3664 (w), 3369 (w), 2964 (w), 2867 (m), 2820 (w), 2061 (s), 1595 (m), 1540 (s), 1493 (w), 1449 (m), 1388 (vs), 1369 (w), 1331 (w), 1259 (w), 1199 (w), 1178 (w), 1154 (w), 1069 (s),

1046 (w), 1024 (m), 997 (s), 904 (m), 823 (m), 759 (m), 716 (vs), 689 (w), 674 (vs), 633 (m), 580 (s), 514 (s), 462 (s), 431(w), 416 (w).

7.2.46. Synthesis of $[Fe_4Y_2(mdea)_4(PhCO_2)_6(N_3)_2(\mu_3\text{-}OH)_2]\cdot MeCN\cdot H_2O$ (46)

Compound **46** was prepared in the same way as compound **40** but using $YCl_3\cdot 6H_2O$ (38 mg, 0.125 mmol) in place of $EuCl_3\cdot 6H_2O$. Yield; 38% based on Y.

Elemental analyses calculated (%) of compound **46** (corresponds to a loss of all lattice MeCN): C 38.37, H 6.06, N 12.34; found: C 38.22, H 5.88, N 12.15.

IR: ν (cm^{-1}): 3666 (w), 3369 (w), 2961 (w), 2870 (m), 2820 (w), 2061 (s), 1595 (m), 1541 (s), 1493 (w), 1452 (m), 1388 (vs), 1372 (w), 1333 (w), 1264 (w), 1199 (w), 1173 (w), 1156 (w), 1069 (s), 1049 (w), 1024 (m), 996 (s), 903 (m), 820 (m), 759 (m), 716 (vs), 689 (w), 675 (vs), 633 (m), 581 (s), 516 (s), 461 (s), 431(w), 414 (w).

7.2.47. Synthesis of $[Cu_2(bpy)_2(PhCH_2PO_2OH)_4]\cdot CH_3OH$ (47)

A mixture of $Cu(OAc)_2\cdot H_2O$ (200 mg, 1 mmol) was dissolved in MeOH (5 mL) was added dropwise over 10 min to a stirred solution of benzylphosphonic acid ($PhCH_2PO(OH)_2$) (172 mg, 1 mmol) and 2,2′-bipyridine (156 mg, 1 mmol) in MeOH (15 mL). The mixture was stirred at ambient temperature for two hours then the solution was filtered and left to stand undisturbed to crystallise via slow evaporation of the solvent. Blue block crystals of compound **47** suitable for X-ray crystallography were obtained after one week. The crystals were filtrated and washed with MeOH. Yield; 45% based on Cu.

Elemental analysis calcd (%) of compound **47** (corresponds to a loss of all lattice MeOH) : C 48,49 H 4.04, N 4.71; found: C 48.26, H 3.99, N 4.61.

IR: ν (cm^{-1}): 3603(m), 3496(w), 3411(w), 3323(w), 3118(w), 3084(w), 3063(w), 3026(w), 3004(w), 2945(w), 2907(w), 1670(w), 1640(w), 1603(s), 1575(w), 1565(w), 1494(s), 1475(m), 1442(s), 1409(m), 1314(m), 1271(w), 1238(vs), 1196(w), 1139(vs), 1115(w), 1063(m), 1029(s), 935(w), 911(w), 901(w), 811(w), 773(vs), 730(m), 697(vs), 660(w), 650(w), 636(w), 589(s), 546(m), 522(vs), 498(w), 475(w), 451(s), 417(w).

7.2.48. Synthesis of $[Cu_2(bpy)_2(PhCH_2PO_2OH)_2(H_2O)_2]\cdot(NO_3)_2\cdot 4H_2O$ (48)

A mixture of $Cu(NO_3)_2.3H_2O$ (240 mg, 1 mmol), benzylphosphonic acid ($PhCH_2PO(OH)_2$) (172 mg, 1 mmol) and 2,2′-bipyridine (156 mg, 1 mmol) was dissolved in of methanol (25 mL). The mixture was stirred at 70 °C for two hours then the solution was filtered and left to stand undisturbed to crystallise via slow evaporation of the solvent. Blue block crystals of compound **48** suitable for X-ray crystallography were obtained after one week. The crystals were filtrated and washed with MeOH. Yield; 55% based on Cu.

Elemental analysis calcd (%) of compound **48**: C 40.25, H 4.34,N 8.29; found: C 40.13, H 4.26, N 8.18.

IR: ν (cm^{-1}): 3084(w), 3077(w), 3065(w), 3054(w), 3036(w), 2918(w), 2413(w), 2034(w), 2016(w), 1981(w), 1945(w), 1921(w), 1880(w), 1749(w), 1601(vs), 1572(m), 1494(s), 1469(m), 1456(w), 1446(vs), 1429(w), 1413(m), 1379(vs), 1314(vs), 1250(m), 1220(m), 1196(w), 1168(w), 1154(w), 1137(w), 1108(w), 1078(m), 1056(vs), 1026(m), 1016(w), 978(w), 964(w), 927(vs), 902(w), 853(w), 841(w), 823(m), 809(m), 771(s), 729(w), 721(w), 700(m), 659(w), 651(w), 636(w), 595(m), 516(m), 491(m), 470(w), 443(w), 419(w).

Chapter 8. Crystallographic data and SHAPE analysis

8.1. Crystallographic Data

Table 8.1. Crystal data of compounds **1**, **3** and **5**

Compound	**1**	**3**	**5**
Formula	$C_{27}H_{38}Dy_2N_6O_{18}$	$C_{46}H_{42}Gd_2O_{16}$	$C_{46}H_{42}Dy_2O_{16}$
Formula weight	1059.63	1127.46	1137.46
Crystal system	Orthorhombic	Monoclinic	Monoclinic
Space group	$Pna2_1$	P $2_1/c$	P $2_1/c$
a/Å	21.6171(8)	9.6286(7)	9.6416(4)
b/Å	8.1007(2)	21.4017(9)	21.4344(11)
c/Å	20.2610(5)	22.0547(11)	22.0152(9)
α/º	90	90	90
β/º	90	90.799(5)	90.837(4)
γ/º	90	90	90
V/Å	3547.98(18)	4544.3(4)	4549.2(4)
Z	4	8	8
T/K	150.15	150.15	150.15
F(000)	2072	2312	2328
Dc/Mg m^{-3}	1.984	1.709	1.723
μ/mm^{-1}	(Ga-Kα) 22.434	(Ga-Kα) 15.913	(Ga-Kα) 17.501
Data measured	17248	26668	21049
Unique data	6460	10597	9275
R_{int}	0.0672	0.0315	0.0616
Data with I ≥2σ(I)	5167	9233	5581
wR_2(all data)	0.2147	0.1028	0.0982
S(all data)	1.014	1.071	0.847
R1[I≥2σ(I)]	0.0876	0.0371	0.0444
Parameters/Restraints	491 /13	594/12	593 /5
Biggest diff. peak/hole/eÅ	+4.068/-1.048	+1.388/-1.879	+1.250/-0.573
Colour of crystal	Colourless needle	Colourless needle	Colourless needle
Diffractometer	Stoe Stadi Vari	Stoe Stadi Vari	Stoe Stadi Vari

Table 8.2. Crystal data of compounds **9**, **13** and **20**

Compound	**9**	**13**	**20**
Formula	$C_{38}H_{72}Dy_2N_2O_{14}$	$C_{66}H_{90}Dy_4N_2O_{26}$	$C_{36}H_{54}Dy_2Fe_2N_{14}O_{18}$
Formula weight	1110	1977.39	1407.63
Crystal system	Triclinic	Triclinic	Monoclinic
Space group	Pī	Pī	C c
a/Å	11.1003(3)	12.1480(6)	18.1252(4)
b/Å	14.3753(5)	13.3595(7)	17.4250(3)
c/Å	16.7760(5)	13.6518(7)	15.8493(3)
α/º	69.166(3)	70.001(5)	90
β/º	89.878(2)	67.942(5)	97.526(2)
γ/º	85.311(3)	88.070(4)	90
V/Å	2492.50(14)	1918.12(19)	4962.59(17)
Z	2	1	4
T/K	293(2)	199.99	180.15
F(000)	1124	972	2784
Dc/Mg m^{-3}	1.479	1.712	1.884
μ/mm^{-1}	(Mo-Kα) 3.031	(Cu-Kα) 21.117	(Mo-Kα) 3.634
Data measured	54224	14303	38676
Unique data	11678	7272	12852
R_{int}	0.0946	0.0393	0.0257
Data with I ≥2σ(I)	8414	5972	12397
wR_2(all data)	0.1187	0.0969	0.1165
S(all data)	1.078	1.045	1.045
R1[I≥2σ(I)]	0.0461	0.0369	0.0445
Parameters/Restraints	535 /109	474/16	667 /9
Biggest diff. peak/hole/eÅ	+1.715/-1.125	+0.988/-1.132	+2.6/-1.181
Colour of crystal	Colourless block	Yellow crystal	Brown block
Diffractometer	Super Nova	Super Nova	Stoe Stadi Vari

Table 8.3. Crystal data of compounds **21, 27** and **28**

Compound	**21**	**27**	**28**
Formula	$C_{82}H_{97}Pr_4Fe_2N_{13}O_{26}$	$C_{82}H_{97}Dy_4Fe_2N_{13}O_{26}$	$C_{76}H_{90}Fe_2Ho_4N_{10}O_{27}$
Formula weight	2356.06	2442.42	2346.99
Crystal system	Triclinic	Triclinic	Triclinic
Space group	Pī	Pī	Pī
a/Å	12.5044(3)	12.3370(4)	12.9532(3)
b/Å	13.7356(3)	13.6145(5)	13.9206(3)
c/Å	15.9969(4)	15.8170(5)	15.3045(3)
α/º	76.787(2)	85.012(3)	63.402(2)
β/º	69.891(2)	69.505(3)	66.654(2)
γ/º	62.503(2)	63.206(4)	62.520(2)
V/Å	2280.55(11)	2213.32(15)	2125.68(10)
Z	1	1	1
T/K	180	180	180
F(000)	1176	1204	1152.0
Dc/Mg m^{-3}	1.716	1.832	1.833
μ/mm^{-1}	(Ga-Kα) 12.825	(Cu-Kα) 20.982	(Ga-Kα) 18.808
Data measured	29381	24546	26486
Unique data	10766	8432	9269
R_{int}	0.0203	0.0432	0.0344
Data with I ≥2σ(I)	10016	7204	7645
wR_2(all data)	0.0827	0.0941	0.1076
S(all data)	1.115	1.045	1.006
R1[I≥2σ(I)]	0.0287	0.0358	0.0393
Parameters/Restraints	581/6	596/13	556/7
Biggest diff. peak/hole / eÅ	+1.165/-0.808	+1.184/-1.115	+1.582/-1.717
Colour of crystal	Yellow needle	Yellow block	Yellow block
Diffractometer	Stoe Stadi Vari	Super Nova	Stoe Stadi Vari

Table 8.4. Crystal data of compounds **31**and **33**

Compound	**31**	**33**
Formula	$C_{87}H_{83.50}Gd_4Fe_2N_{4.50}O_{28}$	$C_{87}H_{83.5}Dy_4Fe_2N_{4.5}O_{28}$
Formula weight	2380.78	2401.78
Crystal system	Triclinic	Triclinic
Space group	Pī	Pī
a/Å	12.2707(4)	12.2130(4)
b/Å	12.8584(5)	12.8391(5)
c/Å	15.2993(8)	15.2748(5)
α/º	73.408(4)	73.346(3)
β/º	71.581(4)	71.419(3)
γ/º	89.562(3)	89.444(3)
V/Å	2185.85(17)	2166.26(14)
Z	1	1
T/K	150.15	150.15
F(000)	1169	1177
Dc/Mg m^{-3}	1.809	1.841
μ/mm^{-1}	(Cu-Kα) 22.562	(Cu-Kα) 21.418
Data measured	24260	23846
Unique data	8305	8258
R_{int}	0.0383	0.0398
Data with I ≥2σ(I)	6461	6436
wR_2(all data)	0.1016	0.0982
S(all data)	1.041	1.027
R1[I≥2σ(I)]	0.0386	0.0378
Parameters/Restraints	539/14	516/3
Biggest diff. peak/hole/eÅ	+0.997/-0.839	+0.747 /-0.745
Colour of crystal	Yellow block	Yellow block
Diffractometer	Super Nova	Super Nova

Table 8.5. Crystal data of compounds **43** and **45**

Compound	**43**	**45**
Formula	$C_{64}H_{81}Dy_2Fe_4N_{11}O_{23}$	$C_{64}H_{81}Er_2Fe_4N_{11}O_{23}$
Formula weight	1920.79	1930.31
Crystal system	Triclinic	Triclinic
Space group	Pī	Pī
a/Å	12.1633(2)	12.1377(2)
b/Å	14.5145(3)	14.5255(2)
c/Å	23.0837(4)	22.9684(3)
α/º	89.544(2)	89.5710(10)
β/º	75.0260(10)	75.2610(10)
γ/º	70.409(2)	70.3260(10)
V/Å	3695.12(13)	3674.00(10)
Z	2	2
T/K	180.15	180.15
F(000)	1924	1932
Dc/Mg m^{-3}	1.726	1.745
μ/mm^{-1}	(Cu-Kα) 17.434	(Ga-Kα) 12.084
Data measured	33273	42742
Unique data	12858	17329
R_{int}	0.0387	0.0284
Data with I ≥2σ(I)	12247	15965
wR_2(all data)	0.1243	0.1092
S(all data)	1.093	1.053
R1[I≥2σ(I)]	0.0440	0.0407
Parameters/Restraints	949/4	949/4
Biggest diff. peak/hole/eÅ	+1.998/-1.428	+1.471/-2.211
Colour of crystal	Orange plate	Orange plate
Diffractometer	Stoe Stadi Vari	Stoe Stadi Vari

Table 8.6. Crystal data of compounds **43** and **45**

Compound	**47**	**48**
Formula	$C_{25}H_{28}CuN_2O_7P_2$	$C_{34}H_{44}Cu_2N_6O_{18}P_2$
Formula weight	593.96	1013.77
Crystal system	Triclinic	Triclinic
Space group	Pī	Pī
a/Å	10.7015(4)	7.5302(3)
b/Å	11.4449(5)	11.1890(4)
c/Å	12.4513(5)	12.3150(5)
α/º	78.681(3)	93.176(3)
β/º	64.548(3)	95.600(3)
γ/º	68.850(3)	91.965(3)
V/Å	1282.70(10)	1030.24(7)
Z	2	1
T/K	150	180
F(000)	614	522
Dc/Mg m^{-3}	1.538	1.634
μ/mm^{-1}	(Ga-Kα) 5.641	(Mo-Kα) 1.194
Data measured	13124	20137
Unique data	5575	8584
R_{int}	0.0512	0.0340
Data with I ≥2σ(I)	5278	6261
wR_2(all data)	0.1701	0.1322
S(all data)	1.051	0.990
R1[I≥2σ(I)]	0.0636	0.0476
Parameters/Restraints	348/0	301/8
Biggest diff. peak/hole / eÅ	+1.498/-1.013	+1.111/-1.113
Colour of crystal	Blue block	Blue block
Diffractometer	Stoe StadiVari	Stoe StadiVari

8.2. SHAPE analysis

A boldface values indicate the closest gemometry acooording to Continuous Shape Measures (CShM). Abbreviations: HP(D*6h*)hexagon, PPY(C*5v*) Pentagonal pyramid, OC(Oh) Octahedron, TPR(D*3h*) Trigonal prism, JPPY (C*5v*) Johnson pentagonal pyramid J2, OP (*D8h*) Octagon, HPY(*C7v*) Heptagonal pyramid, HBPY(*D6h*) Hexagonal bipyramid, CU(*Oh*) Cube, SAPR(*D4d*) Square antiprism, TDD(*D2d*) Triangular dodecahedron, JGBF(*D2d*) Johnson gyrobifastigium J26,

JETBPY(*D3h*) Johnson elongated triangular bipyramid J14, JBTPR (*C2v*) Biaugmented trigonal prism J50, BTPR (*C2v*) Biaugmented trigonal prism, JSD (*D2d*) Snub diphenoid J84, TT (*Td*) Triakis tetrahedron, ETBPY (*D3h*) Elongated trigonal bipyramid, EP (*D9h*) Enneagon, OPY (*C8v*) Octagonal pyramid, HBPY (*D7h*) Heptagonal bipyramid, JTC (*C3v*) Johnson triangular cupola J3, JCCU (*C4v*) Capped cube J8 CCU (*C4v*) Spherical-relaxed capped cube, JCSAPR (*C4v*) Capped square antiprism J10, CSAPR (*C4v*) Spherical capped square antiprism, JTCTPR(*D3h*) Tricapped trigonal prism J51, TCTPR(*D3h*) Spherical tricapped trigonal prism, JTDIC (*C3v*) Tridiminished icosahedron J63, HH (*C2v*) Hula-hoop, MFF (*Cs*) Muffin. PP(D*5h*) Pentagon, vOC (C*4v*) Vacant octahedron, TBPY (D*3h*) Trigonal bipyramid, SPY (C*4v*) Spherical square pyramid, JTBPY (D*3h*) Johnson trigonal bipyramid J12.

8.2.1. SHAPE analysis of compound (1)

Table 8.7. Shape measurement calculations of compound (**1**)

Dy Eight-coordinate	
OP	34.88
HPY	22.02
HBPY	14.68
CU	9.92
SAPR	3.76
TDD	**2.02**
JGBF	14.31
JETBPY	28.79
JBTPR	3.23
BTPR	2.67
JSD	5.04
TT	10.60
ETBPY	24.02

8.2.2. SHAPE analysis of compound (5)

Table 8.8. Shape measurement calculations of compound (**5**)

Dy Eight-coordinate	
OP	29.34
HPY	21.34
HBPY	13.69
CU	11.24
SAPR	2.32
TDD	1.98
JGBF	12.39
JETBPY	27.49
JBTPR	1.67
BTPR	**1.28**
JSD	2.71
TT	11.92
ETBPY	24.45

8.2.3. SHAPE analysis of compound (9)

Table 8.9. Shape measurement calculations of compound (**9**)

Dy Eight-coordinate	
OP	31.00
HPY	23.56
HBPY	12.24
CU	11.47
SAPR	3.07
TDD	**1.48**
JGBF	13.46
JETBPY	26.50
JBTPR	2.98
BTPR	2.74
JSD	3.33
TT	11.88
ETBPY	23.36

8.2.4. SHAPE analysis of compound (13)

Table 8.10. Shape measurement calculations of compound (**13**)

Dy(1) Eight-coordinate		Dy(2) Nine-coordinate	
OP	33.50	EP	34.55
HPY	23.63	OPY	23.06
HBPY	12.63	HBPY	18.56
CU	5.94	JTC	14.55
SAPR	2.91	JCCU	10.23
TDD	**0.56**	CCU	9.19
JGBF	15.54	JCSAPR	1.86
JETBPY	27.72	**CSAPR**	**0.98**
JBTPR	3.39	JTCTPR	2.44
BTPR	3.00	TCTPR	1.62
JSD	3.75	JTDIC	13.37
TT	6.63	HH	11.64
ETBPY	24.73	MFF	1.07

8.2.5. SHAPE analysis of compound (20)

Table 8.11. Shape measurement calculations of compound (**20**)

Fe Hexa-coordinate		Dy Nine-coordinate	
HP	32.98	EP	36.46
PPY	20.20	OPY	23.29
OC	**2.73**	HBPY	18.00
TPR	9.99	JTC	15.51
JPPY	23.63	JCCU	10.84
		CCU	9.25
		JCSAPR	2.01
		CSAPR	**1.30**
		JTCTPR	3.81
		TCTPR	1.94
		JTDIC	12.40
		HH	10.92
		MFF	1.32

8.2.6. SHAPE analysis of compound (27)

Table 8.12. Shape measurement calculations of compound (**27**)

Fe(1) Hexa-coordinate		Dy(1) Eight-coordinate		Dy(2) Nine-coordinate	
HP	33.04	OP	29.30	EP	32.06
PPY	21.08	HPY	22.49	OPY	21.82
OC	**3.36**	HBPY	15.41	HBPY	16.97
TPR	6.63	CU	8.83	JTC	13.37
JPPY	24.14	SAPR	0.95	JCCU	9.12
		TDD	**0.94**	CCU	8.42
		JGBF	15.04	JCSAPR	2.93
		JETBPY	27.77	**CSAPR**	**2.35**
		JBTPR	2.25	JTCTPR	2.39
		BTPR	1.99	TCTPR	2.48
		JSD	3.57	JTDIC	12.32
		TT	9.65	HH	9.29
		ETBPY	23.26	MFF	2.42

8.2.7. SHAPE analysis of compound (33)

Table 8.13. Shape measurement calculations of compound (**33**)

Fe(1) Hexa-coordinate		Dy(1) Eight-coordinate		Dy(2) Eight-coordinate	
HP	33.32	OP	32.50	OP	29.80
PPY	20.07	HPY	21.78	HPY	22.36
OC	**2.09**	HBPY	12.75	HBPY	12.46
TPR	9.76	CU	8.72	CU	8.17
JPPY	24.39	SAPR	3.99	SAPR	3.84
		TDD	**1.31**	**TDD**	**1.69**
		JGBF	11.81	JGBF	11.63
		JETBPY	25.14	JETBPY	26.54
		JBTPR	2.26	JBTPR	3.01
		BTPR	2.43	BTPR	2.80
		JSD	3.61	JSD	4.36
		TT	9.21	TT	8.92
		ETBPY	22.30	ETBPY	21.12

8.2.8. SHAPE analysis of compound (43)

Table 8.14. Shape measurement calculations of compound (**43**)

Fe (1) − Fe (3) Hexa-coordinate		Fe(2)−Fe (4) Hexa-coordinate		Dy Eight-coordinate	
HP	32.26	HP	32.97	OP	29.42
PPY	23.29	PPY	21.64	HPY	20.67
OC	**1.43**	**OC**	**2.92**	HBPY	15.95
TPR	12.47	TPR	7.34	CU	10.68
JPPY	27.37	JPPY	24.76	**SAPR**	**0.70**
				TDD	2.56
				JGBF	14.09
				JETBPY	25.37
				JBTPR	2.27
				BTPR	1.87
				JSD	4.78
				TT	11.51
				ETBPY	21.64

8.2.9. SHAPE analysis of compound (47)

Table 8.15. Shape measurement calculations of compound (**47**)

Cu(1) Five-coordinate	
PP	30.95
vOC	1.95
TBPY	3.00
SPY	**1.07**
JTBPY	6.13

8.2.10. SHAPE analysis of compound (48)

Table 8.16. Shape measurement calculations of compound (**48**)

Cu(1) Five-coordinate	
PP	32.32
vOC	1.19
TBPY	4.66
SPY	**0.85**
JTBPY	7.63

Chapter 9. Methods of characterisation

The main compound of each series in this work is fully crystallographic characterisation by single-crystal X-ray diffraction, while other compounds were confirmed by unit cell and powder XRD. Also, check the purity of all compounds characterisation by powder XRD.

All compounds were characterised by elemental analyses and infrared spectroscopy, to match the theoretical calculation from the crystal structure and experimental part. Optical and magnetic properties were studied in this work.

9.1. X-ray crystallography

The structures were measured using different single crystal X-ray diffractometer (SCXRD): STADIVARI (Mo-Kα, λ = 0.71073 Å; Cu-Kα, λ = 1.5405 Å, detector: Dectris Pilatus 300K (detector: CMOS)), STOE STADIVARI diffractometer with a Dectris Eiger2 R 4M detector using Ga-Kα radiation (λ = 1.34143 Å) from a MetalJet2 s, Stoe IPDS II area detector diffractometer using graphite-monochromated Mo Kα and Rigaku Oxford Diffraction SuperNova E diffractometer (Rigaku Europe, Kemsing, UK) with Mo-Kα and Cu-Kα radiation from a microfocus source.

The structure solution was achieved using Olex2 [499] by dual-space direct-methods (SHELXT), followed by full-matrix least-squares refinement (SHELX-2016) [500, 501], with anisotropic thermal parameters for all the ordered non-H atoms. Organic hydrogen atoms were placed in calculated positions; the coordinates of H(1) were refined.

The equations for the R-factor and goodness of fit S used in the structure refinement are:

$$wR_2 = \{\Sigma [w (F_o^2 - Fc^2)^2] / \Sigma [w (F_o^2)^2 \quad \text{Equation 7.1}$$

$$S = \{\Sigma [w (F_o^2 - Fc^2)^2] / (n-p)^{1/2} \quad \text{Equation 7.2}$$

$$R_1 = \{\Sigma ||F_o| - |Fc||\} / \{\Sigma |F_o|\} \quad \text{Equation 7.3}$$

Where F_o and Fc are the observed and calculated structure factors for each reflection, while n and p are the number of unique reflections (omitting systematic absences) and the total number of parameters, respectively. The weighting factor w is defined as:

$$w^{-1} = \{\sigma^2(F_o^2) + (\alpha P)^2 + bP\} \quad \text{Equation 7.4}$$

where P is;

$$\max(F_o^2, 0) + 2\,Fc^2 / 3 \quad \text{Equation 7.5}$$

wR_2 is the function minimised during the refinement process and all reflections (except those having high negative value or that have flagged manually using OMIT as 'bad reflection") were used in refinement and for the calculation of S.

All Figures in this work were prepared by using the Diamond program version 4 [502] and the packing were prepared by using the Mercury program version 4.3.0 [503].

9.2. Powder X-ray diffraction (PXRD)

X-Ray powder diffraction patterns for all compounds were measured at room temperature using a Stoe STADI-P diffractometer with a Cu-Ka radiation at the Institute of Nanotechnology, Karlsruhe Institute of Technology. Samples were ground and fixed between two plastic sheets with grease (Lithylen®). In addition, some samples were measured in the mother liquid in the capillary–tube method.

9.3. Elemental analysis

The elemental analyses (C, H, and N) were carried out using an Elementar Vario EL analyser.

9.4. FTIR spectroscopy

Fourier transform IR spectra were measured on a Bruker Alpha. In the region, 400 cm^{-1} to 4000 cm^{-1} were performed on transmission mode using 24 scans with a resolution of 4 cm^{-1}. Spectra were obtained to provide a fingerprint of the sample.

9.5. UV-Vis- NIR spectroscopy

UV-Vis-NIR spectra were measured at the Institute of Nanotechnology, Karlsruhe Institute of Technology on a Cary 5000 scan Spectrophotometer UV-Vis-NIR in the range 200 nm to 2000 nm at a scan rate of 600 nm/min. Quartz glass cuvettes were used for the solution sample. Quartz glass plates were used for the solid-state by putting the sample between two plates with a drop of mineral oil also glass film was measured.

9.6. Emission spectroscopy

Fluorescence measurements were performed at the Institute of Nanotechnology, Karlsruhe Institute of Technology on a Cary-Eclipse fluorescence spectrophotometer.

9.7. Magnetic measurements

Magnetic susceptibility measurements were conducted on a Quantum Design MPMS-XL SQUID magnetometer. This magnetometer can work between 1.8 and 400 K with external field up to 7 T. All the measurements were performed on polycrystalline samples. AC susceptibility measurements were performed with an oscillating AC field (0-3T) and frequencies varying from 1 to 1500 Hz. The magnetic data were corrected for sample holder contributions and for diamagnetic contributions calculated from Pascal's constants.

9.8. SHAPE analysis of the metal coordination environmental

The coordination geometries of selected metal centres within the crystal structure were determined using the software 2.1 SHAPE [145, 146].

Chapter 10. Appendix

Appendix A: List of Inorganic compounds

NO	Inorganic compounds
1	$[Dy_2(H_4bdp)(PhCO_2)_2(NO_3)_2]$ NO_3 MeCN
2	$[Eu_2(PhCO_2)_6(CH_3OH)_4]_\infty$
3	$[Gd_2(PhCO_2)_6(CH_3OH)_4]_\infty$
4	$[Tb_2(PhCO_2)_6(CH_3OH)_4]_\infty$
5	$[Dy_2(PhCO_2)_6(CH_3OH)_4]_\infty$
6	$[Eu_2(TipaH_2)_2(Piv)_4]$
7	$[Gd_2(TipaH_2)_2(Piv)_4]$
8	$[Tb_2(TipaH_2)_2(Piv)_4]$
9	$[Dy_2(TipaH_2)_2(Piv)_4]$
10	$[Eu_4(\mu_3\text{-}OH)_2(o\text{-}van)_4(Piv)_6]$ 2MeCN
11	$[Gd_4(\mu_3\text{-}OH)_2(o\text{-}van)_4(Piv)_6]$ 2MeCN
12	$[Tb_4(\mu_3\text{-}OH)_2(o\text{-}van)_4(Piv)_6]$ 2MeCN
13	$[Dy_4(\mu_3\text{-}OH)_2(o\text{-}van)_4(Piv)_6]$ 2MeCN
14	$[Fe_2Pr_2(mdea)_2\{(py)_2C(OCH_3)O\}_2(\mu_4\text{-}O)(N_3)_2(NO_3)_2(CH_3OH)_2]$ H_2O
15	$[Fe_2Nd_2(mdea)_2\{(py)_2C(OCH_3)O\}_2(\mu_4\text{-}O)(N_3)_2(NO_3)_2(CH_3OH)_2]$ H_2O
16	$[Fe_2Sm_2(mdea)_2\{(py)_2C(OCH_3)O\}_2(\mu_4\text{-}O)(N_3)_2(NO_3)_2(CH_3OH)_2]$ H_2O
17	$[Fe_2Eu_2(mdea)_2\{(py)_2C(OCH_3)O\}_2(\mu_4\text{-}O)(N_3)_2(NO_3)_2(CH_3OH)_2]$ H_2O
18	$[Fe_2Gd_2(mdea)_2\{(py)_2C(OCH_3)O\}_2(\mu_4\text{-}O)(N_3)_2(NO_3)_2(CH_3OH)_2]$ H_2O
19	$[Fe_2Tb_2(mdea)_2\{(py)_2C(OCH_3)O\}_2(\mu_4\text{-}O)(N_3)_2(NO_3)_2(CH_3OH)_2]$ H_2O
20	$[Fe_2Dy_2(mdea)_2\{(py)_2C(OCH_3)O\}_2(\mu_4\text{-}O)(N_3)_2(NO_3)_2(CH_3OH)_2]$ H_2O
21	$[Fe_2Pr_4(mdea)_2(mdeaH)_2(\mu_3\text{-}OH)_2(N_3)_2(PhCO_2)_8]$ 3MeCN
22	$[Fe_2Nd_4(mdea)_2(mdeaH)_2(\mu_3\text{-}OH)_2(N_3)_2(PhCO_2)_8]$ 3MeCN
23	$[Fe_2Sm_4(mdea)_2(mdeaH)_2(\mu_3\text{-}OH)_2(N_3)_2(PhCO_2)_8]$ 3MeCN
24	$[Fe_2Eu_4(mdea)_2(mdeaH)_2(\mu_3\text{-}OH)_2(N_3)_2(PhCO_2)_8]$ 3MeCN
25	$[Fe_2Gd_4(mdea)_2(mdeaH)_2(\mu_3\text{-}OH)_2(N_3)_2(PhCO_2)_8]$ 3MeCN
26	$[Fe_2Tb_4(mdea)_2(mdeaH)_2(\mu_3\text{-}OH)_2(N_3)_2(PhCO_2)_8]$ 3MeCN
27	$[Fe_2Dy_4(mdea)_2(mdeaH)_2(\mu_3\text{-}OH)_2(N_3)_2(PhCO_2)_8]$ 3MeCN
28	$[Fe_2Ho_4(mdea)_2(mdeaH)_2(\mu_3\text{-}OH)_2(N_3)_2(PhCO_2)_8]$ 3MeCN H_2O
29	$[Fe_2Y_4(mdea)_2(mdeaH)_2(\mu_3\text{-}OH)_2(N_3)_2(PhCO_2)_8]$ 3MeCN
30	$[Fe_2Eu_4(mdea)_2(o\text{-}van)_2(\mu_4\text{-}O)_2(PhCO_2)_8]$ 2 5MeCN
31	$[Fe_2Gd_4(mdea)_2(o\text{-}van)_2(\mu_4\text{-}O)_2(PhCO_2)_8]$ 2 5MeCN
32	$[Fe_2Tb_4(mdea)_2(o\text{-}van)_2(\mu_4\text{-}O)_2(PhCO_2)_8]$ 2 5MeCN
33	$[Fe_2Dy_4(mdea)_2(o\text{-}van)_2(\mu_4\text{-}O)_2(PhCO_2)_8]$ 2 5MeCN
34	$[Fe_2Ho_4(mdea)_2(o\text{-}van)_2(\mu_4\text{-}O)_2(PhCO_2)_8]$ 2 5MeCN
35	$[Fe_2Er_4(mdea)_2(o\text{-}van)_2(\mu_4\text{-}O)_2(PhCO_2)_8]$ 2 5MeCN
36	$[Fe_2Tm_4(mdea)_2(o\text{-}van)_2(\mu_4\text{-}O)_2(PhCO_2)_8]$ 2 5MeCN
37	$[Fe_2Lu_4(mdea)_2(o\text{-}van)_2(\mu_4\text{-}O)_2(PhCO_2)_8]$ 2 5MeCN
38	$[Fe_2Yb_4(mdea)_2(o\text{-}van)_2(\mu_4\text{-}O)_2(PhCO_2)_8]$ 2 5MeCN
39	$[Fe_2Y_4(mdea)_2(o\text{-}van)_2(\mu_4\text{-}O)_2(PhCO_2)_8]$ 2 5MeCN
40	$[Fe_4Eu_2(mdea)_4(PhCO_2)_6(N_3)_2(\mu_3\text{-}OH)_2]$ MeCN

41	$[Fe_4Gd_2(mdea)_4(PhCO_2)_6(N_3)_2(\mu_3\text{-}OH)_2]$ MeCN
42	$[Fe_4Tb_2(mdea)_4(PhCO_2)_6(N_3)_2(\mu_3\text{-}OH)_2]$ MeCN
43	$[Fe_4Dy_2(mdea)_4(PhCO_2)_6(N_3)_2(\mu_3\text{-}OH)_2]$ MeCN
44	$[Fe_4Ho_2(mdea)_4(PhCO_2)_6(N_3)_2(\mu_3\text{-}OH)_2]$ MeCN
45	$[Fe_4Er_2(mdea)_4(PhCO_2)_6(N_3)_2(\mu_3\text{-}OH)_2]$ MeCN
46	$[Fe_4Y_2(mdea)_4(PhCO_2)_6(N_3)_2(\mu_3\text{-}OH)_2]$ MeCN
47	$[Cu_2(bpy)_2(PhCH_2PO_2OH)_4]$ CH_3OH
48	$[Cu_2(bpy)_2(PhCH_2PO_2OH)_2(H_2O)_2]$ $(NO_3)_2$ $4H_2O$

Appendix B: List of Inorganic compounds were reported

Compounds	inorganic compounds	Reference
Compound **A**	$Na_4[\{Nd(H_2O)\}_2(\mu_2\text{-dptaO})_2]$ $13H_2O$	[318]
Compound **B**	$[Dy(OAc)_3(MeOH)]_\infty$	[319]
Compound **C**	$[Yb_2(TipaH_2)_2(PhCO_2)_4]$	[82]
Compound **D**	$[Dy_4(\mu_3\text{-}OH)_2(o\text{-van})_4(Piv)_4(NO_3)_2]$ CH_2Cl_2 1 $5H_2O$	[156]
Compound **E**	$[Mn_2Dy_2(\mu_4\text{-}O)(Piv)_2(hep)_4(NO_3)_4]$ 3MeCN	[360]
Compound **F**	$[Fe_2Dy_4(L'H)_2(L)_2(\mu\text{-}Piv)_4(\eta^2\text{-}Piv)_2(\mu 2\text{-}\eta^2\text{-}Piv)_2(\mu 3\text{-}OMe)_2]$	[362]
Compound **G**	$[Fe_4Dy_2(\mu_4\text{-}O)_2(Piv)_6(NO_3)_2(Hedte)_2]$ 4MeCN C_6H_5OH	[375]
Compound **H**	$[Fe_4Dy_2(\mu_3\text{-}OH)_2(n\text{-}bdea)_4(PhCO_2)_8]$ MeCN	[379]
Compound **I**	$[Fe_4Dy_2(\mu_3\text{-}OH)_2(nbdea)_4(Piv)_6(N_3)_2]$ 3MeCN	[335]

Appendix C: List of Abbreviations

General Abbreviations

3d	Transition metal ions
4f	Lanthanide ions
Å	Angstrom
FSS	Frequency Selective Structure
PXRD	Powder X-Ray diffraction

S	Spin ground state
SEM	Scanning Electron Microscope
TGA	Thermogravimetric analysis
XRD	X-Ray diffraction

Chemical Abbreviations

$CO(py)_2$	Di-2-pyridyl ketone
Cu	Copper
DMF	Dimethylformamide
$Fe_3O(PhCO_2)$	$[Fe_3O(PhCO_2)_6(H_2O)_3](PhCO_2)$
$Fe_3O(Piv)$	$[Fe_3O(Piv)_6(H_2O)_3](Piv)$
MeCN	Acetonitrile

MeOH	Methanol
N_3^-	Azide ion
NEt_3	Triethylamine
$PhCO_2^-$	Benzoate
Piv^-	Pivalate
PVP	Poly(2-vinylpyridine)

Abbreviations and Terms Used in Magnetism

AC	Alternating-current
C	Curie constant
DC	Direct-current
K	Kelvin
k_B	Boltzmann constant
M	Magnetisation
H	Field
Hz	Hertz
J	Spin-orbit quantum number
Oe	Oersted
QTM	Quantum Tunneling of Magnetisation

SMMs	Single-molecule Magnets
SQUID	Superconductive Quantum Interface Device
T_B	Blocking temperature
U_{eff}	Effective energy barrier of magnetisation
μ_B	Bohr magneton
τ	Relaxation time
τ_o	Pre-exponential factor
χ	molar magnetic susceptibility
χ'	In-phase dynamic susceptibility
χ''	Out-of-phase dynamic susceptibility
VSM	Vibrating Sample Magnetometer

Abbreviations and Terms Used in Optical

cm^{-1}	Wavenumber
FTIR	Fourier transform infrared
NIR	Near Infrared
RF	Radio Frequency
λ	Wavelength
UV-VIS	Ultra violet visible spectroscopy

λ_{em}	Emission wavelength / nm
λ_{ex}	Excitation wavelength / nm
λ_{max}	Maximum wavelength / nm
PL	Photoluminescence
OLEDs	organic light-emitting diodes

Appendix D: List of Figures

Appendix E: List of Tables

Appendix F: List of Schemes

Conference and Workshop Attendance

Workshop	3Met Workshop (Germany)	October 2017
Conference	Spin Begins at 60 (Germany)	December 2019

Publications

Masooma Ibrahim, Ananya Baksi, Yan Peng, Firas Khalil Al-Zeidaneen, Israël M. Mbomekallé, Pedro de Oliveira and Christopher E. Anson. *Synthesis, Characterization, Electrochemistry, Photoluminescence and Magnetic Properties of a Dinuclear Erbium(III)-Containing Monolacunary Dawson-Type Tungstophosphate: [{Er(H_2O)(CH_3COO)($P_2W_{17}O_{61}$)}$_2$]$^{16-}$*. Molecules 2020, **25**, 4229.

Chapter 11. Reference

1. Morrish, A.H., *The physical principles of magnetism*. 2001.
2. Verchuur, G., *Hidden attraction: The mystery and history of magnetism*. 1996, Oxford University Press Inc.
3. Blundell, S.J., *Magnetism: a very short introduction*. 2012: OUP Oxford.
4. Abbas, G., *Synthesis and Characterisation of 4f and 3d-4f Molecular Based Magnets*. Karlsruhe KIT-Bibliothek 2009.
5. Mondal, K.C., *Syntheses, Structures and Properties of F and Df Complexes Using O-vanillin-derived Schiff Base Ligands*. Karlsruhe KIT-Bibliothek 2011.
6. Kurmoo, M., *Magnetic metal–organic frameworks.* Chem. Soc. Rev., 2009. **38**(5): p. 1353-1379.
7. Earnshaw, A., *Introduction to magnetochemistry*. 2013: Elsevier.
8. Maspoch, D., D. Ruiz-Molina, and J. Veciana, *Old materials with new tricks: multifunctional open-framework materials.* Chem. Soc. Rev., 2007. **36**(5): p. 770-818.
9. Kahn, O., *Molecular magnetism.* VCH Publishers, Inc.(USA), 1993: p. 393.
10. Caneschi, A., D. Gatteschi, R. Sessoli, A.L. Barra, L.C. Brunel, and M. Guillot, *Alternating current susceptibility, high field magnetization, and millimeter band EPR evidence for a ground S = 10 state in [Mn12O12(Ch3COO)16(H2O)4].2CH3COOH.4H2O.* J. Am. Chem. Soc., 1991. **113**(15): p. 5873-5874.
11. Sessoli, R., D. Gatteschi, A. Caneschi, and M. Novak, *Magnetic bistability in a metal-ion cluster.* Nature, 1993. **365**(6442): p. 141-143.
12. Sessoli, R., H.L. Tsai, A.R. Schake, S. Wang, J.B. Vincent, K. Folting, D. Gatteschi, G. Christou, and D.N. Hendrickson, *High-spin molecules:[Mn12O12 (O2CR) 16 (H2O) 4].* J. Am. Chem. Soc., 1993. **115**(5): p. 1804-1816.
13. Friedman, J.R., M. Sarachik, J. Tejada, and R. Ziolo, *Macroscopic measurement of resonant magnetization tunneling in high-spin molecules.* Phys. Rev. Lett., 1996. **76**(20): p. 3830.
14. Thomas, L., F. Lionti, R. Ballou, D. Gatteschi, R. Sessoli, and B. Barbara, *Macroscopic quantum tunnelling of magnetization in a single crystal of nanomagnets.* Nature, 1996. **383**(6596): p. 145-147.
15. Lis, T., *Preparation, structure, and magnetic properties of a dodecanuclear mixed-valence manganese carboxylate.* Acta Crystallographica Section B: Structural Crystallography and Crystal Chemistry, 1980. **36**(9): p. 2042-2046.
16. Kloss, A., *Geschichte des Magnetismus*. VDE-Verlag, ©1994.
17. Lecren, L., W. Wernsdorfer, Y.-G. Li, O. Roubeau, H. Miyasaka, and R. Clérac, *Quantum tunneling and quantum phase interference in a [MnII2MnIII2] single-molecule magnet.* J. Am. Chem. Soc., 2005. **127**(32): p. 11311-11317.
18. Carlin, R.L., *The rare earths or lanthanides*, in *Magnetochemistry*. 1986, Springer. p. 237-261.
19. Orchard, A., *Magnetochemistry*. 2003, Oxford: Oxford University Press.
20. *Susceptibility*. Available from: https://en.wikipedia.org/wiki/File:Susceptibility.png.
21. Mondal, K.C., A. Sundt, Y. Lan, G.E. Kostakis, O. Waldmann, L. Ungur, L.F. Chibotaru, C.E. Anson, and A.K. Powell, *Coexistence of Distinct Single-Ion and Exchange-Based Mechanisms for Blocking of Magnetization in a CoII2DyIII2 Single-Molecule Magnet.* Angew. Chem. Int. Ed., 2012. **51**(30): p. 7550-7554.

22. Peng, Y., V. Mereacre, C.E. Anson, and A.K. Powell, *The role of coordinated solvent on Co (ii) ions in tuning the single molecule magnet properties in a {Co II2 Dy III2} system.* Dalton Transactions, 2017. **46**(16): p. 5337-5343.
23. Miller, J.S. and A.J. Epstein, *Molecule-based magnets—an overview.* MRS Bull., 2000. **25**(11): p. 21-30.
24. Piquer, L.R. and E.C. Sañudo, *Heterometallic 3d–4f single-molecule magnets.* Dalton Transactions, 2015. **44**(19): p. 8771-8780.
25. Jankolovits, J., C.M. Andolina, J.W. Kampf, K.N. Raymond, and V.L. Pecoraro, *Assembly of Near-Infrared Luminescent Lanthanide Host (Host–Guest) Complexes With a Metallacrown Sandwich Motif.* Angew. Chem., 2011. **123**(41): p. 9834-9838.
26. Alexandropoulos, D.I., L. Cunha-Silva, L. Pham, V. Bekiari, G. Christou, and T.C. Stamatatos, *Tetranuclear lanthanide (III) complexes with a zigzag topology from the use of pyridine-2, 6-dimethanol: synthetic, structural, spectroscopic, magnetic and photoluminescence studies.* Inorg. Chem., 2014. **53**(6): p. 3220-3229.
27. Guthausen, G., J.R. Machado, B. Luy, A. Baniodeh, A.K. Powell, S. Krämer, F. Ranzinger, M.P. Herrling, S. Lackner, and H. Horn, *Characterisation and application of ultra-high spin clusters as magnetic resonance relaxation agents.* Dalton Transactions, 2015. **44**(11): p. 5032-5040.
28. Ma, Z., L. Wei, E.C. Alegria, L.M. Martins, M.F.C.G. da Silva, and A.J. Pombeiro, *Synthesis and characterization of copper (II) 4'-phenyl-terpyridine compounds and catalytic application for aerobic oxidation of benzylic alcohols.* Dalton Transactions, 2014. **43**(10): p. 4048-4058.
29. Maayan, G. and G. Christou, *'Old'clusters with new function: oxidation catalysis by high oxidation state manganese and cerium/manganese clusters using O2 gas.* Inorg. Chem., 2011. **50**(15): p. 7015-7021.
30. Evangelisti, M., F. Luis, L. De Jongh, and M. Affronte, *Magnetothermal properties of molecule-based materials.* J. Mater. Chem., 2006. **16**(26): p. 2534-2549.
31. Evangelisti, M. and E.K. Brechin, *Recipes for enhanced molecular cooling.* Dalton Transactions, 2010. **39**(20): p. 4672-4676.
32. Hewitt, I.J., J. Tang, N. Madhu, C.E. Anson, Y. Lan, J. Luzon, M. Etienne, R. Sessoli, and A.K. Powell, *Coupling Dy3 triangles enhances their slow magnetic relaxation.* Angew. Chem. Int. Ed., 2010. **49**(36): p. 6352-6356.
33. Dermitzaki, D., G. Lorusso, C.P. Raptopoulou, V. Psycharis, A. Escuer, M. Evangelisti, S.P. Perlepes, and T.C. Stamatatos, *Molecular Nanoscale Magnetic Refrigerants: A Ferrimagnetic {CuII15GdIII7} Cagelike Cluster from the Use of Pyridine-2, 6-dimethanol.* Inorg. Chem., 2013. **52**(18): p. 10235-10237.
34. Liu, J.-L., Y.-C. Chen, F.-S. Guo, and M.-L. Tong, *Recent advances in the design of magnetic molecules for use as cryogenic magnetic coolants.* Coord. Chem. Rev., 2014. **281**: p. 26-49.
35. Jia, R., H.-F. Li, P. Chen, T. Gao, W.-B. Sun, G.-M. Li, and P.-F. Yan, *Synthesis, structure, and tunable white light emission of heteronuclear Zn 2 Ln 2 arrays using a zinc complex as ligand.* CrystEngComm, 2016. **18**(6): p. 917-923.
36. Guo, F.S., B.M. Day, Y.C. Chen, M.L. Tong, A. Mansikkamäki, and R.A. Layfield, *A dysprosium metallocene single-molecule magnet functioning at the axial limit.* Angew. Chem., 2017. **129**(38): p. 11603-11607.

37. Sharples, J.W., D. Collison, E.J. McInnes, J. Schnack, E. Palacios, and M. Evangelisti, *Quantum signatures of a molecular nanomagnet in direct magnetocaloric measurements.* Nature communications, 2014. **5**(1): p. 1-6.
38. Sharples, J.W., Y.-Z. Zheng, F. Tuna, E.J. McInnes, and D. Collison, *Lanthanide discs chill well and relax slowly.* Chem. Commun., 2011. **47**(27): p. 7650-7652.
39. Vincent, R., S. Klyatskaya, M. Ruben, W. Wernsdorfer, and F. Balestro, *Electronic read-out of a single nuclear spin using a molecular spin transistor.* Nature, 2012. **488**(7411): p. 357-360.
40. Bogani, L. and W. Wernsdorfer, *Molecular spintronics using single-molecule magnets.* Nature Materials, 2008. **7**(3): p. 179-186.
41. Katoh, K., H. Isshiki, T. Komeda, and M. Yamashita, *Multiple-decker phthalocyaninato Tb (III) single-molecule magnets and Y (III) complexes for next generation devices.* Coord. Chem. Rev., 2011. **255**(17-18): p. 2124-2148.
42. Chudnovsky, E.M., *Quantum hysteresis in molecular magnets.* Science, 1996. **274**(5289): p. 938-939.
43. Meier, F., J. Levy, and D. Loss, *Quantum computing with spin cluster qubits.* Phys. Rev. Lett., 2003. **90**(4): p. 047901.
44. Leuenberger, M.N. and D. Loss, *Quantum computing in molecular magnets.* Nature, 2001. **410**(6830): p. 789-793.
45. Wernsdorfer, W. and R. Sessoli, *Quantum phase interference and parity effects in magnetic molecular clusters.* Science, 1999. **284**(5411): p. 133-135.
46. Urdampilleta, M., S. Klyatskaya, J.-P. Cleuziou, M. Ruben, and W. Wernsdorfer, *Supramolecular spin valves.* Nature materials, 2011. **10**(7): p. 502-506.
47. Aromi, G. and E.K. Brechin, *Synthesis of 3d metallic single-molecule magnets*, in *Single-molecule magnets and related phenomena*. 2006, Springer. p. 1-67.
48. Peng, Y., *Exploration of CoII-Based (CoII and CoII-4f) Single Molecule Magnets*. Karlsruhe KIT-Bibliothek, 2015.
49. Gao, S. and M. Affronte, *Molecular nanomagnets and related phenomena*. 2015: Springer.
50. Bagai, R. and G. Christou, *The drosophila of single-molecule magnetism:[Mn 12 O 12 (O 2 CR) 16 (H 2 O) 4].* Chem. Soc. Rev., 2009. **38**(4): p. 1011-1026.
51. Chakov, N.E., M. Soler, W. Wernsdorfer, K.A. Abboud, and G. Christou, *Single-molecule magnets: Structural characterization, magnetic properties, and 19F NMR spectroscopy of a Mn12 family spanning three oxidation levels.* Inorg. Chem., 2005. **44**(15): p. 5304-5321.
52. Scheurer, A., A.M. Ako, R.W. Saalfrank, F.W. Heinemann, F. Hampel, K. Petukhov, K. Gieb, M. Stocker, and P. Müller, *Synthesis, Magnetic Properties, and STM Spectroscopy of Cobalt (II) Cubanes [CoII4 (Cl) 4 (HL) 4].* Chemistry–A European Journal, 2010. **16**(16): p. 4784-4792.
53. Saalfrank, R.W., C. Deutscher, S. Sperner, T. Nakajima, A.M. Ako, E. Uller, F. Hampel, and F.W. Heinemann, *Six-membered metalla-coronands. Synthesis and crystal packing: Columns, compartments, and 3D-networks.* Inorg. Chem., 2004. **43**(14): p. 4372-4382.
54. Woodruff, D.N., R.E. Winpenny, and R.A. Layfield, *Lanthanide single-molecule magnets.* Chem. Rev., 2013. **113**(7): p. 5110-5148.
55. Wernsdorfer, W., *CLASSICAL AND QUANTUM MAGNETIZATION PARTICLES AND CLUSTERS.* Advances in, 2001: p. 99.
56. Science, I.E.o. *hysteresis and hysteresis loops*. Available from: http://sciencewise.info/resource/hysteresis_loop/Hysteresis_loop_by_Internet_Encyclopedia_of_Science.

57. hyperphysics. *Variations in Hysteresis Curves*. Available from: http://www.hyperphysics.de/hyperphysics/hbase/solids/hyst.html.
58. Young, H.D., *University Physics*, ed. t. Ed. 1992, Addison-Wesley.
59. Atkins, P. and T. Overton, *Shriver and Atkins' inorganic chemistry*. 2010: Oxford University Press, USA.
60. Bertotti, G., *Hysteresis in magnetism: for physicists, materials scientists, and engineers*. 1998: Academic press.
61. Miller, J.S., *Magnetically ordered molecule-based materials.* Chem. Soc. Rev., 2011. **40**(6): p. 3266-3296.
62. Jones, M., *Design and synthesis of novel lanthanide complexes for luminescent devices*. 2005, Cardiff University.
63. Polyzou, C., *3d/4f-and 4f-metal complexes with interesting magnetic and/or optical properties*. 2016, PATRAS, 2016.
64. Abragam, A. and B. Bleaney, *Electron paramagnetic resonance of transition ions*. 2012: OUP Oxford.
65. Sorace, L., C. Benelli, and D. Gatteschi, *Lanthanides in molecular magnetism: old tools in a new field.* Chem. Soc. Rev., 2011. **40**(6): p. 3092-3104.
66. Liu, S., L. Gelmini, S.J. Rettig, R.C. Thompson, and C. Orvig, *Synthesis and characterization of lanthanide [Ln (L)] 2 complexes of N4O3 amine phenol ligands with phenolate oxygen bridges: evidence for very weak magnetic exchange between lanthanide ions.* J. Am. Chem. Soc., 1992. **114**(15): p. 6081-6087.
67. Sessoli, R. and A.K. Powell, *Strategies towards single molecule magnets based on lanthanide ions.* Coord. Chem. Rev., 2009. **253**(19-20): p. 2328-2341.
68. Long, J., F. Habib, P.-H. Lin, I. Korobkov, G. Enright, L. Ungur, W. Wernsdorfer, L.F. Chibotaru, and M. Murugesu, *Single-molecule magnet behavior for an antiferromagnetically superexchange-coupled dinuclear dysprosium (III) complex.* J. Am. Chem. Soc., 2011. **133**(14): p. 5319-5328.
69. Peng, J.-B., Y.-P. Ren, X.-J. Kong, L.-S. Long, R.-B. Huang, and L.-S. Zheng, *A series of di-, tri-and tetranuclear lanthanide clusters with slow magnetic relaxation for Dy 2 and Dy 4.* CrystEngComm, 2011. **13**(6): p. 2084-2090.
70. Zhang, P., Y.-N. Guo, and J. Tang, *Recent advances in dysprosium-based single molecule magnets: Structural overview and synthetic strategies.* Coord. Chem. Rev., 2013. **257**(11-12): p. 1728-1763.
71. Ishikawa, N., M. Sugita, T. Ishikawa, S.-y. Koshihara, and Y. Kaizu, *Lanthanide double-decker complexes functioning as magnets at the single-molecular level.* J. Am. Chem. Soc., 2003. **125**(29): p. 8694-8695.
72. Kirin, I., *Formation of unusual phthalocyanines of the rare-earth elements.* Russ. J. Inorg. Chem., 1965. **10**: p. 1065-1066.
73. Moskalev, P., G. Shapkin, and A. Darovskikh, *Synthesis and properties of electrochemically oxidized diphthalocyanines of rare earths and americium.* Zhurnal Neorganicheskoj Khimii, 1979. **24**(2): p. 340-346.
74. Tang, J., I. Hewitt, N. Madhu, G. Chastanet, W. Wernsdorfer, C.E. Anson, C. Benelli, R. Sessoli, and A.K. Powell, *Dysprosium triangles showing single-molecule magnet behavior of thermally excited spin states.* Angew. Chem., 2006. **118**(11): p. 1761-1765.
75. Xue, S., X.-H. Chen, L. Zhao, Y.-N. Guo, and J. Tang, *Two bulky-decorated triangular dysprosium aggregates conserving vortex-spin structure.* Inorg. Chem., 2012. **51**(24): p. 13264-13270.

76. James, C. and P. Willand, *THE RARE EARTH COBALTICYANIDE.* J. Am. Chem. Soc., 1916. **38**(8): p. 1497-1500.
77. Osa, S., T. Kido, N. Matsumoto, N. Re, A. Pochaba, and J. Mrozinski, *A tetranuclear 3d− 4f single molecule magnet:[CuIILTbIII (hfac) 2] 2.* J. Am. Chem. Soc., 2004. **126**(2): p. 420-421.
78. Murugesu, M., A. Mishra, W. Wernsdorfer, K.A. Abboud, and G. Christou, *Mixed 3d/4d and 3d/4f metal clusters: Tetranuclear Fe2IIIM2III (MIII= Ln, Y) and Mn2IVM2III (M= Yb, Y) complexes, and the first Fe/4f single-molecule magnets.* Polyhedron, 2006. **25**(2): p. 613-625.
79. Abbas, G., Y. Lan, V. Mereacre, G. Buth, M.T. Sougrati, F. Grandjean, G.J. Long, C.E. Anson, and A.K. Powell, *Synthesis, magnetism, and 57Fe Mossbauer spectroscopic study of a family of [Ln3Fe7] coordination clusters (Ln= Gd, Tb, and Er).* Inorg. Chem., 2013. **52**(20): p. 11767-11777.
80. Abbas, G., Y. Lan, V. Mereacre, W. Wernsdorfer, R. Clérac, G. Buth, M.T. Sougrati, F. Grandjean, G.J. Long, and C.E. Anson, *Magnetic and 57Fe Mössbauer Study of the Single Molecule Magnet Behavior of a Dy3Fe7 Coordination Cluster.* Inorg. Chem., 2009. **48**(19): p. 9345-9355.
81. Baniodeh, A.J., *Cooperative Effects in Non-cyclic and cyclic FeIII/4f Coordination Clusters*. 2013: Cuvillier.
82. Baniodeh, A., C.E. Anson, and A.K. Powell, *Ringing the changes in Fe iii/Yb iii cyclic coordination clusters.* Chemical Science, 2013. **4**(12): p. 4354-4361.
83. Schmidt, S., D. Prodius, G. Novitchi, V. Mereacre, G.E. Kostakis, and A.K. Powell, *Ferromagnetic heteronuclear {Fe4 (Er, Lu) 2} cyclic coordination clusters based on ferric wheels.* Chem. Commun., 2012. **48**(79): p. 9825-9827.
84. Schmidt, S.F., M.P. Merkel, G.E. Kostakis, G. Buth, C.E. Anson, and A.K. Powell, *SMM behaviour and magnetocaloric effect in heterometallic 3d–4f coordination clusters with high azide: metal ratios.* Dalton Transactions, 2017. **46**(45): p. 15661-15665.
85. Schmidt, S.F., C. Koo, V. Mereacre, J. Park, D.W. Heermann, V. Kataev, C.E. Anson, D. Prodius, G. Novitchi, and R.d. Klingeler, *A Three-Pronged Attack To Investigate the Electronic Structure of a Family of Ferromagnetic Fe4Ln2 Cyclic Coordination Clusters: A Combined Magnetic Susceptibility, High-Field/High-Frequency Electron Paramagnetic Resonance, and 57Fe Mössbauer Study.* Inorg. Chem., 2017. **56**(9): p. 4796-4806.
86. Schray, D., G. Abbas, Y. Lan, V. Mereacre, A. Sundt, J. Dreiser, O. Waldmann, G.E. Kostakis, C.E. Anson, and A.K. Powell, *Combined magnetic susceptibility measurements and 57Fe Mössbauer spectroscopy on a ferromagnetic {FeIII4Dy4} ring.* Angew. Chem. Int. Ed., 2010. **49**(30): p. 5185-5188.
87. Abbas, G., M. Ibrahim, S.F. Schmidt, E. Moreno-Pineda, C.E. Anson, and A.K. Powell, *Synthesis of five isostructural tetranuclear Fe2Ln2 (Ln= Gd, Tb, Dy, Ho, Er) complexes with an "inverse butterfly" core.* Polyhedron, 2019. **158**: p. 255-261.
88. Chen, S., *Syntheses, Structures and Properties of FeIII-LnIII Complexes Using N-substituted Diethanolamine Ligands*. Göttingen Cuvillier 2014.
89. Chen, S., V. Mereacre, C.E. Anson, and A.K. Powell, *A single molecule magnet to single molecule magnet transformation via a solvothermal process: Fe 4 Dy 2→ Fe 6 Dy 3.* Dalton Transactions, 2016. **45**(1): p. 98-106.
90. Nayak, S., O. Roubeau, S.J. Teat, C.M. Beavers, P. Gamez, and J. Reedijk, *An S-shaped [Fe4Dy2] complex exhibiting slow relaxation of magnetization: synthesis, magnetism, and*

crystal structures of a family of [Fe4Ln2][Ln] coordination compounds (Ln= Nd, Gd, Tb, Dy, and Ho). Inorg. Chem., 2010. **49**(1): p. 216-221.
91. Ferbinteanu, M., T. Kajiwara, K.-Y. Choi, H. Nojiri, A. Nakamoto, N. Kojima, F. Cimpoesu, Y. Fujimura, S. Takaishi, and M. Yamashita, *A binuclear Fe (III) Dy (III) single molecule magnet. Quantum effects and models.* J. Am. Chem. Soc., 2006. **128**(28): p. 9008-9009.
92. Bünzli, J.-C.G. and S.V. Eliseeva, *Basics of lanthanide photophysics*, in *Lanthanide Luminescence*. 2010, Springer. p. 1-45.
93. Lü, X.Q., W.X. Feng, Y.N. Hui, T. Wei, J.R. Song, S.S. Zhao, W.Y. Wong, W.K. Wong, and R.A. Jones, *Near-Infrared Luminescent, Neutral, Cyclic Zn2Ln2 (Ln= Nd, Yb, and Er) Complexes from Asymmetric Salen-Type Schiff Base Ligands.* Eur. J. Inorg. Chem., 2010(18): p. 2714-2722.
94. Sun, Y.-Q., J. Zhang, and G.-Y. Yang, *A series of luminescent lanthanide–cadmium–organic frameworks with helical channels and tubes.* Chem. Commun., 2006(45): p. 4700-4702.
95. Chi, Y.X., S.Y. Niu, Z.L. Wang, and J. Jin, *Syntheses, Structures and Photophysical Properties of New Heterodinuclear Cd–Ln Coordination Complexes (Ln= Sm, Eu, Tb, Nd, Ho, Er).* Eur. J. Inorg. Chem., 2008(14): p. 2336-2343.
96. Foucault-Collet, A., C.M. Shade, I. Nazarenko, S. Petoud, and S.V. Eliseeva, *Polynuclear SmIII Polyamidoamine-Based Dendrimer: A Single Probe for Combined Visible and Near-Infrared Live-Cell Imaging.* Angew. Chem. Int. Ed., 2014. **53**(11): p. 2927-2930.
97. d'Aléo, A., A. Bourdolle, S. Brustlein, T. Fauquier, A. Grichine, A. Duperray, P.L. Baldeck, C. Andraud, S. Brasselet, and O. Maury, *Ytterbium-Based Bioprobes for Near-Infrared Two-Photon Scanning Laser Microscopy Imaging.* Angew. Chem. Int. Ed., 2012. **51**(27): p. 6622-6625.
98. Foucault-Collet, A., K.A. Gogick, K.A. White, S. Villette, A. Pallier, G. Collet, C. Kieda, T. Li, S.J. Geib, and N.L. Rosi, *Lanthanide near infrared imaging in living cells with Yb3+ nano metal organic frameworks.* Proceedings of the National Academy of Sciences, 2013. **110**(43): p. 17199-17204.
99. Cui, Y., Y. Yue, G. Qian, and B. Chen, *Luminescent functional metal–organic frameworks.* Chem. Rev., 2012. **112**(2): p. 1126-1162.
100. Bünzli, J.-C.G., *Lanthanide luminescence for biomedical analyses and imaging.* Chem. Rev., 2010. **110**(5): p. 2729-2755.
101. Eliseeva, S.V. and J.-C.G. Bünzli, *Lanthanide luminescence for functional materials and bio-sciences.* Chem. Soc. Rev., 2010. **39**(1): p. 189-227.
102. Xu, B., Q. Chen, H.-M. Hu, R. An, X. Wang, and G. Xue, *Hydrothermal syntheses, crystal structures, and luminescence properties of lanthanide-based coordination polymers constructed by sulfonate functionalized imidazophenanthroline derivative ligand.* Crystal Growth & Design, 2015. **15**(5): p. 2318-2329.
103. Ma, X., X. Li, Y.-E. Cha, and L.-P. Jin, *Highly thermostable one-dimensional lanthanide (III) coordination polymers constructed from benzimidazole-5, 6-dicarboxylic acid and 1, 10-phenanthroline: synthesis, structure, and tunable white-light emission.* Crystal growth & design, 2012. **12**(11): p. 5227-5232.
104. Shen, H.-Y., W.-M. Wang, Y.-X. Bi, H.-L. Gao, S. Liu, and J.-Z. Cui, *Luminescence, magnetocaloric effect and single-molecule magnet behavior in lanthanide complexes based on a tridentate ligand derived from 8-hydroxyquinoline.* Dalton Transactions, 2015. **44**(43): p. 18893-18901.

105. Heffern, M.C., L.M. Matosziuk, and T.J. Meade, *Lanthanide probes for bioresponsive imaging.* Chem. Rev., 2014. **114**(8): p. 4496-4539.
106. Bünzli, J.-C.G. and S.V. Eliseeva, *Lanthanide NIR luminescence for telecommunications, bioanalyses and solar energy conversion.* Journal of Rare Earths, 2010. **28**(6): p. 824-842.
107. Bünzli, J.-C.G., S. Comby, A.-S. Chauvin, and C.D. Vandevyver, *New opportunities for lanthanide luminescence.* Journal of rare earths, 2007. **25**(3): p. 257-274.
108. Van Der Ende, B.M., L. Aarts, and A. Meijerink, *Lanthanide ions as spectral converters for solar cells.* PCCP, 2009. **11**(47): p. 11081-11095.
109. Zhang, Q. and X. Huang, *Recent progress in quantum cutting phosphors.* Prog. Mater Sci., 2010. **55**(5): p. 353-427.
110. Suzuki, H., *Organic light-emitting materials and devices for optical communication technology.* Journal of Photochemistry and Photobiology A: Chemistry, 2004. **166**(1-3): p. 155-161.
111. Huang, C.-H., *Rare earth coordination chemistry: fundamentals and applications*. 2011: John Wiley & Sons.
112. Rodriguez-Ubis, J.C., E. Brunet, and O. Juanes, *Lanthanide Ions as Luminescent Probes*, in *Encyclopedia of Metalloproteins*, R.H. Kretsinger, V.N. Uversky, and E.A. Permyakov, Editors. 2013, Springer New York: New York, NY. p. 1077-1087.
113. Crosby, G., R. Whan, and R. Alire, *Intramolecular energy transfer in rare earth chelates. Role of the triplet state.* The journal of chemical physics, 1961. **34**(3): p. 743-748.
114. Parker, D. and J.G. Williams, *Getting excited about lanthanide complexation chemistry.* J. Chem. Soc., Dalton Trans., 1996(18): p. 3613-3628.
115. Petoud, S., G. Muller, E.G. Moore, J. Xu, J. Sokolnicki, J.P. Riehl, U.N. Le, S.M. Cohen, and K.N. Raymond, *Brilliant Sm, Eu, Tb, and Dy chiral lanthanide complexes with strong circularly polarized luminescence.* J. Am. Chem. Soc., 2007. **129**(1): p. 77-83.
116. Chow, C.Y., S.V. Eliseeva, E.R. Trivedi, T.N. Nguyen, J.W. Kampf, S.p. Petoud, and V.L. Pecoraro, *Ga3+/Ln3+ metallacrowns: a promising family of highly luminescent lanthanide complexes that covers visible and near-infrared domains.* J. Am. Chem. Soc., 2016. **138**(15): p. 5100-5109.
117. Zhang, J., P.D. Badger, S.J. Geib, and S. Petoud, *Sensitization of near-infrared-emitting lanthanide cations in solution by tropolonate ligands.* Angew. Chem., 2005. **117**(17): p. 2564-2568.
118. Armelao, L., S. Quici, F. Barigelletti, G. Accorsi, G. Bottaro, M. Cavazzini, and E. Tondello, *Design of luminescent lanthanide complexes: From molecules to highly efficient photo-emitting materials.* Coord. Chem. Rev., 2010. **254**(5-6): p. 487-505.
119. Forsberg, J.H., *Complexes of lanthanide (III) ions with nitrogen donor ligands.* Coord. Chem. Rev., 1973. **10**(1-2): p. 195-226.
120. Richardson, F.S., *Terbium (III) and europium (III) ions as luminescent probes and stains for biomolecular systems.* Chem. Rev., 1982. **82**(5): p. 541-552.
121. Khan, W.U., J. Li, X. Li, Q. Wu, J. Yan, Y. Xu, F. Xie, J. Shi, and M. Wu, *Efficient energy transfer and luminescence properties of Ca 3 Y (GaO) 3 (BO 3) 4: Tb 3+, Eu 3+ as a green-to-red colour tunable phosphor under near-UV excitation.* Dalton Transactions, 2017. **46**(6): p. 1885-1891.
122. Liu, Y.-Y., R. Decadt, T. Bogaerts, K. Hemelsoet, A.M. Kaczmarek, D. Poelman, M. Waroquier, V. Van Speybroeck, R. Van Deun, and P. Van Der Voort, *Bipyridine-Based Nanosized Metal–Organic Framework with Tunable Luminescence by a Postmodification*

with Eu(III): An Experimental and Theoretical Study. The Journal of Physical Chemistry C, 2013. **117**(21): p. 11302-11310.
123. Gruber, J.B., U. Vetter, T. Taniguchi, G.W. Burdick, H. Hofsäss, S. Chandra, and D.K. Sardar, *Spectroscopic analysis of Eu3+ in single-crystal hexagonal phase AlN.* J. Appl. Phys., 2011. **110**(2): p. 023104.
124. Kim, J.H. and P.H. Holloway, *Room-temperature photoluminescence and electroluminescence properties of sputter-grown gallium nitride doped with europium.* J. Appl. Phys., 2004. **95**(9): p. 4787-4790.
125. JD Dunitz, P.H., RH Holm, JA Ibers, CK Jørgensen, JB Neilands, D. Reinen, and RJP Williams *Structure and Bonding, Vol. 24: Photoelectron Spectrometry.* Springer-Verlag, Berlin-Heidelberg-New York 1975, 1976. **80**(6): p. 578-579.
126. Yongjie, C., X. Zhenfang, C. Shuang, and W. Ying, *Synthesis and luminescent properties of terbium complex with 2-amino-4-chlorobenzoic acid.* Journal of Rare Earths, 2016. **34**(3): p. 240-244.
127. Kropp, J.L. and M.W. Windsor, *Comment on the Fluorescence of Trivalent Europium in D2O—H2O Mixtures.* The Journal of Chemical Physics, 1966. **45**(2): p. 761-761.
128. Mantasha, I., M. Shahid, M. Ahmad, R. Arif, S. Tasneem, F. Sama, and I.A. Ansari, *Synthesis, crystal structures, photoluminescence, magnetic and antioxidant properties, and theoretical analysis of Zn (ii) and Cu (ii) complexes of an aminoalcohol ligand supported by benzoate counter anions.* New J. Chem., 2019. **43**(2): p. 622-633.
129. Gurbanov, A.V., S. Hazra, A.M. Maharramov, F.I. Zubkov, F.I. Guseinov, and A.J. Pombeiro, *The Henry reaction catalyzed by NiII and CuII complexes bearing arylhydrazones of acetoacetanilide.* J. Organomet. Chem., 2018. **869**: p. 48-53.
130. Fernandes, T.A., M.V. Kirillova, V. André, and A.M. Kirillov, *Interplay between H-bonding and interpenetration in an aqueous copper (ii)–aminoalcohol–pyromellitic acid system: self-assembly synthesis, structural features and catalysis.* Dalton Transactions, 2018. **47**(46): p. 16674-16683.
131. Sama, F., A.K. Dhara, M.N. Akhtar, Y.-C. Chen, M.-L. Tong, I.A. Ansari, M. Raizada, M. Ahmad, M. Shahid, and Z.A. Siddiqi, *Aminoalcohols and benzoates-friends or foes? Tuning nuclearity of Cu (II) complexes, studies of their structures, magnetism, and catecholase-like activities as well as performing DFT and TDDFT studies.* Dalton Transactions, 2017. **46**(30): p. 9801-9823.
132. Peng, Y., M.K. Singh, V. Mereacre, C.E. Anson, G. Rajaraman, and A.K. Powell, *Mechanism of magnetisation relaxation in {M III2 Dy III2}(M= Cr, Mn, Fe, Al)"Butterfly" complexes: how important are the transition metal ions here?* Chemical science, 2019. **10**(21): p. 5528-5538.
133. Nielsen, M.A. and I. Chuang, *Quantum computation and quantum information*. 2002, American Association of Physics Teachers.
134. Feynman, R.P., *Quantum mechanical computers.* Foundations of physics, 1986. **16**(6): p. 507-531.
135. Loss, D. and D.P. DiVincenzo, *Quantum computation with quantum dots.* Physical Review A, 1998. **57**(1): p. 120.
136. Lehmann, J., A. Gaita-Arino, E. Coronado, and D. Loss, *Spin qubits with electrically gated polyoxometalate molecules.* Nature Nanotechnology, 2007. **2**(5): p. 312-317.
137. wikipedia.org. *Recrystallization*. 25 April 2020; Available from: https://en.wikipedia.org/wiki/Recrystallization_(chemistry).

138. wikipedia.org. *slow liquid diffusion*. 15 January 2007; Available from: https://en.wikipedia.org/wiki/File:X-ray_crystals_-_slow_liquid_diffusion.png.
139. Feuersenger, J., *Synthesis and characterisation of 3d-4f-complexes and their magnetic properties*. 2010, Bordeaux 1.
140. Chemistry, M.D.o. *Growing Quality Crystals*. 2018 Available from: https://web.mit.edu/x-ray/cystallize.html.
141. Ida, H., T. Shiga, G.N. Newton, and H. Oshio, *Syntheses, structures and magnetism of mixed-valence Mn 19 and Mn 21 complexes supported by alkylamine-based alkoxo-bridging ligands.* Inorganic Chemistry Frontiers, 2015. **2**(6): p. 538-543.
142. Kim, Y., Y. Han, J.-W. Hwang, M.W. Kim, and Y. Do, *New titanatranes: characterization and styrene polymerization behavior.* Organometallics, 2002. **21**(6): p. 1127-1135.
143. Nugent, W.A. and R.L. Harlow, *Early transition metal alkoxide complexes bearing homochiral trialkanolamine ligands.* J. Am. Chem. Soc., 1994. **116**(14): p. 6142-6148.
144. Crans, D.C., H. Chen, O.P. Anderson, and M.M. Miller, *Vanadium (V)-protein model studies: solid-state and solution structure.* J. Am. Chem. Soc., 1993. **115**(15): p. 6769-6776.
145. Kirillov, A.M., Y.Y. Karabach, M. Haukka, M.F.C.G. da Silva, J. Sanchiz, M.N. Kopylovich, and A.J. Pombeiro, *Self-assembled copper (II) coordination polymers derived from aminopolyalcohols and benzenepolycarboxylates: structural and magnetic properties.* Inorg. Chem., 2008. **47**(1): p. 162-175.
146. Fernandes, T.A., V. Andre, A.M. Kirillov, and M.V. Kirillova, *Mild homogeneous oxidation and hydrocarboxylation of cycloalkanes catalyzed by novel dicopper (II) aminoalcohol-driven cores.* J. Mol. Catal. A: Chem., 2017. **426**: p. 357-367.
147. Jones, L.F., P. Jensen, B. Moubaraki, J.D. Cashion, K.J. Berry, and K.S. Murray, *The role of diisopropanolamine (dipaH 3) in cluster dimerisation and polymerisation: from spin frustrated S= 5 Fe III 6 clusters to the novel 1-D covalent polymer of mixed valence [Co II 3 Co III] tetramers.* Dalton Transactions, 2005(20): p. 3344-3352.
148. Costes, J.-P., F. Dahan, and F. Nicodeme, *A trinuclear gadolinium complex: structure and magnetic properties.* Inorg. Chem., 2001. **40**(20): p. 5285-5287.
149. Costes, J.-P., F. Dahan, and F. Nicodeme, *Structure-Based Description of a Step-by-Step Synthesis of Homo-and Heterodinuclear (4f, 4f ') Lanthanide Complexes.* Inorg. Chem., 2003. **42**(20): p. 6556-6563.
150. Chen, H., X. Yang, D. Jiang, D. Shi, and L. Zhang, *Construction of NIR luminescent polynuclear lanthanide-based nanoclusters with sensing properties towards metal ions.* Dalton Transactions, 2018. **47**(39): p. 13880-13886.
151. Chen, H., X. Yang, D. Jiang, D. Schipper, and R.A. Jones, *NIR luminescence for the detection of metal ions and nitro explosives based on a grape-like nine-nuclear Nd (iii) nanocluster.* Inorganic Chemistry Frontiers, 2019. **6**(2): p. 550-555.
152. Yang, P.-P., X.-F. Gao, H.-B. Song, S. Zhang, X.-L. Mei, L.-C. Li, and D.-Z. Liao, *Slow magnetic relaxation in novel Dy4 and Dy8 compounds.* Inorg. Chem., 2011. **50**(3): p. 720-722.
153. Zhang, L., P. Zhang, L. Zhao, S.Y. Lin, S. Xue, J. Tang, and Z. Liu, *Two Locally Chiral Dysprosium Compounds with Salen-Type Ligands That Show Slow Magnetic Relaxation Behavior.* Eur. J. Inorg. Chem., 2013. **2013**(8): p. 1351-1357.
154. Wu, J., J. Jung, P. Zhang, H. Zhang, J. Tang, and B. Le Guennic, *Cis–trans isomerism modulates the magnetic relaxation of dysprosium single-molecule magnets.* Chemical science, 2016. **7**(6): p. 3632-3639.

155. Zhang, Y., J. Wu, S. Shen, Z. Liu, and J. Tang, *Coupling Dy3 triangles into hexanuclear dysprosium (III) clusters: Syntheses, structures and magnetic properties.* Polyhedron, 2018. **150**: p. 40-46.
156. Langley, S.K., N.F. Chilton, I.A. Gass, B. Moubaraki, and K.S. Murray, *Planar tetranuclear lanthanide clusters with the Dy 4 analogue displaying slow magnetic relaxation.* Dalton Transactions, 2011. **40**(47): p. 12656-12659.
157. Langley, S.K., B. Moubaraki, and K.S. Murray, *Trinuclear, octanuclear and decanuclear dysprosium (III) complexes: Synthesis, structural and magnetic studies.* Polyhedron, 2013. **64**: p. 255-261.
158. Zou, X., P. Yan, J. Zhang, F. Zhang, G. Hou, and G. Li, *NIR luminescence and catalysis of multifarious salen type ytterbium complexes modulated by anions.* Dalton Transactions, 2013. **42**(36): p. 13190-13199.
159. Hussain, B., D. Savard, T.J. Burchell, W. Wernsdorfer, and M. Murugesu, *Linking high anisotropy Dy 3 triangles to create a Dy 6 single-molecule magnet.* Chem. Commun., 2009(9): p. 1100-1102.
160. Abrahams, A.r., T. Madanhire, E. Hosten, and R. Betz, *Synthesis and characterization of lanthanide complexes prepared with 2-((E)-(1-hydroxy-2-methylpropan-2-ylimino) methyl)-6-methoxyphenol.* J. Coord. Chem., 2017. **70**(12): p. 1994-2014.
161. Liu, T.-Q., P.-F. Yan, F. Luan, Y.-X. Li, J.-W. Sun, C. Chen, F. Yang, H. Chen, X.-Y. Zou, and G.-M. Li, *Near-IR luminescence and field-induced single molecule magnet of four salen-type ytterbium complexes.* Inorg. Chem., 2015. **54**(1): p. 221-228.
162. Ge, J.-Y., H.-Y. Wang, J. Su, J. Li, B.-L. Wang, Y.-Q. Zhang, and J.-L. Zuo, *Modulating the Magnetic Interaction in New Triple-Decker Dysprosium (III) Single-Molecule Magnets.* Inorg. Chem., 2018. **57**(3): p. 1408-1416.
163. Pessoa, J.C., I. Cavaco, I. Correia, I. Tomaz, T. Duarte, and P. Matias, *Oxovanadium (IV) complexes with aromatic aldehydes.* J. Inorg. Biochem., 2000. **80**(1-2): p. 35-39.
164. Vignesh, K.R., S.K. Langley, C.J. Gartshore, B. Moubaraki, K.S. Murray, and G. Rajaraman, *What Controls the Magnetic Exchange and Anisotropy in a Family of Tetranuclear {Mn2IIMn2III} Single-Molecule Magnets?* Inorg. Chem., 2017. **56**(4): p. 1932-1949.
165. Wang, Y.-Z., P. Wang, C. Li, and Y.-Q. Su, *Synthesis, Crystal Structure and Sulfoxidation of an Iron (III) Complex Derived From 3-Methoxysalicylaldehyde.* Synthesis and Reactivity in Inorganic, Metal-Organic, and Nano-Metal Chemistry, 2016. **46**(6): p. 868-871.
166. Lalia-Kantouri, M., C.D. Papadopoulos, A.G. Hatzidimitriou, and S. Skoulika, *Hetero-heptanuclear (Fe–Na) complexes of salicylaldehydes: crystal and molecular structure of [Fe 2 (3-OCH 3-salo) 8· Na 5]· 3OH· 8H 2 O.* Struct. Chem., 2009. **20**(2): p. 177-184.
167. Papadopoulos, C.D., A.G. Hatzidimitriou, G.P. Voutsas, and M. Lalia-Kantouri, *Synthesis and characterization of new addition compounds of bis (substituted-salicylaldehydo) cobalt (II) with 2, 2'-bipyridine (bipy). Crystal and molecular structures of [CoII (3-methoxy-salicylaldehyde) 2 (bipy)]· CH3OH (1) and [CoII (bipy) 3] Br2· 0.5 (5-chloro-salicylaldehydeH)· 1.5 CH3OH (5).* Polyhedron, 2007. **26**(5): p. 1077-1086.
168. Lalia-Kantouri, M., M. Gdaniec, A. Czapik, K. Chrissafis, W. Ferenc, J. Sarzynski, and C.D. Papadopoulos, *Thermoanalytical, magnetic and structural study of Co (II) complexes with substituted salicylaldehydes and neocuproine.* J. Therm. Anal. Calorim., 2012. **109**(1): p. 131-139.

169. Wang, H.-Y., Y.-H. Li, Y.-Q. Ma, Y. Gao, G.-M. Yu, and X.-Y. Yang, *Synthesis and Structures of Mononuclear Co (III) and Cu (II) Complexes Derived from N-[2-(2-Hydroxy-3-methoxybenzylideneamino) cyclohexyl]-2-hydroxybenzamide.* Asian J. Chem., 2014. **26**(3).
170. Sun, H., L. She, S. Fang, and X. Li, *Reaction of acyl (hydrido) cobalt (III) complexes with (2-diphenylphosphanyl) thiophenol and the influence of chelating ligands containing hard/soft donor atoms on the stability of cobalt complexes.* Polyhedron, 2008. **27**(2): p. 854-860.
171. Sen, S., P. Talukder, S.K. Dey, S. Mitra, G. Rosair, D.L. Hughes, G.P. Yap, G. Pilet, V. Gramlich, and T. Matsushita, *Ligating properties of a potentially tetradentate Schiff base [(CH 3) 2 NCH 2 CH 2 N [double bond, length as m-dash] CHC 6 H 3 (OH)(OMe)] with zinc (ii), cadmium (ii), cobalt (ii), cobalt (iii) and manganese (iii) ions: synthesis and structural studies.* Dalton Transactions, 2006(14): p. 1758-1767.
172. Zhang, S.-H., Y. Song, H. Liang, and M.-H. Zeng, *Microwave-assisted synthesis, crystal structure and properties of a disc-like heptanuclear Co (II) cluster and a heterometallic cubanic Co (II) cluster.* CrystEngComm, 2009. **11**(5): p. 865-872.
173. Habib, F., C. Cook, I. Korobkov, and M. Murugesu, *Novel in situ manganese-promoted double-aldol addition.* Inorg. Chim. Acta, 2012. **380**: p. 378-385.
174. Zhang, K., J. Dai, Y.-H. Wang, M.-H. Zeng, and M. Kurmoo, *Microwave and traditional solvothermal syntheses, crystal structures, mass spectrometry and magnetic properties of Co II 4 O 4 cubes.* Dalton Transactions, 2013. **42**(15): p. 5439-5446.
175. Zhang, S.-H., Y.D. Zhang, H.H. Zou, J.J. Guo, H.P. Li, Y. Song, and H. Liang, *A family of cubane cobalt and nickel clusters: syntheses, structures and magnetic properties.* Inorg. Chim. Acta, 2013. **396**: p. 119-125.
176. Tangoulis, V., M. Lalia-Kantouri, M. Gdaniec, C. Papadopoulos, V. Miletic, and A. Czapik, *New type of single chain magnet: pseudo-one-dimensional chain of high-spin Co (II) exhibiting ferromagnetic intrachain interactions.* Inorg. Chem., 2013. **52**(11): p. 6559-6569.
177. Lalia-Kantouri, M., M. Gdaniec, T. Choli-Papadopoulou, A. Badounas, C.D. Papadopoulos, A. Czapik, G.D. Geromichalos, D. Sahpazidou, and F. Tsitouroudi, *Effect of cobalt (II) complexes with dipyridylamine and salicylaldehydes on cultured tumor and non-tumor cells: synthesis, crystal structure investigations and biological activity.* J. Inorg. Biochem., 2012. **117**: p. 25-34.
178. Zhang, S.-H., R.-X. Zhao, G. Li, H.-Y. Zhang, C.-L. Zhang, and G. Muller, *Structural variation from heterometallic heptanuclear or heptanuclear to cubane clusters based on 2-hydroxy-3-ethoxy-benzaldehyde: effects of pH and temperature.* RSC advances, 2014. **4**(97): p. 54837-54846.
179. Zhang, S.-H., R.-X. Zhao, H.-P. Li, C.-M. Ge, G. Li, Q.-P. Huang, and H.-H. Zou, *Structural variation from heterometallic cluster-based 1D chain to heterometallic tetranuclear cluster: Syntheses, structures and magnetic properties.* J. Solid State Chem., 2014. **216**: p. 30-35.
180. Costes, J.-P., L. Vendier, and W. Wernsdorfer, *Structural and magnetic studies of original tetranuclear Co II–Ln III complexes (Ln III= Gd, Tb, Y).* Dalton Transactions, 2011. **40**(8): p. 1700-1706.
181. Zhou, J., S. Fang, H. Sun, and X. Li, *(2-Formyl-6-methoxyphenolato-κ2O, O')-cis-dimethyl-trans-bis (trimethylphosphine-κP) cobalt (III).* Acta Crystallogr. Sect. Sect. E: Struct. Rep. Online, 2006. **62**(12): p. m3451-m3452.

182. Sun, M., J. Wang, Y. Duan, F. Miao, L. Weng, and X. Leng, *Synthesis and structure of bis-(o-vanillin) di-pyridine nickel (II)-pyridine dihydrate.* Chinese Journal of Structural Chemistry, 2001. **20**(1): p. 8-11.
183. Qin, X., S. Ding, X. Xu, R. Wang, Y. Song, Y. Wang, C.-f. Du, and Z.-l. Liu, *Synthesis, structure and magnetic properties of a series of cubane-like clusters derived from Schiff base ligands.* Polyhedron, 2014. **83**: p. 36-43.
184. Wang, Q. and D.-Q. Wang, *Aquabis (o-vanillinato-κ2O, O') nickel (II).* Acta Crystallogr. Sect. Sect. E: Struct. Rep. Online, 2008. **64**(2): p. m298-m298.
185. Zianna, A., G. Psomas, A. Hatzidimitriou, and M. Lalia-Kantouri, *Synthesis, structural, thermal characterization and interaction with calf-thymus DNA and albumins of cationic Ni (II) complexes with 2, 2'-dipyridylamine and salicylaldehydes.* Polyhedron, 2017. **124**: p. 104-116.
186. Zianna, A., G. Psomas, A. Hatzidimitriou, and M. Lalia-Kantouri, *Ni (II) complexes with 2, 2-dipyridylamine and salicylaldehydes: synthesis, crystal structure and interaction with calf-thymus DNA and albumins.* J. Inorg. Biochem., 2016. **163**: p. 131-142.
187. Wang, C.-J., P.-D. Ren, W.-P. Wu, and Z.-B. Zhang, *(2, 2'-Bipyridine)(2-formyl-6-methoxyphenolato) nickel (II) perchlorate.* Acta Crystallogr. Sect. Sect. E: Struct. Rep. Online, 2009. **65**(1): p. m11-m11.
188. Ayikoe, K., R.J. Butcher, and Y. Gultneh, *Tetra-μ3-methanolato-tetrakis [(2-formyl-6-methoxyphenolato) methanolnickel (II)].* Acta Crystallogr. Sect. Sect. E: Struct. Rep. Online, 2010. **66**(11): p. m1487-m1488.
189. Yu, G.-M., L. Zhao, L.-F. Zou, Y.-N. Guo, G.-F. Xu, Y.-H. Li, and J. Tang, *A tetranuclear nickel (II) cubane complex with O-vanillin ligand.* J. Chem. Crystallogr., 2011. **41**(5): p. 606-609.
190. Butcher, R.J., Y. Gultneh, and K. Ayikoé, *Bis [2-(benzylamino) pyridine-κN](2-formyl-6-methoxyphenolato-κ2O1, O6)(nitrato-κ2O, O') nickel (II).* Acta Crystallogr. Sect. Sect. E: Struct. Rep. Online, 2009. **65**(10): p. m1193-m1194.
191. Costes, J.-P., G. Novitchi, L. Vendier, G. Pilet, and D. Luneau, *Magnetic ordering of NiII4 Cubane complexes through hydrogen bonds.* Comptes Rendus Chimie, 2012. **15**(10): p. 849-855.
192. Zhang, S.-H., N. Li, C.-M. Ge, C. Feng, and L.-F. Ma, *Structures and magnetism of {Ni 2 Na 2},{Ni 4} and {Ni 6 II Ni III} 2-hydroxy-3-alkoxy-benzaldehyde clusters.* Dalton Transactions, 2011. **40**(12): p. 3000-3007.
193. Qin, X., Y. Ji, Y. Gao, L. Yan, S. Ding, Y. Wang, and Z. Liu, *Zinc (II) and Nickel (II) Complexes Based on Schiff Base Ligands: Synthesis, Crystal Structure, Luminescent and Magnetic Properties.* Z. Anorg. Allg. Chem., 2014. **640**(2): p. 462-468.
194. Zhao, R.-X., H. Hai, G. Li, H.-Y. Zhang, Q.-P. Huang, S.-H. Zhang, and H.-P. Li, *Room Temperature Syntheses, Structures and Magnetic Properties of Two Heterometallic Tetranuclear Clusters.* J. Cluster Sci., 2014. **25**(6): p. 1541-1552.
195. Manna, S.C., S. Dolai, H. Masu, A. Figuerola, and S. Manna, *Two new μ2-(1, 1-azido) and μ2-(1, 1-phenoxido)-bridged dinuclear nickel (II) complexes: Syntheses, single-crystal structures and magnetic studies.* J. Mol. Struct., 2019. **1180**: p. 849-854.
196. Zhang, Y., X.-M. Zhang, T.-F. Liu, and W.-G. Xu, *Crystal structures and magnetic interactions in nickel (II) dibridged complexes formed by both phenolate oxygen-azide, or methanlate groups.* Transition Met. Chem., 2010. **35**(7): p. 851-858.

197. Ghosh, T.K., P. Mahapatra, S. Jana, and A. Ghosh, *Variation of nuclearity in Ni II complexes of a Schiff base ligand: crystal structures and magnetic studies.* CrystEngComm, 2019. **21**(31): p. 4620-4631.
198. Elerman, Y., A. Elmali, and I. Svoboda, *Crystal structures and magnetic properties of (2, 2'-dipyridyl)-(3-methoxysalicylaldiminato) copper (II) perchlorate and (2, 2'-dipyridyl)-(4-methoxysalicylaldiminato) copper (II) perchlorate.* Zeitschrift für Naturforschung B, 2002. **57**(5): p. 519-523.
199. Dong, F.Y., Y.M. Sun, Y.T. Li, and Z.Y. Wu, *(2-Formyl-6-methoxy-phenolato-κO,O)(perchlorato-κO)(1,10-phenanthroline-κN,N')copper(II).* Acta Crystallogr Sect E Struct Rep Online, 2008. **64**(Pt 5): p. m678.
200. Gao, T., P. Gao, H.-F. Li, J.-W. Zhang, and L.-L. Xu, *catena-Poly [copper (II)-bis (μ-2-formyl-6-methoxyphenolato-κ4O2, O1: O1, O6)-[(methanol-κO) sodium]-μ-perchlorato-κ2O: O'].* Acta Crystallogr. Sect. Sect. E: Struct. Rep. Online, 2012. **68**(2): p. m152-m152.
201. Lin, H., H. Su, and Y.-L. Feng, *Crystal structure of bis (bis (3-methoxysalicylaldehydato) copper (II)) hexakis (adamantylammonium) hexaperchlorate dihydrate,[{Cu (C8H7O3) 2} 2]·(C10H15NH3) 6 (ClO4) 6· 2H2O.* Zeitschrift für Kristallographie-New Crystal Structures, 2006. **221**(2): p. 173-175.
202. Zianna, A., K. Chrissafis, A. Hatzidimitriou, and M. Lalia-Kantouri, *Thermal analysis and structural characterization of copper (II) complexes with salicyladehydes.* J. Therm. Anal. Calorim., 2015. **120**(1): p. 59-66.
203. Mistri, S., V. Bertolasi, and S.C. Manna, *Bis-chelated-(3-methoxy-2-oxo-benzaldehyde)–copper (II) complex: Synthesis, crystal structure, fluorescence property, DFT calculation, and catecholase activity.* Polyhedron, 2015. **88**: p. 101-109.
204. Lin, Z.-D. and W. Zeng, *Aquabis (2-formyl-6-methoxyphenolato) copper (II).* Acta Crystallogr. Sect. Sect. E: Struct. Rep. Online, 2006. **62**(5): p. m1074-m1076.
205. Odabaşoğlu, M., F. Arslan, H. Ölmez, and O. Büyükgüngör, *Synthesis, crystal structures and spectral characterization of trans-bisaquabis (o-vanillinato) copper (II), cis-aquabis (o-vanillinato) copper (II) and aqua [bis (o-vanillinato)-1, 2-ethylenediimin] copper (II).* Dyes and Pigments, 2007. **75**(3): p. 507-515.
206. Yang, Y., P. Gao, J.-L. Yang, H.-G. Hou, and T. Gao, *catena-Poly [[bis (μ-2-formyl-6-methoxyphenolato-1: 2κ4O1, O6: O1, O2) copper (II) sodium]-μ-tetrafluoridoborate-1: 1' κ2F: F'].* Acta Crystallogr. Sect. Sect. E: Struct. Rep. Online, 2012. **68**(1): p. m37-m37.
207. Jia, R., T. Gao, R. Chen, Y. Yang, P. Gao, Y. Wang, and P. Yan, *Syntheses and Structures of Homodinuclear (Na–Na) and Heterodinuclear (Cu–Na, Cu–K) Metal Complexes.* Aust. J. Chem., 2016. **69**(1): p. 20-26.
208. Novitchi, G., G. Pilet, L. Ungur, V.V. Moshchalkov, W. Wernsdorfer, L.F. Chibotaru, D. Luneau, and A.K. Powell, *Heterometallic Cu II/Dy III 1D chiral polymers: chirogenesis and exchange coupling of toroidal moments in trinuclear Dy 3 single molecule magnets.* Chemical Science, 2012. **3**(4): p. 1169-1176.
209. Gao, P., H.-G. Hou, T. Gao, J.-L. Yang, and Y. Yang, *catena-Poly [[bis (μ-2-formyl-6-methoxyphenolato) copper (II) sodium]-μ-nitrato].* Acta Crystallogr. Sect. Sect. E: Struct. Rep. Online, 2011. **67**(11): p. m1522-m1522.
210. Anastasiadou, D., A. Zianna, M. Gdaniec, M.P. Sigalas, E. Coutouli-Argyropoulou, A. Czapik, and M. Lalia-Kantouri, *Unusual coordination mode of 3-methoxysalicylaldehyde in mononuclear zinc (II) complexes with nitrogenous bases: Synthesis, structural characterization and theoretical studies.* Polyhedron, 2015. **87**: p. 275-285.

211. Li, H.-H., Z.-L. You, C.-L. Zhang, M. Yang, L.-N. Gao, and L. Wang, *Zinc and thiocyanate-mediated oxazolidine ring formation in a trinuclear zinc (II) complex: Synthesis, structure, and properties.* Inorg. Chem. Commun., 2013. **29**: p. 118-122.
212. Ghosh, T.K., S. Jana, and A. Ghosh, *Exploitation of the Flexidentate Nature of a Ligand To Synthesize Zn (II) Complexes of Diverse Nuclearity and Their Use in Solid-State Naked Eye Detection and Aqueous Phase Sensing of 2, 4, 6-Trinitrophenol.* Inorg. Chem., 2018. **57**(24): p. 15216-15228.
213. Costes, J.-P., C. Duhayon, L. Vendier, and A.J. Mota, *Reactions of a series of ZnL, CuL and NiL Schiff base and non-Schiff base complexes with MCl 2 salts (M= Cu, Ni, Mn): syntheses, structures, magnetic properties and DFT calculations.* New J. Chem., 2018. **42**(5): p. 3683-3691.
214. Yang, L., J. Li, T.-C. Pu, M. Kong, and Y. Song, *Metal-ion induced ferromagnetic polarization in a mixed-spin system.* Dalton Transactions, 2017. **46**(20): p. 6670-6676.
215. Roy, S., S. Ghosh, D.O. Martins, F. Tuna, and S. Mohanta, *Synthesis, Crystal Structures, and Magnetic Properties of New Hexanuclear MnIII2LnIII4 Complexes: SMM Behavior of the Terbium (III) Analogue.* Eur. J. Inorg. Chem., 2018. **2018**(48): p. 5191-5202.
216. Costes, J.-P., F. Dahan, A. Dupuis, and J.-P. Laurent, *Une famille originale de complexes hétérodinucléaires Co (II)-Ln (III): synthèse et étude magnétostructurale.* Comptes Rendus de l'Académie des Sciences-Series IIC-Chemistry, 1998. **1**(7): p. 417-420.
217. Griffiths, K., P. Kumar, J.D. Mattock, A. Abdul-Sada, M.B. Pitak, S.J. Coles, O. Navarro, A. Vargas, and G.E. Kostakis, *Efficient NiII2LnIII2 electrocyclization catalysts for the synthesis of trans-4, 5-diaminocyclopent-2-enones from 2-furaldehyde and primary or secondary amines.* Inorg. Chem., 2016. **55**(14): p. 6988-6994.
218. Costes, J.-P., F. Dahan, L. Vendier, S. Shova, G. Lorusso, and M. Evangelisti, *Ni II–Ln III complexes with o-vanillin as the main ligand: syntheses, structures, magnetic and magnetocaloric properties.* Dalton Transactions, 2018. **47**(4): p. 1106-1116.
219. Costes, J.-P., F. Dahan, C. Duhayon, and A.J. Mota, *Can novel dinuclear Ni–Gd complexes give supplementary information on the Ni–Gd magnetic interaction?* Polyhedron, 2015. **96**: p. 51-56.
220. Costes, J.P. and L. Vendier, *Structural and magnetic studies of new NiII–LnIII complexes.* Eur. J. Inorg. Chem., 2010. **2010**(18): p. 2768-2773.
221. Upadhyay, A., C. Das, S.K. Langley, K.S. Murray, A.K. Srivastava, and M. Shanmugam, *Heteronuclear Ni (ii)–Ln (iii)(Ln= La, Pr, Tb, Dy) complexes: synthesis and single-molecule magnet behaviour.* Dalton Transactions, 2016. **45**(8): p. 3616-3626.
222. Kırpık, H., M. Kose, M.R. Elsegood, and C.L. Carpenter-Warren, *A new NiCe complex derived from ortho-vanillin: Structural characterization and luminescence properties.* J. Mol. Struct., 2019. **1175**: p. 882-888.
223. Kajiwara, T., K. Takahashi, T. Hiraizumi, S. Takaishi, and M. Yamashita, *Coordination enhancement of single-molecule magnet behavior of Tb (III)–Cu (II) dinuclear systems.* Polyhedron, 2009. **28**(9-10): p. 1860-1863.
224. Hamamatsu, T., K. Yabe, M. Towatari, N. Matsumoto, N. Re, A. Pochaba, and J. Mrozinski, *Synthesis and Magnetic Property of Copper (II)–Lanthanide (III) Complexes [{CuIILLnIII (o-van)(CH3COO)(MeOH)} 2]· 2H2O (LnIII= GdIII, TbIII, and DyIII; H3L= 1-(2-Hydroxybenzamido)-2-(2-hydroxy-3-methoxybenzylideneamino) ethane; o-van= 3-Methoxysalicylaldehydato).* Bull. Chem. Soc. Jpn., 2007. **80**(3): p. 523-529.

225. Chaudhari, A.K., B. Joarder, E. Riviere, G. Rogez, and S.K. Ghosh, *Nitrate-bridged "pseudo-double-propeller"-type lanthanide (III)–copper (II) heterometallic clusters: syntheses, structures, and magnetic properties.* Inorg. Chem., 2012. **51**(17): p. 9159-9161.
226. Costes, J.P., S. Titos-Padilla, I. Oyarzabal, T. Gupta, C. Duhayon, G. Rajaraman, and E. Colacio, *Effect of ligand substitution around the DyIII on the SMM properties of dual-luminescent Zn–Dy and Zn–Dy–Zn complexes with large anisotropy energy barriers: a combined theoretical and experimental magnetostructural study.* Inorg. Chem., 2016. **55**(9): p. 4428-4440.
227. Sampani, S.I., S. Aubert, M. Cattoen, K. Griffiths, A. Abdul-Sada, G.R. Akien, G.J. Tizzard, S.J. Coles, S. Arseniyadis, and G.E. Kostakis, *Dinucleating Schiff base ligand in Zn/4f coordination chemistry: synthetic challenges and catalytic activity evaluation.* Dalton Transactions, 2018. **47**(13): p. 4486-4493.
228. Boulkedid, A.-L., A. Beghidja, C. Beghidja, Y. Guari, J. Larionova, and J. Long, *Synthesis, structure and magnetic properties of a series of dinuclear heteroleptic Zn 2+/Ln 3+ Schiff base complexes: effect of lanthanide ions on the slow relaxation of magnetization.* Dalton Transactions, 2019. **48**(31): p. 11637-11641.
229. Song, X.-Q., P.-P. Liu, C.-y. Wang, Y.-A. Liu, W.-S. Liu, and M. Zhang, *Three sandwich-type zinc (II)–lanthanide (III) clusters: Structures, luminescence and magnetic properties.* RSC advances, 2017. **7**(37): p. 22692-22698.
230. Gao, T., G.M. Li, P. Gao, W.B. Sun, H. Xu, C. Wang, G.F. Hou, and P.F. Yan, *Three-Dimensional Heteropolynuclear Zn4Ln2 Coordination Frameworks: Structure and NIR Luminescent Properties.* Z. Anorg. Allg. Chem., 2011. **637**(14-15): p. 2223-2227.
231. Abbas, G., Y. Lan, G.E. Kostakis, W. Wernsdorfer, C.E. Anson, and A.K. Powell, *Series of isostructural planar lanthanide complexes [LnIII4 (μ3-OH) 2 (mdeaH) 2 (piv) 8] with single molecule magnet behavior for the Dy4 analogue.* Inorg. Chem., 2010. **49**(17): p. 8067-8072.
232. Abbas, G., Y. Lan, G. Kostakis, C.E. Anson, and A.K. Powell, *An investigation into lanthanide–lanthanide magnetic interactions in a series of [Ln2 (mdeaH2) 2 (piv) 6] dimers.* Inorg. Chim. Acta, 2008. **361**(12-13): p. 3494-3499.
233. Malaestean, I.L., A. Ellern, S. Baca, and P. Kögerler, *Cerium oxide nanoclusters: commensurate with concepts of polyoxometalate chemistry?* Chem. Commun., 2012. **48**(10): p. 1499-1501.
234. Qin, L., G.-J. Zhou, Y.-Z. Yu, H. Nojiri, C. Schröder, R.E. Winpenny, and Y.-Z. Zheng, *Topological self-assembly of highly symmetric lanthanide clusters: a magnetic study of exchange-coupling "fingerprints" in giant gadolinium (III) cages.* J. Am. Chem. Soc., 2017. **139**(45): p. 16405-16411.
235. Kemmitt, T., G.J. Gainsford, N.I. Al-Salim, H. Robson-Marsden, and D.V. Sevast'yanov, *Influence of ligand architecture on bridging bond strength in dimeric titanium aminoalkoxy-diolates.* Aust. J. Chem., 2003. **56**(11): p. 1147-1152.
236. Kemmitt, T., N.I. Al-Salim, and G.J. Gainsford, *Formation and Structural Characterisation of an Unusual Cyclic HexamericOxotitanium Complex.* Eur. J. Inorg. Chem., 1999. **1999**(11): p. 1847-1849.
237. Mishra, S., E. Jeanneau, M. Rolland, and S. Daniele, *Structural isomers of iron (III) N-methyl diethanolaminate as sol–gel precursors for iron-based oxide nanomaterials.* RSC advances, 2016. **6**(3): p. 1738-1743.

238. Saalfrank, R.W., A. Scheurer, I. Bernt, F.W. Heinemann, A.V. Postnikov, V. Schünemann, A.X. Trautwein, M.S. Alam, H. Rupp, and P. Müller, *The {Fe III [Fe III (L 1) 2] 3} star-type single-molecule magnet.* Dalton Transactions, 2006(23): p. 2865-2874.
239. Biswas, B., S. Khanra, T. Weyhermüller, and P. Chaudhuri, *A one-pot synthesis of a paramagnetic high-nuclearity nickel (ii) cluster: an octadecanuclear Ni II 16 Na I 2 metal aggregate.* Chem. Commun., 2007(10): p. 1059-1061.
240. Foguet-Albiol, D., K.A. Abboud, and G. Christou, *High-nuclearity homometallic iron and nickel clusters: Fe 22 and Ni 24 complexes from the use of N-methyldiethanolamine.* Chem. Commun., 2005(34): p. 4282-4284.
241. Manos, M.J., E.E. Moushi, G.S. Papaefstathiou, and A.J. Tasiopoulos, *New Zn2+ metal organic frameworks with unique network topologies from the combination of trimesic acid and amino-alcohols.* Crystal growth & design, 2012. **12**(11): p. 5471-5480.
242. Langley, S.K., D.P. Wielechowski, V. Vieru, N.F. Chilton, B. Moubaraki, B.F. Abrahams, L.F. Chibotaru, and K.S. Murray, *A {CrIII2DyIII2} Single-Molecule Magnet: Enhancing the Blocking Temperature through 3d Magnetic Exchange.* Angew. Chem. Int. Ed., 2013. **52**(46): p. 12014-12019.
243. Langley, S.K., C.M. Forsyth, B. Moubaraki, and K.S. Murray, *A fluoride bridged {Cr III 4 Dy III 4} single molecule magnet.* Dalton Transactions, 2015. **44**(3): p. 912-915.
244. Langley, S.K., D.P. Wielechowski, N.F. Chilton, B. Moubaraki, and K.S. Murray, *A family of {CrIII2LnIII2} butterfly complexes: effect of the lanthanide ion on the single-molecule magnet properties.* Inorg. Chem., 2015. **54**(21): p. 10497-10503.
245. Langley, S.K., D.P. Wielechowski, B. Moubaraki, and K.S. Murray, *Enhancing the magnetic blocking temperature and magnetic coercivity of {Cr III2 Ln III2} single-molecule magnets via bridging ligand modification.* Chem. Commun., 2016. **52**(73): p. 10976-10979.
246. Qin, L., J. Singleton, W.P. Chen, H. Nojiri, L. Engelhardt, R.E. Winpenny, and Y.Z. Zheng, *Quantum Monte Carlo Simulations and High-Field Magnetization Studies of Antiferromagnetic Interactions in a Giant Hetero-Spin Ring.* Angew. Chem. Int. Ed., 2017. **56**(52): p. 16571-16574.
247. Rinck, J., G. Novitchi, W. Van den Heuvel, L. Ungur, Y. Lan, W. Wernsdorfer, C.E. Anson, L.F. Chibotaru, and A.K. Powell, *An Octanuclear [CrIII4DyIII4] 3d–4f Single-Molecule Magnet.* Angew. Chem. Int. Ed., 2010. **49**(41): p. 7583-7587.
248. Vignesh, K.R., S.K. Langley, B. Moubaraki, K.S. Murray, and G. Rajaraman, *Large Hexadecametallic {MnIII–LnIII} Wheels: Synthesis, Structural, Magnetic, and Theoretical Characterization.* Chemistry–A European Journal, 2015. **21**(46): p. 16364-16369.
249. Chen, H., C.-B. Ma, M.-Q. Hu, H.-M. Wen, H.-H. Cui, J.-Y. Liu, X.-W. Song, and C.-N. Chen, *Octanuclear Mn III 6 Mn II Ln (Ln= Gd, Dy and Er) clusters with a novel core topology: syntheses, structures, and magnetic properties.* Dalton Transactions, 2013. **42**(14): p. 4908-4914.
250. Vignesh, K.R., S.K. Langley, B. Moubaraki, K.S. Murray, and G. Rajaraman, *Understanding the Mechanism of Magnetic Relaxation in Pentanuclear {MnIVMnIII2LnIII2} Single-Molecule Magnets.* Inorg. Chem., 2018. **57**(3): p. 1158-1170.
251. Mereacre, V., A.M. Ako, R. Clérac, W. Wernsdorfer, I.J. Hewitt, C.E. Anson, and A.K. Powell, *Heterometallic [Mn5-Ln4] Single-Molecule Magnets with High Anisotropy Barriers.* Chemistry–A European Journal, 2008. **14**(12): p. 3577-3584.

252. Chen, H., C.-B. Ma, M.-Q. Hu, H.-M. Wen, and C.-N. Chen, *A family of novel Mn 3 Ln 4 clusters displaying single-molecule magnet behavior.* Dalton Transactions, 2014. **43**(44): p. 16737-16744.
253. Chen, H., C.-B. Ma, L. Sun, and C.-N. Chen, *A family of FeIII4LnIII4 clusters containing derivatised salicylaldoximate ligand: Syntheses, structures and magnetic properties.* Polyhedron, 2017. **132**: p. 90-94.
254. Vignesh, K.R., S.K. Langley, K.S. Murray, and G. Rajaraman, *Exploring the influence of diamagnetic ions on the mechanism of magnetization relaxation in {CoIII2LnIII2}(Ln= Dy, Tb, Ho)"butterfly" complexes.* Inorg. Chem., 2017. **56**(5): p. 2518-2532.
255. Vignesh, K.R., S.K. Langley, K.S. Murray, and G. Rajaraman, *Quenching the Quantum Tunneling of Magnetization in Heterometallic Octanuclear {TMIII4DyIII4}(TM= Co and Cr) Single-Molecule Magnets by Modification of the Bridging Ligands and Enhancing the Magnetic Exchange Coupling.* Chemistry–A European Journal, 2017. **23**(7): p. 1654-1666.
256. Langley, S.K., C. Le, L. Ungur, B. Moubaraki, B.F. Abrahams, L.F. Chibotaru, and K.S. Murray, *Heterometallic 3d–4f single-molecule magnets: ligand and metal ion influences on the magnetic relaxation.* Inorg. Chem., 2015. **54**(7): p. 3631-3642.
257. Langley, S.K., L. Ungur, N.F. Chilton, B. Moubaraki, L.F. Chibotaru, and K.S. Murray, *Single-molecule magnetism in a family of {CoIII2DyIII2} butterfly complexes: effects of ligand replacement on the dynamics of magnetic relaxation.* Inorg. Chem., 2014. **53**(9): p. 4303-4315.
258. Langley, S.K., N.F. Chilton, B. Moubaraki, and K.S. Murray, *Single-molecule magnetism in three related {CoIII2DyIII2}-acetylacetonate complexes with multiple relaxation mechanisms.* Inorg. Chem., 2013. **52**(12): p. 7183-7192.
259. Chen, S., V. Mereacre, Z. Zhao, W. Zhang, and Z. He, *Synthesis, structures and magnetic properties of linear {Co II2 Ln III2} coordination clusters.* New J. Chem., 2018. **42**(2): p. 1284-1289.
260. Mishra, S., J. Zhang, L.G. Hubert-Pfalzgraf, D. Luneau, and E. Jeanneau, *The Interplay between Yttrium and Barium or Copper Trifluoroacetates and N-Methyldiethanolamine: Synthesis of a Heterometallic Y3Cu Trifluoroacetate Complex and a Homometallic Ba-TFA 1D Polymer.* Eur. J. Inorg. Chem., 2007. **2007**(4): p. 602-608.
261. Gatteschi, D. and R. Sessoli, *Quantum tunneling of magnetization and related phenomena in molecular materials.* Angew. Chem. Int. Ed., 2003. **42**(3): p. 268-297.
262. Stamp, P.C. and A. Gaita-Arino, *Spin-based quantum computers made by chemistry: hows and whys.* J. Mater. Chem., 2009. **19**(12): p. 1718-1730.
263. Troiani, F. and M. Affronte, *Molecular spins for quantum information technologies.* Chem. Soc. Rev., 2011. **40**(6): p. 3119-3129.
264. Song, X., M.-H. Chang, and M. Pecht, *Rare-earth elements in lighting and optical applications and their recycling.* JOM, 2013. **65**(10): p. 1276-1282.
265. Amoroso, A.J. and S.J. Pope, *Using lanthanide ions in molecular bioimaging.* Chem. Soc. Rev., 2015. **44**(14): p. 4723-4742.
266. Murthy, C.P., *University Chemistry, Vol. Ii*. 2008: New Age International.
267. Beatty, R., *The Lanthanides*. 2008: Marshall Cavendish.
268. Atwood, D.A., *The rare earth elements: fundamentals and applications*. 2013: John Wiley & Sons.
269. Cui, D., *Molecular catalysis of rare-earth elements*. Vol. 137. 2010: Springer Science & Business Media.
270. Jha, A.R., *Rare earth materials: properties and applications*. 2014: CRC Press.

271. Sauer, M., J. Hofkens, and J. Enderlein, *Handbook of fluorescence spectroscopy and imaging: from ensemble to single molecules*. 2010: John Wiley & Sons.
272. de Bettencourt-Dias, A., *Luminescence of lanthanide ions in coordination compounds and nanomaterials*. 2014: John Wiley & Sons.
273. Eliseeva, S.V. and J.-C.G. Bünzli, *Rare earths: jewels for functional materials of the future.* New J. Chem., 2011. **35**(6): p. 1165-1176.
274. Dei, A. and D. Gatteschi, *Molecular (nano) magnets as test grounds of quantum mechanics.* Angew. Chem. Int. Ed., 2011. **50**(50): p. 11852-11858.
275. Rinehart, J.D. and J.R. Long, *Exploiting single-ion anisotropy in the design of f-element single-molecule magnets.* Chemical Science, 2011. **2**(11): p. 2078-2085.
276. Benelli, C. and D. Gatteschi, *Magnetism of lanthanides in molecular materials with transition-metal ions and organic radicals.* Chem. Rev., 2002. **102**(6): p. 2369-2388.
277. Inomata, Y., T. Takei, and F.S. Howell, *Synthesis and crystal structure of lanthanide metal complexes with N, N-bis (2-hydroxyethyl) glycine.* Inorg. Chim. Acta, 2001. **318**(1-2): p. 201-206.
278. Messimeri, A., C.P. Raptopoulou, V. Nastopoulos, A. Terzis, S.P. Perlepes, and C. Papadimitriou, *Synthesis and physical studies of lanthanide (III) complexes of N, N-bis (2-hydroxyethyl) glycinate (bicinate, bicH2−): molecular and crystal structure of [Gd (O2CMe)(bicH2)(phen)(H2O)](ClO4). phen. 3H2O (phen= 1, 10-phenanthroline).* Inorg. Chim. Acta, 2002. **336**: p. 8-18.
279. Koroteev, P.S., A.B. Ilyukhin, N.N. Efimov, E.V. Belova, A.V. Gavrikov, and V.M. Novotortsev, *Mononuclear and binuclear lanthanide acetates with chelating and bridging triethanolamine ligands.* Polyhedron, 2018. **154**: p. 54-64.
280. Biswas, S., S. Das, J. Acharya, V. Kumar, J. van Leusen, P. Kögerler, J.M. Herrera, E. Colacio, and V. Chandrasekhar, *Homometallic DyIII complexes of varying nuclearity from 2 to 21: synthesis, structure, and magnetism.* Chemistry–A European Journal, 2017. **23**(21): p. 5154-5170.
281. Bag, P., C.K. Rastogi, S. Biswas, S. Sivakumar, V. Mereacre, and V. Chandrasekhar, *Homodinuclear lanthanide {Ln 2}(Ln= Gd, Tb, Dy, Eu) complexes prepared from an o-vanillin based ligand: luminescence and single-molecule magnetism behavior.* Dalton Transactions, 2015. **44**(9): p. 4328-4340.
282. Zahra, A., T. Mahmud, M.N. Tahir, H.A. Shad, H. Rehman, and S. Naseem, *Synthesis, Characterization and Magnetic Studies of Dysprosium Complex,[Dy 2 (TEA) 2 (O 2 CPh) 4· 2H 2 O].* J. Chem. Crystallogr., 2017. **47**(5): p. 151-156.
283. Baniodeh, A., A. Mondal, R. Galeev, A. Sukhanov, R. Eremina, V. Voronkova, C.E. Anson, and A.K. Powell, *How Far can the Anisotropy Deviate from Uniaxiality in a Dy-Based Single-Molecule Magnet? Dinuclear Dy (III) Complex Study.* Appl. Magn. Reson., 2017. **48**(1): p. 101-113.
284. Biswas, S., S. Das, T. Gupta, S.K. Singh, M. Pissas, G. Rajaraman, and V. Chandrasekhar, *Observation of Slow Relaxation and Single-Molecule Toroidal Behavior in a Family of Butterfly-Shaped Ln4 Complexes.* Chemistry–A European Journal, 2016. **22**(51): p. 18532-18550.
285. Biswas, S., P. Kumar, A. Swain, T. Gupta, P. Kalita, S. Kundu, G. Rajaraman, and V. Chandrasekhar, *Phosphonate-assisted tetranuclear lanthanide assemblies: observation of the toroidic ground state in the Tb III analogue.* Dalton Transactions, 2019. **48**(19): p. 6421-6434.

286. Hu, P., L. Yin, N.-n. Mao, F. Yu, B. Li, Z.-x. Wang, and T. Zhang, *A series of six-membered lanthanide rings based on 2, 2-bis (hydroxymethyl)-2, 2', 2 "-nitrilotriethanol: synthesis, crystal structures and magnetic properties.* CrystEngComm, 2017. **19**(32): p. 4807-4814.
287. Chandrasekhar, V., P. Bag, and E. Colacio, *Octanuclear {Ln (III) 8}(Ln= Gd, Tb, Dy, Ho) macrocyclic complexes in a cyclooctadiene-like conformation: manifestation of slow relaxation of magnetization in the Dy (III) derivative.* Inorg. Chem., 2013. **52**(8): p. 4562-4570.
288. Oh, S.J., Y.-S. Choi, S. Hwangbo, S.C. Bae, J.K. Ku, and J.W. Park, *Structure and phosphodiesterase activity of Bis-Tris coordinated lanthanide (III) complexes.* Chem. Commun., 1998(20): p. 2189-2190.
289. Mylonas-Margaritis, I., J. Mayans, S.-M. Sakellakou, C. P Raptopoulou, V. Psycharis, A. Escuer, and S. P Perlepes, *Using the singly deprotonated triethanolamine to prepare dinuclear lanthanide (III) complexes: synthesis, structural characterization and magnetic studies.* Magnetochemistry, 2017. **3**(1): p. 5.
290. Kumar, R., S. Obrai, A.K. Jassal, and M.S. Hundal, *Supramolecular architectures of N, N, N', N'-tetrakis-(2-hydroxyethyl) ethylenediamine and tris (2-hydroxyethyl) amine with La (iii) picrate.* RSC Advances, 2014. **4**(103): p. 59248-59264.
291. Ekkehardt Hahn, F. and J. Mohr, *Synthese und Strukturen von Bis (trietanolamin) lanthanoid-Komplexen.* Chem. Ber., 1990. **123**(3): p. 481-484.
292. Fowkes, A. and W.T. Harrison, *(Nitrato-κ2O, O') bis (triethanolamine-κ4N, O, O', O'') lanthanum (III) dinitrate.* Acta Crystallogr. Sect. C: Cryst. Struct. Commun., 2006. **62**(6): p. m232-m233.
293. Peng, Y., V. Mereacre, A. Baniodeh, Y. Lan, M. Schlageter, G.E. Kostakis, and A.K. Powell, *Effect of Ligand Field Tuning on the SMM Behavior for Three Related Alkoxide-Bridged Dysprosium Dimers.* Inorg. Chem., 2016. **55**(1): p. 68-74.
294. Wang, Y.-X., Q. Xu, P. Ren, W. Shi, and P. Cheng, *Solvent-induced formation of two gadolinium clusters demonstrating strong magnetocaloric effects and ferroelectric properties.* Dalton Transactions, 2019. **48**(6): p. 2228-2233.
295. Starynowicz, P., *Synthesis and structure of bis (triethanolamine) europium (II) diperchlorate.* J. Alloys Compd., 2001. **323**: p. 159-163.
296. Starynowicz, P. and K. Gatner, *An Ytterbium (II) Complex with Triethanolamine.* Z. Anorg. Allg. Chem., 2003. **629**(4): p. 722-726.
297. Vignesh, K.R., D.I. Alexandropoulos, B.S. Dolinar, and K.R. Dunbar, *Hard versus soft: zero-field dinuclear Dy (iii) oxygen bridged SMM and theoretical predictions of the sulfur and selenium analogues.* Dalton Transactions, 2019. **48**(9): p. 2872-2876.
298. Plass, W. and G. Fries, *Synthese und Struktur eines zweikernigen Gadolinium (III)-Komplexes: Magnetische Austauschwechselwirkungen in alkoxyverbrückten Komplexen der Lanthanoiden.* Z. Anorg. Allg. Chem., 1997. **623**(8): p. 1205-1207.
299. Hooper, T.N., S.K. Langley, S. Gómez-Coca, G. Lorusso, E. Ruiz, K.S. Murray, M. Evangelisti, and E.K. Brechin, *Coming full circle: constructing a [Gd 6] wheel dimer by dimer and the importance of spin topology.* Dalton Transactions, 2017. **46**(31): p. 10255-10263.
300. Langley, S.K., K.R. Vignesh, T. Gupta, C.J. Gartshore, G. Rajaraman, C.M. Forsyth, and K.S. Murray, *New examples of triangular terbium (iii) and holmium (iii) and hexagonal dysprosium (iii) single molecule toroics.* Dalton Transactions, 2019. **48**(41): p. 15657-15667.

301. Wang, Y.-X., W. Shi, H. Li, Y. Song, L. Fang, Y. Lan, A.K. Powell, W. Wernsdorfer, L. Ungur, and L.F. Chibotaru, *A single-molecule magnet assembly exhibiting a dielectric transition at 470 K.* Chemical Science, 2012. **3**(12): p. 3366-3370.
302. Chen, Y.-H., Y.-F. Tsai, G.-H. Lee, and E.-C. Yang, *The synthesis, structure, magnetic and luminescent properties of a new tetranuclear dysprosium (III) cluster.* J. Solid State Chem., 2012. **185**: p. 166-171.
303. Gu, Z., L. Li, Q. Bao, and F. Yuan, *Lanthanocene Diolate Complexes: Synthesis, Structures and Catalytic Property for ε-Caprolactone Polymerization.* Chin. J. Chem . 2015. **33**(5): p. 563-567.
304. Langley, S.K., K.R. Vignesh, B. Moubaraki, G. Rajaraman, and K.S. Murray, *Oblate versus Prolate Electron Density of Lanthanide Ions: A Design Criterion for Engineering Toroidal Moments? A Case Study on {LnIII6}(Ln= Tb, Dy, Ho and Er) Wheels.* Chemistry–A European Journal, 2019. **25**(16): p. 4156-4165.
305. Baniodeh, A., N. Magnani, S. Bräse, C.E. Anson, and A.K. Powell, *Ligand field variations: tuning the toroidal moment of Dy 6 rings.* Dalton Transactions, 2015. **44**(14): p. 6343-6347.
306. Langley, S.K., B. Moubaraki, C.M. Forsyth, I.A. Gass, and K.S. Murray, *Structure and magnetism of new lanthanide 6-wheel compounds utilizing triethanolamine as a stabilizing ligand.* Dalton Transactions, 2010. **39**(7): p. 1705-1708.
307. Langley, S.K., B. Moubaraki, and K.S. Murray, *Magnetic properties of hexanuclear lanthanide (III) clusters incorporating a central μ6-carbonate ligand derived from atmospheric CO2 fixation.* Inorg. Chem., 2012. **51**(7): p. 3947-3949.
308. Yuan, F., Z. Gu, L. Li, and L. Sha, *Novel cerium (IV)-diolate complex with a 13-nuclear cerium (IV)-oxo core: Synthesis, molecular structure and catalytic property for ε-caprolactone-polymerization.* Polyhedron, 2017. **133**: p. 393-397.
309. Ruiz-Martínez, A., D. Casanova, and S. Alvarez, *Polyhedral Structures with an Odd Number of Vertices: Nine-Coordinate Metal Compounds.* Chemistry–A European Journal, 2008. **14**(4): p. 1291-1303.
310. Alvarez, S., P. Alemany, D. Casanova, J. Cirera, M. Llunell, and D. Avnir, *Shape maps and polyhedral interconversion paths in transition metal chemistry.* Coord. Chem. Rev., 2005. **249**(17-18): p. 1693-1708.
311. Alvarez, S., D. Avnir, M. Llunell, and M. Pinsky, *Continuous symmetry maps and shape classification. The case of six-coordinated metal compounds.* New J. Chem., 2002. **26**(8): p. 996-1009.
312. Zabrodsky, H., S. Peleg, and D. Avnir, *Continuous symmetry measures. 2. Symmetry groups and the tetrahedron.* J. Am. Chem. Soc., 1993. **115**(18): p. 8278-8289.
313. Sanz, S., K. Ferreira, R.D. McIntosh, S.J. Dalgarno, and E.K. Brechin, *Calix [4] arene-supported Fe III 2 Ln III 2 clusters.* Chem. Commun., 2011. **47**(32): p. 9042-9044.
314. Kahn, M.L., R. Ballou, P. Porcher, O. Kahn, and J.P. Sutter, *Analytical Determination of the {Ln–Aminoxyl Radical} Exchange Interaction Taking into Account Both the Ligand-Field Effect and the Spin–Orbit Coupling of the Lanthanide Ion (Ln= DyIII and HoIII).* Chemistry–A European Journal, 2002. **8**(2): p. 525-531.
315. Alexandropoulos, D.I., K.R. Vignesh, H. Xie, and K.R. Dunbar, *Switching on single-molecule magnet properties of homoleptic sandwich tris (pyrazolyl) borate dysprosium (iii) cations via intermolecular dipolar coupling.* Dalton Transactions, 2019. **48**(28): p. 10610-10618.

316. Cole, K.S. and R.H. Cole, *Dispersion and absorption in dielectrics I. Alternating current characteristics.* The Journal of chemical physics, 1941. **9**(4): p. 341-351.
317. Grahl, M., J. Kötzler, and I. Sessler, *Correlation between domain-wall dynamics and spin-spin relaxation in uniaxial ferromagnets.* J. Magn. Magn. Mater., 1990. **90**: p. 187-188.
318. Miyashita, Y., M. Sanada, M.M. Islam, N. Amir, T. Koyano, H. Ikeda, K. Fujisawa, and K.-i. Okamoto, *Selective formation of lanthanide (III) complexes with polyaminopolycarboxylate: Unprecedented tetranuclear neodymium (III) complex containing alkoxo and carboxylato bridges.* Inorg. Chem. Commun., 2005. **8**(9): p. 785-788.
319. Zheng, Y.Z., Y. Lan, W. Wernsdorfer, C.E. Anson, and A.K. Powell, *Polymerisation of the Dysprosium Acetate Dimer Switches on Single-Chain Magnetism.* Chemistry–A European Journal, 2009. **15**(46): p. 12566-12570.
320. Joarder, B., A.K. Chaudhari, G. Rogez, and S.K. Ghosh, *A carboxylate-based dinuclear dysprosium (III) cluster exhibiting slow magnetic relaxation behaviour.* Dalton Transactions, 2012. **41**(25): p. 7695-7699.
321. Liang, L., G. Peng, G. Li, Y. Lan, A.K. Powell, and H. Deng, *In situ hydrothermal synthesis of dysprosium (III) single-molecule magnet with lanthanide salt as catalyst.* Dalton Transactions, 2012. **41**(19): p. 5816-5823.
322. Song, Y.-m., F. Luo, M.-b. Luo, Z.-w. Liao, G.-m. Sun, X.-z. Tian, Y. Zhu, Z.-J. Yuan, S.-j. Liu, and W.-y. Xu, *The application of single-crystal-to-single-crystal transformation towards adjustable SMM properties.* Chem. Commun., 2012. **48**(7): p. 1006-1008.
323. Evangelisti, M., O. Roubeau, E. Palacios, A. Camón, T.N. Hooper, E.K. Brechin, and J.J. Alonso, *Cryogenic magnetocaloric effect in a ferromagnetic molecular dimer.* Angew. Chem. Int. Ed., 2011. **50**(29): p. 6606-6609.
324. Guo, F.-S., J.-D. Leng, J.-L. Liu, Z.-S. Meng, and M.-L. Tong, *Polynuclear and polymeric gadolinium acetate derivatives with large magnetocaloric effect.* Inorg. Chem., 2012. **51**(1): p. 405-413.
325. Chu, X.-Y., H.-X. Zhang, Y.-X. Chang, Y.-Y. Nie, J.-Z. Cui, and H.-L. Gao, *A series of Ln 2 complexes based on an 8-hydroxyquinoline derivative: slow magnetization relaxation and photo-luminescence properties.* New J. Chem., 2018. **42**(8): p. 5688-5697.
326. Zheng, T.-F., C. Cao, P.-P. Dong, S.-J. Liu, F.-F. Wang, X.-L. Tong, J.-S. Liao, J.-L. Chen, and H.-R. Wen, *Synthesis, structures and magnetocaloric properties of two dinuclear GdIII clusters derived from monocarboxylate ligands.* Polyhedron, 2016. **113**: p. 96-101.
327. Christou, G., *Single-molecule magnets: a molecular approach to nanoscale magnetic materials.* Polyhedron, 2005. **24**(16-17): p. 2065-2075.
328. Ako, A.M., V. Mereacre, R. Clérac, I.J. Hewitt, Y. Lan, C.E. Anson, and A.K. Powell, *High-nuclearity 3d–4f [Fe III 5 Ln III 8] complexes: synthesis, structure and magnetic properties.* Dalton Transactions, 2007(45): p. 5245-5247.
329. Baniodeh, A., N. Magnani, Y. Lan, G. Buth, C.E. Anson, J. Richter, M. Affronte, J. Schnack, and A.K. Powell, *High spin cycles: topping the spin record for a single molecule verging on quantum criticality.* npj Quantum Materials, 2018. **3**(1): p. 1-6.
330. Kaemmerer, H., A. Baniodeh, Y. Peng, E. Moreno-Pineda, M. Schulze, C.E. Anson, W. Wernsdorfer, J. Schnack, and A.K. Powell, *An Inorganic Approach to Stabilizing Nanoscale Toroidicity in a tetraicosanuclear Fe18Dy6 Single Molecule Magnet.* J. Am. Chem. Soc., 2020.

331. Peng, G., G.E. Kostakis, Y. Lan, and A.K. Powell, *Body-wing swapping in butterfly {Fe III 2 Ln III 2} coordination clusters with triethylene glycol as ligand.* Dalton Transactions, 2013. **42**(1): p. 46-49.
332. Peng, G., V. Mereacre, G.E. Kostakis, J.A. Wolny, V. Schünemann, and A.K. Powell, *Enhancement of spin relaxation in an FeDy2Fe coordination cluster by magnetic fields.* Chemistry–A European Journal, 2014. **20**(39): p. 12381-12384.
333. Kizas, C.M., C. Papatriantafyllopoulou, M.J. Manos, and A.J. Tasiopoulos, *Heterometallic FeIII–CeIV complexes from the use of aliphatic aminoalcohol ligands.* Polyhedron, 2013. **52**: p. 346-354.
334. Baca, S., J. van Leusen, M. Speldrich, and P. Kögerler, *Understanding the magnetism of {Fe 2 Ln} dimers, step-by-step.* Inorganic Chemistry Frontiers, 2016. **3**(8): p. 1071-1075.
335. Mereacre, V., F. Klöwer, Y. Lan, R. Clérac, J.A. Wolny, V. Schünemann, C.E. Anson, and A.K. Powell, *Spin relaxation in antiferromagnetic Fe–Fe dimers slowed down by anisotropic DyIII ions.* Beilstein journal of nanotechnology, 2013. **4**(1): p. 807-814.
336. Botezat, O., J. Van Leusen, P. Kögerler, and S.G. Baca, *Ultrasound-Assisted Formation of {Fe6Ln/Y4} Wheel-Shaped Clusters and Condensed {Fe4Ln/Y2} Aggregates.* Eur. J. Inorg. Chem., 2019. **2019**(16): p. 2236-2244.
337. Botezat, O., J. van Leusen, V.C. Kravtsov, P. Kögerler, and S.G. Baca, *Ultralarge 3d/4f Coordination Wheels: From Carboxylate/Amino Alcohol-Supported {Fe4Ln2} to {Fe18Ln6} Rings.* Inorg. Chem., 2017. **56**(4): p. 1814-1822.
338. Zhou, Q., F. Yang, D. Liu, Y. Peng, G. Li, Z. Shi, and S. Feng, *Synthesis, structures, and magnetic properties of a family of 3d–4f [Na 2 Fe 6 Ln 2] complexes (Ln= Y, Gd and Dy): effect of ligands on the connection of inorganic subunits.* Dalton Transactions, 2013. **42**(4): p. 1039-1046.
339. Schmidt, S., D. Prodius, V. Mereacre, G.E. Kostakis, and A.K. Powell, *Unprecedented chemical transformation: crystallographic evidence for 1, 1, 2, 2-tetrahydroxyethane captured within an Fe 6 Dy 3 single molecule magnet.* Chem. Commun., 2013. **49**(17): p. 1696-1698.
340. Serna, Z., N. De la Pinta, M.K. Urtiaga, L. Lezama, G. Madariaga, J.M. Clemente-Juan, E. Coronado, and R. Cortés, *Defective dicubane-like tetranuclear nickel (II) cyanate and azide nanoscale magnets.* Inorg. Chem., 2010. **49**(24): p. 11541-11549.
341. Wang, H.-S., Q.-Q. Long, Z.-B. Hu, L. Yue, F.-J. Yang, C.-L. Yin, Z.-Q. Pan, Y.-Q. Zhang, and Y. Song, *Synthesis, crystal structures and magnetic properties of a series of chair-like heterometallic [Fe 4 Ln 2](Ln= Gd III, Dy III, Ho III, and Er III) complexes with mixed organic ligands.* Dalton Transactions, 2019. **48**(35): p. 13472-13482.
342. Georgopoulou, A.N., R. Adam, C.P. Raptopoulou, V. Psycharis, R. Ballesteros, B. Abarca, and A.K. Boudalis, *Expanding the 3d-4f heterometallic chemistry of the (py) 2 CO and pyCOpyCOpy ligands: structural, magnetic and Mössbauer spectroscopic studies of two Fe II–Gd III co mplexes.* Dalton Transactions, 2011. **40**(32): p. 8199-8205.
343. Wang, H.-S., Y. Chen, Z.-B. Hu, C.-L. Yin, Z. Zhang, and Z.-Q. Pan, *Modulation of the directions of the anisotropic axes of Dy III ions through utilizing two kinds of organic ligands or replacing Dy III ions by Fe III ions.* CrystEngComm, 2019. **21**(36): p. 5429-5439.
344. Bhunia, A., Y. Lan, V. Mereacre, M.T. Gamer, A.K. Powell, and P.W. Roesky, *Salen-Based Coordination Polymers of Iron and the Rare Earth Elements.* Inorg. Chem., 2011. **50**(24): p. 12697-12704.

345. Xiang, H., V. Mereacre, Y. Lan, T.-B. Lu, C.E. Anson, and A.K. Powell, *Direct observation of the role of lanthanides in stabilizing a ferromagnetic spin orientation in a weak Fe III–Fe III antiferromagnet.* Chem. Commun., 2013. **49**(67): p. 7385-7387.
346. Baniodeh, A., V. Mereacre, N. Magnani, Y. Lan, J.A. Wolny, V. Schünemann, C.E. Anson, and A.K. Powell, *Para versus meta ligand substituents as a means of directing magnetic anisotropy in Fe 2 Dy 2 coordination clusters.* Chem. Commun., 2013. **49**(83): p. 9666-9668.
347. Bag, P., J. Goura, V. Mereacre, G. Novitchi, A.K. Powell, and V. Chandrasekhar, *Synthesis, magnetism and Mössbauer studies of tetranuclear heterometallic {Fe III 2 Ln 2}(Ln= Gd, Dy, Tb) complexes: evidence of slow relaxation of magnetization in the terbium analogue.* Dalton Transactions, 2014. **43**(43): p. 16366-16376.
348. Peng, Y., V. Mereacre, C.E. Anson, and A.K. Powell, *Multiple superhyperfine fields in a {DyFe 2 Dy} coordination cluster revealed using bulk susceptibility and 57 Fe Mössbauer studies.* PCCP, 2016. **18**(31): p. 21469-21480.
349. Gao, S., B.-Q. Ma, H.-L. Sun, and J.-R. Li, *Two novel types of Ln2M2 clusters bridged by cyanide and carboxylate simultaneously.* J. Solid State Chem., 2003. **171**(1-2): p. 201-207.
350. Cai, L.-Z., W. Zhang, Z.-X. Zhu, J. Ru, and M.-X. Yao, *Synthesis, structures and magnetic properties of cyano-and amide-bridged FeIII-LnIII tetranuclear heterometallic clusters.* J. Coord. Chem., 2019. **72**(5-7): p. 1097-1107.
351. Song, X.-J., J.-J. Xu, Y. Chen, M. Muddassir, F. Cao, R.-M. Wei, Y. Song, and X.-Z. You, *Synthesis, structures and magnetic properties of cyano-bridged 3d–4f rectangular tetranuclear [FeIII2LnIII2](Ln= Y, Tb, Dy) compounds containing [FeIII (bpy)(CN) 4]− unit.* Polyhedron, 2013. **66**: p. 212-217.
352. Pugh, T., N.F. Chilton, and R.A. Layfield, *A Low-Symmetry Dysprosium Metallocene Single-Molecule Magnet with a High Anisotropy Barrier.* Angew. Chem., 2016. **128**(37): p. 11248-11251.
353. Zhou, H., D.Y. Yu, H.B. Zhou, and A.H. Yuan, *Cyanide-Bridged Tetranuclear REIII2FeIII2 (RE= Y, Tb, Dy) Molecular Squares with 2, 2′: 6′, 2″-Terpyridine as a Capping Ligand.* Z. Anorg. Allg. Chem., 2015. **641**(5): p. 858-862.
354. Alexandru, M.-G., D. Visinescu, S. Shova, W.X. Oliveira, F. Lloret, and M. Julve, *Design of 3d–4f molecular squares through the [Fe {(HB (pz) 3)}(CN) 3]− metalloligand.* Dalton Transactions, 2018. **47**(17): p. 6005-6017.
355. Chen, W.-B., Y.-C. Chen, G.-Z. Huang, J.-L. Liu, J.-H. Jia, and M.-L. Tong, *Cyclic OFF/Part/ON switching of single-molecule magnet behaviours via multistep single-crystal-to-single-crystal transformation between discrete Fe (II)–Dy (III) complexes.* Chem. Commun., 2018. **54**(77): p. 10886-10889.
356. Wang, H.-S., C.-L. Yin, Z.-B. Hu, Y. Chen, Z.-Q. Pan, Y. Song, Y.-Q. Zhang, and Z.-C. Zhang, *Regulation of magnetic relaxation behavior by replacing 3d transition metal ions in [M 2 Dy 2] complexes containing two different organic chelating ligands.* Dalton Transactions, 2019. **48**(27): p. 10011-10022.
357. Huang, W., J.J. Le Roy, S.I. Khan, L. Ungur, M. Murugesu, and P.L. Diaconescu, *Tetraanionic biphenyl lanthanide complexes as single-molecule magnets.* Inorg. Chem., 2015. **54**(5): p. 2374-2382.
358. Grindell, R., B.M. Day, F.-S. Guo, T. Pugh, and R.A. Layfield, *Activation of C–H bonds by rare-earth metallocene-butyl complexes.* Chem. Commun., 2017. **53**(72): p. 9990-9993.

359. Liu, J.-C., J.-W. Zhao, and Y.-F. Song, *1-D Chain Tungstotellurate Hybrids Constructed from Organic-Ligand-Connecting Iron–Lanthanide Heterometal Encapsulated Tetrameric Polyoxotungstate Units.* Inorg. Chem., 2019. **58**(15): p. 9706-9712.
360. Mereacre, V., Y. Lan, R. Clérac, A.M. Ako, I.J. Hewitt, W. Wernsdorfer, G. Buth, C.E. Anson, and A.K. Powell, *Family of MnIII2Ln2 (μ4-O) compounds: syntheses, structures, and magnetic properties.* Inorg. Chem., 2010. **49**(11): p. 5293-5302.
361. Polyzou, C.D., A. Baniodeh, N. Magnani, V. Mereacre, N. Zill, C.E. Anson, S.P. Perlepes, and A.K. Powell, *Squashed {Fe 2 III M 4 III} octahedra (M= Y, Gd, Dy) from the first use of the cyanoacetate ligand in 3d/4f coordination chemistry.* RSC Advances, 2015. **5**(14): p. 10763-10767.
362. Dey, A., S. Das, V. Mereacre, A.K. Powell, and V. Chandrasekhar, *Butterfly-shaped, heterometallic, hexanuclear,[FeIII2LnIII4](LnIII= GdIII, TbIII, DyIII and HoIII) Complexes: Syntheses, structure and magnetism.* Inorg. Chim. Acta, 2019. **486**: p. 458-467.
363. Xiang, H., W.-G. Lu, W.-X. Zhang, and L. Jiang, *A {Cr 2 Dy 4} compressed octahedron: the first sulfate-based single-molecule magnet.* Dalton Transactions, 2013. **42**(4): p. 867-870.
364. Liu, C.-M., D.-Q. Zhang, and D.-B. Zhu, *Hexanuclear [Ni 2 Ln 4] clusters exhibiting enhanced magnetocaloric effect and slow magnetic relaxation.* RSC advances, 2014. **4**(96): p. 53870-53876.
365. Feuersenger, J., D. Prodius, V. Mereacre, R. Clérac, C.E. Anson, and A.K. Powell, *Structure and magnetic properties of hexanuclear 3d–4f clusters with {MnIII2LnIII4}(Ln= Sm, Eu, Gd, Tb, Dy, Ho) core.* Inorg. Chem. Commun., 2011. **14**(12): p. 1851-1854.
366. Xie, Q.-W., A.-L. Cui, J. Tao, and H.-Z. Kou, *Syntheses, structure, and magnetic properties of hexanuclear Mn III 2 M III 4 (M= Y, Gd, Tb, Dy) complexes.* Dalton Transactions, 2012. **41**(35): p. 10589-10595.
367. Chakraborty, A., P. Bag, J. Goura, A.K. Bar, J.-P. Sutter, and V. Chandrasekhar, *Chair-shaped MnII2LnIII4 (Ln= Gd, Tb, Dy, Ho) heterometallic complexes assembled from a tricompartmental aminobenzohydrazide ligand.* Crystal Growth & Design, 2015. **15**(2): p. 848-857.
368. Feuersenger, J., D. Prodius, V. Mereacre, R. Clérac, C.E. Anson, and A.K. Powell, *Synthesis, structure and magnetic properties of hexanuclear CoIII–LnIII clusters.* Polyhedron, 2013. **66**: p. 257-263.
369. Jhan, S.-Y., S.-H. Huang, C.-I. Yang, and H.-L. Tsai, *Structure and magnetic properties of a 3d–4f CoIII2DyIII4 cluster.* Polyhedron, 2013. **66**: p. 222-227.
370. Goura, J., A. Chakraborty, J.P. Walsh, F. Tuna, and V. Chandrasekhar, *Hexanuclear 3d–4f Neutral CoII2LnIII4 Clusters: Synthesis, Structure, and Magnetism.* Crystal Growth & Design, 2015. **15**(7): p. 3157-3165.
371. Zou, H.-H., L.-B. Sheng, F.-P. Liang, Z.-L. Chen, and Y.-Q. Zhang, *Experimental and theoretical investigations of four 3d–4f butterfly single-molecule magnets.* Dalton Transactions, 2015. **44**(42): p. 18544-18552.
372. Zhang, H., R. Liu, J. Zhang, Y. Li, and W. Liu, *Chair-like [Ln III 4 Co III 2](Ln= Dy, Eu, Gd, Tb) clusters including a [Dy III 4 Co III 2] single molecule magnet.* CrystEngComm, 2016. **18**(42): p. 8246-8252.
373. Tian, C.-B., D.-Q. Yuan, Y.-H. Han, Z.-H. Li, P. Lin, and S.-W. Du, *Synthesis, structures, and magnetic properties of a series of new heterometallic hexanuclear Co 2 Ln 4 (Ln= Eu, Gd, Tb and Dy) clusters.* Inorganic Chemistry Frontiers, 2014. **1**(9): p. 695-704.

374. Cremades, E., S. Gómez-Coca, D. Aravena, S. Alvarez, and E. Ruiz, *Theoretical study of exchange coupling in 3d-Gd complexes: Large magnetocaloric effect systems.* J. Am. Chem. Soc., 2012. **134**(25): p. 10532-10542.
375. Akhtar, M.N., V. Mereacre, G. Novitchi, J.P. Tuchagues, C.E. Anson, and A.K. Powell, *Probing Lanthanide Anisotropy in Fe–Ln Aggregates by Using Magnetic Susceptibility Measurements and 57Fe Mössbauer Spectroscopy.* Chemistry–A European Journal, 2009. **15**(30): p. 7278-7282.
376. Cañada-Vilalta, C., T.A. O'Brien, E.K. Brechin, M. Pink, E.R. Davidson, and G. Christou, *Large spin differences in structurally related Fe6 molecular clusters and their magnetostructural explanation.* Inorg. Chem., 2004. **43**(18): p. 5505-5521.
377. Milios, C.J., R. Inglis, A. Vinslava, R. Bagai, W. Wernsdorfer, S. Parsons, S.P. Perlepes, G. Christou, and E.K. Brechin, *Toward a magnetostructural correlation for a family of Mn6 SMMs.* J. Am. Chem. Soc., 2007. **129**(41): p. 12505-12511.
378. Chen, S., V. Mereacre, G.E. Kostakis, C.E. Anson, and A.K. Powell, *Systematic studies of hexanuclear {M III4 Ln III2} complexes (M= Fe, Ga; Ln= Er, Ho): structures, magnetic properties and SMM behavior.* Inorganic Chemistry Frontiers, 2017. **4**(6): p. 927-934.
379. Chen, S., V. Mereacre, D. Prodius, G.E. Kostakis, and A.K. Powell, *Developing a "highway code" to steer the structural and electronic properties of FeIII/DyIII coordination clusters.* Inorg. Chem., 2015. **54**(7): p. 3218-3227.
380. Blake, M.P., N. Kaltsoyannis, and P. Mountford, *Synthesis and reactions of β-diketiminate-supported complexes with Mg–Fe or Yb–Fe bonds.* Chem. Commun., 2013. **49**(32): p. 3315-3317.
381. Blake, M.P., N. Kaltsoyannis, and P. Mountford, *Heterobimetallic complexes containing Ca–Fe or Yb–Fe bonds: synthesis and molecular and electronic structures of [M {CpFe (CO) 2} 2 (THF) 3] 2 (M= Ca or Yb).* J. Am. Chem. Soc., 2011. **133**(39): p. 15358-15361.
382. Goura, J., V. Mereacre, G. Novitchi, A.K. Powell, and V. Chandrasekhar, *Homometallic FeIII4 and Heterometallic {FeIII4LnIII2}(Ln= Dy, Tb) Complexes–Syntheses, Structures, and Magnetic Properties.* Eur. J. Inorg. Chem., 2015. **2015**(1): p. 156-165.
383. Pham, L., K.A. Abboud, W. Wernsdorfer, and G. Christou, *Synthesis, structure and magnetic properties of [FeIII4LnIII2](Ln= Gd, Tb, Dy, Ho) and [FeIII4YIII2] clusters.* Polyhedron, 2013. **66**: p. 205-211.
384. Visinescu, D., L.M. Toma, O. Fabelo, C. Ruiz-Pérez, F. Lloret, and M. Julve, *Low-dimensional 3d–4f complexes assembled by low-spin [FeIII (phen)(CN) 4]− anions.* Inorg. Chem., 2013. **52**(3): p. 1525-1537.
385. Yan, P., F. Zhang, G. Li, J. Zhang, W. Sun, M. Suda, and Y. Einaga, *Synthesis, crystal structures, magnetic and luminescent properties of unique 1D p-ferrocenylbenzoate-bridged lanthanide complexes.* J. Solid State Chem., 2009. **182**(7): p. 1685-1690.
386. Zhao, J.-W., J. Cao, Y.-Z. Li, J. Zhang, and L.-J. Chen, *First tungstoantimonate-based transition-metal–lanthanide heterometallic hybrids functionalized by amino acid ligands.* Crystal growth & design, 2014. **14**(12): p. 6217-6229.
387. Visinescu, D., O. Fabelo, C. Ruiz-Pérez, F. Lloret, and M. Julve, *[Fe (phen)(CN) 4]−: a suitable metalloligand unit to build 3d–4f heterobimetallic complexes with mixed bpym-cyano bridges (phen= 1, 10-phenantroline, bpym= 2, 2'-bipyrimidine).* CrystEngComm, 2010. **12**(8): p. 2454-2465.
388. Efimov, N.N., P.S. Koroteev, A.V. Gavrikov, A.B. Ilyukhin, Z.V. Dobrokhotova, and V.M. Novotortsev, *Magnetic Behavior of Carboxylate and β-Diketonate Lanthanide*

Complexes Containing Stable Organometallic Moieties in the Core-Forming Ligand. Magnetochemistry, 2016. **2**(4): p. 38.
389. Chen, L., F. Zhang, X. Ma, J. Luo, and J. Zhao, *Two types of novel tetra-iron substituted sandwich-type arsenotungastates with supporting lanthanide pendants.* Dalton Transactions, 2015. **44**(28): p. 12598-12612.
390. Chen, Y., L. Sun, S. Chang, L. Chen, and J. Zhao, *Synergistic effect between different coordination geometries of lanthanides and various coordination modes of 2-picolinic acid ligands tuning three types of rare 3d–4f heterometallic tungstoantimonates.* Inorg. Chem., 2018. **57**(24): p. 15079-15092.
391. Qi-Hua, Z., Q.H. Wang, R.B. Fang, and Z.D. Chen, *Synthesis, Crystal Structure and Properties of a New One-Dimensional 3d-4f Compound.* Chin. J. Chem . 2004. **22**(3): p. 264-267.
392. Rocha, J., F.A.A. Paz, F.N. Shi, D. Ananias, N.J. Silva, L.D. Carlos, and T. Trindade, *Mixed-Metal d-f Phosphonate Frameworks–Photoluminescence and Magnetic Properties.* Eur. J. Inorg. Chem., 2011. **2011**(13): p. 2035-2044.
393. Koroteev, P., Z.V. Dobrokhotova, N. Efimov, A. Ilyukhin, and V. Novotortsev, *New binuclear ferrocenecarboxylates of rare-earth metals as precursors for ferrites: Syntheses, structures, and solid-phase thermolysis.* Russian Journal of Coordination Chemistry, 2014. **40**(7): p. 495-504.
394. Johns, N., S.M. Balasekaran, A. Chang, P.K. Bhowmik, and F. Poineau, *Preparation and molecular structure of lanthanum–FcCOO−–DTBbpy complexes.* Inorg. Chim. Acta, 2019. **489**: p. 115-119.
395. Gu, X.-Y., X.-Z. Han, Y.-M. Yao, Y. Zhang, and Q. Shen, *Synthesis and characterization of lanthanide complexes bearing a ferrocene-containing N-aryloxo-β-ketoiminate ligand.* J. Organomet. Chem., 2010. **695**(25-26): p. 2726-2731.
396. Akhtar, M.N., Y. Lan, M.A. AlDamen, Y.-Z. Zheng, C.E. Anson, and A.K. Powell, *Effect of ligand substitution on the SMM properties of three isostructural families of double-cubane Mn 4 Ln 2 coordination clusters.* Dalton Transactions, 2018. **47**(10): p. 3485-3495.
397. Koroteev, P.S., Z.V. Dobrokhotova, A.B. Ilyukhin, N.N. Efimov, D.I. Kirdyankin, A.V. Tyurin, Y.A. Velikodny, M.L. Kovba, and V.M. Novotortsev, *Lanthanide cymantrenecarboxylate complexes with an Ln: Mn ratio of 1: 2 as precursors for LnMn2O5 phases. Synthesis, structure, physicochemical properties, and thermal decomposition.* Polyhedron, 2013. **65**: p. 110-121.
398. Liu, J., C. Ma, H. Chen, M. Hu, H. Wen, H. Cui, X. Song, and C. Chen, *Syntheses, structures and magnetic properties of a family of heterometallic [Mn II 2 Mn III 2 Ln III 2] clusters.* Dalton Transactions, 2013. **42**(7): p. 2423-2430.
399. Modak, R., Y. Sikdar, A. Bieńko, M. Witwicki, M. Jerzykiewicz, and S. Goswami, *Family of MnIII4LnIII2 (LnIII= SmIII, GdIII, DyIII) coordination clusters: Experimental and theoretical investigations.* Polyhedron, 2016. **119**: p. 202-215.
400. Savva, M., K. Skordi, A.D. Fournet, A.E. Thuijs, G. Christou, S.P. Perlepes, C. Papatriantafyllopoulou, and A.J. Tasiopoulos, *Heterometallic MnIII4Ln2 (Ln= Dy, Gd, Tb) Cross-Shaped Clusters and Their Homometallic MnIII4MnII2 Analogues.* Inorg. Chem., 2017. **56**(10): p. 5657-5668.
401. Tang, Q., Y. Sun, H.Y. Li, J.Q. Wu, Y.N. Liang, and Z. Zhang, *Hexanuclear 3d− 4f metal–organic cages assembled from a carboxylic acid-functionalized tris-triazamacrocycle for highly selective fluorescent sensing of picric acid.* Appl. Organomet. Chem., 2019. **33**(4): p. e4814.

402. Li, Q., Y. Peng, J. Qian, T. Yan, L. Du, and Q. Zhao, *A family of planar hexanuclear Co III4 Ln III2 clusters with lucanidae-like arrangement and single-molecule magnet behavior.* Dalton Transactions, 2019. **48**(34): p. 12880-12887.
403. Griffiths, K., G. Novitchi, and G.E. Kostakis, *Synthesis, characterization, magnetic properties, and topological aspects of isoskeletal heterometallic hexanuclear Co II 4 Ln III 2 coordination clusters possessing 2, 3, 4M6-1 topology.* Eur. J. Inorg. Chem., 2016. **2016**(17): p. 2750-2756.
404. Radu, I., V.C. Kravtsov, K. Krämer, S. Decurtins, S.-X. Liu, O.S. Reu, S.M. Ostrovsky, S.I. Klokishner, and S.G. Baca, *Synthesis, characterization, and modeling of magnetic properties of a hexanuclear amino alcohol-supported {CoII2CoIII2DyIII2} pivalate cluster.* The Journal of Physical Chemistry C, 2016. **120**(13): p. 7435-7443.
405. Funes, A.V., L. Carrella, E. Rentschler, and P. Alborés, *Exploring the Slow Relaxation of the Magnetization in CoIII-Decorated {DyIII2} Units.* Chemistry–A European Journal, 2016. **22**(40): p. 14308-14318.
406. Zhao, L., J. Wu, H. Ke, and J. Tang, *Family of Defect-Dicubane Ni4Ln2 (Ln= Gd, Tb, Dy, Ho) and Ni4Y2 Complexes: Rare Tb (III) and Ho (III) Examples Showing SMM Behavior.* Inorg. Chem., 2014. **53**(7): p. 3519-3525.
407. Bhanja, A., R. Herchel, Z. Travnicek, and D. Ray, *Two types of hexanuclear partial tetracubane [Ni4Ln2](Ln= Dy, Tb, Ho) complexes of thioether-based schiff base ligands: synthesis, structure, and comparison of magnetic properties.* Inorg. Chem., 2019. **58**(18): p. 12184-12198.
408. Ke, H., L. Zhao, Y. Guo, and J. Tang, *Syntheses, structures, and magnetic analyses of a family of heterometallic hexanuclear [Ni4M2](M= Gd, Dy, Y) compounds: observation of slow magnetic relaxation in the DyIII derivative.* Inorg. Chem., 2012. **51**(4): p. 2699-2705.
409. Pei, S., Z. Hu, Z. Chen, S. Yu, B. Li, Y. Liang, D. Liu, D. Yao, and F. Liang, *Heterometallic hexanuclear Ni 4 M 2 (M= Dy, Y) complexes: structure and single-molecule magnet for the Dy (iii) derivative.* Dalton Transactions, 2018. **47**(6): p. 1801-1807.
410. Alexandropoulos, D.I., L. Cunha-Silva, J. Tang, and T.C. Stamatatos, *Heterometallic Cu/Ln cluster chemistry: ferromagnetically-coupled {Cu 4 Ln 2} complexes exhibiting single-molecule magnetism and magnetocaloric properties.* Dalton Transactions, 2018. **47**(34): p. 11934-11941.
411. Biswas, S., P. Bag, S. Das, S. Kundu, J. van Leusen, P. Kögerler, and V. Chandrasekhar, *Heterometallic [Cu2Ln3](Ln= DyIII, GdIII and HoIII) and [Cu4Ln2](Ln= DyIII and HoIII) Compounds: Synthesis, Structure, and Magnetism.* Eur. J. Inorg. Chem., 2017. **2017**(8): p. 1129-1142.
412. Gao, G., L. Wang, R. Zhang, C. Xu, H. Yang, and W. Liu, *Hexanuclear 3d–4f complexes as efficient catalysts for converting CO 2 into cyclic carbonates.* Dalton Transactions, 2019. **48**(12): p. 3941-3945.
413. Griffiths, K., J. Mayans, M.A. Shipman, G.J. Tizzard, S.J. Coles, B.A. Blight, A. Escuer, and G.E. Kostakis, *Four new families of polynuclear Zn-Ln coordination clusters. Synthetic, topological, magnetic, and luminescent aspects.* Crystal Growth & Design, 2017. **17**(4): p. 1524-1538.
414. Ängskog, P., M. Bäckström, and B. Vallhagen. *Measurement of radio signal propagation through window panes and energy saving windows*. in *2015 IEEE international symposium on electromagnetic compatibility (EMC)*. 2015. IEEE.

415. Lawrence, J., P. Lubrani, and L. Li, *On the selective deposition of tin and tin oxide on various glasses using a high power diode laser.* Surf. Coat. Technol., 2001. **137**(2-3): p. 235-240.
416. Baetens, R., B.P. Jelle, and A. Gustavsen, *Properties, requirements and possibilities of smart windows for dynamic daylight and solar energy control in buildings: A state-of-the-art review.* Sol. Energy Mater. Sol. Cells, 2010. **94**(2): p. 87-105.
417. Qu, J., J. Song, J. Qin, Z. Song, W. Zhang, Y. Shi, T. Zhang, H. Zhang, R. Zhang, and Z. He, *Transparent thermal insulation coatings for energy efficient glass windows and curtain walls.* Energy and Buildings, 2014. **77**: p. 1-10.
418. Leftheriotis, G. and P. Yianoulis, *Glazings and coatings.* 2012.
419. Huang, H., M. Ng, Y. Wu, and L. Kong, *Solvothermal synthesis of Sb: SnO2 nanoparticles and IR shielding coating for smart window.* Materials & Design, 2015. **88**: p. 384-389.
420. Rosencrantz, T., *Performance of Energy Efficient Windows and solar shading devices.* Lund University, 2005. **3**.
421. Lim, H.S., *Fabrication of frequency selective structure and evaluation of microwave transmission on energy saving glass*. 2015, Universiti Tun Hussein Onn Malaysia.
422. Takeuchi, T., O. Goto, M. Inuduka, T. Narasaki, Y. Tokunaga, H. Bessho, and H. Takeda, *Development of Window Films for Solar Shading and Heat Insulating Applications.* SEI Technical Review, 2012(74): p. 95.
423. Kamalisarvestani, M., R. Saidur, S. Mekhilef, and F. Javadi, *Performance, materials and coating technologies of thermochromic thin films on smart windows.* Renewable and Sustainable Energy Reviews, 2013. **26**: p. 353-364.
424. Korgel, B.A., *Composite for smarter windows.* Nature, 2013. **500**(7462): p. 278-279.
425. Al-Kuhaili, M., S. Ahmad, S. Durrani, M. Faiz, and A. Ul-Hamid, *Energy-saving spectrally-selective coatings based on MoO3/Ag thin films.* Materials & Design, 2015. **73**: p. 15-19.
426. Kiani, G.I., *Passive, active and absorbing frequency selective surfaces for wireless communication applications.* 2008.
427. Heede, R., *Tracing anthropogenic carbon dioxide and methane emissions to fossil fuel and cement producers, 1854–2010.* Climatic Change, 2014. **122**(1-2): p. 229-241.
428. Sohail, S.I. and M.J. Mohammad Zarar, *Frequency selective surface for RF/microwave signal transmission in energy-saving glass.* 2015.
429. Kiani, G.I., A. Karlsson, L. Olsson, and K.P. Esselle. *Glass characterization for designing frequency selective surfaces to improve transmission through energy saving glass windows*. in *2007 Asia-Pacific Microwave Conference*. 2007. IEEE.
430. Ullah, I., X. Zhao, D. Habibi, and G. Kiani. *Transmission improvement of UMTS and Wi-Fi signals through energy saving glass using FSS*. in *WAMICON 2011 Conference Proceedings*. 2011. IEEE.
431. Bouvard, O., M. Lanini, L. Burnier, R. Witte, B. Cuttat, A. Salvade, and A. Schüler, *Structured transparent low emissivity coatings with high microwave transmission.* Appl. Phys. A, 2017. **123**(1): p. 66.
432. Kiani, G.I., L.G. Olsson, A. Karlsson, K.P. Esselle, and M. Nilsson, *Cross-dipole bandpass frequency selective surface for energy-saving glass used in buildings.* IEEE Transactions on Antennas and Propagation, 2010. **59**(2): p. 520-525.
433. Chung, W.-Y., C.-H. Shim, D.-D. Lee, and S.-D. Choi, *Tin oxide microsensor for LPG monitoring.* Sensors and Actuators B: Chemical, 1994. **20**(2-3): p. 139-143.

434. Omura, K., P. Veluchamy, M. Tsuji, T. Nishio, and M. Murozono, *A pyrosol technique to deposit highly transparent, low-resistance SnO2: F Thin films from dimethyltin dichloride.* J. Electrochem. Soc., 1999. **146**(6): p. 2113.
435. Kane, J., H. Schweizer, and W. Kern, *Chemical vapor deposition of transparent, electrically conductive tin oxide films formed from dibutyl tin diacetate.* J. Electrochem. Soc., 1975. **122**(8): p. 1144.
436. Brown, J., P. Haycock, L. Smith, A. Jones, and E. Williams, *Response behaviour of tin oxide thin film gas sensors grown by MOCVD.* Sensors and actuators B: Chemical, 2000. **63**(1-2): p. 109-114.
437. Bruneaux, J., H. Cachet, M. Froment, and A. Messad, *Correlation between structural and electrical properties of sprayed tin oxide films with and without fluorine doping.* Thin Solid Films, 1991. **197**(1-2): p. 129-142.
438. Varghese, O.K., L. Malhotra, and G. Sharma, *High ethanol sensitivity in sol–gel derived SnO2 thin films.* Sensors and Actuators B: Chemical, 1999. **55**(2-3): p. 161-165.
439. Sujatha, C., G.M. Rao, and S. Uthanna, *Characteristics of indium tin oxide films deposited by bias magnetron sputtering.* Materials Science and Engineering: B, 2002. **94**(1): p. 106-110.
440. Homma, H., M. Kentjana, E. Alp, T. Mooney, E. Witthoff, and T. Toellner, *SnO2 grazing-incidence antireflection films for monochromatization of synchrotron radiation: Design, preparation, and characterization.* J. Appl. Phys., 1992. **72**(12): p. 5668-5675.
441. Rella, R., A. Serra, P. Siciliano, L. Vasanelli, G. De, A. Licciulli, and A. Quirini, *Tin oxide-based gas sensors prepared by the sol–gel process.* Sensors and Actuators B: Chemical, 1997. **44**(1-3): p. 462-467.
442. Reddy, M.M. and A. Chandorkar, *E-beam deposited SnO2, Pt–SnO2 and Pd–SnO2 thin films for LPG detection.* Thin Solid Films, 1999. **349**(1-2): p. 260-265.
443. Farber, Y., F. Khonsari-Arefi, and J. Amouroux, *Thin film deposition of conductive tin oxide from tetramethyltin in a low pressure glow discharge diode reactor.* Thin Solid Films, 1994. **241**(1-2): p. 282-286.
444. Czapla, A., E. Kusior, and M. Bucko, *Optical properties of non-stoichiometric tin oxide films obtained by reactive sputtering.* Thin Solid Films, 1989. **182**(1-2): p. 15-22.
445. Karanjai, M.K. and D.D. Gupta, *A simple and novel technique for the deposition of conducting tin dioxide films.* J. Phys. D: Appl. Phys., 1988. **21**(2): p. 356.
446. Dominguez, J., X. Pan, L. Fu, P. Van Rompay, Z. Zhang, J. Nees, and P. Pronko, *Epitaxial SnO 2 thin films grown on (1̄012) sapphire by femtosecond pulsed laser deposition.* J. Appl. Phys., 2002. **91**(3): p. 1060-1065.
447. Supothina, S. and M.R. De Guire, *Characterization of SnO2 thin films grown from aqueous solutions.* Thin Solid Films, 2000. **371**(1-2): p. 1-9.
448. Arai, T., *The study of the optical properties of conducting tin oxide films and their interpretation in terms of a tentative band scheme.* J. Phys. Soc. Jpn., 1960. **15**(5): p. 916-927.
449. Russo, D., C. McKown, C. Roger, J. Brotzman, and J. Stricker, *The influence of film composition on the optical and thermal properties of solar control coatings.* Thin Solid Films, 2001. **398**: p. 65-70.
450. Terrier, C., J. Chatelon, and J. Roger, *Electrical and optical properties of Sb: SnO2 thin films obtained by the sol-gel method.* Thin Solid Films, 1997. **295**(1-2): p. 95-100.
451. Lampert, C.M., *Heat mirror coatings for energy conserving windows.* Solar Energy Materials, 1981. **6**(1): p. 1-41.

452. Hiroko, K., T. Hiromitsu, and A. Kenji, *Near infra-red shielding single or multilayer film and a coating liquid for forming the same.* European Patent, 1999.
453. Elangovan, E. and K. Ramamurthi, *Optoelectronic properties of spray deposited SnO 2: F thin films for window materials in solar cells.* Journal of Optoelectronics and Advanced Materials, 2003. **5**(1): p. 45-54.
454. Taga, Y., *Recent progress in coating technology for surface modification of automotive glass.* J. Non-Cryst. Solids, 1997. **218**: p. 335-341.
455. Dawar, A. and J. Joshi, *Semiconducting transparent thin films: their properties and applications.* Journal of Materials Science, 1984. **19**(1): p. 1-23.
456. Bewilogua, K., G. Bräuer, A. Dietz, J. Gäbler, G. Goch, B. Karpuschewski, and B. Szyszka, *Surface technology for automotive engineering.* CIRP annals, 2009. **58**(2): p. 608-627.
457. Young, P.I. and J.D. Wolfe, *Solar control layered coating for glass windows*. 1990, Google Patents.
458. Openstax. *The Electromagnetic Spectrum*. Available from: https://openstax.org/books/astronomy/pages/5-2-the-electromagnetic-spectrum.
459. Tuchinda, C., S. Srivannaboon, and H.W. Lim, *Photoprotection by window glass, automobile glass, and sunglasses.* Journal of the American Academy of Dermatology, 2006. **54**(5): p. 845-854.
460. Granqvist, C.G., *Handbook of inorganic electrochromic materials*. 1995: Elsevier.
461. Forbes. *The Weaponization Of The Electromagnetic Spectrum*. Available from: https://www.forbes.com/sites/cognitiveworld/2019/04/12/the-weaponization-of-the-electromagnetic-spectrum/#15af99c2699e.
462. Rajendran, V., H. Chang, and R.-S. Liu, *Recent progress on broadband near-infrared phosphors-converted light emitting diodes for future miniature spectrometers.* Optical Materials: X, 2019. **1**: p. 100011.
463. Herschel, W., *XIV. Experiments on the refrangibility of the invisible rays of the sun.* Philosophical Transactions of the Royal Society of London, 1800(90): p. 284-292.
464. Vatansever, F. and M.R. Hamblin, *Far infrared radiation (FIR): Its biological effects and medical applications: Ferne Infrarotstrahlung: Biologische Effekte und medizinische Anwendungen.* Photonics & lasers in medicine, 2012. **1**(4): p. 255-266.
465. Katono, H., Ujiie, T., *KUREHA heat ray absorbing materials.* Convertech, 2006. **34**(6): p. 31-33.
466. Katono, H., *Technology and features of solar heat shielding functional material.* JETI, 2005. **53**(2): p. 93-95.
467. Katono, H.K.T.K., *High performance heat shielding material with high visible transmittance.* Chem Chem Ind., 2005. **58**(11): p. 1339-1341.
468. Katono, H., *Visible light transparency and heat shielding effect of selective near infrared ray absorber.* Sho-Energy, 2005. **57**(10): p. 39-41.
469. Liu, Y., Z. Zhang, X. Chen, S. Xu, and S. Cao, *Near-infrared absorbing dyes at 1064 nm: Soluble dithiolene nickel complexes with alkylated electron-donating groups as Peripheral substituents.* Dyes and Pigments, 2016. **128**: p. 179-189.
470. Cameron, L.A., J.W. Ziller, and A.F. Heyduk, *Near-IR absorbing donor–acceptor ligand-to-ligand charge-transfer complexes of nickel (II).* Chemical science, 2016. **7**(3): p. 1807-1814.
471. Salvador, M.A., P. Almeida, L. Reis, and P. Santos, *Near-infrared absorbing delocalized cationic azo dyes.* Dyes and Pigments, 2009. **82**(2): p. 118-123.

472. Funabiki, K., K. Yagi, M. Nomoto, Y. Kubota, and M. Matsui, *Improvement of the thermal stability of near-infrared-absorbing heptamethinecyanine dyes by anion-exchange from an iodide to fluorine-containing anions.* J. Fluorine Chem., 2015. **174**: p. 132-136.
473. Zorlu, Y., U. Kumru, Ü. İşci, B. Divrik, E. Jeanneau, F. Albrieux, Y. Dede, V. Ahsen, and F. Dumoulin, *1, 4, 8, 11, 15, 18, 22, 25-Alkylsulfanyl phthalocyanines: effect of macrocycle distortion on spectroscopic and packing properties.* Chem. Commun., 2015. **51**(30): p. 6580-6583.
474. Bricks, J.L., A.D. Kachkovskii, Y.L. Slominskii, A.O. Gerasov, and S.V. Popov, *Molecular design of near infrared polymethine dyes: A review.* Dyes and Pigments, 2015. **121**: p. 238-255.
475. Liu, P., F. Gao, L. Zhou, Y. Chen, and Z. Chen, *Tetrathienyl-functionalized red-and NIR-absorbing BODIPY dyes appending various peripheral substituents.* Organic & biomolecular chemistry, 2017. **15**(6): p. 1393-1399.
476. Zeng, X., Y. Zhou, S. Ji, H. Luo, H. Yao, X. Huang, and P. Jin, *The preparation of a high performance near-infrared shielding Cs x WO 3/SiO 2 composite resin coating and research on its optical stability under ultraviolet illumination.* Journal of Materials Chemistry C, 2015. **3**(31): p. 8050-8060.
477. Chao, L., L. Bao, W. Wei, O. Tegus, and Z. Zhang, *Effects of nanoparticle shape and size on optical properties of LaB 6.* Plasmonics, 2016. **11**(3): p. 697-701.
478. Hayashi, N., K. Machida, K. Otawara, A. Hasegawa, and N. Kosaka, *Polymer-soluble thermostable phosphate-ester copper complexes for near-infrared absorbing dyes with weak absorbance in the visible region.* Opt. Mater., 2018. **77**: p. 111-116.
479. Rodgers, G.E., *Introduction to coordination, solid state, and descriptive inorganic chemistry*. New York : McGraw Hill : Primus Custom Pub., ©1999.
480. Purcell, J.C.K.a.K.F., *Chemistry & Chemical Reactivtiy*. Philadelphia : Saunders, 1987.
481. Maggio, S., Q. Zhang, and Z. Zhao, *Free-space optical backplane prototype for telecommunication equipment in the petabit/s range.* Bell Labs Technical Journal, 2013. **18**(3): p. 285-291.
482. Simi, C.G., R. Dixon, M.J. Schlangen, E.M. Winter, and C. LaSota. *Night vision imaging spectrometer (NVIS) processing and viewing tools*. in *Algorithms for Multispectral, Hyperspectral, and Ultraspectral Imagery VII*. 2001. International Society for Optics and Photonics.
483. Bigo, S., *Multiterabit/s DWDM terrestrial transmission with bandwidth-limiting optical filtering.* IEEE Journal of selected topics in Quantum Electronics, 2004. **10**(2): p. 329-340.
484. Sargent, R.B. and N.A. O'Brien, *Dielectric materials for thin-film-based optical communications filters.* MRS Bull., 2003. **28**(5): p. 372-376.
485. Hou, C., Y. Duan, Q. Zhang, H. Wang, and Y. Li, *Bio-applicable and electroactive near-infrared laser-triggered self-healing hydrogels based on graphene networks.* J. Mater. Chem., 2012. **22**(30): p. 14991-14996.
486. Wu, J.-L., F.-C. Chen, M.-K. Chuang, and K.-S. Tan, *Near-infrared laser-driven polymer photovoltaic devices and their biomedical applications.* Energy & Environmental Science, 2011. **4**(9): p. 3374-3378.
487. Asp, A., Y. Sydorov, M. Valkama, and J. Niemelä. *Radio signal propagation and attenuation measurements for modern residential buildings*. in *2012 IEEE Globecom Workshops*. 2012. IEEE.

488. Philippakis, M., C. Martel, D. Kemp, R. Allan, M. Clift, S. Massey, S. Appleton, W. Damerell, C. Burton, and E. Parker, *Application of FSS structures to selectively control the propagation of signals into and out of buildings.* Ofcom ref. AY4464A, 2004.
489. Ragulis, P., Ž. Kancleris, and R. Simniškis, *Transmission and Reflection of Microwave Radioation from Novel Window Panes.* AMEREM-2014, 2014.
490. Rodriguez, I., H.C. Nguyen, N.T. Jorgensen, T.B. Sorensen, and P. Mogensen. *Radio propagation into modern buildings: Attenuation measurements in the range from 800 MHz to 18 GHz*. in *2014 IEEE 80th Vehicular Technology Conference (VTC2014-Fall)*. 2014. IEEE.
491. Börjesson, H., *Radio Wave Propagation in Confined Environments*. 2000, PhD thesis, Lund Institute of Technology, Department of Applied Electronics ….
492. Walker, E.H., *Penetration of radio signals into buildings in the cellular radio environment.* The Bell System Technical Journal, 1983. **62**(9): p. 2719-2734.
493. Cox, D.C., R.R. Murray, and A. Norris, *800-MHz Attenuation Measured In and Around Suburban Houses.* AT&T Bell Laboratories technical journal, 1984. **63**(6): p. 921-954.
494. Widenberg, B. and J.V.R. Rodríguez, *Design of energy saving windows with high transmission at 900 MHz and 1800 MHz.* Electromagnetic Theory Lund Institute of Technology, 2002.
495. Munk, B.A., *Frequency selective surfaces: theory and design*. 2005: John Wiley & Sons.
496. Rafique, U., M. Ahmed, M. Haq, and M. Rana. *Transmission of RF signals through energy efficient window using FSS*. in *2011 7th International Conference on Emerging Technologies*. 2011. IEEE.
497. Kiani, G., L.G. Olsson, A. Karlsson, and K. Esselle, *Transmission of infrared and visible wavelengths through energy-saving glass due to etching of frequency-selective surfaces.* IET microwaves, antennas & propagation, 2010. **4**(7): p. 955-961.
498. Pierce, J.S. and J. Wotiz, *Tris-(hydroxymethyl)-aminomethane Derivatives. I. Polyhydroxyamines1, 2.* J. Am. Chem. Soc., 1944. **66**(6): p. 879-881.
499. Dolomanov, O.V., L.J. Bourhis, R.J. Gildea, J.A. Howard, and H. Puschmann, *OLEX2: a complete structure solution, refinement and analysis program.* J. Appl. Crystallogr., 2009. **42**(2): p. 339-341.
500. Sheldrick, G.M., *SHELXT–Integrated space-group and crystal-structure determination.* Acta Crystallographica Section A: Foundations and Advances, 2015. **71**(1): p. 3-8.
501. Sheldrick, G.M., *Crystal structure refinement with SHELXL.* Acta Crystallographica Section C: Structural Chemistry, 2015. **71**(1): p. 3-8.
502. Bergerhoff, G., M. Berndt, and K. Brandenburg, *Evaluation of crystallographic data with the program DIAMOND.* Journal of research of the National Institute of Standards and Technology, 1996. **101**(3): p. 221.
503. Macrae, C.F., P.R. Edgington, P. McCabe, E. Pidcock, G.P. Shields, R. Taylor, M. Towler, and J. Streek, *Mercury: visualization and analysis of crystal structures.* J. Appl. Crystallogr., 2006. **39**(3): p. 453-457.